



ACME 2011

**Proceedings of the 19th UK National
Conference of the Association for
Computational Mechanics in Engineering**



5 – 6 April 2011
Heriot-Watt University
Edinburgh

Edited by

O. Laghrouche
A. El Kacimi
P. Woodward
G. Medero

ACME 2011

**Proceedings of the 19th UK National
Conference of the Association for
Computational Mechanics in Engineering**

5 – 6 April 2011
Heriot-Watt University
Edinburgh

EXTENDED ABSTRACTS

Edited by

O. Laghrouche
A. El Kacimi
P. Woodward
G. Medero

ISBN 978-0-9565951-1-9

Heriot-Watt University

First published 2011 by

Heriot-Watt University

British Library Cataloguing-in-Publication Data

A catalogue record for this book is available from the British Library

ISBN 978-0-9565951-1-9

Copyright © 2011 Heriot-Watt University. All rights reserved.

No parts of this publication may be produced, stored in a retrieval system, or transmitted in any form or by any means, electronic, mechanical, photocopying, recording or otherwise, without the prior written permission of the Heriot-Watt University, Edinburgh, UK.

Printed and bound by Heriot-Watt University Media Services
Riccarton Campus
Edinburgh EH14 4AS

PREFACE

These Proceedings contain more than 70 extended abstracts of the work presented at the 19th Annual Conference of the UK Association for Computational Mechanics in Engineering (ACME) held at the Heriot-Watt University in Edinburgh on 5th and 6th April 2011.

The Association was founded with the aims of promoting research in computational mechanics in engineering within the UK, and establishing formal links with similar organisations in Europe and the International Association for Computational Mechanics (IACM).

The principal activity of ACME involves the organisation of the annual conference. The first such conference took place at the University College of Wales Swansea in 1993. The conferences have provided a forum for reviewing research activities in many areas of mechanics, with an emphasis on interdisciplinary aspects.

The conferences have proved to be particularly useful events for drawing together researchers from different disciplines, and especially for providing young researchers with opportunities for presenting their work.

The organisers of the 19th ACME Conference took the initiative to organise the 1st ACME School, initially proposed by Professor Nenad Bicanic and other AMCE members. Many thanks to the lecturers of this School: Professor Harm Askes, Professor Jon Trevelyan and Dr. Charles Augarde, who made it happen. It is hoped the ACME School becomes part of the future annual ACME Conferences.

I would like to express my gratitude to the three invited speakers for their contribution to the conference and the time and effort they put.

I would like to acknowledge the assistance of Ms Anne Ormston who has played an invaluable role in organising the Conference.

I hope you enjoy your stay in the historic city of Edinburgh and the ACME meeting.

Omar Laghrouche
Vice-Chairman of ACME 2010/11

CONTENTS

| | Page |
|---------------------------------------------------------------------------------------------------------------------------------------------------------------|------|
| Invited Lectures | |
| CHALLENGES IN THE MODELLING OF PARTICULATES AND MULTI-FRACTURING MATERIALS WITH COUPLED FIELD EFFECTS D. R. J. Owen, Y. T. Feng, K. Han and C. R. Leonardi | 1 |
| MODELLING PHYSICAL DISCONTINUITIES WITH NUMERICAL METHODS K. Davey and R. Darvizeh | 9 |
| BEYOND NAVIER-STOKES: THE CHALLENGES OF UNDERSTANDING NON-EQUILIBRIUM PHENOMENA IN MICROAND NANO-SCALE FLOWS Jason M. Reese and William D. Nicholls | 13 |
| Biomechanics | |
| NON-INVASIVE AND INVERSE PROPERTY ESTIMATION OF ARTERIAL ELASTICITY Amarpal S. Kapoor, Perumal Nithiarasu and Raoul Van Loon | 17 |
| NUMERICAL ANALYSIS OF THE HIP JOINT BONES IN CONTACT Philip Cardiff, Alojz Ivankovic, David FitzPatrick, Rob Flavin and Aleksandar Karac | 21 |
| A BIPHASIC SWELLING MODEL OF THE INTERVERTEBRAL DISC Julien Vignollet, Chris J. Pearce and Lukasz Kaczmarczyk | 25 |
| A ONE-DIMENSIONAL BLOOD FLOW MODEL FOR STUDYING THE EFFECT OF AORTIC ANEURYSMS IN HUMAN ARTERIAL NETWORK Kenny Low, Perumal Nithiarasu and Igor Sazonov | 29 |
| Geomechanics / Material Modelling | |
| RESPONSE OF A TUNNEL DEEPLY EMBEDDED IN A VISCOELASTIC MEDIUM Thomas J. Birchall and Ashraf S. Osman | 33 |
| MODELLING 3D PUNCH INDENTATION USING DISCONTINUITY LAYOUT OPTIMIZATION Samuel J. Hawksbee, Matthew Gilbert and Colin Smith | 37 |
| USING FINITE ELEMENT MODELLING TO ASSESS SUBMARINE SLOPE STABILITY Morelia Urlaub, Antonis Zervos, Peter J. Talling, Doug G. Masson and Chris I. Clayton | 41 |
| AN EVOLUTIONARY APPROACH TO MODELLING COMPACTION CHARACTERISTICS OF SOILS A. Ahangar-Asr, A. Faramarzi, A. Javadi, N. Mottaghifard | 45 |
| UNIQUE CRITICAL STATE HYPERPLASTICITY William M. Coombs, Roger S. Crouch and Charles E. Augarde | 49 |
| COROTATIONAL FORMULATION FOR 3D SOLIDS: ANALYSIS OF GEOMETRICALLY NONLINEAR FOAM DEFORMATION Ł. Kaczmarczyk, T. Koziara and C.J. Pearce | 53 |
| EPR-BASED FINITE ELEMENT ANALYSIS OF SOILS UNDER CYCLIC LOADING Akbar A. Javadi, Asaad Faramarzi, Moura Mehravar and Alireza Ahangar-Asr | 57 |

| | |
|------------------------------------------------------------------------------------------------------------------------------------------------------------------------|-----|
| MATERIAL PLASTIC PROPERTIES CHARACTERIZATION COUPLING EXPERIMENTAL AND NUCLEAR ANALYSIS OF SMALL PUNCH BEAM TESTS Xingguo Zhou, Wenke Pan, Donald Mackenzie | 61 |
| CDPM2: A DAMAGE-PLASTICITY APPROACH TO MODEL THE DYNAMIC FAILURE OF CONCRETE Peter Grassl | 65 |
| A HYSTERETIC MODEL FOR STEEL PLATE SHEAR WALLS A. Faramarzi, M. Mehravar, H. Veladi, A. A. Javadi, A. Ahangar-Asr, M. Mehravar | 69 |
| Multiscale | |
| A ROBUST LOCAL ARC-LENGTH METHOD FOR MULTISCALE PROBLEMS Ahmad Akbari R., Pierre Kerfriden, Timon Rabczuk and Stephane P.A. Bordas | 73 |
| A MICROMECHANICS-ENHANCED FINITE ELEMENT FORMULATION C.J. Pearce, Ł. Kaczmarczyk, P. Grassl and J. Novak | 77 |
| AN ALGORITHM FOR GENERATION OF 3D MESOSTRUCTURE OF CONCRETE FOR FINITE ELEMENT ANALYSIS Zhenhuan Song, Yong Lu | 81 |
| MACRO AND MESO SCALES MODELS TO PREDICT CONCRETE FAILURE AND SIZE EFFECT L.B. Rojas-Solano, P. Grassl, D. Grégoire and G. Pijaudier-Cabot | 85 |
| AN ALTERNATIVE TO MULTISCALE SIMULATORS BASED ON MODEL ORDER REDUCTION FOR NONLINEAR FRACTURE MECHANICS P. Kerfriden, Lee Margetts and S. Bordas | 89 |
| Fracture and Failure Mechanics | |
| MODELLING DAMAGE, FRICTION AND DILATANCY ON STRUCTURAL INTERFACES USING COHESIVE-ZONE MODELS Giulio Alfano and Roberto Serpieri | 93 |
| COHESIVE CRACKING EVOLUTION IN CONCRETE COVER DUE TO REINFORCEMENT CORROSION Hua-Peng Chen, Nan Xiao | 97 |
| AN INTERFACE FAILURE CRITERION IN A MICROMECHANICAL MODEL FOR CONCRETE Iulia Mihai and Tony Jefferson | 101 |
| OVERLOAD EFFECT IN FATIGUE CRACK GROWTH USING A COHESIVE ZONE MODEL H. Dahlan and K. Davey | 105 |
| ON THE MESH DEPENDENCE OF LATTICE MODELS FOR ANALYSING CONCRETE FRACTURE Caroline Fahy, Domenico Gallipoli and Peter Grassl | 109 |
| REDUCED ORDER MODELING FOR NONLINEAR FRACTURE MECHANICS IN A DOMAIN DECOMPOSITION FRAMEWORK Olivier Goury, Pierre Kerfriden, Lee Margetts and Stephane P. A. Bordas | 113 |
| A SCALED BOUNDARY FINITE ELEMENT METHOD FOR NONLINEAR DYNAMIC CRACK PROPAGATION MODELLING E.T. Ooi and Z.J. Yang | 117 |

A DAMAGE-MECHANICS-BASED RATE-DEPENDENT COHESIVE-ZONE MODEL
M. Musto, G. Alfano 121

MODELLING OF FRP-TO-CONCRETE BOND BEHAVIOUR
Y. Tao and J. F. Chen 125

Dynamics and waves

TIME DOMAIN 3D FINITE ELEMENT MODELLING OF TRAIN-INDUCED VIBRATION AT
HIGH SPEED
A. El-Kacimi, P. Woodward, O. Laghrouche and G. Medero 129

WAVE IMPLEMENTATION IN BLADE ELEMENT MOMENTUM THEORY FOR MODELLING
TIDAL STREAM TURBINES
H. C. Buckland, I. Masters and J. Orme 133

DEVELOPMENT OF A FINITE VOLUME ALGORITHM FOR A NEW CONSERVATION
LAWFORMULATION IN STRUCTURAL DYNAMICS
Chun H. Lee, Antonio J. Gil and Javier Bonet 137

USING GRADIENT ELASTICITY THEORIES WITH MICRO-INERTIA TO INCREASE THE
CRITICAL TIME STEP
Harm Askes, Duc C.D. Nguyen and Andy Tyas 141

NUMERICAL MODELLING OF THE DYNAMIC BEHAVIOUR OF A SOIL DEPOSIT
OVERLYING BEDROCK
N. Hamdan, O. Laghrouche, A. El Kacimi, P. Woodward and G. Medero 145

TWO-STEP TAYLOR GALERKIN FORMULATION IN LAGRANGIAN SOLID DYNAMICS
Izian Abd Karim, Javier Bonet and Antonio J. Gil 149

UPDATING FINITE ELEMENT MODEL FROM VIBRATION MEASUREMENTS
Maung Than Soe, Hua-Peng Chen, Kong Fah Tee, and Amir M. Alani 153

CONTROLLING THE CRITICAL TIME STEP VIA THE BIPENALTY METHOD
Jack Hetherington, Antonio Rodriguez-Ferran and Harm Askes 157

DYNAMIC MODELLING USING MIXED STRESS ELEMENTS
G. Edwards, C.J. Pearce and Ł. Kaczmarczyk 161

NUMERICAL CALCULATIONS OF DYNAMIC PRESSURE DURING HOPPER DISCHARGE
USING AN UNCOUPLED ALE-FORMULATION
Yin Wang, Y. Lu and Jin. Y. Ooi 165

ENERGY CONSERVATION OF THE NEWMARK METHOD FOR DYNAMIC CONTACT ANALYSIS
H. Zolghadr Jahromi and B.A. Izzuddin 169

INVESTIGATION OF A NEW ABSORBING BOUNDARY CONDITION FOR TIME STEPPING
SIMULATION OF SEMI-INFINITE ELASTIC MEDIA
G. B. White, A. H. Nielsen and O. Laghrouche 173

Flow in Porous Media / Fluid Dynamics / Fluid-Structure Interaction

COMPUTATIONAL MODELLING OF CONTAMINATED LAND: DEVELOPMENT OF A
COMBINED STOCHASTIC-DETERMINISTIC MODEL FOR MASS TRANSFER IN VARIABLY
SATURATED POROUS MEDIA
Jack M. Barnard and Charles E. Augarde 177

| | |
|-----------------------------------------------------------------------------------------------------------------------------------------------------------------------------------------------|-----|
| PERMEABILITY ASSESSMENT OF HETEROGENEOUS POROUS MEDIA USING THE LATTICE BOLTZMANN METHOD B. D. Jones, Y. T. Feng | 181 |
| PREDICTION OF LAMINARIZATION WITH A ONE EQUATION SPALART-ALLMARAS MODEL Orijji U. Richard and Paul G. Tucker | 185 |
| COMPUTATIONAL MODELLING OF SURFACE TENSION IN FLUID FLOW SIMULATIONS R.J.D. Mackenzie, Ł. Kaczmarczyk and C.J. Pearce | 189 |
| IMMERSED FINITE ELEMENT METHOD FOR FLUID-STRUCTURE INTERACTION Thomas Ruberg, Fehmi Cirak | 193 |
| PREDICTING AIRCRAFT STRUCTURAL RESPONSE TO WATER IMPACT L. Papagiannis and J.C. Campbell | 197 |
| A COUPLING SIMULATION INTERFACE FOR PERFORMANCE-BASED WIND ENGINEERING OF TALL BUILDINGS Gordon H. Clannachan, Nenad Bićanić and Graham M. Copeland | 201 |
| PREDICTION OF LAMINAR SEPARATION BUBBLE USING URANS APPROACH V. Nagabhushana Rao, Richard Jefferson-Loveday and Paul G Tucker | 205 |
| Structures / Stress Analysis / Discrete Systems | |
| THERMO-MECHANICAL ANALYSIS OF STEEL FRAME STRUCTURES USING OPENSEES Jian Jiang and Asif Usmani | 209 |
| EFFICIENT REINFORCED CONCRETE DESIGN USING MODIFIED LINEAR ELASTIC FINITE ELEMENT ANALYSIS Xing Tan, Andrew. J. Deeks | 213 |
| COMPUTATIONAL HOMOGENISATION METHODS FOR FLEXIBLE MARINE RISERS ACCOUNTING FOR STRUCTURAL-TO-STRUCTURAL SCALE BRIDGING Ben Edmans, Giulio Alfano and Hamid Bahai | 217 |
| MODELLING THE RESPONSE OF TRUSSES IN FIRE Panagiotis Kotsovinos, Asif Usmani | 221 |
| FINITE ELEMENT ANALYSIS OF A NOVEL AIRCRAFT SEAT AGAINST STATIC CERTIFICATION REQUIREMENTS (CS 25.561) Omkar Gulavani, Kevin Hughes | 225 |
| APPLICATION FRAMEWORK AND DATA STRUCTURE TO INTRODUCE REAL-TIME STRESS ANALYSIS INTO EARLY DESIGN STAGES M.S. Mohamed, T.M. Foster, J. Trevelyan and G. Coates | 229 |
| DEVELOPMENT AND APPLICATION OF OPENSEES FOR A RC FRAME IN FIRE Jian Zhang, Asif Usmani, Jian Jiang, Yaqiang Jiang, Panagiotis Kotsovinos and Ian May | 233 |
| DAMAGE-BASED FRACTURE ANALYSIS FOR THE EVALUATION OF SEISMIC PERFORMANCE OF RC BRIDGE COULMNS M. O. Benamer, Y. T. Feng | 237 |
| NATURAL FREQUENCIES OF CRACKED ISOTROPIC & SPECIALLY ORTHOTROPIC PLATES USING THE EXTENDED FINITE ELEMENT METHOD S Natarajan, P Baiz, D Roy Mahapatra, T Rabczuk, P Kerfriden and S Bordas | 241 |

A PROJECTED QUASI-NEWTON METHOD FOR DYNAMIC MULTIBODY FRICTIONAL CONTACT PROBLEMS
Tomasz Koziara, Nenad Bicanic 245

MODELLING OF A POST-TENSIONED MODULAR STRUCTURE SYSTEM
Tianxin Zheng, Yong Lu, Asif Usmani 249

Finite Element / Boundary Element / Meshless

ENHANCED RECOVERY TECHNIQUES FOR ACCURATE EVALUATION OF ERROR ESTIMATES IN FE APPROXIMATIONS
Octavio A. González-Estrada¹, Juan José Ródenas, Stéphane P.A. Bordas, Pierre Kerfriden 253

MESH IMPROVEMENT METHODOLOGY FOR EVOLVING GEOMETRIES
Alan Kelly, Chris Pearce and Lukasz Kaczmarczyk 257

RAPID RE-MESHING FOR REAL-TIME THREE-DIMENSIONAL BOUNDARY ELEMENT ANALYSIS
T.M. Foster, M.S. Mohamed, J. Trevelyan and G. Coates 261

DETERMINATION OF POLYNOMIAL C1 SHAPE FUNCTIONS ON TRIANGULAR FINITE ELEMENTS
Stefanos-Aldo Papanicolopoulos and Antonis Zervos 265

A STABILISED FINITE ELEMENT METHOD USING RESIDUAL-FREE BUBBLE ENRICHMENT FOR SEMICONDUCTOR DEVICE SIMULATION
R. Simpson, S. Bordas, P. Kerfriden and A. Asenov 269

THE ANNIHILATION OF PHYSICAL DISCONTINUITIES IN FINITE ELEMENTS
R. Darvizeh and K. Davey 273

FE-EFGM COUPLING USING MAXIMUM ENTROPY SHAPE FUNCTIONS AND ITS APPLICATION TO SMALL AND FINITE DEFORMATION
Zahur Ullah, Charles E. Augarde, Roger S. Crouch and William M. Coombs 277

DRILLING ROTATIONS AND PARTITION OF UNITY BOUNDARY ELEMENT METHOD (PUBEM)
Hing Leung and Pedro M. Baiz 281

AN ISOGOMETRIC BOUNDARY ELEMENT METHOD FOR ELASTOSTATIC PROBLEMS
R.N. Simpson, S.P.A. Bordas, J. Trevelyan and P. Kerfriden 285

AN ELEMENT-FREE GALERKIN SCALED BOUNDARY METHOD
Yiqian He, Haitian Yang and Andrew J. Deeks 291

Challenges in the Modelling of Particulates and Multi-Fracturing Materials with Coupled Field Effects

D. R. J. Owen, Y. T. Feng, K. Han and C. R. Leonardi

Civil & Computational Engineering Centre, Swansea University, Singleton Park, Swansea, SA2 8PP, UK

D.R.J.Owen@swansea.ac.uk

Key Words: *Multi-fracturing solids, multi-field coupling, discrete element modeling, adaptive mesh refinement, lattice Boltzmann solution strategies*

ABSTRACT

Significant progress has been made over the last decade in the effective modeling of the failure and transition from continuum to discontinuum of quasi-brittle materials in many defence, mining and geo-mechanical applications. However, in several problems, the presence of an additional phase, either gaseous, liquid or both, often controls the behaviour of multi-fracturing material systems. Examples of such interaction include fracture induced in rock masses by the presence of fluid flow and the generation of gas pressure fields due to explosive detonation which drives the fracturing process in rock blasting. Although a generic modelling strategy can be developed for a broad range of such problems, nevertheless, some applications require an individual approach to solution. The main objectives of the presentation is to (i) consider the essential issues related to an effective computational implementation of a continuum-discontinuum formulation of quasi-brittle materials under various loading conditions, particularly involving fluid interaction and (ii) model the subsequent flow of fragments within such a secondary medium.

Introduction

Key issues that need to be addressed for the successful modeling of continuous/discontinuous transformation of quasi-brittle materials include (i) the development of constitutive models which govern the material failure; (ii) the ability of numerical approaches to introduce discontinuities such as shear bands and cracks generated during the material failure and fracture process and (iii) the effective simulation of contact between the region boundaries and crack surfaces both during and after the failure process. The numerical treatment of multi-fracturing solids necessitates a blend of continuous and discrete computational processes to provide adequate solution. Modeling aspects related to continuum mechanics include the development of constitutive models for a range of materials under a variety of loading conditions, element technology for near-isochoric deformation conditions, adaptive mesh refinement and damage modelling for prediction of the onset of fracture (de Souza Neto et al. 1998, Klerck et.al 2003, Owen et al. 2004). With the development of fractures, the domain becomes discontinuous in nature and computational issues include strategies for discrete crack insertion that preserve the system energy, adaptive remeshing to accommodate the fracture distribution, global search algorithms to monitor contact between the resulting particle system, development of appropriate contact interaction models and time integration of the system equations. Implementation of the entire solution strategy within a parallel processing environment is a further issue.

Failure Strategies Several fracture criteria available in the literature have been previously employed to predict material failure that may result from the gradual internal deterioration associated with high straining. These predictions remain, to a great extent, relegated to post-simulation analyses. The adoption of a methodology, whereby the coupling between material behaviour and deterioration is considered at the constitutive level during the process simulation offers a more scientifically based alternative to empirical methods with a potential improvement in predictive capability (de Souza et al. 1998). Fracture in quasi-brittle materials is generally an anisotropic phenomenon, with the coalescence and growth of micro-cracks occurring in the directions that attempt to maximise the subsequent energy release rate and

minimise the strain energy density. The optimum propagation paths maintain an orientation normal to the maximum extension strains. The localisation of micro-cracking into effective crack bands results in softening normal to the crack direction. On a continuum basis, fracture is considered in the form of a rate dependent rotating smeared-crack model utilising tensile strain-softening to represent material degradation. The smeared crack model provides a mechanism for directional softening within a continuum framework by envisaging a cracked solid as an equivalent anisotropic continuum with degraded properties in directions normal to crack band orientation. After initial yield the rotating crack formulation introduces anisotropic damage by degrading the elastic modulus in the direction of the current principal stress invariant. The model enforces coincident rotation of the principal axes of orthotropy and the principal strain axes. For the description of material degradation and subsequent discrete fracturing of quasi-brittle materials under multi-axial stress states the Mohr-Coulomb failure criterion, capped Drucker-Prager models or other laws can be coupled with the fully anisotropic tensile smeared crack model (Klerck et al 2003) in which an explicit coupling is introduced between the inelastic strain accrued by the Mohr-Coulomb, or other, yield surface and the anisotropic degradation of the mutually orthogonal tensile yield surfaces.

Although energy dissipation in the crack band model is rendered objective by normalising the softening curve with respect to the specific fracture energy, the spatial localisation is necessarily arbitrary. Localisation occurs in individual elements, resulting in the width of localisation and the crack band spacing depending on the mesh discretisation. Consequently, a non-local averaging of the damage measure is adopted in each orthotropic direction to ensure discretisation objectivity by introducing a length scale to govern the width of the localisation zone. (Klerck et al 2003). When the unloading process within a localisation zone is complete, a discrete (and physical) crack is inserted as described below.

Discrete Crack Insertion The process of inserting a discrete fracture into a continuum based finite element mesh follows three key steps: (i) the creation of a non local failure map that is based upon the weighted nodal averages of the damage within the finite element system; (ii) the failure map is used to determine the onset of fracture within the domain; and (iii) a numerical scheme is employed to perform the topological update whereby a fracture is inserted into the domain, and any additional nodes are inserted and necessary elemental connectivities updated.

The so-called failure factor is typically defined as the ratio of the inelastic fracturing strain and the critical fracturing strain or the ratio of damage and the critical damage. Discrete fracture is realized through the failure factor reaching unity when a discrete fracture of the given orientation is inserted into the finite element mesh, passing through the associated nodal point, which necessitates local mesh refinement in the vicinity of the newly introduced crack in order to provide an adequate element topology.

Contact and Post-Failure Modelling The particles generated under multi-fracturing conditions are highly angular and are represented by multi-faceted solid entities. It is well accepted that such particle angularity is a crucial factor in governing flow characteristics. Due to the large diversity of entity shapes, a two-stage strategy is employed for contact detection (Owen et al., 2004). In the first stage, all objects are approximated by simple rectangular bounding boxes and a list of potential candidates for contact is identified. In the second stage, each potentially contacting pair is locally resolved on the basis of their kinematic relationship, employing the actual geometric shapes involved.

The global contact search can be conducted using either tree-based detection schemes, such as the Augmented Spatial Digital Tree (ASDT), which generally have complexity $O(N \log N)$. Their performance can be improved by incorporating the spatial coherence of objects within successive time instants in the algorithmic framework. More recent developments in this research have focused on cell-based approaches that display $O(N)$ complexity. Contact interaction laws have been implemented within the framework of penalty methods for all contact pairs. The most challenging aspects of the contact treatment include modeling of sharp corner-to-corner contact and maintaining total energy conservation.

Borehole Breakout As a test of the ability of the model to capture the contrasting failure mechanisms exhibited by strong and weak rocks under different confining pressure conditions, Figure 1 illustrates the problem of borehole breakout modeled as a 2D problem. The initial continuum mesh is shown and the

horizontal confining pressure is maintained at a constant value whilst the vertical pressure is incrementally increased at the rate indicated. The properties that describe the behaviour of the material are provided in Owen et al. 2007, where the parameters required are readily identified from standard triaxial and tension tests. In addition to the usual elastic properties, the essential parameters are the tensile strength, compressive strength, fracture energy release rate and the standard Mohr-Coulomb data. An additional parameter is the frictional sliding coefficient on newly created discrete cracks. The material parameters employed correspond to Lac du Bonnet granite (Lee et al. 1993) and the weak sedimentary rock Cardova cream limestone (Haimson et al. 1993).

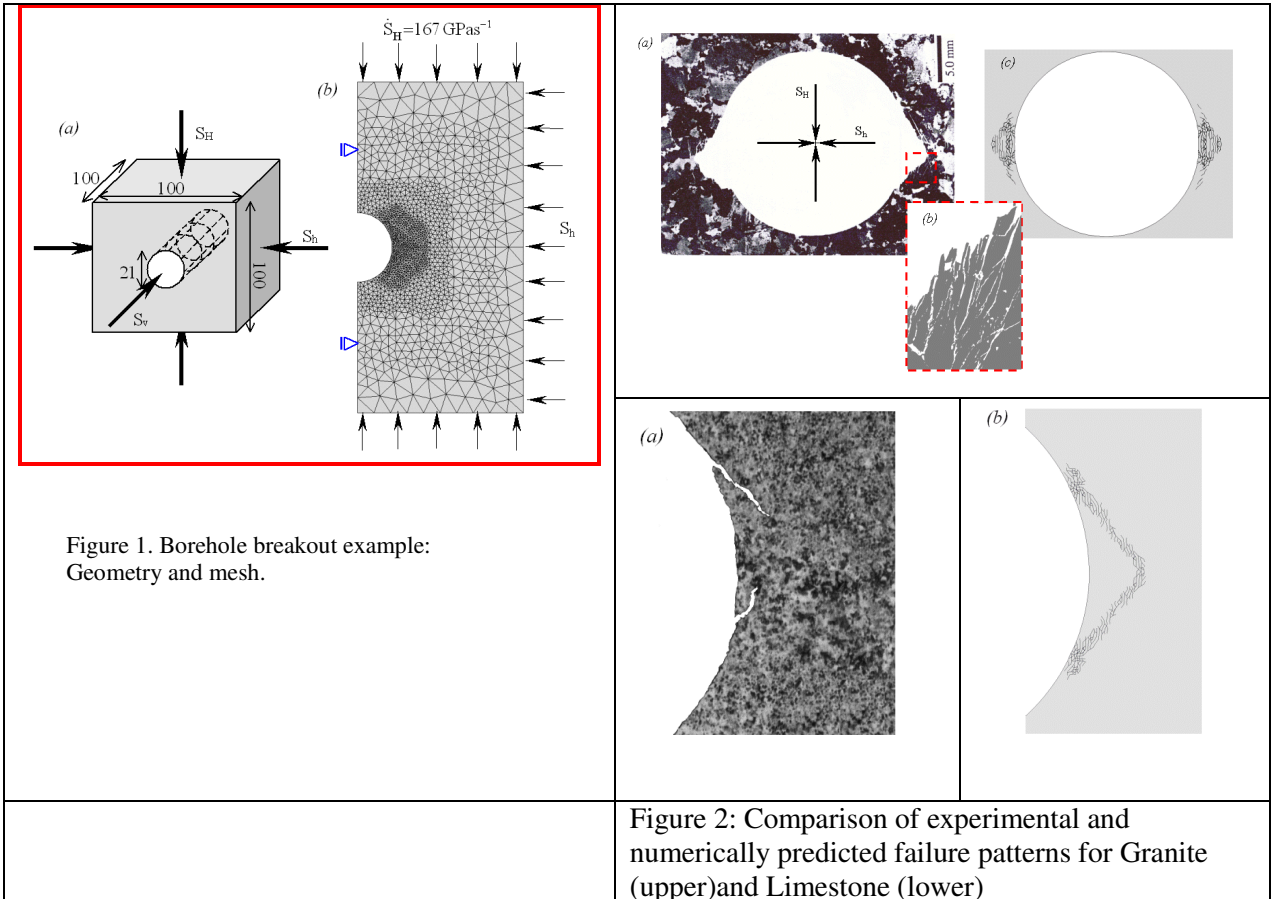


Figure 2 illustrates the fracture patterns developed for the two materials where it is seen that fundamentally different mechanisms are involved. For the granite specimen, Figure 2(a), failure takes place by the development of sub-vertical fractures at the regions indicated and very good agreement is evident between the experimental observations (Lee et al. 1993) and the numerical predictions. In Figure 2(b) similar comparison is made for the Cardova cream limestone, for which failure takes place by the development of fracture shear bands. In the computational model these manifest themselves as distinct crack bands formed by en-echelon systems of tensile fractures. Again, there is a strong correspondence between the experimental failure mode (Haimson et al. 1993) and the numerical simulation. It is important to note that the computational model has been able to reproduce these two fundamentally different failure mechanisms by only changing the relevant material parameters.

Fluid flow within fracturing rock masses

Throughout the geomechanics community there is considerable interest in modelling groundwater flow through fracturing rock masses. Application areas include slope stability problems and hydraulic fracturing in the oil recovery industry. The essential features of such problems are the flow of water both

through individual rock blocks and along joint systems. Consequently, there is a need to model Darcy type seepage within the continuous rock and pipe (sheet in 3D) network flow along the joint planes. This fluid response is strongly coupled to the deformation of the rock arising from loading and progressive fracturing, which in turn is driven by the fluid pressure imposed on the rock. Computationally, these problems can be treated by employing the same mesh that is used to model fracture within individual blocks to represent seepage flow and using compatible joint elements to simulate inter-block fluid flow.

In order to understand the complex interplay between fluid and fractured rock, several approaches and theories have been proposed. One strategy aims to model the flow through cracks without taking into account the flow within the material itself. This simplification is reasonable for soils or rock-like materials with low permeabilities, since the flow along the fractures is dominant. However, an accurate analysis of the in situ stress field can only be obtained if the rock material itself is treated as a porous medium. This is particularly important for rock masses that contain a high degree of small scale fractures resulting in high permeabilities so that the seepage behaviour becomes prominent. The main modelling issues are briefly discussed below.

Constitutive & governing equations for porous materials

The widely used “effective stress” in porous media employs the Biot number which is introduced to take into account the volumetric deformability of the particles. It is related to the bulk modulus of the skeleton and the bulk modulus of the grains. The effective stress is related to the incremental strain and rotation by means of an incremental constitutive relationship involving the rotational stress in the Green-Naghdi rate and a fourth order tensor defined by state variables and the direction of the increment. The governing equations can be written in a u-p formulation that involve (i) the total momentum equilibrium equation for the partially saturated solid-fluid mixture where the acceleration of the fluid relatively to the solid and the convective terms are neglected. This assumption is valid for medium speed and dynamics of lower frequency phenomena, (ii) an equation that ensures mass conservation of the fluid flow in the seepage field and (iii) a mass conservation equation based on a cubic law for the flow within the fracture where an individual fracture is treated as a single confined aquifer. The system defined by the above three governing equations and appropriate boundary conditions describes a well-defined problem which can then be discretized by standard finite elements in space and by a central difference approximation in time.

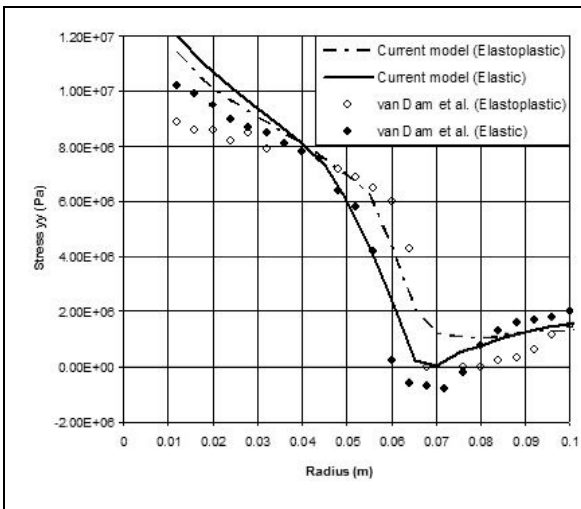


Figure 3. Vertical stress profile in the plane of the fracture for elastic and elasto-plastic simulations.

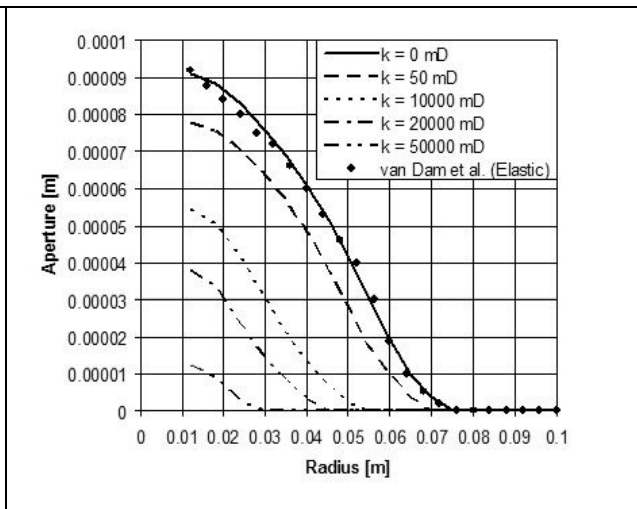


Figure 4. Influence of the leak-off on the size of the fracture.

Numerical example The numerical model presented here is validated against the experimental results published by van Dam et al. 2000. The experiment consists of cubic blocks 0.30m in size, which are loaded in a true triaxial machine to simulate in-situ stress states. After reaching the desired stress state, a high-pressure pump injects fluid to propagate the crack. Artificial rock samples made of cement, plaster and diatomite have been used. The fracturing fluid employed was silicon oil, which approximately behaves as a Newtonian fluid. Further details of the experiments can be found in van Dam et al. 2000.

Three different cases have been considered: elastic, elastoplastic and poroelastic analyses. In the elastic and elastoplastic cases the vertical stress (σ_{yy}) profile has been compared with the ones provided in van Dam et al (2000). In the poroelastic case, different permeabilities for the rock were evaluated in order to verify the influence of the leak-off upon parameters such as length and aperture of the fracture. The permeability varies from 0 to 50000 miliDarcy (mD). The mechanical behavior of the rock is described through a Mohr-Coulomb model which employs the Newton-Raphson method in the return mapping scheme. The cohesion and friction angles are assumed to be given functions of the effective plastic strain. An interface law based on a cohesive-zone model has been used to describe the rupture process at the fracture tip. In this model, the softening curve is obtained through the fracture energy release rate. Within this framework, the fracture is opened when the tensile strength and fracture width reach a critical value.

Figure 3 shows that the vertical stress of the current model (σ_{yy}) agrees well with the results of van Dam et al (2000). The aperture in the elastoplastic case is larger than the elastic case due to the inelastic deformations. Also, the net pressure necessary to propagate the fracture in the elastoplastic case must be higher than in the elastic case. This can be seen in the vertical stress profile, where an increase in (σ_{yy}) is experienced near the fracture tip, which is at the same position in both analyses. Figures 4 shows the aperture profiles in the poroelastic analyses for rocks with different permeabilities. It can be seen that in rocks with higher permeabilities, the length and width of the fracture reduces due to an increase in the leak-off from the fracture to the porous rock.

Rock blasting.

In this application coupling takes place through interaction between the gas pressure due to explosive detonation and the progressively fracturing rock. The most appropriate route to solution is provided by superposing a background Eulerian grid over the Lagrangian mesh used for fracture modelling (Owen et al. 2004). Within this regular Eulerian grid the gas pressure modelling is based on the mass conservation and momentum equations for gas flow employing directional porosities derived from the rock fracture simulation. The coupling takes place through an interdependence between the evolving gas pressure distribution driving the fracturing process which, in turn, provides the porosity distribution which controls the gas pressure. Computationally, solution can be effectively provided through use of a staggered solution scheme based upon time integration of the two fields with partitioned time stepping. The theory of gas flow through rock cracks involves a mass conservation equation in which the component velocities of the gas are related to the gas density and the local directional porosities of the rock mass. The gas velocities are obtained through the momentum equation as a function of the pressure gradients. Since the gas pressure arises from the detonation process, the initial time/pressure relation is obtained using the equation of state for the explosive.

Numerical results are presented below for a HPE test. This is a plan view (plane strain) test case where a borehole of 165 mm diameter, containing an ANFO explosive charge, is located at the centre of a 3m x 3m square rock mass. The meshes employed for the rock fracture and gas pressure development are shown respectively in Figure 5 (a) and (b) and the crack patterns developed at 1000 μ s are illustrated in Figure 5 (c), where the surface cracking due to reflection of the compressive pressure pulse as a tensile wave is readily apparent.

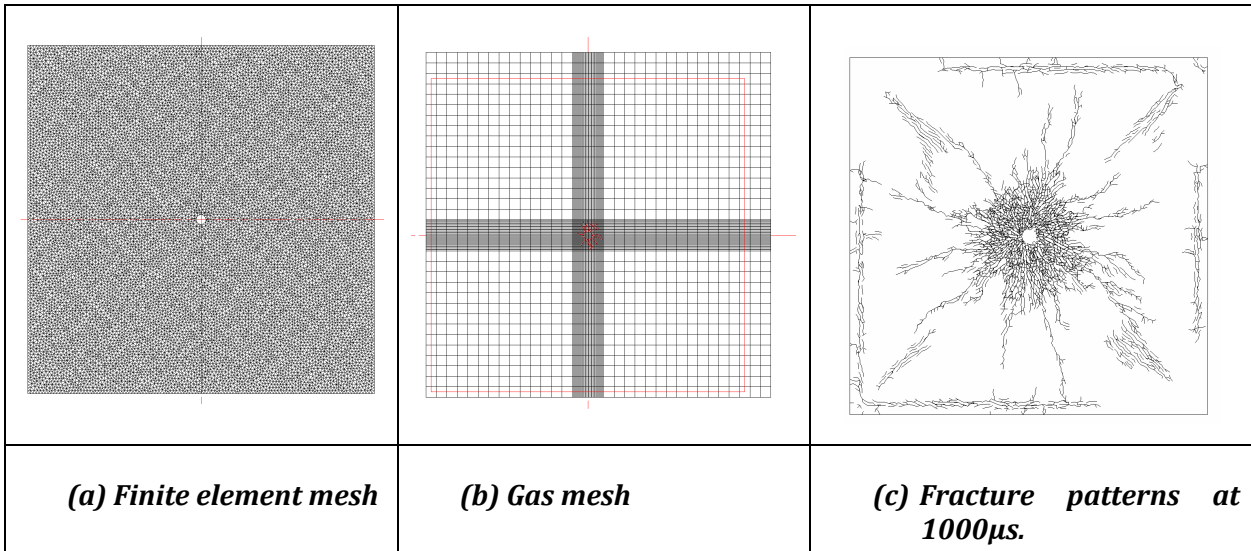


Figure 5. Rock blasting – HPE benchmark test.

Particle transport. The treatment of particle transport problems crucially depends of the size of the particles in relation to the domain size. For small particle sizes, as occur in fluidised beds for example, effective methods have been developed based on background fluid grids in which fluid forces can be computed and applied to particles residing within a particular grid cell. However, for problems in which the particle sizes are large and extend over several grid sizes, alternative solution strategies must be adopted. One option, which is considered here, is to employ a Lattice-Boltzmann (LB) procedure to model the fluid flow. This has the advantage that large particle sizes can be accommodated and moving boundaries of the fluid domain can also be incorporated. Furthermore, employing the Discrete Element Method (DEM) to account for the particle interaction in the problem leads naturally to a combined LB-DEM solution procedure. Key modelling issues involved in this coupled solution strategy (Feng et al. 2007) include the standard LB formulation for fluid flow, the interaction between fluid flow and boundaries and moving particles, incorporation of a turbulence model for high Reynolds number cases, and the interaction between solid particles in the DEM. The powerful modelling ability of the LB-DEM approach is illustrated by an example where a submerged bed of spherical particles of varying sizes are extracted through a vertical column by a vacuum action. An excellent comparison was obtained between experimental measurements and numerical predictions for the mass of excavated material as well as for the profile of the particle bed shown in Figure 6.

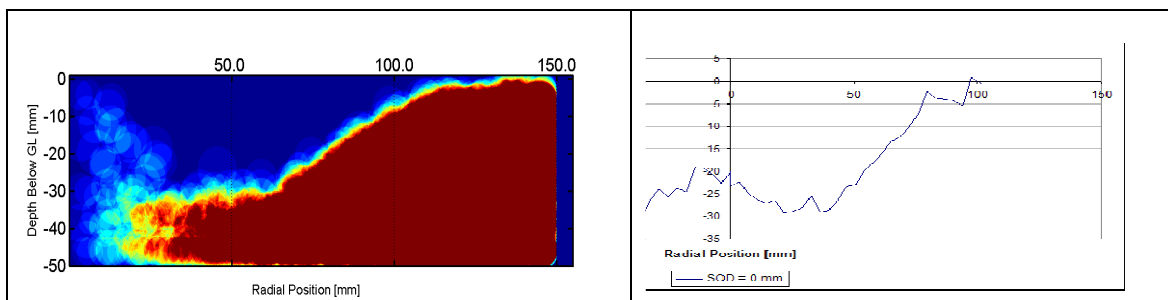


Figure 6. Comparison of numerical prediction and experimental measurement of the excavated bed profile.

Conclusions

The paper highlights the numerical issues related to the modelling of multi-fracturing materials under general mechanical loadings and particularly describes the numerical frameworks necessary to account for the interaction between (fractured) solid masses and fluid/gas phases. It is emphasised that different modelling strategies may need to be applied in order to effectively deal with specific coupling phenomena. Examples have been presented to demonstrate the applicability of the proposed methodology.

Other application areas in which Lattice-Boltzmann approaches can also be effectively used include the modelling of heat transfer between a moving particle system at elevated temperatures and a surrounding pressure driven gas environment, using a double population LB formulation to describe the gas velocity distribution and thermal energy balance (Owen et al. 2008). Additionally, an important issue in block cave mining operations is fines migration in which fine particles that are several orders of magnitude smaller than the main rock fragments flow through the moving particle system. In this multi-scale problem the fines can again be modelled within a LB setting (Owen et al. 2011) using a power law fluid or Bingham plastic formulation to describe the quasi-continuum flow involved, which is then coupled to the DEM modelling of the larger rock fragments.

REFERENCES

1. B. Haimson and I. Song (1993), Laboratory study of borehole breakouts in cordova cream: a case of shear failure mechanism, *Int. J. Mech. Min. Sci. & Geomech. Abstr.*, Vol. 30, No. 7, pp. 1047-1056.
2. M. Lee and B. Haimson (1993), Laboratory study of borehole breakouts in Lac du Bonnet granite: a case of extensile failure mechanism, *Int. J. Mech. Min. Sci. & Geomech. Abstr.*, Vol. 30, No. 7, pp. 1039-1045.
3. de Souza Neto, E.A., Peric, D. and Owen, D.R.J (1998), Continuum modelling and numerical simulation of material damage at finite strains. *Arch. Comput. Meth. Engng*, Vol 5, pp 311-384.
4. D. B. van Dam, P. Papanastasiou and C. J. Pater (2000), Impact of rock plasticity on hydraulic fracture propagation and closure. Paper SPE 78812 presented at the 2000 SPE Annual Technical Conference and Exhibition, Dallas, 1-4 October 2000.
5. P. Klerck, E. J. Sellers and D. R. J. Owen (2003), Discrete fracture in quasi-brittle materials under compressive and tensile stress states, *Comp. Meth. Appl. Mech. Engng*, 193, pp 3035-3056.
6. D. R. J. Owen, Y. T. Feng, E. A. de Souza Neto, F. Wang, M. G. Cottrell, F. A. Pires and J. Yu (2004), The modelling of multi-fracturing solids and particulate media. *Int. J. Num. Meth Engng*, 60(1): 317-340.
7. D. R. J. Owen, Y. T. Feng, M. Labao, C. R. Leonardi, S. Y. Zhao and J. Yu (2007), Simulation of multi-fracturing rock media including fluid/structure coupling, *US-Canadian Rock Mechanics International Conference*, Vancouver, Canada, 27-31 May 2007.
8. Y. T. Feng, K. Han and D. R. J. Owen (2007), Coupled lattice Boltzmann method and discrete element modeling of particle transport in turbulent fluid flows: Computational issues, *Int. J. Num. Meth. In Engng.*, Vol72, pp 1111-1134.
9. D. R. J. Owen, Y. T. Feng, K. Han and C. R. Leonardi (2008), Computational modelling of multi-field problems involving particulate media, *WCCM'08, 8th World Congress for Computational Mechanics*, Venice, Italy, 30th June - 4th July, 2008.
10. D. R. J. Owen, C. R. Leonardi and Y. T. Feng (2011), An efficient framework for fluid-structure interaction using the lattice-Boltzmann method and immersed moving boundaries, *Int. J. Num. Meth Engng*, (In press).

MODELLING PHYSICAL DISCONTINUITIES WITH NUMERICAL METHODS

K. Davey* and R. Darvizeh
School of Mechanical, Aerospace and Civil Engineering,
The University of Manchester, Manchester, M13 9PL, UK

*keith.davey@manchester.ac.uk

Key Words: *non-physical, discontinuities, transport equations, finite element method.*

ABSTRACT

Presented in the paper is new approach that has recently appeared in the literature founded on transport equations and the concept of non-physical variables. The approach can be applied to both mesh and meshfree methods (although restricted here to meshes) and can cater for multiple discontinuities. The non-physical approach permits the precise removal of weak discontinuities arising in the governing transport equations. In order to facilitate the application of the approach the FE equations are presented in the form of weighted transport equations. The method utilises non-physical forms of the physical variables and these forms possess a remarkable source distribution like property at a discontinuity. It is demonstrated in the paper that it is through this property that multiple discontinuities can be exactly removed from an element so facilitating the use of continuous approximations.

1 INTRODUCTION

The development of efficient mesh-based and meshless methods for modelling moving boundary problems continues to be of interest to the research community. Moving boundary problems and material discontinuities offer substantial challenges and many numerical approaches have been proposed. In this paper the method presented in reference [1] and [2] is further investigated and extended to cater for multi-physics typically present in phase change and solid-liquid coupling problems. The focus here is on transport equations rather than the governing partial differential equations or their variational equivalents as these offer advantages hitherto neglected by the research community. Although it is well appreciated that governing partial differential equations can be obtained from transport equations the direct use of transport equations appears at first sight to be limited to finite volume type formulations. However, the recent arrival in the literature of weighted forms of transport equations along with equivalent equations provides a route for numerical formulation that captures desirable conservation properties and discontinuous physics.

2 CONSERVATION LAW FOR A MOVING CV

A conservation law for a moving domain Ω defined by the diffeomorphism $\mathbf{x}(\boldsymbol{\chi}^*, t)$, is

$$\frac{D^*}{D^*t} \int_{\Omega} \rho \psi dV + \int_{\Gamma} \rho \psi (\underline{\mathbf{v}} - \underline{\mathbf{v}}^*) \cdot \underline{\mathbf{n}} d\Gamma = - \int_{\Gamma} \underline{\mathbf{J}} \cdot \underline{\mathbf{n}} d\Gamma + \int_{\Omega} \rho b dV \quad (1)$$

where ρ is density, $\underline{\mathbf{v}}$ is material velocity, $\underline{\mathbf{J}} \cdot \underline{\mathbf{n}}$ is a flux and b is a source term, and where Ω is a control volume which is transported at velocity $\underline{\mathbf{v}}^* = D^* \mathbf{x} / D^* t$, i.e. Ω is time dependent and is a portion of the physical space and moves relative to the physical material.

It is possible to consider a reference control volume Ω^* and define a mapping between points $\boldsymbol{\chi}^* \in \Omega^*$ and points $\mathbf{x} \in \Omega$, i.e. form $\boldsymbol{\chi}^* \mapsto \mathbf{x}(\boldsymbol{\chi}^*, t)$, so that $\underline{\mathbf{v}}^* = D^* \mathbf{x} / D^* t = \partial \mathbf{x}(\boldsymbol{\chi}^*, t) / \partial t$, where the time partial derivative is partial in the sense that $\boldsymbol{\chi}^*$ is held constant when performing the derivative. This concept is essentially identical to that used when defining the material derivative D/Dt and material velocity

$\underline{v} = D\mathbf{x}/Dt = \partial\mathbf{x}(\mathbf{X}, t)/\partial t$ but material points are not necessarily tracked in the case of the mapping $\chi^* \mapsto \mathbf{x}(\chi^*, t)$. Note the use of D^*/D^*t rather than the ordinary derivative d/dt in equations (1) even though these are identical when applied to a function of t . Although the integrals $\int_{\Omega} \rho h dV$ and $\int_{\Omega} \rho dV$ are functions of t the derivative D^*/D^*t is used to immediately relay the notion that Ω is a control volume transported through \underline{v}^* . Although \underline{v}^* is present in equations (1) it cannot influence the value of ψ as this would be physically meaningless. Typical transport equations are:

$$\frac{D^*}{D^*t} \int_{\Omega} \rho dV + \int_{\Gamma} \rho (\underline{v} - \underline{v}^*) \cdot \underline{n} d\Gamma = 0 \quad (2)$$

$$\frac{D^*}{D^*t} \int_{\Omega} \rho e dV + \int_{\Gamma} \rho e (\underline{v} - \underline{v}^*) \cdot \underline{n} d\Gamma = \int_{\Gamma} \underline{v} \cdot \underline{\underline{\sigma}} \cdot \underline{n} d\Gamma - \int_{\Gamma} \underline{q} \cdot \underline{n} d\Gamma + \int_{\Omega} \rho Q dV + \int_{\Omega} \rho \underline{v} \cdot \underline{b} dV \quad (3)$$

$$\frac{D^*}{D^*t} \int_{\Omega} \rho \underline{v} dV + \int_{\Gamma} \rho \underline{v} (\underline{v} - \underline{v}^*) \cdot \underline{n} d\Gamma = \int_{\Gamma} \underline{\underline{\sigma}} \cdot \underline{n} d\Gamma + \int_{\Omega} \rho \underline{b} dV \quad (4)$$

$$\frac{D^*}{D^*t} \int_{\Omega} \rho s dV + \int_{\Gamma} \rho s (\underline{v} - \underline{v}^*) \cdot \underline{n} d\Gamma \geq - \int_{\Gamma} T^{-1} \underline{q} \cdot \underline{n} d\Gamma + \int_{\Omega} \rho T^{-1} Q dV \quad (5)$$

for transport of mass, energy, momentum, and entropy, where $e = u + \frac{1}{2} \underline{v} \cdot \underline{v}$, u and s are internal energy, and entropy per unit mass, $\underline{q} \cdot \underline{n}$ is heat flux, Q represents a heat source, $\underline{\underline{\sigma}}$ is the Cauchy stress tensor and \underline{b} is a body force. The equality arising in equation (5) is as a consequence of irreversibly arising from finite temperature differences and dissipation.

3 MECHANICAL ENERGY EQUATIONS AND DISSIPATION

A particular interest here is the splitting (if possible) of the energy equation (3) into thermal and mechanical parts. To achieve this partition it is shown here that a necessary and sufficient condition is that the solid possesses an entropy function that is dependent on temperature only. Consider for demonstration purposes the deformation of a hyperelastic material.

Theorem 3.1 A hyperelastic material dependent on state variables temperature T and the independent strain components E_{ij} of the Green-Lagrange strain tensor $\underline{\underline{E}}$ has internal energy in the form $u = u^T + u^E$, where u^T and u^E are functions of T and E_{ij} , respectively, if and only if its entropy is dependent on temperature only.

Proof 3.2: The central equation of thermodynamics for the solid is $T ds = du - dw_R$, where reversible differential work $dw_R = \rho_0^{-1} d\omega_0 = \rho_0^{-1} \underline{\underline{S}} : d\underline{\underline{E}}$, and where strain energy $\omega_0(E_{ij}) = \int_0^{E_{ij}} S_{ij} d\tilde{E}_{ij} = \frac{1}{2} \underline{\underline{S}} : \underline{\underline{E}}$, $\underline{\underline{E}}$ is the Green-Lagrange strain measure, which is work conjugate to the 2nd Piola-Kirchoff stress $\underline{\underline{S}}$. Here ρ_0 represents the density in a material reference configuration and by construction $\rho_0 \underline{\underline{\sigma}} : \underline{\underline{\dot{E}}} = \rho \underline{\underline{S}} : \underline{\underline{\dot{E}}}$, where $\underline{\underline{\dot{E}}}$ represents material strain rate and $\underline{\underline{\dot{E}}}$ is the Eulerian strain-rate tensor.

Consider internal energy of the form $u(T, E_{ij})$ with the central equation of thermodynamics $(T ds/dT - \partial u/\partial T) dT = (\partial u/\partial E_{ij} - \rho_0^{-1} S_{ij}) dE_{ij}$ under the assumption $s = s(T)$ and it immediately follows that $\partial^2 u/\partial E_{ij} \partial T = 0$ hence $u = u^T + u^E$ is obtained on integration. Similarly, conversely, assuming internal energy to be of the form $u = u^T + u^E$ gives

$(T \partial s / \partial T - du^T / dT) dT = (\partial u^E / \partial E_{ij} - T \partial s / \partial E_{ij} - \rho_0^{-1} S_{ij}) dE_{ij}$ and heat-mechanical decoupling requires $\partial s / \partial E_{ij} = 0$, i.e. entropy is a function of T only.

Setting $e = u^T + u^E + \frac{1}{2} \underline{v} \cdot \underline{v}$ for the case of a hyperelastic solid, equation (4) readily decouples and yields the mechanical equation,

$$\frac{D^*}{D^* t} \frac{1}{2} \int_{\Omega} \rho \underline{v} \cdot \underline{v} dV + \frac{D^*}{D^* t} \int_{\Omega} \rho \frac{\omega_0}{\rho_0} dV + \frac{1}{2} \int_{\Gamma} \rho \underline{v} \cdot \underline{v} (\underline{v} - \underline{v}^*) \cdot \underline{n} d\Gamma + \frac{1}{2} \int_{\Gamma} \rho \frac{\omega_0}{\rho_0} (\underline{v} - \underline{v}^*) \cdot \underline{n} d\Gamma = \int_{\Gamma} \underline{v} \cdot \underline{\underline{\sigma}} \cdot \underline{n} d\Gamma + \int_{\Omega} \rho \underline{v} \cdot \underline{b} dV \quad (6)$$

and the heat equation,

$$\frac{D^*}{D^* t} \int_{\Omega} \rho h^T dV + \int_{\Gamma} \rho h^T (\underline{v} - \underline{v}^*) \cdot \underline{n} d\Gamma = - \int_{\Gamma} \underline{q} \cdot \underline{n} d\Gamma + \int_{\Omega} \rho Q dV \quad (7)$$

where strain energy $\rho_0^{-1} u^E = \omega_0(E_{ij}) = \frac{1}{2} \underline{\underline{S}} : \underline{\underline{E}}$, ρ_0 represents the density in a reference configuration,

h^T is specific enthalpy, and where use is made of $du^T / dT = dh^T / dT = T ds / dT = c$.

The Clausius-Duhem inequality (5) occurs as a result of irreversibility present in the medium undergoing deformation and heat transfer. In the case of a plastic flow for example the appropriate transport equation including irreversibility is

$$\frac{D^*}{D^* t} \int_{\Omega} \rho s dV + \int_{\Gamma} \rho s (\underline{v} - \underline{v}^*) \cdot \underline{n} d\Gamma = - \int_{\Gamma} T^{-1} \underline{q} \cdot \underline{n} d\Gamma + \int_{\Omega} \rho T^{-1} Q dV + \int_{\Omega} \left(\frac{\underline{\underline{\sigma}} : \underline{\underline{\dot{E}}}}{T} - \frac{\underline{q} \cdot \nabla T}{T^2} \right) dV \quad (8)$$

where the inequalities $\underline{\underline{\sigma}} : \underline{\underline{\dot{E}}} \geq 0$ and $-T^{-2} \underline{q} \cdot \nabla T \geq 0$ lead to inequality (5).

The term $\underline{\underline{\tau}} : \underline{\underline{\dot{E}}}$ is dissipative giving rise to thermal energy and the term $-T^{-2} \underline{q} \cdot \nabla T \geq 0$ represents a loss arising from temperature gradients present in the medium.

4 DEFINITION OF NON-PHYSICAL ENTITIES

Transport equations are utilised to define non-physical enthalpy $\hat{\Psi}$. The prime motivation for the definition of these variables is source-like behaviour that can result at a discontinuity in the associated physical variable [1]. The transport equation definition for $\hat{\Psi}$ is:

$$\frac{D^*}{D^* t} \int_{\Omega} \hat{\Psi} dV = \frac{D^*}{D^* t} \int_{\Omega} \rho \psi dV + \int_{\Gamma} \rho \psi (\underline{v} - \underline{v}^*) \cdot \underline{n} d\Gamma = - \int_{\Gamma} \underline{J} \cdot \underline{n} d\Gamma + \int_{\Omega} \rho b dV \quad (9)$$

The concept of an equivalent governing equation is introduced in reference [1] and extended to multi-discontinuities in [2] but limited there to solidification modelling. The idea is to form alternative transport equations that can be more readily solved using numerical techniques. Unfortunately non-physical variables are found to be dependent on the velocity of the control volume, so careful consideration must be given to their determination. For example, standard control volume methods for the description of a discontinuity travelling through Ω do not apply as the solutions obtained can depend of the front velocity. The problem is that the control volume tracking a discontinuity will in general not be moving with velocity \underline{v}^* and consequently the nature of the non-physical variable is changed. Techniques for the analysis and determination of physical variables on a different moving control volume are required and these are discussed in references [1] and [2]. A discontinuity in ψ at Γ_i gives rise to a source term in non-physical $\hat{\Psi}$ and is described by the transport equation

$$\frac{D^+}{D^+ t} \int_{\Gamma_i} \hat{\Psi}' dV + \int_{\Sigma_i} \hat{\Psi}' (\underline{v}^* - \underline{v}^+) \cdot \underline{t} n d\Sigma = \int_{\Gamma_i} \rho \psi (\underline{v} - \underline{v}^+) \cdot \underline{n} d\Gamma = - \int_{\Gamma_i} \underline{J} \cdot \underline{n} d\Gamma \quad (10)$$

where Σ_i is the boundary for phase boundary Γ_i , and it is assumed that $\hat{\mathbf{h}}_\ell = \hat{\mathbf{h}}_s$, which is a continuity condition invoked by $\hat{\mathbf{h}}$ satisfying equation (10). The jump terms in equation (10) are $]\mathbf{J} \cdot \underline{\mathbf{n}}[= \mathbf{J}_s \cdot (-\underline{\mathbf{n}}_s) + \mathbf{J}_\ell \cdot (-\underline{\mathbf{n}}_\ell)$ and $]\rho\psi(\underline{\mathbf{v}} - \underline{\mathbf{v}}^+) \cdot \underline{\mathbf{n}}[= \rho_s \psi_s(\underline{\mathbf{v}}_s - \underline{\mathbf{v}}^+) \cdot (-\underline{\mathbf{n}}_s) + \rho_\ell \psi_\ell(\underline{\mathbf{v}}_\ell - \underline{\mathbf{v}}^+) \cdot (-\underline{\mathbf{n}}_\ell)$, where subscripts s and ℓ denote different phases.

5 WEIGHTED TRANSPORT EQUATIONS

Consider the following weighted-transport equation,

$$\frac{D^*}{D^*t} \int_{\Omega} W \rho \psi dV + \int_{\Gamma} W \rho \psi (\underline{\mathbf{v}} - \underline{\mathbf{v}}^*) \cdot \underline{\mathbf{n}} d\Gamma - \int_{\Omega} \rho \psi (\underline{\mathbf{v}} - \underline{\mathbf{v}}^*) \cdot \nabla W dV = - \int_{\Gamma} W \mathbf{J} \cdot \underline{\mathbf{n}} d\Gamma + \int_{\Omega} \nabla W \cdot \mathbf{J} dV + \int_{\Omega} \rho W b dV \quad (11)$$

where W is transported invariantly with Ω , i.e. $D^*W/D^*t = 0$.

The equation is arrived at by the introduction of W into the integrals in equation (1) but also by subtracting associated domain integrals involving a derivative of the weighing function for each boundary integral appearing in (1). The form the additional terms take is as a consequence of the divergence theorem applied to the weighted boundary terms. Note also that spatial and temporal derivatives of ψ is avoided, making (11) applicable when a discontinuity is in Ω . Moreover note that on setting $W = 1$, equation (2) is returned, which is in an appropriate form for the finite volume method (FVM). Note however that on applying (11) to an element domain Ω_e and adopting a standard Galerkin weighting gives a finite element formulation in transport form. The full system of FE transport equations with multiple discontinuities removed are:

$$\begin{aligned} \frac{D^*}{D^*t} \int_{\Omega_e / \{\Gamma_k : k \in K_e\}} N_i \hat{\psi} dV &= \int_{\Omega_e} \nabla N_i \cdot \mathbf{J} dV - \int_{\Gamma_e} N_i \mathbf{J} \cdot \underline{\mathbf{n}} d\Gamma + \int_{\Omega_e} \rho N_i b dV - \\ &\sum_{k \in K_e} \frac{D_k^\times}{D_k^\times t} \int_{\Gamma_k^c} N_i \hat{\psi}' dV - \sum_{k \in K_e} \int_{\Sigma_k^c} N_i \hat{\psi}' (\underline{\mathbf{v}}^* - \underline{\mathbf{v}}_k^\times) \cdot \underline{\mathbf{t}} n d\Gamma \end{aligned} \quad (12)$$

where $\Omega_e / \{\Gamma_k : k \in K_e\}$ signifies that integration is in the sense of Lebesgue, and where $K_e = \{k : \Omega_e \cap \Gamma_k \neq \emptyset\}$ which is a subset of $\{k : k = 1 : K\}$. The velocity fields $\underline{\mathbf{v}}_k^\times$ track discontinuities in elements but for convenience match movement of the element boundary. Note that the LHS of equations (12) is continuous and consequently so is the RHS, so discontinuities have been annihilated. The evolution of the source term is determined with the following source transport equation:

$$\frac{D_k^\times}{D_k^\times t} \int_{\Gamma_k^c} \hat{\psi}' d\Gamma + \int_{\Sigma_k^c} \hat{\psi}' (\underline{\mathbf{v}}^* - \underline{\mathbf{v}}_k^\times) \cdot \underline{\mathbf{t}} n d\Sigma = \int_{\Gamma_k^c} \rho \psi (\underline{\mathbf{v}} - \underline{\mathbf{v}}_k^\times) \cdot \underline{\mathbf{n}} d\Gamma = - \int_{\Gamma_k^c}]\mathbf{J} \cdot \underline{\mathbf{n}}[d\Gamma \quad (13)$$

CONCLUSION

The temporal derivatives of $\hat{\psi}$ and ψ are avoided, making the governing equations applicable when a discontinuity is in Ω . The continuous and source like behaviour of $\hat{\psi}$ facilitates the precise removal of discontinuities from the governing system of transport FE equations. It is early days for the theories presented but the transport equations possess conservative properties and capture discontinuous behaviour.

References

- [1] Davey, K and Mondragon, R, *A Non-Physical Enthalpy Method for the Numerical Solution of Isothermal Solidification*, Int. Journal for Numerical Methods in Engineering, 2010. **84**, pp. 214-252.
- [2] Mondragon, R and Davey, K, *Weak Discontinuity Modelling in Solution Modelling*, Computers and Structures, 2011. **89**, pp. 681-701.

BEYOND NAVIER-STOKES: THE CHALLENGES OF UNDERSTANDING NON-EQUILIBRIUM PHENOMENA IN MICRO- AND NANO-SCALE FLOWS

*Jason M. Reese and William D. Nicholls

Department of Mechanical Engineering, University of Strathclyde, Glasgow G1 1XJ, UK

* jason.reese@strath.ac.uk

Key Words: *thermodynamic non-equilibrium; sub-continuum flows, microfluidics, nanofluidics*

ABSTRACT

Micro- and nano-scale fluid systems can behave very differently from their macro-scale counterparts. Remarkably, there is no sufficiently accurate, computationally efficient, and — most importantly — generally agreed fluid dynamic model that encapsulates all of this important behaviour. The only thing that researchers can agree on is that the conventional Navier-Stokes fluid equations are unable to capture the unique complexity of these often locally non-thermodynamic-equilibrium flows. Here, we outline recent work on developing and exploring new models for these flows, highlighting, in particular, slip flow as a quintessential non-equilibrium (or sub-continuum) phenomenon. We describe the successes and failures of various hydrodynamic and molecular models in capturing the non-equilibrium flow physics in current test applications in micro and nano engineering, including the aerodynamic drag of a sphere in a rarefied gas, and the flow of water along carbon nanotubes.

INTRODUCTION

The set of Navier-Stokes-Fourier (NSF) equations, with no-velocity-slip and no-temperature-jump conditions at bounding surfaces, is the traditional model for the transfer of heat and momentum in fluid flows. While it has proven successful for flows ranging from liquids in capillaries to the atmosphere of planets, remarkably it can be a poor predictor when the flow system is either very small (i.e. in micro/nano devices) or very low pressure (e.g. high-altitude air vehicles, spacecraft re-entry), or if the process depends on interactions at the molecular level (e.g. protein folding). This is despite the flows being very typically laminar in such conditions, so simpler in a conventional sense. For example, measured gas flow rates in micro channels are typically a factor of two larger than expected, and drag on a micro sphere is a similar factor smaller [1]. At the nano scale, surface effects such as hydrophobicity, wetting and electrokinetics dominate, and lead to unexpectedly high liquid transport rates in, e.g., carbon nanotubes that different experimentalists not only cannot fully explain but also fail to agree on.

These predictive failures arise from a limiting assumption underlying conventional fluid mechanics: scale-separation — macroscopic flow behaviour is assumed to be independent of the microscopic dynamics of the fluid material [2]. The conventional fluid mechanical model of near-instantaneous local

equilibration of heat and momentum throughout the fluid follows from this, and provides a powerful tool for treating most macro scale flows. However, scale-separation is not always guaranteed in micro and nano scale flows: in these cases we often need to account for the effect of the fluid’s molecular nature on the overall (macro) flowfield. Micro- and millisecond effects are important for micro and nano scale flows, but depend on the outcome of pico- or nanosecond molecular processes [3, 4]. The design of future technologies that exploit micro and nano scale flow components will require the ability to resolve phenomena across scales of at least 8 orders of magnitude in space, and 10 orders of magnitude in time — a formidable multiscale problem.

In this paper we describe some of our most recent computational and theoretical tools we are bringing to bear on this problem. We examine slip flows in microscale gas and nanoscale liquid applications as quintessential non-equilibrium or sub-continuum phenomena that are still not properly understood. We tackle gas and liquid flows alternately in this paper, because we wish to highlight the interesting commonalities between non-equilibrium gas and sub-continuum liquid flows at these small scales.

Thermodynamic non-equilibrium in gases

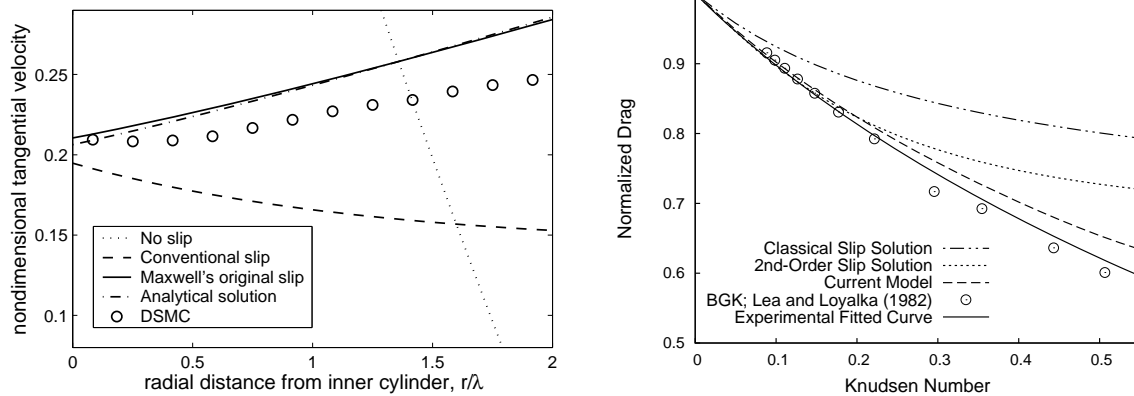
In dilute gas flows, molecules travel in free-flight between brief (binary) collisions with each other or bounding surfaces. The Knudsen number, Kn , indicates the degree of scale independence; in terms of the molecular mean-free-path, λ , and a characteristic length scale, L , of the system (or the local gradient of a relevant flow quantity, Q):

$$\text{Kn} = \frac{\lambda}{L} \cong \frac{\lambda}{Q} \left| \frac{dQ}{dl} \right|. \quad (1)$$

If $\text{Kn} > 0.01$, physical scales are no longer clearly separated, and non-local-equilibrium flow behaviour arises: the flow velocity at a surface takes on a finite “slip” value, and the temperature of the gas near the surface also differs from the surface temperature. At higher Kn the linear NSF constitutive relations themselves become inappropriate. Air flowing at atmospheric pressures in a device with a characteristic length scale of $1\mu\text{m}$ has $\text{Kn} \approx 0.1$ and will show these non-equilibrium (rarefaction) effects. Gas flows in, e.g., micro-pumps or micro-turbines of complex geometry will have a range of Kn : the NSF equations cannot, therefore, be expected to be generally applicable to these flows.

While a molecular-level description of the gas is available through the classical Boltzmann equation — or other kinetic models, such as BGK or ES-BGK — direct solution is computationally expensive. Even the cost of indirect methods, such as the direct simulation Monte Carlo (DSMC) technique, makes complex 3D full-field flow simulation impractical: to resolve micro flow velocities of the order of 0.01 m/s in DSMC, we need roughly 500 million statistical samples of the flowfield at any point [2]. However, variance reduction techniques can be applied to conventional DSMC to create a powerful and more economical method for generating molecular distributions at the most critical points in a flow.

A computationally-efficient gas flow method, but one which has had only modest success to date, is to establish either a Kn -series or a Hermite polynomial approximation to the distribution function in the Boltzmann equation. To first order, i.e. for near-equilibrium flows, both approaches yield the NSF set, but the solution methods can be continued to second and higher orders to incorporate more and more of the salient characteristics of a non-equilibrium flow. Specifying the additional boundary conditions required for the derived higher-moment and higher-order extended hydrodynamic equation sets remains a critical problem. In any case, the complexity of most of the models (Burnett, Grad 13-moment, R13, R26, etc.) is overwhelming, particularly when considering the only modest improvement in accuracy they provide. While they have particular difficulty in resolving strong non-equilibrium phenomena, e.g. the Knudsen layer close to bounding surfaces [5, 6], they may have some use in the “near near-equilibrium” regime [7, 8].



(a) Cylindrical Couette flow ($Kn = 0.5$, argon gas, momentum accommodation coefficient is 0.1), non-dimensional velocity radial profiles. Note the inverted velocity profile, captured by DSMC and an analytical kinetic theory [11].

(b) Normalized drag force on a sphere at various Kn , comparing predictions using the model of [1] with, as noted, Basset's classical slip solution, Cercignani's 2nd-order slip solution, BGK kinetic theory results, and experimental data.

Figure 1: Micro gas flow examples.

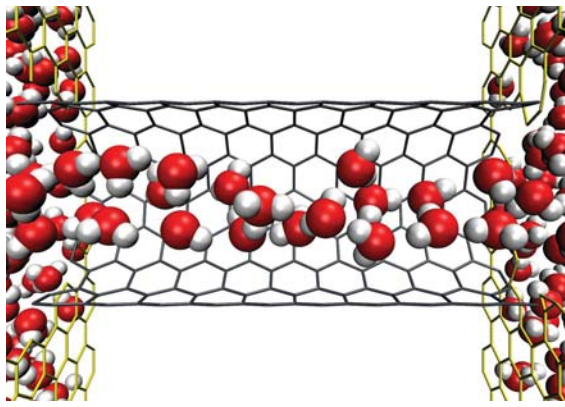
Thermodynamic non-equilibrium in liquids

Non-equilibrium phenomena analogous to that in gases (i.e. slip and non-linear constitutive behaviour) dominate liquid flows at the nanoscale. But identifying and modelling non-equilibrium in liquids is significantly more difficult than for gases: a Knudsen number cannot be ascribed because liquid molecules are constantly moving within each others' potentials, and the length scale for equilibrium breakdown is similar to that at which the continuum-fluid model itself fails. The complexity of material-dependent effects at interfaces cannot be treated by simple phenomenological parameters or by "equivalent fluxes" [9]. Direct molecular simulation of the liquid, however, can simultaneously model these phenomena with minimal simplifying assumptions, and some recent results will be presented below.

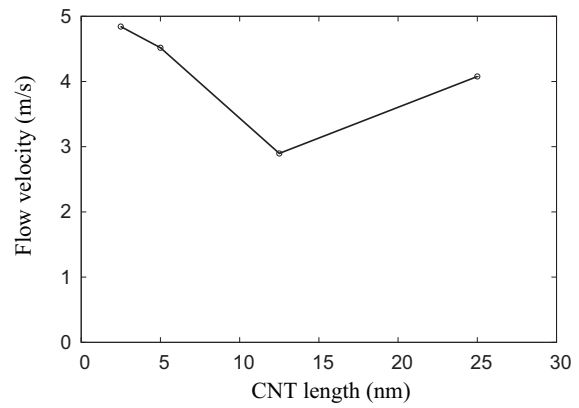
Molecular dynamics (MD) simulations calculate the intermolecular forces between molecules (based on their configuration in space) and then integrate the classical equations of motion using the net force on each molecule. Intermolecular force models can be empirically fitted to experimental data, or derived from first principles. The dynamics of real molecules in collision with real surfaces can then be investigated by accumulating the properties of individual molecules colliding with a (rough) surface lattice of molecules. The major problem again is that, like DSMC, MD is computationally very intensive. For example, to simulate $1\mu s$ of water flow in a $10 \times 20 \times 100$ nm channel would require up to 10 years on a modern PC. However, much of this time is spent in calculating unnecessary molecular detail in parts of the flow that are near to equilibrium [10]. Ultimately, a hybrid framework is called for, which dynamically couples the efficient NSF model in near-equilibrium regions to the detailed molecular dynamics model elsewhere.

References

- [1] Lockerby, D. A. and Reese, J. M., 2008, On the modelling of isothermal gas flows at the microscale, *J. Fluid Mech.*, 604, 235-261.
- [2] Reese, J. M., Gallis, M. A. and Lockerby, D. A., 2003, New directions in fluid dynamics: non-equilibrium aerodynamic and microsystem flows, *Phil. Trans. Roy. Soc. A*, 361, 2967-2988.



(a) Molecular dynamics simulation of water molecules (red and white) transported through a short (7,7) carbon nanotube (green lines), shown in cutaway, that is fixed between two graphene membranes (thin gold lines). The water is moving from an upstream to a downstream reservoir.



(b) Molecular dynamics calculations of variation of water flow velocity with CNT length under 200 MPa pressure difference. The flow enhancement factors (relative to continuum flow expectations) are 71, 126, and 353 for the 5 nm, 12.5 nm and the 25 nm lengths, respectively.

Figure 2: Water transport in carbon nanotubes.

- [3] Borg, M. K., Macpherson, G. B. and Reese, J. M., 2010, Controllers for imposing continuum-to-molecular boundary conditions in arbitrary fluid flow geometries, *Mol. Sim.*, 36, 745-757.
- [4] Macpherson, G. B. and Reese, J. M., 2008, Molecular dynamics in arbitrary geometries: parallel evaluation of pair forces, *Mol. Sim.*, 34, 97-115.
- [5] Lockerby, D. A., Reese, J. M. and Gallis, M. A., 2005, The usefulness of higher-order constitutive relations for describing the Knudsen layer, *Phys. Fluids*, 17, 100609.
- [6] Lockerby, D. A., Reese, J. M. and Gallis, M. A., 2005, Capturing the Knudsen layer in continuum-fluid models of non-equilibrium gas flows, *AAIA J.*, 43, 1391-1393.
- [7] Lockerby, D. A., Reese, J. M. and Struchtrup, H., 2009, Switching criteria for hybrid rarefied gas flow solvers, *Proc. Roy. Soc. A*, 465, 1581-1598.
- [8] Gu, X. J. and Emerson, D. R., 2009, A high-order moment approach for capturing non-equilibrium phenomena in the transition regime, *J. Fluid Mech.*, 636, 177-216.
- [9] Brenner, H. and Ganesan, V., 2000, Molecular wall effects: are conditions at a boundary boundary conditions? *Phys. Rev. E*, 61, 6879-6897.
- [10] Macpherson, G. B. and Reese, J. M., 2006, Molecular dynamics for near surface flows in nano liquid and micro gas systems, 4th ASME Intl Conf Nanochannels, Microchannels & Minichannels, ICNMM2006, 96170.
- [11] Lockerby, D. A., Reese, J. M., Emerson, D. R. and Barber R. W., 2004, Velocity boundary condition at solid walls in rarefied gas calculation, *Phys. Rev. E*, 70, 017303.

NON-INVASIVE AND INVERSE PROPERTY ESTIMATION OF ARTERIAL ELASTICITY

*Amarpal S. Kapoor¹, Perumal Nithiarasu¹ and Raoul Van Loon¹

¹Civil & Computational Engineering Centre, College of Engineering, Swansea University,
Singleton Park, Swansea, SA2 8PP

*A.S.Kapoor.568964@swansea.ac.uk

Key Words: *arterial elasticity; non-invasive; inverse property optimization; blood flow*

ABSTRACT

A non-invasive, patient-specific method for the determination of in-vivo arterial elasticity is proposed here. Inverse property optimization, incorporating a 1D blood-flow model and Levenberg Marquardt Optimization render the possibility of accurately estimating the stiffness of arteries. We begin with a steady state analysis as a starting point, gradually implementing more realistic transient state conditions to finally result in a fully spatial and fully transient scheme. Various meshes representative of healthy and diseased arteries have been simulated successfully. Although the current methodology cannot be directly employed as a clinical practice at this point in time, it provides impetus to carry out work on an advanced level, i.e. 4D (3 spatial dimensions plus time).

1 INTRODUCTION

A brief motivation for the above work is presented in this section.

To have an accurate estimate of arterial elasticity is known to have an important significance in the medical fraternity. It has been long discovered that there is a direct relation between the stiffness of arteries and risk of cardiovascular events [1]. A prior knowledge of arterial elasticity can thus prove to be very important and there has been a rediscovery of this insight with the advent of modern computing framework. A variety of methods have been developed for assessing arterial properties [2]. Most of these methods rely on measuring the pulse wave velocity and assessing the arterial pressure waveforms. These methods provide a single value for the stiffness, which is not always true. Also there are several other factors like age, gender, disease states, smoking habits and possibly others which are not always taken into consideration with these methods. There is another class of methods for arterial elasticity estimation which rely on mechanical testing of specimens, taken from the body. There is an inherent change in material properties as the arteries are removed from the body and is not feasible as a clinical technique, owing to the invasive nature of this method. Moreover, classic risk factors fall short of making accurate predictions of cardiovascular diseases. This is therefore an attempt to develop an engineering based solution to the medical problem being discussed.



Figure 1: *Proposed methodology for arterial elasticity estimation.*

2 METHODOLOGY

The methodology employed for the arterial property estimation algorithm is broadly classified into the following stages as shown in figure 1.

Stage 0 deals with the real-time patient specific data acquisition via dynamic MRI, which captures the displacement of arteries due to distending pressure as the blood flows. Data acquired here acts as a benchmark against which the results of the CFD model are compared. This stage is not included in the current work but is essential in establishing the link between the human body and the CFD model.

Stage 1 constitutes the solution for the forward problem, which employs an explicit scheme to solve the governing 1D equations (1),(2) applied to flow through compliant tubes [3]. The arterial deformation in response to the cardiac output of the heart is artificially obtained from the blood-flow model in terms of the nodal area. The solution procedure also results in the nodal velocity of blood and the nodal pressure is finally evaluated using area and velocity values. The Locally Conservative Taylor-Galerkin method (LCG) that is employed in the solution scheme helps reduce computational effort as it prevents the need to invert huge matrices originating from the conventional assembly process, by treating each element as a separate sub-domain with its own boundaries. Also, the incorporation of discontinuities is simplified in LCG as co-located nodes are permitted to have different properties.

$$\frac{\partial A}{\partial t} + \frac{\partial(Au)}{\partial x} = 0 \quad (1)$$

$$\frac{\partial u}{\partial t} + u \frac{\partial u}{\partial x} + \frac{1}{\rho} \frac{\partial p}{\partial x} + \frac{1}{\rho} \frac{\partial \tau}{\partial x} = 0 \quad (2)$$

It should be noted that for the solution of the forward problem in stage 1, arterial stiffness was assumed to be known, but in real life problems the stiffness is actually not known a priori and its estimation is the hallmark of this work. Even though the forward problem solution is obtained only after using stiffness as an user input, inverse property estimation can be employed to yield the actual stiffness of arteries by making comparisons between the model predicted and experimental data. The Levenberg Marquardt (LM) optimization is used here [4, 5]. It is an iterative technique that locates a local minimum of a multivariate function that is expressed as the sum of squares of several non-linear, real-valued functions. It has been adopted in various data-fitting applications and has become a standard technique for non-linear least squares problems. As a starting point, an objective function incorporating just nodal areas is considered. It is the least square error between the actual and model predicted area (nodal basis). The objective function is as expressed in equation (3).

$$f = \sum_{j=1}^n (A_j - \bar{\bar{A}}_j)^2 \quad (3)$$

where, A_j is a vector of actual nodal areas (experimental data), $\bar{\bar{A}}_j$ is a vector of model predicted nodal areas and j corresponds to the number of nodes. The LM algorithm operates by minimizing this objective function which in a physical sense is equivalent to repeating the forward run in an intelligent manner until the measured displacements equal the model predicted

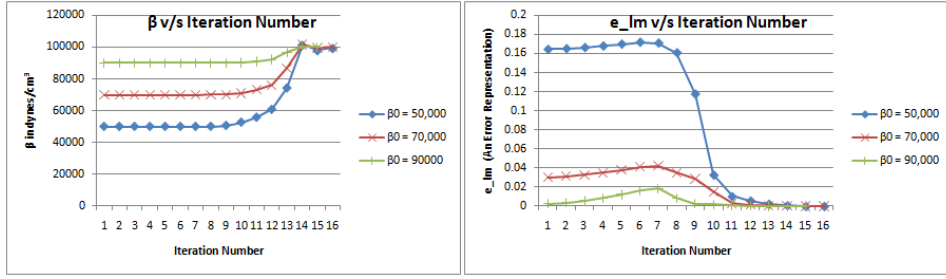


Figure 2: Results for an open artery with different starting values for $\beta = \beta_0$.

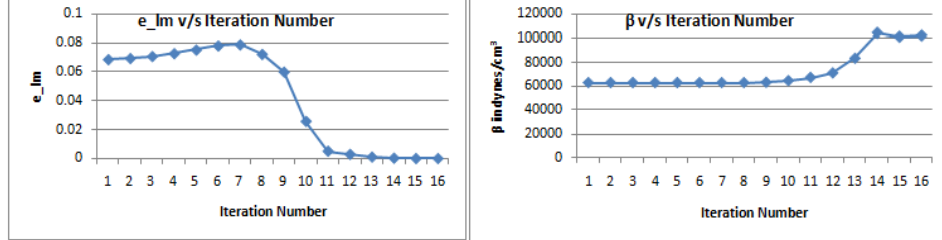


Figure 3: Results for an open artery with linearly distributed values for β .

displacements, which would be indicative of the fact that the current stiffness equals the actual stiffness. It must also be noted that the experimental data here is generated by surrogate means and that no patient data is used for the purpose of this work. The LM algorithm also requires computation of the Jacobian and Hessian matrices (first and second order partial derivatives of area with respect to stiffness respectively) for incrementing/decrementing β (function of Young's Modulus) in every iteration depending on the errors in the current and previous iteration. Analytical evaluation is not possible, hence a numerical finite difference approximation is resorted for, by exploiting the method of perturbations. At every iteration the stiffness values are perturbed slightly (1% of current value) and a forward run is then executed at this value to generate the input arguments required in the forward difference approximation.

3 RESULTS

The proposed methodology is demonstrated to be working very well for 1D simulations considered here. Various meshes indicative of several healthy and diseased states of the artery are considered for the simulations and the errors in the actual and model predicted nodal stiffness are found to be less than 1% (correct $\beta = 100,000$). The variations of the objective function (e_{lm}) and β with iteration number are illustrated for the two cases in figures 2 and 3.

The results shown in the previous section were for a steady pressure pulse applied at the inlet of the artery. The input pressure applied was therefore invariant with time and maintained at a certain constant value. The sampling of variables involved in the objective function evaluation for the optimization routine were based on the values at the end of the cycle time (i.e. last iteration of the forward run). Application of a more realistic input pressure pulse (transient) on the other hand, owing to the inherent iterative nature of the forward run, calls for a need to monitor the variables at the end of every iteration of the forward run. This has a direct effect on the amount of data to be sampled and analyzed by the optimization routine. Several methods like fully transient localised routine, fully transient & fully spatial routine, semi-transient & fully spatial routine and modifications in the objective functions are being worked upon to have a solution to 1D transient property optimization problem.

4 CONCLUSIONS

The following conclusions were derived from the current work:

- Inverse parameter optimization seems to be a feasible technique for material-parameter estimation of human arteries.
- Non-invasive procedures can be employed for determining the arterial material properties.
- A high degree of agreement was observed between the experimental and model predicted values obtained from the Levenberg-Marquardt optimization routine and the error in most cases was found to be less than 1%.
- This study provides the motivation to implement non-invasive and patient-specific arterial material property estimation in multi-dimensions (up to 4D).

Currently, most CFD studies on blood flow simulations rely on an assumed value of elasticity for the arterial walls. Hence, the primary accomplishment of this work was to illustrate the possibility of having a well-defined model for non-invasively extracting the properties of human arteries via inverse optimization.

It is aimed to work towards the development of a new and advanced methodology that could act as a substitute to the current risk assessment and diagnostic procedures being implemented in health care. The evaluation of arterial stiffness can therefore be used as a marker to predict the onset of such disease states (CVD) at a very early stage and could assist in decreasing cardiovascular mortality and increasing life expectancy. With a broader sense, blood vessel elasticity is also important to physiology, clinical problems involving surgery, angioplasty, tissue remodelling, tissue engineering, hypertonology, nephrology, neurology, gynaecology and diabetology.

5 Acknowledgement

The Zienkiewicz Fellowship that made this project possible is highly regarded and acknowledged.

References

- [1] M.O.Rourke. Arterial stiffness, systolic blood pressure, and logical treatment of arterial hypertension. *Hypertension*, 15, 339–347, 1990.
- [2] J.J. Oliver and D.J. Webb. Noninvasive assessment of arterial stiffness and risk of atherosclerotic events. *Arteriosclerosis, Thrombosis, and Vascular Biology: Journal of the American Heart Association*, 23, 554–556, 2003.
- [3] J.P. Mynard and P. Nithiarasu. A 1D arterial blood flow model incorporating ventricular pressure, aortic valve and regional coronary flow using the locally conservative galerkin (LCG) method. *Communications in Numerical Methods in Engineering*, 24, 367–417, 2008.
- [4] Sam Roweis, Levenberg-Marquardt Optimization. In <http://www.LS.nyu.edu/roweis/notes/lm.pdf>, Accessed on Aug. 17, 2010
- [5] M.J. Moulton, L.L. Creswell, R.L. Actis, K.W. Myers, M.W. Vannier, B.A. Szab and M.K. Pasque. An inverse approach to determining myocardial material properties. *Journal of Biomechanics*, 28(8), 935–948, 1995.

NUMERICAL ANALYSIS OF THE HIP JOINT BONES IN CONTACT

*Philip Cardiff¹, Alojz Ivanković¹, David FitzPatrick¹, Rob Flavin¹ and Aleksandar Karač²

¹School of Electronic, Electrical and Mechanical Engineering, University College Dublin, Belfield,
Dublin, D4, Ireland

²University of Zenica, Zenica, Bosnia and Herzegovina

*philip.cardiff@ucd.ie

Key Words: *biomechanics; finite element; finite volume; stress analysis; contact mechanics; hip joint*

ABSTRACT

Total Hip Arthroplasty is a surgical procedure that reforms the hip joint, replacing the pathological joint with an artificial prosthesis. Due to post-operative joint instability, complications such as dislocation are still a significant problem. This research aims to develop a realistic numerical model of a healthy hip joint including Hill-type muscle models and examine its stability. An initial model of the hip joint simulating stance has been developed and two separate material models have been examined. In addition, the effect of including articular cartilage in the model has been investigated.

1 INTRODUCTION

Total Hip Arthroplasty (THA) has progressed considerably over the past 50 years since the late Sir John Charnley ushered in the modern era of low-friction arthroplasties, however significant difficulties still persist. One of the most common complications of THA is the dislocated hip, occurring in up to 10% of primary THAs [1, 2]. This research will focus on improving joint stability, hence lessening risk of dislocation. When a THA is performed, muscles and other soft tissues must be cut to allow insertion of the artificial prosthesis. Following insertion of the prosthesis, these damaged muscles are repaired, and their position can be adjusted to help stabilise the reconstructed joint. As is understandable, it is not possible or ethical to experiment with different muscle positions on patients. By constructing a realistic artificial hip model, the hip stability can be numerically examined. The position and strength of the hip muscles can be altered, and the subsequent effect on hip stability can be examined.

2 METHODS

A 23-year-old male subject was chosen with no congenital or acquired pathology of the hip joint. Computed tomography (CT) and magnetic resonance imaging (MRI) images of the subject's hip joint were acquired. The 3D bone surface geometry was extracted from the scans using open-source software 3D

Slicer [3]; 3D Slicer allows the registration and fusion of CT and MRI data enabling the user to more accurately extract soft and hard tissue. The bone surface meshes were smoothed using a volume preserving Laplacian algorithm [4], before a volume mesh was created. Various different volume meshing software was explored and Ansys ICEM CFD was chosen due to its ability to produce high quality meshes of complex geometry.

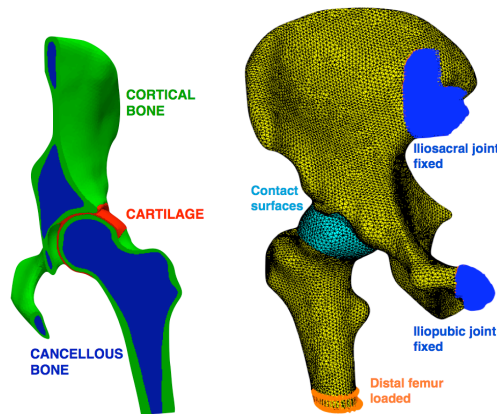


Figure 1: *Sandwich* model (a) material distribution and (b) boundary conditions

3 RESULTS

Two separate numerical approaches are employed to model the hip joint: the finite element approach and the finite volume approach. Commercial software Abaqus is employed using the finite element approach, and open-source software OpenFOAM (Open Field Operation and Manipulation) using the finite volume approach. OpenFOAM is a general 3D based, open source, object-oriented C++ library and was selected due to its ease of customisability.

Two different material properties were considered for the model: a *homogenous* model and a *sandwich* model. The *homogenous* model assumed bone be a homogenous isotropic linear-elastic material with a Young's modulus of 500 MPa and a Poisson's coefficient of 0.2. The *sandwich* model assumed bone to be composed of a flexible cancellous core sandwiched inside a stiffer cortical shell, as shown in figure 1(a). The variable cortical bone thickness was segmented directly from CT scans. The thickness of the cortical bone ranged from almost 10 mm in the femur shaft to less than 1 mm in the ilium and the femur head. Cortical bone was given a Young's modulus of 17 GPa and a Poisson's coefficient of 0.3 [6]. The effect of including a layer of 1 mm constant thickness cartilage on the articular surfaces was examined. The articular cartilage was assumed to have a Young's modulus of 25 MPa and a Poisson's coefficient of 0.45 [5]. The Abaqus *homogenous* model without cartilage contains 384,843 linear C3D4 solid tetrahedral elements. The cartilage volume comprises 17,036 linear C3D6 wedge elements. The Abaqus *sandwich* model uses the same mesh as the *homogenous* model with the appropriate elements assigned cortical bone properties. The OpenFOAM homogenous model contains 10,073 polyhedral cells.

Initially the stance phase of gait has been simulated; a force of 1000 N (approximately 1.2 times body weight) was applied to the distal end of the femur corresponding the ground reaction force experienced by the hip during the stance phase of the gait analysis. The distal femur was fixed in the two directions orthogonal to the applied vertical force. The pelvis was fixed at the iliopubic joint and the iliosacral

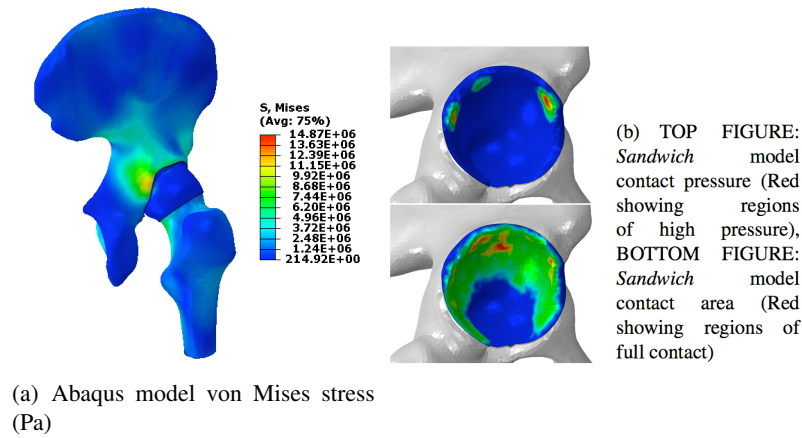


Figure 2: *Sandwich* model stress results

joint corresponding to physiological conditions. The model boundary conditions are shown graphically in figure 1(b). The contact was assumed to be frictionless.

When the *homogenous* model including articular cartilage was simulated, both the Abaqus and the OpenFOAM models gave comparable results with a maximum contact pressure of 10 MPa. When the layer of articular cartilage was excluded from the model, the maximum contact pressure rose considerably to 50 MPa. This increase in contact pressure is due to the absence of articular cartilage to distribute the joint force, resulting in a much lower contact area.

Examining the initial results obtained from the Abaqus *sandwich* model, as expected the stiff cortical bone shell supported the majority of the load. The *sandwich* model with cartilage gave a maximum contact pressure of 14 MPa. Von Mises stress results from the Abaqus *sandwich* model are shown in Figure 2(a). Figure 2(b) shows the region of maximum contact pressure and maximum contact area. When the layer of articular cartilage was excluded from the *sandwich* model, the contact pressure increased appreciably to over 100 MPa. This sizable and unrealistic increase in pressure is due to stiff cortical bone surfaces coming into contact producing a smaller contact area. The OpenFOAM *sandwich* model is currently being developed.

When the Abaqus *sandwich* model was compared with the OpenFOAM and Abaqus *homogenous* models, it was observed that higher stresses are experienced by the articular cartilage in the *sandwich* model. The maximum von Mises stress in the *homogenous* model was 5 MPa, while a maximum von Mises stress of 8 MPa was found in the *sandwich* model. This increase in cartilage stress is due to the cartilage being constrained considerably more by the cortical bone in the *sandwich* model than by the less stiff cancellous bone in the *homogenous* model.

4 CONCLUSIONS

A procedure has been developed to create a patient-specific 3D hip joint model from CT and MRI scans. Cortical bone is segmented separately from cancellous bone, preserving the interface between the two types of bone. Articular cartilage was assumed to have a constant thickness, which has been shown to be a valid assumption [7]. Numerical analysis was performed using both finite element based software Abaqus and finite volume based software OpenFOAM. The stance phase of gait has been simulated using a *homogenous* material model and a *sandwich* material model. The *homogenous* models predicted maximum contact pressures of 10 MPa, while the *sandwich* model predicted maximum contact

pressures of 14 MPa; both models agree well with the range reported in literature of 1–20 MPa [6, 8]. Only the *homogenous* model was simulated in OpenFOAM but the results agree well with the Abaqus *homogenous* model. It has been noted in literature that cortical bone thickness considerably affects the predictions of a numerical model of hip joint mechanics [9]. If cortical bone thickness is over-estimated, it can produce an unrealistically stiff hip joint model. A method to examine the accuracy of the current cortical bone segmentation procedure will be investigated.

In the future, a *CT-based* material model will be implemented in both Abaqus and OpenFOAM. The Young's modulus of each mesh cell using an empirical relationship based on the Hounsfield intensity of the corresponding pixels in the CT images. The *CT-based* models will then be compared with the *homogenous* and *sandwich* models to examine how sensitive the stress results are to material property selection. In addition, the Hill-type muscle models will be incorporated to simulate the mechanics of a full gait cycle. Electromyographical signals obtained from gait analysis will be the primary input to the Hill-type muscle models.

The authors wish to acknowledge the SFI/HEA Irish Centre for High-End Computing (ICHEC) for the provision of computational facilities and support.

References

- [1] M. Von Knoch and D. Berry. Late Dislocation after Total Hip Arthroplasty. *Journal of Bone and Joint Surgery*, 84-A, 1949-1953, 2002.
- [2] R. D. Beckenbaugh and D. M. Ilstrup. Total hip arthroplasty. *The Journal of Bone and Joint Surgery*, 60, 306-313, 1978.
- [3] S. Pieper, B. Lorensen, W. Schroeder and R. Kikinis. The NA-MIC Kit: ITK, VTK, Pipelines, Grids and 3D Slicer as an Open Platform for the Medical Image Computing Community. *Proceedings of the 3rd IEEE International Symposium on Biomedical Imaging: From Nano to Macro*, 1, 698-701, 2006.
- [4] J. Vollmer, R. Mencl and H. Muller. Improved Laplacian Smoothing of Noisy Surface Meshes. *Eurographics*, 18(3), 131-138, 1999.
- [5] F. Bachtar, X. Chen and T. Hisada. Finite element contact analysis of the hip joint. *Medical & biological engineering & computing*, 44(8), 643-51, 2006.
- [6] M. Dalstra, R. Huiskes, A. Odgaard and L. Van Erning. Mechanical and textural properties of pelvic trabecular bone. *Journal of biomechanics*, 26(4-5), 523-535, 1993.
- [7] A. E. Anderson, B. J. Ellis, S. A. Maas and J. A. Weiss. Effects of idealized joint geometry on finite element predictions of cartilage contact stresses in the hip. *Journal of biomechanics*, 43(7), 1351-7, 2010.
- [8] M. Daniel. Contact stresses in the human hip joint - review. *Journal of Biomechanics*, 2(8), 197-203, 2006.
- [9] A. E. Anderson. Computational modeling of hip joint mechanics. *PhD Thesis*, University of Utah, 2007.

A Biphasic Swelling Model of the Intervertebral Disc

*Julien Vignollet, Chris J. Pearce and Lukasz Kaczmarczyk

School of Engineering, University of Glasgow, Rankine Building, Glasgow, G12 8LT

*j.vignollet.1@research.gla.ac.uk

Key Words: *Biomechanics, Biphasic, Swelling, Finite Deformations, Anisotropy*

ABSTRACT

A 3D biphasic swelling model has been derived using mixture theory for soft, hydrated and charged tissues to capture the salient characteristics of the intervertebral disc's behaviour. The model fully couples the solid matrix under finite deformations with the ionised interstitial fluid. The nucleus is assumed to behave isotropically while the fibres in the annulus fibrosus are modelled with a transversely isotropic model. The effects of the fixed negative charges of the proteoglycans, which induce an osmotic pressure responsible for the swelling characteristics of the disc, are accounted for. Preliminary results are presented on an idealised model.

1 INTRODUCTION

The intervertebral disc is a complex multi-phase deformable solid mainly comprised of the nucleus pulposus and the annulus fibrosus (Fig. 1a). The nucleus pulposus is the gelatinous core of the disc, which consists of a charged and hydrated matrix of collagen fibres and an ionised interstitial fluid (up to 85% at the centre). It is enclosed in the annulus fibrosus that is formed by concentric layers of aligned collagen fibre sheets, oriented in an alternating fashion (Fig. 1b).

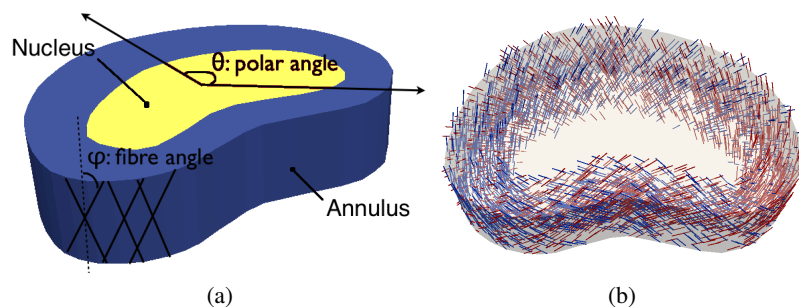


Figure 1: (a) Idealised geometry of the intervertebral disc - (b) Fibre distribution in the annulus fibrosus

The disc also consists of proteoglycans. These are negatively charged and relatively large molecules trapped in the network of collagen fibres, which gives rise to osmosis, resulting in additional mechanical stiffness for the disc under compression and allows it to re-imbibe fluid overnight.

2 MODEL

In an effort to keep an acceptable balance between the model's complexity and the salient features it is able to capture, an anisotropic hyperelastic biphasic swelling model is derived for the intervertebral disc. As the proteoglycans undergo the same deformations as the solid matrix, the osmotic pressure is constitutively determined from the deformation rather than a distinct phase. This offers the advantages of requiring less material parameters than tri- and quadri-phasic models and keeps the number of degrees of freedom relatively low while still accounting for the fluid flow, finite deformations and electro-chemomechanically driven effects.

The biphasic swelling model is based on Ehlers's theory [2]. The linear momentum and mass balance equations are derived for both the fluid and solid phases and then combined together using the principles of mixture theory for saturated and intrinsically incompressible materials. We subsequently obtain Eq. (1) that reflects the coupled nature of the system (solid stress $\boldsymbol{\sigma}^e$ coupled with the osmotic pressure $\Delta\pi$ and the fluid pressure p in the momentum equation; solid velocity coupled with relative fluid velocity in the mass balance equation).

$$\begin{cases} \text{div}(\boldsymbol{\sigma}^e - (\Delta\pi + p)\mathbf{I}) = 0 \\ \text{div}(\mathbf{v}^{solid} + \mathbf{w}) = 0 \end{cases} \quad (1)$$

The fluid flow is described using Darcy's law in its classical form (Eq. 2), with a strain-dependent permeability [5]. The constitutive model of the osmotic pressure is an isotropic generalisation of recent experimental work [3]; because the osmotic pressure is directly related to the concentration of the negative charges that are "attached" to the solid phase, it is inversely proportional to the volume change $J = \det(\mathbf{F})$ of the mixture (Eq. 3).

$$\mathbf{w} = -k\nabla p \quad \text{with} \quad k = k_0 e^{M(J-1)} \quad (2)$$

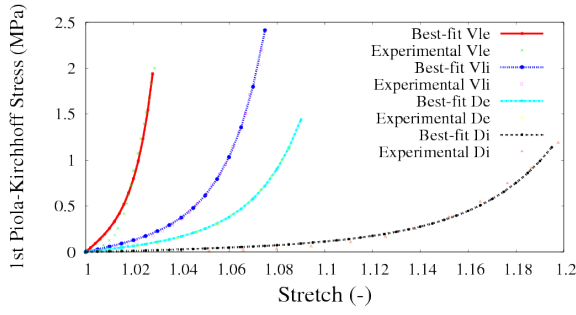
$$\Delta\pi = \frac{\Delta\pi_0}{J} \quad (3)$$

An additive split between the matrix and fibre contributions is adopted for the solid phase: $W_{solid}(\mathbf{C}, I_4, I_6) = W_{iso}(\mathbf{C}) + W_{aniso}(I_4, I_6)$, where the 4th and 6th invariants of the right-Cauchy-Green tensor measure of the square of the fibre's stretch ($I_\alpha = \mathbf{C} : (\mathbf{a} \otimes \mathbf{a})$ where \mathbf{a}_α is the direction of fibre α in the reference configuration). In a first approach, the solid phase is defined using a Neo-Hookean material while the fibres are described using an exponential model [1], which accounts for the fact that the fibres provide stiffness in tension only:

$$\begin{cases} W_{aniso}(I_4, I_6) = 0 & \text{if } I_i \leq 1, i \in \{4, 6\} \\ W_{aniso}(I_4, I_6) = \sum_{\alpha} \frac{k_1}{2k_2} \left(\exp \left[k_2 (I_\alpha - 1)^2 \right] - 1 \right) & \text{if } I_i > 1, i \in \{4, 6\} \end{cases} \quad (4)$$

Material properties for this model were obtained from an iterative best-fit of Holzapfel's experimental results [4]. The 1D stress-stretch curve of a single lamellar sample are plotted on Fig.2. It is interesting to notice that the fibre's stiffness depends not only on the fibre stretch but also the polar angle (Fig. 2).

The set of coupled nonlinear equations is discretised in space (noting the Babuska-Brezzi condition) and in time using a finite difference scheme. The consistently linearised problem is finally implemented in a three-dimensional finite element scheme for high performance computing. An incremental solution scheme is adopted.



| | Vle | Vli | De | Di |
|-------------|--------|-------|-------|-------|
| k_1 (MPa) | 8.34 | 2.11 | 1.12 | 0.23 |
| k_2 | 339.57 | 67.55 | 43.88 | 10.88 |

Figure 2: Experimental results from [4] with best parameters to fit Eq. 4 (Vle: Ventro-lateral external, Vli: Ventro-lateral internal, De: Dorsal external and Di: Dorsal internal)

3 PRELIMINARY RESULTS

Initial validation of the nucleus pulposus were performed against a previously developed 1D model, validated against experimental confined compression data. Qualitative results on an idealised disc are presented, where the geometry, material parameters and boundary conditions are as follows:

1. The idealised geometry is presented in Fig. (1a). The main simplifications are the flat and parallel endplates and straight fibres. The fibre orientation is realistically modelled as a function of the polar angle [4]: $|\varphi| = 23.2 + 0.13\theta$.
2. Although material parameters vary within the disc (e.g. Fig. 2) a single parameter set is used for the nucleus and the annulus across the continuum.
3. The disc is connected, top and bottom, to vertebral bodies that are significantly stiffer than the disc and more permeable than the annulus. Therefore in the current model, the disc is laterally sealed and its top and bottom surfaces cannot expand laterally.

3.1 Compression test

The disc is subjected to compression (5% strain at a rate of $10\mu m.s^{-1}$) in order to verify trends observed with the 1D model. The low permeability (order of $10^{-15}mm/(N.s)$) hinders the fluid flow. Hence, when loaded, fluid is initially only lost near the boundaries, resulting in localised strains, while in the centre there is an increase in fluid pressure.

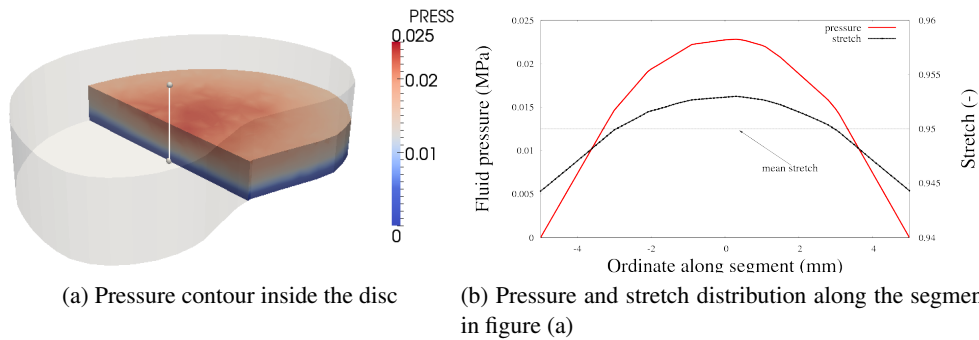


Figure 3: Idealised disc under 5% compressive strain

3.2 Twisting test

In order to verify that the fibres are correctly implemented, the disc is subjected to a torque $\theta = 3^\circ$, with both endplates enforced to remain parallel. The deformations are therefore proportional to the distance from the centre of rotation, which is reflected in Fig. 4a for the fibres experiencing tension. The other family of fibres experiencing compression is not active.

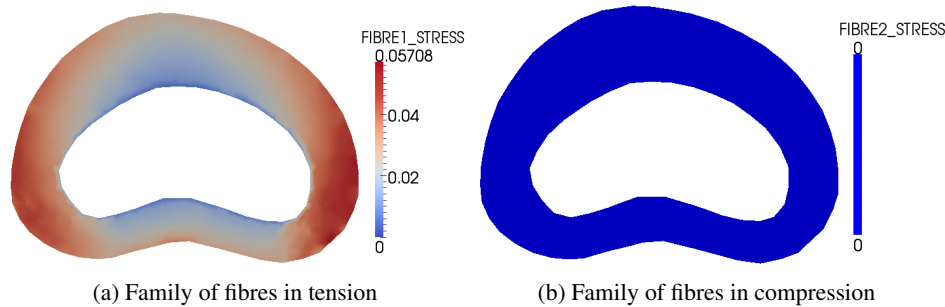


Figure 4: Fibre stress contour plot in the mid-sagittal plane for the twisted disc

4 CONCLUSION

A 3D biphasic swelling, anisotropic and hyperelastic model has been formulated. It captures the salient features of the intervertebral disc such as ionic, stiffening and swelling effects and phase coupling. The early stage results show qualitatively good results. Work is under progress to utilise more realistic geometries and define physiologically correct initial conditions.

References

- [1] R. Eberlein, G.A. Holzapfel, and C. A. J. Schulze-Bauer. An anisotropic model for annulus tissue and enhanced finite element analyses of intact lumbar disc bodies. *Computer Methods in Biomechanics and Biomedical Engineering*, 4(3):209–229, 2001.
- [2] W. Ehlers, N. Karajan, and B. Markert. An extended biphasic model for charged hydrated tissues with application to the intervertebral disc. *Biomechanics and Modeling in Mechanobiology*, 8(8):1617–7959, 2008.
- [3] P. Heneghan and P. E. Riches. The strain-dependent osmotic pressure and stiffness of the bovine nucleus pulposus apportioned into ionic and non-ionic contributors. *Journal of Biomechanics*, 41(11):2411–2416, 2008.
- [4] G. A. Holzapfel, C. A. J. Schulze-Bauer, G. Feigl, and P. Regitnig. Single lamellar mechanics of the human lumbar anulus fibrosus. *Biomechanics and Modeling in Mechanobiology*, 3(3):125–140, 2005.
- [5] W. M. Lai, J. S. Hou, and V. C. Mow. A triphasic theory for the swelling and deformation behaviors of articular-cartilage. *Journal Of Biomechanical Engineering-Transactions Of The Asme*, 113(3):245–258, 1991.

A ONE-DIMENSIONAL BLOOD FLOW MODEL FOR STUDYING THE EFFECT OF AORTIC ANEURYSMS IN HUMAN ARTERIAL NETWORK

Kenny Low*, Perumal Nithiarasu and Igor Sazonov

Civil and Computational Engineering Centre, College of Engineering
Swansea University, Singleton Park, Swansea SA2 8PP, UK

*Corresponding author: 400727@swansea.ac.uk

Key Words: *blood flow; fusiform aortic aneurysm; one-dimensional; locally conservative Galerkin; flow waveforms*

ABSTRACT

The effect of including a fusiform aortic aneurysm into an arterial network is studied and the differences in the waveforms are identified. An existing one-dimensional (1D) model is modified to include the aneurysms and the waveforms are computed using a realistic ventricular pressure. The 1D fluid flow equations are solved using the locally conservative Galerkin (LCG) finite element method. This method provides an explicit element-by-element conservation and naturally incorporates vessel branching, where arteries with different discontinuities are permitted to share the same location at the start of the branch. An example of fusiform thoracic aortic aneurysm with three different sizes, but remain in the same location, is studied and the flow waveforms are compared against a normal adult waveform.

1 INTRODUCTION

Aortic aneurysm is generally a balloon-like bulge formed through weakened arterial wall of the aorta and can be of saccular or fusiform in nature. Fusiforms can be found in the upper or the abdominal part of the aorta. An aneurysm at the upper part is referred to as Thoracic Aortic Aneurysms (TAA) and the one at the lower part is known as Abdominal Aortic Aneurysms (AAA). Aortic aneurysm incidents have steadily increased over the past few decades. Nonetheless, there are still no known precise reasons which affect the weakening of the aortic wall. However, many believed that a number of factors have been related to this disease [1]. Aneurysms often cause no symptoms and are rarely noticed before rupture. To overcome this crisis, aneurysms need to be detected at an early stage [1, 2]. Some studies have been carried out by [2] to investigate the effect of an AAA on the wave propagation both experimentally and using a 1D arterial network model. Nevertheless, if this effect can be evaluated through common pulse sites such as common carotid artery, radial artery and many more, there might be an opportunity for diagnosing aneurysms.

The 1D arterial network models have been used extensively in recent years, primarily to provide a better understanding of the blood flow in the arterial tree. They offer a good compromise between accuracy and cost (computational time) [3]. In this paper, the existing 1D model of [4] with an additional fusiform aneurysm embedded is used to compute the waveforms in the human arterial system using a realistic ventricular pressure as an input. The main objective is to study the effect of blood flow in the presence of an aortic aneurysm in a human arterial network and identify the differences in waveforms.

The governing equations are solved using the LCG finite element method. This method provides explicit element-by-element conservation and reintroduces an interface flux in each element. The element-by-element solution, which is independent of the surrounding elements, offers controlled flexibility thus allowing the introduction of discontinuities along the element boundary [5, 6]. This property is useful in the consideration of vessel branching points such as bifurcations or trifurcations. Arteries with different

discontinuities are permitted to share the same location at the start of the branch in human arterial tree [4].

2 METHODOLOGY

The 1D first order hyperbolic governing equations of an elastic cylindrical vessel of incompressible and Newtonian fluid, based on the mass and momentum conservation laws can be written as [4]:

$$\frac{\partial A}{\partial t} + \frac{\partial(Au)}{\partial x} = 0 \quad (1)$$

$$\frac{\partial u}{\partial t} + \frac{\partial}{\partial x} \left(\frac{u^2}{2} + \frac{p}{\rho} \right) = \frac{1}{\rho} \frac{\partial \tau}{\partial x} \quad (2)$$

where A is the cross-sectional area of the vessel, u is mean velocity of the fluid, p is the internal pressure of the cross-section, ρ is the blood density (assumed to be constant due to incompressibility of blood) and $\tau = \mu(\partial u / \partial r)|_R$ is the shear stress where μ is the dynamic viscosity (constant), r is the radial direction in 3D cylindrical coordinates and R is the vessel radius. In the shear stress term, the inertia component will be neglect while the viscous component is assumed as a fully developed Newtonian steady flow with a parabolic velocity profile (Poiseuille flow) which can be expressed as:

$$\frac{dp}{dx} = \frac{d\tau}{dx} = -\frac{8\pi\mu u}{A} \quad (3)$$

In order to close the system, equations (1) and (2) have to be supplemented with a commonly used pressure-area relation [7] which takes the form:

$$p = p_{ext} + \beta(\sqrt{A} - \sqrt{A_0}), \quad \beta = \frac{\sqrt{\pi}hE}{A_0(1-\sigma^2)} \quad (4)$$

where p_{ext} is the external pressure from the surrounding tissues, A_0 is the unstressed cross-sectional area of the vessel, β is the material properties of the elastic vessel, h is the vessel wall thickness, E is the Young's modulus and σ is the Poisson's ratio.

The explicit semi-discrete form can then be achieved by using the standard second-order Taylor series expansion and the partial differential equation is used to replace the time derivatives with spatial derivatives which can be shown as:

$$\frac{\mathbf{U}^{n+1} - \mathbf{U}^n}{\Delta t} = \mathbf{S}^n - \frac{\partial \mathbf{F}^n}{\partial x} - \frac{\Delta t}{2} \left[\frac{\partial}{\partial x} \left(\frac{\partial \mathbf{F}^n}{\partial \mathbf{U}^n} \mathbf{S}^n - \frac{\partial \mathbf{F}^n}{\partial \mathbf{U}^n} \frac{\partial \mathbf{F}^n}{\partial x} \right) + \frac{\partial \mathbf{S}^n}{\partial \mathbf{U}^n} \frac{\partial \mathbf{F}^n}{\partial x} - \frac{\partial \mathbf{S}^n}{\partial \mathbf{U}^n} \mathbf{S}^n \right] \quad (5)$$

where \mathbf{U} , \mathbf{F} and \mathbf{S} are vectors of the primitive variables, conservative variables and source term respectively. The semi-discrete form will then be further discretised using the LCG finite element method. As with the global Galerkin method, each of the variables is approximated by the standard finite element spatial discretisation. The interface flux can be reintroduced via integration by parts and contained contributions from convective component. In order to achieve local conservation, a simple averaging post-processing procedure is introduced at each time step. The post-processing procedure uses the nodal values from the continuous solution obtained from the previous time-step to provide an accurate interface flux and also establishes connectivity between elements at the next time-step. Full discrete form of the governing equations is shown in [4, 5, 6].

3 RESULTS AND DISCUSSIONS

In this paper, fusiform thoracic aortic aneurysms of size 5cm, 10cm and 15cm as seen in Figure (1) are used to replace the normal aorta of an arterial network [4]. The reason to use such unrealistic size is mainly to justify that aneurysm can affect the blood flow in human body. The blood density and dynamic viscosity were taken to be $\rho = 1060 \text{ kg/m}^3$ and $\mu = 0.035 \text{ poise}$ respectively [4]. A realistic ventricular pressure will act as an input to the model and a detailed description can be found in [4]. Results are computed for one cardiac cycle (0.8s) ‘at rest’ state using all the three different aneurysm sizes stated previously.

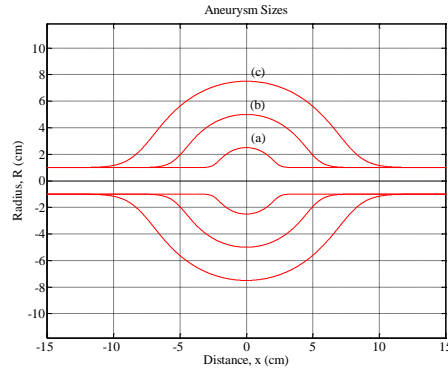


Figure 1: Geometry visualisation of aneurysm sizes of (a) 5cm, (b) 10cm and (c) 15cm respectively.

Figure (2a) shows various waveforms plotted. The first plot compares input pressure, the afterload-corrected left ventricular pressure and the ascending aortic pressure. The second and third plots show the pressure difference and ascending aorta flow respectively. Fourth and fifth plots visualise the left and right coronary flow. The first and second plots of Figure (2b) show the pressure and flow along the aorta respectively. The impact of aneurysm can be shown by the disturbance in waves and similar phenomenon can be found in [2]. Positive and negative wave reflections are found due to the sudden widening of the aorta and they increase significantly as the widening gets larger. The coronary arteries are affected as the distance between the coronary arteries and the location of the aneurysm is small.

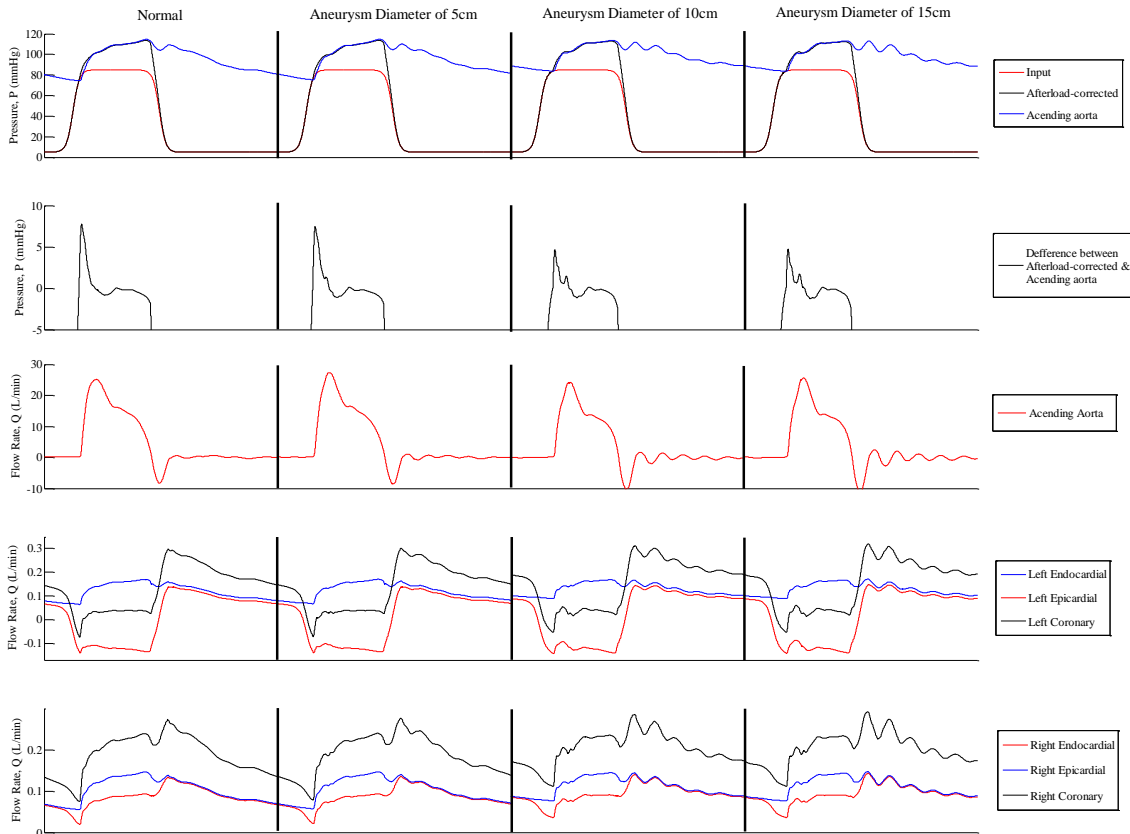


Figure 2a: Simulations of normal and various aneurysm sizes for one cardiac cycle (0.8s) where the medical terms can be shown in [3].

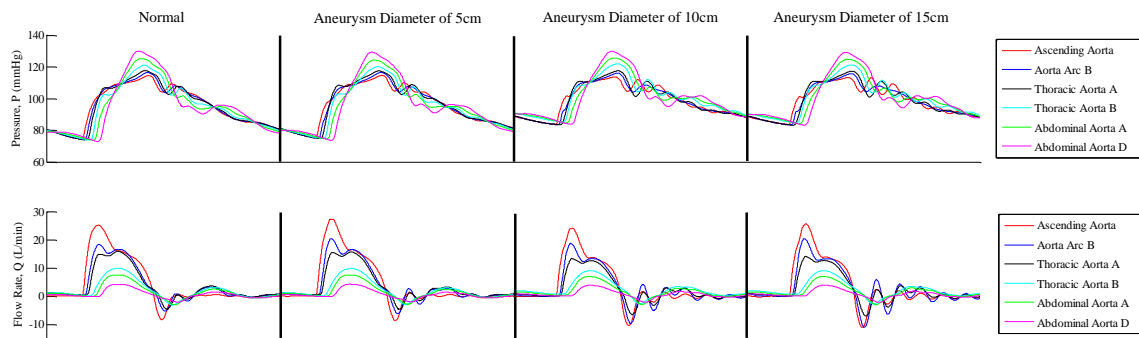


Figure 2b: Simulations of normal and various aneurysm sizes for one cardiac cycle (0.8s) where the medical terms can be shown in [3].

4 CONCLUSIONS AND FUTURE WORK

A 1D model of the human arterial system using the LCG finite element method is presented for normal ‘at rest’ state, for aneurysm sizes of 5cm, 10cm and 15cm. It should be noted that the aim of this paper is to identify arterial waveforms in the presence of a TAA. The example above showed that wave reflections occur when there is a sudden widening in an artery. Future work includes studying the influences of different aneurysm and stenosis shapes.

Acknowledgement

This work is partially funded by Levelhulme Trust grant F/00391/R. The first author acknowledges the financial support received from the College of Engineering.

References

- [1] J.C. Lasheras. The biomechanics of arterial aneurysms. *Annual Review of Fluid Mechanics*, 39, 293-319, 2007.
- [2] A. Swillens, L. Lanoye, J.D. Backer, N. Stergiopoulos, P.R. Verdonck, F. Vermassen and P. Segers. Effect of an abdominal aortic aneurysm on wave reflection in the aorta. *IEEE Transactions on Biomedical Engineering*, 55(5), 1602-11, 2008.
- [3] K.S. Matthys, J. Alastruey, J. Peiro, A.W. Khir, P. Segers, P.R. Verdonck, K.H. Parker and S.J. Sherwin. Pulse wave propagation in a model human arterial network: assessment of 1-D numerical simulations against in vitro measurements. *Journal of Biomechanics*, 40(15), 3476-3486, 2007.
- [4] J.P. Mynard and P. Nithiarasu. A 1D arterial blood flow model incorporating ventricular pressure, aortic valve and regional coronary flow using the locally conservative Galerkin (LCG) method. *Communications in Numerical Methods in Engineering*, 24, 367-417, 2008.
- [5] C.G. Thomas and P. Nithiarasu. An element-wise, locally conservative Galerkin (LCG) method for solving diffusion and convection-diffusion problems. *International Journal for Numerical Methods in Engineering*, 73, 642-664, 2008.
- [6] C.G. Thomas, P. Nithiarasu and R. L. T. Bevan. The locally conservative Galerkin (LCG) method for solving the incompressible Navier-Stokes equations. *International Journal for Numerical Methods in Engineering*, 57, 1771-1792, 2008.
- [7] S.J. Sherwin, V. Franke and J. Peiro. One-dimensional modelling of a vascular network in space-network variables. *Journal of Engineering Mathematics*, 47(3), 217-250, 2003.

RESPONSE OF A TUNNEL DEEPLY EMBEDDED IN A VISCOELASTIC MEDIUM

*Thomas J. Birchall¹ and Ashraf S. Osman¹

¹School of Engineering and Computing Sciences, Durham University, South Road, Durham, DH1 3LE

*t.j.birchall@durham.ac.uk

Key Words: viscoelasticity; creep; tunnels; energy-based solution.

ABSTRACT

This paper presents a three-dimensional energy-based solution for the time-dependent creep response of a deeply embedded and unsupported tunnel, of circular cross-section. Rock behaviour is described in the Laplace domain using Burger's viscoelastic model. The differential equations governing the displacements of the tunnel-rock system and appropriate boundary conditions are obtained using the principle of minimum potential energy. The method produces results with accuracy comparable to that of a finite element analysis but requires much less computation effort.

1 INTRODUCTION

When tunnelling in salt rock or potash in a mining environment, significant time-dependent tunnel closure can occur, as the deformation of these weak rocks is dominated by creep. Creep is also the prime mechanism causing ground squeezing in sheared or faulted rock masses containing mylonite or clay gouge. The efficient and accurate prediction of the time-dependent performance of tunnels located in such rock is a main concern in the design. However, the full three-dimensional (3D) interaction between a tunnel and the surrounding creeping rock is complex. Finite element (FE) analysis with advanced constitutive models can be used to accurately predict the time-dependent response (e.g. [1]), but such analyses are computationally expensive for routine practice. An alternative approach is to idealise the problem as a two-dimensional (2D) plane-strain problem using empirical relations based on field measurements or 3D FE analyses to predict the stresses and displacements in close proximity to the tunnel face (e.g. [2]). However, there are significant uncertainties in extrapolating these empirical relations to different design situations and rock behaviour.

Here we present a 3D approximate solution for the time-dependent response of a semi-infinite and unsupported tunnel which is excavated quasi-instantaneously from a homogeneous, isotropic, viscoelastic, infinite rock body. The rock is assumed to behave volumetrically linear elastic and to exhibit exclusively deviatoric creep which is modelled by the classical Burger's model. The initial in-situ stresses are taken to be isotropic. The potential energy of the tunnel-rock system is expressed in terms of an assumed displacement field. The principle of minimum potential energy is used to obtain the differential equations governing the ground deformation and appropriate boundary conditions.

Burger's model is the simplest linear viscoelastic model that can be used to trace primary and secondary creep deformation. According to Goodman [3] this model is preferable for many practical purposes. This model can be characterised by linear elastic volumetric behaviour and viscoelastic deviatoric behaviour. The relationship between the deviatoric stress s_{ij} and deviatoric strain e_{ij} in the Laplace domain is:

$$\hat{s}_{ij} = 2 \left(\frac{(\eta_1 s^2 + k_1 s)}{\left(\frac{\eta_1}{G_2} \right) s^2 + \left[1 + \left(\frac{G_1}{G_2} \right) + \left(\frac{\eta_1}{\eta_2} \right) \right] s + \left(\frac{G_1}{\eta_2} \right)} \right) \hat{e}_{ij} \quad (1)$$

where

$$\hat{f}(s) = \int_0^{\infty} f(t)e^{-st} dt \quad (2)$$

and where a Kelvin unit is characterized by its shear modulus G_1 and viscosity η_1 , and a Maxwell unit is characterized by its shear modulus G_2 and viscosity η_2 . These creep model parameters can be obtained from laboratory creep experiments.

The differential equations for the rock displacements can be expressed in the Laplace domain and the solution can then be back-transformed into the time domain.

2 ANALYSIS

We consider a tunnel of circular cross-section and radius r_0 (Figure 1(a)). We focus here on the prediction of creep behaviour after the creation of the cylindrical cavity, thus the excavation of the tunnel is assumed to take place instantaneously. The rock surrounding the tunnel is divided into three zones (Figure 1(a)).

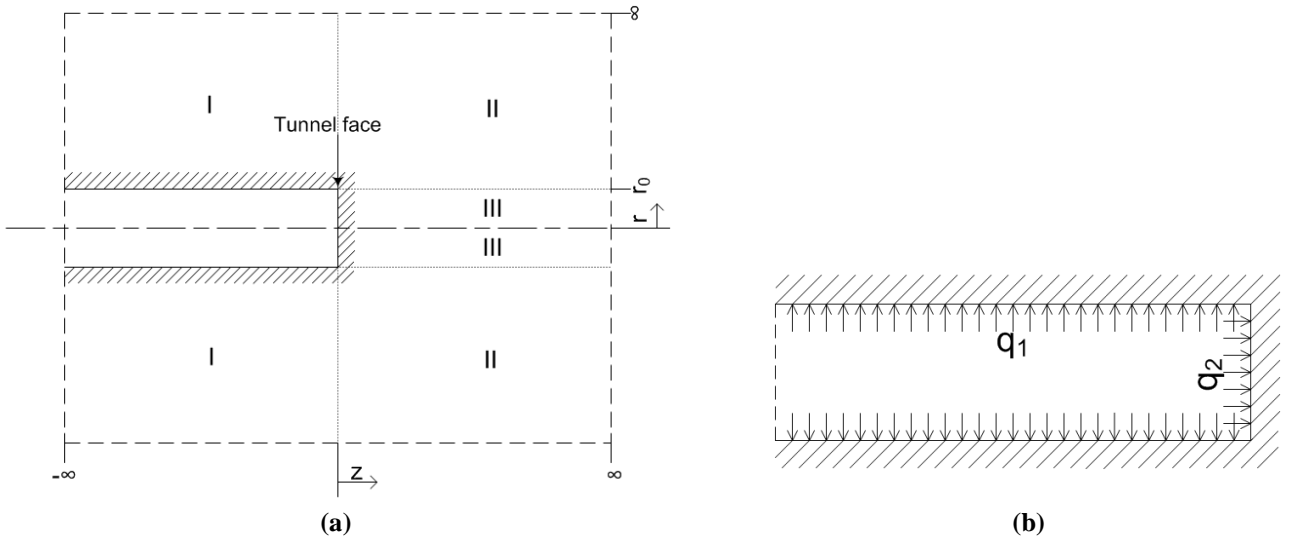


Figure 1: (a) Model geometry and location of zones in which energy is dissipated; (b) Applied pressure.

The displacement field around the cavity is expressed as the product of two separate variables r and z (Table 1), where u_r and u_z are the radial and the longitudinal displacements, respectively. The ψ terms are functions describing the variation of the radial and the longitudinal displacement in the z -direction. The ϕ terms are functions describing the attenuation of rock displacement away from the tunnel axis. As $z \rightarrow -\infty$ the plane-strain condition can be assumed, therefore $\frac{d\psi_{r1}}{dz} = 0$ and $\psi_{z1}(z) = 0$. At a far distance ahead of the tunnel face the displacement reduces to zero, therefore $\psi_{r2}(z) = 0$ and $\psi_{z2}(z) = 0$ as $z \rightarrow \infty$. It is assumed that $\phi_1(r) = 1$ and $\phi_2(r) = 1$ at $r = r_0$ and $\phi_1(r) = 0$ and $\phi_2(r) = 0$ as $r \rightarrow \infty$ (to ensure that rock displacements decrease with radial distance away from the tunnel wall). Finally, it is assumed that $\phi_3(r) = 0$ at $r = 0$ and $\phi_3(r) = 1$ at $r = r_0$ (to ensure compatibility ahead of the tunnel face).

| zone | bounds | $u_r(r, z)$ | $u_z(r, z)$ |
|------|-----------------------------------------------------|-------------------------|-------------------------|
| I | $r_0 \leq r \leq \infty$ $-\infty \leq z \leq 0$ | $\phi_1(r)\psi_{r1}(z)$ | $\phi_2(r)\psi_{z1}(z)$ |
| II | $r_0 \leq r \leq \infty$ $0 \leq z \leq \infty$ | $\phi_1(r)\psi_{r2}(z)$ | $\phi_2(r)\psi_{z2}(z)$ |
| III | $0 \leq r \leq r_0$ $0 \leq z \leq \infty$ | $\phi_3(r)\psi_{r2}(z)$ | $\psi_{z2}(z)$ |

Table 1: Displacements u_r and u_z for each of the rock zones.

The potential energy U of the tunnel-rock system for a linear elastic rock is given by:

$$U = \frac{1}{2} \int_{r_0}^{\infty} \int_0^{2\pi} \int_{-\infty}^{\infty} (\sigma_{rr} \varepsilon_{rr} + \sigma_{\theta\theta} \varepsilon_{\theta\theta} + \sigma_{zz} \varepsilon_{zz} + \tau_{zr} \gamma_{zr}) r dz d\theta dr + \frac{1}{2} \int_0^{r_0} \int_0^{2\pi} \int_{-\infty}^{\infty} (\sigma_{rr} \varepsilon_{rr} + \sigma_{\theta\theta} \varepsilon_{\theta\theta} + \sigma_{zz} \varepsilon_{zz} + \tau_{zr} \gamma_{zr}) r dz d\theta dr \quad (3)$$

where the first integral term represents the internal potential energy of the rock in zones I and II and the second term represents the energy in zone III. Stress-strain relations and strain-displacement relations in cylindrical coordinates, along with the assumed displacement field can then be used to obtain an expression for U in terms of the displacements. Variational principles are then used to obtain expressions for δU and δW . The variation in the external work W is given by:

$$\delta W = \int_0^{2\pi} \int_{-\infty}^0 q_1 r_0 \delta \psi_{r1} dz d\theta + q_2 \pi r_0^2 \delta \psi_{z1} \quad (4)$$

The governing deformation equations can be derived by minimising the energy in the tunnel-rock system:

$$\delta \Pi = \delta U - \delta W = 0 \quad (5)$$

Setting the first variable of the total energy Π equal to zero produces an equation of the form:

$$\delta \Pi = [A(\phi_1) \delta \phi_1] + [B(\phi_2) \delta \phi_2] + [C(\phi_3) \delta \phi_3] + [D(\psi_{r1}) \delta \psi_{r1}] + [E(\psi_{z1}) \delta \psi_{z1}] + [F(\psi_{r2}) \delta \psi_{r2}] + [G(\psi_{z2}) \delta \psi_{z2}] = 0 \quad (6)$$

Since the variations $\delta \phi_1, \delta \phi_2, \delta \phi_3, \delta \psi_{r1}, \delta \psi_{z1}, \delta \psi_{r2}, \delta \psi_{z2}$ are independent, the terms associated with each variation must be equal to zero (e.g. $A(\phi_1) \delta \phi_1 = 0$) to satisfy $\delta \Pi = 0$. Collection of these terms over the related rock domains (e.g. collecting the $\delta \phi_1$ terms for $r_0 \leq r \leq \infty$) forms the differential equations which govern the displacements of the tunnel-rock system. Since the variations are non-zero over the rock domains, the coefficients of the terms must be equal to zero (e.g. $A(\phi_1) = 0$ as shown in equation 7).

$$r \frac{d^2 \phi_1}{dr^2} + \frac{d\phi_1}{dr} - \frac{\phi_1}{r} - \gamma_1 r \phi_1 + \gamma_2 r \frac{d\phi_2}{dr} = 0 \quad (7)$$

Expressions for the boundary conditions are formed by collecting the terms associated with each variation at the appropriate boundaries (e.g. collection of the $\delta \phi_1$ terms at $r=r_0$ and at $r=\infty$). Similarly the remaining governing equations and boundary conditions can be formulated by collection of the other variations. An iterative scheme (Figure 2) is used to solve the governing equations in the Laplace domain. The γ_1 to γ_5 terms in the equations must be sought. Solutions to the differential equations are obtained analytically and numerically using a one-dimensional (1D) finite difference (FD) technique.

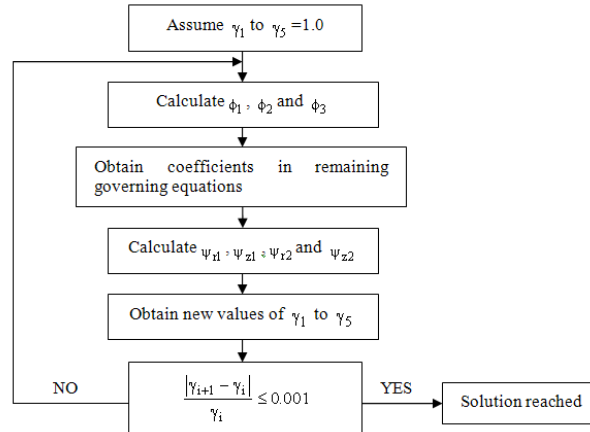


Figure 2: Flowchart of solution procedure for each value of time t.

Displacements are then back-transformed into the time domain using de Hoog's efficient numerical inversion algorithm [4]. A computer program was written using MATLAB to carry out these calculations.

3 RESULTS

The parameters used in the analyses presented here are $r_0=4.57$ m, $q_1=q_2=6.897$ MPa, $\nu=0.2$, $G_1=344.86$ MPa, $\eta_1=239486.1$ MPa Day, $G_2=3448.6$ MPa and $\eta_2=47897222.2$ MPa Day. Figure 3 compares the radial displacement of the proposed energy-based solution with other methods. Figure 3(a) shows that in the plane-strain condition the proposed solution has good agreement with the closed form solution derived by Fahimifar et al. [2]. Figure 3(b) shows that in the region close to the tunnel face the proposed analysis yields results that are comparable with FE analysis and field data.

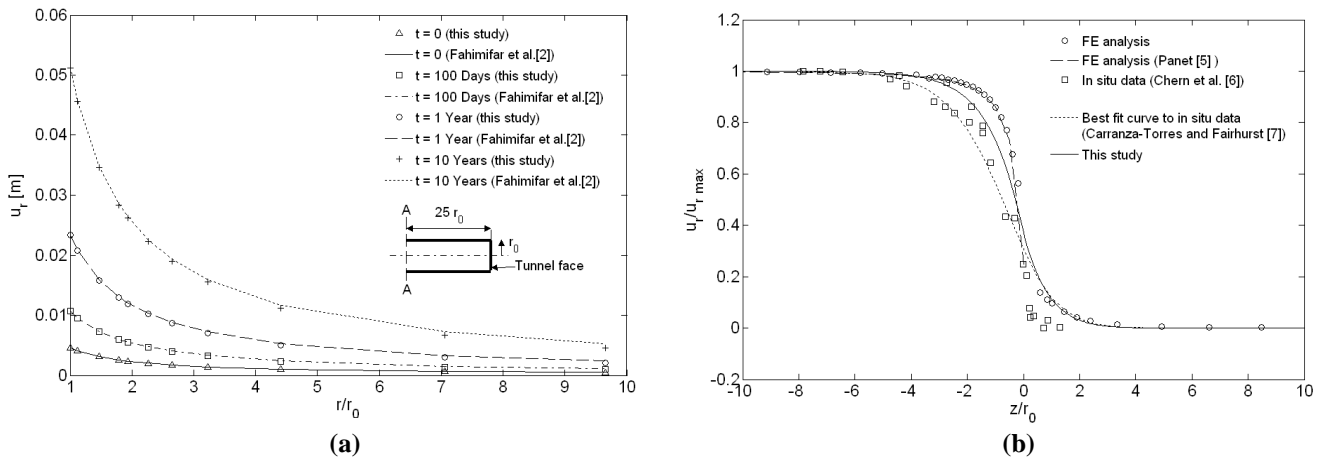


Figure 3: Comparison of radial displacement with: (a) closed form solution; (b) FE analysis and field data ($t=0$).

4 CONCLUSION

A 3D approximate solution for the time-dependent convergence of a deeply embedded and unsupported circular tunnel, driven in a linear viscoelastic rock, was presented. This new approach is comparable with FE analysis, but is faster. In addition the input to our method is accomplished through a simple text file, while the geometry and optimal meshing for an FE analysis requires considerable time. Here Burger's model has been used to describe rock behaviour, however a wide range of constitutive models can be incorporated into this analysis. This new method can be used for the initial design of tunnels.

References

- [1] J. Ghaboussi and G. Gioda. On the time dependent effects in advancing tunnels. *International Journal for Numerical and Analytical Methods in Geomechanics*, 1, 249-269, 1977.
- [2] A. Fahimifar, F.M. Tehrani, A. Hedayat, A. Vakilzadeh. Analytical solution for the excavation of circular tunnels in a visco-elastic Burger's material under hydrostatic stress field. *Tunnelling and Underground Space Technology*, 25(4), 297-304, 2010.
- [3] R.E. Goodman, *Introduction to Rock Mechanics*, 2nd Edition, Wiley: New York, 1989.
- [4] F.R. de Hoog, J.H. Knight, A.N. Stokes. An improved method for numerical inversion of Laplace transforms. *SIAM (Society for Industrial and Applied Mathematics) Journal on Scientific and Statistical Computing*, 3(3), 357-366, 1982.
- [5] M. Panet, *Le calcul des tunnels par la method convergence-confinement*. Presses de l'Ecole Nationale des Ponts et Chaussees, Paris, France, 1995.
- [6] J.C. Chern, F.Y. Shiao, C.W. Yu. An empirical safety criterion for tunnel construction. In Proc. *Regional Symposium on Sedimentary Rock Engineering*, Taipei, Taiwan, 222-227, 1998.
- [7] C. Carranza-Torres and C. Fairhurst. Application of the convergence-confinement method of tunnel design to rock masses that satisfy the Hoek-Brown failure criterion. *Tunneling and Underground Space Technology*, 15(2), 187-213, 2000 (Personal communication with Hoek).

MODELLING 3D PUNCH INDENTATION USING DISCONTINUITY LAYOUT OPTIMIZATION

*Samuel J. Hawksbee¹, Matthew Gilbert¹ and Colin Smith¹

¹Department of Civil and Structural Engineering, University of Sheffield, Sir Frederick Mappin
Building, Mappin Street, Sheffield S1 3JD, UK

*cip09sjh@sheffield.ac.uk

Key Words: *geomechanics; limit analysis; discontinuity layout optimization; bearing capacity*

ABSTRACT

Discontinuity layout optimization (DLO) is a recently developed analysis procedure which has been successfully used to obtain highly accurate limit analysis solutions for a wide range of two-dimensional problems. Here the changes necessary to allow three-dimensional analysis problems to be tackled using DLO are briefly outlined. The resulting formulation involves the use of polygonal potential discontinuities connecting any set of co-planar nodes, along which velocity jumps are permitted. Compatibility is enforced along the edges of the polygonal discontinuities and the minimum collapse load for a given nodal discretization, together with the corresponding collapse mechanism, can be obtained using efficient second order cone programming algorithms. The mechanism produced comprises rigid blocks bounded by the potential discontinuities. In order to validate the formulation, and to demonstrate the potential of the method, the well-known problem of a rough punch bearing on a weightless cohesive material is solved. Despite the use of comparatively coarse nodal discretizations, it is shown that the solutions obtained compare well with published results.

1 INTRODUCTION

Limit analysis is concerned with determining the collapse load of a body or structure. Bounds on the exact collapse load can be obtained by assuming a rigid-plastic material model. Lower bounds can be obtained by enforcing stress equilibrium and yield criteria whilst upper bounds can be obtained by imposing compatibility constraints and the flow rule. Whilst a wide range of computational limit analysis procedures have been developed over the years, here the extremely promising Discontinuity Layout Optimization (DLO) procedure is considered. Originally presented by Smith & Gilbert [?] as a means of obtaining upper bound solutions for plane strain limit analysis problems, DLO has not yet been applied to three dimensional problems. However, in the current contribution the potential for DLO to be applied to three dimensional problems is explored, with the procedure applied to an example problem involving a rough square based punch resting on a weightless cohesive (Tresca) material.

2 DLO FORMULATION

A basic explanation of the plane strain DLO formulation will initially be given with reference to the simple example problem shown in Figure 1; the alterations necessary to permit three dimensional analysis will then be briefly outlined. In Figure 1, a surcharge is applied to a block of soil close to a vertical cut. The area occupied by the block of soil is first populated with nodes as shown in Figure 1(b), with each pair of nodes then interconnected with potential linear discontinuities as shown in Figure 1(c). The critical failure mechanism for the given nodal discretization can then be identified, Figure 1(d).

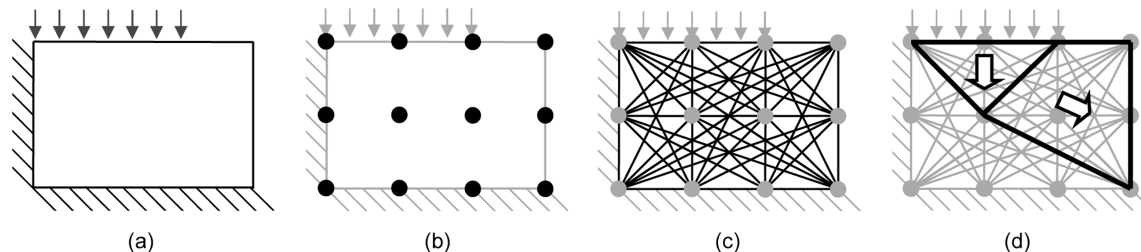


Figure 1: Stages in DLO procedure: (a) starting problem (surcharge applied to block of soil close to a vertical cut); (b) discretization of soil using nodes; (c) interconnection of nodes with potential discontinuities; (d) identification of critical subset of potential discontinuities using optimization (giving the layout of slip-lines in the critical failure mechanism) (after Gilbert et al. [?])

| Reference | Bearing Capacity Factor | |
|----------------------|-------------------------|-------------------------|
| | Other | Lower bound Upper bound |
| Skempton [?] | 6.17 ^a | |
| Gourvenec et al. [?] | | 6.41 |
| | 5.91 ^b | |
| Michalowski [?] | | 6.56 |
| Salgado et al. [?] | 5.52 | 6.22 |
| Present study (DLO) | | 6.42 |

a. Empirical

b. Elasto-plastic finite element

Table 1: Selected published results for a rough square based punch on weightless cohesive (Tresca) material

From Smith & Gilbert [?], the primal kinematic DLO formulation can be written as:

$$\min \lambda \mathbf{f}_L^T \mathbf{d} = -\mathbf{f}_D^T \mathbf{d} + \mathbf{g}^T \mathbf{p}$$

subject to

$$\begin{aligned} \mathbf{B}\mathbf{d} &= \mathbf{0} \\ \mathbf{N}\mathbf{p} - \mathbf{d} &= \mathbf{0} \\ \mathbf{f}_L^T \mathbf{d} &= 1 \\ \mathbf{p} &\geq \mathbf{0} \end{aligned} \tag{1}$$

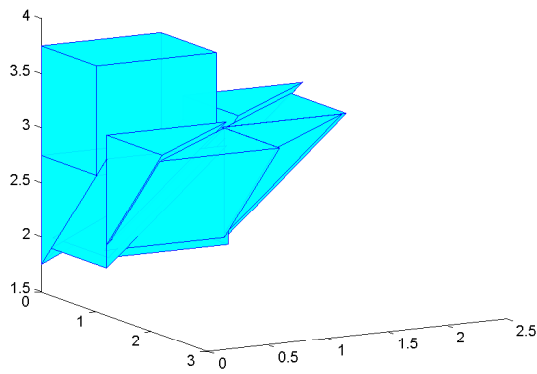
where the problem is formulated in terms of the change in velocity across the potential discontinuities $\mathbf{d}^T = \{s_1, n_1, s_2, n_2, \dots, n_m\}$ and plastic multipliers $\mathbf{p}^T = \{|s_1|, |s_2|, \dots, |s_m|\}$, where s_i and n_i are the shear and normal changes in velocity across discontinuity i and m is the number of discontinuities. \mathbf{B} is a matrix enforcing compatibility at each node while \mathbf{N} enforces the flow rule (associated to the yield criteria). \mathbf{f}_L and \mathbf{f}_D are vectors of live and dead loads respectively and $\mathbf{g}^T = \{c_1 l_1, c_2 l_2, \dots, c_m l_m\}$ where c_i and l_i are the cohesive strength and length of discontinuity i . (A dual equilibrium formulation can also be derived; the reader is referred to Smith & Gilbert [?] for further information.)

The goal is to identify the minimum load factor λ and its associated mechanism, which can be obtained using a suitable linear programming package. The mechanism must consist of rigid blocks bounded by potential discontinuities along which changes in velocity are permitted as illustrated by Figure 1(d). The changes necessary to the formulation for three dimensional analysis are summarized below.

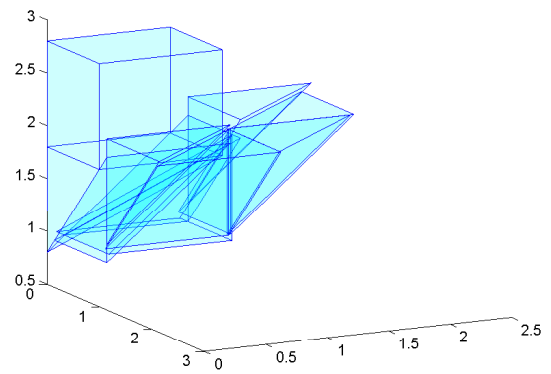
1. Potential discontinuities must now be polygonal rather than linear in form.
2. Three variables per potential discontinuity are now necessary to fully specify the change in velocity at each potential discontinuity (one normal and two shear components). \mathbf{d}^T now becomes $\{s_{11}, s_{12}, n_1, s_{21}, s_{22}, n_2, \dots, n_m\}$, where s_{i1} and s_{i2} are the two shear components of change in velocity across discontinuity i .
3. The resultant of the shear components at each discontinuity must now be calculated in order to find the energy dissipated. This can be done using a conic restraint, $s_{ir} \geq \sqrt{s_{i1}^2 + s_{i2}^2}$; where s_{ir} is the resultant shear change in velocity across discontinuity i . \mathbf{p}^T now becomes $\{s_{1r}, s_{2r}, \dots, s_{rm}\}$.
4. \mathbf{g}^T now equals $\{c_1 a_1, c_2 a_2, \dots, c_m a_m\}$, where a_i is the area of discontinuity i .
5. Compatibility is now conveniently enforced along each edge rather than at each node.
6. A cone programming package must now be used to obtain the minimum.

3 3D PUNCH INDENTATION PROBLEM

To investigate the efficacy of the DLO formulation the well known 3D punch indentation problem is now considered. A rough square based punch, 2 units width, resting on a block of weightless cohesive material, 4 units width and 2 units depth, was analysed though by taking advantage of symmetry only a quarter of the original problem needed to be modelled. The problem was aligned with the x , y and z axis populated with nodes at 1 unit spacings in the x , y and z directions. An optimization problem was then set up using the formulation described previously using MATLAB 7.3.0. The MOSEK optimizer [?], was used to obtain the minimum load factor, equal to the bearing capacity factor. The associated failure mechanism is shown in Figure 2. A bearing capacity factor equal to 6.424 was obtained, which compares reasonably well with the published results for this problem presented in Table 1. This is perhaps slightly surprising considering the very low nodal resolution adopted in this initial study. (Note that the best upper bound solution in the literature was obtained by Salgado et al. [?] using finite element limit analysis.)



(a) opaque discontinuities



(b) translucent discontinuities

Figure 2: Deformed mechanism for rough square based punch (showing a quarter of the square punch)

4 CONCLUSIONS

DLO has been used to obtain upper bounds on the bearing capacity of a rough square based footing resting on weightless cohesive material. The upper bound solution obtained compares reasonably well with the best published upper bound solution, which seems remarkable considering the low nodal resolution employed in this preliminary study. The potential for DLO to be used to obtain upper bound solutions for three dimensional problems has therefore been established and further work is now necessary to ensure this potential is properly realised.

References

- [1] C. Smith and M. Gilbert. Application of discontinuity layout optimization to plane plasticity problem. *Proc. Roy. Soc. A.* 463(2086), 2461-2484, 2007.
- [2] Skempton, A.W. The bearing capacity of clays. *Proc., Building and Research Congress*, Vol 1, London, 180-189.
- [3] S. Gourvenec, M. Randolph and O. Kingsnorth. Undrained bearing capacity of square and rectangular footings. *Int. J. Geomech.*, 6(3), 2006.
- [4] R. L. Michalowski. Upper bound load estimates on square and rectangular footings. *Geotechnique*, 51(9), 787-798, 2002.
- [5] R. Salgado, A.V. Lyamin, S.W. Sloan, and H.S. Yu. Two and three-dimensional bearing capacity of foundations on clay. *Geotechnique*, 54(5), 297-306, 2004.
- [6] M. Gilbert, C.C. Smith, I. Haslam, and T. Pritchard. Application of discontinuity layout optimization to geotechnical limit analysis. *Proc. 7th Eur. Conf. Num. Meth. Geotech. Eng.*, 2010.
- [7] Mosek ApS. The MOSEK optimization toolbox for MATLAB manual. Version 6.0 (revision 85), 2010 [See <http://mosek.com>]

Using Finite Element Modelling to Assess Submarine Slope Stability

*Morelia Urlaub¹, Antonis Zervos², Peter J. Talling¹, Doug G. Masson¹ and Chris I. Clayton²

¹National Oceanography Centre, Southampton, European Way, Southampton, SO14 3ZH

²School of Civil Engineering and the Environment, University of Southampton, SO17 1BJ

*m.urlaub@noc.soton.ac.uk

Key Words: *slope stability; geomechanics; finite elements; critical state; deep sea*

ABSTRACT

Submarine landslides are not only a hazard for the offshore oil and gas industry or telecommunication cables at continental shelves, slopes or deeper water, but also have the potential to trigger tsunamis. They are much larger than their counterparts on land and occur on extremely low slope angles (typically 1 – 2°). Initiation mechanisms for these slides are vital for their prediction but are poorly understood, and in-situ investigations are restricted by a hundreds of meters thick water column. One idea is that rapid asymmetric deposition of sediment on the sea floor causes high rates of overpressure in a low permeability and low stiffness material as typical for marine sediments. We use transient, coupled finite element analysis to predict how the stress state of a submerged finite 2° slope that is subjected to slow continuous, asymmetric loading, changes over time as well as to assess the stability of the slope. The model is used to investigate the emergence of slope instability for different hydraulic conductivities, giving insights into the field conditions necessary for the development of submarine slope failure by overpressure alone.

1 INTRODUCTION

Submarine slope failures that occur at the transition from continent into the deep sea can be far larger than any terrestrial slope failure on land (the Storegga Slide offshore Norway is more extensive than Scotland and contains 300 times the annual sediment load from all of the worlds rivers). Perhaps the most remarkable feature of these huge continental slope failures is that they occur in locations worldwide on gradients of just 2° or less. We are yet to monitor one of these huge underwater landslides in action, and the reason(s) for such large-scale failure on such low gradients are contentious. Scientific drilling in the Gulf of Mexico recently confirmed that high excess pore pressures can be generated in areas of rapid (up to 360 kPa per 1,000 years) sediment accumulation. Low permeabilities prevent sufficiently rapid dewatering and excess pore pressures are produced that are up to 70 % of the lithostatic weight [3]. It might therefore be proposed that rapid sediment accumulation generating high excess pore fluid pressures is a major reason for large-scale submarine slope failure on low (2°) gradients. However, large-scale slope failures also occur on continental margins with much slower sediment accumulation

rates, such as off the coast of Northwest Africa [1]. Deposition rates in this area do not exceed 1.8 kPa per 1,000 years.

Here we undertake a sensitivity analysis of how sediment accumulation rate and permeability influence the stability of low-angle submarine slopes. For this we use a 2D plane strain finite element slope stability model set up in ABAQUS. The model operates on extremely large spatial and temporal scales (modelling several hundreds of kilometers over geological time periods) and includes progressive asymmetric loading. Specific material properties for marine sediments are applied, where necessary via FORTRAN subroutines.

2 FINITE ELEMENT MODELLING

We use the Modified Cam Clay model [8] that is provided in ABAQUS. The slope of the critical state line, M , is calculated from the friction angle, ϕ_{crit} , assuming a purely compressive stress path in plane strain conditions [7]. The sediment is cohesionless and its coefficient of Earth pressure, K_0 , is given by $K_0 = 1 - \sin\phi_{crit}$ [5]. Table 1 lists independent parameters defining the constitutive model.

| Notation | | Value | Reference |
|---------------------------------|------------------------------|-------|--------------------------------------------------------------------------------------------------------------------------------|
| κ | Swelling index | 0.027 | [9, 2] |
| ν | Poisson ratio | 0.3 | [6] |
| λ | Compression index | 0.28 | [9, 2] |
| ϕ'_{crit} [°] | Friction angle | 28 | [9] |
| M | Slope of critical state line | 0.87 | $M = \frac{\sin\phi'_{crit} \cdot 6 \cdot \sqrt{1-b+b^2}}{3 + \sin\phi'_{crit} \cdot 2b - \sin\phi'_{crit}}$, $b = 0.5$, [7] |
| γ_w [kN/m ³] | Specific fluid weight | 10.24 | |
| g [m/s ²] | Gravity | 9.81 | |

Table 1: Spatially and temporarily constant input parameters used in the Modified Cam Clay constitutive model.

A simplified continental margin geometry is adopted (Fig. 1). The area is modelled as one layer without abrupt material changes and only vertical (not lateral) density and permeability gradients. The model domain is partitioned into two regions for meshing purposes. Region 1 comprises the upper 500 m of the sea floor and region 2 covers the deeper part. The mesh consists of 76,050 rectangular plane strain elements and 238,347 nodes. Elements have a size of 10 x 10 m at the sea floor, whilst a coarser mesh size (100 x 100 m) was adopted in region 2 as changes in mechanical properties are less pronounced at these deeper levels [4, 6]. Element sizes further increase towards the model's bottom as well as towards the side boundaries.

Sea floor sediments have an initial void ratio, e , of 3.0 (75 % volume porosity). Sediment porosity, ϕ , and void ratio are related by $\phi = e/(1 + e)$. In region 1 ϕ is defined by $\phi = 0.75 - 0.987z + 0.83z^2$, where z [km] is the depth below the sea floor. This is based on [4]'s empirical porosity relationship for calcareous sediments. In region 2 porosity decreases linearly from 40 % at 500 m below the sea floor, to 10 % at 5000 m below the sea floor. Permeability depends linearly on void ratio and is anisotropic. The horizontal sediment permeability, k_x for $e = 3.0$, i. e. at the sea floor before burial, is 10^{-8} m/s based on oedometer measurements of calcareous sediments compiled by [2]. [10] found vertical permeabilities, k_y , as low as 10^{-13} m/s for mudstones with 40 % porosity, which we use as the lower limit for k_y variations. In order to explore model sensitivity we keep the permeability at the sea floor and in region 2 constant ($k_x = 10^{-8}$ and $k_x = 10^{-12}$, respectively) and vary k at 500 m as well as the anisotropy coefficient, k_x/k_y . Dry density, ρ_{dry} , is directly linked to e as well. At the sea floor $\rho_{dry} = 670$ kg/m³, corresponding to a specific weight, γ , of 1.2 kN/m³. For $e = 0.67$ (500 m below sea floor) $\rho_{dry} =$

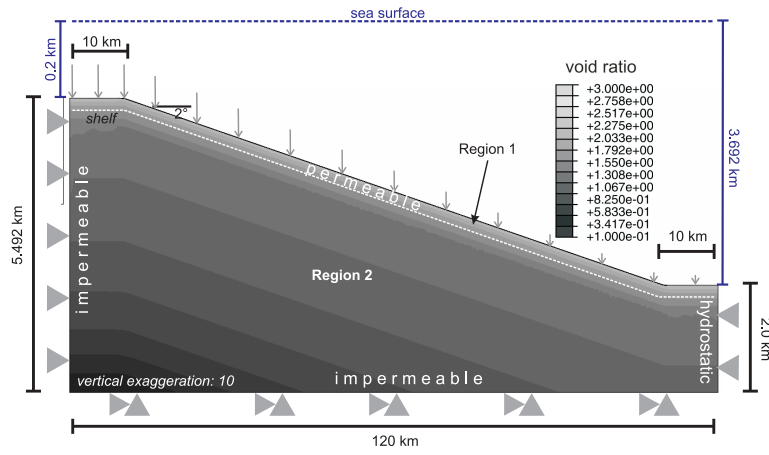


Figure 1: 2D slope model geometry (not to scale) with boundary and loading conditions. Sediment deposition decreases from the shallow end towards the deep sea (grey vertical arrows). Grey shadings represent the initial void ratio (logscale) on which permeability and density depend linearly.

1400 kg/m^3 and $e = 0.1$ (bottom of model) $\rho_{dry} = 1760 \text{ kg/m}^3$. The sediment is assumed fully saturated and normally consolidated. To account for an overconsolidation rate of 1 the size of the yield locus, p_c , is calculated based on the stress state of each node.

The bottom boundary is impermeable and fixed in the vertical and horizontal directions. The landward edge is impermeable as it represents a flow divide, assuming groundwater influence nearer to the continent. The pore pressure at the deep sea side boundary is hydrostatic so that flow into or out of the model is allowed. Both side boundaries are fixed in the horizontal. The sea floor is free to move in any direction and is permeable. However, as deposited sediment is simulated as a surface load the flow normal to the surface is governed by the pore pressure gradient and the vertical permeability. We include gravity and consequently model total pore pressures. The water column is represented as a hydrostatic pressure load on the sea floor, such that there is zero effective stress at the sea floor. Sedimentation is simulated by progressively adding a vertical surface load that decreases from the shelf edge towards the deep sea. Along the shelf the rate is uniform. The decrease is exponential ($e^{-0.032x}$, where $x [km]$ is the distance from the shelf edge), based upon thinning rates of seismic sequences in [1]. $\gamma = 12 \text{ kN/m}^3$ was assumed for the newly deposited fully saturated sediment corresponding to a dry density of 670 kg/m^3 . The peak sedimentation rate at the shelf edge is 0.15 m/ka which equals 1800 kPa over 1 Ma .

3 RESULTS

Several numerical experiments with different vertical permeability gradients and anisotropy ratios were run for 1 Ma . Slope stability is evaluated by analysing vertical effective stress, σ'_v , overpressure ratio (excess pore pressure normalised to σ'_v), u^* , and Factors of Safety (FoS, ratio of available to mobilised strength). In summary, all models are stable. All simulations show an expected increase in vertical effective stress and pore pressure due to overburden. Fluid flow patterns vary within the different models and lateral flow is observed in the models with permeability anisotropy but does not generate significant overpressure ratios at the lower slope. Where permeability is isotropic, fluid flow is purely vertical. To give an example, Fig. 2 shows the model with lowest permeability (k_x decreasing from 10^{-8} to 10^{-11} m/s at 500 m depth, $k_x/k_y = 10$) and a maximum load of 1800 kPa . The maximum overpressure ratio u^* is 0.074 near the shelf edge and at a sub-sea-floor depth of about 1500 m (Fig. 2a). However, in the top 500 m u^* is significantly lower. Fluid flow has a small component towards the foot of slope but is predominantly vertical (as shown by black vectors in Fig. 2a). The FoS is as low as 1.27 below the shelf edge, coinciding with a high overpressure ratio, and at the foot of the slope (Fig. 2b). The FoS contour lines along the slope converge towards the lower slope indicating that the lower slope is less stable than the upper slope. Nevertheless, FoS is > 1 everywhere in the model and so no failure mechanism could

be identified. σ'_v (not shown) is higher at the left and becomes smaller towards the right edge due to asymmetric loading. σ'_v does not show any abnormal pattern and is nowhere near zero.

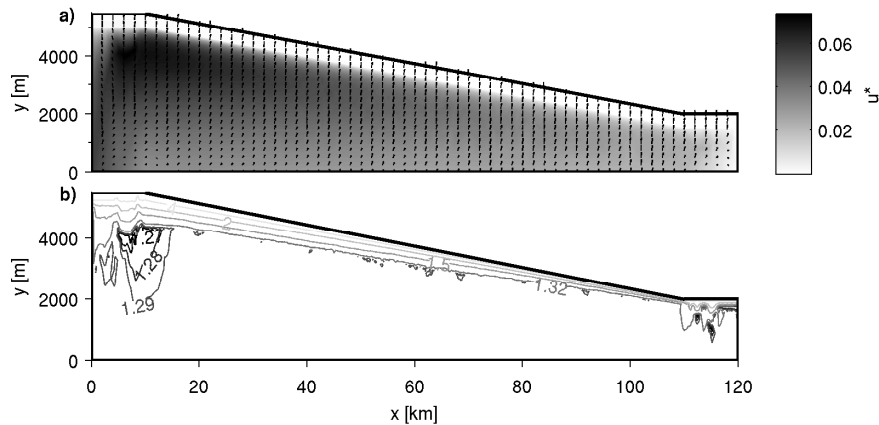


Figure 2: 2D FE solution for (a) overpressure ratio u^* with flow velocity vectors normalised to their absolute magnitude and (b) Factor of Safety calculated at each node after continuous loading with 1800 kPa for a period of 1 Ma. Vertical exaggeration is 5.

4 CONCLUSION

Our work suggests that large-scale failures of slope made of homogeneous low-permeability sediment are in at least some cases not generated by rapid sediment loading alone. It appears that high permeability layers would be needed to allow more rapid lateral fluid flow, or weak layers must be present that are not included in our modelling. The effect of such features on the stability of submarine slopes is where our work is now focussing.

References

- [1] A.A. Antobreh and S. Krastel. Mauritania slide complex: morphology, seismic characterisation and process of formation. *International Journal of Earth Science*, 96, 451–472, 2007.
- [2] K.R. Demars. Unique engineering properties and compression behavior of deep-sea calcareous sediments. In: K.R. Demars and R.C. Chaney (Eds.), *Geotechnical properties, behavior and performance of calcareous soils*, 1982.
- [3] P.B. Flemings, H. Long, B. Dugan, J.T. Germaine, C.M. John, J.H. Behrmann, D.E. Sawyer and Shipboard Scientists. Erratum to "pore pressure penetrometers document high overpressure near the sea floor where multiple submarine landslides have occurred on the continental slope, offshore Louisiana, Gulf of Mexico". *Earth and Planetary Science Letters*, 274, 269–283, 2008.
- [4] E.L. Hamilton. Variations of density and porosity with depth in deep-sea sediments. *Journal of Sedimentary Petrology*, 46(2), 280–300, 1976.
- [5] J. Jaky. The coefficient of earth pressure at rest. *Journal of the Society of Hungarian Architects and Engineers*, 355–358, 1944.
- [6] D.E. Karig and G. Hou. High-stress consolidation experiments and their geological implications. *Journal of Geophysical Research*, 97(B1), 289–300, 1992.
- [7] D.M. Potts and L. Zdravkovic. *Finite Element analysis in geotechnical engineering. Theory*. Thomas Telford, 2001.
- [8] K.H. Roscoe and J.B. Burland. On the generalised stress-strain behaviour of 'wet' clay. In: J. Heyman and F.A. Leckie (Eds.), *Engineering plasticity*. Cambridge University Press, 535–609, 1968.
- [9] P.J. Valent, A.G. Altschaeffl and H.J. Lee. Geotechnical properties of two calcareous oozes. In: Demars, K. R. and Chaney, R. C. (Eds.), *Geotechnical properties, behavior and performance of calcareous soils*, 1982.
- [10] Y. Yang and A.C. Aplin. A permeability-porosity relationship for mudstones. *Marine and Petroleum Geology*, 27, 1692–1697, 2010.

AN EVOLUTIONARY APPROACH TO MODELLING COMPACTION CHARACTERISTICS OF SOILS

***A. Ahangar-Asr, A. Faramarzi, A. Javadi, N. Mottaghifard**

Computational Geomechanics Group, College of Engineering Mathematics and Physical Sciences (CEMPS),
University of Exeter, EX4 4QF

*aa375@ex.ac.uk

Key Words: *maximum dry density, optimum moisture content, evolutionary computing, data mining*

ABSTRACT

An Evolutionary approach is used for prediction of maximum dry density (MDD) and optimum moisture content (OMC) as functions of some physical properties of soil. Evolutionary polynomial regression (EPR) is a data-driven method based on evolutionary computing aimed to search for polynomial structures representing a system. In this technique, a combination of the genetic algorithm (GA) and the least square method is used to find feasible structures and the appropriate parameters of those structures. EPR models are developed based on results from a series of classification and compaction tests from literature. Standard Proctor tests conducted on soils made of four components, bentonite, limestone dust, sand, and gravel, mixed in different proportions. The results of the EPR model predictions are compared with those of a neural network model, a correlation equation from literature and the experimental data. Comparison of the results shows that the proposed models are highly accurate and robust in predicting compaction characteristics of soils. Results from sensitivity analysis indicate that the models trained from experimental data have been able to capture the physical relationships between soil parameters. The proposed models are also able to represent the degree to which individual contributing parameters affect the maximum dry density and optimum moisture content.

1 INTRODUCTION

Many research works have been conducted to relate compaction characteristics of soils to their physical properties. The physical properties used generally include plasticity characteristics, specific gravity, and grain size distribution that are easily attainable from relatively straightforward laboratory tests. However, specific index properties used in the various correlation equations differ considerably. Among the most recent contributions are the work of Wang and Huang [1] who developed regression equations for predicting maximum dry density, optimum water content, and permeability for two levels of compaction degree (90 and 95%). Najjar et al [2] used neuronets to determine the optimum moisture content and maximum dry density of soils. Sinha and Wang [3] proposed models based on the artificial neural network (ANN) to predict permeability, maximum dry density, and optimum moisture content.

This paper introduces a new approach to predict maximum dry density (MDD) and optimum moisture content (OMC) of soils using EPR. EPR is a new data mining technique that overcomes the shortcomings of ANNs by providing a structured and transparent model representing the behaviour of the system. EPR models are developed to relate MDD and OMC to physical properties of the soils. The results of EPR model predictions are compared with those from literature and the experimental data. A parametric study is conducted to assess the level of contribution of each parameter in the developed models.

2 Evolutionary Polynomial Regression (EPR)

EPR is a data-driven method based on evolutionary computing, aimed to search for polynomial structures representing a system. A general EPR expression can be presented as [4]:

$$y = \sum_{j=1}^n F(X, f(X), a_j) + a_0 \quad (1)$$

where y is the estimated vector of output of the process; a_j is a constant; F is a function constructed by the process; X is the matrix of input variables; f is a function defined by the user; and n is the number of terms of the target expression. The general functional structure represented by $F(X, f(X), a_j)$ is constructed from elementary functions by EPR using a Genetic Algorithm (GA) strategy. The GA is employed to select the useful input vectors from X to be combined. The building blocks (elements) of the structure of F are defined by the user based on understanding of the physical process. While the selection of feasible structures to be combined is done through an evolutionary process, the parameters a_j are estimated by the least square method. This technique uses a combination of the genetic algorithm to find feasible structures and the least square method to find the appropriate constants for those structures. In particular, the GA allows a global exploration of the error surface relevant to specifically defined objective functions. By using such objective (cost) functions some criteria can be selected to avoid the overfitting of models, push the models towards simpler structures and avoid unnecessary terms representative of the noise in the data. An interesting feature of EPR is in the possibility of getting more than one model for a complex phenomenon. A further feature of EPR is the high level of interactivity between the user and the methodology. The user physical insight can be used to make hypotheses on the elements of the target function and on its structure. Selecting an appropriate objective function, assuming pre-selected elements based on engineering judgment, and working with dimensional information enable refinement of final models. The level of accuracy at each stage is evaluated based on the coefficient of determination (COD) i.e., the fitness function as:

$$\text{COD} = 1 - \frac{\sum_N (\mathbf{Y}_a - \mathbf{Y}_p)^2}{\sum_N \left(\mathbf{Y}_a - \frac{1}{N} \sum_N \mathbf{Y}_a \right)^2} \quad (2)$$

where \mathbf{Y}_a is the actual output value; \mathbf{Y}_p is the EPR predicted value and N is the number of data on which COD is computed. If the model fitness is not acceptable or the other termination criteria (in terms of maximum number of generations and maximum number of terms) are not satisfied, the current model goes through another evolution in order to obtain a new model. Detailed explanation of the method can be found in [4, 5].

3 EPR model for maximum dry density (MDD)

Five input parameters were used for the EPR model for MDD including dry density of solid phase γ_s expressed in (kg/m^3), fineness modulus (F_m), effective grain size (D_{10}) expressed in (mm), plastic limit (PL) expressed in (%), and liquid limit (LL) expressed in (%). The only output was the maximum dry density. The EPR model developed for maximum dry density is:

$$\text{MDD} = -\frac{1.38 \times 10^7 (D_{10})}{\gamma_s^2} + 1.92(D_{10}) - 6.61 \times 10^{-6} (D_{10}) \cdot PL^2 \cdot LL + 52.35 F_m^2 + 1385.07 \quad (3)$$

Figure 1 shows a comparison between the results of the EPR model predictions for testing data (20% of the whole data) that are not seen by EPR in the training stage and the actual experimental data. Table 1 presents the values of the coefficient of determination (COD) for different MDD models.

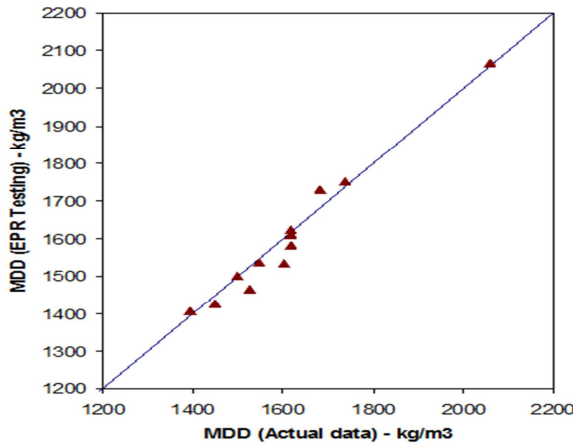


Figure 1. Comparison between the predicted maximum dry density and the actual data

Table 1
COD values for MDD prediction models

| Model | COD values (%) |
|-----------------------|---------------------------|
| EPR | 96 (for testing data) |
| ANN | 98 |
| Wang and Huang (1984) | 95 |

4 EPR model for optimum moisture content (OMC)

Three input variables were used to develop the EPR model for OMC. These are the fineness modulus (F_m), coefficient of uniformity (U), and plastic limit (PL). The EPR model developed to predict the optimum moisture content is:

$$OMC = \frac{9.47}{F_m^3 \cdot U} - \frac{3.57 \times 10^{-5} PL^3}{F_m^2} - \frac{4.55 \times 10^{-3} U}{F_m} + 1.72 \times 10^{-3} PL^2 - 6.36 F_m + 34.09 \quad (4)$$

The optimum moisture content of soils predicted using the EPR model is compared with the experimental data (Figure 2). The values of the coefficient of determination for the different models are shown in Table 2.

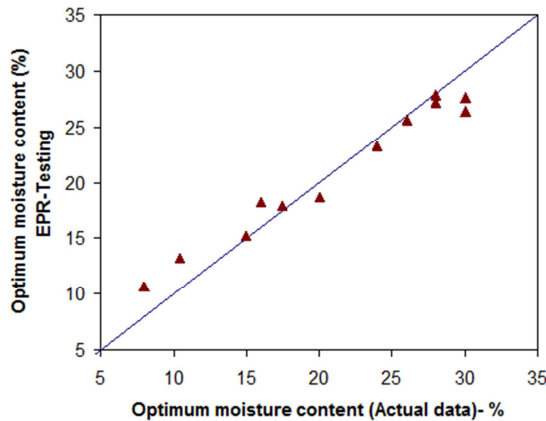


Figure 2. Comparison between the predicted optimum moisture content and the actual data

Table 2
COD values for OMC prediction models

| Model | COD values (%) |
|-----------------------|---------------------------|
| EPR | 94 (for testing data) |
| ANN | 92 |
| Wang and Huang (1984) | 89 |

The results indicate very good performance of the proposed EPR models. Figure 3 shows the sensitivity analysis results conducted. As the fineness modulus increases (the grains get coarser), the optimum moisture content decreases [6]. Increasing the coefficient of uniformity causes the maximum dry density to increase, and the optimum moisture content of the soil decreases accordingly [7]. The results also show that optimum moisture content is greatly affected by fineness modulus and uniformity coefficient and plastic limit appears to have the least effect on optimum moisture content.

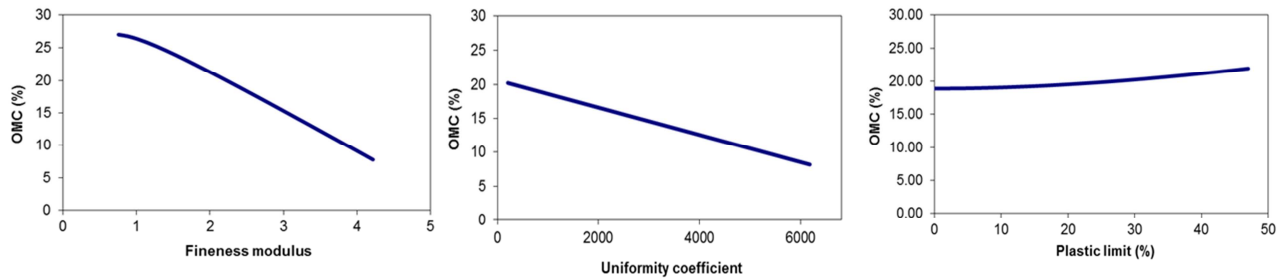


Figure 3. Parametric study results of the optimum moisture content model against; (a): fineness modulus of the soil, (b): uniformity coefficient, and (c): plastic limit

5 Summary and conclusion

Two separate EPR models were developed and validated using a database of experiments involving test data on compaction characteristics of a number of soils. The results of the model predictions were compared with the experimental data as well as results from other prediction models including a neural network. A parametric study was conducted to evaluate the effects of different parameters on compaction characteristics of soils. Comparison of the results shows that the developed EPR models provide very accurate predictions. They can capture and represent various aspects of compaction behaviour of soils directly from experimental data. The developed models present a structured and transparent representation of the system, allowing a physical interpretation of the problem that gives the user an insight into the relationship between the soil compaction behaviour and various contributing physical properties. From practical point of view, the EPR models presented in this paper are very accurate and easy to use. In the EPR approach, no pre-processing of the data is required and there is no need for normalization or scaling of the data. Performance of the models is being tested on a set of unseen data. This allows examining the generalization capabilities of developed models. Thus, an unbiased performance indicator is obtained on the real capability of the models. Another major advantage of the EPR approach is that as more data becomes available, the quality of the prediction can be easily improved by retraining the EPR model using the new data.

References

- [1] M.C. Wang and C.C. Huang. Soil Compaction and Permeability Prediction Models. *Soil Compaction and Permeability Prediction Models (ASCE)*, 110(6), 1063-1083, 1984.
- [2] Y.M. Najjar, I.A. Basheer and W.A. Naouss. On the identification of compaction characteristics by neuronets. *Computers and Geotechnics*, 18(3), 167-187, 1996.
- [3] S.K. Sinha and M.C. Wang. Artificial Neural Network Prediction Models for Soil Compaction and Permeability. *Geotechnical and Geological Engineering*, 26, 47-64, 2008.
- [4] O. Giustolisi and D.A. Savic. A Symbolic Data-driven Technique Based on Evolutionary Polynomial Regression. *Journal of Hydroinformatics*, 8(3), 207-222, 2006.
- [5] A. Javadi and M. Rezaia. A new approach to constitutive modeling of soils in finite element analysis using evolutionary computation. *Journal of Advanced Engineering Informatics*, 23(4), 442-451, 2009.
- [6] B.V. Venkatarama and A. Gupta. Influence of sand grading on the characteristics of mortars and soil-cement block masonry. *Construction and Building Materials*, 22, 1614-1623, 2008.
- [7] L.R. Blots, C.H. Benson and G.P. Boutwell. Estimating Optimum Water Content and Maximum Dry Unit Weight for Compacted Clays. *Journal of Geotechnical and Geo-Environmental Engineering (ASCE)*, 124(9), 907-912, 1998.

UNIQUE CRITICAL STATE HYPERPLASTICITY

* William M. Coombs¹, Roger S. Crouch¹ and Charles E. Augarde¹

¹ Durham University, School of Engineering and Computing Sciences, Durham, DH1 3LE. UK.

*w.m.coombs@dur.ac.uk

Key Words: *Critical State; hyperplasticity; anisotropy; Lode angle dependency; two-surface plasticity; finite deformation mechanics.*

ABSTRACT

Over the last 30 years there has been considerable interest in the extension of the modified Cam Clay constitutive model to include anisotropic material behaviour. Many formulations have been proposed that allow the elliptical yield (or bounding) surface to rotate off the hydrostatic axis, thereby introducing anisotropy. Several of these extensions have included one or more inner yield surfaces that produce inelastic behaviour within the outer surface. However, a Lode angle dependency (LAD), essential for reproducing the behaviour of particulate media, has not been introduced in a satisfactory way in the existing models. Rotating a LAD yield surface has presented challenges for earlier workers, such as maintaining convexity of that surface and uniqueness of the Critical State (CS) cone for differing degrees of anisotropy [1]. This paper overcomes the above difficulties by presenting a two surface anisotropic hyperplasticity model that includes a deviatoric section with a dependency on both (i) the Lode angle and (ii) the intermediate principal stress whilst maintaining a convex yield surface and a unique CS cone for any degree of anisotropy. The model is derived from free-energy and dissipation functions which provide the hyperelasticity law, yield function and direction of plastic flow without any additional assumptions [2]. Through the use of a *target anisotropic* hardening law, as proposed by Wheeler *et al.* [3], the model allows for a unique level of CS anisotropy, in agreement with recent findings from discrete element analyses [4]. An efficient implicit backward Euler stress integration algorithm and derivation of the algorithmic consistent tangent (for both small strain and finite deformation analysis) allows the model to be used in practical boundary value simulations.

1 CONSTITUTIVE FORMULATION

Particulate geomaterials typically demonstrate a dependence of the elastic bulk modulus on the current effective pressure, or equivalently on the current elastic volumetric strain. One common approach in the development of elasticity relations is to specify the elastic shear modulus directly from the bulk modulus, assuming a constant Poisson's ratio. However, this leads to a non-linear elasticity model in which energy can be generated from certain loading cycles [7]. Here we use a variable bulk modulus with a constant shear modulus by adopting an elastic free-energy function of the form

$$\Psi_1 = \kappa p_r \exp\left(\frac{\varepsilon_v^e - \varepsilon_{v0}^e}{\kappa}\right) + G\left(\text{tr}([\gamma^e][\gamma^e])\right) \quad \left(\text{with } \varepsilon_v^e = \text{tr}[\varepsilon^e] \text{ and } [\gamma^e] = [\varepsilon^e] - \frac{1}{3}\varepsilon_v^e[1]\right), \quad (1)$$

where κ is the elastic compressibility index, G is the shear modulus, p_r is the reference pressure, ε_{v0}^e is the elastic volumetric strain at that reference pressure and $[1]$ is the third order identity matrix.

The rate of dissipation for the two-surface model presented here is given by

$$\dot{\Phi} = \underbrace{\sqrt{(\dot{\varepsilon}_{v1}^p + \beta_{ij}\dot{\gamma}_{ij1}^p)^2 A^2 + (\dot{\varepsilon}_{\gamma1}^p B)^2}}_{\dot{\Phi}_1} + \underbrace{\sqrt{(\dot{\varepsilon}_{v2}^p + \beta_{ij}\dot{\gamma}_{ij2}^p)^2 A_f^2 + (\dot{\varepsilon}_{\gamma2}^p B_f)^2}}_{\dot{\Phi}_2}, \quad (2)$$

where $\varepsilon_\gamma^p = \text{tr}([\dot{\gamma}^p][\dot{\gamma}^p])$ and the plastic strain rates ε_v^p and $\{\dot{\gamma}^p\}$ are equivalent to the elastic definitions in (1). The two components of dissipation $\dot{\Phi}_1$ and $\dot{\Phi}_2$ are associated with the outer bounding ($F = 0$) and inner yield ($f = 0$) surfaces, respectively. Following the procedure for developing hyperplastic constitutive models in [8], we obtain the inner-surface yield function as

$$f = (p - p^x)^2 B_f^2 + \{s^\beta\}^T \{s^\beta\} A_f^2 - A_f^2 B_f^2 = 0, \quad \text{with} \quad \{s^\beta\} = \{s\} - \{s^x\} - (p - p^x)\{\beta\} \quad (3)$$

where $p = \text{tr}[\sigma]/3$, $[s] = [\sigma] - p[1]$,

$$A_f = (1 - \gamma)(p - p^x) + (2 - \gamma)\gamma R p_c / 2 \quad \text{and} \quad B_f = \bar{\rho}(\theta) M \left((1 - \alpha)(p - p^x) + \gamma R p_c / 2 \right). \quad (4)$$

$\{\beta\}$ is a traceless measure of the inclination of the yield surfaces' major axis off the hydrostatic axis, p^x and $\{s^x\}$ are the hydrostatic and deviatoric components of the centre of the inner yield surface, $\{\sigma^x\}$, see Figure 1. α and γ control the shape of the yield surfaces¹ and $\bar{\rho}(\theta)$ defines the LAD of the model. M is the classical isotropic gradient of the CS line, R is the relative size of the inner surface to that of the bounding surface; $p_c = p_r \exp(\varepsilon_v^p / (\lambda - \kappa))$. The direction of plastic flow is given by

$$\{g_{,\sigma}\} = \frac{2}{3} \left(B_f^2 (p - p^x) - A_f^2 \{s^\beta\}^T \{\beta\} \right) \{1\} + 2A_f^2 \{s^\beta\}, \quad (5)$$

and the inner surface translates according to

$$\{\dot{\sigma}^x\} = C^x \|\dot{\varepsilon}^p\| \left\{ (1 - R)\{\sigma\} + R p_c \gamma \{ \{1\} + \{\beta\} \} / 2 \right\} + \{\sigma^x\} \left(\varepsilon_v^p / (\lambda - \kappa) - C^x \|\dot{\varepsilon}^p\| \right) + p^x \{\dot{\beta}\}. \quad (6)$$

The first term translates the inner surface towards the image point (see Figure 1), $\{\hat{\sigma}\}$, on the outer surface at a rate controlled by C^x . This translation rule means that the inner surface can touch the outer surface but never intersect it. The second and third terms ensure that the projection centre remains consistent with the isotropic evolution and anisotropic shearing of the outer surface, respectively.

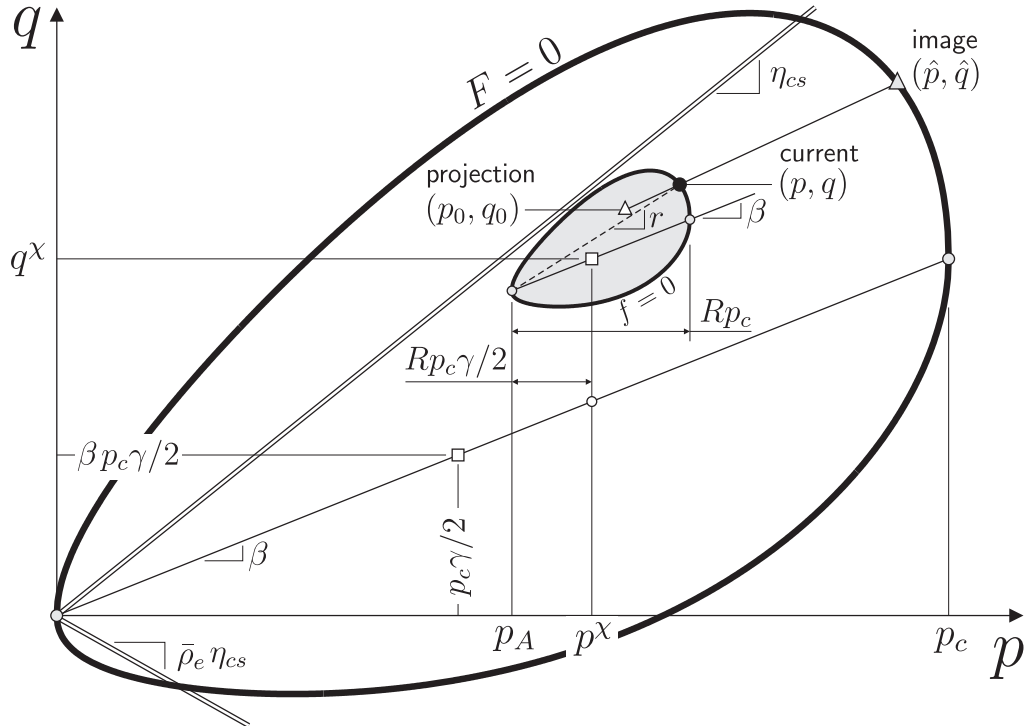


Figure 1: Two surface anisotropic model in p - q stress space.

2 ANISOTROPIC CRITICAL STATE

The two surface model allows for the axes of both the inner yield and outer boundary surfaces to become non-parallel to the hydrostatic axis via a non-zero $\{\beta\}$ (as shown in Figure 1). Here we use the

¹See Coombs and Crouch [8] for more details on the specification and influence of α and γ .

following anisotropic hardening relationship, initially proposed by Wheeler *et al.* [3]

$$\{\dot{\beta}\} = C_{\beta} \left(\left\{ a_{\beta} \{r\} - \{\beta\} \right\} < \dot{\varepsilon}_v^p > + x_{\beta} \left\{ b_{\beta} \{r\} - \{\beta\} \right\} \dot{\varepsilon}_{\gamma}^p \right), \quad (7)$$

where $\langle \cdot \rangle$ is the ramp function of (\cdot) . The local stress ratio, $\{r\}$, controlling the direction of anisotropy evolution, is defined as the deviatoric to volumetric stress ratio measured from the apex of the inner yield surface (see Figure 1). It is given by

$$\{r\} = \left(p - p^x + Rp_c \gamma / 2 \right)^{-1} \left\{ \{s\} - \{s^x\} + Rp_c \gamma \{\beta\} / 2 \right\}. \quad (8)$$

$a_{\beta} \in [0, M]$ and $b_{\beta} \in [0, M]$ act as target values for the evolution of anisotropy from volumetric and deviatoric plastic strains, respectively. x_{β} controls the relative contribution from these two strains and C_{β} governs the absolute rate of evolution. Unlike some anisotropic hardening laws that depend purely on plastic volumetric strains [5,6], (7) gives a unique level of anisotropy at the CS. When approaching the CS, the plastic volumetric strain diminishes and the level of anisotropy tends towards the deviatoric target value $b_{\beta} \{r\}$. The inclination of the yield surface at the CS is independent of the initial anisotropy and the stress path taken to reach this state. It is dependent only on the stress state at the CS. This unique level of fabric anisotropy at the CS results in a unique CS line in the void ratio- $\ln(p)$ plane.

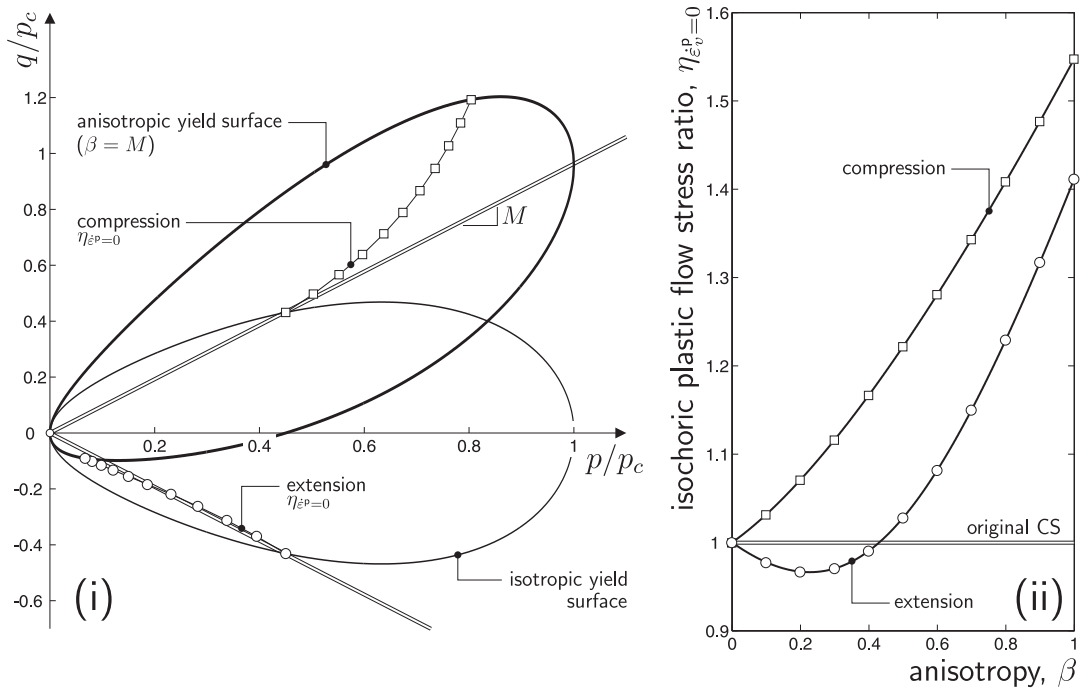


Figure 2: Development of the isochoric plastic flow point with anisotropy using $\alpha = 0.6$, $\gamma = 0.9$ and $M = 1$: (i) p - q stress space and (ii) the $\eta_{\varepsilon_v^p=0}$ stress ratio variation with the level of anisotropy.

The introduction of a non-zero $\{\beta\}$ results in a change of the position of zero volumetric plastic flow on the inner yield and outer bounding surfaces. Setting $\{g_{,\sigma}\}^T \{1\} = 0$ and using the condition that $F = 0$, we obtain a quartic in p/p_c for the position of zero volumetric plastic strains on the bounding surface. The stress ratio of the point on the yield surface with isochoric plastic flow ($\eta_{\varepsilon_v^p} = 0$) for $\beta = \sqrt{\text{tr}([\beta][\beta])}$ between 0 and M is given in Figure 2 (ii). Figure 2 (i) shows the location of these points in normalised p - q stress space. As β increases, $\eta_{\varepsilon_v^p=0}$ under triaxial compression also increases. However, the $\eta_{\varepsilon_v^p=0}$ under triaxial extension initially reduces but then increases to a stress ratio above that of the original CS. When approaching the CS, the volumetric component of plastic flow reduces and the evolution of $\{\beta\}$ is controlled by the deviatoric plastic strains. In the limiting case where $\dot{\varepsilon}_v^p = 0$, $\{\dot{\beta}\}$ becomes

$$\{\dot{\beta}\}_{\dot{\varepsilon}_v^p=0} = C_{\beta} x_{\beta} \left\{ b_{\beta} \{r\} - \{\beta\} \right\} \dot{\varepsilon}_{\gamma}^p. \quad (9)$$

Under continued plastic shearing with no change in state, $\{\dot{\beta}\} \rightarrow \{0\}$ and $\{\beta\}_{cs} = b_{\beta}\{r\}$, where $(\cdot)_{cs}$ denotes a quantity at the CS. If $b_{\beta} = 0$, anisotropy disappears when approaching the CS and $(p/p_c) = \gamma/2$ at a stress ratio $\eta = q/p = M$. When $b_{\beta} \neq 0$, the value of M to obtain the required stress ratio at the CS, η_{cs} , is given by

$$M = \eta_{cs} \left(b_{\beta} \pm \frac{b_M}{A(p/p_c)} \sqrt{\gamma(p/p_c)(2 - \gamma)(1 - (p/p_c))} \right)^{-1} \quad \text{where} \quad b_M = \left((1 - \alpha)(p/p_c) + \frac{\alpha\gamma}{2} \right) \quad (10)$$

By defining the stress ratio and the level of anisotropy at the CS, we can obtain the appropriate M to maintain the unique asymptotic η_{cs} .

3 STRESS INTEGRATION AND LINEARISATION

The constitutive model was integrated using the fully implicit backward Euler method and linearised to obtain the consistent algorithmic tangent². The model was subsequently implemented within a finite deformation finite-element code developed at Durham University (see [9,10] for more details on the numerical framework). This implementation included the derivation of the spatial algorithmic tangent to allow asymptotic quadratic convergence of the global Newton-Raphson solution algorithm.

4 CONCLUSION

The two-surface model presented in this paper incorporates a LAD within an anisotropic yield surface which remains convex and has a unique CS surface. The yield surface anisotropy is introduced via deviatoric shearing. This pressure-dependent translation maintains the convexity of the original surface. When approaching the CS, the volumetric plastic strains reduce to zero and the material moves to a constant state with unbounded deviatoric plastic shearing. At this state the inclination of the yield surface converges to a unique target level of anisotropy. This allows the classical material constant M to be specified such that a the appropriate stress ratio is obtained, maintaining a unique CS.

REFERENCES

- [1] WM Coombs, RS Crouch & CE Augarde, *Influence of Lode Angle Dependency on the Critical State for Rotational Plasticity*, COMPLAS X, E Oñate & DRJ Owen (Eds), Barcelona, 2009.
- [2] IF Collins & GT Houlsby, *Application of thermomechanical principles to the modelling of geotechnical materials*, Proc. R. Soc. Land. A 453 (1997), 1975–2001.
- [3] SJ Wheeler, A Näätänen, M Karstunen & M Lojander, *An anisotropic elastoplastic model for soft clays*, Can. Geotech. J. 40 (2003), 403–418.
- [4] P Fu & YF Dafalias, *Fabric evolution within shear bands of granular materials and its relation to critical state theory*, Int. J. Numer. Anal. Meth. Geomech (2010), DOI: 10.1002/nag.988.
- [5] YF Dafalias, *An anisotropic critical state clay plasticity model*, Proceeding of the 2nd International Conference on Constitutive Laws for Engineering Materials: Theory and applications, 1987.
- [6] AJ Whittle & MJ Kavvas, *Formulation of MIT-E3 Constitutive Model for Overconsolidated Clays*, J. Geotech. Eng.-ASCE 120 (1994), 173–198.
- [7] GT Houlsby, *The use of a variable shear modulus in elastic-plastic models for clays*, Comput. Geotech. 1 (1985), 3–13.
- [8] WM Coombs & RS Crouch, *Algorithmic issues for three-invariant hyperplastic Critical State models*, submitted to Comput. Meth. Appl. Mech. Engrg, 2010.
- [9] WM Coombs & RS Crouch, *Non-associated Reuleaux plasticity: Analytical stress integration and consistent tangent for finite deformation mechanics*, Comput. Meth. Appl. Mech. Engrg. 200 (2011), 1021–1037.
- [10] WM Coombs, RS Crouch & CE Augarde, *70-line 3D finite deformation elastoplastic finite-element code*, NUMGE 7, T Benz & S Nordal (Eds), 151–156, Trondheim, Norway, 2010.

²That is the tangent consistent with the stress integration procedure, see Coombs and Crouch [8] for model details on the stress integration and linearisation procedure for a hyperplastic family of isotropic CS models.

COROTATIONAL FORMULATION FOR 3D SOLIDS: ANALYSIS OF GEOMETRICALLY NONLINEAR FOAM DEFORMATION

*Ł. Kaczmarczyk, T. Koziara and C.J. Pearce

School of Engineering, University of Glasgow, Glasgow

*Lukasz.Kaczmarczyk@glasgow.ac.uk

Key Words: *co-rotational formulation, geometric nonlinearities, finite elements*

ABSTRACT

This paper presents the theory for the Lagrange co-rotational (CR) formulation of finite elements for the geometrically nonlinear analysis of 3D structures. In this paper strains are assumed to be small while there is no restriction on the magnitude of rotations from the reference configuration. A new best fit rotator and consistent spin filter are derived. Lagrange CR formulation is applied to the Hybrid Trefftz Stress elements, although the methodology presented can be applied to other discretization techniques, e.g. finite volume methods, lattice models, discrete element methods. Efficiency of CR formulation can be exploited in post-buckling stability analysis, damage and fracture mechanics, modelling of dynamic fragmentation of bodies made from quasi-brittle materials, solid fluid interactions, analysis of post-stressed structures, discrete body dynamics.

1 INTRODUCTION

The Lagrangian kinematics description for Finite Element Method of geometric nonlinear structures is utilized mainly in two solution techniques, i.e. Total Lagrangian Formulation and Updated Lagrangian Formulation. In this paper we investigate a less common solution technique for geometrically nonlinear problems known as the Lagrange Co-rotational (CR) formulation. In this paper we investigate a less common solution technique for geometrically nonlinear problems, i.e. the Lagrange Co-rotational (CR) formulation.

Key features of the Lagrange CR formulation are efficiency and robustness, i.e. computation of tangent matrices is cheap, the method is easy to parallelize and can be used with various discretization techniques. Large class of problems with finite rotations but small strains, e.g. post-buckling stability analysis, damage and fracture mechanics, modelling of dynamic fragmentation of bodies made from quasi-brittle materials, solid fluid interaction, analysis of post-stressed structures or discrete body dynamics can be solved efficiently with the use of the Lagrange CR formulation.

In this paper, the CR formulation is applied with Hybrid Trefftz Stress (HTS) finite elements. Application of the CR formulation together with HTS elements results in a powerful synergy, which is

exemplified on a case study problem presented in the paper. Although the presented methodology is applied to solid mechanics, the presented method can also be applied to image recovery, where extraction of rigid body motion from image is required.

This paper follows earlier contributions [1, 2, 3], with a full literature review in [3]. Despite the large body of literature on co-rotational formulations, how to construct a best-fit rotation functional remains an open research question. In this paper we introduce a new general best-fit rotation functional in order to derive the rotation operator. Additionally, a new Spin-Filter operator, mapping increments of degrees of freedom into increment of rotation vector, consistent with new best-fit rotation functional is determined.

2 BEST-FIT ROTATION OPERATOR

Computation of the rotation operator for a given displacement field is at the heart of the co-rotational formulation. In our view, an ideal co-rotational formulation should address the following objectives:

- *Versatility.* It must work for static and dynamic problems, with arbitrary discretization of displacements.
- *Rigid bodies.* For rigid body motion, no spurious deformations should develop. Enforcing this will simplify the coupling of FEM-CR methods with multibody dynamics codes [3].
- *Finite stretch and pure shear.* If a element is subjected to a uniform finite stretch or pure shear, no spurious rotation should develop.

In order to find the rotation operator \mathbf{R} , a new functional is proposed here. Stationary points of this functional determine rotation, which complies with the above objectives.

We note, that for a rotation free deformation, the antisymmetric part of the displacement gradient disappears. With that observation at hand, assuming that the rotation is constant in the element domain, the antisymmetric part of the volume averaged deformational displacement (\mathbf{u}^d) gradient is used to construct the best fit rotation operator.

$$\int_{\Omega} \left(\left[\frac{\partial \mathbf{u}^d}{\partial \mathbf{X}} \right] - \left[\frac{\partial \mathbf{u}^d}{\partial \mathbf{X}} \right]^T \right) d\Omega = \mathbf{0} \quad (1)$$

Noting that the antisymmetric part of the displacement gradient has only three non-zero linearly independent components, it can be uniquely expressed by a pseudo-vector $\vec{\mathbf{h}}$. Utilizing that and applying integration by parts, a pseudo-vector $\vec{\mathbf{h}}$ can be expressed by the boundary integral

$$\vec{\mathbf{h}} = \int_{\Gamma} \mathbf{n} \times \mathbf{u}^d d\Gamma = \int_{\Gamma} \text{Spin}[\mathbf{n}] \mathbf{u}^d d\Gamma \quad (2)$$

where \mathbf{n} is the spatial normal vector field on the element boundary Γ . This integration can be undertaken in the current or reference configuration (since the motion is roughly rigid we can assume the Jacobian to be nearly one). A length of the pseudo-vector $\vec{\mathbf{h}}$ is used to formulate the best fit functional. Utilizing

that $\int_{\Gamma} \text{Spin}[\mathbf{N}] \mathbf{X} d\Gamma = 0$, the functional takes form

$$\begin{aligned}
\mathbf{J}(\mathbf{R}) &= \frac{1}{2} [\vec{\mathbf{h}}]^T [\vec{\mathbf{h}}] = \frac{1}{2} \left[\int_{\Gamma} \text{Spin}[\mathbf{n}] \mathbf{u}^d d\Gamma \right]^T \left[\int_{\Gamma} \text{Spin}[\mathbf{n}] \mathbf{u}^d d\Gamma \right] \\
&= \frac{1}{2} \left[\int_{\Gamma} \text{Spin}[\mathbf{RN}] (\mathbf{u} - \mathbf{u}^r) d\Gamma \right]^T \left[\int_{\Gamma} \text{Spin}[\mathbf{RN}] (\mathbf{u} - \mathbf{u}^r) d\Gamma \right] \\
&= \frac{1}{2} \left[\int_{\Gamma} \text{Spin}[\mathbf{N}] \mathbf{R}^T \mathbf{x} d\Gamma \right]^T \left[\int_{\Gamma} \text{Spin}[\mathbf{N}] \mathbf{R}^T \mathbf{x} d\Gamma \right]
\end{aligned} \tag{3}$$

where $\mathbf{N} = \mathbf{R}^T \mathbf{n}$. We note, that the functional expressed in the above form can be applied to problems where displacements are only known on elements boundaries (and can be discontinuous).

The stationary point of this functional lead to a system of non-linear algebraic equations, from which the current rotation operator can be calculated by means of a Newton iterative scheme. It should be noted, that the above procedure permits the the rotation to be calculated independently of the motion history. However, in order to avoid problems with multiple minima and to correctly trace the history of rotation, it is appropriate to initialize the iterative procedure with the most recent value of rotation.

3 Numerical example

In order to present one of the many potential applications of the Lagrange CR formulation we investigate deformation of a hypothetical foam. The mesh was obtained from a high-resolution 3D scan, included as a case study in the Simpleware software [6]. The mesh comprised 95956 tetrahedrons and 40725 nodes. The constitutive parameters of the model were chosen arbitrarily, i.e. $E = 1 \times 10^4$ and $\nu = 0.25$. On the left plate a fully fixed boundary condition was applied. At the right plate tractions in the normal direction were applied. On the front, back, top and bottom sides, displacements in the normal direction are restricted.

Displacement and stress field were approximated using Hybrid-Trefftz finite elements. Two cases were considered with linear and quadratic approximation of displacements. For the first case, second-order polynomial Trefftz functions were used to approximate stresses. For the second case, third-order polynomial Trefftz functions were used to approximate the stress field. This led to models with ~ 5 million DoFs and ~ 10 million DoFs, respectively.

During the analyses, large rotations resulted in local buckling of the foam struts which had a negative impact on the convergence of the Newton method. In order to improve efficiency, arc-length control was introduced.

The Trefftz displacement field is adjoint to the stresses calculated to fulfill equilibrium, hence the displacement vector \mathbf{u} approximation associated with stress functions do not carry any information about translations and rotations. In Figure. 1, displacements are determined using the Trefftz displacement function \mathbf{u} , supplemented with rigid body rotation \mathbf{u}^r . By visual inspection of the figures in this example and in Figure. 1 we can verify an excellent consistency of the calculated rotation operator with the overall deformation.

4 Conclusions

This paper presents a geometrically nonlinear Lagrange co-rotational formulation applied to Hybrid Stress Trefftz Elements. The FE code developed utilises the Portable Extensible Toolkit for Scientific

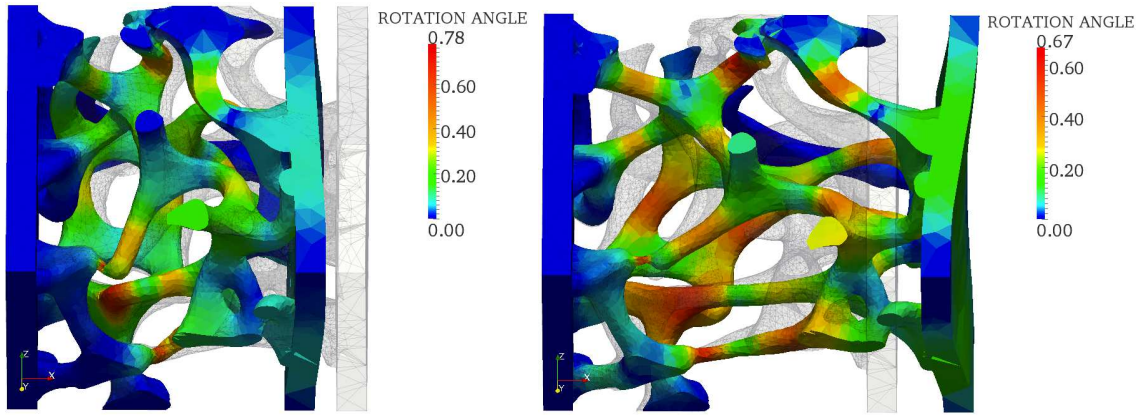


Figure 1: Distribution of magnitude rotations vector.

Computation (PETSc) [4] and A Mesh-Oriented datABase (MOAB) [5]. A new best-fit rotation operator for continuum elements is developed. The best-fit rotation functional is constructed by utilizing a boundary integral over a deformable element/body. Stationary points of the functional lead to a set of three nonlinear equations, solved by means of the Newton method. Formulation of best-fit rotation operator, load vector and tangent matrices was verified by a numerical example of the large deformation of a foam.

References

- [1] B. Nour-Omid, C.C. Rankin, *Finite rotation analysis and consistent linearization using projectors*, Comput. Methods Appl. Mech. Engrg. 93 (1991) 353384.
- [2] M.A. Crisfield, *A consistent corotational formulation for nonlinear three-dimensional beam element*, Comput. Methods Appl. Mech. Engrg. 81 (1990) 131150.
- [3] C.A. Felippa, B. Haugen, *A unified formulation of small-strain corotational finite elements: I. Theory*, Comput. Methods Appl. Mech. Engrg. 194 (2005) 22852335
- [4] Satish Balay and Kris Buschelman and William D. Gropp and Dinesh Kaushik and Matthew G. Knepley and Lois Curfman McInnes and Barry F. Smith and Hong Zhang, *PETSc Web page*, <http://www.mcs.anl.gov/petsc>, 2009.
- [5] Timothy J. Tautges, *MOAB-SD: integrated structured and unstructured mesh representation*, Engineering with Computers, 20(3) 2004 286-293
- [6] *Simpleware Ltd Web page*, <http://www.simpleware.com>
- [7] Samuel A. McDonald, Ghislain Dedreuil-Monet, Yong Tao Yao, Andrew Alderson, and Philip J. Withers, *In situ 3D X-ray microtomography study basic solid state physics comparing auxetic and non-auxetic polymeric foams under tension*, Phys. Status Solidi B, 17 (2010) / DOI 10.1002/pssb.201083975.

EPR-BASED FINITE ELEMENT ANALYSIS OF SOILS UNDER CYCLIC LOADING

Akbar A. Javadi¹, *Asaad Faramarzi¹, Moura Mehravar¹ and Alireza Ahangar-Asr¹

¹Computational Geomechanics Group, College of Engineering, Mathematics and Physical Sciences, University of Exeter, Harrison Building, North Park Road, Exeter, EX4 4QF

*af269@ex.ac.uk

Key Words: *finite element; geomechanics; evolutionary methods; EPR; cyclic loading*

ABSTRACT

In this paper, a new approach is presented for modelling behaviour of soils under cyclic loading. This involves development of a unified approach to modelling of complex materials using evolutionary polynomial regression (EPR) and its implementation in the finite element method. EPR is a data mining technique that generates a transparent and structured representation of the system being studied. The main advantage of an EPR-based constitutive model (EPRCM) over conventional models is that it provides the optimum structure and parameters of the material constitutive model directly from raw experimental (or field) data. The development of the method will be presented followed by the application to study the behaviour of soils under cyclic loading. The results of the analyses will be compared with those obtained from standard finite element analyses using conventional constitutive models. It will be shown that the EPR-based constitutive models offer an effective and unified approach to constitutive modelling of materials with complex behaviour in finite element analysis of boundary value problems.

1 INTRODUCTION

Finite element method has, in recent years, been widely used as a powerful tool in the analysis of engineering problems. In this numerical analysis, the behaviour of the actual material is approximated with that of an idealized material that deforms in accordance with some constitutive relationships. Therefore, the choice of an appropriate constitutive model that adequately describes the behaviour of the material plays an important role in the accuracy and reliability of the numerical predictions. During the past few decades several constitutive models have been developed for various materials including soils. Despite considerable complexities of constitutive theories, due to the erratic and complex nature of some materials such as soils, rocks, composites, etc., none of the existing models can completely describe the real behaviour of these materials under various stress paths and loading conditions.

In this paper a fundamentally different approach is presented for constitutive modelling using Evolutionary Polynomial Regression (EPR) that overcomes some of the shortcomings of the other approaches. In the proposed EPR approach the optimum structure for the material constitutive model representation and its parameters are determined directly from raw data. Furthermore, it provides a transparent and structured representation of the constitutive relationships that can be readily incorporated in a finite element code. Javadi and Rezaia 2009, and Javadi et al. 2009 presented the application of the EPR-based constitutive models in material modelling under monotonic loading situation [1, 2]. However, this paper focuses on the application of the EPR-based constitutive models, to the simulation of behaviour of soils under cyclic loading and its integration in a FE model.

In what follows, the main principles of EPR will be outlined. The application of EPR in modelling of nonlinear constitutive relationships and the implementation of developed EPRCMs in FE analysis will be illustrated. An EPR model will be trained with data from results of a series of synthetic triaxial cyclic loading tests. The trained EPR model will then be incorporated into a finite element model which will in turn be used to analyse the behaviour of the soil under cyclic loading. The training and generalization

capabilities of the EPR in extending the learning to cases of multiple cycles will be investigated.

2 EVOLUTIONARY POLYNOMIAL REGRESSION (EPR)

Evolutionary polynomial regression (EPR) is a data-driven method based on evolutionary computing, aimed to search for polynomial structures representing a system. A general EPR expression can be presented as [3]

$$\mathbf{y} = \sum_{j=1}^n F(X, f(X), a_j) + a_0 \quad (1)$$

where \mathbf{y} is the estimated vector of output of the process; a_0 is a constant; F is a function constructed by the process; X is the matrix of input variables; f is a function defined by the user; and n is the number of terms of the target expression. The general functional structure represented by F is constructed from elementary functions by EPR using a GA strategy. The GA is employed to select the useful input vectors from X to be combined. The building blocks (elements) of the structure of F are defined by the user, based on understanding of the physical processes. While the selection of feasible structures to be combined is done through an evolutionary process the parameters are estimated by the least square method.

EPR is a technique for data-driven modelling. In this technique, the combination of the genetic algorithm to find feasible structures and the least square method to find the appropriate constants for those structures implies some advantages. In particular, the GA allows a global exploration of the error surface relevant to specifically defined objective functions. By using such objective functions some criteria can be set in order to (i) avoid overfitting of models, (ii) push the models towards simpler structures, and (iii) avoid unnecessary terms representative of the noise in data [3]. Application and capability of EPR in modelling and analysing different civil and geotechnical engineering problems have been investigated by the authors, [4, 5]. Detailed explanation of the method is out of the scope of this paper and can be found in [3, 6].

3 EPR FOR CONSTITUTIVE MODELLING

In constitutive modelling using EPR, the raw experimental or in-situ test data are directly used for training the EPR model. In this approach, there are no mathematical models to select and as the EPR learns the constitutive relationships directly from the raw data it is the shortest route from experimental research to numerical modelling. In this approach there are no material parameters to be identified and as more data become available, the material model can be improved by re-training of the EPR using the additional data. Furthermore, the incorporation of an EPR in a finite element procedure avoids the need for complex yield/failure functions, flow rules, etc. An EPR equation can be incorporated in a finite element code/procedure in the same way as a conventional constitutive model. It can be incorporated either as incremental or total stress-strain strategies [2]. In this study the incremental strategy has been successfully implemented in the EPR-based finite element model.

3-1: Input and output parameters

The choice of input and output quantities is determined by both the source of the data and the way the trained EPR model is to be used. A typical scheme to train most of the neural network based material models includes an input set providing the network with the information relating to the current state units (e.g., current stresses and current strains) and then a forward pass through the neural network yielding the prediction of the next expected state of stress and/or strain relevant to an input strain or stress increment [7]. The same idea has been utilized in this work. Thus depending on the problem and the available data, typically the mean stress, deviatoric stress, volumetric strain and shear strain are used as the input parameters representing the current state of stress and strain in a load increment i , and the deviatoric stress and/or volumetric strain corresponding to the input incremental deviatoric strain are used as the output parameters. The database is divided into two separate sets. One set is used for training to obtain the EPR model and the other one is used for validation to appraise the applicability of the trained model.

4 INCORPORATING EPRCM IN FEA

The developed EPRCMs are implemented in the widely used general-purpose finite element code ABAQUS through its user defined material module (UMAT). UMAT updates the stresses and provide the material Jacobian matrix for every increment in every integration point (ABAQUS). In the developed methodology, the EPRCM replaces the role of a conventional constitutive model. The source of knowledge for EPR is a set of raw experimental (or in situ) data representing the mechanical response of the material to applied load. When EPR is used for constitutive description, the physical nature of the input–output data for the EPR is determined by the measured quantities, e.g., stresses, strains, etc. The constitutive relationships are generally given in the following form:

$$\Delta\sigma = \mathbf{D}\Delta\epsilon \quad (2)$$

where \mathbf{D} is material stiffness matrix, also known as the Jacobian. For an isotropic and elastic material, matrix \mathbf{D} is given in terms of Young's modulus, E , and Poisson's ratio, ν . Therefore the function of an EPR-based constitutive model in a FE model (at every element's integration point) is to define E , and ν as follows:

$$E_{\text{EPR}} = \frac{\Delta q^i}{\Delta \epsilon_1^i} \quad (3)$$

$$\nu_{\text{EPR}} = \left(\frac{1 - \frac{\Delta \epsilon_v^i}{\Delta \epsilon_1^i}}{2} \right) \quad (4)$$

5 NUMERICAL EXAMPLE

The application of the method to the analysis of the behaviour of soil under cyclic loading is presented in the following example. In this example, the behaviour of a soil is studied in triaxial tests under cyclic axial loading. The test data for this example were generated by numerical simulation of triaxial experiments. The data for training and validation of the EPR were created by finite element simulation of triaxial cyclic loading tests at constant cell pressures using the modified Cam clay model. The generated data were used to train and test EPRCMs. The EPRCMs were then incorporated in the EPR-based finite element model to represent the soil behaviour under cyclic loading. The results of the EPR-based finite element analyses were compared with those attained using conventional finite element method. The selected EPR models for q and ϵ_v are presented in equations 5(a) and 5(b). After training and validation, the EPRCMs were incorporated in the EPR-based finite element model. The model was then used to simulate the behaviour of the soil in triaxial cyclic loading test at a confining pressure 250 kPa (that has not been used during the training process). The results of the EPR-based finite element analysis are compared with those attained using the conventional FE simulation in Figs. 1(a) and 1(b). It is seen that the results of the EPR-based FE model are in close agreement with those of the conventional FE simulation. It can be seen from the figure that, the EPR-based FE model is capable of solving boundary value problems involving cyclic loading with a good accuracy.

5 DISCUSSION AND CONCLUSION

This paper presented a fundamentally different approach to constitutive modelling of materials in finite element analysis. An EPR-based finite element method was presented for modelling engineering problems. The method is based on the integration of an EPR-based constitutive model in the finite element procedure. In the developed methodology, the EPRCM is used as a unified framework for constitutive modelling of materials in finite element analysis. The model was used to study the behaviour of soils under cyclic loading. It was shown that EPR can learn the complex behaviour of soils under

cyclic loading taking into account the loading history of the soil. It should be noted that, for practical problems, the data used for training of EPRCM should cover the range of stresses and strains that are likely to be encountered in practice. This is due to the fact that EPR models are good at interpolation but not so good at extrapolation.

$$q^{i+1} = \frac{0.0084 (q^i)^2}{\dot{\rho}^2 \varepsilon_v} - \frac{2667.247 (q^i)^2 (\Delta \varepsilon_q)^2}{\dot{\rho} \varepsilon_q} - \frac{0.060714 (q^i)^2 \Delta \varepsilon_q}{\dot{\rho} \varepsilon_v} + \frac{1.8866 \varepsilon_v \Delta \varepsilon_q}{q^i} - \frac{1.9676 q^i \Delta \varepsilon_q}{\varepsilon_v} + \frac{888.4 (q^i)^2 (\Delta \varepsilon_q)^2}{\varepsilon_v} + 104.4964 \dot{\rho} \Delta \varepsilon_q - 1.4 \times 10^{-5} \dot{\rho}^2 + 0.018826 \dot{\rho}^2 q^i \varepsilon_v \Delta \varepsilon_q + 1.0525 q^i - 0.71525 \quad (5a)$$

$$\varepsilon_v^{i+1} = \frac{0.02369 q^i \Delta \varepsilon_q}{\dot{\rho} \varepsilon_q} - \frac{0.4217 q^i \Delta \varepsilon_q}{\dot{\rho}} + \frac{9.3 \times 10^{-6} \varepsilon_q}{q^i} + 0.45727 \Delta \varepsilon_q + 0.99 \varepsilon_v + 0.000041535 \quad (5b)$$

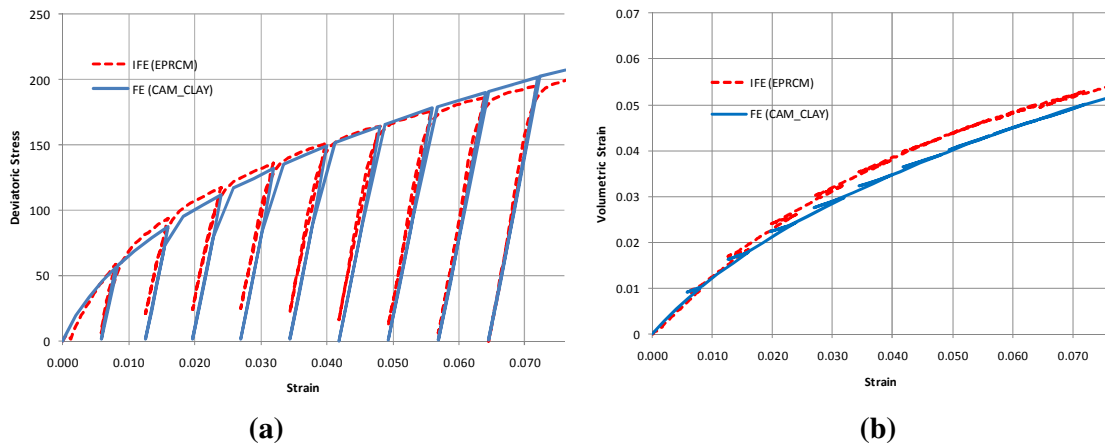


Fig. 1: Comparison between the results of the EPR-based FEA and a conventional FEA for multiple regular loading cycles.

References

- [1] A.A. Javadi and M. Rezaia. Applications of artificial intelligence and data mining techniques in soil modelling. *Geomechanics and Engineering: An International Journal*, 1(1), 53-74, 2009.
- [2] A.A. Javadi, M. Mehravar, A. Faramarzi and A. Ahangar-Asr. An Artificial Intelligence based finite element method. *Transactions on Computers and Intelligent Systems* 1(2), 1-7, 2009.
- [3] O. Giustolisi and D. Savic. A symbolic data-driven technique based on evolutionary polynomial regression. *Journal of Hydroinformatics* 8(3), 207-222, 2006.
- [4] A. Ahangar-Asr, A. Faramarzi and A.A. Javadi. New Approach for Prediction of the Stability of Soil and Rock Slopes, *Engineering Computations*, 27(7), 878-893, 2010.
- [5] M. Rezaia, A. Faramarzi and A.A. Javadi. An evolutionary based approach for assessment of earthquake-induced soil liquefaction and lateral displacement, *Engineering Applications of Artificial Intelligence*, 24(1), 142-153, 2011.
- [6] A. Doglioni, O. Giustolisi, D. Savic and B. Webb. An investigation on stream temperature analysis based on evolutionary computing, *Hydrological Processes*, 22(3), 315-326, 2008.
- [7] J. Ghaboussi, D. Pecknold, M. Zhang and R. Haj-Ali. Autoprogressive training of neural network constitutive models, *International Journal for Numerical Methods in Engineering*, 42(1), 105-126, 1998.

Material plastic properties characterization by coupling experimental and numerical analysis of small punch beam tests

Xingguo Zhou¹, Wenke Pan^{1*}, Donald Mackenzie¹

¹Department of Mechanical Engineering, University of Strathclyde, UK.75 Montrose Street, Glasgow, G1 1XJ
*wenke.pan@strath.ac.uk

Key Words: *small punch beam test; plasticity; material characterization; genetic algorithm*

ABSTRACT

The small punch test method of characterizing material properties was introduced about thirty years ago. It has an advantage over conventional tensile test methods in that only a small sample of material is needed. A disadvantage of the method is that manufacture of the small hemispherical punch head is difficult and expensive due to the high dimensional accuracy requirements. Here an alternative design of punch is presented: a small punch beam test system consisting of a top die, a bottom die and a flat punch with semi-circular cross-section head. By coupling the numerical modelling and experimental results, a genetic algorithm has been used to characterize the material plastic properties.

1 INTRODUCTION

The small punch testing (SPT) technique was developed to characterize material properties in the late 1970s^[1]. In the test, a cylindrical punch with a hemispherical head deforms a thin disc shape specimen, which is clamped between two co-axial hollow cylindrical dies. The punch force and the specimen central displacement are recorded and material properties evaluated through comparison with theoretical or numerical models of deformation. Material properties that have been evaluated by SPT include elastic modulus, plastic deformation properties such as yield stress and tensile strength^[2], creep properties^[3] and fracture properties^[4]. Comparison of SPT results with conventional tensile testing (CTT) method is very encouraging.

One practical advantage of SPT over CTT is that the specimen size is very small and therefore only small samples of material are required for testing. This is particularly useful when testing material from operating plant for life extension programs, as the small amount of material required can often be removed from the surface of components without plant shutdown and intrusive welded repairs are not required afterwards. One disadvantage of SPT is the difficulty and expense of manufacturing the 2.5mm diameter hemi-spherical head punch to the required dimensional accuracy. To overcome this problem, an alternative Small Punch Plane Strain (SPPS) test system with a cylindrical punch contact surface and rectangular test specimen was designed^[5]. The new system has been successfully used to characterize material's plastic properties, with Ramberg-Osgood constitutive relationship employed. Recently, instead of using rectangular specimens, Sehgal *et. al*^[6] used small beam samples for their punch tests. The yield strength and fracture toughness of die steel D3 and Chromium steel H11 were evaluated and compared with the values obtained from standard tests. Their simulated load vs. displacement curves were in good agreement with the results obtained experimentally.

In this paper, a small punch testing system based on a small beam shape specimen and punch similar to that of SPPS is presented. Material properties are evaluated from the deformation through comparison with multi-linear strain hardening Finite Element models of specimen deformation and a genetic algorithm that uses a cost function based on the relative difference between the experimental and testing forces at the top centre of the beam.

2 SMALL PUNCH BEAM TESTING TOOL DESIGN

The small punch beam testing tool system is shown in Figure 1. Similar to conventional small punch test, this tool system includes a punch, a top die and a bottom die. Instead of thin disc shape sample, a beam with rectangle cross-section shape is used. The hollow cylindrical top and bottom dies of the conventional SPT are replaced by top and bottom blocks, each with a narrow through slot. A shallow slot with depth of 1.5mm and width of 2mm is designed for the test beam specimen to sit in. The punch is a rectangular bar with a half-cylinder profile contact surface, overcoming manufacturing difficulties associated with a hemispherical punch. The radius of the punch head is 1.25mm and the width of the punch is 8mm.

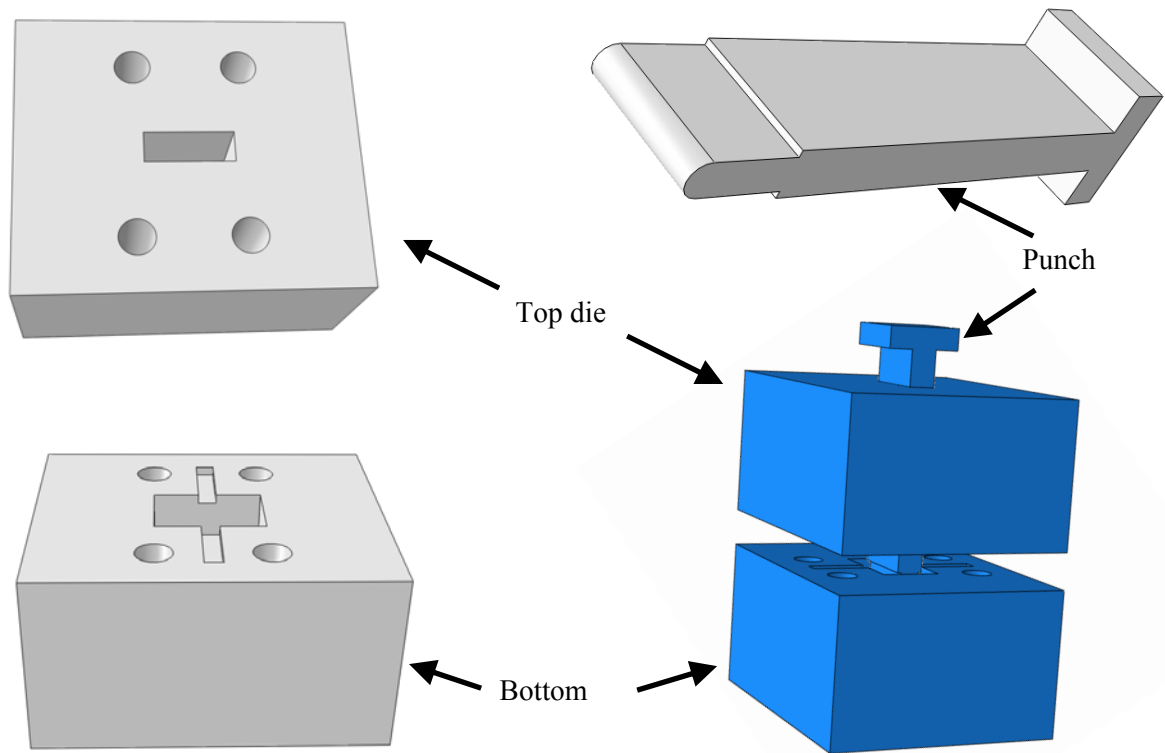


Figure 1 The small punch beam testing tool components

To ensure the specimen is held tightly during the testing, the depth of the slot is 0.2mm less than the height of the beam, therefore sufficient clamping pressure will be applied to the ends of the beam to prevent slip when tightening the screws connecting the top and bottom blocks.

3 FEM NUMERICAL MODELLING

Figure 2 shows a typical three dimensional ABAQUS/implicit finite element model, which consists of punch, top and bottom die and beam specimen. The specimen is Aluminum and the punch high strength steel, which is much stronger than the specimen. The simulation is therefore simplified by assuming the punch to be a rigid body. The dies are modeled using ABAQUS three dimensional 8-node brick element with reduced integration, assuming a linear elastic material. The specimen is modeled using the higher order C3D20R because of the large deformation of the specimen at the centre and near the die shoulder areas. Friction between punch and specimen, specimen and top die and specimen and bottom die is modeled, assuming a friction factor of 0.3. Both top and bottom die surfaces are constrained with no movement allowed along the loading direction. A reference point is defined for the rigid punch and all degrees of freedom of the reference point are constrained apart from the displacement control in the loading direction.

No distinct yield point is observed in stress-strain curves of this type of Aluminum alloy, therefore, the yield stress is defined as the stress corresponding to 0.2% plastic strain. A multi-linear strain hardening material model, as shown in Figure 3, is assumed for analysis. There are three material hardening parameters S1, S2 and S3 to be identified, where S1 and S2 representing stress at the beginning of yield and plastic strain of 0.2%, while S3 representing the ultimate tensile strength. Both material and geometrical nonlinearity are considered in the simulation.

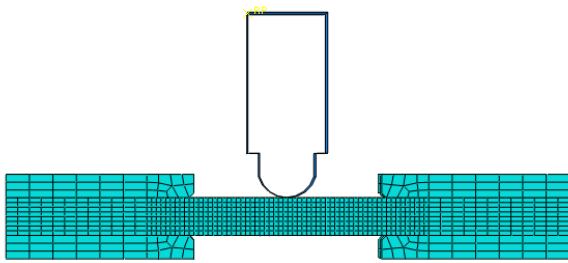


Figure 2 Finite element model

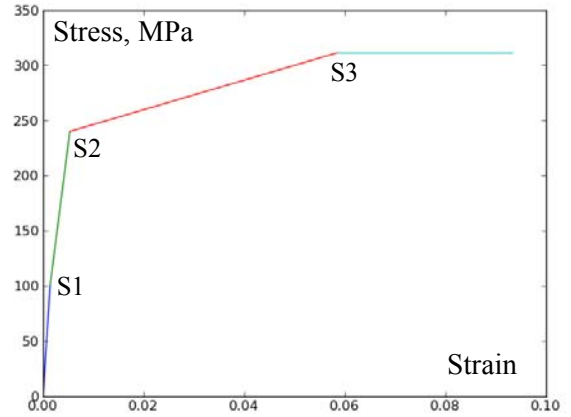


Figure 3 Multi-linear stress strain curve with parameters S1, S2 and S3 to be identified

4 GENETIC ALGORITHM

A Genetic Algorithm (GA) method is applied to characterize the material nonlinear parameters. The flow chart of a general GA optimization procedure is given in Figure 4. Equation 1 shows the formulation of the objective function Φ , which is defined as the square root of the average of the summation of the square of the relative difference between the experimental and numerical results. The fitness is simply chosen as the inverse of the objective function, i.e. $f = \frac{1}{\Phi}$.

$$\Phi = \sqrt{\frac{1}{n} \sum_{i=1}^n \left(\frac{F_i^{cal} - F_i^{exp}}{F_i^{exp}} \right)^2}$$

Equ.1

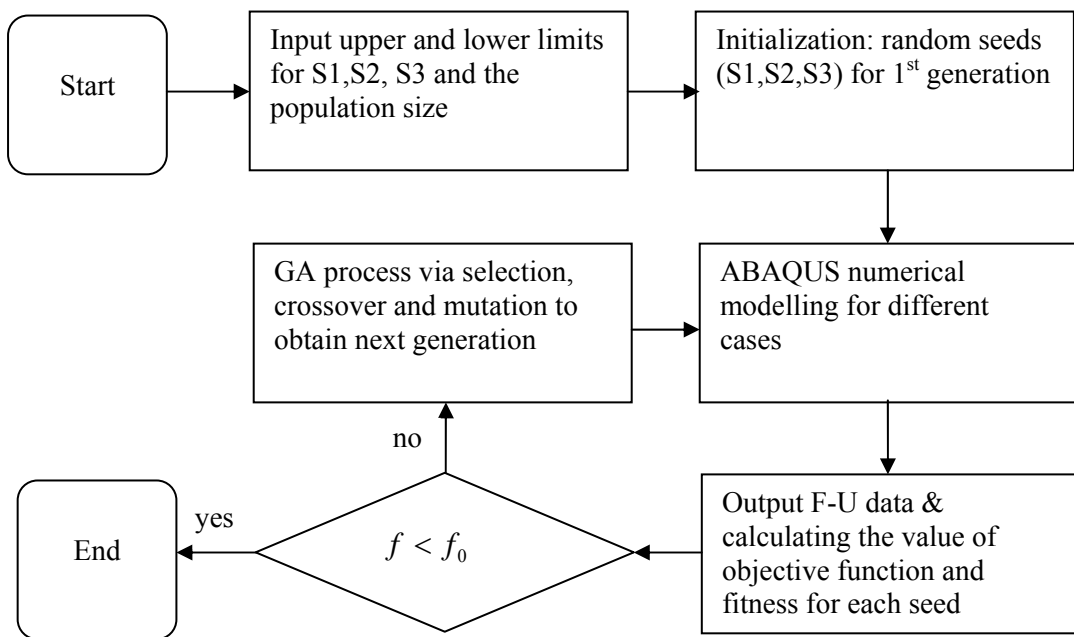


Figure 4 Flow chart of the genetic algorithm

Smaller values of the objective function correspond to the larger values of the fitness. The general GA procedure consists of selection, crossover and mutation, with a higher fitness seed having more chance to be selected and one of the fittest off-spring at each generation always being kept. The GA procedure stops when the convergence criterion is satisfied.

5 RESULTS

The cross-head speed of the press machine used for the test is very slow and the problem is treated as a static problem. Mesh convergence was investigated first, with three cases having different mesh sizes being studied. The results from the finest mesh are used for all the data analysis as the relative error of the calculated displacement at the central point on bottom surface is less than 1.5% if compared with the coarser mesh having roughly twice the mesh size of the finest mesh.

After 20 generations of GA evolution, the best value of the objective function is 6.5%. The values of the material parameters S1, S2 and S3 are 102.2MPa, 219.9MPa and 509MPa respectively. Figure 5 shows the comparison between the numerically predicted force

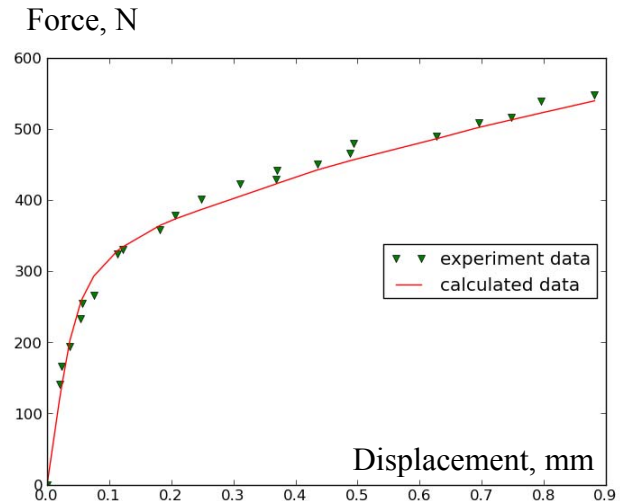


Figure 5 Comparison between the numerically predicted force vs beam top surface central displacement and experimentally obtained curve

versus beam top surface central displacement and that of experimentally obtained force. From this figure, it can be seen that the numerical results are in good agreement with that of experimental results. Due to the fluctuation of the experimental results, it is difficult to obtain better results after 20 iterations. The tested Aluminium has no obvious yield point, but the ultimate tensile stress identified from this GA procedure is very close to 483MPa (relative error is 5%) obtained through conventional tensile testing.

6 CONCLUSIONS AND FUTURE WORK

A small punch beam testing system has been designed and GA method coupled with experimental and numerical results to characterize the material plastic properties. The relative error between the predicted ultimate tensile strength and those obtained by conventional tensile testing method is about 5%. The advantages of this method include the lower cost of manufacturing of the punch, the smaller volume of material required for testing and the GA method predicts the material properties automatically. Future work will be extension of this method to material damage parameters and fracture toughness identification.

References

- [1] Manahan, M.P, Argon, A.S., and Harling O.K., J. of Nuclear Materials, 103&104, North-Holland Publishing Company, 1981, PP. 1545-1550.
- [2] Abendroth, M. and Kuna, M., Computational Materials Science, 28(2003), pp633-644.
- [3] Xiang Ling, Yangyan Zheng, Yingjun You and Yuxin Chen, International Journal of Pressure Vessels and Piping, Volume 84, Issue 5, May 2007, Pages 304-309
- [4] Mao, X., Takahashi, H., J. of Nuclear Material, 1987, vol. 150, North Holland Publi. Co., pp44-52.
- [5] W. Pan, Jim Boyle, Mohd. Ramlan, Craig Dun, Mohd. Ismail, Kenji Hakoda, selected for Czech Metallurgical Journal, Vol. LXIII, 2010, pp.174-179.
- [6] Sehgal, D.K. Husain, A. and Pandey, R.K., Mechanical and Electronics Engineering (ICMEE), 2010, 2nd International Conference, Vol.1, V1-196-V1-199, Kyoto, ISBN: 978-1-4244-7479-0.

CDPM2: A DAMAGE-PLASTICITY APPROACH TO MODEL THE DYNAMIC FAILURE OF CONCRETE

Peter Grassl

School of Engineering, University of Glasgow, Glasgow, United Kingdom

peter.grassl@glasgow.ac.uk

Key Words: *concrete; constitutive model; damage; plasticity; failure*

ABSTRACT

A constitutive model based on the combination of damage mechanics and plasticity is developed to analyse concrete structures subjected to dynamic loading. The aim is to obtain a model, which requires input parameters with clear physical meaning. The model should describe the important characteristics of concrete subjected to multiaxial and rate-depending loading. This is achieved by combining an effective stress based plasticity model with an isotropic damage model based on plastic and elastic strain measures. The model response in tension and multiaxial compression is compared to experimental results in the literature.

1 INTRODUCTION

Concrete is a strongly heterogeneous material, which exhibits a complex nonlinear mechanical behaviour. Failure in tension and low confined compression is characterised by softening which is defined as decreasing stress with increasing deformations. This softening response is accompanied by a reduction of the unloading stiffness of concrete, and irreversible (permanent) deformations, which are localised in narrow zones often called cracks or shear bands. On the other hand, the behaviour of concrete subjected to high confined compression is characterised by a ductile hardening response; that is, increasing stress with increasing deformations. Furthermore, high loading rates are known to significantly increase the strength in tension and compression. These phenomena should be considered in a constitutive model for analysing the dynamic behaviour of concrete structures.

In the present work, the combined damage-plasticity model presented in [2, 3] (CDPM1) is revisited to develop a constitutive model for the rate dependent failure of concrete, which is characterised by its numerical stability, well defined input parameters and flexibility to be adapted to newly developed concrete based materials, such as fibre reinforced concrete. As this model can be seen as an augmentation of CDPM1, it is called here CDPM2. The stress-based plasticity part of the model is based on the effective stress. It includes hardening in the post-peak regime, which is used to model the strain rate

dependence of strength by delaying the onset of damage. The plasticity part is combined with a damage model, which is based on elastic and plastic strain measures and distinguishes between tensile and compressive stress states using an approach similar to those proposed in [6, 7, 1]. The damage model is used to describe the complex strength envelope of concrete. With this combination of plasticity and damage mechanics, it is aimed to provide a computationally efficient model for the dynamic behaviour of concrete. The present extended abstract illustrates some of the features of the model. For a more detailed description, see [4].

2 CONSTITUTIVE MODEL

The damage plasticity constitutive model is based on the following stress-strain relationship:

$$\boldsymbol{\sigma} = (1 - \omega_t) \bar{\boldsymbol{\sigma}}_t + (1 - \omega_c) \bar{\boldsymbol{\sigma}}_c \quad (1)$$

where $\bar{\boldsymbol{\sigma}}_t$ and $\bar{\boldsymbol{\sigma}}_c$ are the positive and negative parts of the effective stress tensor $\bar{\boldsymbol{\sigma}}$, respectively, and ω_t and ω_c are two scalar damage parameters, ranging from 0 (undamaged) to 1 (fully damaged). The effective stress $\bar{\boldsymbol{\sigma}}$ is defined as

$$\bar{\boldsymbol{\sigma}} = \mathbf{D}_e : (\boldsymbol{\varepsilon} - \boldsymbol{\varepsilon}_p) \quad (2)$$

where \mathbf{D}_e is the elastic stiffness tensor based on the elastic Young's modulus E and Poisson's ratio ν , $\boldsymbol{\varepsilon}$ is the strain tensor and $\boldsymbol{\varepsilon}_p$ is the plastic strain tensor. The positive and negative parts of the effective stress $\bar{\boldsymbol{\sigma}}$ in Eq. (1) are determined from the principal effective stress as $\bar{\boldsymbol{\sigma}}_{pt} = \langle \bar{\boldsymbol{\sigma}}_p \rangle_+$ and $\bar{\boldsymbol{\sigma}}_{pc} = \langle \bar{\boldsymbol{\sigma}}_p \rangle_-$, where $\langle \cdot \rangle_+$ and $\langle \cdot \rangle_-$ are positive and negative part operators, respectively, defined as $\langle x \rangle_+ = \max(0, x)$ and $\langle x \rangle_- = \min(0, x)$. In addition, a scalar measure α_c is defined which distinguishes between tensile and compressive stress states. It has the form

$$\alpha_c = \sum_i \frac{\langle \bar{\sigma}_{pi} \rangle_- (\langle \bar{\sigma}_{pi} \rangle_+ + \langle \bar{\sigma}_{pi} \rangle_-)}{\|\bar{\boldsymbol{\sigma}}_p\|^2} \quad (3)$$

where $\langle \bar{\sigma}_{pi} \rangle_+$ and $\langle \bar{\sigma}_{pi} \rangle_-$ are the components of the compressive and tensile part of the principal stresses, respectively. The parameter α_c varies in the range from 0 to 1.

The plasticity model is based on the effective stress and thus independent of damage. The model is described by the yield function, the flow rule, the evolution law for the hardening parameter and the loading-unloading conditions.

The damage part of the present damage-plasticity model is related to elastic and plastic strain measures. The geometrical interpretation of these strain measures for uniaxial tension, hardening plasticity and linear damage evolution are shown in Fig. 1. The part $\omega(\boldsymbol{\varepsilon} - \boldsymbol{\varepsilon}_p)$ is reversible and $\boldsymbol{\varepsilon}_p$ is irreversible.

3 MODEL RESPONSE

The response of the constitutive model is illustrated by several idealised load cases. Firstly, a quasi-static strain cycle is considered, which results in a stress-strain response shown in Fig. 1. The strain is increased from "0" to "1", where the tensile strength of the material is reached. Up to point "1", the material response is elastic-plastic with small plastic strains. With a further increase of the strain from "1" to "2", the effective stress part continues to increase, as the model exhibits hardening, whereas the nominal stress decreases, since the tensile damage variable ω_t increases. A reverse of the strain at

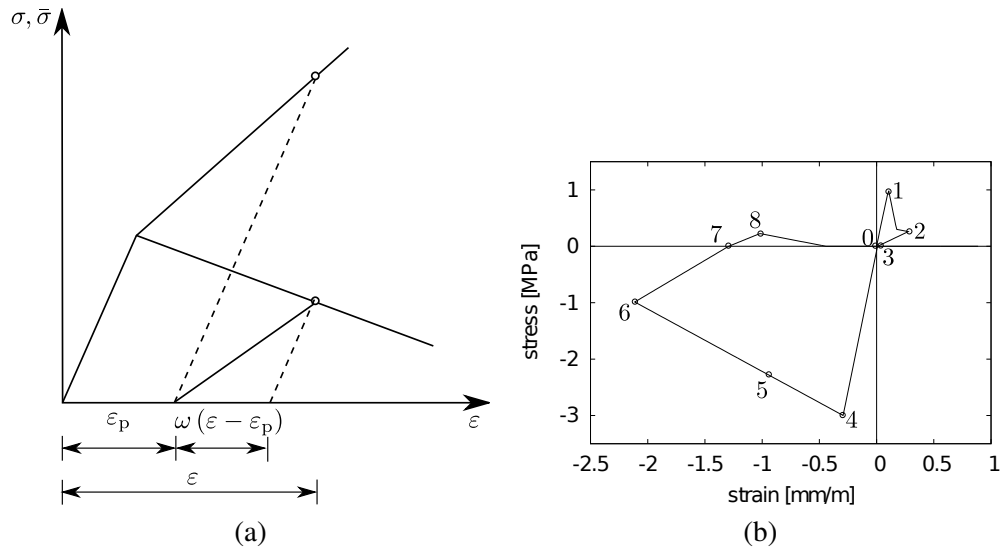


Figure 1: (a) Geometrical meaning of the inelastic strain ε_i for the combined damage-plasticity model. The inelastic strain is composed of reversible $\omega(\varepsilon - \varepsilon_p)$ and irreversible ε_p parts. The dashed lines represent elastic unloading with the same stiffness as the initial elastic loading. (b) Cyclic response obtained with the constitutive model.

point “2” results in an reduction of the stress with an unloading stiffness, which is less than the elastic stiffness of an elasto-plastic model, but greater than the stiffness of an elasto-damage mechanics model. At point “3” when the stress is equal to zero, a further reduction of the strain leads to a compressive response following a linear stress-strain relationship between the points “3” and “4” with the original Young’s modulus E of the undamaged material. This change of stiffness is obtained by using two damage parameters, ω_t and ω_c . At point “3” $\omega_t > 0$, but $\omega_c = 0$. Up to “4” no further plastic strains are generated, since the hardening from “0” to “1” has increased the elastic domain of the plasticity part so much that the yield surface is not reached at “4”. A further decrease of the strain activates the compressive damage variable which leads to a reduction of the nominal stress. At point “5”, the plasticity surface is reached and a subsequent increase of strain results in hardening of the plasticity part. However, the nominal stress, shown in Figure 1b, decreases, since ω_c increases. A second reversal of the strain direction (“6”) changes the stress from tension to compression at “7”, which is again associated with a change of the stiffness.

The second example consists of several tensile loading cases with constant strain strain rates of 1×10^{-6} , 1, 10 and 100 1/s. The corresponding stress strain responses are shown in Fig. 2a. An increase of the loading rate results in a delay of the onset of damage. The initial stiffness is modelled to be independent of the strain rate.

Finally, the model response in triaxial compression is compared to the experimental results reported in [5] (Fig. 2). The material constants for this test are $E = 25$ GPa, $\nu = 0.2$, $f_c = 28$ MPa, $f_t = 2.8$ MPa, $G_{Ft} = 100$ J/m², $G_{Fc} = 15000$ J/m². Overall, the agreement of the model response with the experimental results is very good. The model is able to represent the strength of concrete in multiaxial compression. In addition, the strains at maximum stress agree well with the experimental results.

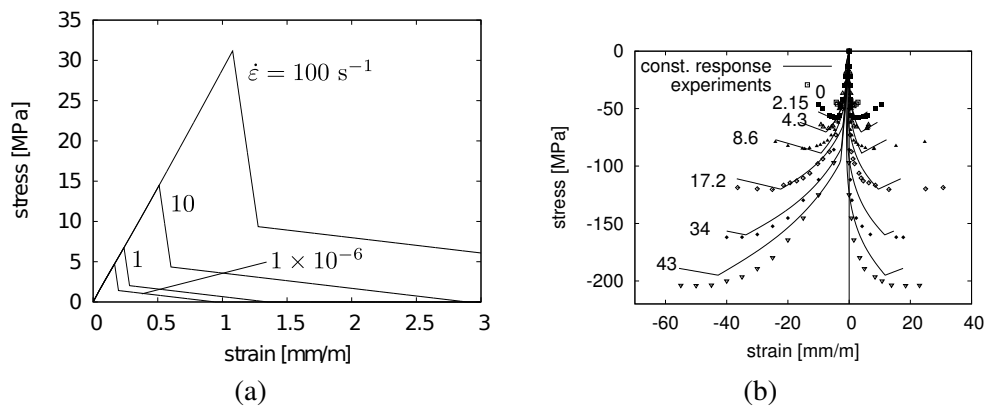


Figure 2: (a) Rate effect in tension: Stress strain response for four tensile strain rates. (b) Confined compression: Model response compared to experiments reported in [5].

4 CONCLUSIONS

The present damage plasticity model combines a stress-based plasticity part with a strain based damage mechanics model. The model response is in good agreement with experimental results for a wide range of loading from uniaxial tension to confined compression. In the next steps, the model will be applied to boundary value problems to evaluate its performance to describe failure processes of concrete mesh-independently. It is expected that the model will perform well for these problems since the softening response is formulated so that the crack band approach can be applied, which is known to lead in many cases to mesh-independent results.

References

- [1] S. Fichant, C. La Borderie, and G. Pijaudier-Cabot. Isotropic and anisotropic descriptions of damage in concrete structures. *Mechanics of Cohesive-Frictional Materials*, 4:339–359, 1999.
- [2] P. Grassl and M. Jirásek. Damage-plastic model for concrete failure. *International Journal of Solids and Structures*, 43(22-23):7166–7196, 2006.
- [3] P. Grassl and M. Jirásek. A plastic model with nonlocal damage applied to concrete. *International Journal for Numerical and Analytical Methods in Geomechanics*, 30:71–90, 2006.
- [4] P. Grassl, U. Nyström, R. Rempling, and K. Gylltoft. A damage-plasticity model for the dynamic failure of concrete. In *8th International Conference on Structural Dynamics*, Leuven, Belgium, 2011.
- [5] I. Imran and S. J. Pantazopoulou. Experimental study of plain concrete under triaxial stress. *ACI Materials Journal*, 93:589–601, 1996.
- [6] J. Mazars. Application de la mécanique de l’endommagement au comportement non linéaire et à la rupture du béton de structure. Thèse de Doctorat d’Etat, Université Paris VI., France, 1984.
- [7] M. Ortiz. An analytical study of the localised failure modes of concrete. *Mechanics of Materials*, 6:159–176, 1987.

A HYSTERETIC MODEL FOR STEEL PLATE SHEAR WALLS

Asaad Faramarzi¹, *Moura Mehravar¹, Hedayat Veladi², Akbar A. Javadi¹, Alireza Ahangar-Asr¹,
Maziar Mehravar³

¹ College of Engineering, Mathematics and Physical Sciences, University of Exeter, UK

² Department of Structural Engineering, University of Tabriz, Iran

³ Department of Civil Engineering, Azad University of Zanjan, Iran

*mm454@ex.ac.uk

Key Words: *Steel plate shear walls; cyclic loading; EPR*

ABSTRACT

In the past few decades, steel plate shear walls (SPSW) have been used in numerous tall buildings as a resistant system against lateral loads. The perceived advantages of these systems in seismic resistant structures include enhanced stiffness, strength and ductility, and stable hysteretic characteristics. Various researchers have studied the behaviour of SPSW under cyclic loading and proposed different models in order to predict the behaviour of these structures under complex loading conditions. In this paper a new approach based on evolutionary polynomial regression (EPR) is proposed, for the prediction of the behaviour of SPSW under cyclic loading using data from laboratory tests on scaled samples of SPSW. It is shown that the EPR model is able to predict the behaviour of SPSW under cyclic loading.

1 INTRODUCTION

A steel plate shear wall (SPSW) consists of steel infill plates bounded by a column-beam system. For the past few decades, experimental and analytical studies have been performed on the use of steel plate shear walls as primary lateral load resisting elements in buildings. Steel plate shear walls have been proposed as viable structural alternatives to resist lateral loads in medium- and high-rise steel construction, particularly in areas of high seismic risk.

Many researchers have studied the behaviour of SPSW under cyclic loading and presented different analytical and numerical models to predict their behaviour. Timler and Kulak (1983) reported a number of static and quasi-static cyclic tests that were performed on large- and small-scale specimens, accompanied with analytical models [1]. Driver et al. (1998) performed a test on a large-scale four-story test specimen of SPSW and developed a nonlinear finite element model for this specimen [2]. They observed a good agreement between the results of the finite element analysis and those of the experiment. Moreover they offered an analytical method based on tension strips for monotonic behaviour. Elgaaly et al. (1993) developed the analytical models that were capable of predicting accurately the behaviour of the wall in the post-buckling domain under monotonic and cyclic loads [3]. Lubell et al. (2000) presented a study on the performance of un-stiffened thin plate shear walls for medium- and high-rise buildings [4]. They performed experimental testing on two single- and one four-story steel shear wall specimens, under cyclic quasi-static loading. The experimental results were then compared with simplified tension field analytical models, based on recommendations in the Canadian code for limit-states design of steel structures. Rezaei et al. (2000) carried out a numerical study using different strip models and compared the results with results of two cyclic tests on single story and one four-story specimens tested at the University of British Columbia [5]. This proposed model predictions illustrated improved correlation with the envelope of cyclic test results achieved from the experimental studies at the University of British Columbia. Alinia and Dastfan (2006) presented a numerical study to investigate the effect of stiffening on the ultimate strength of shear panels [6]. They studied cyclic behaviour of stiffened and unstiffened shear panels. Park et al. (2007) performed an experimental study to investigate the cyclic behaviour of framed steel walls with thin infill plates. They tested five specimens with a single bay and three stories under cyclic lateral

loading and investigated the effects of plate thickness and the strength and compactness of the column [7]. Sabouri-Ghomi and Gholhaki (2008) studied the ductility of thin steel plate shear walls based on ATC-24 protocol and Popov's definition. They tested two three-story unstiffened steel plate shear walls under cyclic loading [8].

On the other hand, in the past few decades, the use of artificial neural networks (ANN) has been introduced as an alternative approach to predict the cyclic behaviour of materials. Yun et al. 2008 (a) presented an approach for ANN-based modelling of the cyclic behaviour of materials [9]. They focused on the issue of hysteric behaviour of material where one strain value may correspond to multiple stresses. In order to overcome on this issue, they introduced two new internal variables in addition to the other ordinary inputs of the ANN-based constitutive material models to help the learning of the hysteretic and cyclic behaviour of the material. The ANN models trained in this way were implemented in a FE model to analyse a boundary value problem (steel beam-column connection) under cyclic loading. Yun et al. 2008 (b) extended the ANN-based cyclic material model developed by Yun et al. 2008 (a) to beam-column connections by adding the mechanical and design parameters as inputs of the ANN model [10].

In this paper, a different approach is presented for modelling cyclic behaviour of SPSW using evolutionary polynomial regression (EPR). In the proposed EPR approach the optimum structure for the model representation and its parameters are determined directly from raw data. Furthermore, it provides a transparent and structured representation of the relationships. In what follows, the main principles of EPR will be outlined. The application of EPR in modelling the cyclic behaviour of SPSW will be illustrated through an example.

2 EVOLUTIONARY POLYNOMIAL REGRESSION

Evolutionary polynomial regression (EPR) is a data-driven method based on evolutionary computing, aimed to search for polynomial structures representing a system. A general EPR expression can be presented as [11]

$$y = \sum_{j=1}^n F(X, f(X), a_j) + a_0$$

where y is the estimated vector of output of the process; a_j is a constant; F is a function constructed by the process; X is the matrix of input variables; f is a function defined by the user; and n is the number of terms of the target expression. The general functional structure represented by $F(X, f(x), a_j)$ is constructed from elementary functions by EPR using a genetic algorithm (GA) strategy. The GA is employed to select the useful input vectors from X to be combined. The building blocks (elements) of the structure of F are defined by the user based on understanding of the physical process. While the selection of feasible structures to be combined is done through an evolutionary process, the parameters a_j are estimated by the least square method.

EPR is a technique for data-driven modelling. In this technique, the combination of the genetic algorithm to find feasible structures and the least square method to find the appropriate constants for those structures implies some advantages. In particular, the GA allows a global exploration of the error surface relevant to specifically defined objective functions. By using such objective (cost) functions some criteria can be selected to be satisfied through the search process. These criteria can be set in order to (a) avoid the overfitting of models; (b) push the models towards simpler structures; and (c) avoid unnecessary terms representative of the noise in data. An interesting feature of EPR is in the possibility of getting more than one model for a complex phenomenon. A further feature of EPR is the high level of interactivity between the user and the methodology. The user physical insight can be used to make hypotheses on the elements of the target function and on its structure (Equation 1). Selecting an appropriate objective function, assuming pre-selected elements in Equation (1) based on engineering judgment, and working with dimensional information, enable refinement of final models. One of the most outstanding features of EPR is that it learns the material behaviour directly from raw experimental data; so the EPR based constitutive model is the shortest route from experimental research (data) to numerical modelling, which is very advantageous especially in modelling of materials with complex behaviour. Furthermore, as more data

becomes available, the material model can be improved by re-training EPR. Detailed explanation of the method can be found in [11].

3. CYCLIC BEHAVIOR MODELLING USING EPR

Data from an experimental test performed by Veladi et al. 2007 were utilized to develop the EPR model [12]. The test was carried out by applying lateral loads through the steel brackets connected to the top beam. In development of the EPR model, δ_i , F_i , $\Delta\delta_i$, $\xi\delta_i$, $\Delta\eta_{\delta,i}$ were used as input and F_{i+1} as the output where the subscript i indicates i^{th} incremental step and δ_i , F_i , $\Delta\delta_i$ are drift, lateral force and the rate of drift in the i^{th} step respectively. As stated before Yun et al. 2008 (a) introduced two additional variables to overcome the issue of hysteresis modelling where one drift value may correspond to multiple lateral forces. This has also been used in the presented study and the following variables have been introduced.

$$\xi_{\delta,i} = F_i \times \delta_i, \quad \Delta\eta_{\delta,i} = F_i \times \Delta\delta_{i+1}$$

At the end of the training process, the selected best EPR model representing the cyclic behaviour of SPSW is:

$$F_{i+1} = 0.99 F_i + 1.8 \times 10^{-6} F_i \Delta \eta_{\delta,i} - 3.9 \times 10^{-12} F_i \Delta \eta_{\delta,i}^2 - 3.3 \times 10^{-13} F_i^2 \Delta \delta_{i+1} \xi_{\delta,i} + 1.5 \times 10^{-7} \delta_i^3 \Delta \eta_{\delta,i}$$

Figure 1 shows a comparison between the results obtained from the EPR model and the experimental data used for training of the EPR. It can be seen that the EPR model can give an excellent prediction of the cyclic behaviour of SPSW.

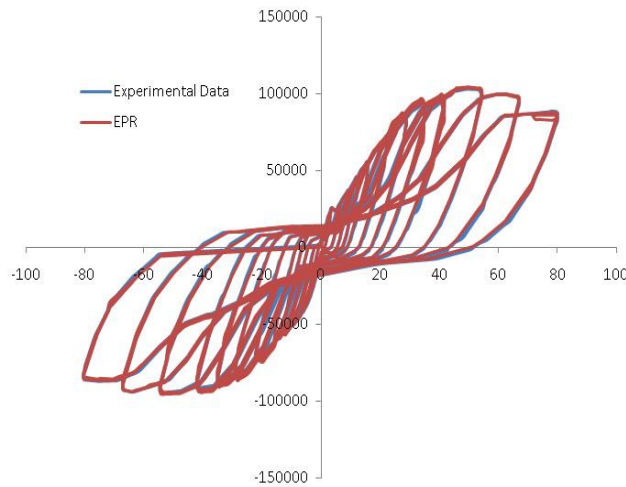


Fig. 1 Results of validation of the EPR model

4. SUMMARY AND CONCLUSIONS

A new approach was introduced to predict the behaviour of steel plate shear walls under cyclic loading based on evolutionary polynomial regression (EPR). EPR models were trained by the data from a cyclic test on a SPSW specimen. In development of the EPR models 5 inputs were used in which two of them were internal variables. EPR models were compared with experimental data and the best EPR model is presented. It was shown that a suitably trained EPR is able to predict the behaviour of SPSW under cyclic loading with a high degree of accuracy.

References

- [1] P.A. Timler, and G.A. Kulak. Experimental study of steel plate shear walls. *Structural Engineering report No. 114, University of Alberta*, 1983.
- [2] R.G. Driver, G.L. Kulak, A.E. Elwi, and D.J.L. Kennedy. FE and simplified models of steel plate shear wall. *Journal of structural Engineering*, 124(2), 121-130, 1998.
- [3] M. Elgaaly. Thin steel plate shear walls behaviour and analysis. *Thin-Walled Structures*, 32, 151-180, 1998.
- [4] A.S. Lubell, H.G.L. Prion, C.E. Ventura, and M. Rezai. Unstiffened steel plate shear wall performance under cyclic loading. *Journal of structural Engineering*, 126(4), 453-460, 2000.
- [5] M. Rezai, C.E. Ventura, and H. G.L. Prion. Numerical investigation of thin unstiffened steel plate shear walls. *Proceeding of 12th WCEE conference, New Zealand*, 2000.
- [6] M.M. Alinia, and M. Dastfan. Cyclic behaviour, deformability and rigidity of stiffened steel shear panels. *Journal of Constructional Steel Research*, 63, 554-563, 2007.
- [7] H. Park, J. Kwack, S. Jeon, W. Kim, and I. Choi. Framed steel plate wall behaviour under cyclic lateral loading. *Journal of structural Engineering*, 133(3), 378-388, 2007.
- [8] S. Sabouri-Ghomi, and M. Gholhaki. Ductility of thin steel plate shear walls. *Asian Journal of civil engineering (building and housing)*, 9(2), 153-166, 2008.
- [9] G.J. Yun, J. Ghaboussi, and A.S. Elnashai. A new neural network-based model for hysteretic behaviour of materials. *International journal for numerical methods in engineering*, 73, 447-469, 2008.
- [10] G.J. Yun, J. Ghaboussi, and A.S. Elnashai. A design-variable-based inelastic hysteretic model for beam-column connections. *Earthquake engineering and structural dynamics*, 37, 535-555, 2008.
- [11] O. Giustolisi and D. Savic. A symbolic data-driven technique based on evolutionary polynomial regression. *Journal of Hydroinformatics* 8(3), 207-222, 2006.
- [12] H. Veladi, A. Armaghani, and A. Davaran. Experimental investigation on cyclic behaviour of steel shear walls. *Asian Journal of civil engineering (building and housing)*, 8(1), 63-75, 2007.

A robust local arc-length method for multiscale problems

Ahmad Akbari R.¹, Pierre Kerfriden¹, Timon Rabczuk², and *Stéphane P.A. Bordas³

¹School of Engineering, Cardiff University, Queen's buildings, Cardiff, UK, CF24 3AA

²Institute of Structural Mechanics, Bauhaus-University Weimar Marienstrae 15, 99423 Weimar,
Germany

³Royal Academy of Engineering/Leverhulme Senior Research Fellow

*stephane.bordas@alumni.northwestern.edu

Key Words: *multiscale, local arc-length, cohesive crack*

ABSTRACT

In this paper, a new local arc-length method has been introduced to follow the snap-back at the microscale as well as in the macroscale for a multiscale problem. First order multiscale computational homogenization (FE2) approach has been employed to study the behaviour of a one dimensional (1D) bar with cohesive cracks in the both scale. The macroscale material properties and constitutive equations are unknown. The local macroscopic constitutive response is determined by solving the related microscale Representative Volume Element (RVE). Each RVE has cohesive cracks whose damage parameters are a function of the displacement jump. The non-damaged part of RVEs are assumed to be linear elastic. In FE2 multiscale methods, the arc-length method is used in the macroscale and the displacement control method is used in the microscale, however, the displacement control cannot follow the snap back. The comparison of the new local arc-length method and conventional local arc-length is presented.

1 Introduction

Almost all materials can be considered as heterogeneous at a specific scale. For example, composites, functionally graded materials, metals, biological materials and materials including micro-cracks can be called heterogeneous at some scales. Multiscale methods are used to solve the problems where information at the macro-level cannot simulate the response of the material. The first order computational homogenization method [1] have been implemented as a multiscale method for the analysis of materials with arbitrary non-linear behaviour at the fine scale. In this method, the macroscopic deformation gradient tensor is used to prescribe the essential boundary conditions on a micro-structural RVE. From the solution of the microscopic RVE, the macroscopic stress tensor and the corresponding tangential stiffness matrix are derived based on the Hill-Mandel condition. In this paper, a 1D bar with cohesive cracks in microscale has been solved by the FE2 method [2]. The macroscopic domain is discretized by

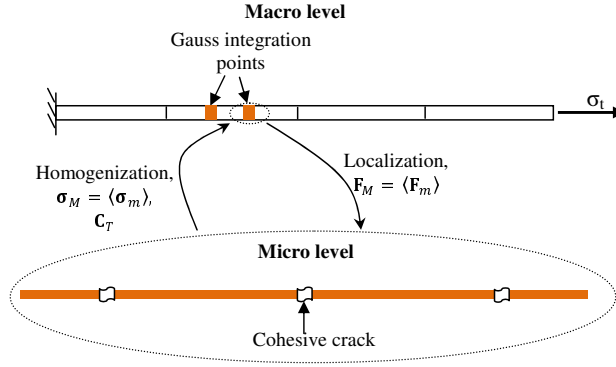


Figure 1: One dimensional bar with cohesive cracks in the microlevel

linear elements. For each integration point, an RVE which includes cohesive cracks has been defined. The following constitutive equation is considered for the damaged zones in the RVE:

$$\begin{aligned} f_c &= k E_0 (1 - d) \llbracket u \rrbracket \\ d &= \min(1, \max(d_0, \llbracket u \rrbracket)) \end{aligned} \quad (1)$$

where f_c is the internal force in the cohesive zone, $k \in]0, 1]$ is a constant coefficient, E_0 is the modulus of elasticity for the non-damaged zone, d_0 is the damage parameter for the last state of equilibrium, and $\llbracket u \rrbracket$ is the displacement jump in the cohesive crack zone.

Three different path-following techniques: displacement control, classic arc-length method [4] and local arc-length method [5], have been applied to study the behaviour of the bar in softening regime. Whereas none of these methods are able to follow the equilibrium equation path completely [6]. A new local arc-length method has been introduced which can track the equilibrium equation in both coarse and the fine scales.

The main difference between the local arc-length and the new local arc-length method is the scale in which the constraint equation is being applied. In the previous local arc-length, the constraint equation enforces the maximum strain of macroscale to remain below some predefined value, but in the new local arc-length method, the constraint equation is applied to the microscale to limit the maximum displacement jump of the RVEs. To solve the equations in an iterative manner, we link the equation of equilibrium in the macroscale to the constraint equation in the microscale through the localization of the macroscale strain as boundary condition of the RVE. The equilibrium equation in the macroscale and the constraint equation in the microscale have been assumed respectively as:

$$\mathbf{R}_f = \mathbf{f}_{in} + \lambda \mathbf{f}_e = \mathbf{0} \quad (2)$$

$$R_c = l_g - \mathbf{c} \mathbf{u}_m = 0 \quad (3)$$

where external force at the macroscale is defined as a load factor λ multiplied with a unit force vector \mathbf{f}_e . l_g is the maximum allowance of jump in the microscale displacement field, \mathbf{u}_m , and $l_g^{k+1} = l_g^k + \Delta l^{k+1}$ where Δl^{k+1} is the increment step size for $(k + 1)$ th step. \mathbf{c} is formal boolean linear operator that indicates the maximum jump in \mathbf{u}_m . We linearise these equations to solve in an iterative fashion by using a Newton-Raphson scheme:

$$\begin{bmatrix} \frac{\partial \mathbf{f}_{in}}{\partial \mathbf{U}_M} & \mathbf{f}_e \\ \frac{\partial R_c}{\partial \mathbf{U}_M} & 0 \end{bmatrix} \begin{bmatrix} \delta \mathbf{U}_M^{k+1} \\ \delta \lambda^{k+1} \end{bmatrix} = - \begin{bmatrix} \mathbf{R}_{in}^k \\ R_c^k \end{bmatrix} \quad (4)$$

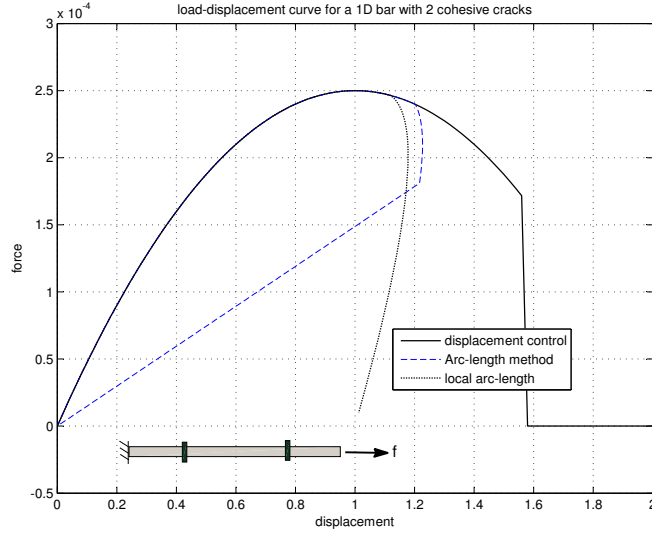


Figure 2: Load-displacement curve for a bar with 2 cohesive cracks

where $\frac{\partial \mathbf{f}_m}{\partial \mathbf{U}_M}$ is the macroscale tangential stiffness matrix which is obtained from homogenization of the microscale RVE, and the \mathbf{U}_M is a displacement vector at the macroscale. $\frac{\partial R_c}{\partial \mathbf{U}_M}$ can be calculated by using the linear relations between the RVE displacement boundary condition, \mathbf{u}_b , and macroscopic strain, $\boldsymbol{\varepsilon}_M$ ($\mathbf{u}_b = \mathbf{D}_b \boldsymbol{\varepsilon}_M$, where $\mathbf{D}_b = [x_l \ x_r]^T$ is the vector position of the RVE boundary nodes). This is written as

$$\frac{\partial R_c}{\partial \mathbf{U}_M} = -\mathbf{c} \frac{\partial \mathbf{u}_m}{\partial \mathbf{U}_M} = -[\mathbf{c}_i \ \mathbf{c}_b] \bar{\mathbf{K}}_m \mathbf{D}_b \mathbf{L} \mathbf{c}_M \quad (5)$$

where $[\mathbf{c}_i \ \mathbf{c}_b]$ is the modified form of \mathbf{c} . \mathbf{L} is the matrix of shape function derivatives at the macroscale, and \mathbf{c}_M is a boolean matrix that indicates the nodal displacement of macroscale element that corresponds to the RVE with the maximum jump. In Eq. (5), the matrix $\bar{\mathbf{K}}_m$ and \mathbf{D}_b are given by

$$\mathbf{u}_m = \bar{\mathbf{K}}_m \mathbf{u}_b, \quad \bar{\mathbf{K}}_m = \begin{bmatrix} -\mathbf{K}_{ii}^{-1} \mathbf{K}_{ib} \\ \mathbf{I}_{bb} \end{bmatrix} \quad (6)$$

where \mathbf{I}_{bb} is identity matrix.

2 Results and discussion

Figure 2 shows the comparison of the load-displacement curves of a bar with two cohesive cracks (in one scale) achieved by three different equilibrium path following techniques: displacement control, conventional arc-length method and local arc-length method. According to this figure, the displacement control technique cannot trace the load displacement curve in the snap back. The classic arc-length technique has passed through the limit point, but it could not trace the load-displacement curve correctly. The local arc-length method can trace the load-displacement curve completely, even in the snap back regime. But in the multiscale method, when we use the local arc-length procedure, it cannot follow the snap-back in the RVE. Since we have to use the displacement control procedure in microscale, the local arc-length fails in the macroscale.

A comparison of the result of local arc-length method and new local arc-length method for the multiscale problem is shown in Fig. 3. It can be seen that the new local arc-length method can trace the equation of equilibrium in snap-back regime for a multiscale problem.

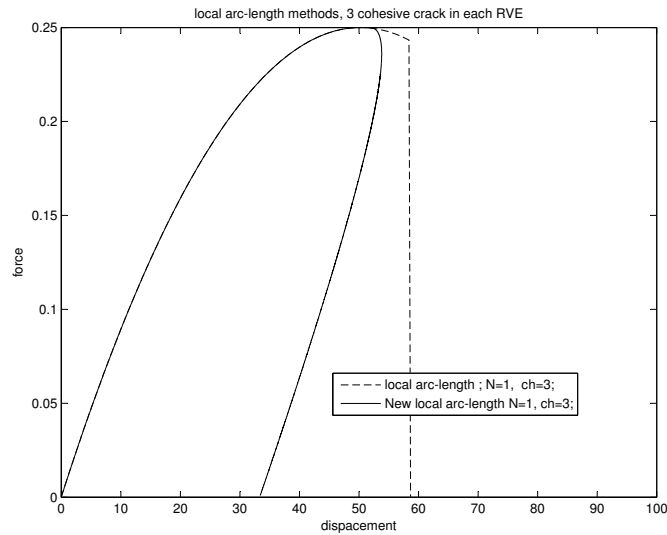


Figure 3: Load-displacement curve in macroscale

Acknowledgements

Stphane Bordas would like to acknowledge the financial support of the Royal Academy of Engineering and of the Leverhulme Trust for his Senior Research Fellowship entitled "Towards the next generation surgical simulators"

The authors also thank the financial support of Cardiff University's Schools of Engineering as well as that of the Overseas Research Student Award (ORSAS) for Mr. Ahmad Akbari R.

References

- [1] Kouznetsova V G, Computational homogenization for the multi-scale analysis of multi-phase materials. Eindhoven, Technische Universiteit Eindhoven, PhD thesis 2002.
- [2] Feyel F, Chaboche JL, FE2 multiscale approach for modelling the elastoviscoplastic behaviour of long ber SiC/Ti composite materials. *Comput. Methods Appl. Mech. Engrg.* 183: 309330, 2000.
- [3] Fish J, Shek K, Pandheeradi M, Shephard M S, Computational Plasticity for Composite Structures Based on Mathematical Homogenization: Theory and Practice, *Comp. Meth. Appl. Mech. Engng.*, Vol. 148, pp. 53-73, 1997.
- [4] Crisfield M A, Accelerated solution techniques and concrete cracking. *Computer Methods in Applied Mechanics and Engineering*, 33(1-3):585-607, 1982.
- [5] Kerfriden P, Gosselet P, Adhikari S, Bordas S P A, Bridging proper orthogonal decomposition methods and augmented Newton-Krylov algorithms: An adaptive model order reduction for highly nonlinear mechanical problems, *Computer Methods in Applied Mechanics and Engineering*, 200 (5-8) 850-866, 2010.
- [6] Gitman, I M, Askes, H., Sluys, L.J.. Representative volume: existence and size determination. *Engineering Fracture Mechanics* 74, 2518-2534, 2007.

A MICROMECHANICS-ENHANCED FINITE ELEMENT FORMULATION

*C.J. Pearce¹, Ł. Kaczmarczyk¹, P. Grassl¹ and J. Novak²

¹School of Engineering, University of Glasgow, Rankine Building, Glasgow

²School of Civil & Environmental Engineering, University of New South Wales, Sydney

*Chris.Pearce@glasgow.ac.uk

Key Words: *micromechanics; equivalent inclusion method; Eshelby's solution; heterogeneous materials; hybrid-stress finite elements*

ABSTRACT

This paper presents a micromechanics-enhanced finite element formulation that accurately captures the mechanical behaviour of heterogeneous materials, yet realized in a computationally efficient manner. The main feature of the technique is that the finite element mesh does not explicitly resolve the heterogeneities. The strategy exploits analytical micromechanics derived by Eshelby for ellipsoidal inclusions in order to determine the mechanical perturbation fields associated with the underlying heterogeneities. Approximation functions for these perturbation fields are then incorporated into a finite element formulation to augment those of the macroscopic fields. In this paper, hybrid-Trefftz stress finite elements are utilised and performance of the proposed formulation is demonstrated with a numerical example.

1 INTRODUCTION

The objective of this work is to develop a Finite Element formulation for modelling the macroscopic mechanical problem that is enhanced to capture the influence of the underlying heterogeneities. In our approach, the Finite Element mesh is not required to explicitly resolve the heterogeneities. Closed-form expressions for the perturbation of the mechanical fields due to the presence of the heterogeneities are determined and these are then utilised to enhance the Finite Element formulation.

The ability to capture the effect of features independently of the underlying finite element mesh, has been an ongoing challenge in computational mechanics research. Partition of Unity methods [1, 2] provide a potential solution to this problem, without mesh refinement, by extending

a given solution space with additional functions and has been successfully applied to problems such as cracks and material interfaces. However, the main focus of this paper is an alternative approach, centred on the Hybrid-Trefftz stress element formulation [3]. This method does not result in additional degrees of freedom, although it does involve an additional, albeit relatively minor, computational overhead.

The heterogeneities, although currently restricted to simple shapes (ellipsoids), can be randomly sized and randomly distributed without reference to the finite element mesh. Therefore, the proposed approach has the potential to be applicable to a wide range of composite materials, such as fibre reinforced composites, porous media, functionally graded materials, etc. Moreover, it can be extended to general inclusion shapes by evaluating the perturbation functions numerically [4].

2 METHODOLOGY

To calculate the perturbation of mechanical fields due to a heterogeneous microstructure, we exploit the *Equivalent Inclusion Method* in conjunction with analytical micromechanics. Our objective is to convert the heterogeneous problem into an equivalent homogeneous problem and to derive analytical expressions for the perturbations of the stress, strain and displacement fields that we can then utilise within a finite element formulation.

Consider a body consisting of clearly distinguishable heterogeneities in a matrix subjected to a displacement and traction field. As a result of the heterogeneities, the mechanical fields (displacement, strains, stresses) experience a perturbation for which can derive closed-form expressions based on analytical micromechanics. It is worth noting that, traditionally, in analytical micromechanics, the *macroscopic* fields are assumed to be uniform across the domain. Here it is assumed that they can be position dependent functions of the Neumann and Dirichlet boundary conditions.

The perturbation fields are determined by employing the *equivalent inclusion method* for a single heterogeneity embedded in a matrix and then extended here for multiple heterogeneities. In the *equivalent inclusion method*, the heterogeneous solid is replaced by an equivalent homogeneous solid with uniform material stiffness everywhere and suitable stress-free eigenstrains applied in the inclusions so that the homogeneous equivalent solid has the same mechanical fields as the original heterogeneous solid. It can be shown that the stress perturbation depends on the stiffness of the different material phases, the macroscopic strain field and the geometry of the heterogeneity. This closed-form expression for the stress perturbation is at the heart of the proposed finite element enrichment.

In the case of multiple inclusions, it is necessary to introduce an iterative *self-balancing* procedure to ensure that the solution correctly reflects the influence of multiple inclusions. This procedure iteratively modifies the eigenstrain inside any given inclusion, to account for the influence of the remaining inclusions. This methodology can then be utilised to formulate an enhanced Finite Element formulation, whereby appropriate approximation functions for the mechanical perturbation fields based on the analytical micromechanics briefly described above, which can then augment the standard FE macroscopic field approximations.

Practically, the perturbation field approximation functions are determined *a priori* as a linear combination of the perturbation fields evaluated analytically for six load cases, with self-equilibrium enforced by means of the *self-balancing* algorithm discussed above. Each load case corresponds to a unit component of the macroscopic strain vector.

3 NUMERICAL EXAMPLE

The proposed modelling strategy is also demonstrated on an example with a large number of inclusions. A 3D L-shaped specimen with fully fixed boundary conditions on the right surface of the right-hand arm and normal traction applied on the top surface of the left-hand arm is analysed, see Fig. 1. The length of the plate is 300 in both x and y direction, the depth is 150 in z direction. The Young moduli were chosen as $E = 1$ and $E = 2$ for matrix and inclusion respectively. Poisson's ratio was $\nu = 0.1$ for both material phases. The microstructure comprised 2,523 spherical inclusions varying in size between 4 and 8 with a normal distribution (Figure 1(b)). All units are consistent.

The solution for three different mesh densities are compared in Figures 1(c)-(d). These results show that the complex stress distribution resulting from the heterogeneities can be captured and that the solution is converging with mesh refinement. Further local mesh refinement near corners and stress concentrations is possible, although this was not undertaken in this case.

4 CONCLUSIONS

A new micromechanics-enhanced finite element formulation has been presented for modelling the influence of a large number of heterogeneities in composite materials in a computationally efficient manner. The strategy exploits analytical micromechanics derived by Eshelby for ellipsoidal inclusions in order to determine the mechanical perturbation fields as a result of the underlying heterogeneities. Approximation functions for these perturbation fields are then incorporated into a finite element formulation to augment those of the macroscopic fields. A significant feature of this approach is that the finite element mesh does not explicitly resolve the heterogeneities. The proposed technique has been implemented into a hybrid-Trefftz stress (HTS) element formulation and it has been shown that the resulting enhanced elements (C-HTS) require significantly fewer degrees of freedom to capture the detailed mechanical response compared to standard finite elements.

References

- [1] N. Moës and J. Dolbow and T. Belytschko. A finite element method for crack growth without remeshing. *International Journal for Numerical Methods in Engineering*, 46(1), 131150, 1999.

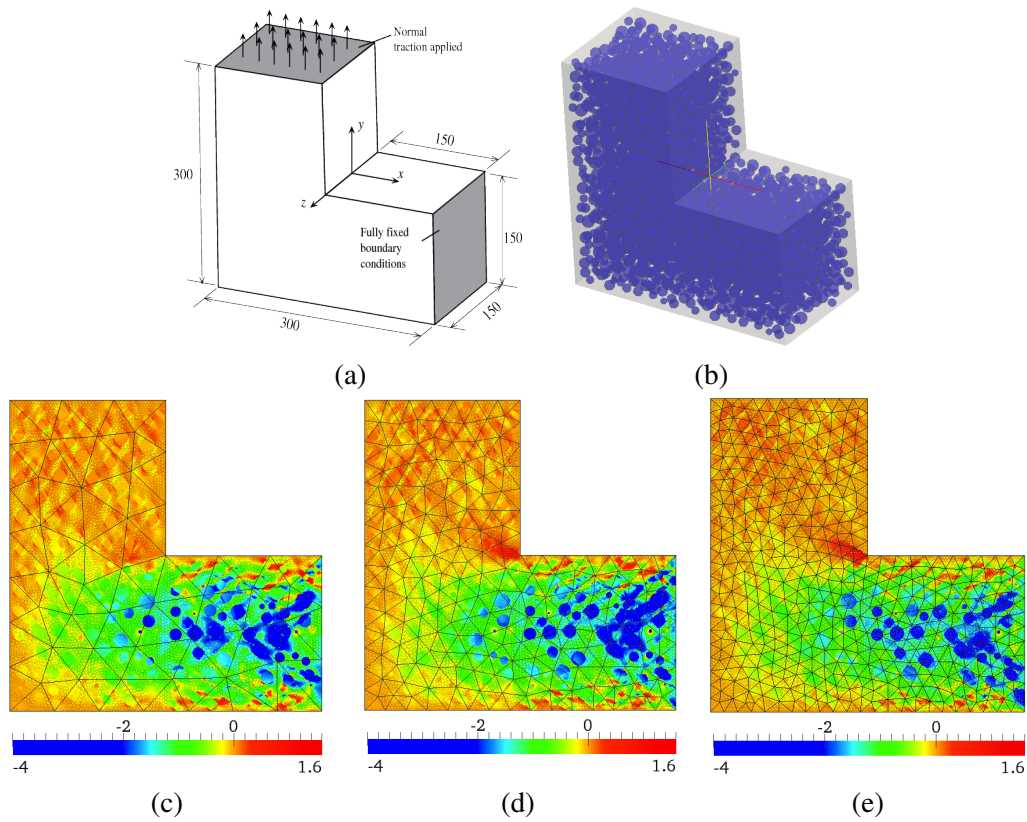


Figure 1: L-shaped specimen a) geometry, b) microstructure comprising 2,523 spherical inclusions. Plots of σ_{xy} resulting from c) coarse mesh, d) medium mesh and e) fine mesh.

- [2] G.N. Wells, L.J. Sluys and R. De Borst. Simulating the propagation of displacement discontinuities in a regularised strain-softening medium. *International Journal for Numerical Methods in Engineering*, 53, 1235-1256, 2002.
- [3] Ł. Kaczmarczyk and C.J. Pearce. A corotational hybrid-Trefftz stress formulation for modelling cohesive cracks. *Computer Methods in Applied Mechanics and Engineering*, 198, 1298 - 1310, 2009.
- [4] V. Maz'ya and G. Schmidt. *Approximate approximations*, American Mathematical Society, Providence, RI, 2007.

AN ALGORITHM FOR GENERATION OF 3D MESOSTRUCTURE OF CONCRETE FOR FINITE ELEMENT ANALYSIS

Zhenhuan Song, Yong Lu *

Institute for Infrastructure and Environment, Joint Research Institute for Civil and Environmental Engineering,
School of Engineering, University of Edinburgh, The King's Buildings, Edinburgh EH9 3JL, UK

*yong.lu@ed.ac.uk

Key Words: *heterogeneity; mesoscale model; three-dimensional; computational methods*

ABSTRACT

This paper is concerned about an efficient algorithm for the automatic generation of realistic 3D mesostructure for concrete-like materials. A geometric concept, called convex hull, is adopted for the representation of aggregates, and this makes it possible to utilize the relevant theorems and algorithms in the field of computational geometry. A take-and-place procedure is employed to facilitate the generation of the complete mesostructure. Associated techniques are developed for fast detection of particle inclusion-intersection. The formation of the ITZ as well as the meshing of the whole mesostructure is also briefly discussed, together with an example of FE simulation.

1 INTRODUCTION

Numerical modelling at the mesoscale for heterogeneous materials such as concrete has attracted great interest in the scientific community due to its various advantages for investigating into the mechanisms governing the bulk behaviour of such materials.

The mesostructure of concrete is complex and includes three phases: aggregates, mortar matrix, and the interface transition zone (ITZ). Different levels of mesoscale models have been proposed in the literature depending on the choice of the aggregate geometry and the material laws for individual phases. Simple shapes such as round, ellipse and sphere have been commonly used to represent the aggregates, while a better approximation with polygon has also been applied in some 2D models [1-2].

For 3D mesoscale modelling of concrete, a common approach is to use spheres or mixed spheres and ellipsoids to represent aggregates. Polytopes is obviously a better approximation but their use in 3D is much more difficult. In the present study, a geometric concept called convex hull is adopted to represent the geometry of aggregates. This makes it possible to utilize the relevant theorems and algorithms in the field of computational geometry for the generation of individual aggregates. A take-and-place procedure is employed to facilitate the creation of complete mesostructure for a sample object. Meshing of the mesostructure of the sample object is carried out using a Delaunay-refinement based mesh generator. Subsequent FE analysis is performed using a general purpose transient analysis code.

2 AGGREGATE PARTICLE GENERATION

Typically, the particle shape and surface texture of aggregates can be classified as: rounded or well-rounded, irregular (naturally), flaky (thickness is much smaller than the other two dimensions), elongated (length is considerably larger). A classic approach to model the shape of gravel aggregates is based on the morphological analysis developed by Beddow and Meloy [3]. In this approach, the trace of aggregate shape is represented as a Fourier series:

$$r(\theta) = r_0 + \sum_{m=1}^{\infty} A_m (\cos m\theta + x) \quad (1)$$

where r_0 is average radius. The second term on the right hand side reflects the characteristic of the particle contour where A_m represents the magnitude and m represents frequency. Based on this rule, the shape of a gravel particle can be approximated by a series of short straight line segments [1]. The approximation of 2D angular particles using polygons is straightforward, as can be seen in applications such as [1, 2].

In the present study, we use a geometric concept called convex hull, which is the minimum convex set containing a series of randomly generated points, to represent 3D aggregate particles. Flaky and elongated shapes can subsequently be created by shrinking and elongation.

2.1 Generating Regular aggregate particle

The generation of a random-shaped convex hull starts from a set of random points. Each point in the list is represented in the spherical coordinates by radius r , inclination angle θ and azimuth angle ψ , which are all random numbers from a uniform distribution:

$$\begin{aligned} r &\sim U[r_0 - d/2, r_0 + d/2] \\ \theta &\sim U[0, 2\pi] \\ \varphi &\sim U[0, \pi] \end{aligned} \quad (2)$$

where r_0 is the nominal size discretised from a specified aggregate grading curve (such as Fuller curve) and d is the discretization length. The spherical coordinates are then transformed to Cartesian coordinates. There is no clear criterion for the choice of the number of random points. More points tends to result in a shape closer to quasi-sphere, while fewer points gives a simpler polytope. Experience from many trials shows that a number between 10 and 20 is appropriate.

The so-called beneath-beyond method, which is a classic algorithm for the generation of convex hull [4], is used to construct a particle. Fig. 1 depicts the above procedure and a resulting particle shape.

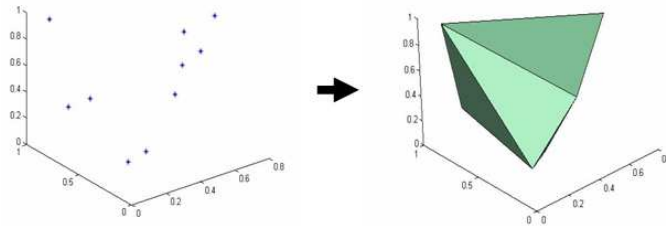


Fig. 1. Formation of a convex hull from 10 random points

2.2 Generating flaky or elongated aggregates

A flaky or elongated aggregate can be created on the basis of the regular convex hull generated in section 2.1. Both flaky and elongated shapes may be implemented by introducing a shrinkage (or elongation) factor s on one dimension. To keep the volume constant during shrinking or elongation, the remaining dimensions are adjusted in the opposite way. This process may be described by

$$R'_x = s * R_x \quad R'_y = R_y / \sqrt{s} \quad R'_z = R_z / \sqrt{s} \quad (3)$$

where R is the coordinates of each vertex and the ratio s is taken as a random number between 0.5 and 1.5. To ensure shrinkage is done in a random orientation, the coordinates are rotated to a random direction after shrinking through a rotational transformation matrix.

Fig. 2 gives a few examples of individual aggregate shapes generated with 10 random points.

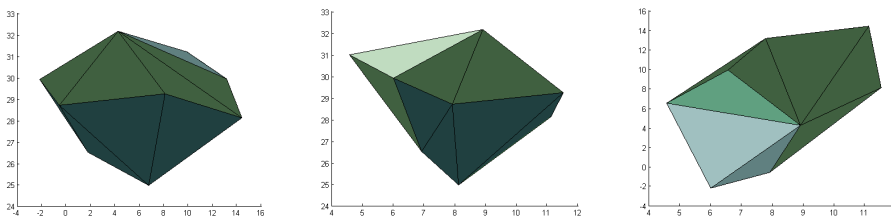


Fig. 2. Illustration of variation of aggregate particles

3 SIMULATING CONCRETE MESO-STRUCTURES

Different methods exist for the generation of a complete 3D meso-structure for a given sample volume such as a cube. Herein the so-called take-and-place procedure is employed. In this procedure, individual particles are generated (taken) and iteratively placed in the bounded space until a target volumetric ratio is satisfied. The procedure has been used to generate concrete structure in 2D and sphere-shaped 3D aggregates in the literature. To improve the efficiency in the inclusion-intersection check, a pre-detection algorithm and a fast inclusion detection method are incorporated.

The inclusion check is to avoid the inclusion or intersection of the currently generated aggregate particle with any existing particles. This is traditionally done by checking the current particle against all existing ones. Herein a pre-detection algorithm is used to identify the existing polytopes that may “possibly” intersect with the current one, such that more detailed checking is only required on these limited number of particles. This is done by introducing the concept of bounding sphere, which is defined as a sphere that shares the same centre with a convex hull and covers all vertices, as shown in Fig. 3(a). The inclusion or intersection between bounding spheres can be identified easily by checking the relation between the summation of the radii and distances of centres involved. Subsequent inclusion-intersection check only needs to be carried out for polytopes whose bounding spheres intersect with that of the current particle.

A linear time algorithm, proposed by Dobkin [5], is employed for determining the distance between two convex hulls. The algorithm is based on a hierarchical representation of convex hulls. Once the hierarchy representation is constructed, the detection of intersection can be done by iteratively calculating the distance between two particles. Fig. 3(b) shows an illustrative example of the structure of aggregate particles for a 50 mm cube sample.

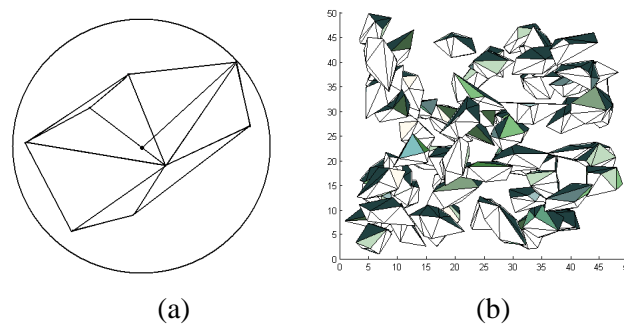


Fig. 3. (a) particle with bounding sphere; (b) aggregate structure with fixed size

In the present mesoscale model, the ITZ phase is represented by a thin layer of solid elements around individual aggregates. A shrinking strategy is employed to generate the ITZ layer. The shrinking of each aggregate is done with respect to the centre of the particle. The layer between the boundaries before and after shrinking forms the ITZ for each aggregate.

4 FINITE ELEMENT MESHING AND EXAMPLE ANALYSIS

After the generation of the ITZ domain, the remainder of the space in the sample cube automatically forms the mortar matrix. Due to the existence of randomly shaped aggregate particles, the mesostructure is highly unstructured. Triangle and tetrahedral meshing techniques are the most common forms of unstructured mesh generation in 2D and 3D. Available algorithms for meshing an unstructured domain include Octree, advancing front and Delaunay refinement. The meshing code used in this research, TetGen [6] is one type of Delaunay refinement. An example of the 3D structure and meshing result is shown in Fig.4.

As an illustration, a standard concrete compressive test is simulated after the complete generation of the finite element mesoscale model. Loading is applied through a velocity boundary imposed to the top of the cube while the bottom is fixed. Both friction-free and infinite-friction conditions on the loading and reaction faces are simulated, respectively. The material parameters used in the simulation are the same as in our previous pseudo 3D study [7]. The transient dynamic analysis code LS-DYNA is employed to

perform the simulation using an explicit time integration procedure, which enables an easy realisation of dynamic loading.

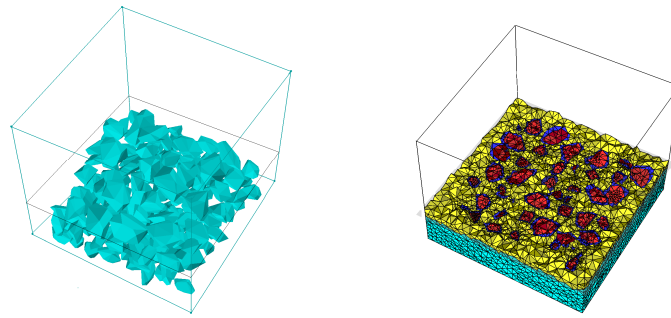


Fig.4. (a) aggregate particles on the bottom of the cube; (b) mesh for all three phase

Fig. 5 shows the predicted stress-strain relations with a loading rate of 10/s, and the final damage contours under the two end face friction conditions, respectively. The results resemble well typical experimental observations. It can be seen that in the friction-free case, the loading surface is severely damaged, while in the fully constrained case the loading face remains intact due to confinement effect.

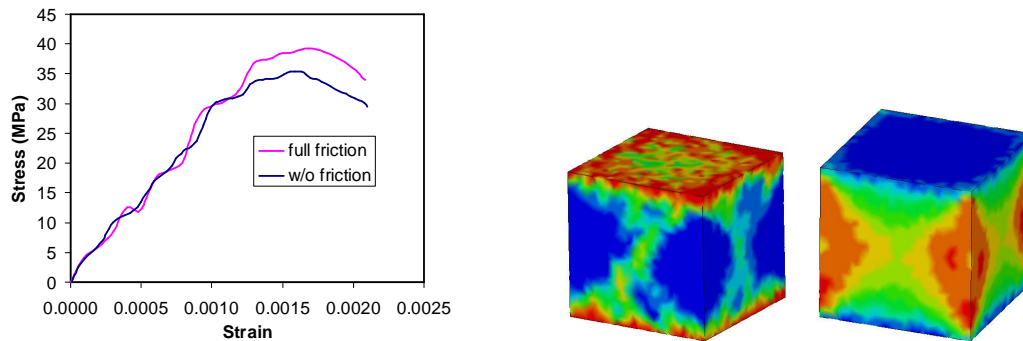


Fig.5. Stress and strain relation (left) and damage contours (right)

5 CONCLUDING REMARKS

3D mesostructure of concrete-like heterogeneous materials can be effectively generated using the proposed methodology. 3D mesoscale finite element model can then be developed on this basis. Implementation of the 3D mesoscale model with a general-purpose finite element code allows for the analysis under complex and dynamic loading conditions.

References

- [1] Z.M. Wang, A.K.H. Kwan and H.C. Chan, Mesoscopic study of concrete I: generation of random aggregate structure and finite element mesh, *Computers and Structures* 70(5), 533-544, 1999.
- [2] Caballero, I. Carol and C.M. López, 3D meso-mechanical analysis of concrete specimens under biaxial loading, *Fatigue Fract Eng Mater Struct*, 30, 877–886, 2007.
- [3] Beddow J.K. and T. Meloy, *Testing and characterization of powders and fine particles*. Heyden and Son Ltd. 1980.
- [4] H. Edelsbrunner, *Algorithms in Combinatorial Geometry*. Springer, 1987.
- [5] D. Dobkin and D. Kirkpatrick, A linear algorithm for determining the separation of convex polyhedra, *J. Algorithms* 6, 381-392, 1985.
- [6] H. Si, *Tetgen- A Quality Tetra Mesh Generator and a 3D Delaunay Triangulator*, User's Manual, 2009.
- [7] Y. Lu, Z.H. Song and Z.G Tu, Analysis of Dynamic Response of Concrete Using a Mesoscale Model Incorporating 3D Effects, *International Journal of Protective Structures*, 1(2), 197-218, 2010.

MACRO AND MESO SCALES MODELS TO PREDICT CONCRETE FAILURE AND SIZE EFFECT

L.B. Rojas-Solano¹, P. Grassl², *D. Grégoire¹ and G. Pijaudier-Cabot¹

¹Laboratoire des Fluides Complexes et leurs Réservoirs, Université de Pau et des Pays de l'Adour,
Campus Montauray, 64600 Anglet, France

²School of Engineering, University of Glasgow, Glasgow G128LT, United Kingdom

*david.gregoire@univ-pau.fr

Key Words: *size effects; mesoscopic damage model; macroscopic damage model; crack; concrete*

ABSTRACT

The purpose of this paper is to examine the capabilities of continuum based and discontinuum based (discrete) models to describe the continuous – discontinuous transition involved during crack propagation. It aims to capture the size effect for different specimen geometries and their different boundary effects. For this purpose, size effect tests have been performed on three point bending specimens with different notch lengths. Such a comparison involving different initial notch lengths is unique mainly because the experimental test data were not available previously. The macroscopic description fails to reproduce size effects whereas the mesoscopic model is able to recover them for each tested configuration. The microstructure intrinsically incorporated into the meso-model allows the evolution of non local interactions whereas these interactions are homogenized in the continuum model through the internal length in a way which seems too simplistic.

1 INTRODUCTION

In quasi-brittle materials, cracks exhibits a finite size fracture process zone (FPZ). Macro-cracking is the result of progressive material damage in which micro-cracks appear first in a rather diffuse way into a fracture process zone, and then coalescence occurs in order to form the macro-crack. A consequence of the existence of such a FPZ is the structural size effect explained as the dependence of the nominal strength on the size of structure.

This work aims to examine the performances of continuum based and discontinuum based (discrete) models to describe the process of concrete fracture through their capabilities of describing structural size effect. For this purpose size effect tests have been performed on three point bending specimens with different notch lengths [1].

2 MACROSCOPIC MODEL

The strain-softening material is supposed to be isotropic described with a scalar damage model. Temperature and time-dependent effects are neglected. Therefore, the stress-strain relation is classically written:

$$\sigma = (1 - D)C : \varepsilon \quad (1)$$

where σ , C , ε are respectively the stress, stiffness and strain tensors and D is the damage scalar variable ($0 < D < 1$) which represents the material degradation.

Damage evolution is based on Mazars' definition and is governed by the Kuhn-Tucker loading-unloading conditions.

$$g(\varepsilon_{eq}, x) = \varepsilon_{eq}(\varepsilon) - \kappa; \quad g(\varepsilon, \kappa) \leq 0; \quad \dot{\kappa} \geq 0; \quad \dot{\kappa} g(\varepsilon, \kappa) = 0; \quad \varepsilon_{eq} = \sqrt{\sum_{k=1}^3 \langle \varepsilon_k \rangle_+^2}; \quad (2)$$

In this paper we shall be interested in damage due to tension loads only and D is estimated through:

$$D(\varepsilon_{eq,x}) = 1 - (1 - A_t) \frac{\varepsilon_{D_0}}{\varepsilon_{eq}(x)} - \frac{A_t}{e^{B_t(\varepsilon_{eq}(x) - \varepsilon_{D_0})}} \quad (3)$$

Where ε_{eq} is the equivalent strain, $\langle \varepsilon_i \rangle_+$ the positive part of the principal strains, ε_{D_0} is the damage threshold, κ is the history variable, the largest ever reached value of the equivalent strain. A_t, B_t are model parameters representing the exponential softening of the material. Classical values of the model parameters are provided in (Mazars, 1986) and (Pijaudier-Cabot et al., 1991).

The non-local formulation is based on integral-type non local damage models proposed by Pijaudier-Cabot and Bažant (1987):

$$\bar{\varepsilon}_{eq}(x) = \frac{1}{\Omega_r(x)} \int_{\Omega} \psi_0(x, \xi) \varepsilon_{eq}(\xi) d\xi, \quad \Omega_r(x) = \int_{\Omega} \psi_0(x, \xi) d\xi, \quad \psi_0(x, \xi) = \exp\left(\frac{-4\|x - \xi\|^2}{l_{c_0}}\right) \quad (4)$$

where Ω is the volume of the structure, Ω_r is a representative volume introduced in a way that the non-local operator does not affect the uniform field, $\bar{\varepsilon}_{eq}$ is the non-local strain, ψ_0 is a Gaussian weight function and l_{c_0} is the internal length of the non-local continuum which is related to the fracture process zone size.

3 MESOSCOPIC MODEL

At the mesoscopic scale, the aggregates, the mortar and the interfacial transition zones are modelled as different phases with different materials properties. The aggregates are assumed to be linear elastic and stiffer than the matrix and the interfacial transition weaker than the matrix with a random distribution of tensile strength and fracture energy.

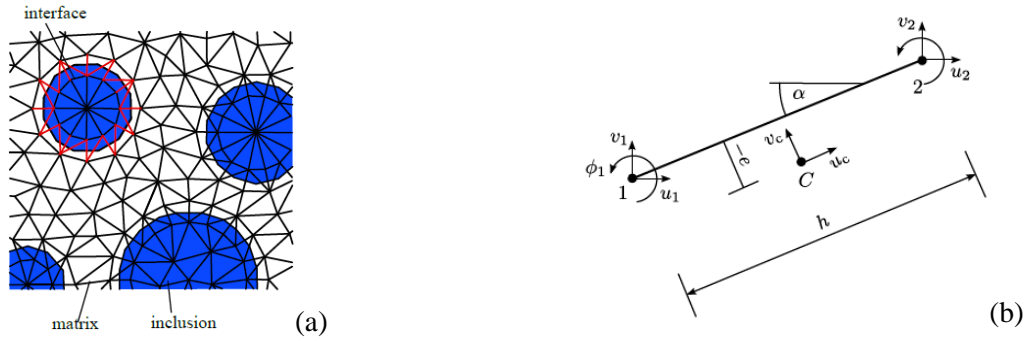


Figure 1. (a) Special arrangement of lattice elements. (b) One lattice element in the global coordinate system.

The mechanical response of the heterogeneous material is determined by discrete lattice elements combined with a local damage model, as described in Figure 1.

Each lattice node possesses three degrees of freedom: two translations u, v and one rotation ϕ . Thus, the displacement discontinuities at point C , $u_c = (u_c, v_c, \phi_c)^T$, are linked to displacements at the nodes $u_e = (u_1, v_1, \phi_1, u_2, v_2, \phi_2)^T$. The displacement discontinuities are transformed into strains $\varepsilon = (\varepsilon_n, \varepsilon_s, \varepsilon_\phi)^T = u_c / h$ and then the nominal stresses is calculated as $\sigma = (\sigma_n, \sigma_s, \sigma_\phi)^T$. Whereas the stress-strain relation and the damage evolution are the same as the ones introduced in the macroscopic model, here the equivalent strain is not computed from Mazars' law but it corresponds to an elliptic envelope in the $\sigma_n - \sigma_s$ stress plane, as proposed in [3].

$$\varepsilon_{eq}(\varepsilon_n, \varepsilon_s) = \frac{1}{2} \varepsilon_0 (1 - c) + \sqrt{\left(\frac{1}{2} \varepsilon_0 (c - 1) + \varepsilon_n\right)^2 + \frac{c \gamma^2 \varepsilon_s^2}{q^2}} ; f_c = c f_t \quad (5)$$

Where γ is the Poisson's ratio of the material and c is ration of the compressive strength to the tensile strength (f_c and f_t). The softening curve of stress-strain response in uniaxial tension is defined by the relation

$$\sigma = f_t \exp\left(-\frac{w_c}{w_f}\right), \quad w_c = Dh\varepsilon, \quad G_{ft} = f_t w_f \quad (6)$$

where w_c is considered as an equivalent crack opening under monotonic uniaxial tension, h the distance between lattice nodes and w_f determines the initial slope of softening curve and is related to meso-level fracture energy.

4 DESCRIPTION OF EXPERIMENTS

Three different geometries were analysed. Three notch lengths $a = 0.5D, 0.2D, 0$ and four beam depths $D = 0.4, 0.2, 0.1, 0.05m$ were studied. The thickness was kept constant for all sizes and equal to $b = 0.05m$. The distance between supports was $L = 2.5D$. All the characteristics of the beams are detailed in Figure 2. The materials properties $E = 37$ MPa, $\gamma = 0.21$, $f_t = 3.9$ MPa, $\sigma_c = 42.3$ MPa were identified by compression and splitting tests.

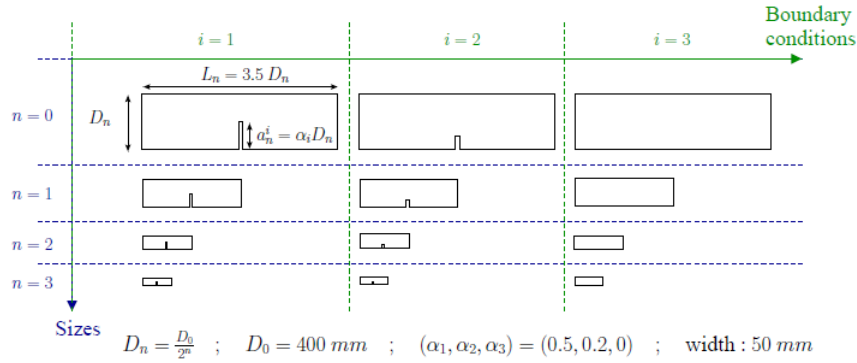


Figure 2. Beam specimen geometries.

Three points bending tests were then performed on each beam. This type of experiments has, to our knowledge, never been carried out before. The main aim of this campaign was the establishment of an important database of curves Force vs. Crack opening mouth. More details about the experiments can be found in [1].

5 NUMERICAL ANALYSIS

The macroscopic analysis has been performed using the finite element code Cast3m [4]. The computations at the mesoscale were performed with a cohesive model developed by Grassl (2009). Parameters f_t and G_f are the mean values of the random fields of tensile strength and fracture energy respectively.

The results of both mesoscopic and macroscopic approaches have been compared to the experimental ones. Figure 3 shows the results in term of size effects for long notched and unnotched beams. It is important to note that each curve in Figure 3 (b) corresponds to an average of 100 computations with different mesostructures and random fields. We can observe that mesoscopic results are in good agreement with the experimental datas whereas the macroscopic approach is not able to represent the size effect. The same holds for the two others geometries tested, for beams with a small notch and for beams without notch.

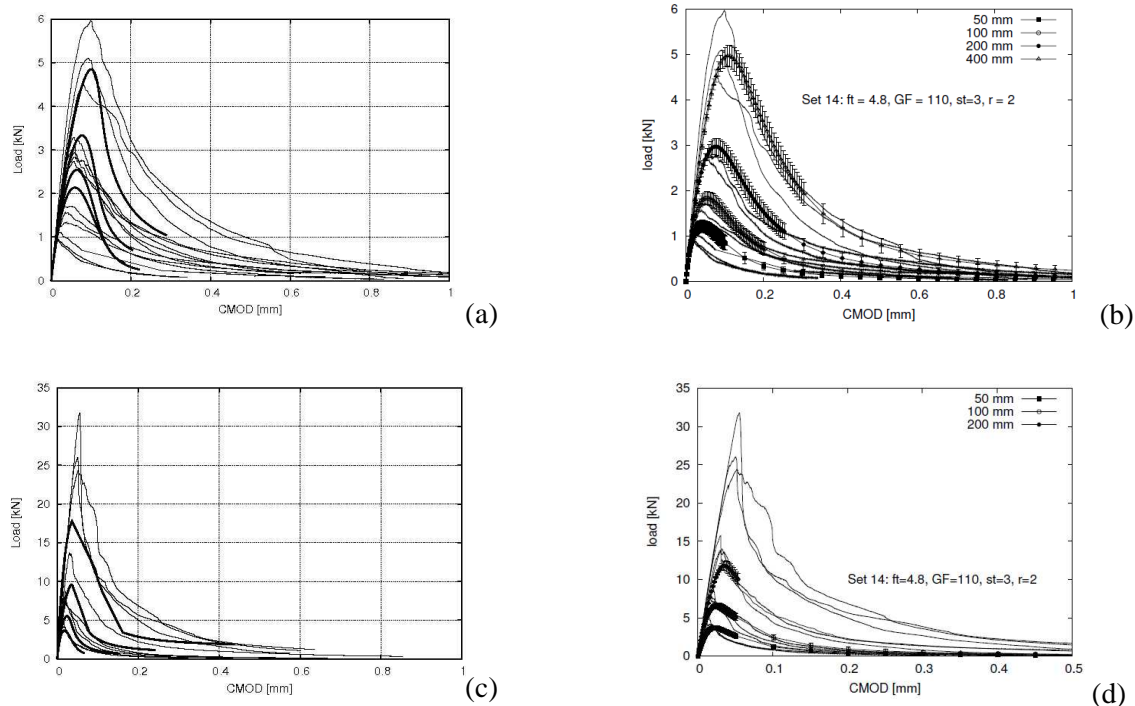


Figure 3. Load versus CMOD for the beams with the notch $a = 0.5D$ and $a = 0$ (a) and (c) results with macroscopic model. (b) and (d) results with mesoscopic model.

7 CONCLUSIONS

In this paper, original experimental data has been used for determining size and geometry effects in quasibrittle materials. The experimental results have been used as reference results for comparison between two numerical models. The macroscopic approach based on finite elements combined with a continuum non local formulation failed to reproduce size effects whereas the mesoscopic approach, based on lattice method was able to recover them for each configuration tested. The microstructure intrinsically introduced into the meso-model allows the evolution of non local interaction whereas these interactions do not evolve in the continuum model which seems to be a too simplistic approximation.

ACKNOWLEDGEMENTS

Financial support from ERC advanced grant FailFlow (27769) is gratefully acknowledged.

References

- [1] D. Grégoire, L.B. Rojas-Solano and G. Pijaudier-Cabot. Failure and size effect for notched and unnotched concrete beams. To be submitted. International Journal of Fracture, 2011.
- [2] Z. Bazant. J. Planas. Fracture and size effect in concrete and other quasibrittle materials, CRC, 1998.
- [3] P. Grassl and M. Jirasek. Meso-scale approach to modelling the fracture process zone of concrete subjected to uniaxial tension. Int. J. Solids Struct, 47, 957–968, 2010.
- [4] www-cast3m.cea.fr

An alternative to multiscale simulators based on model order reduction for nonlinear fracture mechanics

*P. Kerfriden¹, Lee Margetts² and S. Bordas¹

¹Cardiff University, School of Engineering, Queen's building, The Parade, Cardiff CF243AA

² University of Manchester, Research Computing Services, Devonshire House, Oxford Road, Manchester M13 9PL

*kerfridenp@cardiff.ac.uk

Key Words: *nonlinear fracture; model order reduction; Newton-Krylov; augmented conjugate gradient*

ABSTRACT

We present an adaptive model order reduction for parametrised nonlinear fracture mechanics. Efficient corrections of the initial reduced space, provided by the proper orthogonal decomposition, are performed on-the-fly during the solution process. The proposed strategy establishes a bridge between model order reduction and full-scale augmented Newton-Krylov solvers. We demonstrate its efficiency through numerical examples.

1 INTRODUCTION

The simulation of failure in complex materials has been one important issue throughout engineering. Micro and mesoscale models have demonstrated their ability to predict complex phenomena such as crack initiation and propagation. However, these models usually describe the material at a very fine scale compared to the size of the structure, which leads to large numerical problems. Various multiscale computational strategies have been developed to tackle this important issue, such as enrichment techniques, homogenization strategies [2], domain decomposition methods, or model order reduction [3, 6].

Among them, the Proper Orthogonal Decomposition-based (POD) is a valuable tool for deriving efficiently a multiscale computational method, in the sense that no *a priori* physical understanding of the different scales involved is required. It consists in using a set of potential solutions to the initial, potentially large problem (snapshot) and extracting, by a spectral analysis, a few basis vectors spanning a space of small dimension in which the solution to the, initially large, numerical problem is well approximated [6]. This technique is efficient when speed is more important than accuracy, for instance in the case of early stage design.

In the context of structural problems involving plasticity or damage, a severe drawback limits the direct application of POD-based model order reduction. The initial snapshot might be too poor to represent accurately the solution of the damaged structure. This can happen if: (i) The “*a priori*” mechanical understanding of the structure is too poor, which might result in a bad choice of the snapshot simulations. (ii) The number of parameters involved is too important, the snapshot needed to compute a relevant reduced basis might be too large or (iii) strong topological changes in the structure occur.

We propose here a novel strategy that couples these two approaches. Our vision is that if complex changes in the topology of the structure appear (local crack initiation for instance), they can only be accurately predicted by solving the fine scale model, at least locally. This can be done, for instance,

by adding the finite element shape functions to the snapshot, or by using localisation techniques. However, the long-range effects of these topological changes do not require the fine description, and can be obtained by coarsely solving the full system of equations. Therefore, when the global residual exceeds a given threshold value, we propose to obtain a loose solution on the full system. The new vector obtained is used to enrich the reduced basis.

This strategy can be interpreted as a bridge between “exact” preconditioned Newton-Krylov strategies [5], and projection-based model order reduction methods (like the POD) for nonlinear problems. Indeed, setting the residual threshold to a low value leads to the former strategy, while setting it to a high value leads to the latter. An intermediate value yields an adaptive model order reduction method with control of the global residual. We show that this method permits to obtain an “on-the-fly”, cheap, correction to the reduced model in the case of parametrised nonlinear fracture mechanics.

2 Projection-based Model order reduction.

We consider the generic problem of quasi-static evolution of irreversible damage processes in a deformable solid. The rate-effects are neglected and the solution field (displacement) is looked for under the assumption of small perturbation. We introduce a classical finite element space discretization for the spatial derivatives. A time discretization scheme is performed to integrate the resulting semi-discrete problem over the time interval $[0, T]$. The procedure consists in finding a set of consecutive solutions at times $(t_n)_{n \in \llbracket 0, n_t \rrbracket}$. At any time t_{n+1} of the analysis, one needs to solve a nonlinear vectorial equation of the form:

$$\underline{\mathbf{F}}_{\text{Int}} \left(\underline{\Delta \mathbf{U}}, \left(\underline{\mathbf{U}}|_{t_m} \right)_{m \in \llbracket 0, n \rrbracket} \right) + \underline{\mathbf{F}}_{\text{Ext}} = \underline{\mathbf{0}} \quad (1)$$

where the vector of increment in the nodal displacement unknowns $\underline{\Delta \mathbf{U}} \in \mathbb{R}^{n_u}$ (n_u is the number of nodal unknowns introduced in the finite element discretization) is defined by $\underline{\Delta \mathbf{U}} = \underline{\mathbf{U}}|_{t_{n+1}} - \underline{\mathbf{U}}|_{t_n}$, $\underline{\mathbf{F}}_{\text{Int}} \in \mathbb{R}^{n_u}$ and $\underline{\mathbf{F}}_{\text{Ext}} \in \mathbb{R}^{n_u}$ are respectively the classical internal and external force vectors.

The increments in the solution vector are searched for in a space of small dimension (several orders smaller than the number of finite element degrees of freedom). Let us call $\underline{\mathbf{C}}$ the matrix whose n_c columns $(\underline{\mathbf{C}}^k)_{k \in \llbracket 1, n_c \rrbracket} \in (\mathbb{R}^{n_u})^{n_c}$ (also called Ritz vectors) form a basis of this space. Applied to the reduction of problem (1), the increment in the solution field is approximated by:

$$\underline{\Delta \mathbf{U}} = \underline{\mathbf{C}} \underline{\alpha} \quad (2)$$

where we introduced the reduced state variables $\underline{\alpha} \in \mathbb{R}^{n_c}$. Problem (1) is classically modified by introducing a Galerkin orthogonality condition: the residual $\underline{\mathbf{R}} = \underline{\mathbf{F}}_{\text{Int}}(\underline{\mathbf{U}}|_{t_n} + \underline{\mathbf{C}} \underline{\alpha}) + \underline{\mathbf{F}}_{\text{Ext}}$ of equation (1) is required to be orthogonal to any test vector $\underline{\delta \mathbf{U}}^* = \underline{\mathbf{C}} \underline{\delta \alpha}^*$ belonging to the space spanned by the Ritz vector. The reduction of problem (1) takes the following form:

$$\underline{\mathbf{C}}^T \left(\underline{\mathbf{F}}_{\text{Ext}} + \underline{\mathbf{F}}_{\text{Int}}(\underline{\mathbf{U}}|_{t_n} + \underline{\mathbf{C}} \underline{\alpha}) \right) = \underline{\mathbf{0}} \quad (3)$$

This nonlinear problem can be solved by a Newton solution strategy.

The reduced basis used in the paper is computed prior to the actual simulation by the classical Snapshot Proper Orthogonal Decomposition approach [6].

3 “On-the-fly” corrections of the Ritz basis based on Krylov iteration

Updating the reduced space is done during the Newton algorithm used to solve (3) at current time step t_{n+1} . At iteration i of the Newton solver, if the solution to the reduced problem (3) is sufficiently converged, one can evaluate the residual of the full problem (1). If the norm of this residual is larger than a certain tolerance (i.e.: an error criterion), the following linear system is considered to compute a correction to the current Ritz basis $\underline{\mathbf{C}}^i$:

$$\underline{\bar{\mathbf{K}}}_1^i \underline{\delta \mathbf{U}} = \underline{\mathbf{R}}^i \quad (4)$$

$\underline{\underline{\mathbf{K}}}_T^i$ is an approximation of the consistent tangent stiffness $\underline{\underline{\mathbf{K}}}_T^i = \frac{\partial \mathbf{F}_{\text{Im}}(\mathbf{U})}{\partial \mathbf{U}} \Big|_{\mathbf{U}=\mathbf{U}^i}$ of the full problem, while $\underline{\mathbf{R}}^i$ is the residual of the initial system of equations (1) for $\mathbf{U} = \mathbf{U}|_{t_n} + \underline{\underline{\mathbf{C}}}^i \underline{\alpha}^i$. An approximate solution to this problem is searched for in two supplementary spaces:

$$\underline{\delta \mathbf{U}} = \underline{\delta \mathbf{U}}_C + \underline{\delta \mathbf{U}}_K \quad \text{where} \quad \begin{cases} \underline{\delta \mathbf{U}}_C \in \text{Im}(\underline{\underline{\mathbf{C}}}^i) \\ \underline{\delta \mathbf{U}}_K \in \text{Im}(\underline{\underline{\mathbf{C}}}^i)^{\perp_{\underline{\underline{\mathbf{K}}}_T^i}} = \text{Ker}(\underline{\underline{\mathbf{C}}}^{iT} \underline{\underline{\mathbf{K}}}_T^i) \end{cases} \quad (5)$$

$^{\perp_{\underline{\underline{\mathbf{K}}}_T^i}}$ denotes the $\underline{\underline{\mathbf{K}}}_T^i$ -orthogonality. $\underline{\delta \mathbf{U}}_C$ is the exact solution of the linearisation of reduced problem (3). $\underline{\delta \mathbf{U}}_K$ is a correction searched by a Krylov solver projected in space $\text{Ker}(\underline{\underline{\mathbf{C}}}^{iT} \underline{\underline{\mathbf{K}}}_T^i)$ and set to a loose tolerance (10^{-1} is a typical value for the stopping criterion). The resulting solution, which is $\underline{\underline{\mathbf{K}}}_T^i$ -orthogonal to the current reduced space by construction, is used to update the Ritz basis:

$$\underline{\underline{\mathbf{C}}}^{i+1} = \left(\underline{\underline{\mathbf{C}}}^i \quad \frac{\underline{\delta \mathbf{U}}_K}{\|\underline{\delta \mathbf{U}}_K\|} \right) \quad (6)$$

Newton iteration $i + 1$ is solved using the corrected reduced basis. Successive corrections may be performed until the tolerance on the norm of the residual of the full problem is reached [4].

4 Results

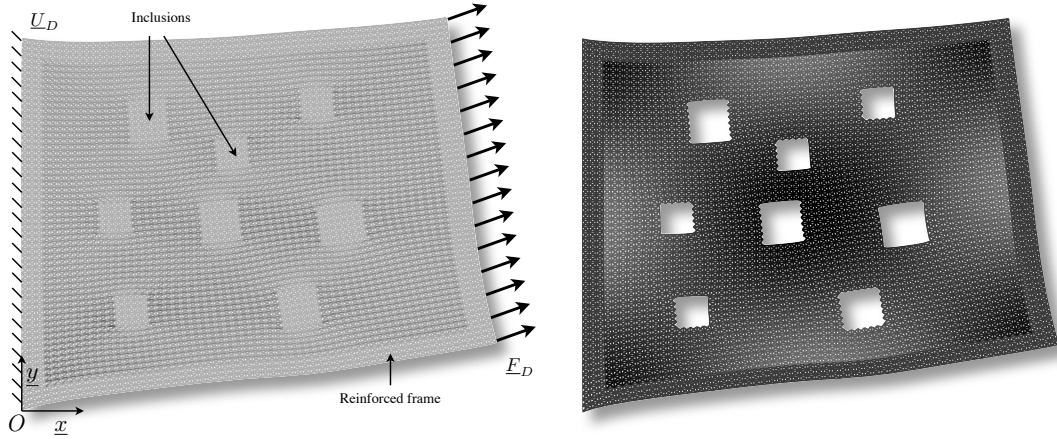


Figure 1: Reference problem and associated solutions (left), where darker colours correspond to higher value of damage, and Young's modulus cosinusoidal distribution (right), where darker colours correspond to higher values of the stiffness parameter.

The structure under consideration is an elastic damageable lattice structure represented in figure 1. The load is parametrised by its angle. An other parameter is introduced to control the spatial distribution of the material stiffness.

We want an approximation of the response surface of the total dissipated energy at failure as a function of the two parameters of the model. This surface is made by performing 16 simulations, the response surface being linearly interpolated between these points. 4 of these simulations are performed on the initial system of equations, until failure of the structure. The solution vectors are sorted by a singular value decomposition, and the 12 remaining simulations are performed by the proposed corrective model order reduction.

The results are plotted in figure 2. The error in the dissipated energy monotonically decreases when the correction threshold decreases. This justifies our statement that the strategy establishes a bridge between model order reduction methods and full-scale preconditioned Newton/Krylov solvers. The additional CPU time is low compared to a basic POD method, which predicts the dissipation with an average error greater than 100%. The computational time increases with the distance of the current solution to the snapshot space (larger number of corrections required), and can be reduced by a better choice of the initial simulations ([1]).

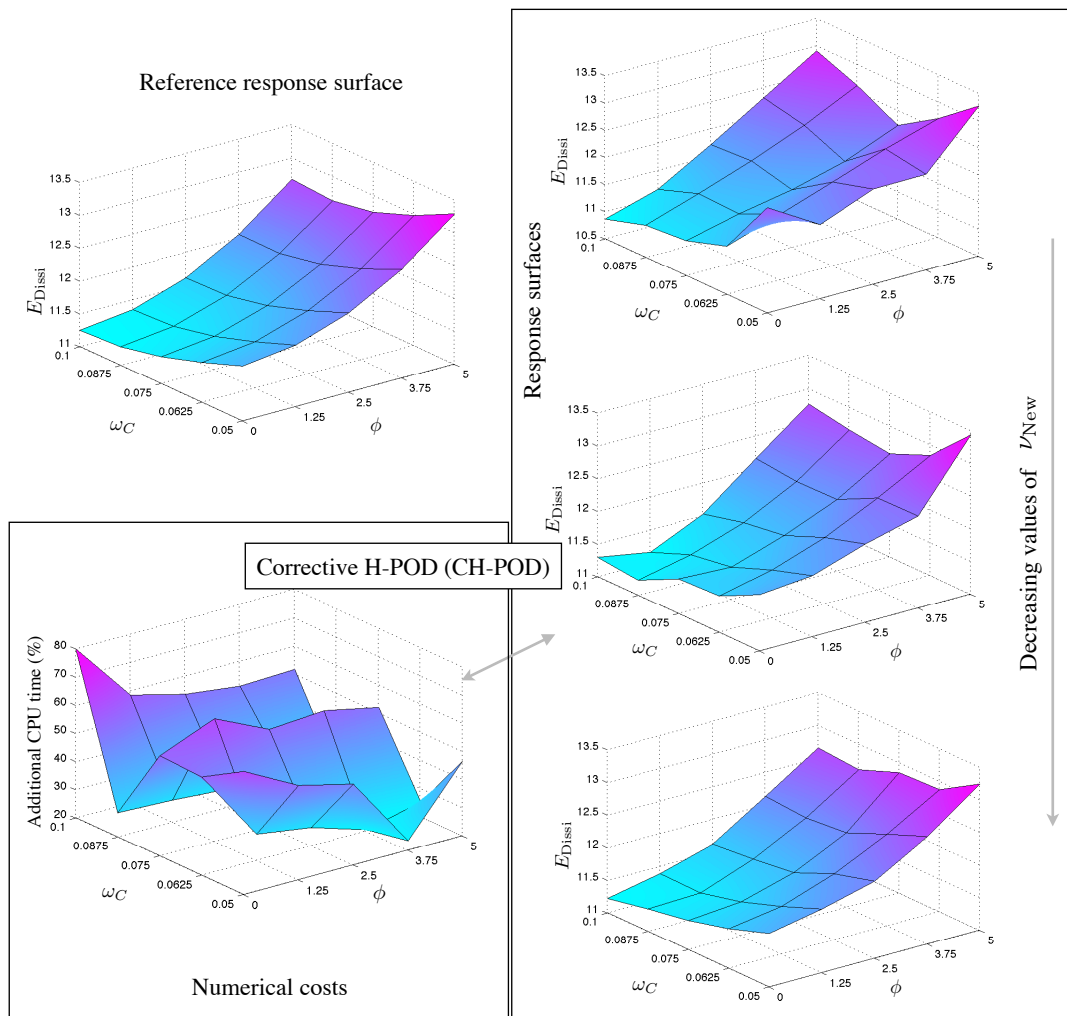


Figure 2: Response surface obtained in the reference case, and when using the CH-POD for various values of the reduced model error criterion, and CPU time for each of the 25 simulations (additional CPU times with respect to the ones obtained by applying hyperreduction).

References

- [1] M. Barrault, Y. Maday, N.C. Nguyen, and A.T. Patera. An 'empirical interpolation' method: application to efficient reduced-basis discretization of partial differential equations. *Comptes Rendus de Mathématique*, 339(9):667–672, 2004.
- [2] J. Fish, K. Shek, M. Pandheeradi, and M. S. Shephard. Computational plasticity for composite structures based on mathematical homogenization: Theory and practice. *Computer Methods in Applied Mechanics and Engineering*, 148:53–73, 1997.
- [3] K. Karhunen. Über lineare methoden in der wahrscheinlichkeitsrechnung. *Annales Academiae Scientiarum Fennicae Series A1, Mathematical Physics* 37, 37:1–79, 1947.
- [4] P. Kerfriden, P. Gosselet, S. Adhikari, and S. Bordas. Bridging proper orthogonal decomposition methods and augmented newton-krylov algorithms: an adaptive model order reduction for highly nonlinear mechanical problems. *Computer Methods in Applied Mechanics and Engineering*, 200(5-8):850–866, 2010.
- [5] F. Risler and C. Rey. Iterative accelerating algorithms with krylov subspaces for the solution to large-scale nonlinear problems. *Numerical algorithms*, 23:1–30, 2000.
- [6] L. Sirovich. Turbulence and the dynamics of coherent structures. part I: coherent structures. *Quarterly of Applied Mathematics*, 45:561–571, 1987.

MODELLING DAMAGE, FRICTION AND DILATANCY ON STRUCTURAL INTERFACES USING COHESIVE-ZONE MODELS

*Giulio Alfano¹ and Roberto Serpieri²

¹School of Engineering and Design, Brunel University, Kingston Lane UB8 3PH, Uxbridge, UK

²Dipartimento di Ingegneria, Univ. degli Studi del Sannio, Piazza Roma, 2, 82100 Benevento, Italy

*giulio.alfano@brunel.ac.uk

Key Words: *interface elements; multiscale; damage mechanics.*

ABSTRACT

Recently proposed approaches for the development of cohesive-zone models which account for the interaction between interface damage, friction and dilatancy are reviewed in this paper. After a brief illustration of the main ideas behind the models and of some numerical results validating their effectiveness some open issues for future research are discussed.

1 INTRODUCTION

The interaction between damage and friction along structural interfaces is a complex problem which is strongly dependent on how microcracks grow and coalesce and how much energy is dissipated because of frictional slipping at the micro-scale. The geometry of the microstructure or of the interface itself can also play an important role particularly when a dilatant response is observed at the macro-scale. An accurate description of all these processes could be obtained through an adequate micromechanical model, which is computationally very expensive. On the other hand, when the overall behaviour of a structural interface is the main interest, a cohesive-zone model (CZM) may be effective enough to capture the mechanics of crack initiation and growth. In particular, a number of CZMs have been proposed in which the effect of friction is somehow accounted for, see [1,2] among many others. In these models the interaction between frictional slips at the microscale and the damage evolution at the meso-scale is mainly derived on a phenomenological basis, which makes their range of applicability somehow limited. To overcome such limitations a more general approach was presented in [3]. It hinges on a strictly meso-mechanical interpretation of the cohesive-zone concept in the framework of damage mechanics, which makes the derivation of interface constitutive laws conceptually simpler, physically well motivated and easy to generalise. The model was enhanced to account for dilatancy firstly in [4] and then, using an alternative original approach, in [5]. The latter method is based on a small-scale description of the geometry of the interface in the form of a periodic arrangement of distinct micro-planes, the interaction within each of these surfaces being governed by the CZM proposed in [3]. In this paper, after a brief illustration of the the main ideas behind the models presented in [3–5] some numerical results will be reviewed and open issues for future research are discussed.

2 CZM FORMULATION AND NUMERICAL RESULTS

The key idea behind the CZM proposed in [3] is that at the meso-mechanical scale an infinitesimal representative interface area (RIA) can be partitioned into an ‘undamaged’ part dA_u and a ‘damaged’ part dA_d ; on the ‘undamaged’ part the interface is fully bonded while on the ‘damaged’ part a unilateral contact with friction occurs. Denoting by dA the area of the RIA and by D the ratio dA_d/dA it results that $dA = dA_u + dA_d$, where $dA_u = (1 - D) dA$ and $dA_d = D dA$ (Figure 1.a).

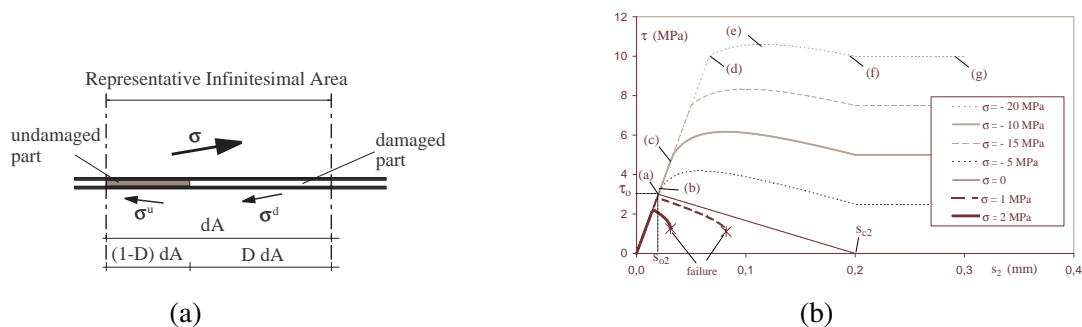


Figure 1: Meso-mechanical modelling of interfaces: (a) RIA and (b) interface response to a prescribed slip history and constant confining stress.

The damaged area is the meso-scale interpretation of a high number of micro-cracks at the micro-structural scale within an interface layer with a small but finite thickness and the assumption is made that the relative displacement s is constant along the entire RIA. Therefore, an interface model can be easily derived by following 4 steps: (i) introducing a relation between the stress σ^u acting on the undamaged part and s which reflects the behaviour of the material in the real finite-thickness interface; (ii) introducing a unilateral contact relation between the stress σ^d acting on the undamaged part and s which can incorporate friction; (iii) recovering the overall stress σ by using the simplified homogenisation formula $\sigma = (1 - D) \sigma^u + D \sigma^d$; (iv) postulating an evolution law for D which reflects the physics of crack growth for the specific case under consideration.

In Figure 1.b the shear stress is plotted against the mode-II relative displacement for different prescribed normal components of the normal stress σ when a linear elastic model is used on dA_u and a Coulomb friction model with no dilatancy is used on dA_d . The curves show that the model well captures (i) the residual tangential stress due to friction after complete decohesion, (ii) the increase of the peak load with a higher confining stress whereby the energy dissipated because of internal friction increases even before complete decohesion occurs and (iii) the recovery of mixed-mode behaviour for a tensile normal stress.

The same model was used to simulate the failure of a masonry wall under combined compression and shear and a push-out test for fibre-reinforced composites, the latter being schematically described in Figure 2.a, with the obtained load-displacement curve reported in Figure 2.b and compared with available experimental results. For more details on the input data and on the results of these and other simulations the reader is referred to [3].

In many problems dilatancy plays a fundamental role. Therefore, in [4] the model presented in [3] was enhanced by simply including dilatancy in the frictional contact law used on dA_d . However, in some cases the dilatant behaviour is linked to a specific geometry of the interface, which led the authors of this paper to propose a different method in [5], which is essentially multiscale. This consists of (i) defining a macro-scale problem with a smooth (for example, flat) interface; (ii) defining a micro-scale

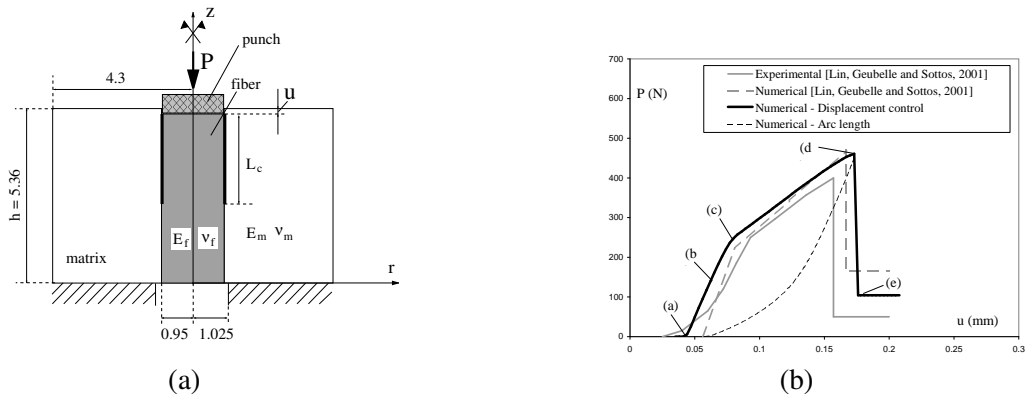


Figure 2: Push-out test: (a) geometry/loading and (b) numerical and experimental load vs -displacement.

problem by considering a representative unit area (RUA) of the interface made of a number of microplanes, each one characterised by its normalised length and its normal direction; (iii) assuming that the dimension of the RUA is significantly larger than the dimension of the RIA of Figure 1.a and that on each microplane the model by Alfano and Sacco [3] is used (i.e. no dilatant behaviour on each microplane); (iv) assuming that the same relative displacement with respect to the common reference system of the macro problem is used on each microplane; (v) solving the problem for each micro-plane at the integration point level and recovering the total homogenised stress as a suitably weighted sum of all the stress components on the microplanes.

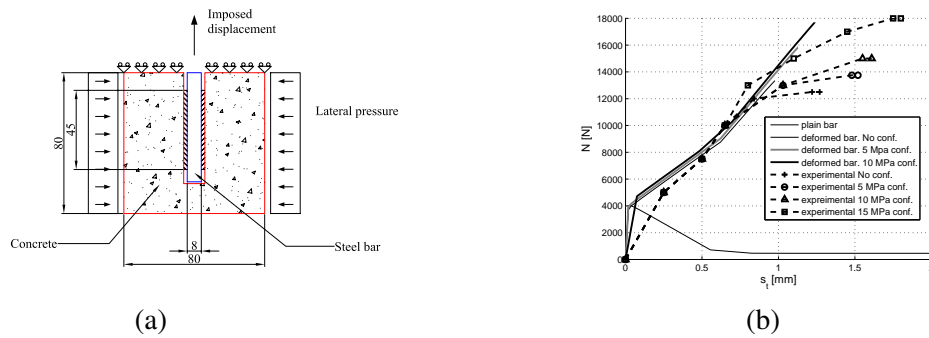


Figure 3: Pull-out test: (a) geometry, loading and constraints and (b) numerically [5] and experimentally [6] computed load-displacement curves.

Figure 3.b reports the load-displacement curve obtained by simulating the pull-out test of a steel bar from a concrete block schematically described in Figure 3.a compared with the experimental results reported in [6]. For more details on the input data and on the results of these and other simulations the reader is referred to [5].

3 DISCUSSION AND OUTLOOK FOR FUTURE RESEARCH

The reported numerical results show good agreement with experimental data, which shows the effectiveness of the proposed approaches. In the case of the pull-out test the agreement is good but not excellent,

which indicates that some aspects of the physical behaviour are not perfectly captured. One aspect that is not simulated in our model in the case of the bond-slip between concrete and ribbed steel bars is localised crushing of concrete, which plays a non-negligible role. However, the generality of the framework is demonstrated by the fact that localised concrete crushing can be accounted for by introducing an elasto-plastic relationship on dA_u , an improvement which will be explored in future work. This flexibility of the formulation also results in a quite wide range of potential applications. For example, some authors report an experimentally observed dilatant behaviour of the fibre-matrix interface during push-out tests. In such a case, the agreement with the experimental results would have not been so good in [3] but the enhanced models proposed in [4] or [5] could be accurate enough.

More generally, the procedure briefly summarised in Section 2 and fully reported in [3–5] can be considered the key-stone to build any CZM. Any constitutive law can be introduced on the dA_u (e.g., elastic, elastoplastic, rate-dependent, etc.) and any contact law (with or without friction, with or without dilatancy) can be introduced on dA_d . In this respect, to introduce dilatancy, the use of a dilatant friction model on dA_d , as done in [4], seems easier. On the other hand, an issue of length scale can be raised: is the dilatant response due to roughness within microcracks at the microscale, or is it due to the roughness of the actual geometry of the interface, i.e. at a larger scale with respect to the RIA of Figure 1.a? One answer could be that in the former case the best approach is the one used in [4] whereas in the latter, for example in the case of the bond-slip interaction between a ribbed steel bar and concrete, the new method proposed by the authors in [5] seems superior. In fact, the above question seems to be related to a deeper theoretical issue regarding the multiscale nature of the approaches. In [3] two scales are involved, the meso-scale, where the interface is a zero-thickness surface and the micro-scale, where micro-cracks grow and nucleate. In [5] a third scale appears, that is the scale of the interface roughness generating interlocking. Therefore, future work can revisit these models within the more rigorous framework of multi-scale computational homogenisation.

References

- [1] G. Bolzon and G. Cocchetti. Direct assessment of structural resistance against pressurized fracture. *International Journal for Numerical Methods in Geomechanics*, 27(5), 353-378, 2003.
- [2] G. Giambanco, S. Rizzo and R. Spallino. Numerical analysis of masonry structures via interface models. *Computer Methods in Applied Mechanics and Engineering*, 190(49-50), 6493-6511, 2001.
- [3] G. Alfano and E. Sacco. Combining interface damage and friction in a cohesive-zone model. *International Journal for Numerical Methods in Engineering*, 65(5), 542-582, 2006.
- [4] G. Alfano, S. Marfia and E. Sacco. A cohesive damage-friction interface model accounting for water pressure effect on crack propagation. *Computer Methods in Applied Mechanics and Engineering*, 196(1-3), 192-209, 2006.
- [5] R. Serpieri and G. Alfano. Bond-slip analysis via a thermodynamically consistent interface model combining interlocking, damage and friction. *International Journal for Numerical Methods in Engineering*, 85(2), 164-196, 2010.
- [6] C. La Borderie and G. Pijaudier-Cabot. Influence of the state of the stress in concrete on the behavior of steel concrete interface. *Proc. of the Fracture Mechanics of Concrete Structures. Breckenridge, Colorado, USA*, 1992.

COHESIVE CRACKING EVOLUTION IN CONCRETE COVER DUE TO REINFORCEMENT CORROSION

Hua-Peng Chen^{1*}, Nan Xiao^{1,2}

1. School of Engineering, University of Greenwich at Medway, Chatham Maritime, Kent, ME4 4TB, UK
2. College of Civil Engineering and Architecture, Zhejiang University, Hangzhou, 310058, China

*Corresponding Author, h.chen@gre.ac.uk

Key Words: *concrete cracking; tensile softening; reinforcement corrosion; nonlinear FE analysis*

ABSTRACT

The paper presents a new analytical model and numerical simulations to study the evolution of radial cracking around a corroding steel reinforcement bar embedded in concrete. The concrete cover for the corroding rebar is modelled as a thick-walled cylinder subject to axisymmetrical displacement constraint at the internal boundary generated by expansive products due to reinforcement corrosion. A bilinear softening curve reflecting realistic concrete property, together with the crack band theory for concrete fracture, is applied to model the residual tensile stress in the cracked concrete. A governing equation for directly solving the crack width in cover concrete is established for the proposed analytical model and the general solution is obtained. The analytical predictions are examined by comparing with the published experimental data and nonlinear finite element analyses are also performed for the problem to verify the developed analytical model. Validations show that the experimental and finite element simulation results agree with the results predicted by the proposed analytical model.

1. INTRODUCTION

The serviceability and durability of concrete structures may be seriously affected by the corrosion of steel reinforcement in structures that are exposed to aggressive environments. Reinforcement corrosion consumes original steel rebar, generates much lighter rust products and creates expansive layer at the interface between the reinforcement and the surrounding concrete cover. As corrosion progresses, the expansive displacement at the interface generated by accumulating rust products causes tensile stress in the hoop direction within the concrete cover, leading to radial splitting cracks in the concrete. Although many investigations have been undertaken during last two decades regarding the influence of reinforcement corrosion and concrete cracking on the performance of reinforced concrete structures, limited work has been done on the theory of cracking evolution in cover concrete during the progress of reinforcement corrosion with reference to realistic concrete material properties such as tensile softening behaviour of the cracked concrete and crack band spacing in the concrete cover.

The paper presents a new approach for studying the evolution of cover concrete cracking due to reinforcement corrosion, based on the thick-walled cylinder model for the concrete cover and the cohesive crack model for the cracked concrete, which is examined by reported experimental measurements and non-linear finite element simulations.

2. THEORY

In the thick-walled cylinder model for cover concrete cracking induced by reinforcement corrosion, as shown in Figs. 1(a) and (b), the reinforcing steel bar has an initial radius R_b embedded in concrete with a clear cover thickness C . The restraint at the internal boundary of the concrete cover could be represented by a prescribed displacement caused by expansive steel rebar corrosion products. Liu and Weyers [1] estimated the mass of rust products M_r over time t from

$$M_r(t) = (4.2 \times 10^{-2} \pi R_b i_{corr} t)^{\frac{1}{2}} \quad (1)$$

where i_{corr} is mean annual corrosion current per unit length. To accommodate the volume increase due to steel corrosion, the prescribed displacement at the interface over time $\bar{u}_b(t)$ is given by

$$\bar{u}_b(t) = R_r - R_b = \sqrt{R_b^2 + \frac{\gamma_m}{\pi} M_r(t)} - R_b \quad (2)$$

where coefficient γ_m is associated with densities of original steel and corrosion rust. The prescribed displacement will be considered as the internal boundary condition of the boundary-value problem for the evolution of cover concrete cracking.

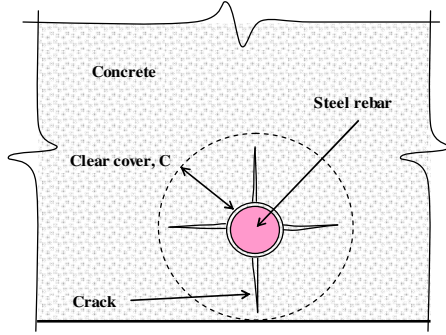


Fig. 1 (a) Idealisation of cover concrete

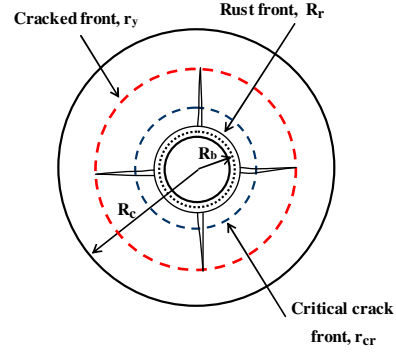


Fig. 1 (b) Geometry of cylinder model

Based on the assumption that the steel rebar has uniform corrosion at the surface, the thick-walled cylinder model for cover concrete cracking can be considered as an axisymmetrical problem and further treated as a plane stress problem. When the hoop stress reaches the tensile strength of concrete, the radial splitting cracks propagate from the bond interface (R_b) in axisymmetrical directions to the same radius (r_y) until reaching the free surface of concrete cover (R_c), as shown in Fig. 1(b).

On the other hand, concrete cracking could be modelled as a process of tensile softening if the cracking is considered as cohesive and the crack width does not exceed a limited value [2]. The function (softening curve) can be determined from experiments and may be utilised to replace the stress-strain relations in the theories such as plasticity. The bilinear softening curve adopted in the present study and expressed as

$$\sigma_w = f_t (a - bW) \quad (3)$$

where σ_w is the tensile stress crossing cohesive cracks, coefficients a and b are defined in the CEB-FIB Model Code and associated with normalised critical and ultimate crack widths W_{cr} and W_u , f_t is the tensile strength of concrete, and W is dimensionless variable that normalises actual crack width $w(r)$ to a non-dimensional form and defined as

$$W = \frac{f_t}{G_F} w(r) \quad (4)$$

where G_F is the fracture energy of concrete. From the crack band theory for the fracture of concrete, the total number of cracks n_c separating cracking bands appearing at cover surface (R_c) is estimated from

$$n_c = \frac{2\pi R_c}{L_c} \quad (5)$$

in which L_c is minimum admissible crack band width estimated from $L_c \approx 3d_a$ in which d_a is maximum aggregate size of concrete. From the defined constitutive equation and relationship between strain and the radial displacement u , the governing equation of displacement can be obtained from stress equilibrium equation by

$$\frac{d^2u}{dr^2} + \frac{1}{r} \frac{du}{dr} - \beta \frac{u}{r^2} = 0 \quad (6)$$

where the reduction factor of residual tensile stiffness β is defined as

$$\beta = \frac{\varepsilon_\theta^e}{\varepsilon_\theta^e + \varepsilon_\theta^f} = \left[1 + \frac{bl_0 W}{(a-bW)r} \right]^{-1} \quad (7)$$

The total hoop strain ε_θ of the cracked concrete consists of fracture strain ε_θ^f and linear elastic strain between cracks ε_θ^e , defined, respectively, as

$$\varepsilon_\theta^f = \frac{n_c w(r)}{2\pi r} = bl_0 \frac{f_t W}{E r} \quad ; \quad \varepsilon_\theta^e = \frac{\sigma_\theta}{E} = \frac{f_t}{E} (a - bW) \quad (8)$$

From the total hoop strain ε_θ , the radial displacement u of the cracked concrete is calculated from

$$u = \varepsilon_\theta r = \frac{f_t}{E} [(a - bW)r + bl_0W] \quad (9)$$

where material coefficient $l_0 = n_c l_{ch} / 2\pi b$ in which l_{ch} is characteristic length $l_{ch} = EG_F / f_t^2$. The governing equation (6) now can be rewritten for directly solving normalised crack width W as

$$(l_0 - r) \frac{d^2W}{dr^2} + (l_0 - 3r) \frac{1}{r} \frac{dW}{dr} = 0 \quad (10)$$

The general solution to the second-order linear homogeneous differential equation is

$$W = C_1 \left[\frac{1}{l_0(l_0 - r)} - \frac{1}{l_0^2} \ln \frac{|l_0 - r|}{r} \right] + C_2 \quad (11)$$

where constant coefficients C_1 and C_2 in the general solution can be determined from two boundary conditions of the boundary-value problem.

In the case of crack propagation before crack width at rebar surface reaches critical value, the thick-walled cylinder is now divided into two zones, an intact outer ring ($r_y^+ \leq r \leq R_c$) and a cracked inner ring ($R_b \leq r \leq r_y^-$). In the intact outer ring, the tensile hoop stress reaches the concrete tensile strength f_t at the crack front (r_y^+) and the external surface (R_c) remains free, expressed as

$$\sigma_\theta \Big|_{r=r_y^+} = f_t, \quad \sigma_r \Big|_{r=R_c} = 0 \quad (12)$$

From the boundary conditions, the normalised crack width over the cracked inner ring is given by

$$W = \frac{\delta(l_0^{cr}, r) - \delta(l_0^{cr}, r_y)}{\delta(l_0^{cr}, R_b) - \delta(l_0^{cr}, r_y)} W_b^{cr} \quad (13)$$

where a crack width function associated with material coefficient l_0 and radius r is defined as

$$\delta(l_0, r) = \frac{1}{l_0(l_0 - r)} - \frac{1}{l_0^2} \ln \frac{|l_0 - r|}{r} \quad (14)$$

and the normalised crack width at the rebar surface is calculated from

$$W_b^{cr}(t) = \frac{1}{b^{cr}(l_0^{cr} - R_b)} \left(\frac{E}{f_t} \bar{u}_b(t) - a^{cr} R_b \right) \quad (15)$$

and crack front (r_y) can be determined by the continuity condition of radial stress crossing the intact and cracked zones, expressed as

$$r_y(l_0^{cr} - r_y) \left[\delta(l_0^{cr}, r_y) - \delta(l_0^{cr}, R_b) \right] \left[(1 + \nu) + (1 - \nu^2) \frac{R_c^2 - r_y^2}{R_c^2 + r_y^2} \right] = (1 - \alpha) \frac{W_b^{cr}}{W_{cr}} \quad (16)$$

The radial stress at the external boundary of the cracked zone (r_y^-) is given by

$$\sigma_r \Big|_{r=r_y^-} = \frac{f_t}{1 - \nu^2} \left[(1 + \nu) - \frac{(1 - \alpha)}{r_y(l_0^{cr} - r_y) [\delta(l_0^{cr}, r_y) - \delta(l_0^{cr}, R_b)]} \frac{W_b^{cr}}{W_{cr}} \right] \quad (17)$$

When the crack front reaches the concrete cover surface ($r_y = R_c$), the displacement at the internal boundary of the thick-walled cylinder at time T_c can be determined from

$$\bar{u}_b(T_c) = \left\{ 1 + (1 + \nu) \frac{R_c}{R_b} (l_0^{cr} - R_b)(l_0^{cr} - R_c) [\delta(l_0^{cr}, R_c) - \delta(l_0^{cr}, R_b)] \right\} \frac{f_t}{E} R_b \quad (18)$$

Consequently, the time to cracking T_c can be estimated from Eqs. (2) and (1), which is a function of concrete cover dimensions, material properties of cover concrete and reinforcement corrosion rate.

The above procedure can be further used for the full development of cracking in the cover concrete such as the cases when crack width at rebar surface exceeds critical value and when the concrete cover is completely cracked, where the boundary conditions at internal and external surfaces are different.

3. NUMERICAL EXAMPLE

A numerical example is utilised to demonstrate the cracking development in concrete cover due to reinforcement corrosion predicted by the proposed approach. The material properties for the specimens utilised in [1] are taken as tensile strength $f_t = 3.3\text{MPa}$, elastic modulus of concrete $E = 27\text{GPa}$, fracture energy $G_f = 83\text{N/m}$, critical and ultimate crack widths $w_{cr} = 0.03\text{mm}$ and $w_u = 0.2\text{mm}$. The plot in Fig. 2 presents curves for the cracked front r_y propagating with time from the rebar surface to the concrete cover surface. The crack width at the concrete cover surface w_c shown in Fig. 3 increases abruptly when crack front reaches the free cover surface due to sudden release of energy. After the time to cracking, the crack width w_c is close to that at the rebar surface w_b and becomes ultimate cohesive width at last. The theoretical predictions of the crack width over time are also compared with the experimental measurements by Andrade et al. [3], and the predicted results lie between the maximum and minimum measured crack widths and are in good agreement with the experimental data.

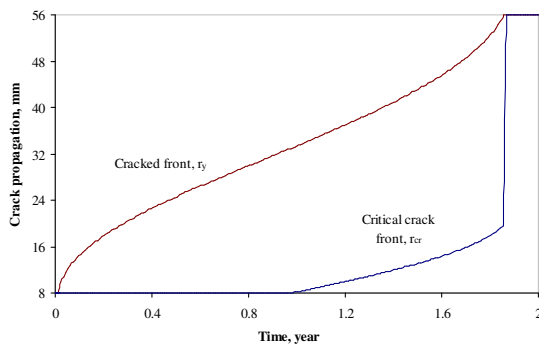


Fig. 2 Propagation of cracked front (r_y) and critical crack front (r_{cr}) with time t .

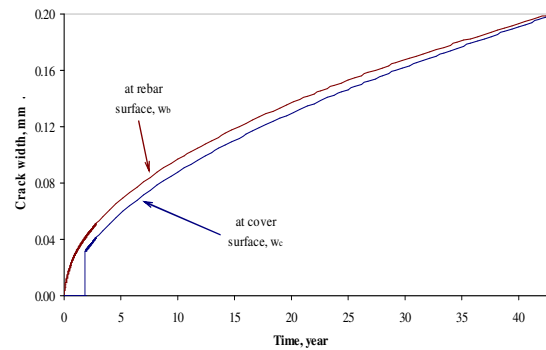


Fig. 3 Crack widths at rebar surface (w_b) and at cover surface (w_c) with time t .

The problem is analysed by finite element software DIANA where softening cohesive concrete model is adopted. The results of crack propagation from the interface to the cover surface and the crack width at the interface from FE simulations are presented in Fig. 4, which match with the theoretical results.

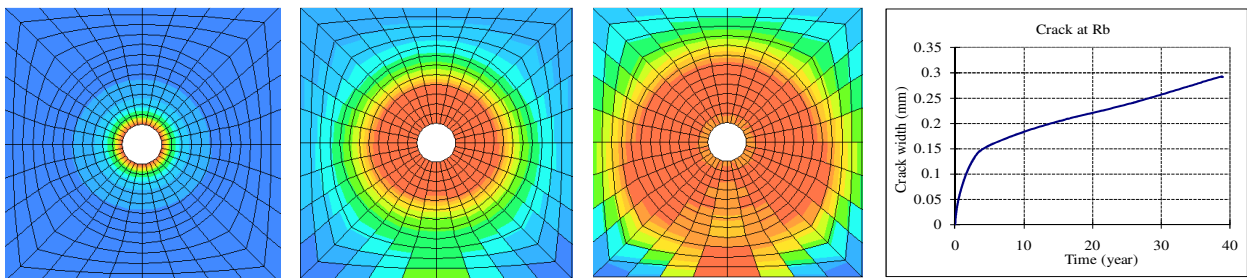


Fig. 4 Crack propagation in the cover concrete and predicted crack width from FE simulations.

4. CONCLUSIONS

The proposed analytical method can effectively simulate the evolution of radial cracking around a corroding steel reinforcement bar embedded in concrete, which can be verified by existing experimental data and finite element simulations.

REFERENCES

- [1] Liu, Y., Weyers, R.E., 1998. Modelling the time-to-corrosion cracking in chloride contaminated reinforced concrete structures. *ACI Materials Journal* 95 (6), 675–681.
- [2] Bažant, Z.P., Planas, J., 1998. *Fracture and Size Effect in Concrete and Other Quasibrittle Materials*. CRC Press, Boca Raton, Florida USA.
- [3] Andrade, C., Alonso, C., Molina, F.J., 1993. Cover cracking as a function of bar corrosion: Part I - Experimental test. *Materials and Structures* 26 (8), 453-464.

AN INTERFACE FAILURE CRITERION IN A MICROMECHANICAL MODEL FOR CONCRETE

*Iulia Mihai¹ and Tony Jefferson¹

¹School of Engineering, Cardiff University, Queen's Buildings, The Parade, Cardiff, CF24 3AA

*MihaiIC1@cardiff.ac.uk

Key Words: *micromechanics; cementitious composites; exterior point Eshelby*

ABSTRACT

New developments for simulating microcracking in cementitious composite materials are presented. A microcrack initiation criterion based upon the exterior point Eshelby solution which aims to model the onset of micro-cracking in the interfacial transition zone between aggregate particles and the cement matrix is proposed. The adopted solution captures tensile stress concentrations in the proximity of inclusion – matrix interfaces in directions lateral to a compressive loading path. The criterion is subsequently applied in a constitutive model - initially formulated by Jefferson and Bennett [1-2] - that employs micromechanical solutions of a two-phase composite comprising a matrix phase, spherical inclusions, penny-shaped microcracks randomly distributed in the matrix and combines these with a rough crack contact component. The effective properties of the two-phase composite are obtained using the Mori-Tanaka homogenization scheme. The two-phase formulation is able to predict the build-up of tensile stresses within the matrix phase under uniaxial compression stresses. However, it is the employment of the damage initiation criterion that positions the onset of micro-cracking in a region adjacent to the matrix-inclusion boundary and enables the use of realistic material properties for obtaining a correct cross-cracking response. Numerical results that demonstrate the potential of the model to capture key characteristics of the mechanical behaviour of concrete are presented.

1 INTRODUCTION

The development of an accurate and robust constitutive model for cementitious composite materials such as concrete has been a challenge for researchers for many years. Many macroscopic models based on damage and plasticity theories have been proposed and implemented in commercial FE codes with varying degrees of success however they often use parameters that are difficult to determine and thus far no one model has been able to fully simulate all aspects of the complex behaviour of concrete.

An alternative approach to phenomenological models is offered through the development of models based on micromechanical theories which aim to relate the macroscopic behaviour observed in experiments to simple physical mechanisms modelled at micro and meso scales. In recent years several models have been proposed that employ a micromechanical solution of an elastic solid containing penny-shaped microcracks and various damage evolution laws [3-5].

The present work follows on from the micromechanics based constitutive model formulated by Jefferson and Bennett [1, 2]. A crack initiation criterion based upon the so-called exterior point Eshelby solution is proposed for modelling the onset of micro-cracking in the aggregate-cement paste interface.

2 MICROMECHANICS BASED CONSTITUTIVE MODEL

The model simulates a two-phase composite comprising a matrix (m), spherical inclusions (Ω) and penny-shaped microcracks with rough surfaces randomly distributed within the matrix phase. A brief summary with key equations is presented below.

The Eshelby inclusion solution and the Mori-Tanaka averaging scheme for a non-dilute distribution of inclusions were employed in deriving the elastic properties of the two-phase composite. The overall constitutive relationship for the composite is as follows

$$\bar{\boldsymbol{\sigma}} = \mathbf{D}_{m\Omega} : (\bar{\boldsymbol{\varepsilon}} - \boldsymbol{\varepsilon}_a) \quad (1)$$

where $\bar{\boldsymbol{\sigma}}$ and $\bar{\boldsymbol{\varepsilon}}$ are the average far-field stress and the average far-field strain respectively,

$\mathbf{D}_{m\Omega} = (f_\Omega \mathbf{D}_\Omega : \mathbf{T}_\Omega + f_m \mathbf{D}_m) : (f_\Omega \mathbf{T}_\Omega + f_m \mathbf{I}^{4s})^{-1}$ is the elasticity tensor of a two-phase composite, $\mathbf{T}_\Omega = \mathbf{I}^{4s} + \mathbf{S}_\Omega : [(\mathbf{D}_\Omega - \mathbf{D}_m) : \mathbf{S}_\Omega + \mathbf{D}_m]^{-1} : (\mathbf{D}_m - \mathbf{D}_\Omega)$, f_m and f_Ω represent the volume fractions of the matrix and inclusion phases respectively ($f_m + f_\Omega = 1$), \mathbf{S}_Ω is the interior-point Eshelby tensor [6], \mathbf{D}_Ω and \mathbf{D}_m are the elasticity tensors for the inclusion and matrix phase respectively and \mathbf{I}^{4s} is the fourth order identity tensor.

The added strain $\boldsymbol{\varepsilon}_a$ due to a series of randomly distributed penny-shaped microcracks was derived in [1] based on Budiansky and O'Connell's solution [6] in which the crack density function was interpreted in terms of a directional damage parameter ω ($0 \leq \omega \leq 1$). Transforming and adding the contributions of microcracks from all possible directions gives:

$$\boldsymbol{\varepsilon}_a = \left(\frac{1}{2\pi} \int_{2\pi} \int_{\pi/2} \mathbf{N}^T : \mathbf{C}_L : \mathbf{N} \frac{\omega(\theta, \psi)}{1 - \omega(\theta, \psi)} \sin(\psi) d\psi d\theta \right) : \bar{\boldsymbol{\sigma}} \quad (2)$$

In which \mathbf{C}_L is the compliance tensor in the local coordinate system of a microcrack and \mathbf{N} the stress transformation tensor. The evolution of the damage parameter ω is essentially governed by the local strains [1].

A transition function Ξ was introduced in the model to simulate the fact that microcracking in early stages is controlled by the matrix stress whereas the later stages, in which cracking progresses towards macro-crack formation, are governed by the average stress [2]. Hence, equation (1) becomes:

$$\bar{\boldsymbol{\sigma}} = \left(\mathbf{I}^{4s} + \frac{\mathbf{D}_{m\Omega}}{2\pi} \int_{2\pi} \int_{\pi/2} \mathbf{N}^T : \mathbf{C}_L : \mathbf{N} : \Xi \frac{\omega(\theta, \psi)}{1 - \omega(\theta, \psi)} \sin(\psi) d\psi d\theta \right)^{-1} : \mathbf{D}_{m\Omega} : \bar{\boldsymbol{\varepsilon}} \quad (3)$$

A rough crack closure component was then implemented to model the recovery of stress on microcracks that regain contact. In each direction the local stress was written as a summation of the average stress on intact material and the recovered stress on debonded material that regains contact.

$$\mathbf{s}_\alpha = [(1 - \omega) \mathbf{D}_L : \boldsymbol{\varepsilon}_L] + [H_f(\boldsymbol{\varepsilon}_L) \omega \boldsymbol{\Phi}(m_g, \boldsymbol{\varepsilon}_L) : \boldsymbol{\varepsilon}_L] \quad (4)$$

H_f is a reduction function that decreases from 1 to 0 as the potential for shear transfer reduces with increasing crack opening, $\boldsymbol{\Phi}(m_g, \boldsymbol{\varepsilon}_L)$ is the contact matrix in which m_g is the slope of the interlock contact surface and describes roughness of the crack surface [1]. $\mathbf{D}_L = \mathbf{C}_L^{-1}$ and $\boldsymbol{\varepsilon}_L$ is the local strain tensor. Removing the elastic compliance from equation (4), the added compliance including contact $\mathbf{C}_{c\alpha}$ becomes:

$$\mathbf{C}_{c\alpha} = \left[(1 - \omega) \mathbf{I}^{2s} + H_f \omega \boldsymbol{\Phi} \right]^{-1} - \mathbf{I}^{2s} \cdot \mathbf{C}_L \quad (5)$$

Replacing $\frac{\omega}{1 - \omega} \mathbf{C}_L$ with $\mathbf{C}_{c\alpha}$ in equation (3) the average stress-average stress relationship is obtained:

$$\bar{\boldsymbol{\sigma}} = \left(\mathbf{I}^{4s} + \frac{\mathbf{D}_{m\Omega}}{2\pi} \int_{2\pi} \int_{\pi/2} \mathbf{N}^T : \mathbf{C}_{c\alpha} : \mathbf{N} : \Xi \sin(\psi) d\psi d\theta \right)^{-1} : \mathbf{D}_{m\Omega} : \bar{\boldsymbol{\varepsilon}} \quad (6)$$

The integration over a hemisphere in equation (6) is evaluated numerically by employing McClaurin integration rule with 29 sample directions.

3 EXTERIOR POINT ESHELBY BASED CRACK INITIATION

Experiments suggest that microcracking is initiated in the interfacial transition zone between aggregate particles and cement matrix and is caused by a build-up in tensile stresses, shear stresses or both [7]. In an attempt to simulate this particular mechanism a microcrack initiation criterion was formulated based upon the exterior point Eshelby solution which provides the expression of the total strain/stress field outside an ellipsoidal inclusion embedded in an infinite elastic matrix [8].

$$\boldsymbol{\varepsilon}_{m\Omega}(\mathbf{x}) = \boldsymbol{\varepsilon}_0 + \mathbf{S}_E(\mathbf{x}) : \boldsymbol{\varepsilon}^* \quad (7)$$

$$\boldsymbol{\sigma}_{m\Omega}(\mathbf{x}) = \boldsymbol{\sigma}_0 + \mathbf{D}_m : \mathbf{S}_E(\mathbf{x}) : \boldsymbol{\varepsilon}^* \quad (8)$$

in which $\boldsymbol{\varepsilon}_0$ and $\boldsymbol{\sigma}_0$ are the applied far-field strain and stress respectively, $\boldsymbol{\varepsilon}^*$ is an inhomogeneity-induced eigenstrain and $\mathbf{S}_E(\mathbf{x})$ is the exterior-point Eshelby tensor. The explicit components of the exterior point Eshelby tensor are derived in [8] for spheroidal inclusion and in [9] for spherical inclusions.

A full account of the development of the microcrack initiation criterion using the exterior point Eshelby solution for spherical inclusions is given in [10]. An illustrative diagram showing the lateral stress distribution outside a spherical inclusion for a uniaxial compressive load case is presented in Figure 1. The exterior point Eshelby solution is able to capture sharp gradients adjacent to an inclusion-matrix interface that generates a peak in the stress field.

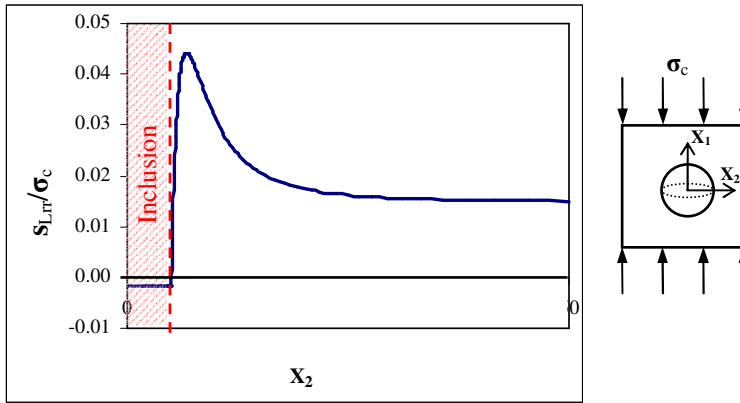


Figure 1. Lateral stress distribution outside a spherical inclusion

The use of this peak tensile stress in the crack initiation condition (i.e. in simplified terms, damage is initiated when the peak stress becomes greater than or equal to the tensile strength of the interface) enables the use of realistic and meaningful material properties- i.e. elastic moduli of the two phases and measured aggregate-mortar interface strength parameters- to simulate lateral splitting in uniaxial compression, a primary damage mechanism [10]. Moreover, the above solution is able to place microcrack initiation at the matrix-inclusion interface without having to introduce a separate interface component into the model.

4 RESULTS AND CONCLUSION

Numerical results for a uniaxial compression strain path obtained with the micromechanical model including the exterior point Eshelby based crack initiation criterion and using realistic material data justified in [10] are presented in Figure 2.

The micromechanical model and the crack initiation criterion presented are able to simulate successfully micromechanisms that lead to failure while employing realistic and meaningful material parameters. Many more examples and comparisons with experimental data are presented in the full description of the model [10].

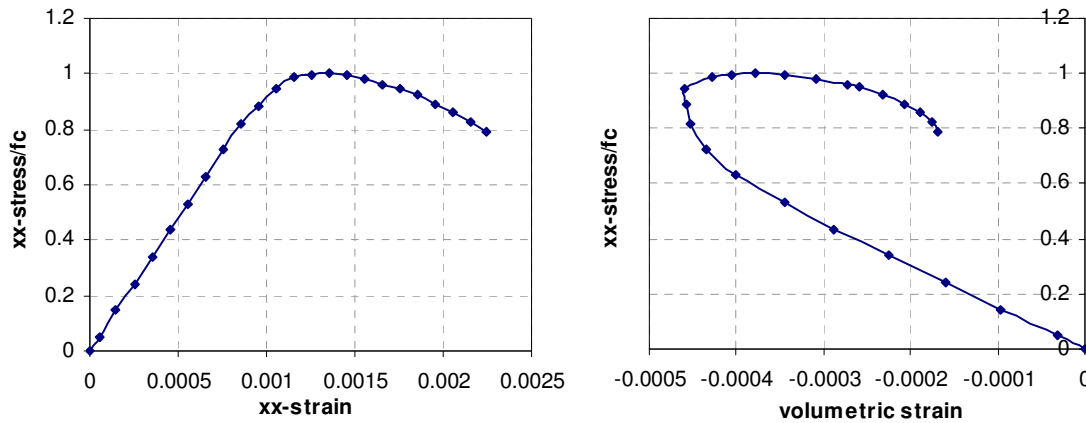


Figure 2. Uniaxial compression prediction (compression ϵ_v)

References

- [1] A.D. Jefferson, T. Bennett. Micro-mechanical damage and rough crack closure in cementitious composite materials. *International Journal for Numerical and analytical methods in Geomechanics*, 31(2), 133-146, 2007
- [2] A.D. Jefferson, T. Bennett. A model for cementitious composite materials based on micro-mechanical solutions and damage-contact theory. *Computers and Structures*, 88, 1361-1366, 2010
- [3] V Pensée, D Kondo, L Dormieux. Micromechanical analysis of anisotropic damage in brittle materials. *Journal of Engineering Mechanics ASCE*, 889-897, 2002
- [4] B. Pichler, C. Hellmich, H.A. Mang. A combined fracture-micromechanics model for tensile strain-softening in brittle materials, based on propagation of interacting microcracks. *International Journal for Numerical and Analytical Methods in Geomechanics* 31, 111-132, 2007
- [5] Q Z Zhu, D Kondo, J F Shao. Micromechanical analysis of coupling between anisotropic damage and friction in quasi brittle materials: Role of the homogenization scheme. *International Journal of Solids and Structures*, 45, 1385-1405, 2008
- [6] S. Nemat-Nasser, M. Hori. *Micromechanics: overall properties of heterogeneous materials*. North-Holland, 1999
- [7] J G M van Mier. *Fracture processes of concrete*, CRC Press, 1997
- [8] J.W. Ju, L.Z. Sun. A Novel Formulation for the Exterior-Point Eshelby's Tensor of an Ellipsoidal Inclusion. *Journal of Applied Mechanics ASME*, 66, 570 – 574, 1999
- [9] S. Li, R.A Sauer, G. Wang. The Eshelby Tensors in a Finite Spherical Domain – Part I: Theoretical Formulations. *Journal of Applied Mechanics* 74, 770 – 783, 2007
- [10] I.C. Mihai, A.D. Jefferson. Exterior point Eshelby microcrack initiation criterion for a material model for cementitious composite materials. *International Journal of Solids and Structures*, Submitted for publication 2011

OVERLOAD EFFECT IN FATIGUE CRACK GROWTH USING A COHESIVE ZONE MODEL

H. Dahlan and K. Davey*
School of Mechanical, Aerospace and Civil Engineering,
The University of Manchester, Manchester, M13 9PL, UK

*keith.davey@manchester.ac.uk

Key Words: fatigue, overload, cohesive elements, finite element method.

ABSTRACT

The precise numerical modelling of fatigue is recognised to be computationally expensive and potentially can involve the analysis of many thousands of cycles. A particular phenomenon of interest in this paper is the *overload effect* which occurs when increased loading is sporadically superimposed on constant-amplitude fatigue loading. The *overload effect* is an unexpected increase in the number of cycles to component failure. The numerical analysis of the overload effect in fatigue-crack growth is presented in this paper. The simulation of a discontinuity on a predefined crack path under cyclic loading is achieved by means of a cohesive zone model incorporated into Code_Aster. The model introduces irreversibility into the constitutive relationships by means of damage accumulation with cyclic loading. The traction-separation relationship underpinning the cohesive zone model is not required to follow a predetermined path, but is dependent on irreversibility introduced by decreasing the critical traction value. The results of computation demonstrate the model can capture the overload phenomenon. It is demonstrated in the paper that a single overload can be sufficient to retard crack growth rate and under certain conditions can even arrest crack growth altogether. The effects of boundary constraint are also presented in the paper.

1 INTRODUCTION

During service, many structures are occasionally subject to cyclic overload, which is observed to decelerate the fatigue crack growth rate. The cause of this deceleration is usually attributed to plasticity induced crack closure, strain hardening, crack tip blunting, and crack deflection. The plastic zone is thought however to be of major importance as its presence can result in the generation of compressive residual stresses which then act as a reduction factor contributing to crack growth retardation. Various empirical models have been proposed each pertaining to relate to a particular phenomenon, i.e. crack closure [1], compressive residual stress [1,2] and variants of the empirical model proposed by Wheeler [3,4]. Similarly, exponential models have been developed that determine not only parameters related with overload but also residual life [5]. The difficulty with these empirical models is that they do not capture completely the physics of fatigue crack growth and have a limited range of applicability. The phenomena of fatigue crack growth can in principle be described with the aid of a computational model. Adopting a mechanism-based approach rather than as empirical method should in principle provide greater insight to support the development of more realistic computational models although invariably at the price of increased complexity and computational cost.

A particular mechanistic computational model that has been applied to model fatigue is that of the cohesive zone model. The cohesive zone model can capture the nonlinear behaviour occurring in the process zone and also can be paired with a plasticity model to account for bulk material deformation and is especially useful in simulating fatigue behaviour for materials that violate small-yielding assumptions at the crack tip. Cohesive zone fatigue models are most commonly implemented in finite element codes and provide a mechanism for element interface separation. In fatigue models, the traction-separation relationship underpinning the cohesive zone model is not required to follow a predetermined path, but is dependent on irreversibility introduced within the model. Various cohesive models have been proposed with some incorporating a degrading peak traction stress under cyclic loading and unloading [6] along with incremental changes in stiffness [7]. In this work, the degrading peak-traction approach is incorporated along with the adoption of a irreversibility parameter. This model is implemented in

Code_Aster [8] but brief details are presented in the following section.

2. Cohesive zone model

In the cohesive zone model considered here the irreversible crack behaviour is controlled by an internal variable κ , which is defined as the accumulation of normal separation δ_n during loading cycles. The irreversibility results as a consequence of the growth of this parameter which is non-negative. In an incremental form the relationship between κ and δ_n is defined as $\kappa^i = \kappa^{i-1} + \langle \delta_n^i - \delta_n^{i-1} \rangle$.

The traction-separation relationship can be considered in three stages, which are: initial shape, damage processing and post fracture as illustrated in Figure 2.1. In first stage (initial shape), the accumulation of normal separation is still zero ($\kappa^{i-1} = 0$) the normal traction σ_n is a function of current normal separation, δ_n^i , which can be expressed as $\sigma_n(\delta_n^i) = \sigma_c \left(1 - \frac{\delta_n^i}{\delta_c}\right)$ for $0 < \delta_n^i \leq \delta_c$, otherwise it is zero,

where δ_c is the critical normal separation at which fracture occurs and σ_c is the critical normal stress, beyond which incipient separation begins. For the second stage (damage processing), the normal separation κ^i increases during the cyclic process with $0 < \kappa^{i-1} < \delta_c$. The normal traction $\sigma_n = 0$ for

$0 < \delta_n^i \leq \delta_n^{i-1}$ and $\delta_n^i > d_c$, but for $\delta_n^{i-1} < \delta_n^i < d_c$ is defined to be $\sigma_n(\kappa^i) = \sigma_c \left(1 - \frac{\kappa^i}{\delta_c}\right)$ where

$$d_c = \frac{\delta_c S_c}{\sigma_c} \quad \text{and} \quad S_c = \sigma_c \left(1 - \frac{\kappa^{i-1} - \delta_n^{i-1}}{\delta_c}\right) \quad (\text{see Figure 2.1}).$$

For the third stage (post fracture) when the crack is open, $\kappa^{i-1} \geq \delta_c$, the normal traction σ_n is zero for $0 < \delta_n^i$ and a contact condition is applied when $\sigma_n(0) \leq 0$. The irreversible behaviour is illustrated in Figure 2.2 with vertical lines denoting loading and unloading.

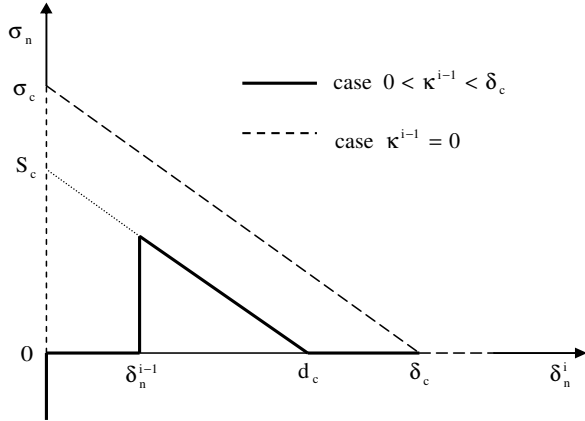


Figure 2.1 Schematic of cohesive law

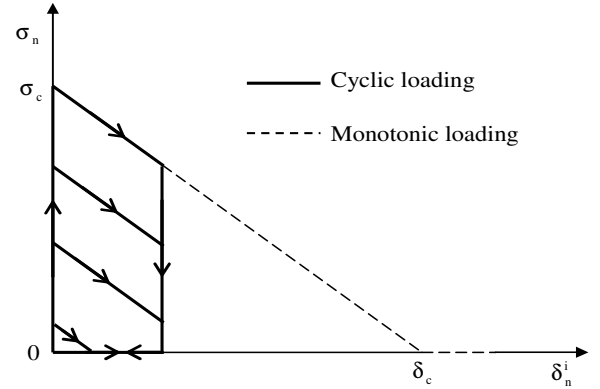


Figure 2.2 Evolution of traction during monotonic and cyclic loading with the cohesive law

3. IMPLEMENTATION OF COHESIVE ZONE MODEL

3.1 Model Description

In the present work, a model consisting of 17.7 mm crack length with 50 mm of height (h) and 52 mm of width (w) is analysed. The crack propagation is assumed to proceed along the axis of symmetry of the model. The assumed symmetry means that only half the model is simulated. The cohesive interface of 163 elements are placed along the symmetry line from the initial crack tip to the outer boundary. The model is meshed with 12680 quadratic-triangular elements. The mechanical properties of the material used for linear-elastic analysis are: $E = 72$ GPa, $\sigma_{ys} = 300$ MPa, $\nu = 0.3$ and $G_{IC} = 9.5$ N/mm. The critical stress σ_c is taken as 350 MPa for plane stress and the plastic modulus $E_T = 1.39$ GPa to represent linear-kinematic hardening. In the case of constant amplitude loading (CAL), a stress loading of 15 MPa

is applied uniformly on the edge top of plate as a sinusoidal function as shown on Figure 3.1 (b). The model have three different boundary conditions, i.e.

1. Constraint left edge, $D_x = 0$ and bottom edge, $D_y = 0$ (LC) as shown in Figure 3.1 (a).
2. Constraint right edge, $D_x = 0$ and bottom edge, $D_y = 0$ (RC).
3. Constraint point A, $D_x = 0$, $D_y = 0$ and bottom edge, $D_y = 0$ (NC).

For single cycle overloading (SOL), a single stress overloading (S_{ol}) of 30 MPa is applied at the first cycle and a stress loading (S_{max}) of 15 MPa is applied uniformly on the top edge of the plate as a sinusoidal function as shown on Figure 3.1(c). A overload ratio $SOL = S_{ol} / S_{max} = 2.0$ and a load ratio $R = S_{max} / S_{min} = 0$ is applied for all tests. The model has boundary conditions: constraint left edge, $D_x = 0$ and bottom edge, $D_y = 0$ (LC) as shown in Figure 3.1 (a).

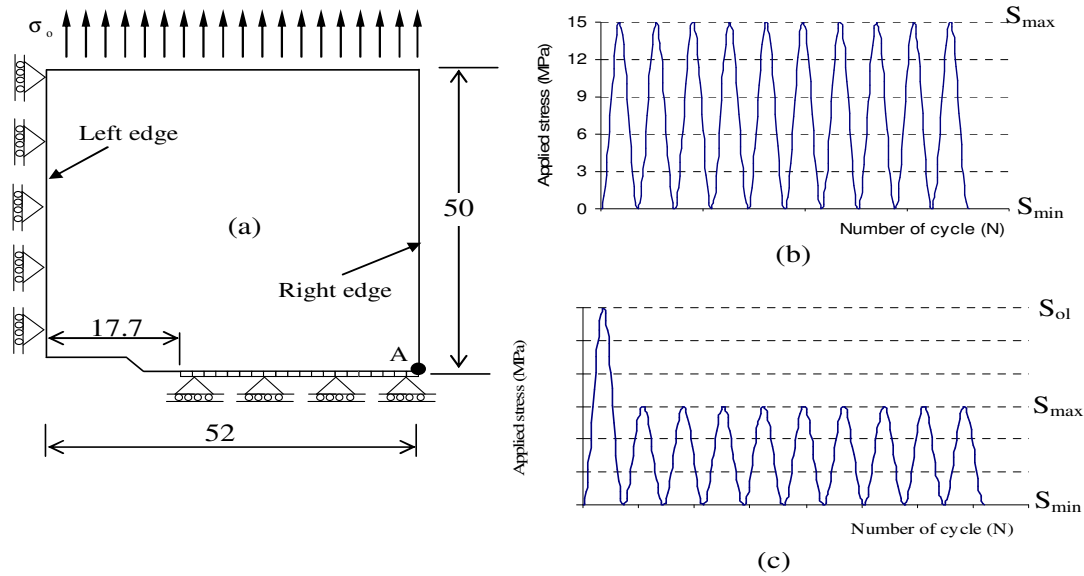


Figure 3.1 The schematics of models: (a) dimensions and boundary condition (LC) (b) constant amplitude cyclic loading (CAL) (c) single overload (SOL)

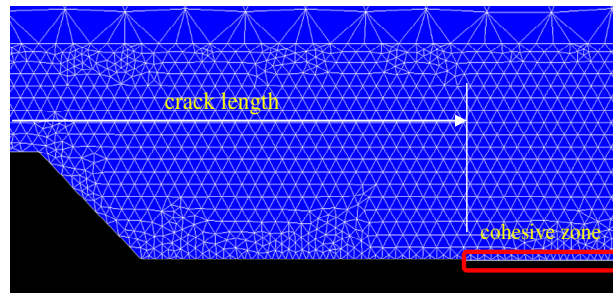


Figure 3.2 The cohesive element model in Code_Aster

3.2 Results and discussion

Figure 3.3 shows the effect of boundary conditions on crack propagation with the number of cycles (N). The NC constraint condition has the highest crack growth rate. This is caused by the lack of constraint in both edges which leads to higher stress levels at the crack tip when contrasted against the other constraint conditions. Constraints near the crack tip (LC) produces low stress levels ahead of the crack tip, which results in an increase in the number of cycles to failure.

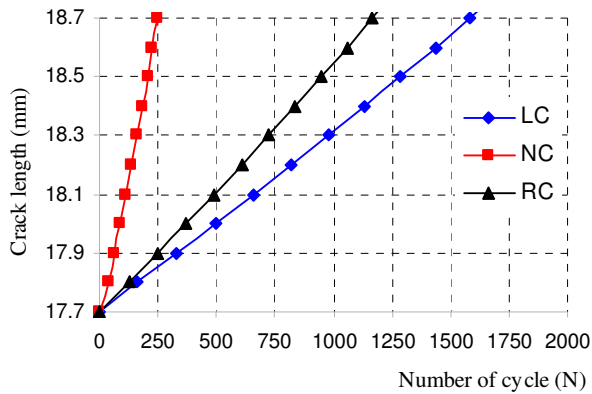


Figure 3.3 The effect of various boundary condition respect to number of cycle

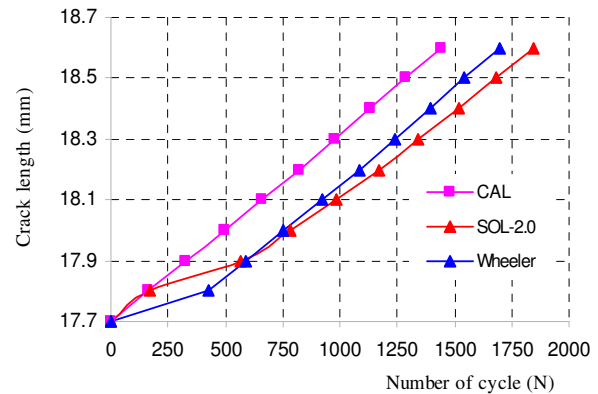


Figure 3.4 The effect of various single overload (SOL) in crack growth rate

The effect of a single overload (at $N=1$) in crack growth rate is presented in Figure 3.4. It is apparent on examination of this figure that the crack growth rate begins to retard once the overload is applied. However it clearly decelerates after the first element fails then eventually follows a similar rate of crack growth as seen with constant amplitude loading (CAL). The numerical results are contrasted with Wheeler's model utilising the material parameters found in reference [5]. This shows that both results are in broad agreement in general although errors are apparent immediately following the application of an overload. In addition, as the number of cycles becomes large the crack growth rate predicted by Wheeler's empirical model is lower. This demonstrates the limitation of an empirical model to accurately account for all loading conditions.

4. Conclusion

The results of the computation demonstrate that a cohesive zone model can capture the overload phenomenon. It is demonstrated that a single overload can be sufficient to retard crack growth rate. The boundary constraint has an effect on crack growth rate by modifying stress levels at the crack tip.

References

- [1] W. Elber. Fatigue crack closure under cyclic tension. *Journal Engineering Fracture. Mechanics.* 2, 37–45, 1970.
- [2] O.E. Wheeler. Spectrum loading and crack growth, *Journal Basic Engineerin. Trans ASME, Ser D,* 94(1),81–6, 1972.
- [3] H. Xiaoping, T. Moan, and C. Weicheng, An engineering model of fatigue crack growth under variable amplitude loading. *International Journal of Fatigue,* 30, 2–10, 2008.
- [4] G.A. Harmain. A model for predicting the retardation effect following a single overload. *Theoretical and Applied Fracture Mechanics,* 53, 80-88, 2010.
- [5] J.R. Mohanty, B. B. Verma and P.K. Ray. Prediction of fatigue crack growth and residual life using an exponential model: Part II (mode-I overload induced retardation). *International Journal of Fatigue,* 31, 425-432, 2009.
- [6] A. Ural, V. R. Krishnan, K. D. Papoulia. A cohesive zone model for fatigue crack growth allowing for crack retardation. *International Journal of Solids and Structures,* 46, 2453-2462, 2009.
- [7] O. Nguyen, E.A. Repetto, M. Ortiz, and R.A. Radovitzky. A cohesive model of fatigue crack growth. *International Journal Fracture,* 110, 351–369, 2001.
- [8] J. Laverne, Lois de comportement cohésives CZM_xxx_xxx et pilotage du chargement. *de référence du Code_Aster R7.02.11,* 1-19, 2010.

ON THE MESH DEPENDENCE OF LATTICE MODELS FOR ANALYSING CONCRETE FRACTURE

Caroline Fahy, Domenico Gallipoli and Peter Grassl

School of Engineering, University of Glasgow, Oakfield Avenue, Glasgow, G12 8LT

c.fahy.1@research.gla.ac.uk, {domenico.gallipoli, peter.grassl}@glasgow.ac.uk

Key Words: *fracture; lattice; concrete; computational methods*

ABSTRACT

The present work is part of a project on modelling corrosion induced cracking and spalling in reinforced concrete structures. In the first step, the aim is to investigate the accuracy and robustness of lattice approaches to modelling fracture in concrete. This paper presents a comparative study of the influence of mesh size on predicted fracture trajectories which are also compared to experimental data. Two separate problems were analysed using three mesh sizes for each. The results obtained from these analyses are presented in this work.

1 INTRODUCTION

Lattice models have been used to study the behaviour of a number of softening materials, such as concrete. This work investigates the performance of one of these models when combined with an isotropic damage law. The constitutive law used within this model is outlined in the following section. The influence of mesh size on the resulting fracture patterns and load-displacement curves is examined. The results of the analyses are compared with those of experimental tests reported in the literature.

2 LATTICE MODEL

In the model outlined below, discretisation of the material continuum is based on Voronoi and Delaunay tessellations with random geometries [2]. Lattice elements correspond to the edges of a Delaunay triangulation [2]. The edges of the Voronoi polygons are used to scale the stiffness of the elements. The inelastic response of the lattice element is described by an isotropic damage approach, which corresponds to a continuous reduction of the element's stiffness [3]. The main equations of this constitutive model are as follows. The stress-strain law is defined as

$$\boldsymbol{\sigma} = (1 - \omega) \mathbf{D}\boldsymbol{\varepsilon} \quad (1)$$

where $\boldsymbol{\sigma} = \{\sigma_n, \sigma_s, \sigma_\phi\}^T$ is the nominal stress vector (comprising of normal, shear and rotational stresses), ω is a damage parameter, \mathbf{D} is the elastic stiffness and $\boldsymbol{\varepsilon} = \{\varepsilon_n, \varepsilon_s, \varepsilon_\phi\}^T$ is the strain vector (comprising of normal, shear and rotational strains). The elastic stiffness is defined as

$$\mathbf{D} = \begin{pmatrix} E & 0 & 0 \\ 0 & \gamma E & 0 \\ 0 & 0 & E \end{pmatrix} \quad (2)$$

and depends on the model parameters E and γ which are used to relate the continuum properties of the specimen to the local properties of the lattice element. E and γ are calculated as follows

$$\gamma = \frac{1 - 3\nu}{\nu + 1} \quad (3)$$

$$E = \frac{E_c}{1 - \nu} \quad (4)$$

Here, ν is Poisson's ratio and E_c is the Young's modulus of the continuum specimen. At present there is no direct way of determining the tensile strength and fracture energy of the lattice elements from the tensile strength and fracture energy of the continuum specimen. For the analyses carried out in this work, it was initially assumed that the continuum and discrete tensile strength and fracture energy were equal. However, comparison with experimental data showed this assumption was incorrect and the tensile strengths and fracture energies for both specimens were modified to achieve a better quantitative agreement with the experimental load-displacement curve. An exponential softening curve was used to describe the stress crack opening part of the model.

3 SIMULATION OF FRACTURE TESTS

Two tests were chosen to investigate the influence of mesh size on concrete fracture. Each fracture test was analysed using three different mesh sizes and a comparison of the influence of the different mesh sizes on the curved fracture pattern was carried out. The specimens modelled, the parameters assumed and the results from the analyses are outlined in the following sections.

3.1 FOUR-POINT SHEAR TEST

The first simulation modelled the four-point shear test of a single-edge-notched (SEN) beam tested by Arrea and Ingraffea [1]. The geometry of the specimen, along with the loading setup and the crack trajectories obtained in the experiments are shown in Fig. 1. The material parameters chosen for the lattice elements were as follows: $E = 36.58$ GPa, $\gamma = 0.3898$, $\bar{f}_t = 2.8$ MPa and $G_F = 112$ J/m². The first two parameters correspond to elastic properties of the continuum model of $E_c = 30$ GPa and $\nu = 0.18$. Figure 1 below shows the failure patterns obtained from the analysis. The displacement was calculated as the difference of the vertical displacements at the bottom nodes on each side of the notch (referred to as the Crack-Mouth-Shear-Displacement). The load-CMSD curves for the three meshes are compared to the experimental results in Fig. 2.

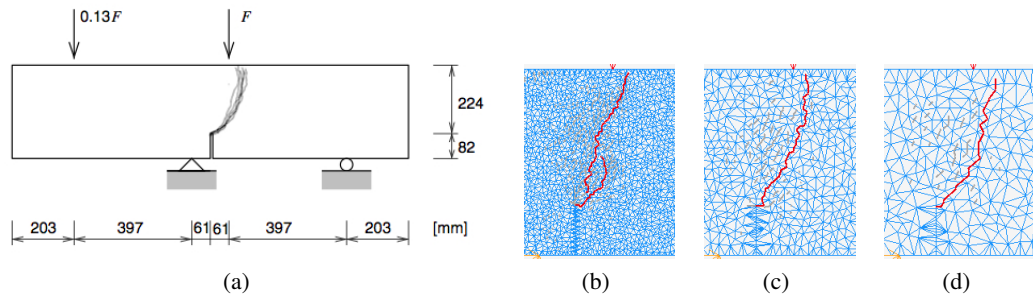


Figure 1: Influence of mesh size on the crack trajectory in the SEN test: (a) Experimental setup and crack trajectories [1], (b) Fine Mesh, (c) Medium Mesh, (d) Coarse Mesh.

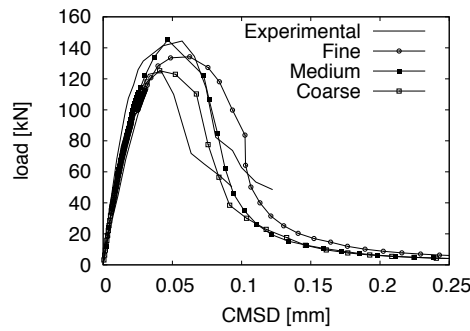


Figure 2: Load-CMSD curve.

3.2 DOUBLE-EDGE-NOTCHED SPECIMEN

The second simulation modelled the double-edge-notched (DEN) shear test performed by Noor-Mohamed [4]. The geometry and experimental setup can be seen in Fig. 3. The model parameters were chosen as the following: $E = 36.25$ GPa, $\gamma = 0.3333$, $\bar{f}_t = 1.95$ MPa and $G_F = 71.5$ J/m². The first two parameters correspond to the elastic material properties for the continuum specimen $E_c = 29$ GPa and $\nu = 0.2$. As with the previous analyses, three different mesh refinements were used to inspect the influence of mesh size on the crack patterns. This test requires two stages of loading. During the first stage, the specimen is loaded by an increasing shear force, P_s , until a value of 10kN is reached. For the second stage, this shear force is kept constant and the specimen is stretched under displacement control in the vertical direction which generates a reaction force P . The crack trajectories obtained during the analyses are seen in Fig. 4 and a comparison between the load-displacement curve for each mesh and the experimental results is shown in Fig. 3.

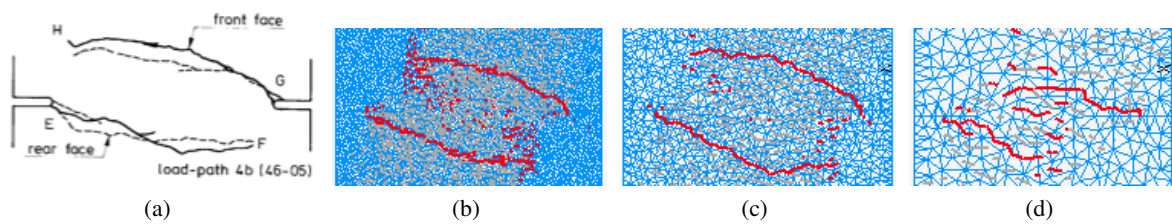


Figure 4: Influence of mesh size on the crack trajectory in the DEN test: (a) Experimental crack pattern, (b) Fine Mesh, (c) Medium Mesh, (d) Coarse Mesh.

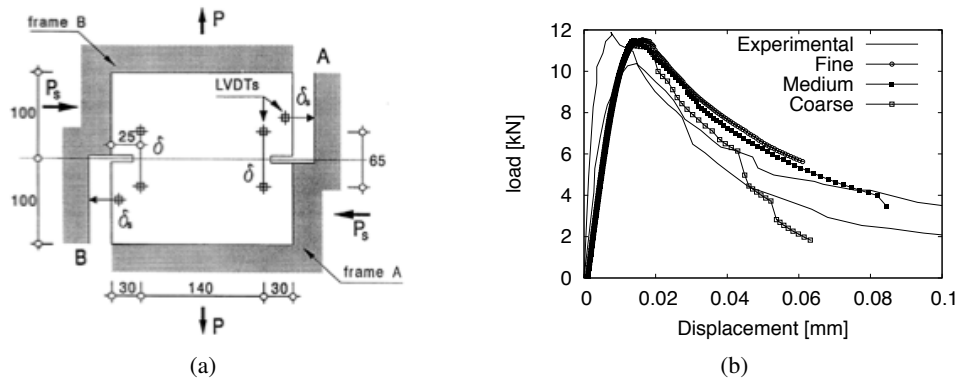


Figure 3: The DEN specimen (a) geometry and loading [4], (b) Load-Displacement Curves.

4 DISCUSSION OF RESULTS

The lattice model outlined in this work was used to successfully reproduce fracture patterns on two concrete specimens. A reduction in the tensile strength and the fracture energy of the lattice elements allowed for the load-displacement curves to be obtained in agreement with experimental tests while calculating accurate crack trajectories of fracture patterns. It has been observed that the size of the mesh can influence the trajectory of the crack pattern. The coarse mesh for the DEN specimen in particular was poor at modelling the crack pattern, both in the extent and direction of crack, and was not able to model continuity of the crack. However, load-displacement curves are mesh independent.

References

- [1] M Arrea and AR Ingraffea. Mixed-mode crack propagation in mortar and concrete. Department of Structural Engineering, Cornell University, 1982.
- [2] J Bolander and S Saito. Fracture analyses using spring networks with random geometry. *Engineering Fracture Mechanics*, 61(5-6):569–591, November 1998.
- [3] P Grassl and M Jirásek. Meso-scale approach to modelling the fracture process zone of concrete subjected to uniaxial tension. *International Journal of Solids and Structures*, 47(7-8):957–968, April 2010.
- [4] M Nooru-Mohamed. *Mixed-mode fracture of concrete: an experimental approach*. PhD thesis, Delft University of Technology, 1992.

Reduced order modeling for nonlinear fracture mechanics in a domain decomposition framework

*Olivier Goury¹, Pierre Kerfriden¹, Lee Margetts² and Stéphane P. A. Bordas¹

¹ University of Cardiff, Queen's Buildings, The Parade, Cardiff, CF24 3AA

² University of Manchester, Devonshire House, Oxford Road, Manchester, M13 9PL

*gouryOM@cardiff.ac.uk

Key Words: *Model Order Reduction; Domain Decomposition Method; Balancing Domain Decomposition; Hyper-Reduction; Proper Orthogonal Decomposition*

ABSTRACT

This paper proposes to merge domain decomposition methods with model order reduction methods for the first time in the context of fracture mechanics. On one side, domain decomposition methods are a well-known way to divide a large mechanical problem into several smaller pieces easier to solve. It is very suitable to parallel computing since those subproblems can be solved independently using a coarse global problem to link the solutions together. On the other side, model order reduction methods are used to reduce the size of a problem using usually projections of the space of unknowns onto spaces of much smaller dimensions. This enables to solve problems faster while keeping accuracy. This is a critical point in the field of virtual surgery or rapid virtual prototyping. In this paper, we propose to use the balancing domain decomposition method coupled with the proper orthogonal decomposition method. To save time for assembling the stiffness matrix, the hyper-reduction method will be used.

1 INTRODUCTION

When solving large non-linear mechanical problems, the discretisation using finite element method leads to the resolution of linear systems of the type $Ku = f$, where K is the stiffness matrix, u the displacement and f some force applied on the domain studied. The size of the mesh used is limited by the computational power available. Domain decomposition techniques are one way to take advantage of parallel computers, since the basic idea is to subdivide the main domain into a number of subdomains, typically as many as the number of processors available. Description and use of those methods are given in [1], [2], [3], [4]. The problem is reformulated so that we end up with a global coarse problem usually solved in parallel using a Krylov-subspace method along with smaller easier systems to solve on each subdomain. One way to make it even more efficient will be to reduce the local problems using model order reduction (MOR). This will allow us to solve even larger problems. MOR is used for example in [5], [6], [7], [8].

In this paper we formulate the strategy using the balancing domain decomposition (BDD) technique coupled with the proper orthogonal decomposition (POD). An issue arising from using the POD is

the fact that despite the time we gain by solving smaller problems, the stiffness matrix is still fully assembled and this operation takes most of the runtime. This issue can be tackled by using a technique of hyper-reduction which consists of assembling only selected parts of the stiffness matrix which speeds up significantly the algorithm.

2 BALANCING DOMAIN DECOMPOSITION

In the BDD method, first described in [9], the main domain is divided into several subdomains. The continuity between the subdomains is guaranteed by forcing the degrees of freedom to be equal on the interfaces. The problem is formulated and discretised on each subdomain (E) in the form $K^{(E)}u^{(E)} = f^{(E)}$. For clarity we will skip the superscript (E) in the following. By separating the internal degrees of freedom from the interface degrees of freedom, the systems can be rewritten in the form:

$$\begin{bmatrix} K_{ii} & K_{ib} \\ K_{bi} & K_{bb} \end{bmatrix} \begin{bmatrix} u_i \\ u_b \end{bmatrix} = \begin{bmatrix} f_i \\ f_b \end{bmatrix} \quad (1)$$

In the usual BDD method the internal degrees of freedom are condensed on the interface with intervention of the Schur complement. This leads to the system:

$$S_p u_b = F_c \quad \text{with} \quad S_p = K_{bb} - K_{bi} K_{ii}^{-1} K_{ib} \quad \text{and} \quad F_c = F_b - K_{bi} K_{ii}^{-1} F_i \quad (2)$$

The Schur complement system (also called interface problem or coarse problem) can be solved in parallel iteratively using a Krylov-subspace method such as the conjugate gradient or GMRes (or BiCGSTAB) in a non-symmetric case.

The u_i are then found on each subdomain using the equation: $u_i = K_{ii}^{-1}(F_i - K_{ib}u_b)$. The matrices K_{ii} are relatively small and those problems are solved using direct methods.

3 INTRODUCTION OF PROPER ORTHOGONAL DECOMPOSITION INTO THE BDD FORMULATION

The proper orthogonal decomposition is a model order reduction method. The idea is to first create a set of simple solutions as representative as possible called the snapshot. With the use of the singular value decomposition (SVD), an orthonormalised space of much smaller dimension is selected. It is on that space that we will then look for the solution of our problem. A key point is how the snapshot is created. One way to do that is for example to take solutions from previous time steps, orthonormalise them and take that basis as the projection space. Some other strategies include solving a family of simple problems related to the problem to be solved, orthonormalise the solutions and select only a few modes through use of the SVD.

We are here trying to reduce the internal degrees of freedom so instead of looking for $u = \begin{bmatrix} u_i \\ u_b \end{bmatrix}$, we will be looking for $u = \begin{bmatrix} C_i \alpha \\ u_b \end{bmatrix}$.

We are not reducing the degrees of freedom present on the interface, but only the internal ones. C is the basis of the projection space. α is a dimensionless vector of small size.

On each subdomain, we then have to solve:

$$\begin{bmatrix} K_{ii} & K_{ib} \\ K_{bi} & K_{bb} \end{bmatrix} \begin{bmatrix} C_i \alpha \\ u_b \end{bmatrix} = \begin{bmatrix} K_{ii} C_i & K_{ib} \\ K_{bi} C_i & K_{bb} \end{bmatrix} \begin{bmatrix} \alpha \\ u_b \end{bmatrix} = \begin{bmatrix} f_i \\ f_b \end{bmatrix} \quad (3)$$

This system is overdetermined since we still have the same number of equations but we reduced the number of unknowns. We will take care of that using a Galerkin method which consists of saying that the residual should be orthogonal to the solution space: $\forall u^* = \begin{bmatrix} C_i \alpha^* \\ u_b^* \end{bmatrix}, \begin{bmatrix} C_i \alpha^* \\ u_b^* \end{bmatrix}^T (K \begin{bmatrix} C_i \alpha \\ u_b \end{bmatrix} - F_c) = 0$

This is equivalent to:

$$K_{red} \begin{bmatrix} \alpha \\ u_b \end{bmatrix} - F_c = 0, \quad \text{with} \quad K_{red} = \begin{bmatrix} C_i^T K_{ii} C_i & C_i^T K_{ib} \\ K_{bi} C_i & K_{bb} \end{bmatrix} \quad (4)$$

which is now a well-defined system of much smaller dimension than the original one in equation (1).

4 ASSEMBLING THE STIFFNESS MATRIX USING HYPER-REDUCTION

A significant amount of the runtime is spent in assembling the stiffness matrix. The fact we reduced the local problems, and hence made the resolution faster is wasted by spending much more time assembling the stiffness matrix. This feels particularly wrong since, even though we calculate the full stiffness matrix exactly, we reduce it then significantly using the POD. A way to handle that is called hyper-reduction. It was first described in [10], and developed in [11]. The basic idea is to select only a little number of equations so that only a little part of the stiffness matrix need to be assembled, reducing significantly the execution time. Consider E a boolean operator that selects n_h equations out of the n_i ones corresponding to the internal degrees of freedom. The POD reduced equations then become:

$$\begin{bmatrix} E^T & 0 \\ 0 & Id \end{bmatrix} (K \begin{bmatrix} C_i \alpha \\ u_b \end{bmatrix} - f) = 0 \quad (5)$$

As before we use the Galerkin orthogonality condition to guarantee that the system we have is squared. The space we want the residual to be orthogonal to is not the full space spanned by the reduced basis C anymore, but the hyperreduced space of smaller dimension of it: $C^T E$. We then obtain the following system:

$$\begin{bmatrix} C^T & 0 \\ 0 & Id \end{bmatrix} \begin{bmatrix} E & 0 \\ 0 & Id \end{bmatrix} \begin{bmatrix} E^T & 0 \\ 0 & Id \end{bmatrix} (K \begin{bmatrix} C_i \alpha \\ u_b \end{bmatrix} - f) = 0$$

which is equivalent to:

$$\begin{bmatrix} C_i^T E E^T K_{ii} C_i & C_i^T E E^T K_{ib} \\ K_{bi} C_i & K_{bb} \end{bmatrix} \begin{bmatrix} \alpha \\ u_b \end{bmatrix} = \begin{bmatrix} C_i^T E E^T F_i \\ F_b \end{bmatrix} \quad (6)$$

In practice the operator E is not computed. The effect of matrix $E E^T$ on K_{ii} is to replace some of its lines by zeros. The matrix $E E^T K_{ii}$ is assembled instead of K_{ii} . This is a much faster operation since many lines are zeros.

The choice we make for the selected equations can have a dramatical influence on the results. Choosing well the equations means choosing the ones having the largest influence on the residual. This is a hard task since we have to select those equations a priori. One simple strategy is to consider the values of $K C_i$ and F at the beginning of the algorithm and keep the components having the highest absolute value. Those are ones the most likely to have the largest influence on the residual.

When used with right parameters, we have expectations for this BDD-POD using hyper-reduction strategy to speed up significantly the resolution of non-linear mechanical problems.

Acknowledgements

The authors thank the financial support of EPSRC High End Computing Studentship for Mr. Olivier Goury as well as the support of Cardiff and Glasgow Universitys Schools of Engineering. Pierre Kerfriden and Stéphane Bordas would like to also acknowledge the financial support of the Royal Academy of Engineering and of the Leverhulme Trust for S. Bordas' Senior Research Fellowship entitled Towards the next generation surgical simulators which funded P. Kerfriden's post in 2009-2010 and allowed him to lay the foundations for the work presented in this paper.

References

- [1] Gosselet, P., Rey, C. Non-overlapping domain decomposition methods in structural mechanics. *Archives of Computational Methods in Engineering* Vol 13. Num 4. Pages 515-572. 2006
- [2] Farhat C., Roux F.-X., Implicit Parallel Processing in Structural Mechanics, *Comp. Mech. Adv.*, II(1): 1-124, 1994
- [3] P. Kerfriden, O. Allix, and P. Gosselet. A three-scale domain decomposition method for the 3D analysis of debonding in laminates, *Computational Mechanics*, 44(3) :343-362, 2009
- [4] Lloberas Valls O., Rixen D.J., Simone A., Sluys L.J., A Domain Decomposition Approach To Multiscale Analysis For Structure With Softening Materials, *proc. 7th Euromech Solid Mech. Conf.*, 2009
- [5] L. Sirovich. Turbulence and the dynamics of coherent structures. part I : coherent structures, *Quarterly of Applied Mathematics*, 45 :561-571, 1987
- [6] Barrault M., Maday Y., Nguyen N.C., Patera A.T., An empirical interpolation method: application to efficient reduced-basis discretization of partial differential equations. *Compt. Rend. Math.*, 339: 667-672, 2004.
- [7] Carlberg, K., Bou-Mosleh, C. and Farhat, C. , Efficient non-linear model reduction via a least-squares Petrov-Galerkin projection and compressive tensor approximations. *Int. J. for Num. Meth. in Eng.*, 2010
- [8] F. Chinesta, A. Ammar, and E. Cueto. Proper generalized decomposition of multiscale models, *International Journal for Numerical Methods in Engineering*, 83(8-9) :1114-1132, 2010
- [9] J. Mandel Balancing domain decomposition *Communications in Numerical Methods in Engineering*, 9, 233–241, 1993.
- [10] D. Ryckelynck A priori hyperreduction method: An adaptive approach. *Journal of Computational Physics*, Vol.202, 346–366, 2005.
- [11] D.Ryckelynck, F.Chinesta, E.Cueto, and A.Ammar. On the a priori model reduction: overview and recent developments, *Archives of Computational Methods in Engineering, State of the Art Reviews*, 13(1) :91-128, 2006.

A SCALED BOUNDARY FINITE ELEMENT METHOD FOR NONLINEAR DYNAMIC CRACK PROPAGATION MODELLING

E.T. Ooi ¹and *Z.J. Yang

¹School of Engineering, the University of Liverpool, L69 3GQ

*zjyang@liv.ac.uk

Key Words: *scaled boundary finite element method, dynamic fracture mechanics, cohesive crack model, fast crack propagation, remeshing, quasi-brittle materials*

ABSTRACT

This study develops a scaled boundary finite element method (SBFEM) for modelling fast cohesive crack propagation in quasi-brittle materials subjected to transient dynamic loadings. In this method, the elastic bulk material is modelled by SBFEM subdomains and the cracks by nonlinear cohesive interface finite elements that are automatically inserted by a remeshing procedure. The global equation system is solved using an implicit time integration algorithm. Because all the solutions (displacements, stresses, velocities, accelerations) are semi-analytical in a subdomain, this method offers a few advantages over other methods, such as accurate calculation of stress intensity factors without using fine crack-tip meshes, simpler remeshing, more accurate yet efficient mesh mapping, and the need of much fewer degrees of freedom for the same accuracy. A concrete beam under mode-I fracture was modelled to validate the method.

1 INTRODUCTION

The scaled boundary finite element method (SBFEM), developed in 1990s [1], is a semi-analytical method combining the advantages of the finite element method (FEM) and the Boundary element method (BEM). It discretises subdomain boundaries only but no fundamental solutions and singular integrations are needed. Therefore, the FEM's wide applicability and the BEM's simplicity in remeshing are both retained. Another significant advantage is that stress singularities at cracks or corners are analytically represented by the stress solutions so that accurate stress intensity factors (SIFs) can be calculated directly by definition. As such, fine crack-tip meshes or singular elements as required by the FEM are not needed. In addition, discretising domains in the SBFEM can be much more flexible than in the FEM. These advantages of the SBFEM were recently exploited by the authors to develop models for linear and nonlinear fracture with single and multiple cracks subjected to quasi-static loadings [2-4]. These studies demonstrate that: (i) remeshing is very simple and only leads to slight increases in degrees of freedom (DOFs); (ii) the semi-analytical nature of SBFEM makes mesh mapping extremely simple but very accurate, which contributes greatly to numerical stability and convergence in solving highly nonlinear equation systems; and (iii) it also allows a structure to be modelled by much fewer DOFs than the FEM. These features appear to just overcome the challenges faced by FEM for modelling fracture problems.

We recently developed a linear elastic fracture mechanics (LEFM)-based SBFEM procedure for dynamic fracture modelling with excellent results [5]. This study further extends the developed procedure to model nonlinear dynamic fracture problems by incorporating cohesive interface elements to model the fracture process zone which is characteristic to quasi-brittle materials.

1 METHODOLOGY

1.1 The scaled boundary finite element method

A domain of analysis is illustrated in Figure 1(a) as an example. The domain is divided into 3 subdomains. Figure 1(b) shows the details of Subdomain 1. The subdomain is represented by scaling a defining curve S relative to a scaling centre. A normalized radial coordinate ζ is defined, varying from zero at the scaling centre and unit value on S . A circumferential coordinate η is defined around the defining curve S . A curve similar to S defined by $\zeta=0.5$ is shown in Figure 1b. The coordinates ζ and η form a local coordinate system used in all the subdomains and simple coordination transformation equations exist for each subdomain.

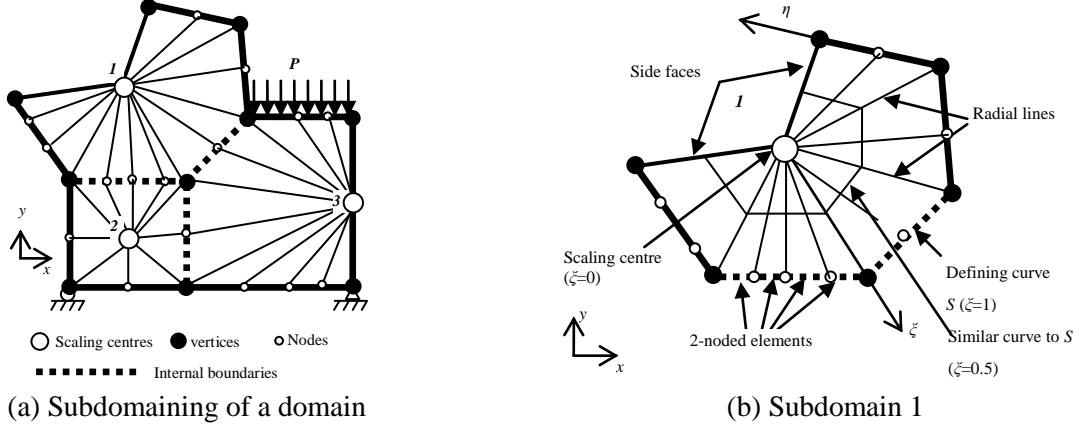


Fig. 1 The concept of the scaled boundary finite element method

The displacements of any point (ζ, η) in a subdomain are assumed as

$$\mathbf{u}(\zeta, \eta) = \mathbf{N}(\eta)\mathbf{u}(\zeta) \quad (1)$$

where $\mathbf{u}(\zeta)$ are the displacements along the radial lines and are *analytical* with respect to ζ . $\mathbf{N}(\eta)$ is the shape function matrix in the circumferential direction.

1.2 Time integration

In elastodynamics, the dynamic equilibrium equation of a domain without damping is derived as [5]

$$\mathbf{M}\ddot{\mathbf{U}} + \mathbf{K}\mathbf{U} = \mathbf{P} \quad (2)$$

where \mathbf{M} and \mathbf{K} are the global mass and stiffness matrices by assembling contributions of all subdomains, \mathbf{P} the global load vector, \mathbf{U} and $\ddot{\mathbf{U}}$ the nodal displacement and acceleration vectors, respectively. For nonlinear fracture problems, \mathbf{K} includes stiffness matrices of cohesive interface elements and depends on \mathbf{U} , i.e., $\mathbf{K} = \mathbf{K}(\mathbf{U})$. The time integration algorithm of Hughes [6] based on the average acceleration method is used to solve Eq. 2 in this study. At time step $n+1$

$$\mathbf{U}_{n+1} = \Delta t(\dot{\mathbf{U}}_{n+1} + \dot{\mathbf{U}}_n)/2 + \mathbf{U}_n, \quad \dot{\mathbf{U}}_{n+1} = \Delta t(\ddot{\mathbf{U}}_{n+1} + \ddot{\mathbf{U}}_n)/2 + \dot{\mathbf{U}}_n \quad (3)$$

Substituting Eq. 3 into Eq. 2 leads to

$$\mathbf{B}\mathbf{U}_{n+1} + \mathbf{F}(\mathbf{U}_{n+1}) = \mathbf{P}_{n+1} + \mathbf{G}_{n+1} \quad (4)$$

where $\mathbf{F}(\mathbf{U}_{n+1}) = \mathbf{K}(\mathbf{U}_{n+1})\mathbf{U}_{n+1}$ is the internal force vector and

$$\mathbf{B} = 4\mathbf{M}/\Delta t^2, \quad \mathbf{G}_{n+1} = \mathbf{B}\mathbf{U}_n + 4\mathbf{M}\dot{\mathbf{U}}_n/\Delta t + \mathbf{M}\ddot{\mathbf{U}}_n \quad (5)$$

Eq. 4 can be solved using the Newton-Raphson iterative method. In the iteration $(i+1)$

$$\mathbf{U}_{n+1}^{(i+1)} = \mathbf{U}_{n+1}^{(i)} + \Delta\mathbf{U}_{n+1}^{(i)} \quad (6)$$

where $\Delta\mathbf{U}_{n+1}^{(i)}$ satisfies the linear equation

$$[\mathbf{B} + \mathbf{K}_T(\mathbf{U}_{n+1}^{(i)})]\Delta\mathbf{U}_{n+1}^{(i)} = \mathbf{P}_{n+1} + \mathbf{G}_{n+1} - \mathbf{B}\mathbf{U}_{n+1}^{(i)} - \mathbf{F}(\mathbf{U}_{n+1}^{(i)}) \quad (7)$$

where $\mathbf{K}_T = \partial\mathbf{F}/\partial\mathbf{U}$ is the tangential stiffness matrix. Eq. 7 is repeatedly solved until the convergence criterion is satisfied

$$\|\Delta \mathbf{U}_{n+1}^{(i+1)}\| \leq \varepsilon \|\mathbf{U}_{n+1}^{(i+1)} - \mathbf{U}_n\| \quad (8)$$

where ε is the error tolerance and a small number.

Calculating \mathbf{K}_T in every iteration in Eq. 7 may be computationally costly. The initial stiffness matrix at the beginning of the time step is used instead in all the iterations (the modified Newton-Raphson method).

After \mathbf{U}_{n+1} is calculated from Eq. 4, the fields of displacement, velocity and acceleration in a subdomain are calculated by

$$\mathbf{u}(\xi, \eta) = \mathbf{N}(\eta) \sum_{i=1}^N c_i \xi^{\lambda_i} \boldsymbol{\varphi}_i, \quad \dot{\mathbf{u}}(\xi, \eta) = \mathbf{N}(\eta) \sum_{i=1}^N \dot{c}_i \xi^{\lambda_i} \boldsymbol{\varphi}_i, \quad \ddot{\mathbf{u}}(\xi, \eta) = \mathbf{N}(\eta) \sum_{i=1}^N \ddot{c}_i \xi^{\lambda_i} \boldsymbol{\varphi}_i \quad (9)$$

where N is the number of degrees of freedom of the subdomain, λ_i and $\boldsymbol{\varphi}_i$ are eigen values and vectors of an eigen problem for the subdomain, and c_i , \dot{c}_i and \ddot{c}_i are constants determined by nodal displacements, velocities and accelerations of the subdomain boundary, which are subsets of \mathbf{U} , $\dot{\mathbf{U}}$ and $\ddot{\mathbf{U}}$, respectively. The stresses in the subdomain are calculated by

$$\boldsymbol{\sigma}(\xi, s) = \mathbf{DB}^1(s) \left[\sum_{i=1}^N c_i \lambda_i \xi^{\lambda_i-1} \boldsymbol{\varphi}_i \right] + \mathbf{DB}^2(s) \left[\sum_{i=1}^N c_i \xi^{\lambda_i-1} \boldsymbol{\varphi}_i \right] \quad (10)$$

It is clear that all the state variables in Eqs 9-10 are analytical in the radial direction ξ . The stress intensity factors can be calculated from Eq. 10 by definition [5].

2 NUMERICAL EXAMPLE

A three-point-bending concrete beam with material properties and dimensions shown in Fig. 2 was modelled. The measured experiment load history for strain rate $1.48s^{-1}$ [7] was used in the analysis, with time step $\Delta t=0.010ms$ and crack propagation length $\Delta a=2.7mm$. As in [7-8], a dynamic tensile strength $13.10MPa$ was used for crack initiation with a dynamic traction-separation softening curve shown in Fig. 3 for cohesive elements to model crack propagation.

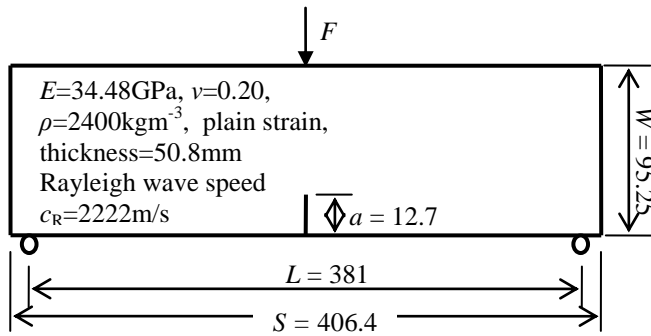


Fig. 2 A concrete beam under three point bending

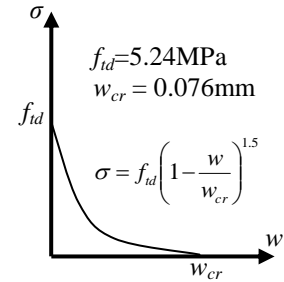
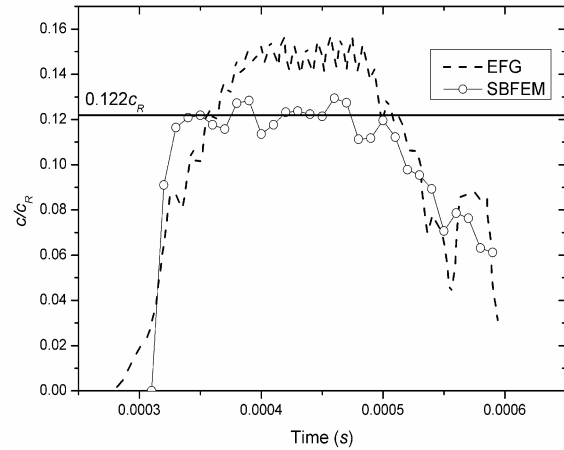
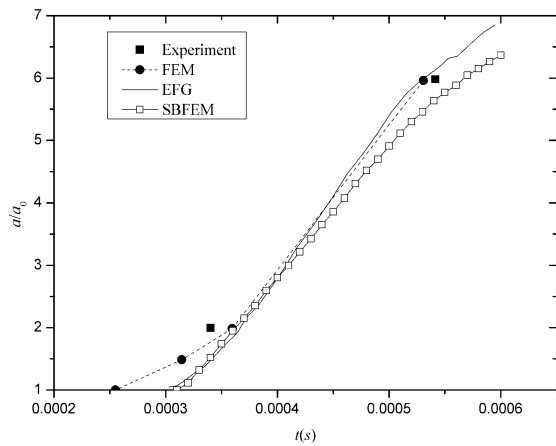
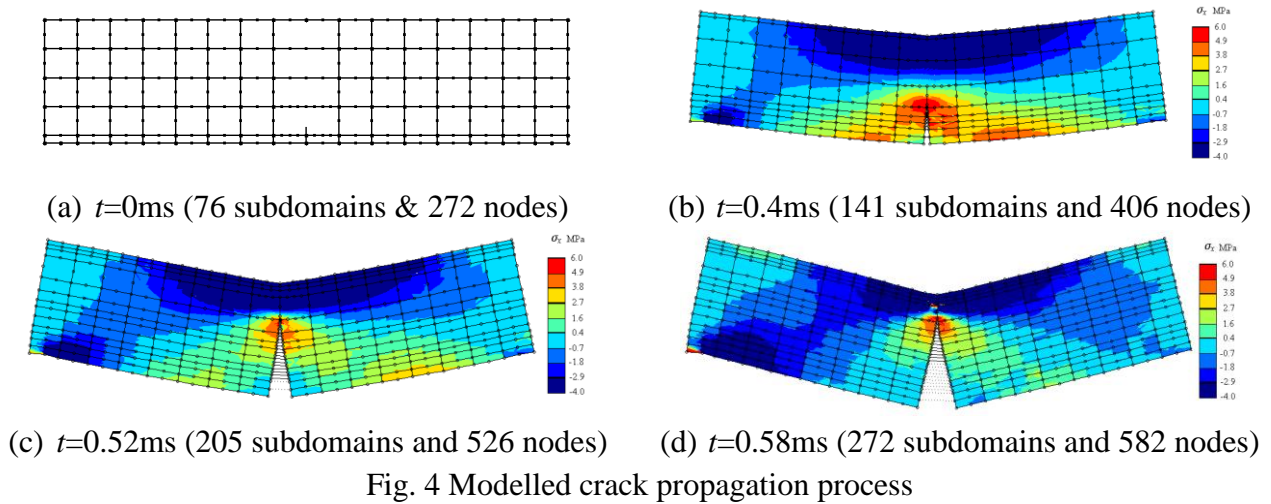


Fig. 3 Dynamic softening curve for cohesive elements

Fig. 4 shows the initial mesh and deformed meshes at three time instances. The number of subdomains and nodes in the final mesh increases to 221 and 562 from 76 and 272 in the initial mesh, respectively. It may be noted that 3999 nodes and 3840 integration cells were used to model the same problem by Belytschko et al. [8] using an Element-free Galerkin (EFG) method. Fig. 5 compares the predicted crack length history with experimental data and FEM results in [7] and EFG results in [8]. The present method predicted that the crack started to propagate at $t=0.3ms$, compared with $0.260ms$ in the experiment [7] and $0.278ms$ in [8], respectively. The predicted crack velocity history is shown in Fig. 6. The present method predicted a velocity plateau at $0.124c_R$, which is closer to the experimental value $0.122c_R$ [7] than $0.15c_R$ as predicted by EFG [8].



Acknowledgement

This project is funded by EPSRC UK (Project No: EP/F00656X/1).

References

- [1] Wolf JP and Song CM. *Finite-element modelling of unbounded media*. Chichester, John Wiley and Sons, 1996.
- [2] Yang ZJ (2006). Fully automatic modelling of mixed-mode crack propagation using scaled boundary finite element method. *Engineering Fracture Mechanics* 73(12):1711-1731.
- [3] Yang ZJ and Deeks AJ. (2007). Fully-automatic modelling of cohesive crack growth using a finite element-scaled boundary finite element coupled method. *Engineering Fracture Mechanics* 74(16): 2547-2573.
- [4] Ooi ET and Yang ZJ (2009). Multiple cohesive crack propagation using a finite element-scaled boundary finite element coupled method. *Engineering Analysis with Boundary Elements* 33(7): 915-929.
- [5] Ooi ET and Yang ZJ (2011). Modelling dynamic crack propagation using the scaled boundary finite element method. *International Journal of Numerical Methods in Engineering*, in press (DOI:10.1002/nme.3177).
- [6] Hughes TJR (1976) Stability, convergence and growth and decay of energy of the average acceleration method in nonlinear structural dynamics. *Computer & Structures* 6: 313-324.
- [7] Du J, Yon JH, Hawkins NM, Arakawa K and Kobayashi AS (1992). Fracture process zone for concrete for dynamic loading. *ACI Materials Journal* 89: 252-258.
- [8] Belytschko T, Organ D and Gerlach C (2000). Element-free Galerkin methods for dynamic fracture in concrete. *Computer Methods and Applied Mechanics in Engineering* 187: 385-399.

A DAMAGE-MECHANICS-BASED RATE-DEPENDENT COHESIVE-ZONE MODEL

*M. Musto¹, G. Alfano¹

¹School of Engineering and Design, Brunel University, Kingston Lane, UB8 3PH, Uxbridge

*marco.musto@brunel.ac.uk

Key Words: *interface elements; viscoelasticity; thermodynamics; damage mechanics*

ABSTRACT

An effective and general approach to the derivation of cohesive-zone models for the analysis of crack initiation and growth in rate-dependent materials is described in this paper. The constitutive law of the interface material is enriched adding internal variables in the framework of thermodynamics of irreversible processes. Both the internal variables and their evolution laws are chosen considering the physics of crack formation, which is specifically exploited in this work for rubber-like materials. Some results of the interface response for a prescribed relative-displacement history are presented.

1 INTRODUCTION

Laminated materials are widely used in engineering practice. Their characteristic structure poses novel problems to the analyst, as they introduce some additional failure modes, when compared to homogeneous materials. Numerous investigations have focused on delamination, which represents a characteristic local failure mode, potentially leading to structural collapse, and many techniques have been developed to model the problem, a summary being provided in [1].

In this paper attention is devoted to the ‘cohesive zone model’ in which a traction - separation law is introduced which also provides, in the case of infinitesimal elastic deformations, the link to Linear Elastic Fracture Mechanics as its integral equals the critical energy release rate.

The rate dependence of the mechanical response leading to crack initiation and / or growth can not be neglected for a wide class of engineering applications. The complexity of the problem and the presence of numerous competing factors are evident from the fact the fracture toughness may not show a monotonic trend with respect to crack speed, even when the latter is small enough not to consider inertial effects [2-4]. Furthermore, even when such trend is monotonic, the fracture toughness can increase with crack speed for some materials and decrease for others [2-4]. It has been also suggested that "stick - slip" behaviour can depend from the rate dependence of the fracture mechanism in the process zone [5].

The overall rate dependence can arise as a consequence of the rate dependence of the interface in itself, of the bulk material, or of both. A number of cohesive zone models and modelling strategies have been presented covering these different assumptions and are reviewed in Ref. [6]. They are quite successful in capturing many of the aspects of the rate-dependent nature of the interface damage and debonding. On the other hand, it is the authors’ opinion that more work can be done to develop a general, physically well based cohesive element, without resorting to any phenomenological law other than basic physical and engineering understanding. Such an attempt is made in [6] and in this paper we summarise the main ideas and provide some of the results which demonstrate the effectiveness of the proposed approach.

Our aim is to capture the rate dependence within the process zone of the interface in itself regardless of the behaviour of the surrounding material. First, we postulate the existence of an intrinsic fracture energy of the material, which is not rate-dependent. This is related to an elastic energy threshold needed to break bonds at the micro or possibly, the atomistic scale. By using a general meso-mechanical approach to the development of cohesive-zone models which has been proposed in [7], the overall rate-dependence of the energy dissipation on the interface is simply the result of the rate dependence of the deformation on any infinitesimal parts of the interface where cohesion has not yet been lost. For the purposes of validating the concept, we will then restrict ourselves to linear visco-elasticity, but the overall formulation is presented for the most general case to underline its general validity. Also, the treatment is restricted to a pure mode-

I problem.

2 COHESIVE ZONE FORMULATION

In the proposed mesomechanical approach the finite thickness process zone is replaced with a zero-thickness interface over which a scalar field of the internal variable damage is defined. To this end, a ‘representative infinitesimal area’ (RIA) dA of the interface is subdivided into an undamaged part dA_u and a damaged part dA_d . The damaged parameter is defined as $D = dA_d/dA$ and ranges from 0, for the undamaged points of the interface, to 1 for the fully damaged points (Figure 1.b). This decomposition is done on an infinitesimal area and does not correspond to a decomposition of the process zone into two different sub-zones.

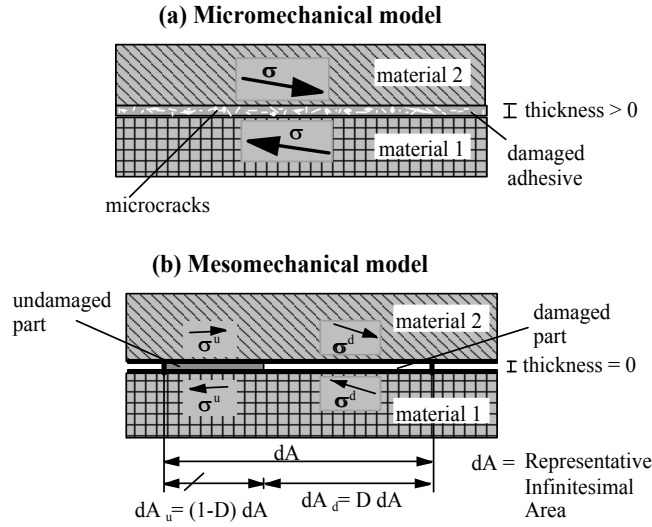


Figure 1: (a) micromechanical and (b) mesomechanical modelling..

In this description any constitutive law can be used for the undamaged part of the interface. In addition, the formulation can be enriched with a further internal variable describing damage. In this way, following the classic definition of damage due to Kachanov, a general expression of the cohesive zone free energy ψ can be introduced as follows:

$$\psi = \mathbf{d} \cdot \tilde{\Psi}(\delta_i, \delta_j) \quad (1)$$

where $\tilde{\Psi}$ represents a vector of free energies for the undamaged material, δ_i and δ_j represent observable and internal variables respectively and \mathbf{d} is a vector of internal variables associated with the evolution of damage. The choice of the number and type of the internal variables is arbitrary and depends of course on the phenomenon being addressed.

The great flexibility and power of the procedure lies in that these variables can be chosen *ad hoc* to represent a vast range of physical phenomena occurring within the material.

For the purposes of this work attention is devoted to rubber-like materials, and linear viscoelasticity has been chosen as a sufficiently accurate framework to model the process zone in first approximation.

It has to be stressed that the presented formulation can be very simply enriched using more complex material constitutive laws for the undamaged portion of the interface. Bearing this in mind we deemed though appropriate, for the purposes of the proof of concept, to initially present results obtained resorting to the simplest available time-dependent law. On this instance we focused on a thin rubber interface.

The Standard Linear Model (see Figure 2) is chosen to describe the undamaged part of the interface. An internal variable δ_e is introduced, which represents the elastic part of the displacement on the Maxwell arm of the model. Hence, in our case and referring to Figure 2, the free energy can be written as follows:

$$\tilde{\Psi} = \begin{bmatrix} \tilde{\psi}_1(\delta) \\ \tilde{\psi}_2(\delta_e) \end{bmatrix} \quad (2)$$

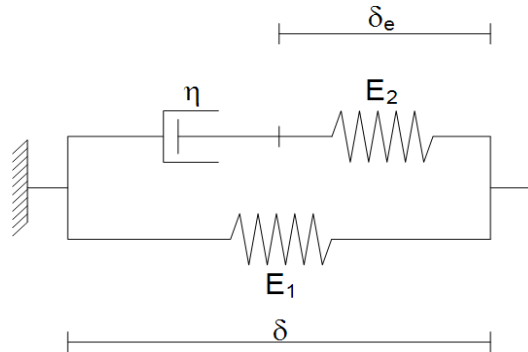


Figure 2: Rheological model

where δ is the total relative displacement on the interface and $\tilde{\psi}_1$ and $\tilde{\psi}_2$ represent the free energies in the elastic arm and in the Maxwell arm, respectively. The damage variables are collected in the vector $\mathbf{d} = [1 - D_1 \quad 1 - D_2]^T$. For more details on the physical meaning of the damage parameters D_1 and D_2 , as well as further insight into their micro-structural justification the reader is referred to Ref. [6]. In this context we limit ourselves to observe that D_1 and D_2 represent the damage parameters in the elastic and in the Maxwell arm, respectively, and that the former can be regarded as representative of the load-bearing chains in the rubber while the latter simulates the behaviour of the entangled chains.

To close the problem evolution laws for the damage internal variables are needed. As far as D_1 is concerned, due to its physical nature we postulate that its evolution is related to the stored energy in the elastic arm. In particular, we chose an evolution law presented in [1], according to which a damage threshold for the free energy is introduced, dependent on D_1 . Furthermore, as a result of the above interpretation we deem it acceptable to assume in first approximation that $D_2 = D_1$.

3 NUMERICAL EXAMPLES

The cohesive-zone model briefly described in Section 2 has been implemented as constitutive law for 6-noded interface elements for its use within general non-linear finite-element analyses. We refer to Ref [6] for a validation of the proposed procedure against experimental tests for a double-cantilever specimen made of steel arms sandwiching a thick rubber layer to which they are bonded with a strong adhesive. Here we report the results of a single-element test in which the relative-displacement history has been prescribed to linearly increase from $t = 0$ to $t = 1$ and different relaxation times λ have been considered. Furthermore, the intrinsic fracture energy associated with the elastic arm is $G_c = 10 \text{ N mm}^{-1}$, the initial stiffness of the elastic and the Maxwell arms are 6 and 4 N mm^{-3} and the first-cracking relative displacement for the elastic arm is 0.75 mm.

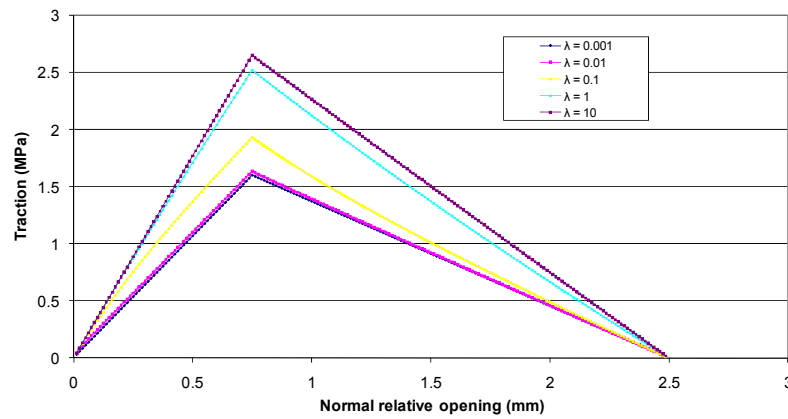


Figure 3: Traction vs. Displacement for different relaxation times.

4 CONCLUSIONS AND FURTHER WORK

In this paper a general framework for the development of rate-dependent interface models has been presented which is based on a strict mesomechanical interpretation of the interface constitutive law and a thermodynamically based damage-mechanics formulation. The detailed micro-structural behaviour is accounted for through *a priori* homogenisation and in this first developments of the formulation, with a view to better presenting the proof of concept, the model has deliberately been kept simple by considering linear stiffness and viscosity and one single Maxwell arm. On the other hand, the generality of the formulation allows one to enrich the expressions of the free energies and the definition of evolution for the damage parameters as much as needed to increase the accuracy of the prediction and to account for the complexity of the material response, which together with the extension to mixed-mode analysis will be the subject of future work.

References

- [1] G. Alfano and M. A. Crisfield. Finite element interface models for the delamination analysis of laminated composites: mechanical and computational issues. *International Journal for Numerical Methods in Engineering*, 50(7):1701-1736, 2001.
- [2] R. Frassine, M. Rink and A. Pavan. Viscoelastic effects on the interlaminar fracture toughness of epoxy / carbon fibre. *International Journal of Composite Materials*, 27:921-933, 1993.
- [3] R. Frassine and A. Pavan. Viscoelastic effects on the interlaminar fracture behaviour of thermoplastic matrix composites: I. Rate and temperature dependence in unidirectional PEI / carbon-fibre laminates. *Journal of Composite Science Technology*, 54:193-200, 1995.
- [4] R. Frassine, M. Rink and A. Pavan. Viscoelastic effects on the interlaminar fracture behaviour of thermoplastic matrix composites: II. Rate and temperature dependence in unidirectional peek / carbon-fibre laminates. *Journal of Composite Science Technology*, 56:1253-1260, 1996
- [5] G.A. Maugin. *The thermomechanics of nonlinear irreversible behaviours*. World Scientific, Singapore, 1999.
- [6] M. Musto and G. Alfano. A thermodynamically based cohesive-zone model for the analysis of rate-dependent crack growth. To be submitted to *International Journal of Solids and Structures*.
- [7] D.H. Allen and C.R. Searcy. A micromechanical model for a viscoelastic cohesive zone. *International Journal of Fracture*, 107:159-176, 2001.
- [8] G. Alfano and E. Sacco. Combining interface damage and friction in a cohesive-zone model. *Int. J. Num. Meth. Eng.*, 2006, 68(5): 542-582.

MODELLING OF FRP-TO-CONCRETE BOND BEHAVIOUR

Y. Tao and J. F. Chen *

Institute for Infrastructure and Environment, School of Engineering, The University of Edinburgh, UK

*j.f.chen@ed.ac.uk

Key Words: FRP; concrete; debonding; finite element analysis; damage; plastic degradation

ABSTRACT

The bond behaviour between fibre reinforced polymer (FRP) composite and concrete plays a crucial role in structures strengthened with externally bonded FRP. This bond behaviour has been extensively investigated experimentally but much less research has been concerned with the numerical simulation chiefly due to difficulties in accurately modelling the complex behaviour of concrete. This paper proposes a robust finite element (FE) model for simulating the bond behaviour in the entire loading process in the pull-off test. A concrete damage plasticity model based on the plastic degradation theory is proposed. It is shown that the model produces results in very close agreement with test data

1 INTRODUCTION

Extensive research on the bond behaviour between fibre reinforced polymer (FRP) composite and concrete in the last two decades because it plays a crucial role in structures strengthened with externally bonded FRP. The bond behaviour is typically investigated experimentally using the pull-off test of FRP-to-concrete bonded joints (e.g. [1]). This paper is concerned with numerical modelling of the bond behaviour using the finite element (FE) method.

Typical failure in the pull-off test occurs in the concrete a short distance away from the adhesive-concrete interface. The bond behaviour is thus controlled by the behaviour of the concrete. Existing FE studies on the problem may be classified into three approaches all of which do not explicitly model the thin adhesive layer: a) direct model where the behaviour of concrete is accurately modelled in a meso-scale with an appropriate constitutive model; b) interface model where the bond behaviour is modelled using a layer of interface elements; and c) crack band model which assumes that debonding takes place within a band in the concrete adjacent to the concrete-FRP interface and a modified constitutive law for the concrete in this band.

The purpose of this study is to develop a general predictive model, using the aforementioned direct model, based on the concrete damage plasticity model available in FE software ABAQUS, incorporating a proposed plastic degradation model.

2 MODELLING OF CONCRETE

The smeared crack approach is adopted in this study as it is impossible to track multiple cracks, especially the numerous micro-cracks in the pull off test where failure occurs within a few millimetres in the concrete adjacent to the FRP. One of the drawbacks in the smeared concrete model is that it involves the strain localisation phenomenon due to strain-softening of concrete. This is overcome by adopting the crack band theory [2]:

$$w = h \int \varepsilon_{ct} \quad (1)$$

where w is crack opening width, h is the width of the crack band and ε_{ct} is the crack strain caused by the opening of micro-cracks. The crack band width h represents the effective width of the fracture process

zone over which micro-cracks are assumed to be uniformly distributed. In FE analysis, the cracking strain is assumed to be uniformly distributed over h which is in turn related to the element size, type and integration scheme.

The concrete is modelled using the isotropic plasticity model available in ABAQUS and an isotropic damage model. Under uniaxial compression, it is described by the following stress strain relationship proposed by Saenz [3]:

$$\sigma = \frac{E_0 \varepsilon}{1 + \left(\frac{E_0 \varepsilon_p}{\sigma_p} - 2 \right) \left(\frac{\varepsilon}{\varepsilon_p} \right) + \left(\frac{\varepsilon}{\varepsilon_p} \right)^2} \quad (2)$$

where σ and ε are respectively the compressive stress and strain, σ_p and ε_p are the experimentally determined maximum stress and its corresponding strain which are taken to be the cylinder strength f'_c (MPa) and 0.002 respectively. The elastic modulus of the concrete E_0 is estimated from $E_0 = 4730 \sqrt{f'_c}$ (MPa) following ACI318.

Under uni-axial tension, the problem involves tensile cracking. The fracture energy G_F is treated as a material property of the concrete. The stress-crack opening displacement relationship proposed by Hordijk [4] is adopted:

$$\frac{\sigma_t}{f_t} = \left[1 + \left(c_1 \frac{w_t}{w_{cr}} \right)^3 \right] e^{\left(-c_2 \frac{w_t}{w_{cr}} \right)} - \frac{w_t}{w_{cr}} (1 + c_1^3) e^{(-c_2)} \quad (3)$$

$$w_{cr} = 5.14 \frac{G_F}{f_t} \quad (4)$$

where w_t is the crack opening displacement, w_{cr} is the crack opening displacement at the complete loss of tensile stress, σ_t is the tensile stress normal to the crack direction, f_t is the concrete uniaxial tensile strength, and $c_1=3.0$ and $c_2=6.93$ are constants determined from tensile tests of concrete. f_t and G_F may be estimated from the CEB-FIB model:

$$f_t = 1.4 \left(\frac{f'_c - 8}{10} \right)^{\frac{2}{3}}, \text{ MPa} \quad (5)$$

$$G_F = (0.0469 d_a^2 - 0.5 d_a + 26) \left(\frac{f'_c}{10} \right)^{0.7}, \text{ N/mm} \quad (6)$$

in which d_a is the maximum aggregate size which is assumed to be 20mm if no test data is available in the present study. Once the stress-crack opening displacement relationship is known, the stress-strain relationship can be determined for each element based on its size through Equation 1. The Poisson's ratio $\nu=0.2$ is assumed in the present model.

The isotropic scale damaged stiffness in ABAQUS under uniaxial loading can be represented by :

$$\sigma = (1 - d) D_0 (\varepsilon - \bar{\varepsilon}^p) \quad (7)$$

where σ , ε and $\bar{\varepsilon}^p$ are respectively the stress, total strain and equivalent plastic strain in the loading direction; D_0 is the initial (undamaged) stiffness and d is the damage variable. The degraded stiffness is:

$$D = (1 - d) D_0 \quad (8)$$

This is illustrated in Fig. 1 for the case of uni-axial tension.

In the plastic degradation theory, the stiffness degradation is associated with the plastic deformation instead of the total deformation [5]. It is proposed in this study that the ratio of the plastic strain with stiffness degradation to that without stiffness degradation, ρ , is proportional to the cohesion of the material. In the case of uni-axial tension, this ratio is expressed as (Fig. 1):

$$\rho = \frac{\bar{\varepsilon}_t^p}{\varepsilon_t^p} = \frac{c}{c_{\max}} \quad (9)$$

For the case of uni-axial tension, the stiffness degradation variable d_t can be found from the geometrical relationships between the variables in Fig. 1 as:

$$d_t = \frac{(1 - \rho)\varepsilon_t^p}{(1 - \rho)\varepsilon_t^p + \sigma_t/E_0} \quad (10)$$

The same expression applies under uni-axial compression by replacing the tensile strength with the compressive strength.

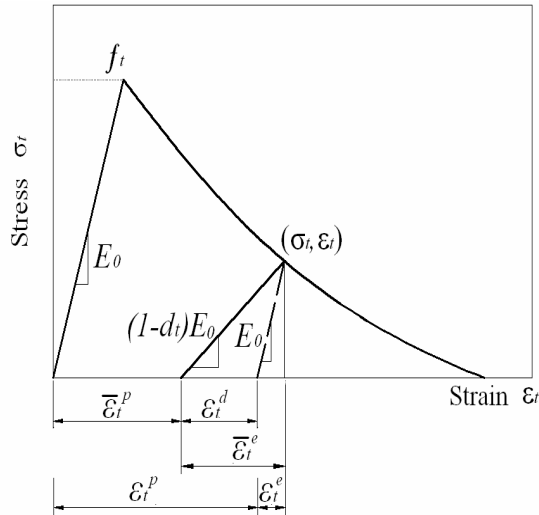


Figure 1. Stress-strain relationship of concrete under uniaxial tension

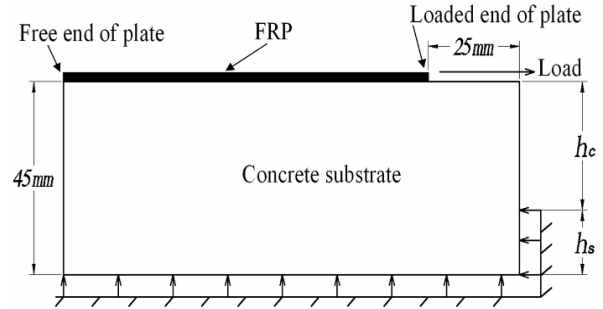


Figure 2. FE model of pull-off test

3 FE MODELLING OF PULL-OFF TEST

A 45 mm thick concrete prism as shown in Figure 2 was modelled as a plane stress problem in the FE analysis. This thickness is smaller than most specimens used in the experiments but the rest of the concrete should have little effect on the FE results as the pull-off test commonly fails by debonding in concrete a few millimeters away from the FRP-concrete interface. The thickness of the FRP plate t_p is set equal to 1 mm but the modulus of elasticity of the plate E_p is modified so that the plate has the actual axial stiffness $E_p t_p$. The concrete is modelled using mono-size square elements with four integration points. Rots' [6] recommendation is adopted that the characteristic length for a square element with 4 integration points is $\sqrt{2}e$ where e is the element side length. The FRP is modelled using the same element with matching mesh. Based on the results of a mesh convergence analysis, the 1mm mesh was used in the paper on the balance of accuracy and computational economy.

4 COMPARISON OF FE PREDICTIONS WITH TEST RESULTS

The proposed FE model has been used to simulate pull-off tests reported in [1], [7] and [8] failed by debonding. Figures 3 and 4 show the predicted and measured load-slip curve at the loaded end for two specimens: specimen II-5 in [1] and specimen No. 1 in [7]. Clearly the predictions are in close agreement with test data for both specimens in the whole loading range.

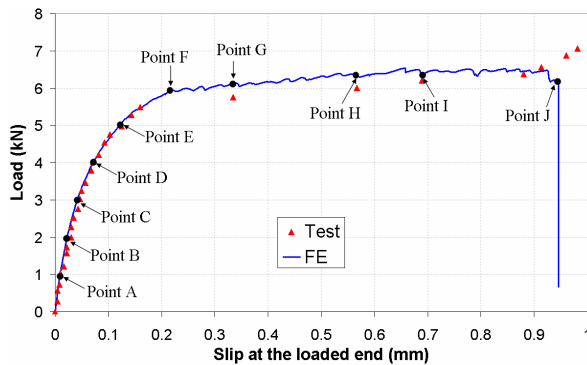


Figure 3. FE prediction versus test for specimen II-5 in [1]

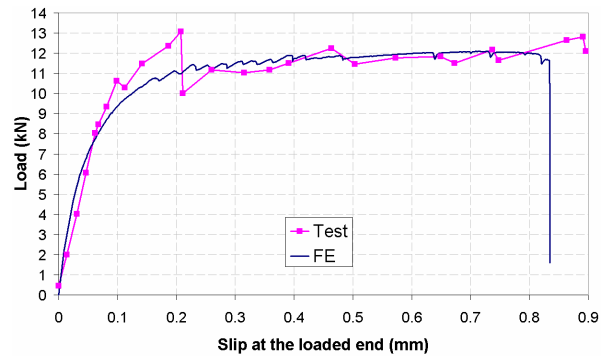


Figure 4. FE prediction versus test for specimen No. 1 in [7]

5 CONCLUSIONS

A plastic degradation model based the concrete damage plasticity theory has been proposed in this paper to simulate the bond behaviour between FRP and concrete. The proposed model has been implemented in ABAQUS to model the FRP-to-concrete bond behaviour in the pull-off test. It has been shown that the model can accurately predict the bond behaviour in the whole loading process and the numerical results are in very close agreement with test data from the literature.

6 ACKNOWLEDGEMENT

The authors would like to acknowledge the support from the Scottish Funding Council for the Joint Research Institute between the University of Edinburgh and Heriot-Watt University which forms part of the Edinburgh Research Partnership in Engineering and Mathematics (ERPem). They would also like to acknowledge the support from the UK Engineering and Physical Sciences Research Council (EPSRC) and Shell for providing the first author the Dorothy Hodgkin Postgraduate Award.

References

- [1] Yao, J., Teng, J. G. and Chen, J. F. 2005. Experimental study on FRP-to-concrete bonded joints. *Composites Part B: Engineering* 36(2):99-113.
- [2] Bažant, Z. and Oh, B. 1983. Crack band theory for fracture of concrete. *Materials and Structures* 16(3):155-177.
- [3] Saenz, L. P. 1964. Discussion of equation for the stress-strain curve of concrete-by Desayi, P. and Krishan, S. *ACI Journal* 61(9):1229-1235.
- [4] Hordijk, D. A. 1991. *Local Approach to Fatigue of Concrete*. PhD thesis, Delft University of Technology, Delft.
- [5] Lubliner, J., Oliver, J., Oller, S. and Oñate, E. 1989. A plastic-damage model for concrete. *International Journal of Solids and Structures* 25(3):299-326.
- [6] Rots, J. G. 1988. Computational modeling of concrete fracture. PhD thesis, Delft University of Technology, Delft.
- [7] Ali-Ahmad, M., Subramaniam, K. and Ghosn, M. 2006. Experimental investigation and fracture analysis of debonding between concrete and FRP sheets. *Journal of Engineering Mechanics* 132(9):914-923.
- [8] Wu, Z. S., Yuan, H., Yoshizawa, H. and Kanakubo, T. 2001. Experimental/analytical study on interfacial fracture energy and fracture propagation along FRP-concrete interface. *ACI International SP201(8):133-152*.

TIME DOMAIN 3D FINITE ELEMENT MODELLING OF TRAIN-INDUCED VIBRATION AT HIGH SPEED

*A. El-Kacimi¹, P. Woodward¹, O. Laghrouche¹ and G. Medero¹

¹School of the Built Environment, Heriot-Watt University, Edinburgh EH14 4AS, UK

Key Words: *structures; geomechanics; computational methods*

ABSTRACT

In this work, the effect of the soil parameters on the ground induced vibration due to a high speed moving train is numerically investigated through 3D finite element (FE) modelling. These include the Rayleigh wave speed and the damping ratio at different train speeds in the sub-critical and super-critical ranges. The developed 3D finite element model uses 20 noded brick elements for the track components for the sleepers, the ballast and the sub-grade. 3D beam-column elements are considered to describe the rail. The time integration is performed explicitly. The far field of the soil is truncated and absorbing boundary conditions are incorporated. Preliminary validation in the case of a static point load acting on homogeneous half space is carried out and results to study the vibration attenuation of the ground response when harmonic point loading is applied on the free surface of a single layer overlying bedrock are presented. The compression wave cut-off frequency is accurately estimated in terms of the frequency content, as theoretically predicted. Parametric studies are also conducted to show the effect of ground vibration when the train exceeds the Rayleigh ground wave speed.

1 Introduction

The study of the train induced vibration in railway and ground in civil and transportation engineering aims mainly to ensure the safety of the train operations, prevent track geometry deterioration and also protect the environment nearby buildings and the human comfort. In the soft ground areas, the train speed may exceed the soil Rayleigh speed which produces strong vibrations due to the resonance of the track structure. The design of safe and cost effective railway track requires a realistic track model which can describe its actual behaviour under moving vehicle loading. An adequate model should take into account the sleeper-ballast interaction, the spread of the moving load on the adjacent sleepers via the rail and afterwards into the multi-layered sub-grade.

Most early works attempted to provide analytical or semi-analytical solutions of moving load induced ground vibration. In ref. [1], Eason investigated a 3D steady-state problem, where a uniform half space is subjected to moving load at uniform speed. Singh and Kuo [2] developed an analytical solution for the response of an elastic half space under a moving circular load. Krylov [3], [4] derived an analytical prediction model for train-induced ground vibration, the track being modelled as a beam on an elastic foundation. Dieterman and Metrikine [6] investigated the steady-state response of a beam on an elastic

half-space for the simulation of the track vibration under train moving loads. De Barros and Luco [5] proposed a method giving the steady-state displacements and stresses within a multilayered viscoelastic half-space due to a buried or surface point load moving along a horizontal straight line. Jones *et al.* [7] gave the analytical solution of an elastic half space subjected to a moving rectangular harmonic. Lefeuvre-Mesgouez *et al.* [8] derived a semi-analytical solution of the half space ground response due to a vertical harmonic moving strip load. A complete bibliography references of research works related to the topic can be found in [9]. The obtained theoretical solutions are, however, mostly complex and require the numerical evaluation of integral formulations, with restrictions on the geometry and the material properties of the considered problem.

With the rapid progress of computer Technologies, numerical approaches based on the FE, the boundary element methods or coupled together become powerful tools in solving soil dynamic problems. However, there remain some difficulties with these approaches in dealing with the boundary and wave reflection between interfaces.

In this paper, a 3D FE model is developed for simulating the dynamic response of railway track. Multilayered ground and material damping are incorporated. The model may also deal with material non-linearity, especially of the ballast layer, and multi degree of freedom model for the vehicle. Lysmer and Kuhlemeyer absorbing boundary conditions [10] are implemented to take into account the radiation damping to infinity. The next section describes briefly the railway track model adopted to obtain dynamic responses due to moving loads.

2 3D coupled train-track FE model

The developed model includes railway track components such as the rail, railpad, sleeper, ballast/subballast and multi-layered subgrades, as illustrated in Figure 1 (left). A linear constitutive soil

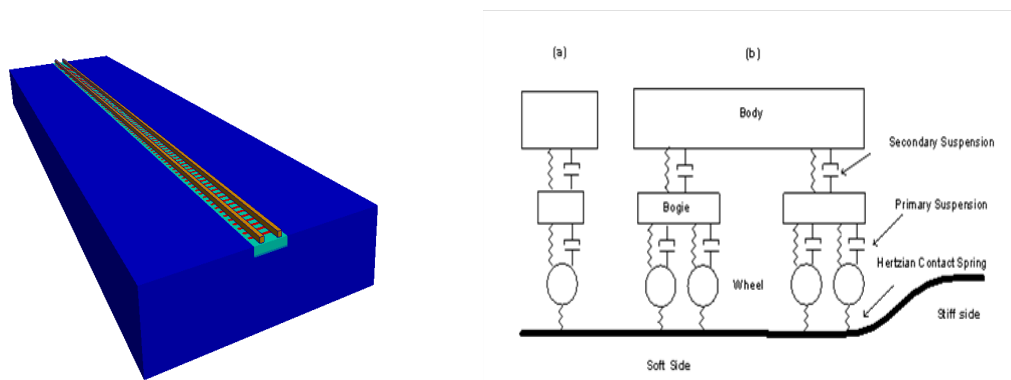


Figure 1: Schematic layout of 3D coupled train-track model.

model describing the wave propagation in a linearly isotropic medium is implemented. Viscous boundary conditions are incorporated to overcome the artificial stress wave reflections inside the physical domain.

The vehicle dynamic may be governed by quarter, fourth or full train model see Figure 1 (right). The quarter train model consists of bogie, train body and the corresponding suspension systems. The subgrade is meshed into 20 noded brick elements and the beam column element is considered for the rail. The resulting system of ordinary differential equations is approximated by an explicit time integration scheme with mass lumping.

3 Numerical results

Preliminary numerical validation dealing with uniform half space subjected to a constant point load was conducted. The obtained results are shown in Figure 2. A test problem of constant harmonic point load acting on a single layer overlying bedrock is also considered. The soil layer depth is $H = 10\text{m}$ and the material properties are: elastic modulus $E \simeq 0.15\text{GPa}$, Poisson ration $\nu = 0.35$ and density $\rho = 1,500\text{kg/m}^3$. It follows that the shear velocity of the soil is $C_S \simeq 192\text{m/s}$ and the compressional wave velocity is $C_P \simeq 400\text{m/s}$. Since the vertical vibration results mainly from the compressional waves, the resonance frequency should be roughly close to the compressional resonance frequencies $f_P = \frac{(2n-1)C_P}{4H}$, $n > 0$. By virtue of this formula the cut-off frequency is 10 Hz. It is observed from the results of Figure 2 that the numerical solution is in good agreement with the Boussinesq solution. Moreover, the cut-off frequency is accurately reproduced by the 3D FE model (see Figure 3). Figures 4 and 5 show the response in time and frequency domain at an observation point and the displacement magnitude for the coupled train-track model. It is clearly seen from the results that higher vibration is observed at the supercritical Rayleigh speed.

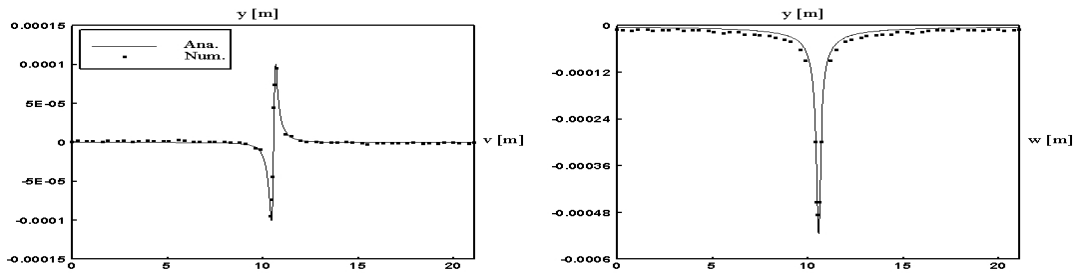


Figure 2: FE vs. Boussinesq's solutions.

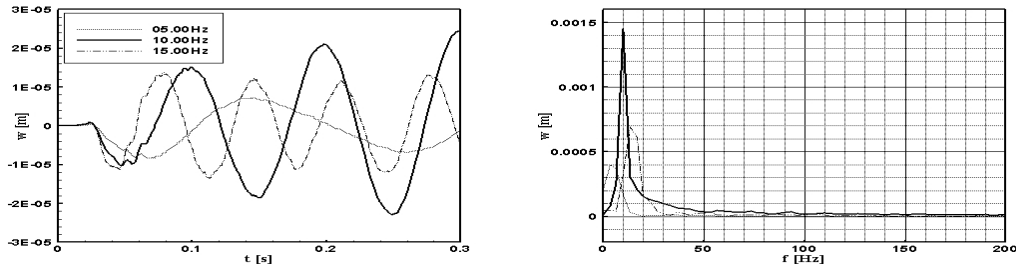


Figure 3: Vertical displacement: (left) the time domain response and (right) the frequency content.

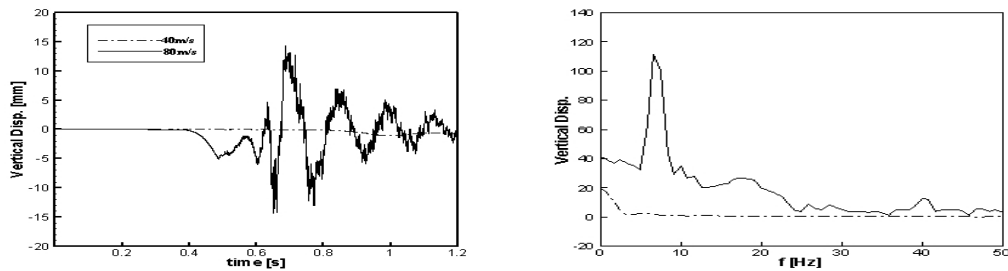


Figure 4: Vertical displacement: (left) the time domain response and (right) the frequency content.

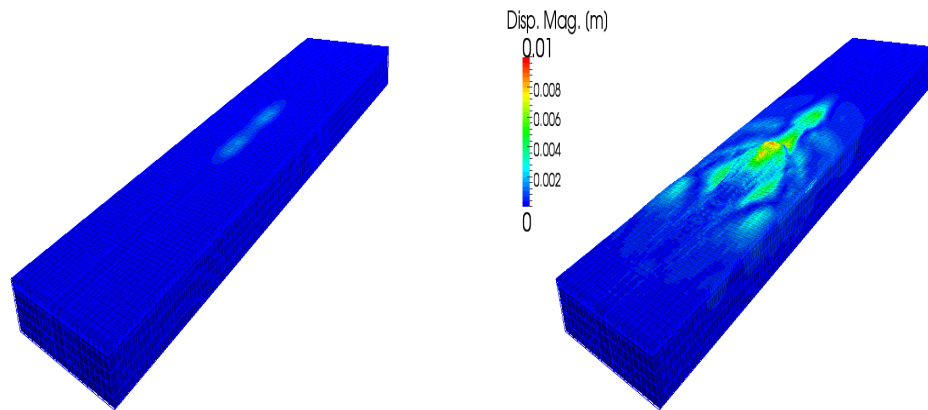


Figure 5: Displacement magnitude: (left) subcritical and (right) supercritical ranges.

In Figure 4 the damping is set to zero to illustrate the resonant response.

References

- [1] G.Eason. The stresses produced in a semi-infinite solid by a moving surface force. *Int J Eng Sci*, 2, 581–609, 1965.
- [2] S.K Singh and J.T. Kuo. Response of an elastic half space to uniformly moving. *J. Appl. Mech*, 1, 109–115, 1970.
- [3] V.V. Krylov and C. Ferguson. Calculation of low-frequency ground vibrations from railway trains. *Applied Acoustics*, 42, 199–21, 1994.
- [4] V.V. Krylov. Generation of ground vibration by superfast trains. *Applied Acoustics*, 44, 149–164, 1995.
- [5] F.C.P. De Barros and J.E. Luco. Response of a layered visco-elastic half-space to a moving point load. *Wave Motion* 19, 189210, 1994.
- [6] H.A. Dieterman and A.V. Metrikine. Steady-state displacements of a beam on an elastic half-space due to a uniformly moving constant load. *Eur J Mech A/Solids*, 6(2): 295–306, 1997.
- [7] D.V. Jones, D. Le Houedec and M. Petyt. Ground vibrations due to a rectangular harmonic load. *J.of Sound and Vibration*, 212(1): 61-74, 1998.
- [8] G. Lefeuvre-Mesgouez, D. Le Houédec and A.T. Peplow. Ground vibration in the vicinity of a high-speed moving harmonic strip load. *J. of Sound and Vibration*, 231(5): 1289–1309, 2000.
- [9] Y.M. Cao, H. Xia and G. Lombaert. Solution of moving load induced soil vibrations based on the Betti-Rayleigh Dynamic Reciprocal Theorem. *Soil Dyn. and Earth. Eng.*, 30, 470–480, 2010.
- [10] J. Lysmer and R.L. Kuhlemeyer. Finite dynamic model for infinite media. *J. of the Eng. Mech., ASCE*, 95 (EM4): 859877, 1969.

WAVE IMPLEMENTATION IN BLADE ELEMENT MOMENTUM THEORY FOR MODELLING TIDAL STREAM TURBINES

* H. C. Buckland¹, I. Masters¹ and J. Orme²

¹Marine Energy Research Group, Swansea University, Singleton Park, Swansea SA2 8PP, UK

²Swantubines Ltd. Digital Technium, Singleton Park, Swansea SA2 8PP, UK

*513924@swansea.ac.uk

ABSTRACT

A study of the non-linear and three-dimensional effects of a regular wave incident on a tidal turbine using Blade Element Momentum Theory and Chaplins stream function wave theory. BEMT is a method of modelling the performance of wind and marine turbines by combining one-dimensional momentum theory with rotational momentum and blade element theory. Chaplins stream function uses linear wave theory in a moving frame of reference to describe an incident wave front. The limitations and compatibility of BEMT and the stream function theory are discussed. Results for a freely rotating turbine are presented in the frequency, time and Tip Speed Ratio (TSR) domains. The turbine data used has been validated against tank testing by Bahaj et al.[1] and the Garrad Hassan Tidal Bladed software [6].

1 INTRODUCTION

Blade element momentum theory (BEMT) is used within MatLab to simulate the performance of a tidal turbine with low computational time when compared to traditional CFD codes. BEMT is derived for the general case of a turbine with an infinite number of infinitely thin blades. The inclusion of corrections and wave theory adapts BEMT to model the performance of a real turbine which can be used to validate the scheme against experimental data. Blade element momentum theory combines one dimensional momentum theory with blade element theory. In each case, two sets of equations are obtained for the turbines' axial force and torque, dT and dFa . Blade element theory partitions the rotor blades along their lengths into elements of length dr . Each is assumed to be a two-dimensional foil, implying lift and drag characteristics produce all the loadings[2] which can be summed over the blade length and number of blades N . The lift and drag coefficients, C_L and C_D , are found by interpolation from a lookup table of these values for the specific blade dimensions.

One dimensional momentum theory with rotational momentum models the turbine as a frictionless permeable actuator disc in a control flow stream bounded by a stream tube[8, 5] and uses Bernoulli's equation to compare pressure over the disc. It was first derived as a way of calculating the incoming velocity needed in blade element theory. It takes the azimuthally averaged axial and tangential induction factors, a and b , over the whole blade and so must be calculated with tip and hub loss corrections, combined together as a total loss F . This gives two sets of equations both describing torque and axial force and derived from complimenting theories[2]. As there are the four unknowns, dT , dFa , a and b , this is now a closed system. The system is resolved by using the least squares method within the MatLab constrained minimum toolbox FMINCON for the function g , by changing a and b such that,

$$g_1 = (dT_1 - dT_2)^2 = (N \frac{1}{2} \rho V^2 cr (C_L \cos \phi - C_D \sin \phi) dr - 4bF (1 - a) \rho U \ r^3 \pi dr)^2 \quad (1)$$

$$g_2 = (dFa_1 - dFa_2)^2 = (N \frac{1}{2} \rho V^2 c (C_L \sin \phi + C_D \cos \phi) dr - 4F\pi r \rho U^2 a(1-a) dr)^2 \quad (2)$$

$$g = g_1 + g_2 \quad (3)$$

Where c is the element chord and V is the local blade element velocity which is effected on by wave theory. U is the far upstream flow velocity and is taken as the hub height velocity and so is also effected by wave theory. By minimising g the difference between the blade element and momentum theory results for axial force, dFa and torque dT are minimised.

2 CHAPLIN'S STREAM FUNCTION WAVE THEORY

The stream function wave theory describes a 2D, irrotational, periodic wave of permanent form in the wave frame of reference, i.e. moving with wave speed C . Therefore the problem reduces to one of steady flow. The stream function is $\psi(x, y)$ where $\frac{\partial \psi}{\partial y} = v$ and $\frac{\partial \psi}{\partial x} = u - C$. By normalising the constant in the dynamic free surface boundary condition, the total head can be found, which is constant for a given wave. It is defined as:

$$Q = y + \frac{v^2 + (u - C)^2}{2g} \quad \text{on } y = \eta(x) \quad (4)$$

All conditions, apart from 4, can be satisfied by choosing a stream function of order N with the form:

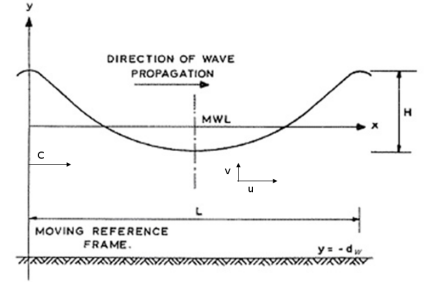
$$\psi(x, y) = -\frac{L}{T}x + \sum_{n=1}^N a_n \sinh \frac{2\pi n(d+y)}{L} \cos \frac{2\pi nx}{L} \quad (5)$$

The first term is the wavelength multiplied by frequency and the x position in the frame of reference and represents the mean resulting flow from choosing a moving frame of reference. The summation represents the wave disturbance. The numerical problem defined by this formulation of wave theory is to determine the unknown values of a_1, a_2, \dots, a_N and L and $\psi(x, \eta)$ such that the remaining condition of total head 4 is satisfied as closely as possible. In Dean's formulation[4], by specifying the mean water depth, total head and wave period, the parameters a_1, a_2, \dots, a_N and L are found using least squares method to minimise the errors of 4. The unknown parameter values are initially estimated and, from there, the solution progresses iteratively, using the modified form of the Gauss Method. The sum of squares of the boundary condition errors are minimised for a solution[3]. Total head, Q , is unknown and so was interpolated by Dean using the input parameter of wave height. However, most integral wave properties, such as total head, do not peak at maximum wave height, but before the maximum wave height[3]. This fact increases with wave steepness and creates 2:1 mapping therefore Dean's solution of interpolation is increasingly inaccurate with wave steepness[3]. Chaplin suggests total head should be abandoned as an input parameter and proceeds by creating a non-dimensionalised problem.

$$= \frac{\psi(x, y)}{\psi(x, \eta)}, \quad X = \frac{x}{L}, \quad D = \frac{d}{L}, \quad S = \frac{d+y}{L}, \quad A = \frac{a}{\psi(x, \eta)} \quad (6)$$

The new input parameters for the numerical problem are average water depth, d , wave period, T , and wave height, H . The independent unknowns to be found are now D and the surface height above the sea bed, S_1, S_2, \dots, S_{J-2} at positions along the x axis, x, x_2, \dots, x_{J-2} , in the moving frame of reference, between a crest and a trough. The non-dimensionalised stream function reads,

$$= A_{N+1}X + \sum_{n=1}^N A_n \sinh 2\pi n S \cos 2\pi n X \quad (7)$$



The coefficients A_n cannot be derived directly by the method of Fourier analysis since the function $A_n \sinh 2\pi n S_j \cos 2\pi n X_j$ and X_j are not orthonormal [3]. They are, however, linearly independent and so, using the Schmidt process, a set of orthonormal functions can be generated. A series of orthonormal functions $\phi_1(X_j), \phi_2(X_j), \dots, \phi_{N+1}(X_j)$ can be defined by the matrix equation, with the dummy variable k :

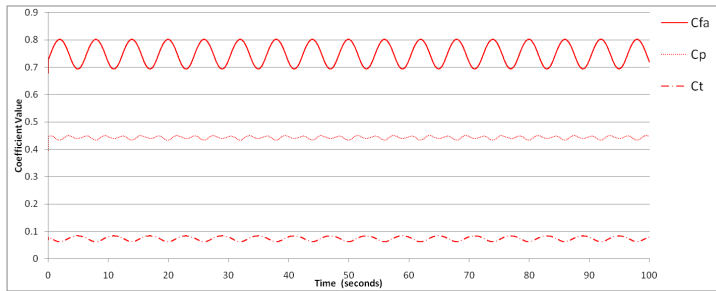
$$\zeta_{n,j} = C_{n,k} \phi_{k,j} \quad \text{where } \phi_{k,j} = \phi_k(X_j) \quad n = 1, 2, \dots, N+1 = 1, 2, \dots, J \quad (8)$$

Where C is a lower triangular matrix. The elements of the n th row of ϕ are then found from:

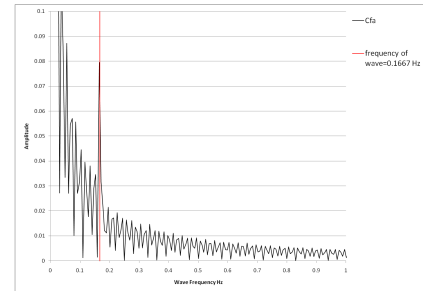
$$\phi_{n,j} = \frac{-\sum_{k=1}^{n-1} C_{n,k} \phi_{k,j} + \zeta_{n,j}}{C_{n,n}} \quad j = 1, 2, \dots, J \quad (9)$$

This method is repeated until all the elements of the matrices ϕ and C are known. Unfortunately, the round up error of this means that the component vectors of ϕ become progressively less orthogonal. Therefore a correction by Davies is applied. The problem is now a system of J non-linear equations and $J - 1$ unknowns and can now be directly solved using the Gauss non-linear least-squares method. Although this method is more complex than Dean's formulation, there is no interpolation error as the total head of the wave is calculated directly from the input wave height. The Chaplin stream function theory is compatible with BEMT as the wave velocities are simply coupled to the tidal velocities to give a combined flow velocity for a number of points in the x, y and z directions which are stored in a velocity matrix. This can then be used to compute the exact flow velocity at the blade element position in blade element theory, V and the upstream flow velocity, U , in momentum theory. Although Chaplin's wave theory can accommodate a non-uniform tidal flow by altering the speed at which the moving frame of reference propagates, this is not a realistic approximation. If the flow were to be non-uniform the fluid is no longer irrotational and the Laplace equation is not valid. This complicates the expansion so that the formulation is not easily incorporated into BEMT. The approach taken is suggested by Swan [10] and utilises Chaplin's wave theory purely to produce wave motion components of flow velocity without consideration for current effects. Addition is then used to combine these components with the tidal flow velocity components, which are calculated independently of the wave motion. The hydrodynamic force on the turbine due to the accelerative wave loadings is implemented using Morison's equation [9]. However, this approach is theoretically dubious as wave and tidal flows do not act independently of each other. This model cannot capture the rotation of flow which may occur and the effect of the current velocity on the dispersion of the waves.[7]

3 RESULTS

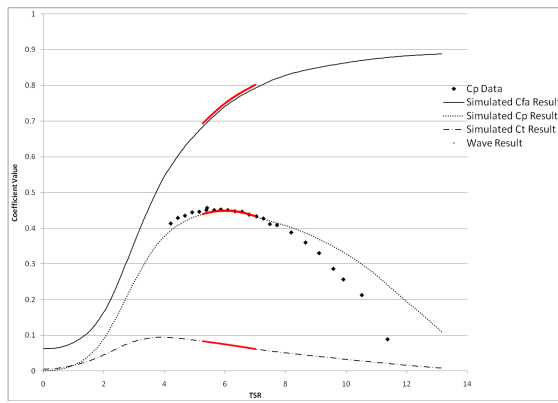


(a) The effect of wave motion with time

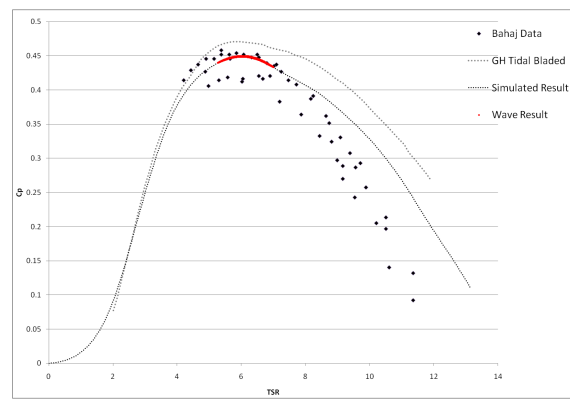


(b) Frequency study

The Bahaj 1m diameter rotor was successfully simulated using this scheme and the specifics of the experiment are outlined in [1]. The experimental data is corrected for blockage effects. The free stream tidal flow was 1.73m/s for the case where the blades are pitched at 20° as compared here. However all conditions investigated in [1] can be successfully simulated by this scheme. Figure 1(a) shows the force coefficients oscillate in the presence of a wave. The wave period is 6s and the height 4m. The coefficients oscillate from positive to negative without resistance. If the wave motion becomes more significant this could be undesirable as the rotor speed increases and decreases with wave trough and crest affecting the TSR which can default the power coefficient from its peak at



(c) TSR study with wave motion and compared to experimental data from the paper by Bahaj et. al. [1]



(d) Comparison with Bahaj experimental data and Garrad Hassan Tidal Bladed software [6]

TSR=6. By using Fast Fourier Transformation the magnitude of axial force coefficient with wave frequency can be shown as in Figure 1(b). As the simulated wave is of period 6 seconds a sharp peak is shown at the corresponding wave frequency of 0.1667Hz. The magnitude of the peak corresponds to the magnitude of C_{Fa} oscillations. As the regular, sinusoidal, Chaplin waves pass over the rotor the power and torque coefficients circulate up and down the TSR curves repeatedly with each wavelength. Instead of operating at peak C_P , TSR=6, the power is reduced with every peak and trough down either side of the peak as in Figure 1(c). Finally the results are compared to those of the Garrad Hassan Tidal Bladed turbine simulation software in Figure 1(d). It is shown that this scheme agrees well with experimental data and the commercial Garrad Hassan scheme and that wave motion can be incorporated into a BEMT model using Chaplin's stream function theory.

References

- [1] A.S. Bahaj, A.F. Molland, J.R. Chaplin, and W.M.J. Batten. Power and thrust measurements of marine current turbines under various hydrodynamic flow conditions in a cavitation tunnel and a towing tank. *Renewable Energy*, Volume 32(Issue 3):407–426, 2007.
- [2] T. Burton, N. Jenkins D. Sharpe, and E. Bossanyi. *Wind Energy Handbook*. John Wiley and Sons, Ltd, West Sussex, England, 2001.
- [3] John R Chaplin. Developments of stream-function wave theory. *Coastal Engineering*, 3:179–205, 1979.
- [4] R.G. Dean. Stream function representation of non-linear ocean waves. *Geophysical Research*, 70, 1965.
- [5] R. T. Griffiths and M. G. Woolard. Performance of the optimal wind turbine. *Applied Energy, Applied Science Publishers Ltd. Essex, England*, Volume 4, 1978.
- [6] Garrad Hassan and Partners Ltd. Development of a design tool for axial flow tidal stream devices. *BERR Emerging Energies Technology programme, AEA Energy and Environment*, 2008.
- [7] John Chapman Ian Masters and James Orme. A three-dimensional tidal stream turbine hydrodynamic performance model. In *Proc. World Renewable Energy Congress (WREC X)*, 2008.
- [8] I. Masters, J. Orme, M. Willis, and J. Chapman. A robust blade element momentum theory model for tidal stream turbines including tip and hub loss corrections. *Proceedings of the Institute of Marine Engineering, Science and Technology Part A Journal of Marine Engineering and Technology*, 10:25–35, January 2011.
- [9] J. Orme. Dynamic performance modelling of tidal stream turbines in ocean waves. *PhD Thesis, Civil and Computational Engineering, Swansea University*, 2006.
- [10] C. Swan, I. Cummins, and R. James. An experimental study of two-dimensional surface water waves propagating on depth-varying currents. part 1. regular waves. *Journal of Fluid Mechanics*, 428:273–304, 2001.

DEVELOPMENT OF A FINITE VOLUME ALGORITHM FOR A NEW CONSERVATION LAW FORMULATION IN STRUCTURAL DYNAMICS

Chun H. Lee*, Antonio J. Gil and Javier Bonet

Civil and Computational Engineering Centre, College of Engineering
Swansea University, Singleton Park, Swansea SA2 8PP, UK

*Corresponding author: 371363@swansea.ac.uk

Key Words: *First Order Conservation Laws, Finite Volume Method, Locking*

ABSTRACT

Recently, a new mixed formulation for explicit Lagrangian rapid dynamic analysis, based upon the formulation of a first order hyperbolic system of conservation laws, has been introduced [1, 2]. In this paper, a new finite volume algorithm is proposed for the numerical solution of the formulation mentioned above. The methodology will be shown to be capable of alleviating volumetric locking both in the analysis of nearly incompressible dynamics applications and in bending dominated situations. It is worth noting that this finite volume discretisation, particularly based on constant quadrilaterals, leads to second order convergence for velocities, displacements and stresses. A state-of-the-art shock capturing technique [3] is introduced so as to avoid spurious oscillation in the vicinity of sharp gradients. To this end, a number of numerical examples will be examined in order to demonstrate the robustness and general capabilities of the proposed approach.

1 INTRODUCTION

In general, the traditional solid dynamics formulation, where its primary variable is the displacement field, is solved by standard Finite Element (FE) spatial discretisation together with a family of Newmark time integration schemes. However, the resulting space-time discretised formulation presents a series of shortcomings. First, Newmark's method has a tendency for high frequency noise to persist in the solution and most importantly, its accuracy is remarkably degraded once artificial damping is employed. Some minor modifications were introduced to improve the accuracy of numerical dissipation without the inclusion of a discontinuity sensor [4], which consequently made the Newmark scheme unsuitable for problems where shocks are present. Additionally, it is well known that using linear elements in displacement-based FE leads to second order convergence for displacements but one order less for strains and stresses.

It is also known that constant stress elements exhibit volumetric locking in incompressible or nearly incompressible applications; for instance, plastic flows involving large isochoric strains. In order to eliminate the locking phenomena, a variety of different approaches have been developed. First, p-refinement

can be introduced where high order interpolating functions are adopted [7]. Another general approach is to introduce a three-field Hu-Washizu type of variational principle, which enables the use of independent kinematic descriptions for the volumetric and deviatoric deformations [5]. In particular, the mean dilatation technique, in which a constant interpolation for volumetric variables over an element is involved, is widely accepted. This specific technique is alternatively known as selective reduced integration, where the volumetric stress components are suitably underintegrated. Unfortunately, this scheme cannot be applied within the context of low order elements such as linear triangles and tetrahedrons as these elements have already used the simplest gaussian quadrature rule. In [6], Bonet and Burton suggested that the volumetric strain energy is approximated by evaluating averaged nodal pressures in terms of nodal volumes while the deviatoric component is treated in a standard manner. However, the resulting solution behaved poorly in bending dominated cases. To circumvent this difficulty, Dohrmann *et.al* [7] proposed a new linear tetrahedron by applying nodal averaging process to the whole small strain tensor. Furthermore, Bonet *et.al* extended this application to large strain regime with the idea of employing an averaged nodal deformation gradient tensor as the main kinematic variable [8].

This paper offers an alternative computational framework to prevent the detrimental locking effects by developing a mixed formulation that permits the use of any low order elements. Insofar as the formulation is expressed as a system of conservation laws, where both the velocities and deformation gradient tensor are the primary conserved variables, stresses converge at the same rate as velocities and displacements. Moreover, this system of equations can be discretised using a Finite Volume methodology, typically based on the use of Riemann solvers and shock capturing schemes.

2 METHODOLOGY

The new formulation of Lagrangian explicit dynamics solid mechanics is crucially governed by two physical laws, namely the momentum balance principle and the deformation gradient conservation principle. Mathematically, they can be written as

$$\begin{aligned} \frac{\partial \mathbf{p}}{\partial t} - \nabla_0 \cdot \mathbf{P} &= \rho_0 \mathbf{b} \\ \frac{\partial \mathbf{F}}{\partial t} - \nabla_0 \cdot (\mathbf{v} \otimes \mathbf{I}) &= \mathbf{0}, \end{aligned} \quad (1)$$

where $\mathbf{p} = \rho_0 \mathbf{v}$ is the linear momentum per unit of material volume, ρ_0 represents the material density, \mathbf{v} is the velocity field, \mathbf{b} stands for the body force per unit mass, \mathbf{F} indicates the deformation gradient tensor, \mathbf{P} describes the first Piola-Kirchhoff stress tensor and ∇_0 denotes a material gradient operator in undeformed space. During irreversible processes, it is essential to solve for an additional state variable, that is the first law of thermodynamics, which can be formulated as

$$\frac{\partial E}{\partial t} + \nabla_0 \cdot (\mathbf{Q} - \mathbf{P}^T \mathbf{v}) = s, \quad (2)$$

where E is the total energy per unit of undeformed volume, \mathbf{Q} describes the heat flux vector and s represents the heat source. For simplicity, this paper only deals with an isothermal process where the heat flux \mathbf{Q} and the energy source term, s , can be ignored. Hence, this process allows the energy balance principle, Eqn. (2), to be uncoupled from the rest of the system (1). These conservation laws, viz.(1) and (2), have to be supplemented by a constitutive law so as to close the coupled system, that is, $\mathbf{P} = \partial \psi(\mathbf{F}, \alpha) / \partial \mathbf{F}$. Here, ψ is the Helmholtz free energy function per unit of undeformed volume and α denotes the hardening variable of the dissipative model.

The spatial semi-discretisation is performed on a standard cell-centred cartesian grid, where the primary variables are defined at the centroids of the cells. Under this circumstance, any control volume can be identified with the existing grid and typically, the field variables are approximated in every cell by means of piecewise constant shape functions, which yield first order accuracy in space. Higher order spatial accuracy can be achieved by introducing a suitable reconstruction procedure for variables within each cell. The discontinuity at every cell interface motivates the use of a Riemann solver to evaluate the flux. Inasmuch as the higher order spatial method does not prohibit unphysical oscillations in the vicinity of discontinuities, a shock capturing technique which incorporates the Van Leer nonlinear limiter is introduced [3]. Furthermore, the semidiscrete nonlinear evolution equations will be advanced forward in time by using a TVD Runge-Kutta time stepping scheme.

3 NUMERICAL EXAMPLES

A series of examples will be examined in order to illustrate the performance of the proposed methodology. The first example which will be considered is that of the wave propagation on a one-dimensional elastic cable. The left end of the cable is fixed and any forcing function can be applied to its free right end. By applying a step function force, Fig.(1a) presents the stress history of a square wave at fixed end. A mesh convergence analysis is also performed where a sinusoidal forcing function is adopted; see Fig.(1b). Moreover, we have chosen a simple example of cantilever beam subjected to a sudden constant vertical load at its free end. The purpose of this example is to show the behaviour of the proposed algorithm in bending-dominated situations. Fig.(2) depicts the deformed configurations obtained with standard Finite Element technique and the new Finite Volume method at a particular time instant.

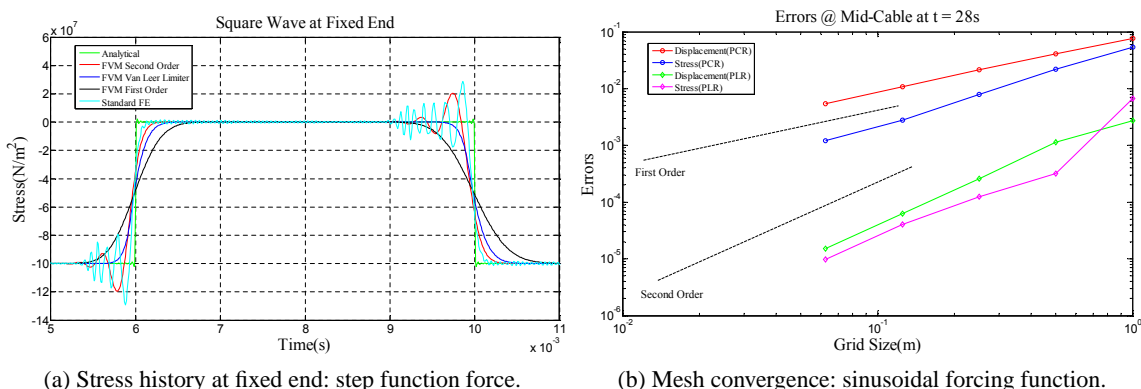


Figure 1: One-dimensional elastic cable.

4 CONCLUSIONS

A new Finite Volume computational methodology in cartesian grids is presented for the numerical solution of a new mixed formulation based upon a first order hyperbolic system of conservation laws. This new formulation, which is of mixed velocity-deformation gradient tensor, enables the stresses converge at the same rate as velocities and displacements, and also permits the use of any low order elements without volumetric locking and bending difficulty. Furthermore, the use of constant stress elements

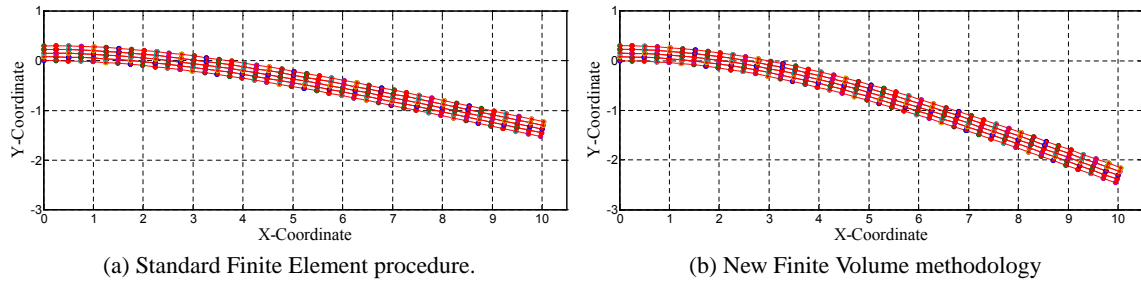


Figure 2: Shear locking behaviour.

results in a faster and easy-to-implement code. In this paper, it is worth noting that the algorithm proposed performs better than displacement-based model in the presence of shock waves. In addition, we have also shown that the new Finite Volume algorithm presents a clear advantage over a traditional displacement formulation in bending dominated problem. The overall numerical strategy provides a good compromise between accuracy and speed of computations.

References

- [1] J. Peraire, P. Persson, Y. Vidal, J. Bonet and A. Huerta. A discontinuous Galerkin formulation for Lagrangian dynamic analysis of hyperelastic materials. *VII World Congress of Computational Mechanics*, Los Angeles, 2006.
- [2] J. Bonet and A.J. Gil. Two step Taylor-Galerkin solution of Lagrangian explicit dynamic solid mechanics. *8th World Congress on Computational Mechanics(WCCM8)*, Venice, 2008.
- [3] E.F. Toro. Riemann solvers and numerical methods for fluid dynamics: a practical introduction, second edition, Springer-Verlag, 2006.
- [4] J. Chung and G.M. Hulbert. A time integration algorithm for structural dynamics with improved numerical dissipation: the generalized α method. *Journal of Applied Mechanics*, 60, 371–375, 1993.
- [5] J. Bonet and R.D. Wood. Nonlinear continuum mechanics for finite element analysis, second edition, Cambridge university press, 2008.
- [6] J. Bonet and A.J. Burton. A simple average nodal pressure tetrahedral element for incompressible and nearly incompressible dynamic explicit applications. *Communications in Numerical Methods in Engineering*, 14, 437–449, 1998.
- [7] C.R. Dohrmann, M.W. Heinstein, J. Jung, S.W. Key and W.R. Witkowski. Node-based uniform strain elements for three-node triangular and four-node tetrahedral meshes. *International Journal for Numerical Methods in Engineering*, 47, 1549–1568, 2000.
- [8] J. Bonet, H. Marriott and O. Hassan. An averaged nodal deformation gradient linear tetrahedral element for large strain explicit dynamic applications. *Communications in Numerical Methods in Engineering*, 17, 551–561, 2001.

USING GRADIENT ELASTICITY THEORIES WITH MICRO-INERTIA TO INCREASE THE CRITICAL TIME STEP

*Harm Askes, Duc C.D. Nguyen and Andy Tyas

Department of Civil and Structural Engineering, University of Sheffield, United Kingdom
h.askses@sheffield.ac.uk

Key Words: *gradient elasticity; micro-inertia; length scale; explicit dynamics; critical time step*

ABSTRACT

The critical time step of conditionally stable time integrators, such as the explicit central difference scheme, can be increased by incorporating *micro-inertia* terms in the governing equations. This is shown for two types of micro-inertia, both of which are special cases of the 1964 Mindlin theory of elasticity with microstructure. Closed-form expressions for the critical time step are derived for a number of standard finite elements with micro-inertia enrichment.

1 INTRODUCTION

Explicit time integration is the most popular method to carry out time domain analysis in computational mechanics. The advantages are its ease of implementation and the minimal computational efforts per time step. However, the drawback is that explicit time integration schemes are only conditionally stable, that is, the time step must be chosen smaller than a so-called critical time step, otherwise the numerical solution can become unstable. The critical time step depends on the element size and on the speed of sound of the material. The latter can be manipulated by employing micro-structural enrichments of the usual equations of continuum mechanics. In particular gradient elasticity theories provide a simple framework by which the classical equations of elasticity are extended with strain gradient and/or inertia gradients. In particular, the use of inertia gradients has been shown to lead to increased critical time steps [1]. The speed of sound of the higher frequencies is lowered by the long-range interaction introduced by the higher-order inertia effects, and this affects the eigen-frequencies of the individual finite elements which set the critical time step.

Section 2 starts with a brief review of the general gradient elasticity theory of Mindlin [3], which includes strain gradients as well as inertia gradients. Two particular cases of inertia gradients will be considered, whereby in the discretised equations the micro-inertia terms are proportional to the diffusivity matrix or to the stiffness matrix. Closed-form expressions for the critical time step are derived in Section 3 for a number of standard finite elements, including three-noded triangles and four-noded squares.

2 ELASTICITY WITH MICRO-INERTIA

In the 1960s, Mindlin derived an elasticity theory whereby the microstructural effects were captured by inertia gradients and strain gradients [3], that is

$$\rho \ddot{u}_i - b_1 \ddot{u}_{j,i,j} - b_2 \ddot{u}_{i,j,j} = (\lambda + \mu) u_{j,i,j} + \mu u_{i,j,j} - 2(a_1 + a_2 + a_5) u_{j,i,j,kk} - 2(a_3 + a_4) u_{i,j,jkk} \quad (1)$$

where u are the displacements, ρ is the mass density, λ and μ are the Lamé constants, and standard index notation is used. The parameters a_i that accompany the strain gradients are irrelevant for the purpose of this paper, hence we will take $a_1 + a_2 + a_5 = 0$ as well as $a_3 + a_4 = 0$. The remaining two parameters b_1 and b_2 are related to micro-inertia, but it is more convenient to rewrite them in term of internal length scales ℓ_1 and ℓ_2 as $b_1 = \rho \ell_1^2$ and $b_2 = \rho \ell_2^2$. Thus, Eq. (1) is simplified as

$$\rho (\ddot{u}_i - \ell_1^2 \ddot{u}_{j,i,j} - \ell_2^2 \ddot{u}_{i,j,j}) = (\lambda + \mu) u_{j,i,j} + \mu u_{i,j,j} \quad (2)$$

Two special cases of this equation will be considered, namely $\ell_1^2 = 0$ and $\ell_1^2 = \ell_2^2 \cdot (\lambda + \mu) / \mu$, which are referred to as Type I and Type II micro-inertia, respectively. The first special case is obtained by taking $\ell_1^2 = 0$. The weak form of Eq. (2) is written as

$$\int_{\Omega} \mathbf{w}^T \rho (\ddot{\mathbf{u}} - \ell^2 \nabla^2 \ddot{\mathbf{u}}) dV = \int_{\Omega} \mathbf{w}^T \mathbf{L}^T \mathbf{C} \mathbf{L} \mathbf{u} dV \quad (3)$$

where \mathbf{C} contains the elastic moduli, \mathbf{w} is a generic test function, \mathbf{L} and ∇ are the usual differential operators, and ℓ_2 is replaced by ℓ . Integration by parts results in

$$\int_{\Omega} \mathbf{w}^T \rho \ddot{\mathbf{u}} dV + \int_{\Omega} \sum_{\xi} \frac{\partial \mathbf{w}^T}{\partial \xi} \rho \ell^2 \frac{\partial \ddot{\mathbf{u}}}{\partial \xi} dV + \int_{\Omega} (\mathbf{L} \mathbf{w})^T \mathbf{C} \mathbf{L} \mathbf{u} dV = \text{boundary terms} \quad (4)$$

with a summation over the three spatial coordinates x , y and z . Using finite element shape functions \mathbf{N} for the trial function \mathbf{u} and the test function \mathbf{w} yields

$$[\mathbf{M} + \ell^2 \mathbf{D}] \ddot{\mathbf{u}} + \mathbf{K} \mathbf{u} = \mathbf{f} \quad (5)$$

where \mathbf{M} and \mathbf{K} are the standard mass matrix and stiffness matrix. Furthermore, the diffusivity matrix \mathbf{D} is defined by

$$\mathbf{D} = \int_{\Omega} \sum_{\xi} \frac{\partial \mathbf{N}^T}{\partial \xi} \rho \frac{\partial \mathbf{N}}{\partial \xi} dV \quad (6)$$

Such a micro-inertia modification of the mass matrix was also suggested by [5].

The second special case is found by taking $\ell_1^2 = \ell_2^2 \cdot (\lambda + \mu) / \mu$. The weak form of Eq. (2) can then be written as

$$\int_{\Omega} \mathbf{w}^T \rho \ddot{\mathbf{u}} dV = \int_{\Omega} \mathbf{w}^T \mathbf{L}^T \mathbf{C} \mathbf{L} (\mathbf{u} + \tau^2 \ddot{\mathbf{u}}) dV \quad (7)$$

where a time scale τ is defined via

$$\tau^2 = \ell_1^2 \frac{\rho}{\lambda + \mu} = \ell_2^2 \frac{\rho}{\mu} \quad (8)$$

Integration by parts results in

$$\int_{\Omega} \mathbf{w}^T \rho \ddot{\mathbf{u}} dV + \int_{\Omega} (\mathbf{L} \mathbf{w})^T \mathbf{C} \mathbf{L} (\mathbf{u} + \tau^2 \ddot{\mathbf{u}}) dV = \text{boundary terms} \quad (9)$$

and subsequent finite element discretisation results in

$$[\mathbf{M} + \tau^2 \mathbf{K}] \ddot{\mathbf{u}} + \mathbf{K} \mathbf{u} = \mathbf{f} \quad (10)$$

Using the stiffness matrix to modify the mass matrix was suggested earlier in [2, 4].

3 CRITICAL TIME STEP INCREASED WITH MICRO-INERTIA

For explicit time integration algorithms, the critical time step Δt_{crit} can be found from

$$\Delta t_{\text{crit}} = \frac{2}{\omega_{\text{max}}} \quad (11)$$

where ω_{max} is the maximum eigenfrequency of the finite element mesh, usually estimated by the largest eigenvalue of a single element. Thus, a small eigenvalue problem must be solved, that is

$$\det(-\omega^2 [\mathbf{M} + \mathbf{M}_m] + \mathbf{K}) = 0 \quad (12)$$

whereby $\mathbf{M}_m = \ell^2 \mathbf{D}$ for Type I micro-inertia and $\mathbf{M}_m = \tau^2 \mathbf{K}$ for Type II micro-inertia. Symbolic operation software can be used to find closed-form expressions for the maximum eigenfrequency for a range of simple, two-dimensional finite elements. However, certain assumptions about the element geometry must be made to keep the resulting expressions simple and of practical use. The first example concerns bilinear, four-noded square elements. The element size is denoted as h and a plane stress assumption is used. Assuming Type I micro-inertia, Eq. (12) results in

$$\begin{aligned} \{2E(3-\nu) - \omega^2 \rho(3h^2 + 8\ell^2)(1-\nu^2)\}^2 \cdot \{4E - \omega^2 \rho(h^2 + 4\ell^2)(1-\nu)\} \\ \cdot \{4E - \omega^2 \rho(h^2 + 4\ell^2)(1+\nu)\}^2 = 0 \end{aligned} \quad (13)$$

where E and ν are the Young's modulus and Poisson's ratio, so that

$$\Delta t_{\text{crit}} = \frac{h}{c_e} \cdot \sqrt{(1-\nu) \left(1 + \frac{4\ell^2}{h^2}\right)} \quad (14)$$

where $c_e = \sqrt{E/\rho}$ is the elastic bar velocity. The eigenvalue problem of Type II micro-inertia reads

$$\begin{aligned} \{2E(3-\nu) - \omega^2 \rho(3h^2(1-\nu^2) + 2\tau^2 c_e^2(3-\nu))\}^2 \\ \cdot \{4E - \omega^2 \rho(h^2(1-\nu) + 4\tau^2 c_e^2)\} \{4E - \omega^2 \rho(h^2(1+\nu) + 4\tau^2 c_e^2)\}^2 = 0 \end{aligned} \quad (15)$$

by which

$$\Delta t_{\text{crit}} = \frac{h}{c_e} \cdot \sqrt{1-\nu + \frac{4\tau^2 c_e^2}{h^2}} \quad (16)$$

The second example concerns a right-angle linear three-noded triangle, whereby the two shortest sides each have length h . The Type I micro-inertia eigenvalue problem reads

$$\begin{aligned} \{E(6h^2 + 27\ell^2) - \omega^2 \rho(h^4 + 12h^2\ell^2 + 27\ell^4)(1+\nu)\}^2 \\ \cdot \{27E^2 - \omega^2 E\rho(12h^2 + 54\ell^2) + \omega^4 \rho^2(h^4 + 12h^2\ell^2 + 27\ell^4)(1-\nu^2)\} = 0 \end{aligned} \quad (17)$$

which gives

$$\Delta t_{\text{crit}} = \frac{h}{c_e} \cdot \sqrt{\frac{4(1-\nu^2) \left(1 + \frac{3\ell^2}{h^2}\right) \left(1 + \frac{9\ell^2}{h^2}\right)}{6 + \frac{27\ell^2}{h^2} + 3\sqrt{1 + 3\nu^2} \left(1 + \frac{3\ell^2}{h^2}\right) \left(1 + \frac{9\ell^2}{h^2}\right)}} \quad (18)$$

Conversely, the eigenvalue problem of Type II micro-inertia yields

$$\{6E - \omega^2 \rho (h^2(1 + \nu) + 6\tau^2 c_e^2)\} \cdot \{27E^2 - \omega^2 E \rho (12h^2 + 54\tau^2 c_e^2) + \omega^4 \rho^2 (h^4(1 - \nu^2) + 12h^2 \tau^2 c_e^2 + 27\tau^4 c_e^4)\} = 0 \quad (19)$$

and

$$\Delta t_{\text{crit}} = \frac{h}{c_e} \cdot \sqrt{\frac{4 \left(1 + \frac{3\tau^2 c_e^2}{h^2}\right) \left(1 + \frac{9\tau^2 c_e^2}{h^2}\right) - 4\nu^2}{6 + \frac{27\tau^2 c_e^2}{h^2} + 3\sqrt{1 + 3\nu^2}}} \quad (20)$$

4 Discussion

In this paper, micro-inertia extensions of classical elasticity have been explored as a means to increase the critical time step of explicit time integration. Two types of micro-inertia have been considered, whereby the modification of the mass matrix adopts the format of the diffusivity matrix (Type I) or the stiffness matrix (Type II). Both types can be interpreted as special cases of Mindlin's 1964 theory of elasticity with strain gradients and inertia gradients. Figure 1 demonstrates the effects of micro-inertia on the critical time step of four-noded bilinear square and three-noded linear triangular elements. Important increases of the critical time step can be observed, which are governed by the microstructural parameters ℓ and/or τ .

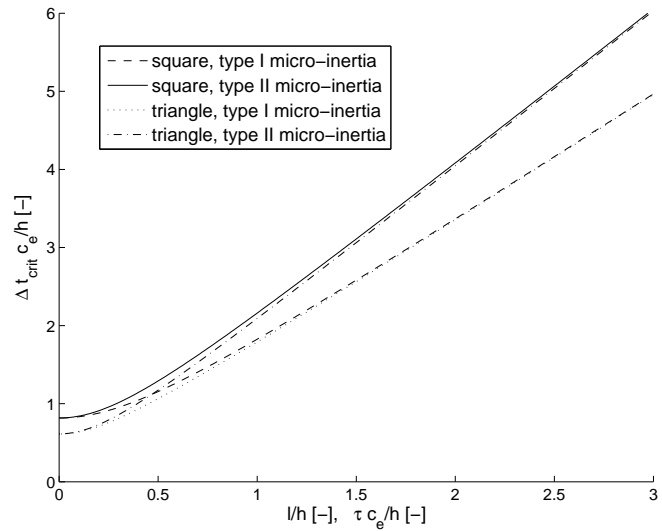


Figure 1: Effects of micro-inertia on critical time step

References

- [1] H. Askes, B. Wang, and T. Bennett, *Element size and time step selection procedures for the numerical analysis of elasticity with higher-order inertia*, J. Sound Vibr. **314** (2008), 650–656.
- [2] R.W. Macek and B.H. Aubert, *A mass penalty technique to control the critical time increment in explicit dynamic finite-element analysis*, Earthq. Engng. Struct. Dyn. **24** (1995), 1315–1331.
- [3] R.D. Mindlin, *Micro-structure in linear elasticity*, Arch. Rat. Mech. Analysis **16** (1964), 52–78.
- [4] L. Olovsson, K. Simonsson, and M. Unosson, *Selective mass scaling for explicit finite element analyses*, Int. J. Numer. Meth. Engng. **63** (2005), 1436–1445.
- [5] P. Plecháč and M. Rousset, *Implicit mass-matrix penalization of Hamiltonian dynamics with application to exact sampling of stiff systems*, Multisc. Mod. Simul. (SIAM) **8** (2010), 498–539.

Numerical modelling of the dynamic behaviour of a soil deposit overlying bedrock

N. Hamdan¹, O. Laghrouche¹, A. El Kacimi¹, P. Woodward¹ and G. Medero¹

¹School of the Built Environment, Heriot Watt University, Edinburgh, EH14 4AS

nh60@hw.ac.uk, o.laghrouche@hw.ac.uk

Key Words: *wave propagation; finite elements; consistent transmitting boundary; frequency domain*

ABSTRACT

A two-dimensional numerical model is used to simulate the propagation of waves in a homogeneous soil deposit overlying bedrock. The finite element method is adopted in the frequency domain under plane strain conditions. To simulate the infinite extent of the medium, in the lateral directions, the consistent transmitting boundary developed by Waas [1] is implemented. The numerical model is validated by checking the effectiveness of the transmitting boundary to radiate waves away towards infinity and by considering the dynamic behaviour of a soil layer over bedrock.

1 INTRODUCTION

The finite element method has been widely used for engineering applications where the computational domain is of finite extent. In problems dealing with unbounded media, such as wave propagation in soils, special treatment is required at the boundary of the computational domain to allow waves to radiate away towards infinity. If no treatment is used, incoming waves will reflect back from the domain boundaries and the solution would be affected by spurious waves. Therefore, some type of absorbing conditions must be applied at the artificial boundaries in order to overcome wave reflection and also reduce the size of the problem.

Several authors have developed various absorbing boundaries to separate what they referred to as 'the soil box or the soil island' from the infinite media. These boundaries prevent to some extent impinging waves from reflecting back to the soil box. Waas [1] was among the pioneers who worked intensively on developing transmitting boundary conditions for soil dynamic problems. They were implemented for the study of the dynamic behaviour of various foundation types in soil media.

2 PROBLEM FORMULATION

Figure 1 shows a schematic diagram of a traditional dynamic soil-structure interaction problem. A semi-infinite soil medium is divided into three regions. The central region I, overlying a rigid base, may contain some kind of discontinuities such as foundations, tunnels or wave barriers. The left and right-hand regions, II and III, are assumed to extend horizontally to infinity. The finite element method is adopted to analyze the central region by discretizing the domain into 4-node bilinear finite elements with two degrees of freedom at each node; horizontal and vertical displacements. A direct stiffness method is used to formulate the element mass and stiffness matrices.

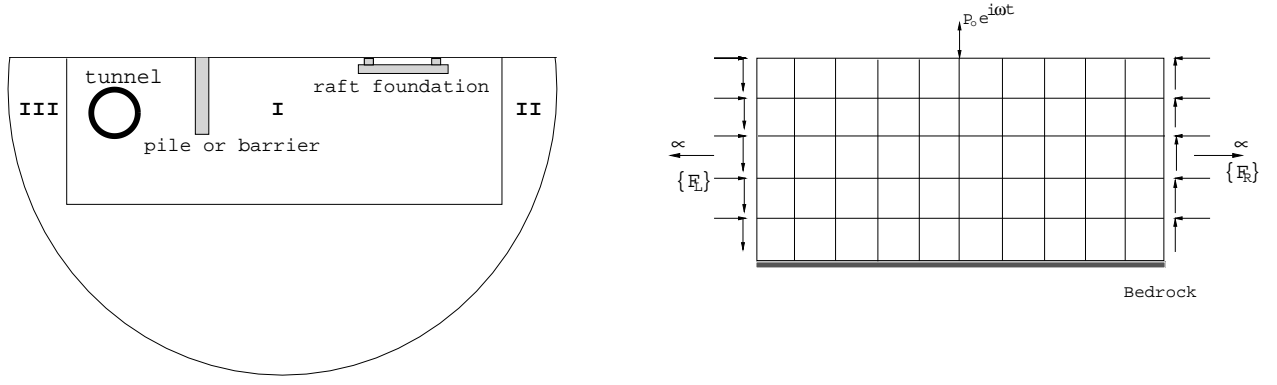


Figure 1: Schematic representation of the problem and Finite Element discretization.

Both regions II and III are subdivided into horizontal layers where the displacements are assumed to vary linearly with the depth and exponentially in the infinite direction, with a wave number k . Considering the free vibration of the domains and ensuring their dynamic equilibrium leads to the quadratic eigenvalue problem

$$[k^2 \mathbf{A} + ik\mathbf{B} + \mathbf{G} - \omega^2 \mathbf{M}] \{\mathbf{U}\} = \{\mathbf{0}\} \quad (1)$$

where the matrices \mathbf{A} , \mathbf{B} , \mathbf{G} , and \mathbf{M} are obtained from the geometry and material properties of the horizontal layers. The eigenvalue problem (1) of dimension $2n$, where n is the number of layers, is first reduced to a first order problem but with the dimension increased to $4n$. Half of the eigenvalues, with positive imaginary part, represent waves travelling in $x \geq 0$ and the other half represents waves travelling in $x \leq 0$. The displacement field is therefore written as a combination of all mode shapes which leads to nodal forces on the right and left sides of the central domain, respectively, of the form

$$\{\mathbf{F}_R\} = -[\mathbf{R}] \{\mathbf{U}_R\} \quad \text{and} \quad \{\mathbf{F}_L\} = -[\mathbf{L}] \{\mathbf{U}_L\} \quad (2)$$

where \mathbf{U}_R and \mathbf{U}_L are the nodal displacement vectors of the right and left boundaries. They are parts of the global displacement vector \mathbf{U} . The matrices \mathbf{R} and \mathbf{L} are deduced from the eigenvalues and eigenmodes of expression (1). Given that the displacements \mathbf{U}_R and \mathbf{U}_L are unknown, the finite element system of the central domain has the following form

$$[(1 + 2i\xi) \mathbf{K} - \omega^2 \mathbf{M} + \mathbf{R} + \mathbf{L}] \{\mathbf{U}\} = \{\mathbf{P}\} \quad (3)$$

The global matrices \mathbf{K} and \mathbf{M} are obtained from assembling the element stiffness and mass matrices of the central domain. The problem (3) is linear and a direct solver, such as the Gauss elimination approach, is used for the solution. The time variable is omitted by considering a steady state problem.

3 NUMERICAL RESULTS

This section deals with numerical tests aiming at validating the above presented model. First, the ability of the consistent transmitting boundary to allow the incoming waves to radiate away towards infinity is checked by varying the horizontal extent of the computational domain. Then, the ability of the model to capture the dynamic behaviour of a soil deposit overlying bedrock is checked against a 1D wave propagation analytical model.

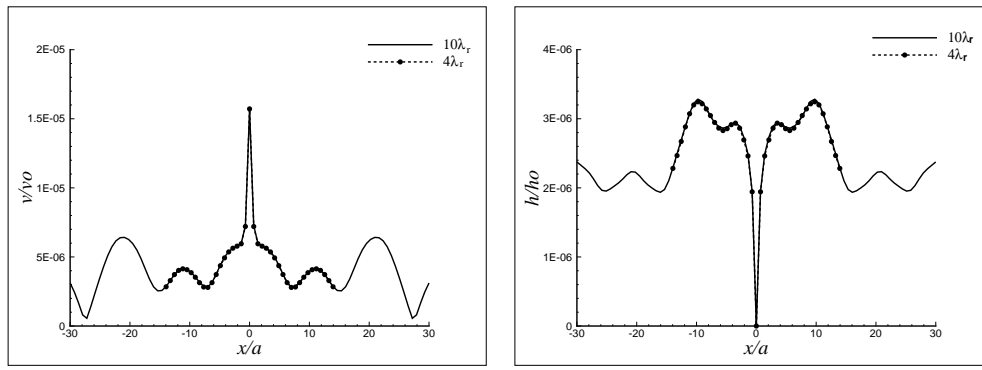


Figure 2: Displacements at the surface of the domain, (left) vertical displacements, (right) horizontal displacements.

A soil deposit of $4\lambda_R$ extent, where λ_R is the Rayleigh wavelength, is subjected at its surface to a harmonic point load of 1kN with a frequency of 20Hz. For the same problem, the domain is extended horizontally to $10\lambda_R$, while keeping all other parameters unchanged. Figure 3 shows the vertical and horizontal displacements at the surface of the domain for both extents. Obviously the results are in very good agreement. This informs us about the ability of the consistent transmitting boundary used above to make the artificial lateral boundaries transparent to the impinging waves. It is worth mentioning that when the presented model is used without the consistent transmitting boundary, the results for the domain extents $4\lambda_R$ and $10\lambda_R$ show significant differences. In all tests, a discretization level of at least 10 nodal points per λ_R is maintained to model the wave pattern.

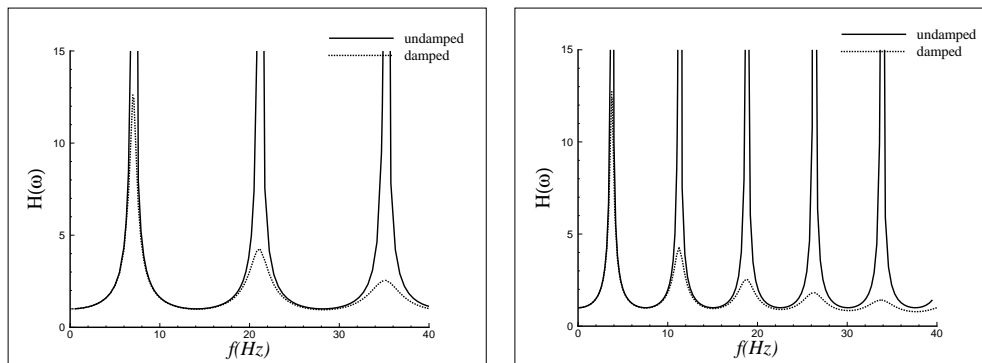


Figure 3: Theoretical results of the variation of surface displacements with frequency, (left) vertical displacements, (right) horizontal displacements.

The following numerical tests deal with the dynamic behaviour of a soil layer of 10m thickness overlying a rigid base. According to theory [2], resonance will occur at an infinite number of natural frequencies. These are depicted in Figure 3 which shows the modulus of the transfer function, representing the ratio between the maximum displacement at the surface and the maximum displacement near the rigid base, for both vertical and horizontal displacements, in the case of damped and undamped soils. This phenomenon is numerically shown by considering the maximum displacements at the surface of the soil deposit for increasing frequency, such as shown in Figure 4. An example of resonance is shown in Figure 5 where the vertical and horizontal displacements are shown for various frequencies. By considering the area A under the displacement curve, normalized with a unit area A_0 , the natural frequencies

shown in Figure 4 are in very good agreement again with those predicted theoretically in Figure 3. For example, the fundamental frequency of the vertical displacements is theoretically determined to be 7.03Hz. Numerically, it is estimated to be around 7Hz, which is very close.

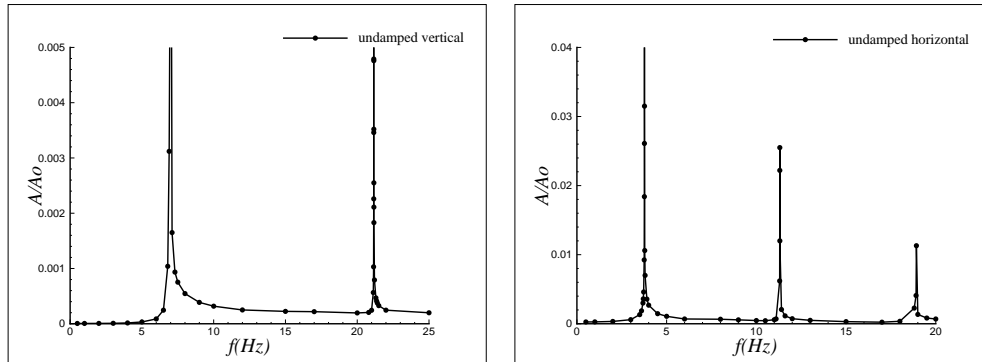


Figure 4: Numerical results of the variation of surface displacements with frequency, (left) vertical displacements, (right) horizontal displacements.

Overall, the results show clearly that the presented model is capable of radiating the waves away towards infinity in the horizontal direction. It is also capable of simulating the behaviour of a soil layer over bedrock. More numerical tests are currently being carried out in order to further validate this model by considering the efficiency of the consistent transmitting boundary when the external harmonic loads are on the lateral artificial boundaries of the computational domain. Also, the effect of different discretization levels and use of unstructured mesh grids are to be studied.

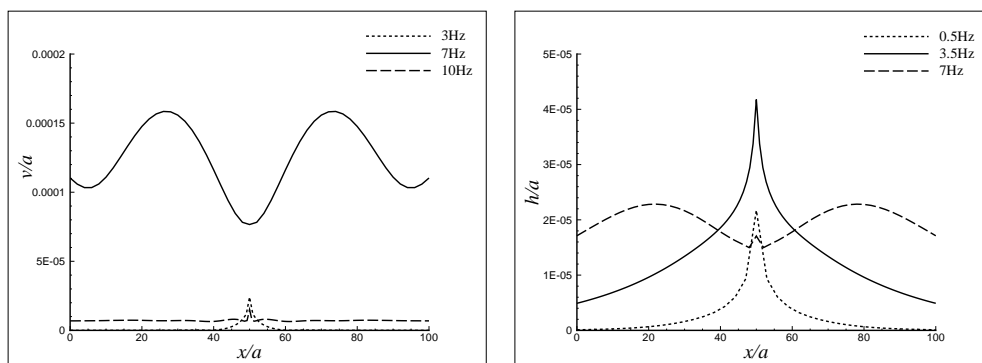


Figure 5: Vertical and horizontal displacements at the surface of a soil deposit overlying bedrock.

References

- [1] G. Waas. Linear two-dimensional analysis of soil dynamics problems in semi-infinite layered media, PhD Dissertation, University of California, Berkeley, 1972.
- [2] S. L. Kramer. Geotechnical earthquake engineering. Prentice Hall, 1996.

TWO-STEP TAYLOR GALERKIN FORMULATION IN LAGRANGIAN SOLID DYNAMICS

Izian Abd Karim¹, Javier Bonet² and Antonio J. Gil²

¹Department of Civil Engineering, University of Putra Malaysia, Serdang, Selangor, 43400

²College of Engineering, University of Swansea, Swansea, SA2 8PP

*390902@swansea.ac.uk

Key Words: *Taylor-Galerkin; solid dynamics; Lagrangian formulation*

ABSTRACT

The purpose of this paper is to propose a Lagrangian finite element formulation for solving solid dynamics problems based on a mixed approach where the unknowns are both momentum and deformation gradient. This scheme is expressed as a first order conservation law which is then integrated in time and discretized in space using the two-step Taylor-Galerkin developed in fluid dynamics [1, 2]. The proposed algorithm allows the using of linear triangles elements without volumetric locking or difficulties in bending applications. A viscous term is also introduced to eliminate high frequencies in the solution. The performance of the algorithm is verified by solving some 1D and 2D test cases involving small and large deformation problems. The numerical results have been compared to the analytical solution and standard Newmark scheme. The results performed well and achieved second order of accuracy.

1 INTRODUCTION

Over the last decade, computational methods of solid dynamics have become a major field of interest both at the research and industrial levels. The comprehensive understanding of many problems in solid dynamics such as shock propagation, impact mechanics, large deformation, moving boundaries and highly nonlinear waves has advanced significantly. In fast structural dynamics, the explicit Lagrangian finite element formulation is often used to model the solid as it automatically satisfies mass conservation. The classical finite element solid dynamics formulation is based on the central difference time integration of the second order dynamic equilibrium equation for the displacements [3]. This approach converges to second order accuracy for displacements but only to first order precision for stresses if linear elements are used. The low order elements such as triangles and tetrahedra exhibit volumetric locking and difficulties in bending application. Furthermore, the displacement based finite elements is unsuitable for the shock propagation problem as it is related to the short wave propagation. This paper is devoted to targeting these difficulties by proposing the formulation based on the first order conservation laws very similar to the systems encountered in first order wave propagation problems.

The proposed scheme is integrated in time and discretized in space using the two-step Taylor-Galerkin

which is well developed and widely used in fluid dynamics finite element formulation [1,2,4]. The scheme has been successfully applied in electromagnetic wave problems [5]. The algorithm allows the use of triangular elements which can prevent the locking effects and perform well in bending application. In this paper, the primary problem variables are based on the mixed formulation where the unknowns are both momentum and deformation gradient.

2 METHODOLOGY

In this section, the governing equation of the first order equation are developed based on mixed formulation. Similar mixed approach conservation law formulation have been used by other authors in Eulerian system [6,7]. Three conservation laws or so-called *balance laws* related to the Lagrangian dynamic system are considered. They are the conservation of linear momentum, deformation gradient and energy;

$$\frac{\partial \mathbf{p}}{\partial t} - \nabla_0 \cdot \mathbf{P} = \rho_0 \mathbf{b} \quad (1)$$

$$\frac{\partial \mathbf{F}}{\partial t} - \nabla_0 \cdot \left(\frac{1}{\rho_0} \mathbf{p} \otimes \mathbf{I} \right) = \mathbf{0} \quad (2)$$

$$\frac{\partial E}{\partial t} + \nabla_0 \cdot \left(\mathbf{Q} - \frac{1}{\rho_0} \mathbf{P}^T \mathbf{p} \right) = 0 \quad (3)$$

where ρ_0 is the density in the reference configuration, $\mathbf{p} = \rho_0 \mathbf{v}$ is the linear momentum, \mathbf{P} is the first Piola-Kirchhoff stress tensor, \mathbf{b} is the external body forces, \mathbf{F} is the deformation gradient, E is the total energy per unit initial volume and \mathbf{Q} is the heat flux vector in the reference configuration.

The above equations can be combined into a general conservation law system of first order equations as;

$$\frac{\partial \mathbf{u}}{\partial t} + \frac{\partial \mathcal{F}_I}{\partial X_I} = \mathcal{S} \quad (4)$$

where \mathbf{u} is the vector unknowns, \mathcal{F}_I is the flux tensor and \mathcal{S} is the source term.

A two-step explicit Taylor-Galerkin finite element method is used to solve the above equations. A general Taylor series expansion of $t = t^{n+1}$ provides;

$$\mathbf{u}^{n+1} = \mathbf{u}^n + \Delta t \frac{\partial \mathbf{u}^n}{\partial t} + \frac{\Delta t^2}{2} \frac{\partial^2 \mathbf{u}^n}{\partial t^2} \quad (5)$$

Neglecting the source term, the first step or *predictor step* will obtain the piecewise linear unknowns in the elements at intermediate time $t = t^{n+\frac{1}{2}}$ as;

$$\mathbf{u}^{n+\frac{1}{2}} = \mathbf{u}^n - \frac{\Delta t}{2} \frac{\partial \mathcal{F}_I^n}{\partial X_I} \quad (6)$$

The second step or *corrector step* given as;

$$\mathbf{u}^{n+1} = \mathbf{u}^n - \Delta t \frac{\partial \mathcal{F}_I^{n+\frac{1}{2}}}{\partial X_I} \quad (7)$$

Let $\Delta \mathbf{u} = \mathbf{u}^{n+1} - \mathbf{u}^n$. Proceeding with the standard Galerkin method, multiply the above equation by a shape function N_a and integrate over the domain V to get the following scheme;

$$\mathbf{M} \Delta \mathbf{u} = \Delta t \int_V \mathcal{F}_I^{n+\frac{1}{2}} \frac{\partial N_a}{\partial X_I} dV - \Delta t \int_{\partial V} N_a \mathcal{F}_N^{n+\frac{1}{2}} dA \quad (8)$$

where \mathbf{M} is the lumped mass matrix and $\mathcal{F}_N = \mathcal{F}_I N_I$.

3 RESULTS AND DISCUSSION

Fig. 1a shows a cantilever bar under axial load. The bar is analysed using a one dimensional mesh comprised of 100 elements using small strains constitutive relationship. Fig. 1b shows the velocity at tip end of the elastic material bar under constant step-function load $T=0.001$ N. The result shows that the two-step Taylor-Galerkin scheme predicts the correct time of the shock and having less oscillations compared to the Newmark scheme.

Fig.2 shows the results obtained when the bar is analysed under the sine-function load $T=0.001\sin(0.1t)$ N. The normal stress at mid-span of the bar is compared using the various number of mesh elements. It can be observed that the solution converges as the mesh become finer and there is good agreement in comparison with the analytical solution.

For 2D example, the cantilever beam is analysed under the step-function point load using linear triangular mesh. Fig. 3b shows the deflected shape of the beam as well as the shear stress contour. The result clearly shows that the using of triangular mesh did not cause any bending difficulties.

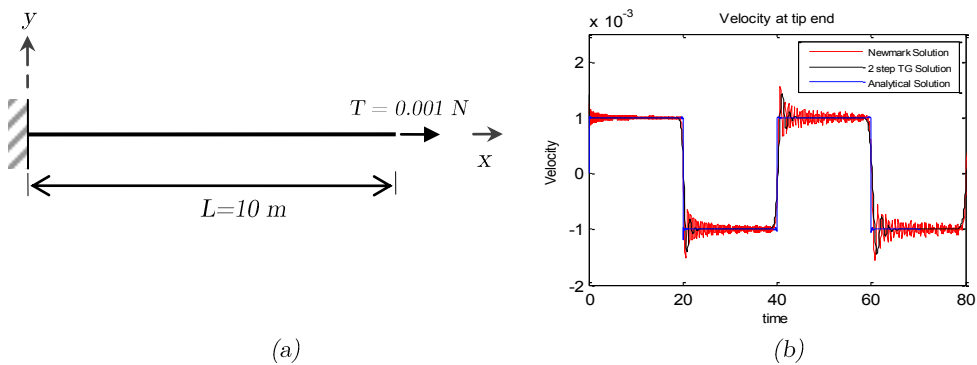


Figure 1: (a) A 1D cantilever bar under axial load (b) Velocity evolution at the tip end

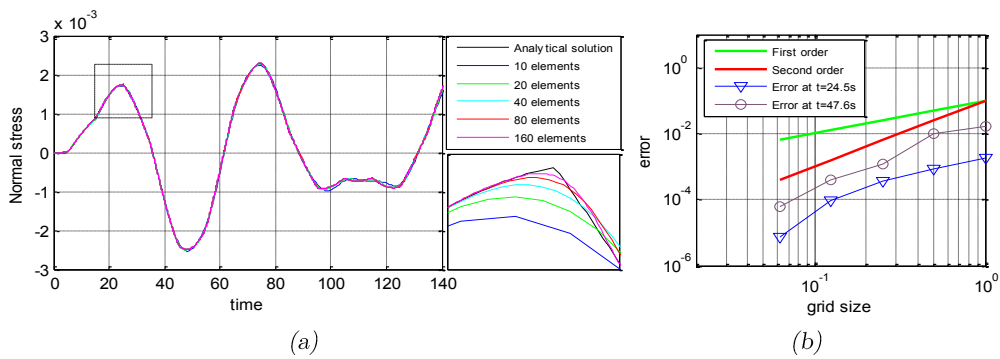


Figure 2: (a) Stress evolution at mid-span of 1D bar under sine-function axial loading (b) Convergence error

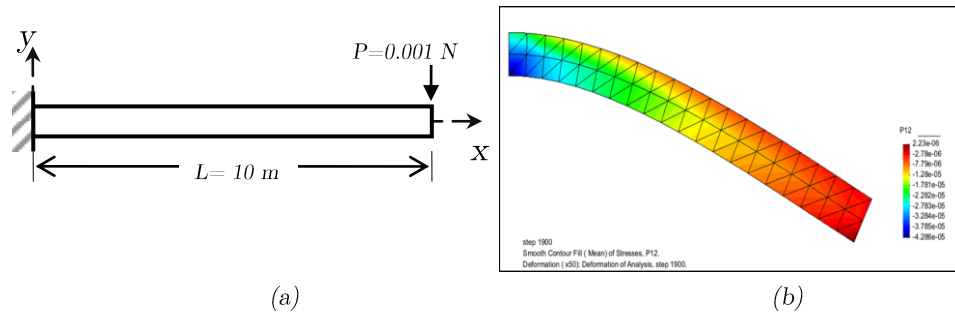


Figure 3: (a) A 2D cantilever beam under point load (b) The deflected shape and shear stress smooth contour

4 CONCLUSION

The preliminary numerical study of the performance of two-step Taylor-Galerkin scheme has been presented in this paper. The present method can be used in 1D and 2D without the difficulty in bending. The convergence study shows that the mixed formulation can achieve second order accuracy for stresses. Further studies are ongoing to investigate the performance of the scheme on the large deformation and plasticity problems.

References

- [1] O.C. Zienkiewicz and R.L. Taylor. *The finite element method*, 5th. Edition, Vol. 3, McGraw Hill, 2000.
- [2] R. Lohner, K. Morgan and O. C. Zienkiewicz. An adaptive finite element procedure for compressible high speed flows. *Computer Methods in Applied Mechanics and Engineering*, 51, 441-465, 1985.
- [3] D.J. Benson. Computational methods in Lagrangian and Eulerian Hydrocodes *Computer Methods in Applied Mechanics and Engineering*, 99, 235-394, 1992.
- [4] J. Peraire. A finite method for convection dominated flows. *PhD Thesis*. University College of Swansea, 1986.
- [5] K. Morgan, P.J. Brookes, O. Hassan and N.P. Weatherill. Parallel processing for the simulation of problems involving scattering of electromagnetic waves. *Computer Methods in Applied Mechanics and Engineering*, 152, 157-174, 1998.
- [6] J.A. Trangenstein and P. Colella. A higher order godunov method for modeling finite deformation in elastic-plastic solid. *Communications on Pure and Applied Mathematics*, 44:41100, 1991.
- [7] G.H. Miller and P. Colella. A high order eulerian godunov method for elasticplastic flow in solids. *of Computational Physics*, 167:131176, 2002.

UPDATING FINITE ELEMENT MODEL FROM VIBRATION MEASUREMENTS

Maung Than Soe, Hua-Peng Chen*, Kong Fah Tee, and Amir M. Alani

School of Engineering, University of Greenwich at Medway, Chatham Maritime, Kent, ME4 4TB, UK

*Corresponding Author, h.chen@gre.ac.uk

Key Words: *model updating; vibration measurement; mode shape; natural frequency*

ABSTRACT

Experimentally measured modal data of a structure play an important role in structural condition assessment. In reality, the measured and theoretically predicted vibration characteristics of the structure are different. This paper presents a model updating methodology of a space frame building model to improve the correlation between physical and its mathematical model with the information of only measured eigendata available. Parameters for material properties and geometric properties are employed to represent the modifications of system parameters. A set of nonlinear equations have to be utilized to solve for the modifications of structural parameters because only a few number of modified eigendata are known. Neither model reduction nor mode shape expansion is required for modal updating because information about incomplete measured modal data can be directly employed. Computational procedures based on the derived nonlinear governing equations are presented for eigendata modification and model updating. This process is finally applied to a 4-story steel frame test structure. Modal parameters are extracted from the vibration measurements. The results from the experiment show that the analytical model is improved after model updating such that modified natural frequencies are closed to the experimental natural frequencies.

Introduction

Several methods for structural system identification have been developed in the past two decades. There are certain differences in modal parameters of the structure between the numerical analysis and the model testing. There is a need to modify the structural model in order to match the results of test and the analytical model. The finite element (FE) model updating methods are often utilized to adjust the mathematical model using the measured modal data to maximize the correlation between the numerical and experimental results. Model updating methods based on sensitivity analysis are usually employed for updating a numerical model, such that it can exactly reproduce an incomplete set of measured eigendata. In the studies of Fox and Kapoor [1], sensitivity analysis based on eigenvalue and eigenvector derivatives were utilized for the dynamic reanalyses of a structure. However, the efficiency of these sensitivity analysis methods is limited because these methods are complicated and suitable for small modifications of structural parameters. In this study, the new model updating technique, which was recently proposed by Chen [2] is utilized to modified structural and modal parameters. A four story steel frame building model is built for experimental purpose. Predicted modal parameters of the structure are required in such a way that the modification can be observed. The test structure is excited in several places by impact hammer. Accelerations are measured from the beam-column joints by a number of accelerometers for certain period of time. Modal parameters are extracted from the measured acceleration. Information on measured eigendata available are employed in model updating to represent the modifications of structural parameters. The results show that the model updating procedures discussed here can be utilized to adjust the analytical model correctly using information about only a limited number of modified eigendata.

Model updating

Numerical correlation and model updating techniques has been utilizing over the recent years. Modal parameters from vibration measurements are employed to represent the structural modification. It is assumed that structural parameters characterize at element level. The perturbations of structural stiffness matrix and mass matrix are then defined as,

$$\Delta K = \sum_{j=1}^{NP} \alpha_j K_j, \quad \Delta M = \sum_{j=1}^{NP} \beta_j M_j \quad (1)$$

where α_j and β_j are stiffness and mass matrix coefficient. In this study, measured eigendata from model testing are directly utilized in model updating.

Model updating from only eigenvalue available

In the case of modified eigenvalues are known and eigenvector are not available, nonlinear equations have to be used to solve for the modifications of structural parameters. The i th eigenvalue λ_i^* and the corresponding eigenvector ϕ_i^* for the modified structural system are expressed by Chen [2] as,

$$\lambda_i^* = \lambda_i + \Delta\lambda_i \quad (2)$$

$$\phi_i^* = \phi_i + \Delta\phi_i \quad (3)$$

$\Delta\lambda_i$ and $\Delta\phi_i$ are perturbations of eigenvalue and eigenvector respectively. They can be expressed as,

$$\Delta\lambda_i = \frac{\phi_i^T [\Delta K - \lambda_i \Delta M] \{\phi_i + \Delta\phi_i\}}{1 + \phi_i^T \Delta M \{\phi_i + \Delta\phi_i\}} \quad (4)$$

$$\Delta\phi_i = \sum_{k=1, k \neq i}^{NC} C_{ik} \phi_k \quad (5)$$

where, C_{ik} is mode participation factor.

$$C_{ik} = \frac{[\sum_{j=1}^{NP} (a_{kji}^K \alpha_j - \lambda_i^* a_{kji}^M \beta_j) + \sum_{j=1}^{NP} \sum_{l=1, l \neq i, k}^{NC} (a_{kjl}^K \alpha_j - \lambda_i^* a_{kjl}^M \beta_j) C_{il}]}{[\lambda_i^* - \lambda_k - \sum_{j=1}^{NP} (a_{kjk}^K \alpha_j - \lambda_i^* a_{kjk}^M \beta_j)]} \quad (6)$$

Sensitivity coefficients associated with structural parameters and eigenvector are defined as,

$$a_{iji}^{K*} = \phi_i^T K_j \phi_i^*, \quad a_{iji}^{M*} = \phi_i^T M_j \phi_i^* \quad (7a)$$

$$a_{kjl}^K = \phi_k^T K_j \phi_l, \quad a_{kjl}^M = \phi_k^T M_j \phi_l \quad (7b)$$

Initial C_{ik} is assumed to be zero. The estimates of both parameters α_j and β_j are then computed from the following equation.

$$\sum_{j=1}^{NP} a_{iji}^{K*} \alpha_j - \lambda_i^* \sum_{j=1}^{NP} a_{iji}^{M*} \beta_j - \Delta\lambda_i = 0 \quad (8)$$

The Tikhonov regularisation algorithm incorporating with L-curve criterion is employed for general ill-conditioned system to estimate the structural parameters α_j and β_j . After the initial α_j and β_j are acquired from Eq (8), the next approximation for the mode participation factors C_{ik} can be calculated from Eq (6). Then, the modified eigenvectors ϕ_i^* are calculated using Eq (3) and Eq (5). Consequently, Eq (6) and Eq (8), as well as Eq (3), are used recursively to compute further approximation for α_j and β_j as well as C_{ik} and the preceding recursive process is repeated until the convergence for system parameters α_j and β_j is achieved.

Model updating from eigenvalue and incomplete eigenvector available

It is assumed that the information about measured frequencies and incomplete measured mode shape ψ_i^{a*} for the modified structural dynamic system is available. The i th eigenvector for the modified structural system then can be expressed by

$$\phi_i^* = \phi_i^{a*} + \phi_i^{u*} \quad (9)$$

Incomplete set of measured mode shapes ψ_i^{a*} are obtained and need to be factored by v_i in order to make the measured mode shapes close to the corresponding part of the analytical mode shapes.

$$\phi_i^{a*} = v_i \psi_i^{a*}, \quad \text{in which mode scale factor } v_i = \frac{\phi_i^{aT} \psi_i^{a*}}{\psi_i^{a*T} \psi_i^{a*}} \quad (10)$$

The modified mode shape ϕ_i^{u*} is computed from

$$\phi_i^{u*} = \phi_i^u + \Delta\phi_i^u \quad (11)$$

where the change of unknown vector $\Delta\phi_i^u$ is expressed as,

$$\Delta\phi_i^u = \sum_{l=1, l \neq i}^{NC} C_{il} \phi_l^u \quad (12)$$

Consequently, the i th complete eigenvector for the modified system ϕ_i^* is obtained from

$$\phi_i^* = \phi_i^a + \sum_{l=1, l \neq i}^{NC} C_{il} \phi_l^u \quad (13)$$

in which ϕ_i^a is defined as,

$$\phi_i^a = v_i \psi_i^{a*} + \phi_i^u \quad (14)$$

Mode scale factor v_i has to be updated for each iteration because ϕ_i^{a*} must be scaled in such a way as to be close to ϕ_i^{u*} . The first estimation for α_j and β_j is then obtained from

$$\sum_{j=1}^{NP} a_{ji}^{K*} \alpha_j - \lambda_i^* \sum_{j=1}^{NP} a_{ji}^{M*} \beta_j - \phi_i^{a*} = 0 \quad (15)$$

where the sensitivity coefficient vectors are defined as

$$a_{ji}^{K*} = \sum_{k=1}^N \frac{\phi_k^T K_j \phi_i^*}{(\lambda_i^* - \lambda_k)} \phi_k^a, \quad a_{ji}^{M*} = \sum_{k=1}^N \frac{\phi_k^T M_j \phi_i^*}{(\lambda_i^* - \lambda_k)} \phi_k^a \quad (16)$$

in which the modified eigenvectors ϕ_i^* are calculated using Eq (13) and the mode participation factors C_{ik} can be obtained from Eq (6). The set of nonlinear equations (8) and (15) are utilized for an iterative solution procedure to solve for system parameters α_j and β_j . Similarly, the initial mode participation factors C_{ik} are assumed to be equal to zero. The first estimation for α_j and β_j is then obtained from Eq (15). The next estimation for the mode participation factors C_{ik} is obtained from Eq (6). The modified eigenvectors ϕ_i^* then can be calculated using Eq (13). Therefore, Eq (8) and Eq (15), as well as Eq (13), are used recursively to compute further estimation for α_j and β_j as well as C_{ik} until the condition of convergence for α_j and β_j is satisfied.

Numerical example

A 3D steel frame building model is used as an experimental structure to demonstrate the effectiveness of the proposed techniques for finite element model updating. The test structure has 4 stories with 40 structural elements including beams, columns and braces, fixed into a rigid steel base plate. The analytical model used has 20 nodes and 40 elements with a total of 120 degree of freedoms (DOF). All structural members have the same material properties with Young's modulus $E = 2.0 \times 10^{11} \text{ N/m}^2$, density $\rho = 7800 \text{ kg/m}^3$, cross-sectional area of column and beam elements is 0.0002 m^2 and bracing is $3.848 \times 10^{-7} \text{ m}^2$. The geometric properties of the structure and element numbers are shown in Fig. 1. Accelerometers are placed at node 5 to 20 measuring only translation displacement reading in Y-direction as shown in Fig. 1. The data set of acceleration is recorded from the excitation of impact hammer by using NI data acquisition device and Labview Signalexpress commercial software. Modal parameters including frequencies and mode shape measurements are extracted from MEscape VES software.

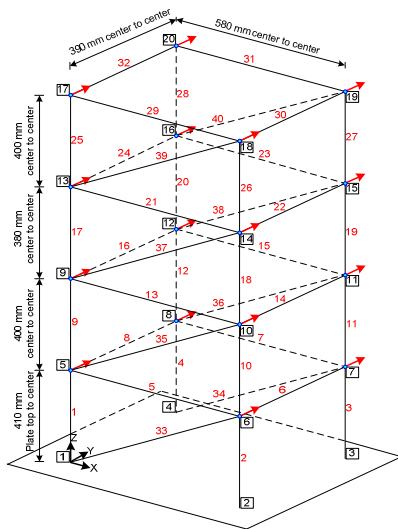


Figure 1. Experimental Structure

Table 1. Natural frequencies for analytical, tested and updated models (Hz)

| Mode | Analytical | Tested | Modified | MAC diagonal value |
|------|------------|--------|----------|--------------------|
| 1 | 10.3552 | 10.3 | 10.2849 | 0.9998 |
| 2 | 25.9379 | 24.3 | 25.9889 | 0.9998 |
| 3 | 31.7607 | 32.2 | 32.2441 | 0.9990 |
| 4 | 45.2474 | 46.0 | 45.7889 | 0.9990 |
| 5 | 51.8178 | 51.4 | 51.8654 | 0.9953 |
| 6 | 65.5715 | 60.3 | 65.7223 | 0.9946 |
| 7 | 70.6418 | 70.4 | 70.9379 | 0.9757 |

The modal properties of the modified structure were computed using the new model updating techniques from eigendata obtained from vibration measurements. The updated natural frequencies through a succession of iterations are listed in Table 1 along with the analytical predictions and experimental results. Results in Table 1 show that structural parameters for stiffness and mass at each element could be correctly adjusted when information about only seven natural frequencies and/or incomplete mode shapes are employed.

Conclusion

The modal parameters including stiffness and mass of a structural system can be updated using the proposed techniques for finite element model updating. The adjusted model closely reproduces the modal data obtained for experimental model for model updating. The results obtained, therefore, show that only a limited measured vibration modal data is required to correctly update the structural parameters such as stiffness and/or mass parameters at element level.

References

- [1] RL Fox and MP Kapoor. Rates of changes of eigenvalues and eigenvectors. *AIAA Journal*, Vol.6, No.12, 2426-2429, 1968.
- [2] HP Chen. Nonlinear perturbation theory for structural dynamic systems. *AIAA Journal*, Vol.43, No.11, 2412-2421, 2005.
- [3] JR Wu and QS Li. Structural parameter identification and damage detection for a steel structure using a two-stage finite element model updating method. *Journal of Constructional Steel Research*, Vol.62, No.3, 231-239, 2006.

CONTROLLING THE CRITICAL TIME STEP VIA THE BIPENALTY METHOD

*Jack Hetherington¹, Antonio Rodríguez-Ferran² and Harm Askes¹

¹University of Sheffield, Department of Civil and Structural Engineering, Mappin Street,
Sheffield S1 3JD, UK

²Universitat Politècnica de Catalunya, Laboratori de Càlcul Numèric, Jordi Girona 1–3,
08034 Barcelona, Spain

*cip09jeh@sheffield.ac.uk

Key Words: *penalty method; constraints; finite element method; critical time step; bipenalty method*

ABSTRACT

It is well known that standard penalty methods can decrease the critical time step of time domain dynamic finite element analyses. The bipenalty method utilises both stiffness and mass penalties in order to impose constraints that have a minimal effect on the eigenfrequencies (and therefore the critical time step) of a finite element system. One way of achieving this goal is to find a ratio of stiffness and mass penalty parameters—the critical penalty ratio (CPR)—that does not affect the maximum eigenfrequency of a system. Here we present a new method of calculating the CPR associated with a finite element formulation through examination of the generic eigenvalue problem. Advantages of the method compared with existing solutions include increased simplicity and generality, and the ability to consider multiple constraints.

1 INTRODUCTION

Penalty methods are a popular technique for imposing constraints in structural analyses. In their most common form penalty constraints are implemented by adding large values of stiffness, referred to as *penalty parameters*, to the stiffness matrix of a system. Penalty methods are more flexible than direct imposition, and are often favoured over Lagrange multipliers for their simplicity and the fact that additional variables do not enter the formulation. The most obvious drawback is that constraints are only approximately imposed; however, errors can usually be kept within acceptable bounds.

In time domain dynamic analysis there is a further problem: when employing conditionally stable time integration schemes, traditional stiffness penalties can decrease the critical time step, potentially increasing computational expense and, if unaccounted for, causing instabilities in the solution [1]. One method that can be used to counter this effect is the so-called *bipenalty method*. This involves the use of mass penalties along with stiffness penalties in order to keep the maximum eigenfrequency at the

desired value; in this way, the critical time step can be kept constant even after adding large penalty parameters into the system.

The ratio between stiffness and mass penalties that ensures the critical time step is unaffected is referred to as the *critical penalty ratio* (CPR), and a method for calculating it was first given in [2]. However, the calculation method suffers from the drawbacks that it does not account for multiple constraints and, since the eigenproblem associated with the full, penalised system must be analysed, becomes increasingly difficult to employ for more complex element types. Bipenalty formulations have also been developed by Asano [3], and Paraskevopoulos et al. [4], although neither formulation provides a method by which the CPR can be calculated.

In this paper, we present a method of calculating the CPR for a given finite element which relies only upon the maximum eigenfrequency of the *unpenalised* element system, giving greater simplicity and generality. An arbitrary number of absolute constraints are accounted for in the formulation.

2 THE BIPENALISED PROBLEM

The critical time step for the central difference time integration scheme is given by

$$t_{\text{crit}} = \frac{2}{\omega_{\text{max}}} \quad (1)$$

where ω_{max} is the maximum eigenfrequency of an individual finite element. Therefore, to keep the critical time step constant after the additional of penalties, we must ensure that the maximum eigenfrequency is not affected. The eigenfrequencies are found, for the unpenalised problem (UP), from

$$\mathbf{K} - \omega_i^2 \mathbf{M} \mathbf{u}_i = \mathbf{0} \quad (2)$$

where \mathbf{K} and \mathbf{M} are the stiffness and mass matrices, respectively, and the eigenvectors \mathbf{u}_i and corresponding eigenfrequencies ω_i form the n solutions. The bipenalised problem (BP), in which absolute constraints have been applied to the first k DOF, is given by

$$[\mathbf{K} + \mathbf{K}^{\text{P}}] - \omega_i^2 [\mathbf{M} + \mathbf{M}^{\text{P}}] \mathbf{u}_i = \mathbf{0} \quad (3)$$

where \mathbf{K}^{P} and \mathbf{M}^{P} contain the stiffness and mass penalty parameters, α_{s} and α_{m} , and are of the form

$$\mathbf{K}^{\text{P}} = \alpha_{\text{s}} \begin{bmatrix} \mathbf{I}_k & \mathbf{0} \\ \mathbf{0} & \mathbf{0} \end{bmatrix}; \quad \mathbf{M}^{\text{P}} = \alpha_{\text{m}} \begin{bmatrix} \mathbf{I}_k & \mathbf{0} \\ \mathbf{0} & \mathbf{0} \end{bmatrix} \quad (4)$$

where \mathbf{I}_k is the identity matrix of size $k \times k$. The n solutions of the BP are given by \mathbf{u}_i and ω_i . For a detailed derivation of the bipenalty method for absolute constraints, see [2].

3 RELATING CPR TO MAXIMUM EIGENFREQUENCY

The relationship we have established between the CPR and the maximum unpenalised eigenfrequency can be stated simply as

$$R_{\text{crit}} = \omega_{\text{max}}^2 \quad (5)$$

That is, (for large penalty parameters) the critical penalty ratio can be found from the square of the maximum unpenalised eigenfrequency. The full proof requires showing the following three things:

1. If $R = \omega_n^2$, there is no eigenfrequency of the BP that exceeds the maximum eigenfrequency of the UP.
2. If $R = \omega_n^2$, the eigenpair (ω_n, \mathbf{u}_n) , an eigensolution of the UP, is also an eigensolution of the BP.
3. If the penalty ratio is selected such that $R > \omega_n^2$, the maximum eigenfrequency of the BP is greater than that of the UP, for large α_m .

Unfortunately, we only have space to provide proof of the first point here. Items 2 and 3 above are considered to be an extension of that original proof, and will be provided in a separate publication.

In the following we make use of the Rayleigh quotient, defined as

$$\rho(\mathbf{v}) = \frac{\mathbf{v}^T \mathbf{K} \mathbf{v}}{\mathbf{v}^T \mathbf{M} \mathbf{v}} \quad (6)$$

where \mathbf{v} is any non-zero vector. A useful property of the Rayleigh quotient is that it is bounded by the minimum and maximum eigenvalues of the system [5]. That is,

$$\omega_1^2 \leq \rho(\mathbf{v}) \leq \omega_n^2 \quad (7)$$

Now, if we consider the Rayleigh quotient of the BP, we have

$$\rho_{\text{BP}}(\mathbf{v}) := \frac{\mathbf{v}^T (\mathbf{K} + \mathbf{K}^p) \mathbf{v}}{\mathbf{v}^T (\mathbf{M} + \mathbf{M}^p) \mathbf{v}} = \frac{\mathbf{v}^T \mathbf{K} \mathbf{v} + \alpha_s \|\mathbf{v}^p\|^2}{\mathbf{v}^T \mathbf{M} \mathbf{v} + \alpha_m \|\mathbf{v}^p\|^2} \quad (8)$$

where \mathbf{v}^p is a vector containing only the first k entries of \mathbf{v} (i.e., the entries associated with the bipenalised DOF only). Now we assume that $R = \omega_{\text{max}}^2$, as stated in (5), and substitute in the Rayleigh quotient of the UP, $\rho_{\text{UP}}(\mathbf{v})$. Taking into account (7) we then have

$$\rho_{\text{BP}}(\mathbf{v}) = \frac{\rho_{\text{UP}}(\mathbf{v}) \mathbf{v}^T \mathbf{M} \mathbf{v} + R \alpha_m \|\mathbf{v}^p\|^2}{\mathbf{v}^T \mathbf{M} \mathbf{v} + \alpha_m \|\mathbf{v}^p\|^2} \leq \omega_n^2 \frac{\mathbf{v}^T \mathbf{M} \mathbf{v} + \alpha_m \|\mathbf{v}^p\|^2}{\mathbf{v}^T \mathbf{M} \mathbf{v} + \alpha_m \|\mathbf{v}^p\|^2} = \omega_n^2 \quad (9)$$

Therefore, $\rho_{\text{BP}}(\mathbf{v})$ is bounded from above by ω_n^2 , which means that *no eigenvalue of the BP can be larger than the largest eigenvalue of the UP, if we set $R = \omega_{\text{max}}^2$* . After extending the proofs to include all three of the items provided earlier, we assert that the relationship given in (5) holds true, and, given that, the CPR for a given element type can be calculated as follows:

1. Derive the element stiffness and mass matrices.
2. Solve $\det \mathbf{K} - \omega_i^2 \mathbf{M} = 0$ for ω_i .
3. Select $\max(\omega_i)$ and calculate CPR from $R_{\text{crit}} = \omega_{\text{max}}^2$.

4 NUMERICAL VERIFICATION

In order to verify the method, the CPR is calculated using the process above for a few simple element types. The elements are then used to form a 10 m cantilever beam, with a constant point force of 10 kN acting vertically downwards at its tip. The boundary conditions (rigid supports) are applied using the bipenalty method, with a constant stiffness penalty parameter, $\alpha_s = 10^{13}$ N/m. The material properties are $E = 10^9$ N/m², $\rho = 1000$ kg/m³ and $\nu = 0.3$ in all cases. The central difference scheme time integration scheme is used, with a critical time step, so that the stability of each analysis can be assessed. The results (given in Table 1) show t_{unstable} , the time at which instability is first detected; here we assume instability has occurred when the maximum displacement reaches 10^{10} m. For brevity, details of the individual element formulations will not be provided here, but will be given in a separate publication.

We see from the results that using $R = R_{\text{crit}}$ is safe in all cases; no instability is detected in the first 60 s of any analysis. Increasing the penalty ratio by even a small amount causes instability to occur, demonstrating the crisp boundary provided by the CPR.

| Element type | Mass matrix | t_{unstable} (s) | | | |
|-------------------------------|-------------|---------------------------|------------------------|-------------------------|-------------------|
| | | $R = 1.01R_{\text{crit}}$ | $1.001R_{\text{crit}}$ | $1.0001R_{\text{crit}}$ | R_{crit} |
| Square, selective integration | Lumped | 0.225898 | 0.712834 | 2.702412 | - |
| | Consistent | 0.115931 | 0.363251 | 1.190708 | - |
| Right-angled triangle | Lumped | 0.163204 | 0.508923 | 1.833244 | - |
| | Consistent | 0.081602 | 0.261625 | 1.842588 | - |
| Parallelogram | Lumped | 0.219030 | 0.693978 | 2.845849 | - |
| | Consistent | 0.097597 | 0.307217 | 1.001001 | - |

Table 1: Time at which instability was detected for various values of R , for a few common plane stress elements. Blank entries indicate that no instability was detected within 60 s.

5 CONCLUSIONS

This work presents a simple method of finding the CPR for a given finite element formulation directly from its maximum unpenalised eigenfrequency. This allows the use of the bipenalty method in order to ensure that the critical time step of a conditionally stable time domain analysis is not affected by the addition of penalties.

Closed form expressions for the CPR can be found for simple element types; however, it is clear that closed form expressions will not be available for more complex elements, due to difficulties regarding element formulation and finding an analytical solution to the associated eigenvalue problem. However, numerical methods (e.g., direct iteration) are available for calculating the maximum eigenfrequency of a system, and future work will investigate how best to utilise them in order to select suitable penalty parameters. In addition, extending the proof given above to include relative constraints, such as those used in contact-impact problems, will be the subject of further research.

References

- [1] T. Belytschko and M. Neal. Contact-impact by the pinball algorithm with penalty and Lagrangian methods. *International Journal for Numerical Methods in Engineering*, 31(3):547–572, 1991.
- [2] H. Askes, M. Caramés-Saddler, and A. Rodríguez-Ferran. Bipenalty method for time domain computational dynamics. *Proceedings of the Royal Society A: Mathematical, Physical and Engineering Sciences*, 466(2117):1389–1408, 2010.
- [3] N. Asano. A penalty function type of virtual work principle for impact contact problems of two bodies. *Bulletin of the Japan Society of Mechanical Engineers*, 29(257), 1986.
- [4] E. A. Paraskevopoulos, C. G. Panagiotopoulos, and G. D. Manolis. Imposition of time-dependent boundary conditions in FEM formulations for elastodynamics: critical assessment of penalty-type methods. *Computational Mechanics*, 45(2-3):157–166, 2010.
- [5] K.-J. Bathe. *Finite element procedures*. Prentice Hall, Englewood Cliffs, 1996.

DYNAMIC MODELLING USING MIXED STRESS ELEMENTS

*G. Edwards¹, C.J. Pearce¹ and Ł. Kaczmarczyk¹

¹School of Engineering, University of Glasgow, Glasgow, G12 8LT

*g.edwards.1@research.gla.ac.uk

Key Words: *structures; hybrid-Trefftz; dynamic loading; heterogeneous material*

ABSTRACT

The overall mechanical response of many materials is rooted in the behaviour of the heterogeneous microstructure. There are a number of microstructure-driven phenomena such as wave dispersion and size effects that can be investigated by a detailed modelling of the material microstructure. This paper develops a formulation for the modelling of heterogeneous materials subject to dynamic loading and supplements the work of Kaczmarczyk and Pearce[2] for a hybrid-Trefftz (HT) stress element formulation for the modelling of cohesive cracks in heterogeneous materials subject to static loads. Here a mixed formulation is considered.

1 INTRODUCTION

The “Trefftz method” was first introduced in 1926 by Erich Trefftz[3] and was the start point for the development of the formulation which will be discussed in this paper. In a classical finite element there is one continuous field covering the domain of the element, Ω_e , where the displacements at any point in the element relates to the strains and stresses. In the hybrid formulation [2], two fields were present, one within the element domain Ω_e and one on the element boundary, Γ_e . However, for the modelling of dynamic problems, the hybrid formulation cannot be used and an alternative mixed formulation is considered instead.

The features of the mixed formulation presented here are:

- Displacement boundary conditions and displacement compatibility are enforced in weak integral sense.
- Traction boundary conditions and stress compatibility are enforced in a strong integral sense.
- Compatibility of accelerations associated with the mixed approximation fields is enforced in a strong integral sense.

Furthermore, the equilibrium equation for dynamic problem is fulfilled locally inside the element domain. This element has been designed for dynamics problems of fracturing quasi-brittle heterogeneous materials, where accurate representation of the stress field is considered more important than the representation of the displacement field.

2 MIXED FORMULATION

The work presented here is largely based on the work of Teixeira de Freitas [1] and Kaczmarczyk and Pearce[2]. In the formulation, an element, e , is considered with domain Ω_e which has a boundary $\Gamma = \Gamma_\sigma \cup \Gamma_u$, where $\Gamma_\sigma \cap \Gamma_u = \emptyset$. The prescribed displacements are given as $\bar{\mathbf{u}}$ on Γ_u while the tractions on the boundary of the element are given by $\bar{\mathbf{t}}$ on Γ_σ . The body forces were eliminated for simplicity in this case. The governing relations between displacements, strains and stresses are as follows:

$$\mathbf{L}^T \boldsymbol{\sigma} = \mathbf{L}^T \mathbf{S}_v \mathbf{v} = \rho \ddot{\mathbf{u}} \quad \text{in } \Omega_e \quad (1)$$

$$\boldsymbol{\varepsilon} = \mathbf{C} \boldsymbol{\sigma} = \mathbf{C} \mathbf{S}_v \mathbf{v} \quad \text{in } \Omega_e \quad (2)$$

$$\mathbf{L} \mathbf{u} = \mathbf{L} \mathbf{U}_v \mathbf{v} = \boldsymbol{\varepsilon} \quad \text{in } \Omega_e \quad (3)$$

$$\mathbf{u} = \bar{\mathbf{u}} \quad \text{on } \Gamma_u \quad (4)$$

$$\mathbf{N} \boldsymbol{\sigma} = \bar{\mathbf{t}} \quad \text{in } \Gamma_\sigma \quad (5)$$

$$\mathbf{u}(t = 0) = \mathbf{u}_0 \quad \text{in } \Omega \quad (6)$$

$$\dot{\mathbf{u}}(t = 0) = \dot{\mathbf{u}}_0 \quad \text{in } \Omega \quad (7)$$

where \mathbf{L} is the differential operator, \mathbf{S}_v is the matrix of stress approximation functions in the element, \mathbf{U}_v is the displacement approximation functions derived from \mathbf{S}_v and \mathbf{v} is the vector of stress degrees of freedom.

The stress approximation functions S_v are derived from an assumed displacement approximation field with the element using Legendre polynomials shown in (8).

$$P_m(x) = \frac{1}{2^m m!} \frac{d^m}{dx^m} [(x^2 - 1)^m] \quad (8)$$

As stated above, compatibility between the accelerations derived from the mixed approximation fields was enforced in a strong integral sense. The displacements within the element are approximated independently of the stress approximation field as:

$$\mathbf{u} = \mathbf{U}_\Omega \mathbf{q} \quad (9)$$

Thus the compatibility relation for accelerations is given by:

$$\int_{\Omega} \mathbf{w}_3^T (\rho^{-1} \mathbf{L}^T \mathbf{S}_v \mathbf{v} - \mathbf{U}_\Omega \ddot{\mathbf{q}}) d\Omega = 0 \quad (10)$$

where \mathbf{w}_3 is the weighting function chosen as $\rho \mathbf{U}_\Omega$ and this ensure that the integral above has the dimensions of energy.

Applying the Newmark method for time integration and supplementing equations from [2] by the acceleration compatibility equation above, yields the following linear system of equations:

$$\begin{bmatrix} \mathbf{F} & -\mathbf{A}^T + \mathbf{M}^T \\ \mathbf{A} - \mathbf{M} & \frac{1}{\Delta t^2 \alpha} \mathbf{B} \end{bmatrix} \begin{bmatrix} \Delta \mathbf{v} \\ \Delta \mathbf{q} \end{bmatrix} = \begin{bmatrix} \mathbf{p}_u - \mathbf{F} \mathbf{v}_n - \mathbf{M}^T \mathbf{q}_n + \mathbf{A}^T \mathbf{q}_n \\ \mathbf{p}_\sigma - \mathbf{A} \mathbf{v}_n - \mathbf{B} \left[\frac{-1}{\Delta t \alpha} \dot{\mathbf{q}}_n - \frac{1}{\alpha} \left(\frac{1}{2} - \alpha \right) \ddot{\mathbf{q}}_n \right] + \mathbf{M} \mathbf{v}_n \end{bmatrix} \quad (11)$$

$$\begin{aligned}\mathbf{F} &= \int_{\Omega} \mathbf{S}_v^T \mathbf{C} \mathbf{S}_v d\Omega \\ \mathbf{A} &= \int_{\Gamma} \mathbf{U}_{\Gamma}^T \mathbf{N} \mathbf{S}_v d\Gamma \\ \mathbf{p}_u &= \int_{\Gamma_u} (\mathbf{N} \mathbf{S}_v)^T \bar{\mathbf{u}} d\Gamma\end{aligned}$$

$$\begin{aligned}\mathbf{p}_{\sigma} &= \int_{\Gamma_{\sigma}} \mathbf{U}_{\Gamma}^T \bar{\mathbf{t}} d\Gamma \\ \mathbf{B} &= \int_{\Omega} \mathbf{U}_{\Omega} \rho \mathbf{U}_{\Omega} d\Omega \\ \mathbf{M} &= \int_{\Omega} \mathbf{U}_{\Omega}^T \mathbf{L}^T \mathbf{S}_v d\Omega\end{aligned}$$

where α is a Newark time integration parameter and Δt is the time step used. This system of equations can be solved on element level using static condensation that will lead to a symmetric, positive definite system stiffness matrix.

3 RESULTS

Simple static and dynamic benchmark problems have been considered to validate the formulation and its computer implementation. First a simple problem comprising two triangular elements subject to uniaxial tension is presented. The results for this static analysis are shown in Figure 1 and Figure 2.

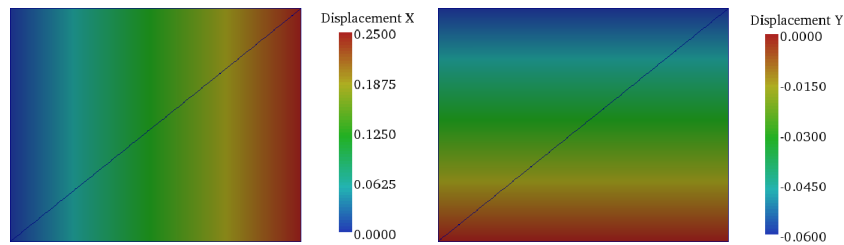


Figure 1: Displacement Results for Static Case of New Formulation

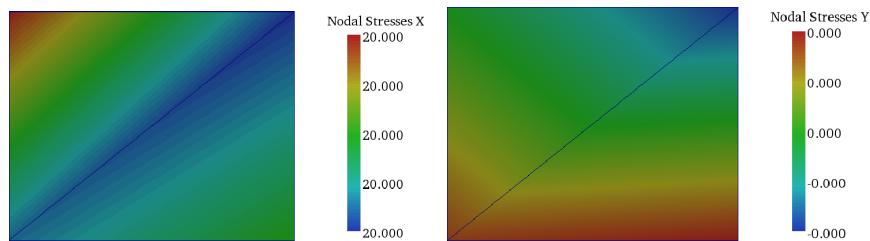


Figure 2: Stress Results for Static Case of New Formulation

Second, a bar comprising 4 triangular elements was subject to a constant velocity at every node in the x direction and the results for the 10th time step are shown in Figure 3.

4 CONCLUSIONS

In conclusion, a new formulation for a mixed stress element for dynamic problems has been presented which represents an extension of a hybrid stress finite element formulation. The next stage of this work is to validate the formulation for more complex dynamic loading scenarios. Furthermore, the formulation will be applied to 3D problems.

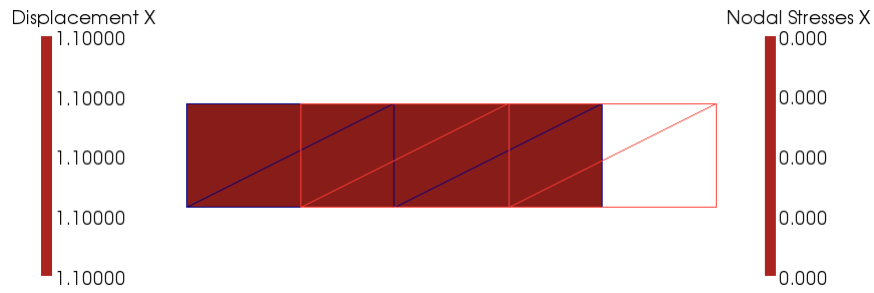


Figure 3: Results for Constant Velocity Applied at Each Node at 10th Time Step

References

- [1] J Freitas. Formulation of elastostatic hybrid-Trefftz stress elements. *Computer Methods in Applied Mechanics and Engineering*, 153(1-2):127–151, January 1998.
- [2] Łukasz Kaczmarczyk and Chris J. Pearce. A corotational hybrid-Trefftz stress formulation for modelling cohesive cracks. *Computer Methods in Applied Mechanics and Engineering*, 198(15-16):1298–1310, March 2009.
- [3] E. Trefftz. Ein Gegenstück zum ritzschen Verfahren. *In: Proc. 2nd Int. Cong. Appl. Mech.*, pages 131–137., 1926.

NUMERICAL CALCULATIONS OF DYNAMIC PRESSURE DURING HOPPER DISCHARGE USING AN UNCOUPLED ALE-FORMULATION

*Yin Wang, Y. Lu and Jin. Y. Ooi

Institute for Infrastructure & Environment, School of Engineering, Univ. of Edinburgh, Edinburgh, EH9 3JL, UK

*yin.wang @ed.ac.uk

Key Words: *silos and hoppers; ALE; Finite Element; granular solid; discharge pressure*

ABSTRACT

This paper describes a finite element analysis of the granular flow in a conical silo hopper, which has been performed to investigate the dynamic phenomena that can occur during discharge. The behaviour of the stored solid was modelled using a continuum mechanics approach formulated in an Arbitrary Lagrangian Eulerian (ALE) frame of reference. The temporally averaged discharge pressures obtained from the FE simulation are compared with those from the most commonly quoted theoretical solutions and are found to be in good agreement. The predicted dynamic events are studied and the results provide useful insight into the fluctuating pressure patterns often observed in silo discharge experiments.

1 INTRODUCTION

Silos are widely used for the storage of bulk solid in industry. In the design of silos, the pressure acting on the silo walls during filling and discharge are the main loads that need to be determined for design. Silo pressure during filling and storing are generally accepted to be well represented by Janssen type pressure equation [1]. However during discharge, the silo pressure tends to exhibit temporal and spatial variations and more work is needed to define the discharge pressure more accurately [2,3]. The present study describes results of a finite element simulation carried out using an Uncoupled Arbitrary Lagrangian-Eulerian (ALE) formulation with an explicit time integration scheme. The method is able to simulate the silo discharge process without mesh distortion problem which are often encountered in the modeling of granular flow involving very large deformation such as silo discharge [4]. The dynamic events predicted by the present simulation were studied to provide further insight into the fluctuating pressure patterns often observed in silo discharge experiments. The oscillating discharge pressures were found to be dominated by two major frequencies at about 5 Hz and less than 1 Hz, respectively. The causes for these events have been investigated which lead to the conclusion that the stress wave and moving shear zone phenomena are responsible for these effects.

2 ALE MODEL IMPLEMENTATION

The Lagrangian and Eulerian are two major descriptions of motion used in the algorithm of continuum mechanics. In a purely Lagrangian formulation, it is difficult to describe large deformation because the element mesh can become severely distorted in the computational domain when no remeshing is used or when a remeshing operation becomes ineffective. In a purely Eulerian formulation, problems may arise when free surface condition, prescribed boundary condition or continuum deformation with history-dependent constitutive relations are considered. In order to overcome the shortcomings of both formulations and to combine their best features, an Arbitrary Lagrangian-Eulerian technique has been developed [5]. In this method, the mesh is neither connected to the material nor fixed spatially but can be prescribed in an arbitrary manner. Meanwhile, the convective term is introduced in a remap of state

variables between material and mesh.

The entire silo discharge process is simulated using ALE method available in the program Abaqus/Explicit code [6]. As a result, the deformation process is split into a Lagrangian phase and an Eulerian phase combined with a smoothing phase, as shown in Fig. 1. In Lagrangian phase, the material body deforms from its material configuration to its spatial one with a high distortion of the spatial discretization. In order to reduce the distortion a smoothing phase is then applied, which leads to the final spatial discretization. This allows the computation of convective terms and further to obtain history-dependent variables in Eulerian phase.

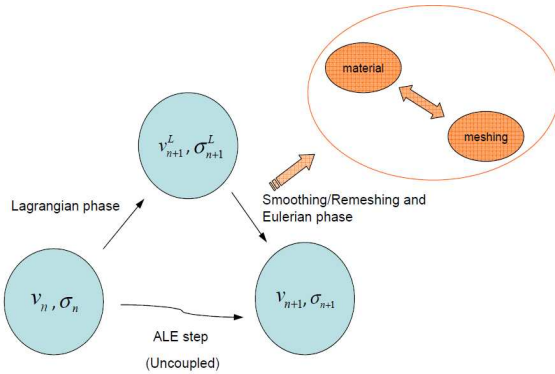


Fig. 1 ALE solution process: history-dependent variables (v_n, σ_n) in n time step

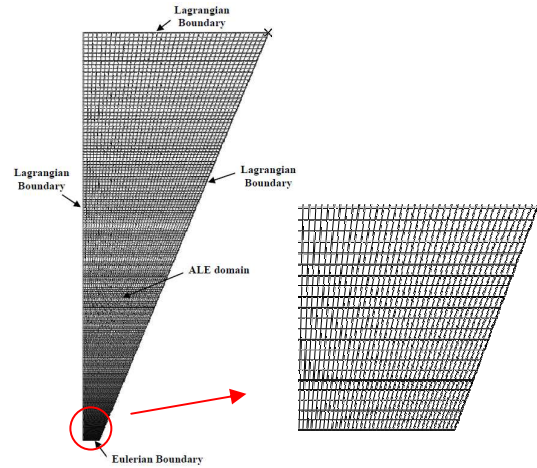


Fig. 2 Discretization grid and ALE boundary definitions

An explicit time integration method was used [6]. The hopper was modelled as an axisymmetric structure. Fig. 2 shows the ALE mesh for the granular solid. An adaptive mesh constraint of zero-movement was applied to each node at the outlet, while an Eulerian surface-defined region is defined to the outlet edge to enable the granular solid to flow out through the outlet. A Lagrangian surface-defined region is applied to the other three boundaries of the solid domain (see Fig 2). The solid-wall contact was modelled using the Coulomb friction model with a constant wall friction coefficient and a penalty constraint enforcement method to control the contact behaviour by relating the constraint normal pressure to the penetration distance. Full details about the definition and choice of parameters in the ALE model can be found in Wang et al. [7].

2 FE RESULTS

The predicted wall normal pressure distributions during filling and discharge are compared with the theoretical solutions in Fig. 3. This shows a reasonable agreement with a greater discrepancy during the discharge phase: the discrepancy is not surprising since Walker's solution [8] for discharge is based on static equilibrium in a horizontal solid slice of conical hopper. Fig. 5 shows the time series for the predicted normal pressure during the discharge at three different positions at the hopper wall. Similar fluctuations has been reported in experimental observations e.g. Ostendorf et al. [9] as shown in Fig. 4. A frequency spectrum analysis for the pressure at point b was made with a Fourier transformation (Fig. 6), which shows two dominant frequencies, one at less than 1 Hz and the other at about 5 Hz.

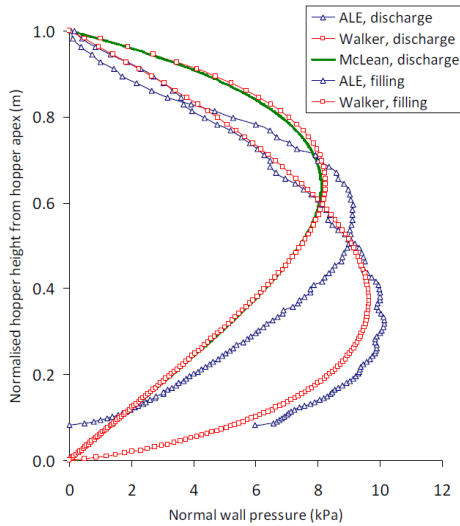


Fig. 3 Wall normal pressure in the conical hopper

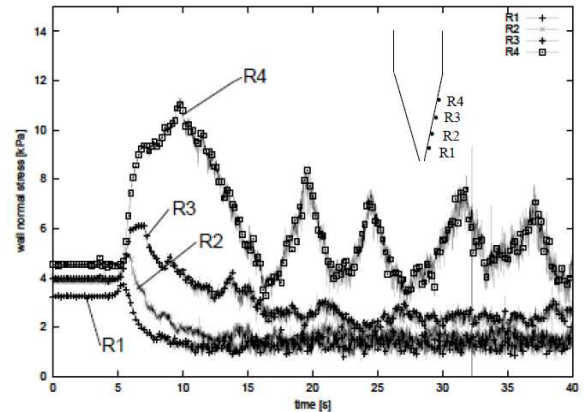


Fig. 4 Wall pressures at various positions during discharge, experimental results by Ostendorf et al., 2003 [9]

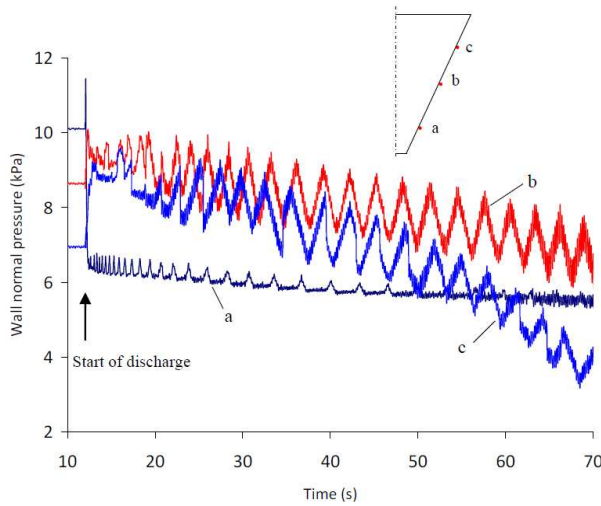


Fig. 5 Wall normal pressures at various positions during discharge by the ALE model

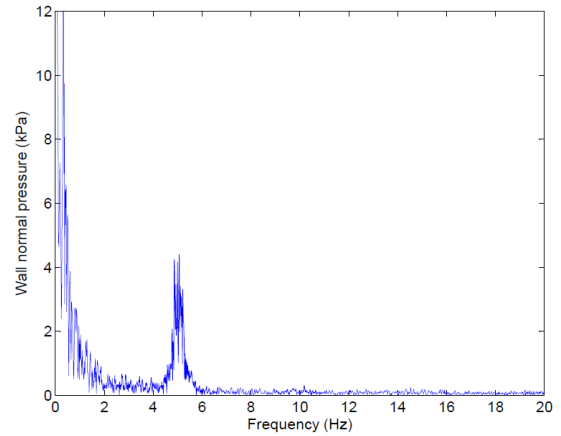


Fig. 6 Frequency spectrum of the predicted normal wall pressure by ALE at point *b*

3 DISCUSSION ON FLUCTUATING PRESSURE

The frequency of any longitudinal wave travelling within the granular solid in the hopper can be estimated from the wave equation for an elastic bar of hopper height with free ends [10].

$$f_n = \sqrt{\frac{E(1-\nu)}{\rho(1+\nu)(1-2\nu)}} / 2h_f = \sqrt{\frac{550000(1-0.3)}{1000(1+0.3)(1-2 \cdot 0.3)}} / 2 \cdot 2.64 \cong 5.2 \text{ Hz}$$

where E denotes the modulus of elasticity, ν is the Poisson's ratio, ρ is the mass density of the fill and h_f is the height of the fill in the hopper. This confirms that the about 5 Hz fluctuations at very small amplitudes in the predicted pressure is caused by the longitudinal wave propagation.

For the fluctuation at much larger amplitudes with frequencies of less than 1 Hz, a probable explanation can be found by studying evolution of shear zone and slip-stick wall motion during discharge. An examination of the propagation of the shear failure zones during discharge (not shown here due to space constraint) reveals an intermittent shear failure arching zone located in the upper half of the hopper. Associated with that, the displacement of the solid adjacent to the wall shows a slip-stick motion as indicated in Fig. 7. Each slip was found to correspond to a reduced stress ratio in the arching shear zone identified. The frequency of the slip-stick motion and intermittent shear zone are all less than 1 Hz which provides a plausible explanation for these larger pressure fluctuations. Further interpretation about the

pressure fluctuations can be found in Wang et al. [6].

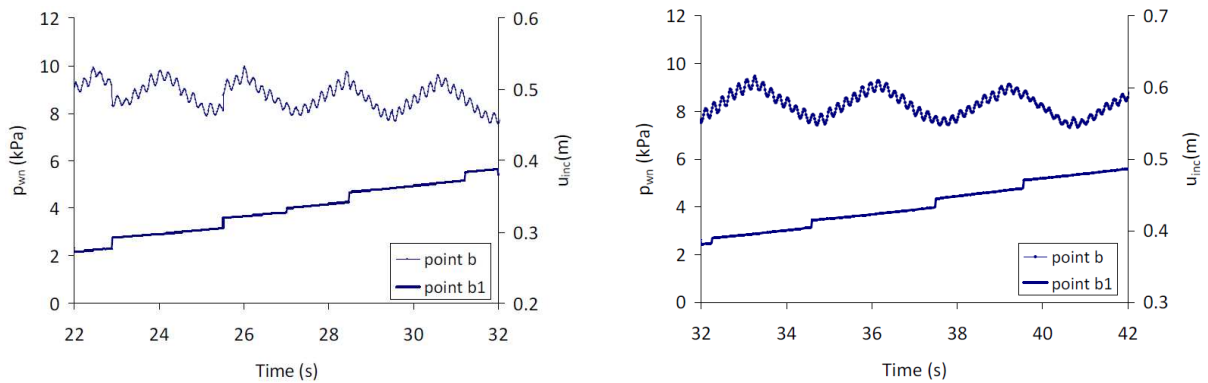


Fig. 7 Wall normal pressure (p_{wn}) at point b and slip displacement (u_{inc}) at point $b1$ at the hopper wall

4 CONCLUSIONS

A finite element analysis of hopper discharge using an uncoupled ALE approach has been successfully performed. An appropriate material model and realistic description of solid-wall interface behaviour are required to obtain proper predictions. The predicted discharge pressures are in good agreement with the theoretical solutions. The dynamic pressure fluctuations have been analyzed and investigated thoroughly. The predicted fluctuations exhibited two primary frequencies. By analyzing the wave effect and the development history of shear zones and slip-stick wall motion, the governing mechanisms have been identified. Further exploration using the ALE model is underway to study the effect of discharge rate and silo geometry.

References

- [1] H.A. Janseen. Versuche uber getreidedruck in silozellen. *Zeitschrift des Vereines Deuischer Ingenieure*, 39 (35), 1045-1049, 1895.
- [2] J.M. Rotter. *Guide for the economic design of circular metal silos*, 1st Edn, Vol.I, Spon Press, 2001.
- [3] J.Y. Ooi and J.M. Rotter. Elastic predictions of pressures in conical silo hoppers. *Engineering Structures*, 13, 1, Jan, 2-12, 1991.
- [4] M.A. Martinez, I. Alfaro and M. Doblare. Simulation of axisymmetric discharging in metallic silos: Analysis of the induced pressure distribution and comparison with different standards. *Engineering Structures*, 24, 1561-1574, 2002.
- [5] J. Donea and A. Huerta. *Finite element methods for flow problems*. 1st Edn, Vol.I, Wiley Press, 2003.
- [6] Hibbitt, Karlsson & Sorensen Inc. 2008. ABAQUS/Explicit user's manual, version 6.8.
- [7] Yin. Wang, Y. Lu and Jin.Y. Ooi Pressure prediction for silo discharge using ALE technique. Internal Report. School of Engineering, University of Edinburgh, 2010.
- [8] D.M. Walker. An approxiamte theory for pressures and arching in hoppers. *Chemical Engineering Science*, Vol.21, 975-997, 1966.
- [9] M. Ostendorf, J. Schwedes, J.U. Bohrsen and H. Antes. Dynamic measurement and simulation of bulk solids during silo discharge. *TASK QUARTERLY*, 7(4), 611-621, 2003.
- [10] S. Prakash, *SOIL DYNAMICS*, 1st Edition, Vol. 1, McGraw-Hill, 1981.

ENERGY CONSERVATION OF THE NEWMARK METHOD FOR DYNAMIC CONTACT ANALYSIS

*H. Zolghadr Jahromi and B.A. Izzuddin

Department of Civil and Environmental Engineering
 Imperial College London, London SW7 2AZ, U.K.

*hamed.jahromi08@imperial.ac.uk

Key Words: *energy conservation; Newmark method; contact analysis; computational methods; finite element method*

ABSTRACT

Solution procedures typically used in finite element analysis programs for contact problems are generally based on displacement constraints via Lagrangian multipliers or penalty functions. It is widely established that the well-known average acceleration Newmark scheme with a Lagrangian displacement constraint leads to spurious energy gain/loss upon contact which cannot be controlled with the refinement of temporal and/or spatial discretisation [1]. The penalty method also suffers from a non-physical energy gain/loss upon contact [2], though better accuracy in energy conservation may be achieved through temporal refinement. However, satisfying both the acceptable penetration criteria and energy conservation can lead to an excessively small time-step. Accordingly, a Lagrangian velocity constraint methodology is suggested with the Newmark average acceleration method for frictionless energy conserving dynamic contact analysis. It is further demonstrated that an approximate displacement constraint is achieved by enforcing the associated velocity constraint, while the magnitude of the gap can be reduced by temporal refinement. Moreover, it is shown that the energy conservation of contacting systems can be achieved through refining the mesh and/or reducing the time-step size. Hence, the proposed method leads to a more robust algorithm which can accurately model the interactions of solids subject to dynamic contact, while avoiding the need for very small time-steps or the determination of the requirements for the penalty stiffness a priori. Finally, numerical studies are presented to highlight the relative advantages of the Lagrangian velocity constraint method combined with the Newmark scheme for application in dynamic contact analysis using finite element procedures.

1 INTRODUCTION

The solution of highly nonlinear dynamic phenomena in solid and structural mechanics has received considerable attention over the years (e.g. [3]). In this context, the numerical simulation of dynamic contact problems is of great importance due to its frequent application in engineering practice. For this purpose, several methods were developed based on Lagrangian multipliers or penalty functions in an attempt to impose the impenetrability conditions in dynamic contact analysis. The kinematic constraints of impenetrability used in finite element analysis programs commonly work in conjunction with implicit step-by-step integration schemes such as the well-known Newmark average acceleration (so called ‘trapezoidal rule’) and the Midpoint rule. Notwithstanding that the trapezoidal and Midpoint rules show unconditional stability and energy conservation in the linear elastic regime, much work can be found in the literature regarding the loss of those characteristics in dynamic contact analysis (e.g. [1-2]). It is now well established that, rather than a necessary spectral radius criteria, a sufficient condition for unconditional stability in the nonlinear regime can be achieved through the conservation or decay of the total energy within a time-step [4] given as:

$$U_{n+1} - U_n + K_{n+1} - K_n \leq W_{n+1}^{ext} - W_n^{ext} \text{ or } [U]_n^{n+1} + [K]_n^{n+1} \leq [W]_n^{n+1} \quad (1)$$

where, for $i \in \cup_{n=0}^{k-1} \{n\}$ and $n \in \mathbb{N}_0$, the variables U_i , K_i and W_i are respectively the strain energy, kinetic

energy and the work done at time t_i for a given temporal discretisation $\cup_{n=0}^{k-1} \{t_n, t_{n+1}\} = \{0, t_1, \dots, t_k\}$ of the time interval of interest¹.

Several algorithmic energy controlling strategies based on Lagrangian multipliers [1] and penalty functions [2] were proposed for dynamic contact analysis, using the ‘Energy-Momentum Method’ introduced by Simo and Tarnow [3]. However, this method lacks generality for application in common nonlinear finite element analysis programs, since it requires the evaluation of the internal energy at the mid-point of each time-step during analysis. Therefore, specific consideration is given in this paper to different algorithms enforcing the contact constraints using the Newmark family of methods, which enable energy conservation for frictionless linear elastic dynamic contact problems. For these cases, it is shown that a proposed algorithm based on Lagrangian velocity constraint ensures unconditional stability and leads to improved accuracy and convergence by means of temporal and/or spatial refinement.

2 THE NEWMARK METHOD

The single step Newmark method is considered here for dynamic analysis of frictionless contact problems. In this method, the solution for the equation of motion is obtained via the discrete equations:

$$\{d_{n+1}\} = \{d_n\} + \Delta t \{v_n\} + \Delta t^2 \left((1/2 - \beta) \{a_n\} + \beta \{a_{n+1}\} \right) \quad (2)$$

$$\{v_{n+1}\} = \{v_n\} + \Delta t \left((1 - \gamma) \{a_n\} + \gamma \{a_{n+1}\} \right) \quad (3)$$

where $\Delta t = t_{n+1} - t_n$ is the time-step for a given temporal discretisation; $\{d_n\}$, $\{v_n\}$ and $\{a_n\}$ are nodal kinematic matrices for displacement, velocity and acceleration evaluated at t_n , respectively; β and γ are algorithm parameters defining the characteristics of temporal discretisation. To investigate the numerical stability of the Newmark method associated with the nonlinearity in dynamic contact phenomena, the incremental energy balance of a linear elastic system is considered for nodal contact problems. For this system, assuming a constant and symmetric mass matrix during the analysis time interval, the incremental energy balance in terms of the nodal kinematic matrices is:

$$[U + K]_n^{n+1} = \{\Delta d\}^T \left\{ 1/2(f_{n+1} + f_n) + (\gamma - 1/2)\Delta f \right\} - 1/2(\beta - 1/2\gamma)\Delta t^2 \left[\{a\}^T [M] \{a\} \right]_n^{n+1} \quad (4)$$

$$- (\gamma - 1/2) \left(\{\Delta d\}^T [k_T] \{\Delta d\} + (\beta - 1/2\gamma)\Delta t^2 \{\Delta a\}^T [M] \{\Delta a\} \right)$$

$$\text{where for } i \in \cup_{n=0}^{k-1} \{n\} \rightarrow [M] \{a_i\} + [k_T] \{d_i\} = \sum f_i^{ext} + \sum f_i^{contact} = f_i$$

It can be shown using eq. 4 that for $\beta = \gamma/2 = 0.25$ (i.e. average acceleration scheme) the total potential energy is conserved for a linear elastic system under free vibration. However, the response of this system using Newmark parameters $\beta \neq \gamma/2$ and $\gamma = 1/2$ suffers from a periodic energy fluctuation. Therefore, in this paper, special consideration is given to the Newmark average acceleration scheme.

3 FRICTIONLESS CONTACT CONSTRAINTS

Several methods have been developed over the recent decades to model the dynamic contact phenomenon by enforcing constraints on the displacements of the nodes for the contacting body (called ‘master body’) and the associated nodes/ surface of the impacted body (called ‘slave body’). The conventional penalty spring and Lagrangian displacement multiplier are typical examples of this.

3.1 Lagrangian displacement constraint

In this method for frictionless dynamic contact analysis, the so called ‘Kuhn-Ticker’ kinematic conditions are introduced via a multiplier into the equation of total potential energy, as illustrated below:

$$(i). g_N(d, t_i) = g(d, t_i) \cdot \bar{n} \geq 0 \quad (5)$$

¹ The notation $[\]_n^{n+1}$ defines the incremental difference of the variable within the time step $[t_n, t_{n+1}]$ (i.e. $[\chi]_n^{n+1} = \chi_{n+1} - \chi_n$).

$$(ii). f_i^{contact} \approx f^{contact}(d, t_i) = \tau(d, t_i) \cdot \bar{n} \geq 0$$

$$(iii). f_i^{contact} \cdot g_N(d, t_i) = 0$$

Where $g(d, t_i)$ and $\tau(d, t_i)$ represent, respectively, the closest distance vector and the pressure between the solids along the contact boundaries at the time t_i , and \bar{n} is the unit outward normal to the current contact slave surface. Based on this, the analytical study of the total incremental energy for nodal contact in the linear elastic system (eq. 7) shows that, the energy gain/loss for the trapezoidal rule will occur in two time steps: 1) initial contact $[t_n, t_{n+1}]$, and 2) rebound $[t_{n+k}, t_{n+k+1}]$, where k is the number of time steps in contact. From eq. 1 the sum of incremental energy over the contact duration $[t_n, t_{n+k+1}]$ is equal to:

$$[K_i + U_i]_n^{n+k+1} = [g_N(d, t_n)]^T \cdot \{1/2(f_{n+1})\} + [g_N(d, t_{n+k+1})]^T \cdot \{1/2f_{n+k}\} \quad (6)$$

It is observed that, for persistent contact analysis, the trapezoidal rule combined with the Lagrangian displacement multiplier leads to severe oscillations in the displacements of contacting nodes. Hence, this method leads to numerical instability which cannot be resolved by spatial and/or temporal discretisation.

3.2 Penalty function

For the penalty method, the displacement constraint is enforced via a stiff penalty spring (kp) located at the position of contact to prevent large penetration between different boundaries. Similar to the Lagrangian displacement constraint, undesirable energy alteration is observed for contact analysis of a linear elastic system with the use of trapezoidal rule and the penalty spring:

$$[K_i + U_i]_n^{n+k+1} = 1/2(g_N(d, t_n))^T kp(g_N(d, t_{n+1})) + 1/2(g_N(d, t_{n+k+1}))^T kp(g_N(d, t_{n+k})) \quad (7)$$

According to eq. 7, with the use of suitable penalty stiffness, better accuracy in energy conservation and contact response can be achieved through refinement of analysis time steps. However, defining appropriate penalty stiffness remains the main drawback of this method.

3.3 Lagrangian velocity constraint

Based on eq. 6, the numerical instability observed with the Lagrangian displacement multiplier is caused by the cumulative energy gain during multiple contacts of the discretised system. For the persistent contact case, this energy instability can be linked to the lack of kinematic constraints which cause severe velocity and displacement oscillation of the contacting nodes. Accordingly, by derivation of the normality 'Kuhn-Tucker' condition with respect to time and holding the equality in equation 5(i) a condition for zero gap function rate is achieved for persistent dynamic contact analysis. The zero gap rate constraint, herein called as velocity constraint, is generally not captured with time-step algorithms using the Lagrangian displacement constraint or the penalty springs. In this paper, a velocity constraint multiplier is suggested with the trapezoidal rule to achieve a robust algorithmic solution procedure for frictionless dynamic contact analysis, written as:

$$\lambda(d, t_i) \cdot \dot{g}_N(d, t_i) = 0 \quad (8)$$

where $\dot{g}_N(d, t_i)$ is the normal gap rate function for corresponding nodal contact nodes evaluated at time t_i and $\lambda(d, t_i)$ is the corresponding Lagrangian multiplier.

4 CASE STUDY

Elastic impact of two identical rods, one initially stationary ($v_0^{slave} = 0$) and the other one moving with constant unit velocity ($v_0^{master} = 1$), is considered to illustrate the advantages of the Lagrangian velocity method against the conventional ones. The rods have unit cross section ($A=1$) as well as unit Young's modulus ($E=1$) and material density ($\rho=1$). The robustness of the suggested algorithmic method as well as its effective characteristic in modelling the dynamic contact constraints is illustrated in Fig. 1. Furthermore, it is shown that, the method can achieve better accuracy in terms of energy conservation and dynamic response through mesh refinement (Fig. 1(b)) or reducing the analysis time-step (Fig. 1(c)).

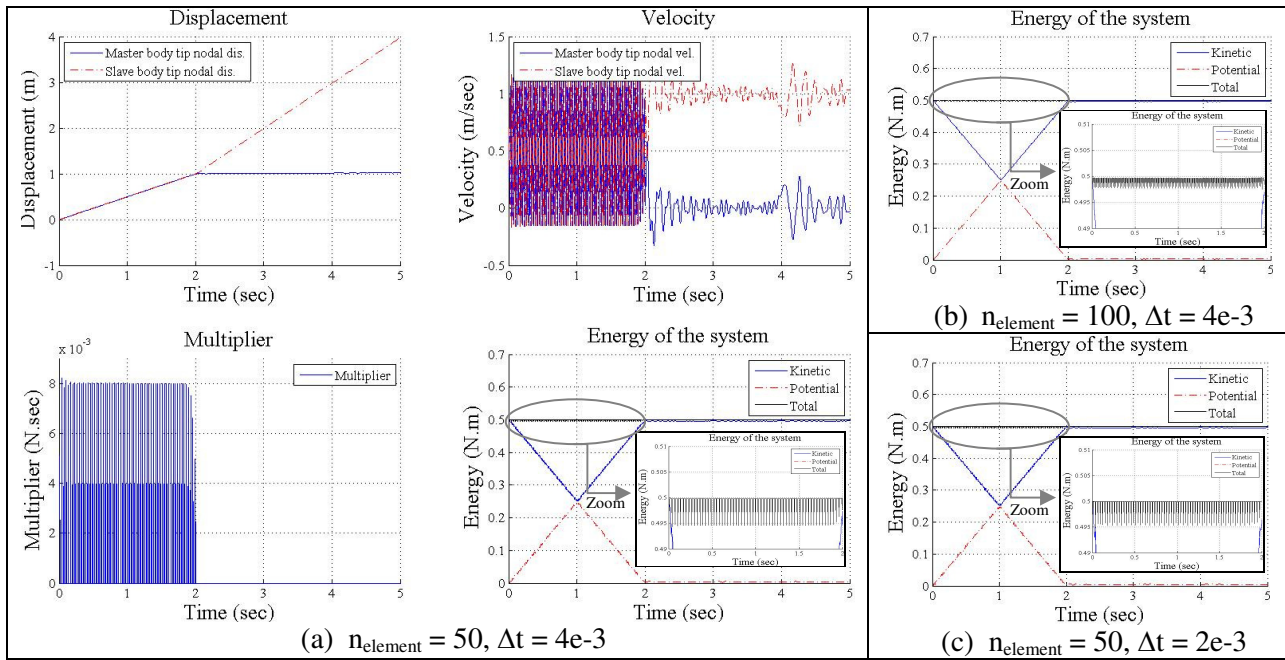


Fig. 1. Impact response of two rods using trapezoidal rule with Lagrangian velocity constraint.

5 Conclusion

It is widely established that the conservation or decay in the total energy of the system can ensure the desirable unconditional stability in nonlinear dynamic analysis. In this respect, dynamic contact analysis has received extensive attention due to its inherent nonlinearity. In this paper, the energy conservation of the Newmark family of integration methods is assessed for frictionless dynamic contact analysis of linear elastic structures. To investigate the energy stability, the incremental energy formulation of the trapezoidal rule is considered for both the penalty method and Lagrangian displacement constraint. It is noted that, for the case of Lagrangian displacement constraint, the cumulative energy error cannot be reduced by further refinement in the analysis time-step and finite element mesh due to high frequency oscillations in the displacement of the contacting nodes.

An algorithmic energy conserving method based on a Lagrangian velocity constraint and the trapezoidal rule is suggested to eliminate the spurious displacement oscillation caused by temporal and finite element discretisation. In addition to the persistency condition, the method efficiently achieves a good approximation of the displacement constraint the magnitude of which can be reduced by temporal refinement. The main characteristics of the proposed method are its applicability to typical nonlinear finite element analysis programs and its robustness (unconditional stability) with respect to the inherent nonlinearity in frictionless dynamic contact problems. Finally, it is shown in Figs. 3(b and c) that, unlike methods based on Lagrangian displacement constraints, the proposed method achieves better accuracy in the response with refinement of the spatial and/or temporal discretisation.

References

- [1] T.A. Laursen and V. Chawla, Design of energy conserving algorithms for frictionless dynamic contact problems. *Int. J. Numer. Meth. Engng.*, 40, 863-886, 1997.
- [2] F. Armero and E. Petocz, Formulation and analysis of conserving algorithm for frictionless dynamic contact/impact problems. *Comput. Meth. Appl. Mech. Engrg.*, 158(3-4), 269-300. 1998.
- [3] J.C. Simo, N. Tarnow, and K.K. Wong, Exact energy-momentum conserving algorithms and symplectic schemes for nonlinear dynamics. *Comput. Meth. Appl. Mech. Engrg.*, 100(1), 63-116, 1992.
- [4] D. Kuhl, and M.A. Crisfield, Energy-conserving and decaying algorithms in non-linear structural dynamics. *Int. J. Numer. Meth. Engng.*, 45, 569-599, 1999.

INVESTIGATION OF A NEW ABSORBING BOUNDARY CONDITION FOR TIME STEPPING SIMULATION OF SEMI-INFINITE ELASTIC MEDIA

G. B. White¹, A. H. Nielsen² and O. Laghrouche¹

¹School of the Built Environment, Heriot-Watt University, Edinburgh, EH14 4AS

²Jacobs, 95 Bothwell Street, Glasgow, G2 7HX

gbw2@hw.ac.uk

Key Words: *absorbing boundary condition; elastic waves; semi-infinite media; wave propagation;*

ABSTRACT

Many boundary conditions have been created to eliminate the reflection of outgoing propagating waves in the finite element analysis of semi-infinite media. However, many of these are not efficient and allow some waves to be reflected. A new absorbing boundary condition has been proposed by Nielsen^[1] and aims to fully absorb outgoing waves. Using Maple 13, an incident P-wave case and incident S-wave case were analyzed using the theory of Lysmer and Kuhlemeyer^[2] and then using the theory of the new proposed absorbing boundary condition. The results of the Lysmer and Kuhlemeyer analysis demonstrate that whilst the boundary conditions can absorb energy, they still are not perfect and allow some outgoing propagating waves to be reflected. However, the results of the new absorbing boundary conditions show that for all the incident angles, the reflection coefficients of the P-wave and S-wave are evaluated as zero. This suggests that there is complete energy absorption at the boundary. Whilst the theory from the proposed absorbing boundary condition is promising, it has yet to be fully tested and validated.

1 INTRODUCTION

Structural and civil engineers can use computer software to understand the interaction between a structure and the soil it is founded on. However, when carrying out such a computer analysis on a dynamic problem such as an earthquake, the outgoing propagating waves hit the boundaries of the model. Rather than propagating beyond the boundary, the waves are reflected back into the model's domain. The waves become trapped within the model, Figure 1. As the model no longer represents semi-infinite media accurately, the analysis is altered.

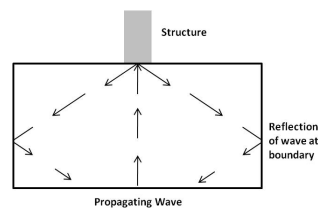


Figure 1 - Wave Reflection

A solution to overcome this problem is to apply absorbing boundary conditions (ABCs) at the boundaries of the model. One such ABC is the viscous boundary that was developed by Lysmer and Kuhlemeyer. Whilst the ABC can absorb propagating waves, it still results in some waves being reflected into the model. Despite this, it is a popular method and is still used in analysis today.

Much research has gone into creating a boundary condition that can achieve complete energy absorption. Many ABCs, such as the ones developed by Higdon and Wolf, improve the accuracy, but still allow for energy to be reflected. In 2008, a new ABC was proposed by Nielsen. The ABC is said to deliver an exact solution for analysis in the time domain and is capable of full absorption, but has yet to be validated. The purpose of this paper is to understand how the new ABC theory works, by using it to analyse two incident wave cases and comparing it with another ABC method that has been tried and tested.

2 THEORY

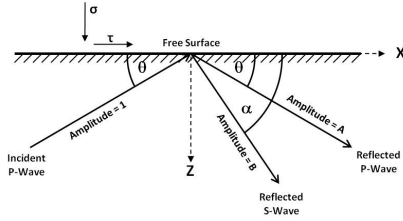


Figure 2 - Incident P-wave Case

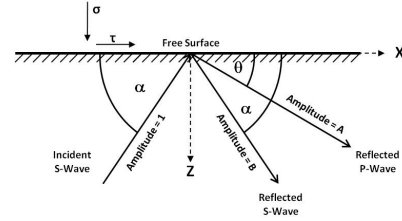


Figure 3 - Incident S-wave Case

The viscous boundary theory and the new ABC theory are used in the analysis of an incident P-wave and an incident S-wave. First, consider an incident P-wave propagated towards the free surface boundary at angle θ , Figure 2. As the wave hits the free surface boundary, a reflected P-wave of angle θ and S-wave of angle α are produced. However, in a computer model we are not interested in the free surface, but the use of an artificial boundary to shorten the semi-infinite domain. To prevent waves reflecting at the artificial boundaries, ABCs are imposed on them.

In the case of the incident P-wave, the displacement potentials of the P-wave, ϕ , and S-wave, ψ , are

$$\phi(x, z, t) = e^{ik(ct+z\tan\theta-x)} + Ae^{ik(ct-z\tan\theta-x)} \quad (1)$$

$$\psi(x, z, t) = Be^{ik(ct-z\tan\alpha-x)} \quad (2)$$

where ω is the frequency, c is the velocity, k is the wave number and A and B are the amplitudes of the reflected P-wave and S-wave respectively, and are also known as the reflection coefficients. It should be noted, that the amplitude of the incident wave is arbitrary as the interest lies in the amplitudes of the reflected waves. These expressions were used to obtain the horizontal and vertical displacements, u and w . Using the displacements obtained, expressions for the normal stress and shear stress were obtained. These were then applied to the viscous boundary theory and then to the new ABC theory. For an incident S-wave case, Figure 3, an incident S-wave of angle α , hits the free surface boundary and produces a reflected P-wave of angle θ and a reflected S-wave of angle α . The displacement potentials of the S-wave and P-wave are

$$\phi(x, z, t) = Ae^{ik(ct-z\tan\theta-x)} \quad (3)$$

$$\psi(x, z, t) = e^{ik(ct+z\tan\alpha-x)} + Be^{ik(ct-z\tan\alpha-x)} \quad (4)$$

Horizontal and vertical displacements were derived from these and then used to obtain expressions for the normal and shear strain. These were then applied to both theories, as done in the previous analysis.

2.1 Lysmer and Kuhlemeyer Viscous Boundary

This absorbing boundary condition was developed for a semi-infinite system, where a convex boundary is used to separate an inner region from an outer region. All sources of excitement would be contained within the inner region. Propagation of energy would first occur from within the inner region and head towards the convex boundary. As the energy reaches the boundary, it would then pass into the exterior region. To keep the same behaviour, it was determined that a boundary could absorb the propagating energy^[2]. This led to the development of the viscous boundary which acts as normal and shear viscous dashpots supporting the convex boundary for use in the time domain. The conditions are expressed as

$$\sigma_{zz} = \rho c_p \dot{w} \quad (5)$$

$$\tau_{xz} = \rho c_s \dot{u} \quad (6)$$

where σ is the normal stress, τ is the shear stress, c_p is the P-wave velocity, c_s is the S-wave velocity, \dot{w} is the normal velocity and \dot{u} is the tangential velocity.

In the analysis of the incident P-wave, the displacement expressions given above were inserted into the viscous boundary, (5) and (6). Using Maple 13, these were then evaluated to determine expressions for the reflected amplitudes, A and B . In order to gain such expressions, the angle of the reflected S-wave, was related to the angle of the P-wave, using Snell's law. With amplitudes obtained, the energy ratio, (7), was evaluated over all incident angles.

$$\frac{E_r}{E_i} = A^2 + \left(\frac{c_s}{c_p}\right) \frac{\sin\alpha}{\sin\theta} B^2 \quad (7)$$

The analysis for the incident S-wave is similar to the analysis of the incident P-wave. However, it should be noted that a critical angle exists for the incident S-wave. It can be calculated using

$$\alpha_{crit} = \cos^{-1}\left(\frac{c_s}{c_p}\right) \quad (8)$$

When the incident S-wave is propagated at the critical angle, a reflected P-wave is produced at an angle of 0° . However, if the incident angle of the S-wave is smaller than the critical angle, a boundary wave is created, which decays exponentially with the depth. Due to this, the energy ratio must be calculated in two steps. When the incident angle of the S-wave is greater than or equal to the critical angle, the energy ratio is calculated using

$$\frac{E_r}{E_i} = B^2 + \left(\frac{c_p}{c_s}\right) \frac{\sin\theta}{\sin\alpha} A^2 \quad (9)$$

and when the incident S-wave angle is less than the critical angle, the energy ratio is calculated using

$$\frac{E_r}{E_i} = B_i^2 + B_r^2 \quad (10)$$

where B_i is the imaginary solution of amplitude B and B_r is the real solution of amplitude B . This energy ratio equation does not contain the energy from the boundary wave produced, as it does not add or remove energy from the boundary[2]. By plotting the energy ratio against the angle of incidence, for both the incident P-wave and S-wave case, the following graphs were obtained.

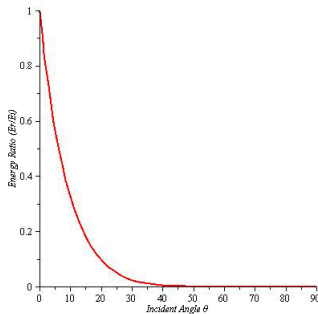


Figure 4 - Energy Ratio vs P-wave incident angle

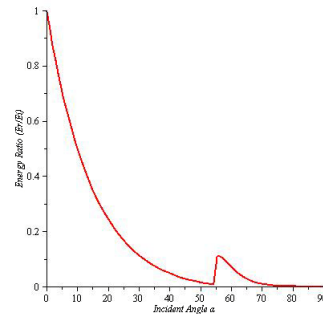


Figure 5 - Energy ratio vs S-wave incident angle

By looking at Figure 4 for the incident P-wave, we can see that when the incident angle is greater than 50° , there is complete absorption. Between 30 and 50 degrees, there is still a considerable amount of energy absorbed, but some energy is reflected. As the incident angle becomes smaller, less energy is absorbed and when the incident angle is 0° , there is complete reflection. Figure 5 for the incident S-wave also displays the same relationship. These results indicate that whilst the viscous boundary is a method capable of complete absorption, it depends on the incident angle.

2.2 New Absorbing Boundary Condition

The new absorbing boundary conditions derived by Nielsen are different for an incident P-wave and

incident S-wave^[1]. For an incident P-wave, the conditions are expressed as

$$\sigma_{zz} = \Delta(\lambda + \mu(1 - \cos 2\theta)) \quad (11)$$

$$\tau_{xz} = -\Delta\mu\sin 2\theta \quad (12)$$

where σ_{zz} is the normal stress, τ_{xz} is the shear stress, λ and μ are the Lamé coefficients and Δ is the dilatation, as the P-wave is a dilatational wave. The dilatation can be calculated using

$$\Delta = \frac{\partial u}{\partial x} + \frac{\partial w}{\partial z} \quad (13)$$

In the incident P-wave analysis, the normal and shear expressions derived earlier, were applied to the new P-wave boundary conditions, (11) and (12). Using Maple 13, these were then used to gain expressions for the reflected amplitudes, A and B , and then evaluated over all angles of incidence. As for an incident S-wave, the new boundary conditions are expressed as

$$\sigma_{zz} = 2\omega\sin 2\theta \quad (14)$$

$$\tau_{xz} = -2\omega\mu\cos 2\theta \quad (15)$$

where σ_{zz} is the normal stress, τ_{xz} is the shear stress, λ and μ are the Lamé coefficients and ω is the rotation, as the S-wave is a shear wave. The rotation can be calculated using

$$\omega = \frac{1}{2} \left(\frac{\partial w}{\partial x} - \frac{\partial u}{\partial z} \right) \quad (16)$$

As with P-wave analysis, the normal and shear expressions that were derived earlier, were applied to the new boundary conditions, (14) and (15). Snell's law was used to relate the P-wave angle to the S-wave angle and Maple 13 was used to obtain expressions for the reflected amplitudes, A and B , and then evaluated over all angles of incidence. The energy ratio can be calculated using the same equations used in the viscous boundary theory^[2]. If the energy ratio is then plotted against the incident angle for both the incident P-wave and S-wave cases, no curve is obtained. This is because the reflection coefficients, A and B , are evaluated to as 0 for all incident angles, indicating that no reflection takes place.

3 CONCLUSION

In conclusion, it is clear that the Lysmer and Kuhlemeyer viscous boundary condition is practical to implement in a code for its simplicity. However, in practice it is dependent on the angle of incidence. For normal incidence of waves on an artificial boundary, it leads to complete absorption of energy. But as the angle of incidence becomes smaller, most of the energy is reflected. This is unlike the newly proposed ABC which is shown to display complete absorption over all angles of incidence. This is proven theoretically but will require further validation through implementation in a finite element code.

References

- [1] Nielsen, A. H. A new Boundary Condition for Analysis of Semi-infinite Media in Time Domain. *SECEED Newsletter*, 2008, Vol. 21, 1
- [2] Lysmer, J and Kuhlemeyer, R. L. Finite Dynamic Model for Infinite Media, *Journal of the Engineering Mechanics Division Proceedings for ASCE*, 1969, Vol. 95
- [3] Higdon, R. L. Radiation Boundary Conditions for Elastic Wave Propagation. *SIAM Journal on Numerical Analysis*, 1990, Vol. 24, 4
- [4] Wolf, J. P. Soil-structure Interaction Analysis in Time Domain. *Nuclear Engineering and Design*, 1989, Vol.111, 3

Computational modelling of contaminated land: Development of a combined stochastic-deterministic model for mass transfer in variably saturated porous media.

*Jack M. Barnard¹ and Charles E. Augarde¹

¹School of Engineering and Computing Sciences, Durham University
South Road, Durham, DH1 3LE, UK

*jack.barnard@durham.ac.uk

Key Words: *mass transport, porous media, random-walk, stochastic methods*

ABSTRACT

A new model to describe water movement and mass transport in remediated contaminated land is being developed. The model will be able to deal with differing climatic conditions, describe mass transfer and basic reaction systems and will contain some characterisation of the resulting uncertainty. An overview of some of the methods used in attempts to describe mass transport in porous media and some of the issues encountered is presented here. In particular the issues of numerical dispersion, anomalous transport and uncertainty about subsurface heterogeneity are discussed. In addition the use of stochastics in accounting for the uncertain nature of subsurface heterogeneity will be briefly discussed.

1 Introduction

A new model is being developed to allow for long term prediction of the effectiveness of a new technology for the remediation of contaminated land as part of the EPSRC funded ROBUST project¹. The uncertainty of subsurface conditions in contaminated land and the nature of risk assessment mean that probabilistic methods are likely to play a significant role in the development of this model.

2 The Advection-Dispersion-Reaction Problem

The description of mass transfer in variably saturated porous media can be divided into two problems, water flow and mass transfer. In the model under construction here the water flow problem will be solved by the application of finite element analysis (FEA) to Richards' equation and the use of the primary variable switching method (PVSM)[6][5]. This involves switching the primary variable in the problem depending on the saturation of the soil. Volumetric water content θ is used in unsaturated conditions and pressure head ψ is used in saturated or close to saturated conditions. This method can deal with problems which vary quickly between saturated and unsaturated conditions efficiently. The solution of the flow field is then used to solve the advection-dispersion-reaction (ADR) equation [1]

$$\frac{\partial c}{\partial t} + v \cdot \nabla c = \nabla \cdot (D \nabla c) + Q \quad (1)$$

where c is solute concentration, v is pore water velocity, D is a combined dispersion-diffusion term and

¹<http://www.robustdurham.org.uk/>

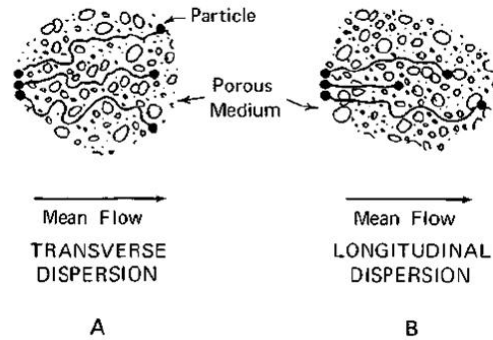


Figure 1: Dispersion in porous media due to variations in flow path (adapted from Prickett *et al.* 1981 [9])

Q represents sources and sinks including reactions. Advection is the transport of mass by the movement of the medium as it is within. Diffusion is the movement of mass causing reductions in concentration gradients due to random walk of particles. Dispersion is the spreading of material due to velocity variations within pores and variations in flow path [Figure 1].

3 Numerical Solutions

The solution of the ADR equation generally involves the solution of the advection term separately. Trying to solve the advection term using standard FEA soon leads to problems, the chief of which being numerical dispersion. Fluxes in porous media tend to be of the order that distance travelled by a particle in a time step $(Vc/\theta)\Delta t$ is smaller than the distance between nodes. Therefore the concentration of a solute in the pore fluid arriving at any node at any time generally has to be interpolated from the nodal data. This process is conceptualised in the single step reverse particle tracking (SRPT) method (*e.g.*[3]). In this method the location of a fictitious particle which will arrive at node i at time $t = n$ is found. The concentration at this location at time $t = n - \Delta t$ is interpolated from the nodal concentrations and transferred to node i at time $t = n$. This method causes numerical dispersion of sharp concentration gradients [Figure 2].

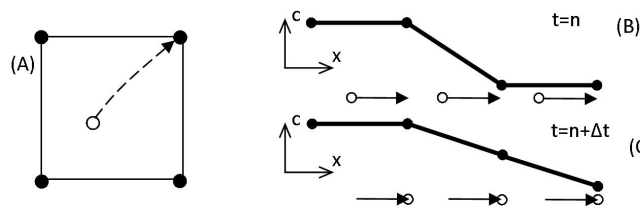


Figure 2: A schematic diagram showing particle movement within the SRPT scheme (A) and the effect of numerical dispersion(B,C). (A) The particle arriving at the top right node at $t = n + \Delta t$ travels along the path shown by the arrow. It's location at $t = n$ is shown by the open circle. (B,C) The particles, shown by open circles move as shown by the arrows during one timestep. Due to the interpolation of the solute concentration between nodal locations the concentration front is smoothed out.

To combat the problem of numerical dispersion the continuous forward particle tracking (CFPT) method was developed [8]. In the CFPT method a cloud of particles is placed within the domain. The particles are moved according to the generated flow field and then projected onto the nodes to form a concentration field. This method effectively eliminates numerical diffusion but is more computationally intensive than SRPT as it requires a much larger number of particles. As numerical dispersion is more of a problem around sharp concentration gradients adaptive versions of the CFPT method [8] have been developed to remove particle clouds and revert to the SRPT method when concentration gradients drop

below a certain threshold. In both the SRPT and CFPT methods the dispersive transport is solved by the standard finite element method.

The CFPT method produces results in good accordance with analytical solutions assuming that dispersive transport behaves according to a Fickian model. Laboratory testing (*e.g.*[2]) has shown that the ADR equation does not fit well to transport in heterogeneous porous media and that the transport does not fit a Fickian description. Levy and Berkovitz [7] show that even in grain size sorted sands that this is the case. A qualitative depiction of this is shown in Figure 3. Tortuosity and the presence of preferential flow paths and stagnant areas lead to the spreading of material in an anomalous fashion. In systems where the porous media is more heterogeneous the effect is enhanced. A schematic representation of the difference between normal Fickian transport and this anomalous or non-Fickian transport is shown in Figure 4.

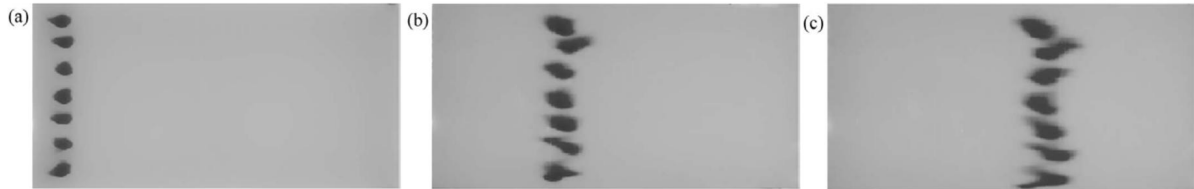


Figure 3: Dispersion of ink in porous media due to variations in flow path. Flow field is continuous and from left to right (adapted from[7]).

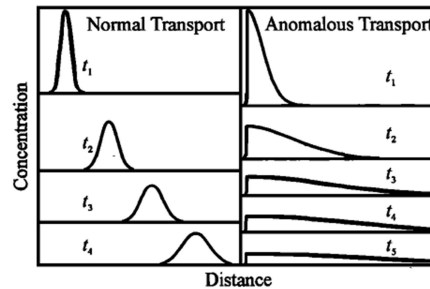


Figure 4: A schematic representation of the difference between normal (Fickian) and anomalous (non-Fickian) transport (from [2]).

4 Stochastic Methods

Due to the uncertain nature of subsurface heterogeneity the problem cannot be addressed in a deterministic fashion. Instead dispersive transport can be characterised as a stochastic variable. The continuous time random walk (CTRW) method [9] uses the same method for solving the advective term as the ADR equation but replaces the Fickian FE solution of the diffusive and dispersive transport with a random walk procedure. A random number generator fitted to a normal distribution is used to determine the dispersive component of transport. A limit on the maximum deviation from the mean in terms of the standard deviation is often imposed [9]. This value is then multiplied by the standard deviation $\sigma = \sqrt{2D^*t}$ where t is time and D^* is a combined dispersion-diffusion term. The particle is moved a random distance in the longitudinal and transverse direction producing a random spreading of the concentration field [Figure 5].

The continuous time random walk (CTRW) method deals with the uncertainty associated with dispersion of a contaminant caused by variations in flow paths within a porous medium. Another uncertain variable in a porous medium is how the hydraulic conductivity changes throughout the medium. If a characterisation of the variability of hydraulic conductivity within a soil type, generally fitted to log-normal distribution [4], can be obtained then the hydraulic conductivity can be treated as a random variable in the same fashion as the dispersive flux in the CTRW method. This random hydraulic conductivity can be used as a single realisation or as part of a Monte Carlo simulation. The amount of

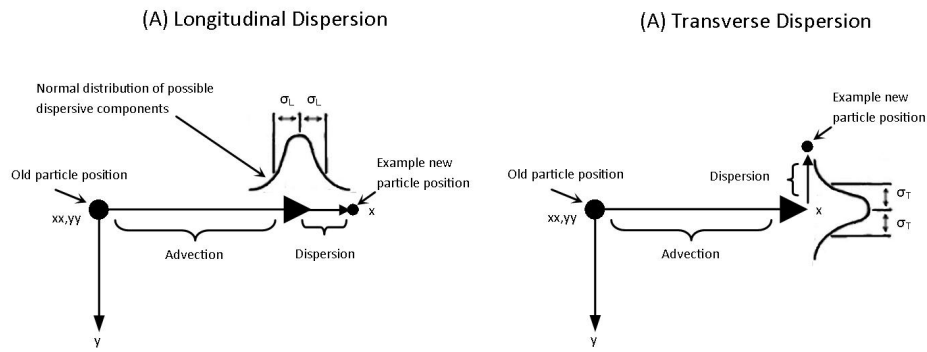


Figure 5: The general scheme for the continuous time random walk (CTRW) method (adapted from [9]).

computing time and power needed to run Monte Carlo simulations of mass transfer problems in porous media is prohibitive [4] so the simulations in this project will probably use single or small numbers of realisations. An introduction to the application of stochastic methods to flow and transport in porous media can be found in [4].

5 Conclusion

A brief overview of some of the issues surrounding mass transfer in porous media has been presented. These methods are being applied in the development of a new numerical model to describe the long term effectiveness of a novel remediation technique for contaminated land. The applications of probabilistic methods are an important aspect of model development and are being applied to mass transport and may be extended to include soil water retention properties and Monte Carlo simulations.

References

- [1] J. Bear and Cheng A. H.-D. *Modeling Groundwater Flow and Contaminant Transport*, volume 23 of *Theory and Application of Transport in Porous Media*. Springer, 2010.
- [2] B. Berkowitz, H. Scher, and S.E. Silliman. Anomalous transport in laboratory-scale, heterogeneous porous media. *Water Resources Research*, 36(1):149–158, 2000.
- [3] R.T. Cheng, V. Casulli, and S.N. Milford. Eulerian-Lagrangian solution of the convection-dispersion equation in natural coordinates. *Water Resources Research*, 20(7):944–952, 1984.
- [4] G. Dagan and S.P. Neuman. *Subsurface flow and transport: a stochastic approach*. Cambridge Univ Pr, 1997.
- [5] H.J.G. Diersch and P. Perrochet. On the primary variable switching technique for simulating unsaturated-saturated flows. *Advances in Water Resources*, 23(3):271–301, 1999.
- [6] P. A. Forsyth, Y. S. Wu, and K. Pruess. Robust numerical methods for saturated-unsaturated flow with dry initial conditions in heterogeneous media. *Advances in Water Resources*, 18(1):25 – 38, 1995.
- [7] M. Levy and B. Berkowitz. Measurement and analysis of non-Fickian dispersion in heterogeneous porous media. *Journal of Contaminant Hydrology*, 64(3-4):203–226, 2003.
- [8] S.P. Neuman. Adaptive Eulerian–Lagrangian finite element method for advection–dispersion. *International Journal for Numerical Methods in Engineering*, 20(2):321–337, 1984.
- [9] T.A. Prickett, T.G. Naymik, and C.G. Lonquist. A ‘Random Walk’ Solute Transport Model for Selected Groundwater Quality Evaluations. *Illinois State Water Survey Bulletin*, 65, 1981.

Permeability Assessment of Heterogeneous Porous Media Using the Lattice Boltzmann Method

*B. D. Jones, Y. T. Feng

College of Engineering, Swansea University, Singleton Park, Swansea, SA1 8PP

*403113@swan.ac.uk

Key Words: *lattice Boltzmann, porous media; fluids; x-ray micro-tomography; bounceback*

ABSTRACT

Material characterisation is one of the most important aspects of accurate numerical modelling; correct material properties must be obtained for the correct behaviour to be observed. Traditionally permeability is measured by applying a constant/falling head test to a material sample, where such tests may involve many samples at varying pressure gradients. However current X-Ray micro-tomography techniques allow us to avoid physical lab tests by providing the ability to reproduce a voxelised representation of the internal structure of a porous medium. The Lattice Boltzmann Method may then be used to model a pressure induced flow field within the sample so that permeability may be numerically approximated. Typically this process is carried out after a thresholding procedure has been applied to the voxelised geometry to split it into definite solid and void spaces, at the expense of accuracy of the geometry. In an attempt to better represent the porous medium, a partial bounceback condition could be applied to the Lattice Boltzmann scheme allowing us to consider directly the raw voxel values and avoiding the need for any thresholding procedure. To validate this hypothesis two test cases were explored; flow past a periodic array of cylinders by use of a unit cell model, and flow through a simple heterogeneous porous medium. Results were compared with analytical expressions where available, and published expressions for permeability evaluation of porous media. Results were found to be in good agreement with the available expressions.

1 INTRODUCTION

Porous media represent a broad range of materials which may be encountered in a variety of industries, from oil production to textiles, yet the assessment procedure for permeability evaluation has, for the most part, gone unchanged for many years. When an organisation requires the permeability of a material to be evaluated, they must typically gather a set of samples of sufficient size and submit them to a laboratory where a constant/falling head test may be applied. Preparation and testing of these samples can leave them unsuitable for subsequent tests, and for media with anisotropic permeability the number of samples required for accurate permeability evaluation may easily be doubled when compared to a sample with isotropic permeability for a true scientific test. The research presented herein is focused on applying the Lattice Boltzmann method (LBM) to permeability assessment by considering the microstructural geometry of a porous media, represented by a voxelised scan of a porous sample generated by use of x-ray micro-tomography. An alternate form of the bounceback “no-slip” boundary condition was explored with respect to its use in this field.

2 THE LATTICE BOLTZMANN METHOD

The Lattice Boltzmann Method^[1] (LBM) has become a popular method in the field of porous media flow modelling^[2,3], in large part due to the simplicity of constructing a lattice which may represent heterogeneous porous media. Since the LBM operates on a regular lattice, in most cases a square lattice, one can avoid the complexities of meshing routines required by more traditional methods such as the Finite Volume technique.

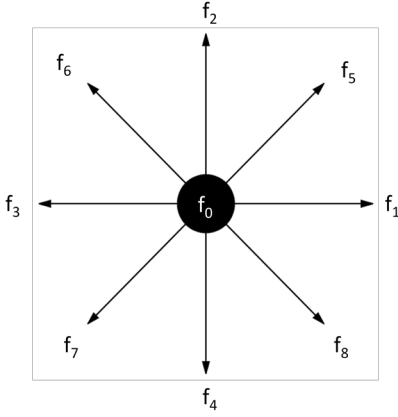


Figure 1 - The Lattice Site

The standard D2Q9 Lattice Boltzmann scheme with an LBGK collision term^[4] operates on a square lattice of connected lattice sites, figure 1 shows a diagram of a D2Q9 lattice site. Each lattice site is connected to its neighbours by 8 vectors, e_i , and each vector has a particle distribution function (PDF), f_i , associated with it along with a ninth “rest” PDF. The evolution of these PDF’s is defined by the LBGK Lattice Boltzmann equation:

$$f_i(\mathbf{x} + \mathbf{e}_i \delta_t, t + \delta_t) - f_i(\mathbf{x}, t) = \frac{1}{\tau} (f_i^{eq}(\mathbf{x}, t) - f_i(\mathbf{x}, t))$$

Macroscopic values of density and momentum can be calculated by use of the following simple equations respectively:

$$\rho = \sum_i f_i, \quad \rho \mathbf{u} = \sum_i \mathbf{e}_i f_i$$

For a no-slip condition to be imposed within a lattice Boltzmann domain one can simply apply what’s known as the “bounceback” boundary condition^[5], where a site which represents a solid body interface simply reflects any momentum transferred to it. This operation is represented by the following equation:

$$f_i(\mathbf{x} + \mathbf{e}_i \delta_t, t + \delta_t) = f_{-i}(\mathbf{x}, t)$$

Where f_{-i} is the PDF whose associated vector is in the opposite direction to the vector associated with f_i . This operation occurs instead of the LBM evolution equation for a given bounceback site. In order to represent the voxelised microstructural geometry of porous media using the LBM and the standard bounceback condition, one must therefore split the computational domain into lattice sites which represent either fluid space or solid space. However a voxelised geometry does not result in this polarised representation, instead a voxel is given a value between 0 and 1 which represents the degree to which the voxel is filled with solid matter, in order to better represent this voxelised geometry it is proposed that a partial bounceback condition be imposed rather than the standard “full way” bounceback condition. To this end, the partial bounceback condition proposed by Noble and Torczynski^[8] was used; this condition is applied to all sites within the domain and modifies the standard LBGK LBM equation to read:

$$f_i(\mathbf{x} + \mathbf{e}_i \delta_t, t + \delta_t) - f_i(\mathbf{x}, t) = [1 - B(\mathbf{x})] \Omega_i^{BGK} + B(\mathbf{x}) \Omega_i^S$$

$$\Omega_i^{BGK} = \frac{1}{\tau} (f_i^{eq}(\mathbf{x}, t) - f_i(\mathbf{x}, t))$$

There is some ambiguity in the literature as to a suitable expression for Ω_i^S , to this end the following two expressions were tested.

$$\Omega_i^S = f_{-i}(\mathbf{x}, t) - f_i(\mathbf{x}, t) + f_i^{eq}(\rho, \mathbf{U}_s) - f_{-i}^{eq}(\mathbf{x}, t)$$

$$\Omega_i^S = f_{-i}(\mathbf{x}, t) - f_i(\mathbf{x}, t) + f_i^{eq}(\rho, \mathbf{U}_s) - f_{-i}^{eq}(\rho, \mathbf{U}_s)$$

The variable B, determines the strength of the bounceback operation so that for B equal to one, a lattice site is seen to exhibit full way bounceback behaviour and for B equal to zero the lattice site is seen to exhibit purely fluid behaviour. For the case that B has a value between zero and one, the lattice site would have some permeability attached to it and behave in itself as a porous medium.

3 TEST CASES

To validate the use of this partial bounceback model in this way, two test cases were explored. The first test case is based upon the works of Gebart^[6] and Lee and Yang^[7], who have proposed expressions for the permeability of an ordered periodic array of cylinders representative of aligned fibres in fabrics or composites. A unit cell cylinder model was adopted, and a pressure drop applied across this unit cell cylinder. The pressure induced velocity field was approximated using the standard LBGK LBM with both full way and partial bounceback boundary conditions. Once an approximation for the steady state velocity field was achieved, Darcy’s law was applied to calculate the permeability of the domain. The unit cell cylinder model was tested for varying resolution and varying porosity.

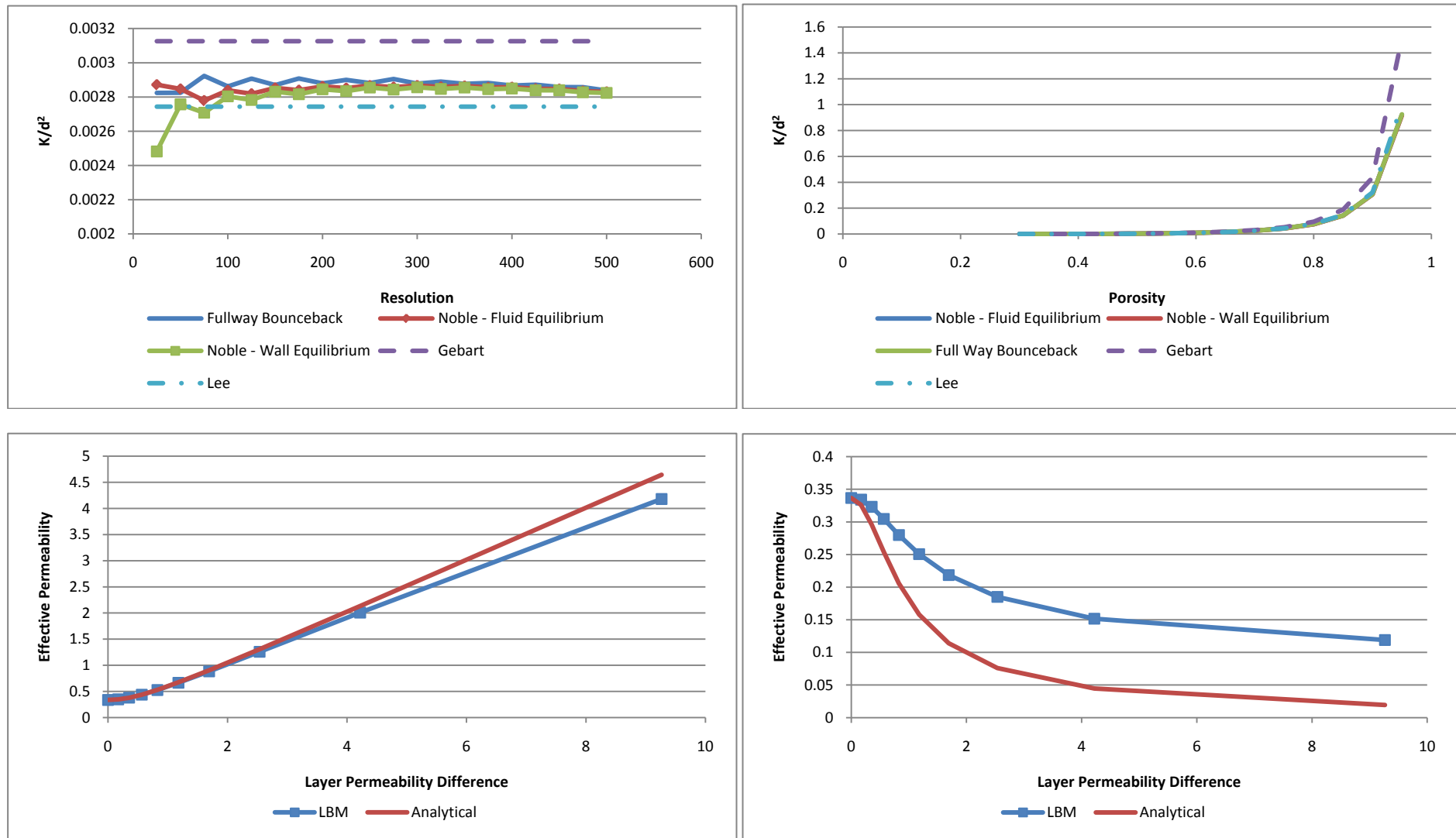


Figure 2 – Results of Test Cases

Top: Results for Unit Cylinder Test; Radius Normalised Permeability Variation with Resolution (Left), Radius Normalised Permeability Variation with Porosity (Right)
Bottom: Results for Heterogeneous Porous Media; In Parallel (Left), In Series (Right)

The second test case which was explored was that of two simple heterogeneous porous media, each consisting of two homogeneous regions of different permeability aligned in parallel for the first medium, and in series for the second medium. Once again an approximation for the steady state velocity field was gained by using the standard LBGK LBM, however due to the nature of the domain only the partial bounceback condition could be applied. These simple heterogeneous porous media were tested for increasing permeability difference; approximate values for effective permeability were then compared with analytical expressions^[8] for effective permeability of these simple porous media.

The results for both test cases are presented in figure 2. For the unit cell cylinder test, good agreement can be shown when results are compared with both Gebart's expression and Lee and Yang's expression, though a better correlation with Lee and Yang's expression can be seen. The second test case shows good agreement between numerical and analytical permeability for the "in parallel" porous medium, with results diverging only slightly as the permeability difference is increased. The correlation between numerical and analytical results for the "in series" porous medium is not so good. Though the two trends exhibit similar behaviour, the results are extremely divergent as the permeability difference is increased.

5 CONCLUSION

Noble's Partial Bounceback condition was applied to permeability assessment of simple heterogeneous porous media with results compared to proposed expressions for permeability approximation and analytical permeability. It was shown that in general numerical results are in good agreement with these expressions. However there is still room for improvement, especially with respect to the heterogeneous porous medium with two regions of differing permeability in series. Since the full way bounceback is unable to deal with regions of a microstructural geometry which are intrinsically porous, and the partial bounceback condition demonstrates similar accuracy to the full way bounceback condition when representing a definite fluid/solid boundary; it can be seen that the partial bounceback condition proposed by Noble is more suitable than the full way bounceback condition for considering the voxelised microstructural geometry of a heterogeneous porous medium.

References

- [1] X. He and L.S. Luo. Theory of the lattice Boltzmann method: From the Boltzmann equation to the lattice Boltzmann equation. *Physical Review E*, 56(6), 6811-6917, 1997.
- [2] A. Nabovati, E. W. Llewellyn and A. C. M. Sousa. A General model for the permeability of fibrous porous media based on fluid flow simulations using the lattice Boltzmann method. *Composites: Part A* 40, 860-869, 2009.
- [3] E. S. Boek and Maddalena Venturoli. Lattice-Boltzmann studies of fluid flow in porous media with realistic rock geometries. *Computers and Mathematics with Applications* 59, 2305-2314, 2010.
- [4] P.L. Bhatnagar, E.P. Gross and M. Krook. A Model for Collision Processes in Gases. I. Small Amplitude Processes in Charged and Neutral One-Component Systems. *Physical Review* 94, 511-525, 1954.
- [5] Q. Zhou, S. Hou and G.D. Doolen. Analytical solutions of the lattice Boltzmann BGK model. *Journal of Statistical Physics* 81, 319-334, 1995.
- [6] B.R. Gebart. Permeability of Unidirectional Reinforcements for RTM. *Journal of Composite Materials*, 26(8), 1100-1133, 1992.
- [7] S.L. Lee and J.H. Yang. Modeling of Darcy-Forchheimer drag for fluid flow across a bank of circular cylinders. *International Journal of Heat and Mass Transfer*, 40(13), 3149-3155, 1997.
- [8] Y. Gao and M. M. Sharma. A LGA Model for Fluid Flow in Heterogeneous Porous Media. *Transport in Porous Media* 17, 1-17, 1994.
- [9] D. R. Noble and J. R. Torczynski. A Lattice Boltzmann Method for Partially Saturated Computational Cells. *International Journal of Modern Physics*, 9(8), 1-13, 1998.

PREDICTION OF LAMINARIZATION WITH A ONE EQUATION SPALART-ALLMARAS MODEL

*Oriji U. Richard ¹ and Paul G. Tucker ¹

¹Whittle Lab, Department of Engineering, University of Cambridge, 1 JJ Thompson Avenue, Cambridge, CB3 0DY.

*uro20@cam.ac.uk

Key Words: *Spalart-Allmaras model; Laminarization; Unstructured grids; RANS; CFD; Acceleration parameter; Accelerating boundary layer*

ABSTRACT

The one equation Spalart-Allmaras (SA) turbulence model, which is the most popular industrial turbulence model, has been modified to predict the effect of boundary layer laminarization. Like most other Reynolds averaged Navier Stokes (RANS) models, the original SA model is insensitive to boundary layer acceleration. The modified version proposed here preserves the original models behavior in regions where the criteria determining the onset of laminarization is not exceeded. The model has been implemented in an unstructured Computational Fluid Dynamics (CFD) code, for acceleration parameters ranging from 1.5×10^{-6} to 3.5×10^{-6} . The modification is based on a proposition by Jones and Launder, this being that the Van Driest damping function constants must become variables for accelerating flows. This is because the viscous sub-layer thickens in a laminarizing boundary layer. The modified SA model shows encouraging agreement with measurements for idealized (sink) flows.

1. INTRODUCTION

It is generally agreed that a turbulent boundary layer will transition to laminar flow if subjected to a sufficiently severe favorable pressure gradient (FPG). The dimensionless acceleration parameter $K = (\nu / U_e^2) \times (dU_e / dx)$ is used to discern the onset of laminarization [1]. Under mild acceleration there is only a partial reversion to laminar state and for strong accelerations there is a complete reversion to laminar flow [1-2]. Unlike the laminar to turbulent transition, laminarization is usually accompanied by certain flow features, such as the thickening of the viscous sub layer, a departure of the mean velocity profile from the logarithmic ‘law of the wall’, a thinning of the boundary layer, a decrease in the momentum thickness Reynolds number (R_2) and an increase in the shape factor (H). Flows which tend to laminarize however tend to pose challenges for RANS turbulence models as these models remain effectively turbulent in regions where experiments would suggest turbulent decay [3]. For a RANS model to predict the correct physics under these conditions, it would have to stop the global production of turbulence energy during laminarization and resume net production afterwards.

2. GOVERNING EQUATION

The SA low Reynolds number model is one of the most widely used turbulence model for aerospace applications. It solves a transport equation for an intermediate variable $\tilde{\nu}$. The SA model uses the Boussinesq hypothesis to relate the Reynolds stress $-\overline{u_i u_j}$ to the gradient of the mean velocity

$$-\overline{u_i u_j} = \nu_t \left(\frac{\partial u_i}{\partial x_j} + \frac{\partial u_j}{\partial x_i} \right) \quad (1)$$

The transport equation for the one equation SA model can be written as:

$$\frac{\partial \tilde{v}}{\partial t} + u_j \frac{\partial \tilde{v}}{\partial x_j} = C_{b1}(1 - f_{t2})\hat{S}\tilde{v} + \frac{1}{\sigma} \left[\frac{\partial}{\partial x_j} \left((v + \tilde{v}) \frac{\partial \tilde{v}}{\partial x_j} \right) + C_{b2} \frac{\partial \tilde{v}}{\partial x_i} \frac{\partial \tilde{v}}{\partial x_i} \right] - \left[C_{w1} f_w - \frac{C_{b1}}{\kappa^2} f_{t2} \right] \left(\frac{\tilde{v}}{d} \right)^2 \quad (2)$$

The turbulent eddy viscosity is calculated from the relationship with \tilde{v} as:

$$v_t = \rho \tilde{v} f_{v1}, \quad f_{v1} = \frac{\chi^3}{\chi^3 + C_{v1}^3}, \quad \chi = \frac{\tilde{v}}{v} \quad (3)$$

Where f_{v1} is the damping function, $C_{v1} = 7.1$ and the analogy from Mellor and Herring's notation [4] introduced in the original paper by Spalart and Allmaras gives $\chi = \kappa y^+$. This later relationship holds from the wall to the log layer with $\kappa = 0.41$. Due to brevity, the full description of the terms and modeling constants is not explained here but can be found in the original paper [5]

3. TURBULENCE MODEL MODIFICATION

The approach used in this work for the prediction of laminarization gains its basis from [6]. Van Driest proposed a near wall theory for turbulent flow that at a distance away from the wall, the eddies were not damped by the effect of wall proximity and close to the wall the viscosity and wall blocking influenced the near wall eddies. The damping factor was thus proposed as $V_D = 1 - \exp(-y^+/A^+)$ where $A^+ = 26$. Van Driest's theory meant that the mixing length had to be represented by the equation $l = \kappa y [1 - \exp(-y^+/A^+)]$. However, Launder and Jones [1] proposed a modification to Van Driest function stating that for FPG turbulent boundary layer sink flow the A^+ was representative of the sub layer thickness. Suggesting that the Van Driest constant A^+ would become a variable proportional to a laminarization parameter. Hence a linear theoretical correlation is given by:

$$\begin{aligned} L \leq 1.9 \times 10^{-3}, & \quad A^+ = 26 \\ L > 1.9 \times 10^{-3}, & \quad A^+(K) = 11 + (7.9 \times 10^3)L \end{aligned} \quad (5)$$

$$L = K C_f^{3/2} \quad (6)$$

Two methods of synthesizing the Jones and Launder Proposal with the SA model are explored here. These are described below.

METHOD 1 (Van Driest Type)

For Method 1, the y^+ Van Driest damping function is taken with y^+ replaced with χ/κ .

$$D_V = 1 - \exp\left(-\chi/\kappa A^+\right) \quad (7)$$

For an accelerated boundary layer the A^+ is modified based on the proposition by Jones and Launder. With this A^+ is a variable $A^+\{K\}$. It is expressed as a function of the dimensionless acceleration parameter. Hence we can state equation (5) as

$$D_{JL} = 1 - \exp\left(-\chi/\kappa A^+\{K\}\right) \quad (8)$$

The subscript JL indicates that the acceleration parameter is based on the Jones and Launder proposition. The difference between D_V and D_{JL} is then calculated. This is an estimate of the damping increase needed to account for acceleration. It is subtracted from the SA f_{v1} damping function to give the following new function.

$$D_{diff} = D_V - D_{JL} \quad (9)$$

$$f_{v1,new} = \max\{(f_{v1} - D_{diff}), 0\} \quad (10)$$

The eddy viscosity is calculated as:

$$v_t = \rho \tilde{v} f_{v1,new} \quad (11)$$

METHOD 2 (Mellor and Herring Type)

In a similar approach to Method 1, we introduce an analogy that represents the variation of A^+ with K in the Van Driest damping, however this is more directly added to the f_{v1} damping function. We define χ_A where the subscript A, denotes the growth of the viscous sub layer. Using this we redefine f_{v1} as

$$f_{v1,new} = \frac{(\chi/\chi_A)^3}{(\chi/\chi_A)^3 + C_{v1}^3} \quad (12)$$

where

$$\chi_A = \max(1.0, \kappa A^+ \{K\}) \quad (13)$$

4. PROBLEM DESCRIPTION

The code adopted for the calculations in this work is the in house Rolls-Royce HYDRA code. The discretization of the Reynolds average Navier-Stokes equation is based on an edge based finite volume scheme. Hydra is an unstructured solver and solves 2D and 3D RANS equation from a user specified boundary condition. The present calculation is for an incompressible flow over a flat plate for different K values. K is changed by varying the geometry's inlet to exit area ratio (AR) and maintaining a constant inlet free stream Mach number. The two dimensional flat plate geometry used in this calculation has a full length of 2.0m. It has been designed such that a zero pressure gradient (ZPG) 0.8m length section is followed by a 0.6m FPG section and terminated by a 0.6m ZPG length for flow recovery. A hexahedral grid is used. A low Reynolds number calculation was performed with $y^+ < 1$. The grid used 549 points in the stream wise direction and 205 (for the least acceleration parameter) for the normal direction. A grid independence study was also carried out doubling the grid points in all directions.

5. RESULTS AND DISCUSSION

The model in ZPG and adverse pressure gradient (AVG) still possess its normal formulation by the original author [5] except in region of strong FPG where the modification is automatically turned on. In Figure 1, a profile for Reynolds shear stress for varying acceleration is shown. The modified SA model for $K=1.5 \times 10^{-6}$ shows good agreement with Jones and Launder's measurements. The peak stress value is around 0.0008 and the Reynolds shear stress profile shows a decrease as it moves further away from the wall. Figure 2 shows the variation of H with K for the modified SA prediction. The solutions indicate that an increase in K tends to shift the value of the shape factor towards a laminar solution which can be explained as the effect of the viscous sub layer thickening. Consequently, the variations of R_2 with K as shown in Figure 3 suggest a decrease in the R_2 for increasing value of K . For $K=3.5 \times 10^{-6}$, R_2 reaches a value around 310. Figure 4 shows a departure of the mean velocity profile for $K=2.5 \times 10^{-6}$ from the logarithmic law of the wall. This departure is however not achievable with the standard SA model as it is not able to predict laminarization.

6. CONCLUDING REMARKS

This work is part of an on going work on crosswind flow around the lip of an aero engine intake lip. The flow around the nacelle lip tends to laminarize under severe acceleration and separate. On the basis of this motivation, an extensive study was carried out for boundary layers that tend to laminarize. This has been examined for sink flow cases. Preliminary calculations using the standard SA model showed this model to be insensitive to predicting laminarization as also mentioned in [3]. The predictions here are all for the modified SA model (method 1 was not as sensitive as method 2 since it did not have the original trend as the f_{v1} damping function and the predicted results show encouraging agreement with Jones and Launder's measurements for sink flow.

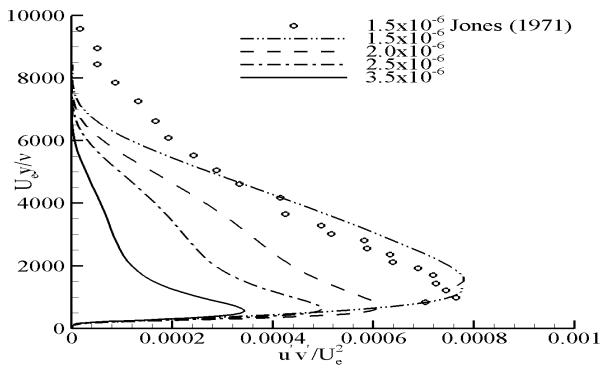


Figure 1. Reynolds shear stress profile for sink flow boundary layer.

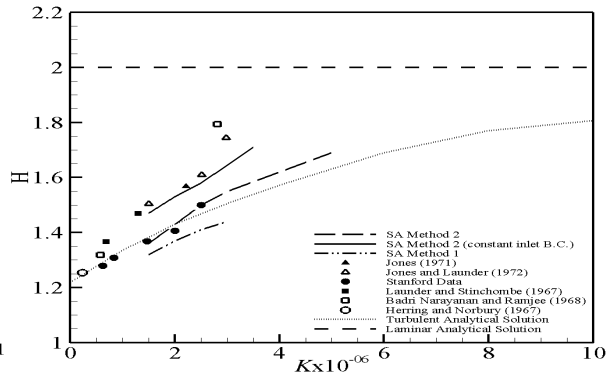


Figure 2. Variation of H with K for sink flow boundary layer [7-12]

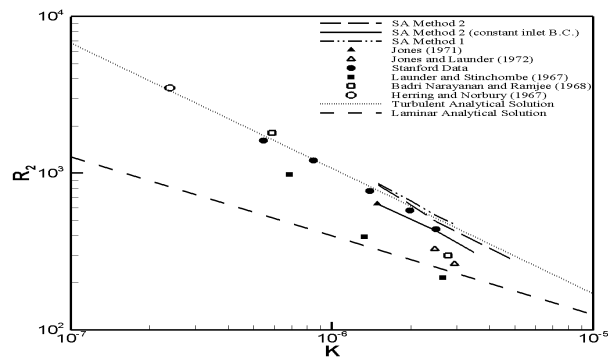


Figure 3. Variation of R_2 with K for sink flow boundary layer. [7-12]

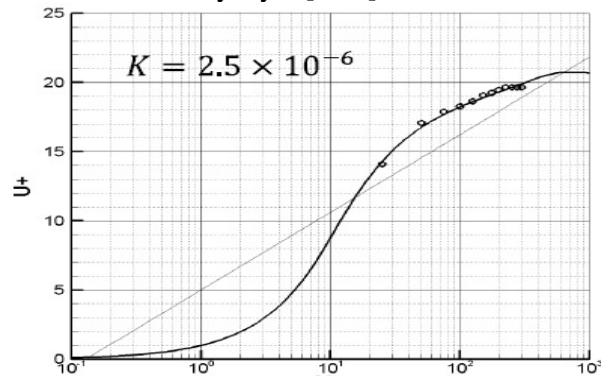


Figure 4. Mean Velocity Profile for accelerating boundary layer.

ACKNOWLEDGEMENT

We like to thank the EPSRC and Rolls-Royce for the CASE award that funded this research.

REFERENCE

- [1] Launder B.E., and Jones W.P., (1968) "On the prediction of Laminarization", Presented at a meeting of the ARC Heat and Mass Transfer Sub-committee, April 5.
- [2] Piomelli U., Balaras E., and Pascarelli A., (2000) "Turbulent structures in accelerating boundary layers", Journal of Turbulence, Vol. 1, Art. No. N1
- [3] Rumsey C.L. and Spalart P.R (2008) "Turbulence model behaviour in low Reynolds number regions of aerodynamic flowfields", AIAA-2008-4403
- [4] Mellor G.L. and Herring H.J. (1968) "Two methods of calculating turbulent boundary layer behaviour based on numerical solution of the equation of motion", Proc. Conf. Turb. Boundary Layer., Stanford.
- [5] Spalart P.R. and Allmaras S.R., (1992) "A One-Equation turbulence model for aerodynamic flows", La Recherche Aerospaciale, No. 1, 1992, pp. 5-21.
- [6] Van Driest E.R., (1956) "On turbulent flow near a wall," AIAA Vol. 23, no. 11, pp1007-1011, 1036
- [7] Herring, H.J. & Norbury, J.F. 1967 Experiments on equilibrium turbulent boundary layers in favourable pressure gradients. J. Fluid Mech. 27, 541.
- [8] Badri Narayanan, M.A. & Ramjee, V. 1968 On the criteria for reverse transition in a two-dimensional boundary-layer flow. India Inst. Sci. Rep. AE 68 FM1.
- [9] Launder, B.E. & Stinchcombe, H.S. 1967 Non-normal similar boundary layers. Imperial college, Mech. Engng Dept. Rep. TWF/TN/21.
- [10] Schraub, F.A. & Kline, S.J. 1965 Stanford University, Mechng Dept. Rep. MD-12
- [11] Jones W.P. & Launder B.E. 1972 Some properties of sink flow turbulent boundary layers. J. Fluid Mech. 56, 337
- [12] Jones W.P. 1971 Laminarization in strongly accelerated boundary layers. Ph.D. thesis, University of London.

COMPUTATIONAL MODELLING OF SURFACE TENSION IN FLUID FLOW SIMULATIONS

*R.J.D. Mackenzie¹, Ł. Kaczmarczyk¹ and C.J. Pearce¹

¹School of Engineering, University of Glasgow, Glasgow, G12 8LT

*r.mackenzie.2@research.gla.ac.uk

Key Words: *surface tension; computational methods; fluid dynamics; surface acoustic waves*

ABSTRACT

Previous attempts to model a fluid free surface have encountered some problems because of the computational techniques adopted. Such techniques typically use an Eulerian approach to formulate the governing equations; a fixed control volume with the fluid particles moving through it. As such this method does not accurately depict the flexibility of free surface flows because the boundaries of the problem are changing constantly in time.

In our initial work we adopt the Particle Finite Element Method. This approach adopts a Lagrangian mesh, allowing for a much more efficient tracking of individual fluid particles as the control volume moves in context with the fluid particles. Separation of particles from the main FE mesh is allowed and hence a much more accurate depiction of the free surface flow and wave splashing is achieved.

Further improvement is still possible and these will be described in this paper. These developments include an Arbitrary Eulerian Lagrangian (ALE) formulation of the governing equations and the introduction of surface tension. Surface tension is an important fluid property that determines the shape of fluid droplets as the fluid aims to minimise surface area. By initially modelling surface tension for a single droplet, the method can be included in larger scale problems such as breaking wave modelling, as well as small scale liquid actuation problems involving surface acoustic waves (SAW). Such analysis will lead to the design of more efficient microfluidic SAW devices for microfluidic applications, for example within the drug delivery and food industries.

1 INTRODUCTION

Surface tension is an important fluid property that has a direct affect on the shape of fluid droplets. To gain an understanding in the mechanism of surface tension is of great benefit for both large scale fluid free surface tracking problems and small scale liquid actuation problems involving surface acoustic waves (SAW). The implementation of surface tension in computational models will have a more obvious affect on the accuracy of small scale problems where results are dependent on only a single fluid droplet or collection of droplets. However, its importance in the modelling of wave splashing and fluid separation should not be discounted, as accurate tracking of droplets breaking away from and rejoining the main fluid body effects the way the body moves as a whole.

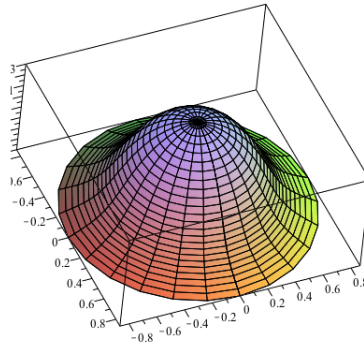


Figure 1.1: Shape of Droplet when subjected to a Surface Acoustic Wave

The work of Alghane et al. [1] saw a method of microscale mixing and pumping using surface acoustic waves (SAW). Whilst this produced several good results, the method used exclusively an Euler mesh and it was assumed that the shape of the droplet is spherical. This is not always the case and as such Alghane et al. did not include surface tension in their analysis. This is what our work aims to implement and Figure 1.1 shows our preliminary semi-analytical result of a fluid droplet resting on a solid surface subject to SAW.

2 METHODS OF FORMULATING THE GOVERNING EQUATIONS

Traditionally, Eulerian algorithms (spatial descriptions) were widely used in fluid dynamics to formulate the governing equations. A Eulerian approach assesses a specific location in the space through which a fluid flows as time passes; this is known as the control volume. The mesh points, comprising the finite element (FE) mesh, are stationary and the fluid particles pass through the mesh, therefore tracking of individual fluid particles is not possible as the properties of each particle can only be assessed whilst they pass through the control volume.

Onate et al. [6] describe an alternative method which they implement in their work. A Lagrangian approach (material description) adopts a system where each node in the FE mesh represents a fluid particle and the motion of an individual particle is followed through time by moving the control volume in context with the particle. An additional benefit of this approach is the fact that particles are allowed to freely move and can even separate from the main FE mesh. However, frequent remeshing of the continuum is required and large distortions are not easily followed. Use of a Lagrangian formulation has been termed as the Particle Finite Element Method (PFEM) by Onate et al. and is used in their work involving analysis of large fluid bodies.

It would appear, however, that neither a solely Eulerian or Lagrangian formulation give an entirely satisfactory outcome and hence, we will implement later in our work, a third approach known as the Arbitrary Lagrangian Eulerian (ALE) approach, as described in Figure 2.1.

ALE combines the most favourable features of both other formulations and this allows for modelling of greater distortions and with more resolution. Figure 2.1 shows a point that represents a given particle and that the point defined in material coordinates can be mapped to spatial coordinates using $x = \varphi(X, t)$ or to mesh space using $\chi = \Psi^{-1}(X, t)$. Additionally, the same point can be mapped from mesh space to spatial coordinates using $x = \Phi(\chi, t)$. Now a velocity of w is applied to the mesh in mesh space. To map from material coordinates to mesh space for the same particle we use $\chi = \Psi^{-1}(X, t + dt)$ and to map from material coordinates to spatial coordinates for the same particle we use $x = \varphi(X, t + dt)$ where dt is the time increment. However, to map from mesh space to spatial coordinates for the same particle we must use the expression $x = \Phi(\Psi^{-1}(X, t + dt), t + dt)$ but to map to the same mesh point we use $x = (\Psi^{-1}(X, t + dt), t)$. Thus the equivalent velocity in spatial coordinates is made up of two parts, $Fwd\tau$ and \hat{v} .

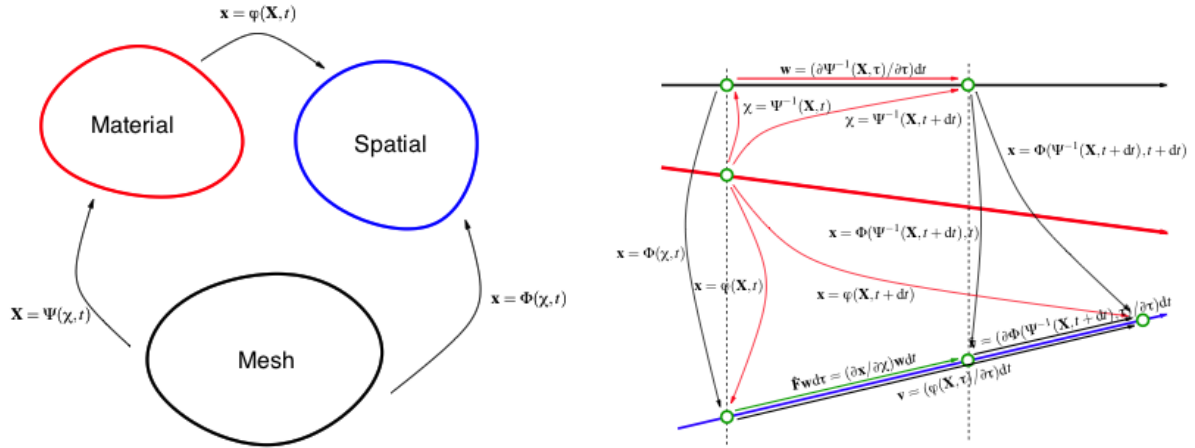


Figure 2.1: Arbitrary Lagrangian Eulerian Mapping

3 ANALYSIS OF A LARGE SCALE DAM BREAK PROBLEM

In our initial work, the PFEM was used in the analysis of a dam break problem to assess the motion of a body of fluid moving under gravity and to examine the motion of wave breaking. The computational code was developed based upon a physical experiment undertaken by Janosi et al. [4], the geometry of which is shown in Figure 3.1. The analysis is formulated from the Navier-Stokes equations that describe the motion of a fluid based upon the conservation of mass, momentum and energy, see Eq. 3.1, where ρ is the fluid density, u is the fluid velocity, t is time, p is the pressure, μ the dynamic viscosity, and F represents body forces. The fluid modelled is incompressible and this is because, in the micro-fluid problems that follow, volume change is negligible at micro-scales.

$$\rho \frac{Du}{Dt} = -\nabla p + \mu \nabla^2 u + F \quad (3.1)$$

The analysis made use of the tools MOAB (Mesh Oriented dataBase)[5], PETSc (Portable, Extensible Toolkit for Scientific Computation)[7], and CGAL (Computational Geometry Algorithms Library)[2]. MOAB stores the mesh and hold information pertaining to the mesh, whilst PETSc solves the system of non-linear algebraic equations, and CGAL assists in mesh and alpha shape creation.

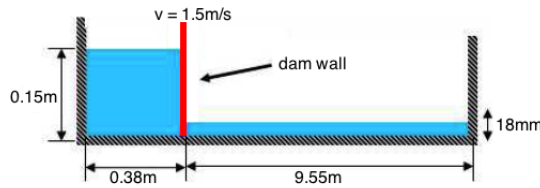
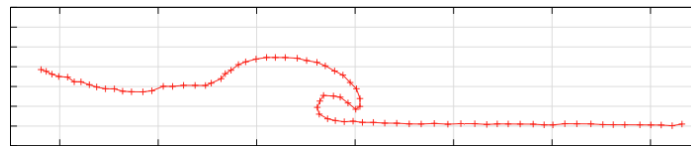
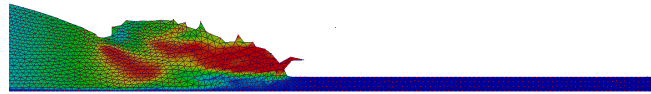


Figure 3.1: Geometry of Dam Break Problem

Photographs were taken during the physical experiment and these were compared to the free surface profile found from our model. Whilst there was a level of correlation to the photographs in terms of the profile of the fluid surface, the fluid in the computational model moved too quickly compared to that in the photographs and wave breaking was achieved at an earlier time than that observed by Janosi et al., see Figure 3.2. This is because turbulence has not been taken into account in our model. Whilst turbulence is a necessary requirement for large scale problems, in the small scale micro-fluid problems that follow it is not important and therefore has not been added into this analysis.



(a) Free Surface Profile from Janosi et al. Experiment



(b) Free Surface Profile from Computational Analysis

Figure 3.2: Comparison of Free Surface Profiles

4 SURFACE TENSION AND FUTURE IMPLEMENTATION

Surface tension is a property of the fluid surface that allows it to resist external force. It is caused by cohesive forces within the fluid due to the surface molecules only having neighbouring molecules on one side and therefore a non-zero net force. This causes the fluid to attempt to reduce its surface area. Surface tension is responsible for the shape of fluid droplets because of this cohesive force and in a zero-gravity environment, fluid droplets will form near perfect spheres.

We have begun to model surface tension in our work. The first step was to examine Total Lagrangian elements (TL elements) as described by Felippa [3]. The displacement of these elements and the current strains and stresses in them are related back to the reference geometry. A simple analysis was developed to assess these elements and to gain an understanding of the elements in general terms.

The next step is to use the tools of MOAB, PETSc and CGAL to model a single droplet of fluid and to identify the edges of the mesh that are on the fluid-air interface. Of course, these edges will change constantly as the droplet moves across a surface or actuates in a certain location and therefore, the identification of surface edges must occur every time step. The analysis will identify these edges and apply a surface tension value to them and thus better model the behaviour of fluid droplets subjected to SAW.

References

- [1] M Alghane, B X Chen, Y Q Fu, Y Li, J K Luo, and A J Walton. Experimental and Numerical Investigation of Acoustic Streaming Excited by using a Surface Acoustic Wave Device on a 128\AA° YX-LiNbO₃ Substrate. *Journal of Micromechanics and Microengineering*, 21(1):015005, January 2011. ISSN 0960-1317.
- [2] CGAL. Computational Geometry Algorithms Library. <http://www.cgal.org>.
- [3] C. Felippa. Nonlinear Finite Element Methods - The TL Bar Element. <http://www.colorado.edu/engineering/cas/courses.d/NFEM.d/>.
- [4] Imre M Janosi, Jan Dominique, K. Gabor Szabo, and Tamas Tel. Turbulent Drag Reduction in Dam-Break Flows. *Experiments in Fluids*, 37:219–229, 2004. doi: 10.1007/s00348-004-0804-4.
- [5] MOAB. Mesh-Oriented datABase. <http://trac.mcs.anl.gov/projects/ITAPS/wiki/MOAB>.
- [6] E Onate, S.R Idelsohn, F Del Pin, and R Aubry. The Particle Finite Element Method-An Overview. *International Journal*, 1(2):267–307, 2004.
- [7] PETSc. Portable Extensible Toolkit for Scientific Computation. <http://www.mcs.anl.gov/petsc>, 2011.

Immersed Finite Element Method for Fluid-Structure Interaction

Thomas R berg¹, *Fehmi Cirak¹

¹Department of Engineering, University of Cambridge, Trumpington Street, Cambridge, CB2 1PZ

*f.cirak@cam.ac.uk

Key Words: *fluid-structure interaction; finite elements; immersed boundary methods*

ABSTRACT

A finite element technique is presented which does not rely on body-fitted meshes. This method is tailored for the numerical analysis of fluid flow around moving and highly flexible objects as in the context of fluid-structure interaction. A variationally consistent penalty method is used for the treatment of no-slip boundary conditions and LBB-stability is achieved by means of a subdivision stabilisation technique. The full interaction between incompressible fluid flow and elastic structures is handled by strong coupling.

1 INTRODUCTION

The numerical analysis of many fluid-structure interaction problems, such as, e.g., flapping flight or hemodynamics, faces the difficulty of exceedingly large structural motions and deformations. In this context, standard finite element methods suffer from severe mesh distortions and therefore require complicated mesh adaptation algorithms. This defect is our main motivation to favour immersed finite element techniques which do not rely on any mesh generation but operate on simple Cartesian grids [1].

Obviously, the imposition of Dirichlet boundary conditions, i.e., the no-slip at the structural surface, is not straightforward. Here, we use a modification of the variationally consistent penalty method, commonly referred to as Nitsche's method [2], in which these boundary conditions are treated as natural conditions and a penalty term is added purely for stability reasons.

The finite element discretization is based on *b*-splines [3] which allow for arbitrary approximation orders. The use of implicit surface representations for the immersed objects adds an extra degree of robustness and flexibility to the numerical computations. This is verified by the examples presented here.

Another technical difficulty arises from cells which are traversed by the boundary Γ_D such that their contribution to the system matrix is vanishingly small. Since arbitrary surface motions are allowed, this problem requires a robust solution. Therefore, we employ on a special preconditioner as given in [3].

2 IMMERSSED FLUID SOLVER

Consider the incompressible Navier-Stokes equations in a fluid domain Ω with density ρ and viscosity μ formulated in the stress divergence form

$$\rho \left(\frac{\partial \mathbf{u}}{\partial t} + (\mathbf{u} \cdot \nabla) \mathbf{u} \right) - \nabla \cdot \boldsymbol{\sigma}(\mathbf{u}, p) = \mathbf{f}, \quad \nabla \cdot \mathbf{u} = 0, \quad \mathbf{x} \in \Omega \quad (1)$$

with the fluid stress $\boldsymbol{\sigma}(\mathbf{u}, p) = -p\mathbf{I} + \mu(\nabla \mathbf{u} + \nabla \mathbf{u}^\top)$. The corresponding boundary conditions are

$$\mathbf{u} = \bar{\mathbf{u}}, \quad \mathbf{x} \in \Gamma_D, \quad \text{and} \quad \mathbf{t}(\mathbf{u}, p) = \boldsymbol{\sigma}(\mathbf{u}, p) \cdot \mathbf{n} = \bar{\mathbf{t}}, \quad \mathbf{x} \in \Gamma_N, \quad (2)$$

on the boundary parts Γ_D and Γ_N such that $\Gamma = \partial\Omega = \Gamma_D \cup \Gamma_N$. In practical terms, the Dirichlet conditions on Γ_D will be the inflow and no-slip boundary conditions, whereas Γ_N refers to the outflow boundary.

The weak form that we use incorporates both boundary conditions as natural conditions and reads: find (\mathbf{u}, p) such that

$$\begin{aligned} 0 = & \rho \int_{\Omega} \left(\frac{\partial \mathbf{u}}{\partial t} + (\mathbf{u} \cdot \nabla) \mathbf{u} \right) \cdot \mathbf{v} \, d\mathbf{x} + \int_{\Omega} \boldsymbol{\sigma}(\mathbf{u}, p) : \nabla \mathbf{v} \, d\mathbf{x} - \int_{\Omega} q(\nabla \cdot \mathbf{u}) \, d\mathbf{x} - \int_{\Omega} \mathbf{f} \cdot \mathbf{v} \, d\mathbf{x} \\ & - \int_{\Gamma_N} \bar{\mathbf{t}} \cdot \mathbf{v} \, ds - \int_{\Gamma_D} \mathbf{t}(\mathbf{u}, p) \cdot \mathbf{v} \, ds - \int_{\Gamma_D} \mathbf{t}(\mathbf{v}, q) \cdot (\mathbf{u} - \bar{\mathbf{u}}) \, ds - \gamma \int_{\Gamma_D} (\mathbf{u} - \bar{\mathbf{u}}) \cdot \mathbf{v} \, ds \end{aligned} \quad (3)$$

for all admissible (\mathbf{v}, q) .

Since the weak form (3) is formulated without essential boundary conditions, it allows for more freedom in the choice of the finite element discretization. In view of the final application to fluid-structure interaction with large deformations, our choice is an orthogonal grid with b -spline shape functions. The finite element approximations are thus

$$\mathbf{u}_h(\mathbf{x}) = \sum B_i(\mathbf{x}) \mathbf{u}_i \quad \text{and} \quad p_h(\mathbf{x}) = \sum \tilde{B}_j(\mathbf{x}) p_j \quad (4)$$

with the b -splines B_i and \tilde{B}_j of specific polynomial degree. In order to fulfil the LBB-stability condition, we choose equal polynomial degrees for B_i and \tilde{B}_j but approximate the velocities on a grid which is one level finer than the grid used for the pressure. Using the refinability property of b -splines, we actually operate exclusively on the finer grid but mimic the coarse grid splines \tilde{B}_j as linear combinations of fine grid splines, i.e., $\tilde{B}_j = \sum s_{jk} B_k$ with a predefined mask s_{jk} .

3 FLUID-STRUCTURE COUPLING

For the interaction between fluid and elastic structures, we combine the fluid solver as described in the previous section with a structures solver which can handle large deformations. In order to represent the complete interaction between these media, a strong coupling iteration is used, see, e.g., [4]. Therefore, at each discrete time point t_n the following iteration scheme is carried out

- given the location and surface velocity of the structure, solve the fluid problem for the velocity and pressure fields;
- evaluate the surface tractions that the fluid applies on the structure surface;
- solve the structure problem for its new location and velocities;
- if converged go to the next time step, otherwise iterate again.

4 RESULTS

As example applications of the presented method, consider the viscous flow in a two-dimensional channel around deformable objects. Two such examples are depicted in the top row of figure 1: a circle and a beam. On the left side of the channel, parabolic inflow is prescribed and the immersed objects deform elastically in response to the fluid forces acting on them. Based on the characteristic length $c = 0.2$ for the circle and $c = 0.51$ for the beam, the Reynolds numbers are $Re = 80$ and 204 , respectively. The immersed objects are modelled by dynamic large-deformation beam elements with bending stiffnesses of $EI = 5.6 \cdot 10^{-4}$ and $2.6 \cdot 10^{-3}$, respectively.

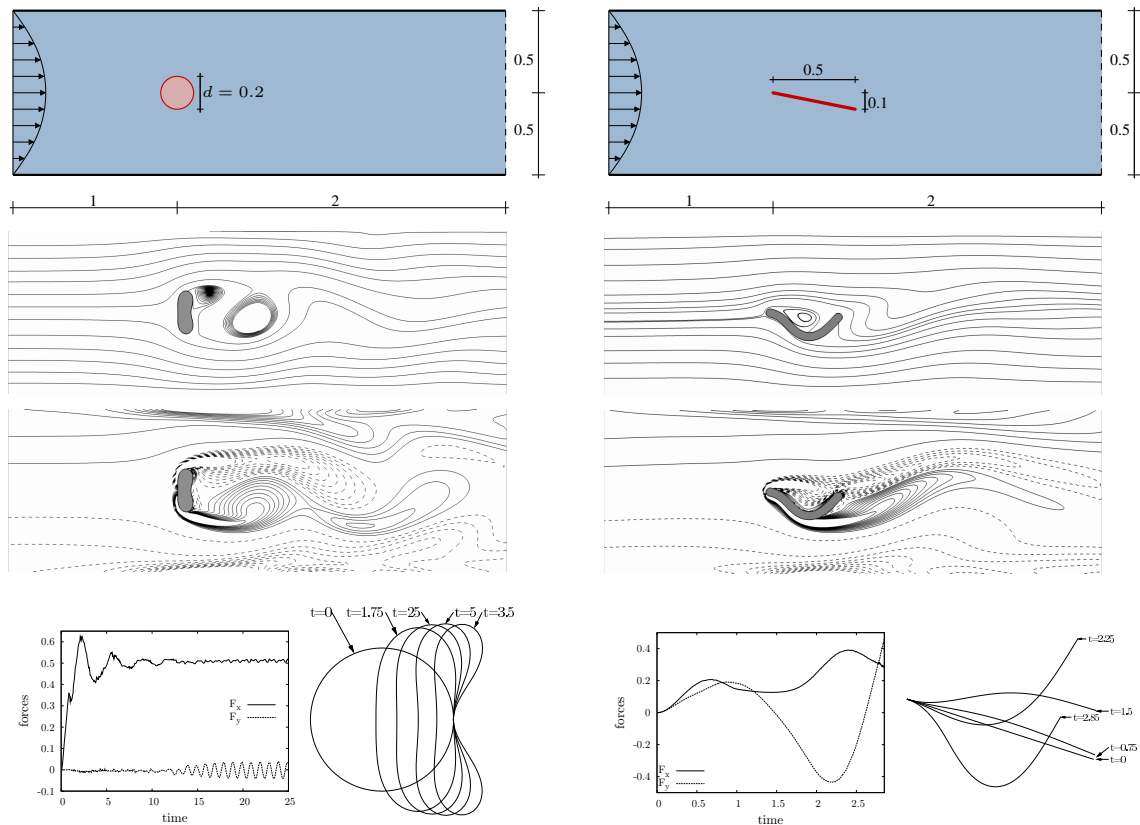


Figure 1: Flow around a cylinder (left) and an inclined beam (right): problem description (top), streamline and vorticity snapshots (middle), forces acting on and deformed shapes of the immersed object (bottom)

In the case of the circle, the deformation reaches a steady state and the flow field around is adapted to it. After some initial time, the typical vortex shedding appears as clearly visible in the streamline and vorticity plots. This effect is reflected by the force history. The beam, on the other hand is first deflected upwards due to the inflow. This upward deflection reaches a point where the flow applies in turn a downward force on the object. The deformation builds up and becomes unstable.

References

- [1] R. Mittal and G. Iaccarino. Immersed boundary methods. *Annual Review of Fluid Mechanics*, 37, 239–261, 2005.
- [2] R. Stenberg. On some techniques of approximating boundary conditions in the finite element method. *Journal of Computational and Applied Mathematics*, 63, 139–148, 1995.
- [3] K. Höllig. *Finite Element Methods with B-splines*. SIAM Frontiers in Applied Mathematics, 2003.
- [4] U. Küttler and W.A. Wall. Fixed-point fluid-structure interaction solvers with dynamic relaxation. *Computational Mechanics*, 43, 61–72, 2008.

Predicting aircraft structural response to water impact

L. Papagiannis* and J.C. Campbell

School of Engineering, Cranfield University, Cranfield, Bedfordshire, MK43 0AL.

* l.papagiannis@cranfield.ac.uk

Key Words: ditching; fluid-structure interaction; coupled FE-SPH

ABSTRACT

As a part of the aircraft certification process, manufacturers are obliged to show that following a water landing, known as ditching, the aircraft will be able to stay afloat in order to allow the safe disembarkation of passengers. Improved design tools are required to support cost-effective design and entry into service of aircraft containing new materials and structures. Detailed analysis of ditching using a transient finite element structural model requires a suitable fluid model. One approach is to use the Smoothed Particle Hydrodynamics (SPH) method to represent the fluid, allowing a coupled fluid-structure analysis to be performed. This approach is established for vertical impacts on water, but has limited application to ditching as key aspects of the flow physics that occurs at high speed are not included in the model. Aspects such as cavitation and suction influence the structural response and must be included in any suitable tool. This paper discusses the current state of the art with respect to ditching analysis using the SPH method. The key missing aspects of the flow physics are discussed, including the challenges related to including them in a coupled model.

1 INTRODUCTION

A ditching event is described as the planned water landing of an aircraft. As a part of the aircraft certification process, manufacturers are obliged to show that following a ditching, the aircraft will be able to stay afloat in order to allow the safe disembarkation of passengers [1]. High impact loads during ditching can cause structural damage that allows water to enter the fuselage, posing a risk to the safe egress of the passengers [2]. In a water impact the loads experienced by the fuselage are not the same as from impact on a hard surface with the fuselage skin forming a key part of the load path, figure 1. The structural integrity of the aircraft following the ditching is a key feature in survivability. It is shown from data collected between 1959 until 1996 that most fatalities are a result of drowning rather than direct crash injuries [1].

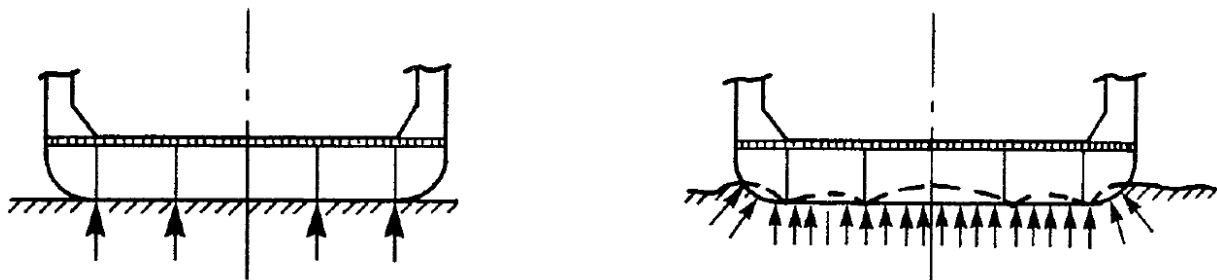


Figure 1: Loading of a structure during a hard surface impact (left) and a soft/fluid surface (right) [3].

Typically the configuration of an aircraft during ditching is similar to the landing configuration but with the landing gear retracted. This means that the first point of contact is the lower aft section of the fuselage. Following the first impact there can be a strong pitch down moment on the aircraft, resulting in

a second impact on the forward fuselage and potentially nose diving. It must be noted that during a ditching event there are other factors outside the control of the crew like the state of the water (sea state) that can have a significant effect on the behaviour of the aircraft when impact occurs [4].

The classical approach to ditching design uses scale model experimental data, over a range of conditions, to derive structural loads. Increasingly this has been supplemented by simple analytical models for the water behaviour. A consequence of this classical approach is that ditching certification for novel fuselage shapes, structural concepts or materials is expensive and time consuming. Improved numerical tools are required that can predict the structural loads and response during ditching

So far water impact simulations that include a deformable structure have been focused on vertical impact, see for example Pentecote et al. [5]. The ability of these simulation techniques to predict fixed-wing aircraft ditching, which is characterised by a high initial horizontal velocity, is limited. Important aspects of the flow physics such as cavitation, ventilation and suction are omitted. These physical effects significantly influence the pressure distribution and deformation of the skin and hence the structural response cannot be predicted without them.

2 WATER BEHAVIOUR DURING DITCHING

A ditching event includes complex fluid-structure interaction. There are several important phenomena that influence the structural loading from the fluid. In this section these will be briefly introduced.

Air cushioning

During the impact, trapped air between the object and the fluid provides a cushioning effect [6], referred to as air cushioning. The presence of this air cushion alters the structural loads, in particular initial impact pressures. As the amount of trapped air increases, initial impact pressures become lower [6].

Suction

Suction occurs where the fluid pressure is low, resulting in an outward force on the structure. During ditching, the aft part of the fuselage can experience a region of suction that potentially can generate both local structural loads as well as a significant pitch up moment [4].

Cavitation

Cavitation is the result of the phase change of the fluid from liquid to vapour [7], occurring where the liquid pressure falls below the vapour pressure. The typical result is a cloud of vapour bubbles forming in the fluid. The primary relevant effect of cavitation for the structural loads during ditching is that it acts as a limit on local suction forces from the fluid.

Ventilation

Ventilation occurs when air enters between the structure and the fluid [8]. It is often linked to cavitation as the low fluid pressures that cause cavitation also draw in air.

3 DITCHING MODELLING

Non-linear explicit finite element analysis is well established in the crash analysis field for the prediction of structural response, see for example Fasanella and Jackson [9]. The requirement for ditching analysis is a suitable fluid model that can be robustly coupled with the structural model. One approach in use is to model the fluid with the Smoothed Particle Hydrodynamics (SPH) method, a contact algorithm is used for coupling the fluid model with the structural model. SPH is a meshless Lagrangian method that uses a pseudo-particle interpolation method to compute smooth field variables. Each SPH particle has a mass, Lagrangian position, Lagrangian velocity, and internal energy; other quantities are derived by interpolation or from constitutive relations. A detailed explanation of the SPH method is given by

Monaghan [10].

The coupled finite element-SPH approach has been applied to a range of fluid structure impact problems [5,11]. One example is the impact on water of an aluminium structure, characteristic of a helicopter cabin sub-floor [11]. Experimental data is available [12] for the impact of the structure on water. In the experiment the structure was mounted on a trolley and dropped with an impact velocity of 7.95 m/s. The total mass on the structure and trolley was approximately 600 kg. A finite element model of the sub-floor structure was constructed using shell elements with appropriate elastic-plastic material properties. The trolley was represented as a rigid mass, and time history information for the trolley acceleration was measured. The initial state of model is shown in figure 2 and consists of approximately 38000 shell elements and 61500 SPH particles. The overall deformation of the FE structure is consistent with the deformation observed in the experiment, figure 3.

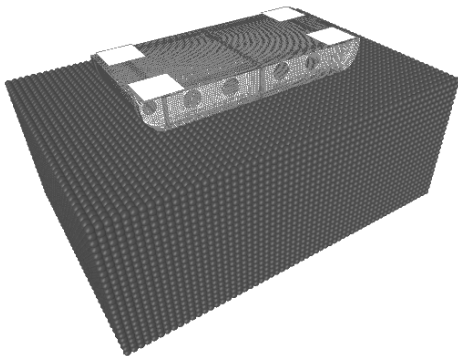


Figure 2: Initial problem setup.

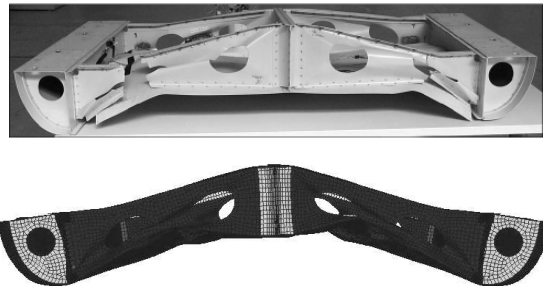


Figure 3: Comparison of deformed shape of test article and FE mesh.

With respect to published ditching simulation results there are some common characteristics [5,11,13]. The water is modelled as a simple inviscid compressible fluid using a simple equation of state to define the pressure-volume relationship. Where ditching simulations with a forward velocity have been attempted [5], the same simple fluid model has been used.

At present the important phenomena identified in section 2 are not represented within a coupled finite element-SPH analysis. Air is not included in the models as its inclusion would significantly add to the cost and complexity of the analyses. The suction force is not represented [14], as the contact algorithms used do not allow tensile forces to be generated between the fluid and structure. Simple cavitation models that use a cut-off value to limit the pressure have been investigated [15-16], but the suitability of this approach for high-speed water flow past a body has not been investigated.

4 FUTURE DEVELOPMENT

It is understood that in high velocity water impacts the complex phenomena that occur in the water flow can have a significant effect on the structural integrity of a structure. While the analysis of vertical impact of structures on water is established, the simplified fluid models used mean that they can not be directly applied to ditching analysis of fixed wing aircraft. The objective of this PhD research project is to develop and demonstrate an improved coupled finite element/SPH modelling methodology that is capable of predicting the response for a deformable structure subject to impact on water at a high horizontal velocity. The research will concentrate on the development of an improved fluid model and fluid-structure interaction model that incorporates the effects of the phenomena identified.

Acknowledgement

L. Papagiannis is funded by the EPSRC through the Cranfield University Doctoral Training Account.

References

- [1] Patel, A.A. and Greenwood R.P. Jr. "Transport water impact and ditching performance". *Final Report DOT/FAA/AR-95/54*, US Department of Transportation (1996).
- [2] Streckwall H., Lindenau O. and Bensch L. "Aircraft ditching: a free surface/ free motion problem." *Archives of civil and mechanical engineering* VII, no. 3 (2007): 177-190.
- [3] Zimmermann R.E., Warrick J.C., Lane A.D., Merritt N.A. and Bolukbasi A.O. "Aircraft Crash Survival Design Guide. Volume III: Aircraft Structural Crash Resistance" *U.S. Army Aviation Research & Technology Activity Report USAAVSCOM TR 89-D-22C* (1989).
- [4] Smith, A. G., C. H.E. Warren, and D. F. Wright. *Investigations in the Behaviour of Aircraft When Making a Forced Landing on Water (Ditching)*. Ministry of Supply Aeronautical Research Council Reports and Memoranda, 1957.
- [5] Pentecote N., Kohlgruber D. and Kamoulakos A. "Simulation of water impact problems using the smoothed particle hydrodynamics method." *ICD Proceedings*. (2003).
- [6] Bullock, G.N., A.R. Crawford, P.J. Hewson, M.J.A. Walkden, and P.A.D. Bird. "The influence of air and scale on wave impact pressures." *Coastal Engineering*, vol. 42 (2001): 291-312.
- [7] Franc, J.-P. Physics and Control of Cavitation. In *Design and Analysis of High Speed Pumps* (pp. 2-1 – 2-36). Educational Notes RTO-EN-AVT-143, Paper 2. Neuilly-sur-Seine, France: RTO. (2006) Available from: <http://www.rto.nato.int/abstracts.asp>.. (accessed 01 10, 2011).
- [8] Faltinsen O.M. *Hydrodynamics of High - Speed Marine Vehicles*. New York: Cambridge University Press (2005)
- [9] Fasanella E.L. and Jackson K.E. "Best practices for crash modelling and simulation" Technical report NASA/TM-2002-211944 (2002).
- [10] Monaghan, J. J. "Smoothed particle hydrodynamics." *Reports on Progress in Physics*, vol. 68 (2005): 1703-1759.
- [11] Patel M.H., Vignjevic R., Campbell J.C. "An SPH Technique for Evaluating the Behaviour of Ships In Extreme Ocean Waves", *International Journal of Maritime Engineering* 151 (2009) 39-47.
- [12] Vigliotti A., "Metallic specimen test report, D.6.5.1.2." *CAST (Crashworthiness of helicopters on water: design of structures using advanced simulation tools)*. EU Framework V project, Contract GARD-CTI999-01728, CIRA, Italy. (2003)
- [13] Francesconi E., Anghileri M. "A numerical - experimental investigation on crash behaviour of skin panels during a water impact comparing ALE and SPH approaches." *7th European LS-DYNA Conference*. Salzburg, Austria, (2009)
- [14] Streckwall, H., O. Lindenau, and L. Bensch. "Aircraft ditching: a free surface/ free motion problem." *Archives of civil and mechanical engineering* VII, no. 3 (2007): 177-190.
- [15] Zardoni L. "Cavitation modelling in DYNA3D" MSc Thesis, Cranfield University (2005)
- [16] Ma, Q. W., Andrews D.J. "On techniques for simulating effects of cavitation associated with the interaction between structures and underwater explosions using LS-DYNA." *3rd European LS-DYNA Conference*. Paris, France (2001)

A Coupling Simulation Interface for Performance-Based Wind Engineering of Tall Buildings

***Gordon H. Clannachan¹, Nenad Bićanić² and Graham M. Copeland¹**

¹Department of Civil Engineering, University of Strathclyde, John Anderson Building, Glasgow, G4 0NG

²Department of Civil Engineering, University of Glasgow, Rankine Building, Glasgow, G12 8LT

*gordon.clannachan@strath.ac.uk

Key Words: *performance-based design; wind engineering; tall buildings; fluid-structure interaction; coupling interface*

ABSTRACT

A Performance-Based Wind Engineering (PBWE) framework for assessing the serviceability limit state of tall buildings is considered. The immediate focus is on a key component of this procedure which involves creating an appropriate coupling interface between two independent fluid and structural solvers. The fluid solver (ANSYS FLUENT) uses the finite volume method to model the wind field and predict the wind-induced loads. The structural solver (Strand7) applies the finite element method to model the resulting dynamic response. The requirement of the coupling algorithm is to appropriately consider the interaction phenomena involving the wind and the tall building. Clearly, no single coupling algorithm exists which may be appropriate for all fluid-structure interaction problems; the choice depends on an appropriate level of detail and accuracy in a given simulation setting and has a significant impact on the computational demand and accuracy. The decision on the level of complexity for this particular coupling problem is related to the inherently probabilistic context of the PBWE framework and its ability to account for a whole range of uncertainties. The code for the coupling interface has been developed using Microsoft VBA and its functionality will be demonstrated using a case study of a standard 49-storey tall building. Attention will be focused on its capabilities and the potential consequences of its limitations.

1 INTRODUCTION

Modern design trends and advances in engineering materials have encouraged the demand for taller and more slender buildings. This pattern induces inherent structural flexibility and heightens concerns regarding Aeolian risk. Complete structural failure caused by the wind is extremely unlikely. Instead, the primary concerns are related to serviceability failures such as damage to non-structural components and unacceptable occupant comfort conditions due to building motion. Intrinsic uncertainties arise in such Wind Engineering problems due to the complexity and stochastic nature of both the loading and response parameters. This paper explores the potential for adopting a probabilistic approach to Wind Engineering of tall buildings. The proposed framework implements advanced numerical simulation methods to model the fluid-structure interaction (FSI) phenomena. An appropriate coupling simulation interface between the independent fluid and structural solvers is an essential component.

2 PERFORMANCE-BASED WIND ENGINEERING

Performance-based design (PBD) offers a novel approach for handling the risks faced by structures in a probabilistic context, rationally reducing these risks for both design and retrofitting strategies [1]. The concepts of PBD have developed predominantly in Seismic Engineering. The last decade, however, has seen a gradual increase towards adapting these established frameworks for Fire, Blast and Wind Engineering [2]. The fundamental aim of Performance-Based Wind Engineering (PBWE) is to ensure that key structural damage limitations associated with the risk of wind loading are satisfied with an

acceptable probability throughout the design life of the structure. The probabilistic context of PBD can incorporate the inherent uncertainties associated with Wind Engineering.

Researchers from the Pacific Earthquake Engineering Research (PEER) Centre in Berkeley developed an effective PBD framework for Seismic Engineering [3]. Early attempts have since been made at the Sapienza University of Rome at extending this theory to Wind Engineering to assess the performance of long-span bridges [2]. The procedure has been subdivided into five clearly-defined sequential stages. The first stage, Intensity Measure (IM), involves characterising a range of relevant Aeolian events based on the site-specific wind environment. The mean wind speed and turbulence properties of each IM event are dependent on key variables such as height, risk of exceedance, terrain roughness, directionality, and local topography. The Interaction Parameter (IP) phase entails a series of analyses that consider the interaction effects between the derived range of IM wind events and the tall building. The probabilistic assessment of the resultant structural response is based on a chosen measure of Engineering Demand Parameter (EDP) i.e. interstorey drift, root-mean-square acceleration, or peak displacement. The Damage Measure (DM) identifies the structural damage as a consequence of the EDP response. The DM limits can be based on life safety, structural integrity, or functionality requirements and must be appropriate for the considered risk. Finally, the Decision Variable (DV) translates the DM estimates into a quantifiable measure of likely losses from Aeolian risk throughout the design life of the structure. The performance, or adequacy, of the structural design can be decided on the basis of these results.

The focus of the current research is to introduce advanced simulation techniques to support such a PBWE framework and address weaknesses identified by previous studies. Specifically, the techniques of Computational Fluid Dynamics (CFD) and Computational Structural Mechanics (CSM) will be implemented into PBWE. It is intended that the former will offer an improved characterisation of the wind field and prediction of the subsequent wind loading, while the latter will provide a detailed prediction of the resultant dynamic response of the tall building. The proposed numerical improvements require an efficient coupling interface to communicate between the fluid (ANSYS FLUENT) and structural (Strand7) solvers during the Interaction Parameter analyses.

3 COUPLING ALGORITHM FOR FLUID-STRUCTURE INTERACTION

A range of different coupling algorithms are available and each has its own advantages and limitations. The coupling strategies can be classified as monolithic, partitioned (or staggered), and one-way. Clearly, no single coupling algorithm is ideally suited for all FSI problems; the choice depends on an appropriate level of detail and accuracy vs. uncertainty in a given simulation setting and has a significant impact on the computational demand and accuracy.

Monolithic coupling simultaneously solves the entire fully coupled set of governing equations for both the fluid and structural domains. Full aeroelastic effects can be considered to evaluate the movement-induced excitation caused by the structural motion. However, this method is computationally very demanding and difficult to implement, particularly for multi-degree-of-freedom (MDOF) problems [4]. A partitioned approach independently solves each domain; it moves intermittently between the fluid and structural solver throughout the simulation. Coupling is achieved by specifying continuity conditions between the mesh motions of each domain. The strength of coupling depends on the number of iterations performed to achieve convergence at each transition. The computational requirements are clearly less demanding than monolithic coupling. Nonetheless, it has been identified that this method also presents difficulties when applied to MDOF problems [5]. A one-way strategy allows the fluid solver to predict a range of pressure histories before transferring these loads to the structural solver to determine the dynamic response. The underlying assumption is the motion of the structure has a negligible effect on the flow pattern and thereby the algorithm does not account for aeroelastic phenomena. This coupling method is suited to relatively stiff structures.

The probabilistic nature of PBWE and its ability to account for uncertainties suggest the basic one-way coupling strategy can be adopted. The algorithm has been developed within the Visual Basic Application (VBA) in Microsoft Excel. The mean velocity and turbulence profiles from each of the characterised IM wind events act as inflow conditions for separate unsteady CFD analyses in ANSYS FLUENT. A series of monitors across the tall building record the predicted pressures throughout the simulations. The coupling interface exports the database of pressure histories from each IM wind event as a collection of forcing functions and assigns these to the corresponding locations on the Strand7 structural model. The

algorithm initiates the dynamic structural solver and extracts the acceleration history for the EDP response. An overall assessment of the EDP results gives a distribution of the acceleration data. The DM is based on acceleration levels which cause unacceptable occupant comfort conditions. If the specified DV threshold is exceeded then the tall building design must be revised to increase the stiffness.

4 ILLUSTRATIVE EXAMPLE: 49-STOREY TALL BUILDING

The performance of the coupling interface will be demonstrated by applying the enhanced PBWE framework to a 49-storey standard tall building. The structure has a rectangular prismatic shape and its dimensions are $D = 30$ m, $B = 45$ m and $H = 180$ m. The lateral stability of the structural system is provided by a concrete core and provides a fundamental natural frequency of 0.26 Hz. An acceleration range between 4-12 milli-g is generally accepted as causing unacceptable occupant comfort conditions. An agreed DV strategy would specify that this acceleration threshold is not exceeded on more than n instances throughout the design life. The overall assessment requires the full range of IM wind events to be simulated. This example here details a procedure for a single IM wind event only, in the overall PBWE framework an analogous procedure needs to be repeated for sampled (e.g. hypercube) IM events. The geometry of the computational domain in ANSYS FLUENT is chosen large enough to ensure the flow is not constrained at the tall building and the obstacle effects on the inflow and outflow are eliminated. The building is oriented with the incident wind normal to one of the wider faces. Equations for the vertical profiles of mean wind speed and turbulence were written in C programming language and interpreted in ANSYS FLUENT. The reference mean wind speed at the building height was 41 ms^{-1} . The domain gives a 0.9% blockage ratio and is shown along with the boundary conditions in Figure 1. The mesh generation strategy is aimed at computational efficiency, i.e. at providing a number of elements as low as feasibly possible, while satisfying near-wall meshing requirements. Figure 2 shows the grid arrangement on the boundary surfaces. The main characteristic of the mesh style is that it uses a grid nesting technique; the tall building is nested in a rectangular cylinder about four times larger than itself. The zones outside the nest use a fully structured mesh of hexahedral elements, while an unstructured mesh is applied within the nest volume. This meshing scheme allows the near-wall region at the building faces to be fine enough and the outlying extents of the domain to be more appropriately coarser. The generated grid has 2.96×10^6 elements.

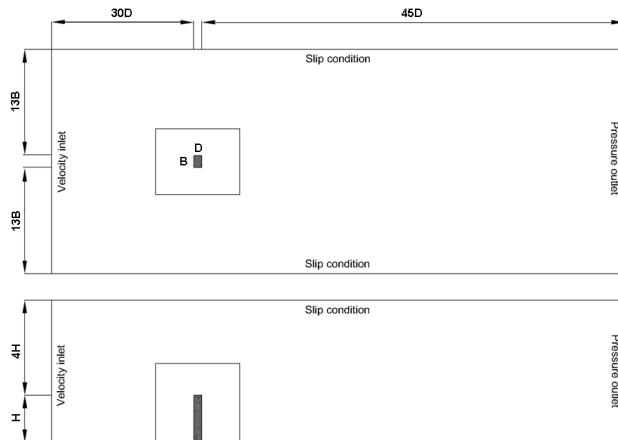


Figure 1. Domain and boundary conditions

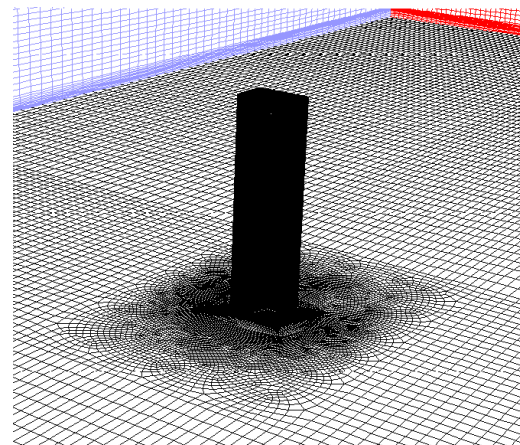


Figure 2. Surface mesh for the fluid field

The transport equations were solved using the RANS $k-\epsilon$ turbulence model with RNG modifications. The CFD computations were performed on a high-performance computer in the Faculty of Engineering at the University of Strathclyde. A total of 8 CPUs were used in parallel for the simulation. The numerical time step was 5×10^{-3} s and 24000 steps (5 subiterations) were iterated to provide a flow time of 120 s. A total of 90 CPU hours were required. The surface monitors recorded the predicted pressures at 0.1 s intervals and stored this data in an external .out file format.

The VBA coupling interface code extracted the wind pressures from the generated output files and imported this data as a series of forcing functions into the Strand7 structural model. The coupling

algorithm was then responsible for assigning these force histories to the corresponding positions on the building envelope for a linear transient dynamic analysis of the structural response.

The detailed finite element model was created in Strand7 using a total of 12327 beam and 40791 plate elements (Figure 3). Modal superposition involving the first 20 natural eigenvalues was performed and the structural damping was estimated using the Rayleigh method. The transient settings corresponded to the conditions specified in the fluid solver. The CSM simulation required 22 CPU hours on a standard desktop machine. The estimated EDP history of the absolute top floor acceleration is shown in Figure 4. It can be seen that the predicted values for this particular IM event do not exceed the threshold leading to unacceptable occupant comfort conditions. However, an overall assessment in the context of the PBWE framework requires a full range of determined IM wind events to be completed.

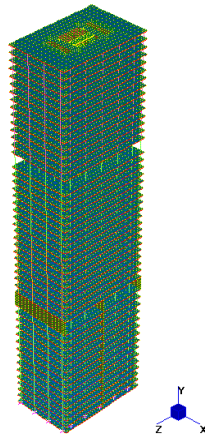


Figure 3. Strand7 finite element model

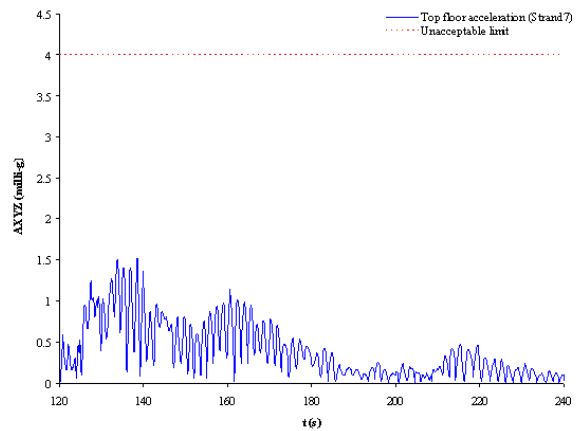


Figure 4. Top floor EDP absolute acceleration response

5 CONCLUSIONS

An enhanced PBWE framework for tall building design has been proposed. A probabilistic approach to Wind Engineering can incorporate the intrinsic uncertainties associated with such problems. The aim is that the introduction of advanced computational methods will improve the wind field characterisation, prediction of wind loads, and estimation of dynamic structural response. The paper has identified the importance of an appropriate coupling simulation interface to communicate between the fluid and structural solver. The role of the coupling algorithm has been demonstrated by following the proposed PBWE framework for a 49-storey standard tall building design using an illustrative, single IM wind event. In the overall PBWE framework an analogous procedure needs to be repeated many times. The adopted one-way coupling strategy has a limited range of applications and is not appropriate for FSI analyses of highly-flexible structures such as aircraft wings or suspension bridges. It must be assured that the effect of aeroelastic phenomena can be safely neglected or otherwise considered in the context of the simulation setting.

References

- [1] G. Augusti and M. Ciampoli, Performance-Based Design in risk assessment and reduction, *Probabilistic Engineering Mechanics*, 23, 496-508, 2008.
- [2] F. Petrini, M. Ciampoli, and G. Augusti, A probabilistic framework for Performance-Based Wind Engineering. In: *Proc. 5th European and African Conference on Wind Engineering*, Florence, Italy, 19-23 July, 2009.
- [3] J. Moehle and G.G. Deierlein, A framework methodology for performance-based earthquake engineering. In: *Proc. World Conference on Earthquake Engineering*, Vancouver, Canada, 1-6 August, 2004.
- [4] M.M. Joosten, *Analysis of Gauß-Seidel solution strategy for coupled problems based on a one-dimensional model problem*, M.Res. Swansea University, 2007.
- [5] Braun and Awruch, Aerodynamic and aeroelastic analyses on the CAARC standard tall building model using numerical simulation. *Computers and Structures*, 87, 564-581, 2009.

Prediction of Laminar Separation Bubble using URANS approach

* V. Nagabhushana Rao¹, Richard Jefferson-Loveday¹ and Paul G Tucker¹

¹Whittle Laboratory, University of Cambridge, 1 JJ Thomson Ave., Cambridge, CB3 0DY, United Kingdom

*nrv24@cam.ac.uk

Key Words: *laminar Separation bubble; transition; turbulence; URANS*

ABSTRACT

The performance of different Unsteady RANS models were evaluated against DNS, for a boundary layer separating over a flat plate, subjected to a prescribed adverse pressure gradient. With minimal fine-tuning, the decay of free stream turbulent kinetic energy was matched with the value predicted by DNS at the point of separation. A reasonable agreement on predicting the trends of the velocity profiles, streamwise velocity fluctuations and shear stress, was obtained by the URANS models. However, a larger separation bubble is predicted by all the models. The streamwise evolution of skin friction coefficient and the contours of turbulent kinetic energy showed that the delay in the production of sufficient turbulent kinetic energy to suppress the bubble, resulted in a larger separation bubble. While using SA model, the turbulent to laminar viscosity ratio, VR , at the inlet is shown to be a crucial parameter to reproduce a laminar separation bubble. Rational solutions could only be obtained using ‘transition by contact’ process.

1. INTRODUCTION

Numerous DNS [see e.g. 1, 10, 11, 12]; LES [see e.g. 2, 7] and URANS [see e.g. 3, 4] simulations have been carried out in the literature, to study the flow physics of the laminar separation bubble. While the URANS is computationally affordable, it fails to predict the sub scales. On the other hand, although LES and DNS simulations resolve the sub scales effectively, the associated computational cost is a major hurdle for their usage in industrial applications. The solution lies, either in developing a model which would be a trade off between the two or in extracting the details provided by the DNS in improving the existing URANS. While the former is gaining a substantial attention, the current work attempts to focus on the later part of it. A standard RANS model usually fails to predict the separation if run fully turbulent. Either the transition location has to be specified or the transition terms have to be coupled with the models to predict the separation [9]. Another alternative is to use the turbulence models with low values of free-stream turbulence variables [2, 10]. The present investigation explores the usage of this alternative, along with the details provided by the DNS, to predict the effects on transition.

2. FLOW CONFIGURATION

2.1 Computational Domain

The test case considered herein, is the flow over a flat plate with a sharp leading edge. Similar configuration was investigated in great detail [6, 9, 11] and DNS results are available for this case to compare with. The upper boundary of the computational domain is specifically contoured to impose an adverse streamwise pressure gradient for $x/L > 0.3$ as shown in Figure 1. This is representative of the flow around the leading edge of a LP turbine blade. At sufficiently low Reynolds number of 60000 [2], the flow fails to sustain the strong enough pressure gradient and separates in the laminar region. The simulations were carried out on an adequate fine grid of 512 x 128.

2.2 Boundary Conditions

As shown in Figure 1, a slip wall (or a free slip) condition is imposed on 1) the upper wall and 2) in the region upstream of the leading edge of the lower boundary of the flat plate ($-0.5 < x < 0.0$), with the

strategy of saving the computational points, thus allowing a coarser mesh in this region. This strategy was proposed by Wissink and Rodi [11]. While a no slip boundary condition is imposed on the flat plate ($x > 0$), a simple convective (or the non-reflective) boundary condition was used at the outlet.

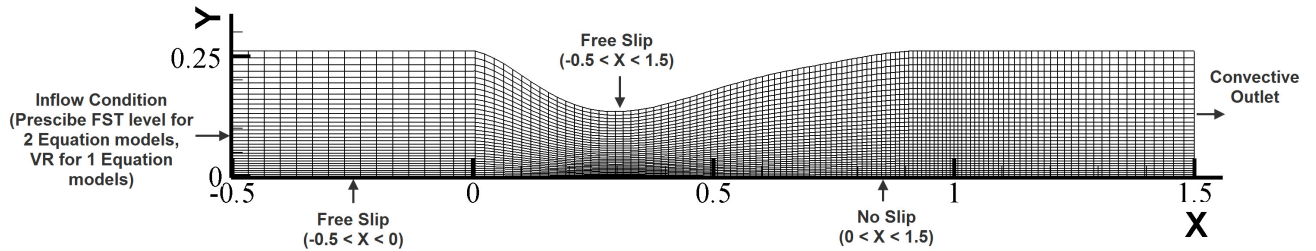


Figure 1. Computational Domain, grid (512x128, every 4th node shown) and the boundary conditions considered.

An inlet free stream turbulence intensity level (FSTI) of 1% was specified for the two equation models ($k-\epsilon$ (Launder-Sharma [8]), $k-\omega$, $k-\omega$ MSST, $k-\omega$ BL). Figure 2 shows the decay of FSTI predicted by two equation turbulence models along streamwise direction at a cross-stream location of $y/L = 0.065$, in accordance with Wissink and Rodi [11]. It is evident that both the URANS (with inlet FSTI of 1%) and DNS (with an inlet FSTI of 5%) reach the similar level of FSTI at the point of separation, thus providing a basis for comparing the results. The k , ϵ and ω values at the inlet were specified based on the FSTI and the length scale prescribed by Lardeau [6]. This essentially reduces the incoming turbulent kinetic energy and the dissipation rates, thus aiding in the formation of separation bubble. It was noticed that with a higher level of FSTI, the URANS failed to predict the separation bubble.

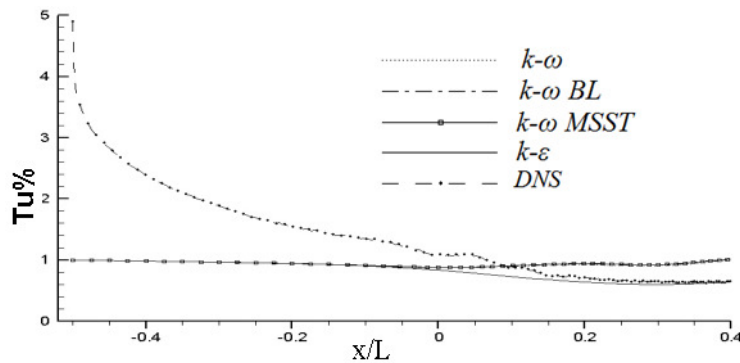


Figure 2. Comparison of the decay of free stream Turbulence Intensity predicted by two equation turbulence models in stream wise direction at a cross-stream location of $y/L = 0.065$

For the solution of different turbulence models, the BOFFS code [5] was used. It is essentially a multi-block; structured, curvilinear solver which uses the second-order centred fluxes with an additional smoothing term containing a tuning parameter. Crank-Nicolson scheme is used for temporal discretization.

3. URANS RESULTS

The simulations were carried out at a Reynolds number of 60,000, based on the chord length L and the inflow velocity U , identical to Re used in the work of Wissink and Rodi [11]. Investigations for four different two-equation turbulence models ($k-\epsilon$, $k-\omega$, $k-\omega$ -MSST and $k-\omega$ -BL) are presented. With URANS, the flow field is averaged over consecutive time intervals. A pseudo steady state is considered to have been achieved if the averaged flow field remains invariant over two successive time intervals. The streamwise velocity distribution for the turbulence models are compared at seven locations on the flat plate and illustrated in figure 3. The flow is accelerated upto a streamwise location of $x/L = 0.3$, where the throat is located and then decelerates downstream. Although the velocity profiles agree fairly well with the DNS till x/L of 0.5, considerable deviation creeps in for the rest of the domain.

Figure 4(a) shows the plots of the skin friction coefficient along the flat plate. For all the models, the separation was observed at a streamwise location of around 0.38 which is in close agreement with the predictions of Wissink and Rodi [11].

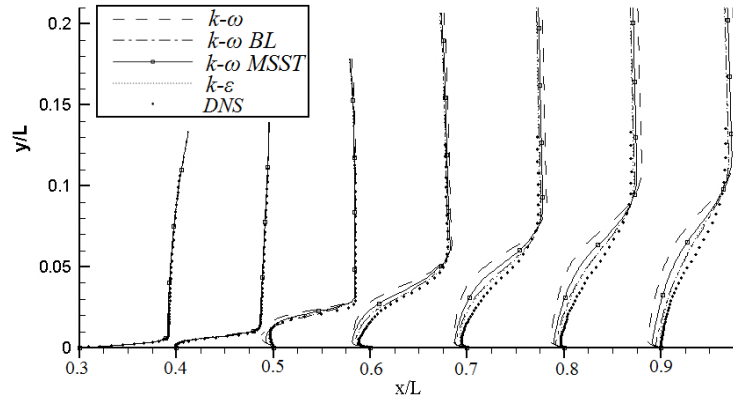


Figure 3. Comparison of streamwise velocity profiles predicted by two equation turbulence models with DNS at seven different stations, over the length of the separation bubble.

As the phenomenon itself is unsteady, the reattachment point oscillates in space with time. However, with the time averaged flow field, an averaged separation bubble was obtained. All the models predicted a larger separation bubble compared to DNS (DNS plot is not shown in the figure, as we had only discrete data). Of all the models, the $k-\epsilon$ model predicts a smaller separation bubble while the $k-\omega$ model predicts the largest. This could be attributed to the combined effect of the low free stream values at the inlet which were imposed to predict transition (as discussed in section 2.2) and the maximum turbulent kinetic energy being located far too downstream as shown in the contour plots of turbulent kinetic energy in Figure 4(b).

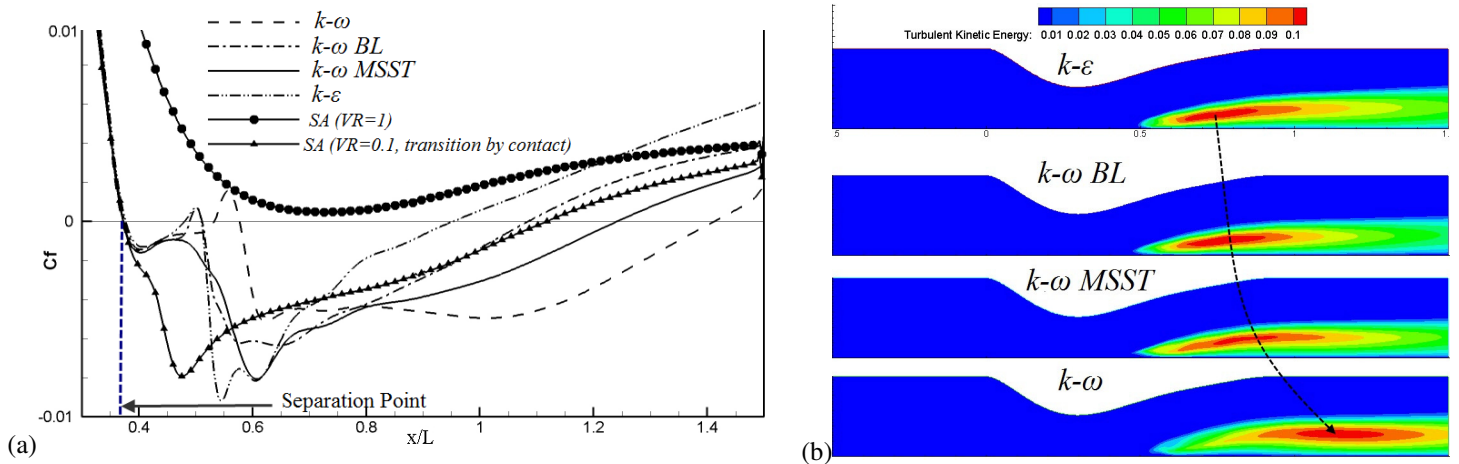


Figure 4. Comparison of (a) Streamwise evolution of Skin Friction coefficient and (b) contours of turbulent kinetic energy, excluding SA, (arrow shows the shift in the location of peak turbulent energy) for different turbulence models.

Since Spallart-Allmaras turbulence model is widely used in industrial applications, its performance in exploring the laminar separation bubble is also attempted. The turbulent to laminar viscosity ratio (VR) at the inlet is a crucial parameter. The streamwise evolution of skin friction coefficient for $VR=0.1$ and 1 is also illustrated in Figure 4(a). Very low values of VR in the range of 0 to 0.1 could predict the separation bubble as observed by Catalano [2] and Spallart and Strelets [10]. $VR = 0$ at the inlet and $\mu_t > 0$ within the domain, as an initialization yields plausible results that are virtually identical to those for $VR = 0.1$ and this is a more rational process. There is no turbulence entering the detached shear layer. The transition, referred as ‘transition by contact’ [10], occurs due to the contact of return flow of the turbulent fluid with the laminar fluid in the separation bubble. We intend to study this phenomenon further as it could occur spontaneously in complex flows in which laminar regions are allowed.

Comparison of streamwise RMS velocity fluctuations and shear stress of the turbulence models with DNS is addressed in Figures 5(a) and 5(b) respectively. Although the trends captured by URANS are in accordance with the DNS, the peaks of both the parameters is quite low for $0.5 < x/L < 0.7$.

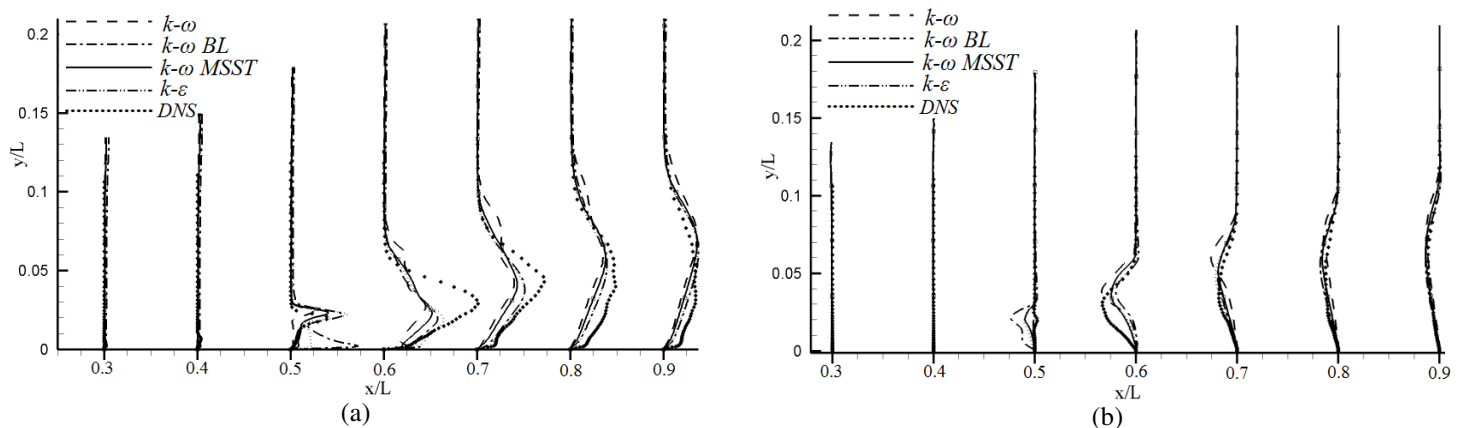


Figure 5. Comparison of (a) streamwise velocity fluctuations and (b) shear stress of turbulence models with DNS.

4. CONCLUSIONS

The performance of $k-\epsilon$, $k-\omega$, $k-\omega$ -MSST and $k-\omega$ -BL models were evaluated for a boundary layer separating over a flat plate, subjected to a prescribed adverse pressure gradient. The decay of free stream turbulent kinetic energy was adjusted to match the value predicted by DNS at the point of separation. The results obtained were compared against DNS and a reasonable agreement on mean velocity profiles, streamwise velocity fluctuations and shear stress was noticed. However, the models predict a larger separation bubble due to the delay in the production of enough turbulent kinetic energy to suppress the bubble. This was illustrated by the skin friction coefficient plot and the accompanying turbulent kinetic energy contours. The importance of choosing the appropriate value of turbulent to laminar viscosity ratio at the inlet, when using the SA model, was illustrated and the interest to study the phenomenon of ‘transition by contact’ is highlighted.

REFERENCES

- 1) M. Alam and N. D. Sandham. Direct numerical simulation of short laminar separation bubbles with turbulent reattachment. *Journal of Fluid Mechanics* 410, 1-28, 2000.
- 2) P. Catalano. Aerodynamic Analysis of Low Reynolds Number Flows. *PhD Thesis*, University of Naples Federico, 2009.
- 3) Hadžić and K. Hanjalić. Separation-induced transition to turbulence: Second-moment closure modelling. *Flow, Turbulence and Combustion* 63, 153-173, 2000.
- 4) R.J.A Howard, M. Alam, and N. D. Sandham. Two-equation turbulence modelling of a transitional separation bubble. *Flow, Turbulence and Combustion* 63, 175-191, 2000.
- 5) R. Jefferson-Loveday. Numerical simulations of unsteady impingement jet flows. *PhD thesis*, Swansea University, 2008.
- 6) S. Lardeau and M. A. Leschziner. Modelling and Simulation of Laminar Separation, Transition and Turbulent Reattachment. *Personal Communication*.
- 7) S. Lardeau, N. Li and M. A. Leschziner. Large eddy simulation of transitional boundary layers at high free-stream turbulence intensity and implications for RANS modeling. *Journal of Turbomachinery* 129, 311-317, 2007.
- 8) B. E. Launder and B. I. Sharma. Application of the Energy-Dissipation Model of Turbulence to the Calculation of Flow Near a Spinning Disc. *Letters in Heat and Mass Transfer* 1, 131-138, 1974.
- 9) D. Nürnberger and H. Greza. Numerical investigation of unsteady transitional flows in turbomachinery components based on a RANS approach. *Flow, Turbulence and Combustion* 69, 331-353, 2002.
- 10) P. R. Spalart and M.K. Strelets. Mechanisms of transition and heat transfer in a separation bubble. *Journal of Fluid Mechanics* 403, 329-349, 2000.
- 11) J. G. Wissink and W. Rodi. DNS of a laminar separation bubble affected by free-stream disturbances. *Direct and large-eddy simulation V: proceedings of the fifth international ERCOFTAC Workshop on Direct and Large-eddy simulation, held at the Munich University of Technology*, 213-220, 2004.
- 12) J. G. Wissink and W. Rodi. DNS of a laminar separation bubble in the presence of oscillating external flow. *Flow, Turbulence and Combustion* 71, 311-331, 2000.

Thermo-mechanical Analysis of Steel Frame Structures Using OpenSees

Jian Jiang and Asif Usmani

School of Engineering, The University of Edinburgh, Edinburgh EH9 3JF, United Kingdom

jian.jiang@ed.ac.uk

Key Words: *THERMO-MECHANICAL; STEEL FRAME; OPENSEES*

ABSTRACT

The OpenSees framework is extended to deal with the frame structures in fire conditions. OpenSees is an object-oriented, open source software framework developed at UC Berkeley and has so far been focused on providing an advanced computational tool for analyzing the non-linear response of structural frames subjected to seismic excitations. To deal with thermo-mechanical analysis of structures, new load classes are created to define the temperature distribution across the section of the element, which is built up with “fibres”. Existing material classes are modified to account for the temperature-dependent material properties according to the Eurocode3. The existing beam-column element classes are modified to include interfaces to the updated material at elevated temperature and section with temperature field and to take account of the thermally induced forces and deformations. Some benchmark cases are studied to verify the performance of thermal-mechanical analysis in OpenSees including steel frame and composite beam in Cardington test. The analysis procedures being developed for structures under fire in OpenSees will make it easier for users to define temperature-dependent material properties (based on codes or experiment data) and allow for non-uniform temperature distribution along an element. This work is part of wider project at the University of Edinburgh which, upon completion, will provide another user-friendly platform for structural fire engineering analyses. More importantly however, because of its open access and availability to all, this work will help towards OpenSees becoming a “community code” promoting collaboration between research groups. Furthermore, it will enable the analysis of structures subject to a sequence of man-made or natural hazards, an important topic in the context of the community’s increasing concern with structural robustness, resilience and sustainability.

1 INTRODUCTION

Many finite element program codes have been written to simulate the structural behaviour at elevated temperature and the results are compared well with the test data from Cardington test. These include specialist programs such as ADAPTIC(Song 1995; Izzuddin 1996), FEAST (Liu 1988; Liu 1996), SAFIR (Franseen 2000), VULCAN (Bailey 1995; Huang 2000) and commercial package such as ABAQUS and DIANA. The specialist programs are cost-effective but lack generality and versatility because they are always developed to focus on some special feature of structural behaviour in fire. OpenSees is an open-source object-oriented software framework developed at UC Berkeley. OpenSees has so far been focussed on providing an advanced computational tool for analysing the non-linear response of structural frames subjected to seismic excitations. Given that OpenSees is open source and has been available for best part of this decade it has spawned a rapidly growing community of users as well as developers who have added considerably to it’s capabilities over this period, to the extent that for the analysis of structural frames it has greater capabilities than that of many commercial codes.

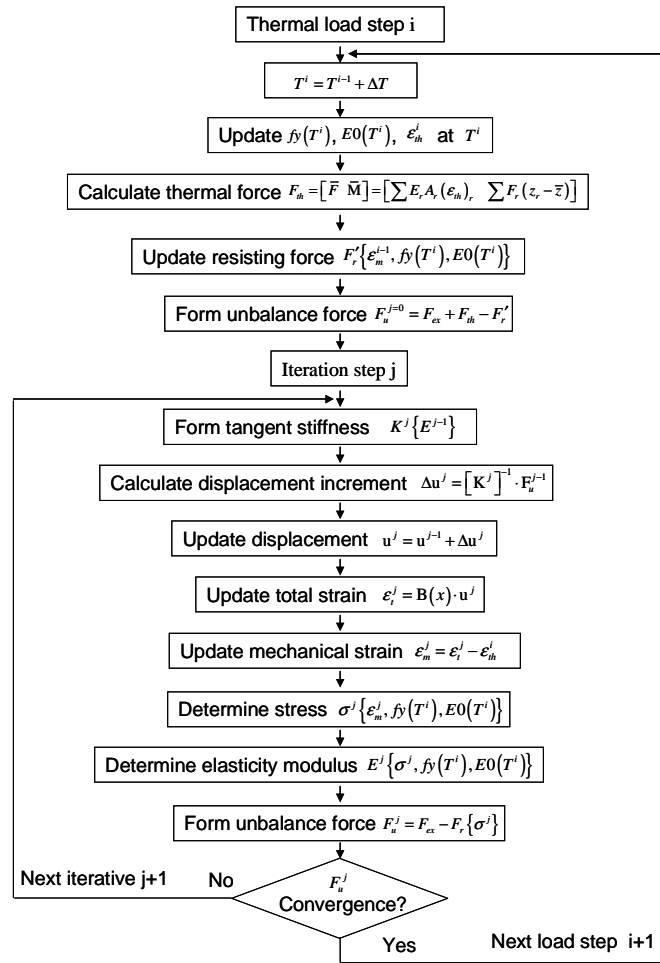


Figure 1. Flowchart for thermal-mechanical analysis in OpenSees

2 Thermo-mechanical analysis in OpenSees

The OpenSees framework was chosen to develop thermo-mechanical analysis of frame structures by adding new thermal load class and modified temperature dependent material classes (shown in Figure 2). Based on existing beam element *dispBeamColumn2d* (Taucer and Filippou 1991), the flowchart of the thermo-mechanical analysis in OpenSees is shown in Figure 1. New thermal load class `<Beam2dTemperatureLoad>` is created to store the temperature distribution along the section consisting of temperature and coordinate, the temperature of each fiber will be determined by the interpolation of the temperature at the nearest coordinate point according to its location. Also the temperature dependent material properties are modified from the existing material bilinear steel material according to Eurocode 3 (ENV 1993-1-2).

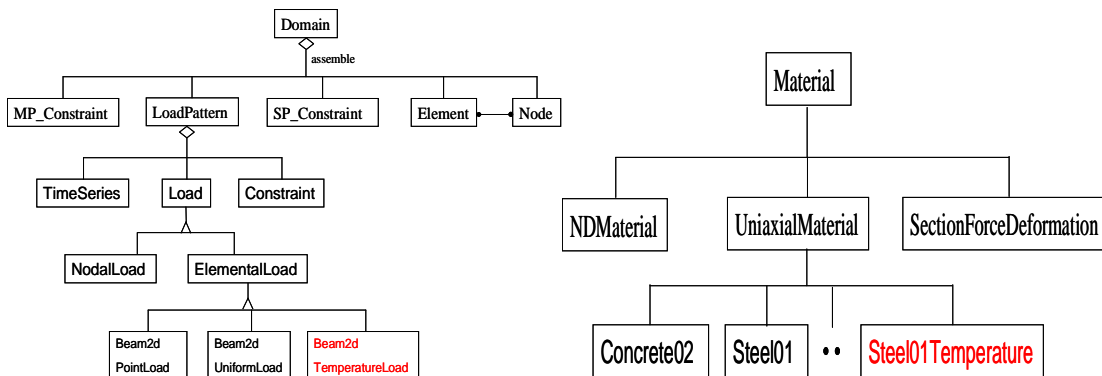


Figure 2. Class diagram for thermal load and material in OpenSees

3 Validation

In order to establish the validity of the present thermo-mechanical analysis in OpenSees, two benchmark examples are conducted and the comparisons have been made with experimental data and ABAQUS. These include a fully restrained beam subjected to uniform temperature rise and a uniformly heated steel frame test.

3.1 Restrained beam under thermal expansion

Figure 3 shows a beam, only the left half of which is subjected to a uniform temperature increment from ambient to 1000°C. The temperature-dependent material properties are taken from Eurocode3 (ENV 1993-1-2). The horizontal displacement and stress at midspan of the beam against temperature are shown in Figure 4. The results are consistent with that of ABAQUS.

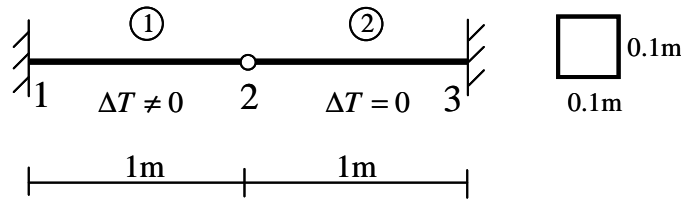
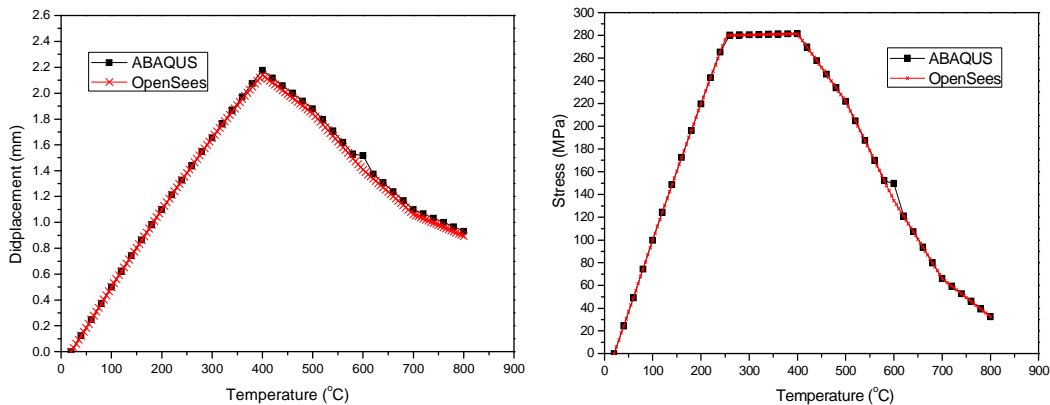


Figure 3. Schematic of restrained beam subjected to uniform temperature rises



(a) horizontal displacement of node 2

(b) stress of node 2

Figure 4. Results of Restrained beam under thermal expansion

3.2 Steel frame test

Two steel frames were tested, with a schematic diagram shown in Figure 5. The results shown in Figure 6 agree well with the experimental data (Rubert 1986).

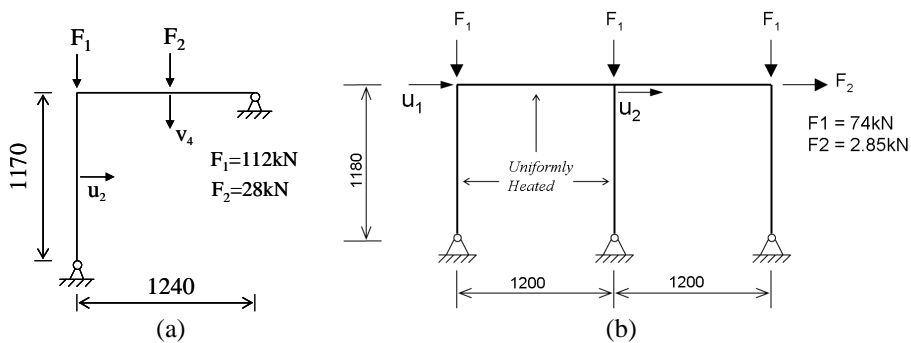


Figure 5. Schematic of the tested steel frames (mm): (a) frame EHR3; (b) frame ZSR1

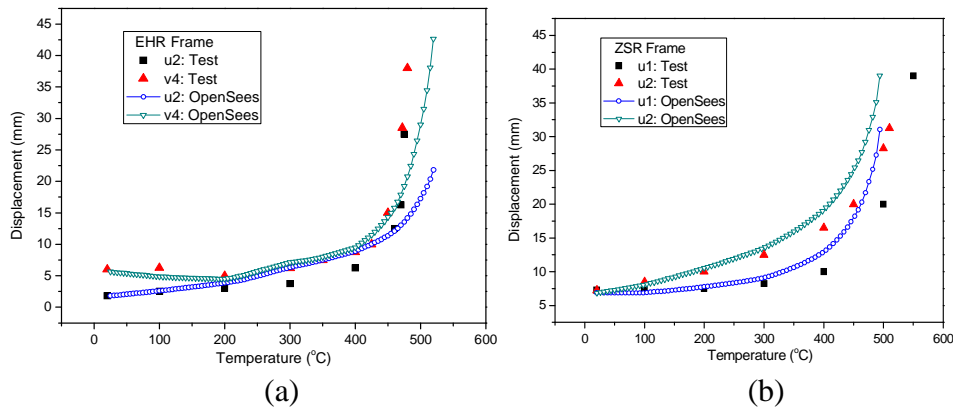


Figure 6. Comparison between predicted and test deflection results:
 (a) frame EHR3; (b) frame ZSR1

Conclusions

The present extended OpenSees shows good performance to deal with the thermo-mechanical analysis of structures under fire conditions. Further work should be done to develop a series of temperature-dependent material class according to different code and make the 3D beam element and shell element available for thermo-mechanical analysis .

References

- [1] Bailey, C. G. (1995) "Simulation of the structural behavior of steel-framed buildings in fire", PhD thesis, Department of Civil and Structural Engineering, University of Sheffield, UK.
- [2] ENV 1993-1-2. Design of steel structures, Part 1.2: general rules — structural fire design. Eurocode 3 Part 1.2, 2005
- [3] Franssen, J. M., Kodur, V. K. R. and Mason, J. (2000) User's manual for SAFIR2001, A computer program for analysis of structures submitted to the fire, University of Liege, Belgium.
- [4] Huang, Z. H., Burgess, I. W. and Plank, R.J. (2000) "Effective stiffness modeling of composite concrete slabs in fire", *Engineering structures* 22: 1133-1144.
- [5] Izzudin, B. A. (1996) "Quartic formulation for elastic beam-columns subject to thermal effects", *ASCE Journal of Engineering Mechanics* 122(9): 861-871.
- [6] Liu, T. C. H. (1988) "Thermal modeling of steel portal frame behavior", PhD thesis, Department of Civil Engineering, University of Manchester, UK.
- [7] Liu, T. C. H. (1996) "Finite element modeling of behavior of steel beams and connection in fire", *Journal of Constructional Steel Research* 36(2):181-199.
- [8] Rubert, A. and Schaumann, P. (1986) "Structural steel and plane frame assemblies under fire action", *Fire Safety Journal*, 10, 173-184.
- [9] Song, L., Izzudin, B.A., Elashai, A. S. (1995) "Nonlinear analysis of steel frames subjected to explosion and fire loading", *Proceedings of the International Conference on Structural Dynamics, Vibration, Noise and Control*, Hong Kong, December.
- [10] Taucer, F. F. Filippou, F. C. (1991) "A Fiber Beam-column element for seismic response analysis of reinforced concrete structures". Report of University of California, Berkeley.

Efficient Reinforced Concrete Design Using Modified Linear Elastic Finite Element Analysis

Xing Tan ¹, *Andrew. J. Deeks ²

¹ School of Civil & Resource Engineering, University of Western Australia,
Crawley, Western Australia 6009, Australia

² School of Engineering and Computing Sciences, Durham University,
South Road, Durham, DH1 3LE

xing.tan@durham.ac.uk¹, *a.j.deeks@durham.ac.uk²

Key Words: *Strut-and-tie; Linear elastic; Deep beam; Stress redistribution; Stress singularities*

ABSTRACT

Although the strut and tie approach has become a rational and reasonable approach for the design of non-flexural members in concrete structures, the approach may lead to suboptimal design, as much of the material present in the member is neglected. Other difficulties, such as the amount of time consumed and the designer dependency of the solutions, have been encountered in its implementation. To avoid these problems, design may be undertaken using conventional linear elastic finite element analysis, which can yield more efficient designs with less material usage. However, the conventional linear elastic finite element method is also inefficient when the non-flexural members contain stress singularities, such as occur in a deep beam with square or rectangular web openings. These stress singularities lead to singular stress fields which always violate the yield criterion. The modified linear elastic finite element method proposed in this paper successfully removes the stress singularities by adjusting the elastic modulus in certain regions. The conventional strut-and-tie method and the new stress redistribution method are used to design a deep beam example with two web openings. The performance of the design resulting from the new method is assessed through non-linear finite element analysis. The results show that the proposed approach is safe, and is also more efficient than the strut-tie approach.

1. Introduction

The strut-and-tie approach is widely used for the design of non-flexural members, such as deep beams, corbels and nibs. This method has proved to be useful in the design and analysis of such disturbed regions of structural members (Marti P, 1985). While effective, this strut and tie modelling approach has some shortfalls, not only because it only considers the concrete within each compressive strut and does not utilize the capacity of the concrete outside of the identified struts, but also because it requires the designer to use their experience to identify the most suitable arrangement for the struts and ties. This may be difficult for members with complex shape, particularly those containing penetrations (Tjhin TN & Kuchma DA, 2002). Consequently designs produced using this approach might be conservative and designer-dependent. In another words, such an approach may lead to an inefficient design for members, wasting concrete. Since reducing carbon emissions due to construction activity is now of significant interest, and the production of concrete is a major generator of carbon, reducing the amount of concrete in a design is one way of reducing the carbon emissions of a construction project.

To avoid these shortcomings of the strut-tie method, the current Australian Concrete design code (AS3600) permits the use of linear elastic finite element analysis (LEFEA) to design the reinforced concrete members (Standards Australia, 2005). By using LEFEA, the stress field is computed directly using the finite element method, eliminating the need for designers to identify a suitable arrangement of struts and ties. This allows the contribution of concrete outside the conventional compressive struts to the

load carrying of the structure to be included, which means the approach can yield more efficient designs with less material usage.

However, when members contain stress singularities associated with particular geometric discontinuities or boundary conditions, such as occur in a deep beam with square or rectangular web openings, the conventional linear finite element method cannot be applied, as stresses close to the singularities always violate the max stress permitted in the concrete, and the lower bound theorem of plasticity cannot be applied (Ashour A & Yang KH, 2008). This paper presents a new approach which overcomes this difficulty.

2. Modified linear elastic finite element method

This paper proposes a rational approach to solve the above-mentioned stress singularity problem when using finite element analysis for the design of deep beams with web openings. For structural design considering stress singularities, the actual behaviour of the material should be taken into consideration. The existence of stress singularities is not realistic, because engineering materials, including concrete, yield or fail locally at some finite level of stress, never reaching the infinite stress state predicted by linear elastic stress field analysis (Barber JR, 2002). In reality the concrete at such points would crack, and removing the stress singularities altogether. The modified linear elastic finite element method proposed in this paper successfully removes the stress singularities by adjusting the elastic modulus in certain regions, which effectively reduces local stresses and redistributes them to the surrounding elements. Since the redistributed stress field is both in internal equilibrium and equilibrates the applied loads, this stress field can be used to design the member, applying the lower bound theory of plasticity.

It is well-known (Logan DL, 2002; Timoshenko S, 1969) that when applying the finite element method, the elastic modulus E is taken as constant when the material is homogeneous and elastic. The approach proposed here artificially modifies the constitutive matrix by using an elastic modulus $E(s,t)$ which varies in terms of the local spatial coordinates (s,t) of the element, but keeps Poisson's ratio constant. The isoparametric shape functions used to approximate the displacement field are also used to define the variation of elastic modulus between nodal values. Thus the constitutive matrix for plane stress is:

$$[D] = \frac{E(s,t)}{(1-\nu^2)} \begin{bmatrix} 1 & \nu & 0 \\ \nu & 1 & 0 \\ 0 & 0 & \frac{1-\nu}{2} \end{bmatrix} \quad \text{with} \quad E(s,t) = \sum_{i=1}^n N_i E_i$$

3 Practical implementation

In the work reported here, Matlab is used to implement a custom element and to perform the linear finite element analysis. In the analysis, when the compressive stress in the beam exceeds the specified compressive strength limit, the elastic modulus is adjusted to try to reduce the stress to an acceptable value. This iterative process is continued until the entire stress field meets the compressive stress limit. This generally involves 4 stages:

Stage 1: Specify the finite element model with initial constant young's modulus, and conduct the analysis as per usual; Stage 2: If needed, soften the peak stress exceeding the yield criterion by adjusting the elastic modulus at appropriate nodes, maintaining the Poisson's ratio constant all the time; Stage 3: Re-run the analysis with the modified model and to see whether all the yield criterion are satisfied. If they are not, return to stage 2, otherwise continue to stage 4; Stage 4: Find out the suitable reinforcement dimension to carry all the principal tensile stresses in the concrete.

For stage 2, the rules used to adjust the Elastic modulus are:

$$E_i^k = \begin{cases} \varepsilon \left(\frac{\phi 0.9 f_c'}{\sigma_{3,i}^{k-1}} \right) E_i^{k-1} & \text{for } \sigma_{1,i}^{k-1} \leq f_{ct}' \\ \varepsilon \left(\frac{\phi 0.54 f_c'}{\sigma_{3,i}^{k-1}} \right) E_i^{k-1} & \text{for } \sigma_{1,i}^{k-1} > f_{ct}' \end{cases} \leq E_i^{k-1}$$

Here, the subscript i indicates the node under consideration, while the superscript k denotes the iteration

number. When the relationship is used to adjust the material properties in certain specified areas, the effective compressive strength factor specified by the concrete code (Standards Australia, 2005) is taken into consideration in this rule. A factor ε less than one is chosen to reduce the elastic modulus by a greater ratio to improve the rate of convergence. In addition, before proceeding to step 2, the elastic modulus is specified as zero at the points of singularity to effectively remove them from the stress field.

As the resulting stress field is statically admissible and able to satisfy the yield condition (Ashour A & Yang KH, 2008), softening the material around the corner is a rational and reasonable way to remove the stress singularities and redistribute the stress, it can be used for design. Unlike non-linear finite element analysis, the position of reinforcing steel and the thickness of the beam do not need to be defined in advance. Non-linear finite element analysis is useful to verify designs, but cannot be used efficiently to produce designs.

Figure 1: Dimensions of the beam

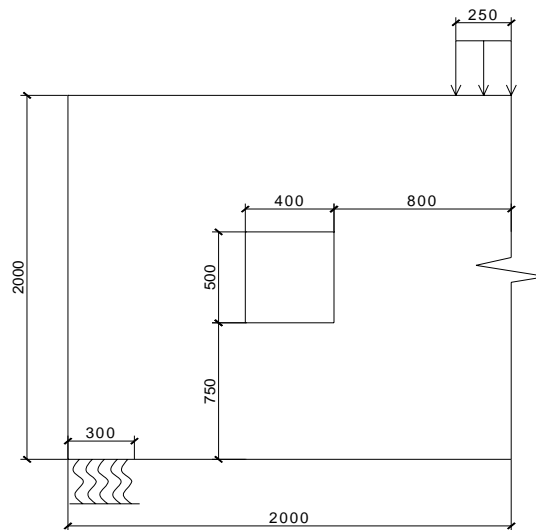
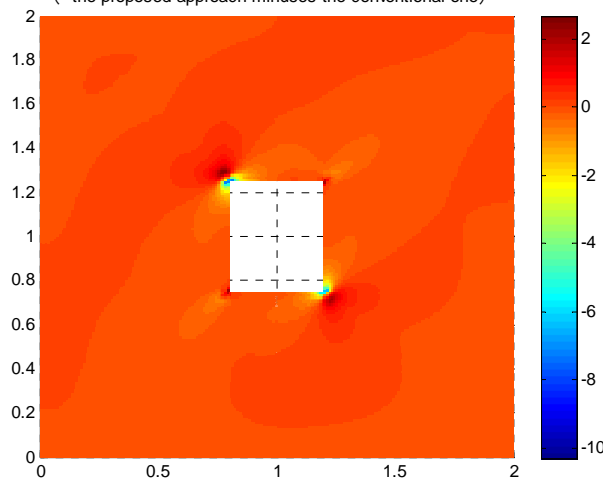


Figure 2: Principal Compressive Stress Difference (the proposed approach minus the conventional one)



4. Application example

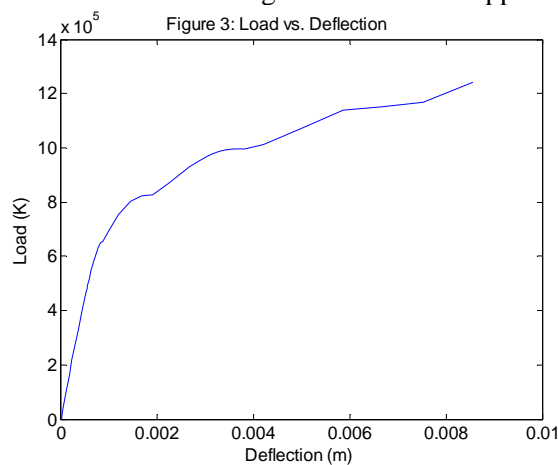
The design (using $f'_c = 25\text{MPa}$ concrete) of a simple deep beam with two rectangular openings with a point load ($P=1000\text{KN}$) applied over a bearing length of 500mm at the centre of the beam is investigated. To avoid the occurrence of stress singularities in the supports, relatively soft spring supports are assumed. The dimensions of the beam are shown as figure 1. For comparison, the two different design approaches are used to design this beam, and the cost comparison is shown in Table 1. The difference in the principal

compressive stress field between conventional and modified linear stress analysis is plotted in Figure 2. From the above example, the conclusion can be drawn that the stress redistribution method solves the problem of stress singularities confronted in a conventional Linear Stress Analysis approach and leads to a more efficient design than the conventional strut and tie method.

| Table 1: Cost Comparison | | |
|-----------------------------|-------------------------------------------------|----------------------------|
| Design Approaches | Quantity of Steel at Mid-span (mm^2) | Thickness of Concrete (mm) |
| Conventional Strut-and-Tie | 1250 | 246 |
| Modified Linear Elastic FEA | 970 | 214 |

5. Verification

To verify the safety of this proposed approach, ABAQUS/CAE is used to conduct non-linear finite element analysis of the final design produced by the new approach. The load vs. deflection curve (presented in Figure 3) shows that the ultimate mid-span load is about 1240KN, compared to the ultimate design load of 1000KN. This result means the design is safe and the approach is reasonable.



6. Conclusions and future work

This paper presents a stress redistribution method based on modified linear elastic finite element analysis, which is a new tool for designing complex non-flexural members, such as deep beams with openings. The new method was shown to lead to more efficient solutions than the conventional design approaches for such concrete structure members. Preliminary tests of the proposed design were performed using non-linear finite element analysis, which showed the method leads to safe designs. As the stress field resulting from this new method is statically admissible and able to satisfy the yield condition, designs generated using this method will reach or exceed the ultimate design load, in accordance with the lower bound theory of plasticity. Future work should include conducting full scale experimental tests to verify the designs produced by this proposed approach.

References

- [1] Ashour A, Yang KH. Application of plasticity theory to reinforced concrete deep beams: a review. *Magazine of Concrete Research*. 2008.
- [2] Logan DL. *A first course in the finite element method*, 3rd edn, Brooks/Cole, Pacific Grove, CA 2002.
- [3] Marti P. Basic Tools of Reinforced Concrete Beam Design. *ACI Journal*.1985; 82(1):46-56.
- [4] Standards Australia 2005. *Dr05252 Concrete Structures-Draft for public Comment Australia Standard*.
- [5] Timoshenko S. *Theory of Elasticity*, 3rd edn, McGraw-Hill, New York. 1969.
- [6] Tjhin TN, Kuchma DA. Computer-based tools for design by strut-and-tie method: advances and challenges. *ACI Structural Journal* 2002; 99 (5).

COMPUTATIONAL HOMOGENISATION METHODS FOR FLEXIBLE MARINE RISERS ACCOUNTING FOR STRUCTURAL-TO-STRUCTURAL SCALE BRIDGING

*Ben Edmans¹, Giulio Alfano¹ and Hamid Bahai¹

¹School of Engineering and Design, Brunel University, Uxbridge, Middlesex, UB8 3PH

*mepgbde@brunel.ac.uk

Key Words: *Homogenisation; Flexible Pipes; Nonlinear Structures; Boundary Conditions*

ABSTRACT

In recent years, computational homogenisation techniques for simulating complex materials and structures have evolved to be able to incorporate structural elements and displacement discontinuities in model formulations. However, their extension to scale-bridging between two models each comprised of structural elements remains relatively unexplored. Such an extension requires careful modification of averaging procedures and the microscopic boundary conditions used.

The authors present a structural-to-structural computational homogenisation technique applied to unbonded flexible pipes, where large scale response is dominated by interlaminar sliding. Using a specially developed beam element as the macro-scale model, selection of appropriate boundary conditions for testing each generalized strain state on a nonlinear shell-based detailed model is discussed in the context of the Hill-Mandel macrohomogeneity principle. Aspects of the detailed model and computational issues arising in the detailed model are discussed.

1 INTRODUCTION

The computational homogenisation approach is a well-developed tool for the analysis of composites and problems involving complex structures at different length scales (Geers et al., 2007). The standard two-scale first-order homogenisation procedure for continua is a nested algorithm in which a micro-scale model is activated as a subroutine for selected material points in the macro-scale model. The macro-scale model passes strains to the subroutine, which tests the Representative Volume Element (RVE) under appropriate boundary conditions, and returns averaged stresses. The Hill-Mandel principle of equivalence of virtual work on macro- and micro-scales is used to formulate boundary condition restrictions and averaging procedures. Recent work (Kouznetsova et al., 2002; Coenen et al., 2010) has involved extending the first-order computational homogenisation scheme to problems involving discontinuities, fracture and thin shells. Work on shells involves passing higher-order strain measures consistently between a continuum and a structural model.

Unbonded flexible pipes and risers are key components in the subsea oil and gas industry. Key structural requirements include high flexural compliance combined with high axial stiffness and high resistance to external pressure. Analytical tools used for design and operational assessment deal with either 1) global dynamic analysis of riser configurations, or 2) local fatigue analysis. The coupled nature of these problems prompts enquiry into whether a multi-scale approach could fulfil both roles, increasing accuracy by removing the need for modelling assumptions and enabling the practical prediction of the long-term local effects of large-scale dynamical response of risers to cyclic loads, such as wave motion and vortex-induced vibration.

2 FLEXIBLE PIPE HOMOGENISATION: SPECIAL FEATURES

The application of computational homogenisation procedures to flexible pipes differs in several regards from other traditional applications. Firstly, formulations involving structural elements require passing generalised stresses and strains between the models in a consistent manner, when measures used in one model may not be explicitly calculated in the other. Secondly, the detailed model is discontinuous; the ability of components to slide over each other is the principal mechanism governing the global nonlinear response. This can cause numerical difficulties when testing the RVE under typical boundary conditions. Thirdly, the detail required by a realistic small-scale model would make a nested solution algorithm too computationally demanding for practical industrial applications.

The standard first-order computational homogenisation is based on three principles: 1) the Hill-Mandel macrohomogeneity condition, which states that virtual work done by the stresses at each macroscopic material point equals the RVE-averaged microscopic virtual work done by stresses on the detailed model; 2) identification of the continuum deformation gradient of the linearised large-deformation kinematic description of the material as a macroscopic strain; measure, and corresponding identification of the higher-order terms as the microscopic displacement fluctuation field, 3) identity of macroscopic and RVE-averaged microscopic measures in the limiting case of the RVE volume tending to zero.

To use these principles in the context of a structural-structural homogenisation, each of them must be modified by 1) replacing continuum with generalised stress and strain measures, 2) replacing the deformation gradient with a “beam operator” describing the part of the microscopic displacement field that is a function of the macroscopic generalised strains 3) replacing volumetric averaging with section averaging

Further details of the formal equivalence and implications for homogenisation procedures will be given in a forthcoming article (Edmans et al., 2011).

Instead of attempting a nested procedure, we present a framework in which the (modified) computational homogenisation theory is used to select appropriate boundary conditions for running a series of simulations on the detailed model. In these analyses, the nonlinear response of the RVE to a chosen set of macroscopic generalised strains that have clear physical meaning (e.g. bending) is computed. The stresses resulting from these tests are then averaged using a procedure justified by the modified theory. This enables a set of generalised stress-strain curves to be produced. A nonlinear macroscopic constitutive model can then be proposed that approximates these results, the parameters of which can be determined from curve-fitting. These parameters may then be used for global analyses using the macroscopic model alone.

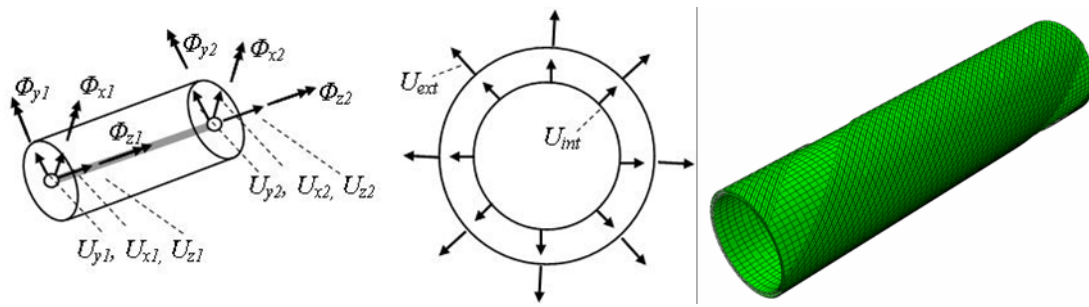


Figure 1: (a) Translational and rotational DOFs of beam(b) Radial DOFs (c) Detailed finite element model (outer layer and some wires removed)

3 BEAM MODEL

The large-scale analysis uses a three-dimensional beam model. The beam incorporates the flexible pipe constitutive model developed by Alfano et al. (2009) and Bahtui (2008), embedded in a corotational element. The constitutive model relating beam stress resultants to generalised strains incorporates two radial nonstandard strain measures. The relation between generalised stresses and strains is modelled as generalised non-associative plasticity, displaying characteristic hysteresis in bending. Previous comparison of this constitutive model with detailed finite element simulations have shown good agreement in predicting behaviour.

4 DETAILED MODEL

The detailed model was created using the finite element package ABAQUS 6.9 (Fig. 1 (c)). All physically distinct components of the pipe were considered as separate entities, modelled with linear shell elements, with surface-to-surface frictional contact between all components. The pressure armour and carcass layers of a flexible pipe are self-interlocking strips with complex sections; for this reason, these layers were modelled as equivalent orthotropic homogenous cylinders with appropriate constants.

The infinite through-thickness stiffness of the shell elements was compensated by enforcing contact with a penalty method. Following de Souza et al. (2010), penalty stiffnesses were chosen to model the actual through-thickness compliance of the contacting shells. Independent comparison with other analytical models showed that this modification significantly improved accuracy.

Periodic boundary conditions were used to implement the four standard generalised strains, while uniform traction boundary conditions were used to apply the pressure-related terms. This is because internal and external pressure data is either prescribed, or is passed to the structural analysis by a coupled CFD simulation.

5 NUMERICAL RESULTS

To demonstrate the performance of the beam element, the riser configuration shown in Figure 2(a) was modelled. A sinusoidally varying vertical displacement was applied to the top node. Hysteretic behaviour near the touch-down point is observed (Fig. 2(b)).

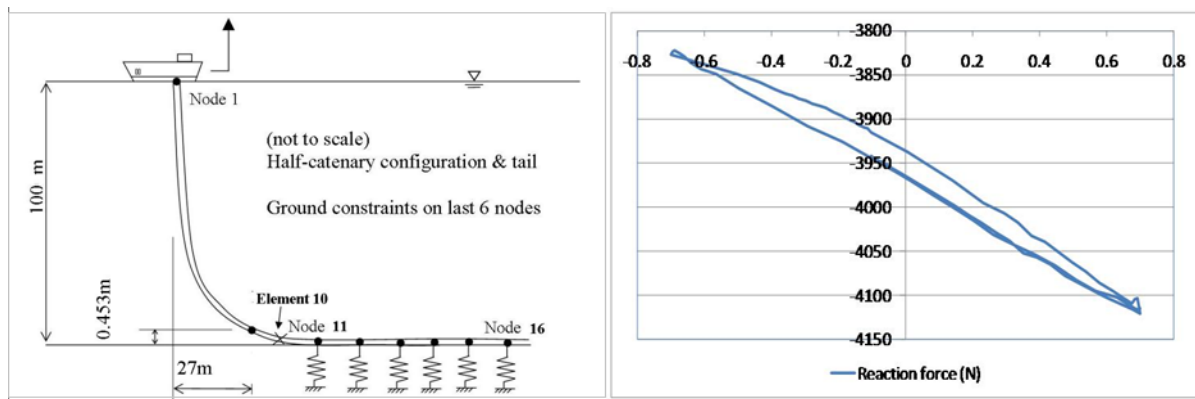


Figure 2: (a) Riser configuration (b) Top node vertical displacement vs. vertical reaction. Evaluated at node 1

6 CONCLUSIONS

A homogenisation procedure for the analysis of unbonded flexible pipes is proposed. Based on computational homogenisation principles, a sequential procedure for testing a detailed RVE composed of shell finite elements and multiple contact interactions is described, aimed at establishing parameters of a macroscopic beam model. Some modification of the computational homogenisation theory is required, and numerical issues must be addressed. The authors contend that extension of the computational homogenisation framework should enable theoretically-justified determination of equivalent material properties for a wider range of engineering structures.

References

- Alfano, G., Bahtui, A., Bahai, H., 2009. Numerical derivation of constitutive models for unbonded flexible risers. *International Journal of Mechanical Science*.
- Bahtui, A., 2008. Development of a constitutive model to simulate unbonded flexible riser pipe elements. Ph.D. thesis, Brunel University, UK.
- Coenen, E., Kouznetsova, V., Geers, M., August 2010. Computational homogenization for heterogeneous thin sheets. *Internat. J. Numer. Methods in Engrg.* 83 (8–9), 1180–1205.
- de Souza, J. R. M., Viero, P. F., et al, C. M., June 2010. An experimental and numerical study on the axial compression response of flexible pipes. In: *Proc. ASME 2010 29th Int. Conf. on Offshore, Ocean and Arctic Engineering*.
- Edmans, B., Alfano, G., Bahai, H., 2011. Nonlinear multi-scale homogenisation of unbonded flexible risers: Theoretical and computational issues. To be submitted to *Internat. J. of Solids and Structures*.
- Geers, M., Coenen, E., Kouznetsova, V., 2007. Multi-scale computational homogenisation of thin sheets. *Modelling and Simulation in Materials Science and Engineering* 15, 393–404.
- Kouznetsova, V., Geers, M., Brekelmans, W., 2002. Multi-scale constitutive modelling of heterogeneous materials with a gradient-enhanced computational homogenisation scheme. *Internat. J. Numer. Methods in Engrg.* 54, 1235–1260.

MODELLING THE RESPONSE OF TRUSSES IN FIRE

* Panagiotis Kotsovinos¹, Asif Usmani¹

¹ University of Edinburgh, School of Engineering and Electronics, Edinburgh, United Kingdom

*p.kotsovinos@ed.ac.uk

Key Words: *structures in fire; OpenSees; trusses; nonlinear finite elements; object-oriented framework*

ABSTRACT

The response of structures under different fire scenarios is a complex phenomenon, and in order to represent it efficiently, a software is required that can analyse the inherent nonlinear behaviour under elevated temperatures due to second order effects of large deflections, progressive softening of materials with temperature rise and the effect of thermal expansion. Furthermore, it is also important for such software to have the flexibility of adding new capabilities and to be accessible to users or researchers for modification of existing methods and procedures. A truss element has been implemented within the object oriented nonlinear finite element framework OpenSees, primarily designed for earthquake engineering simulations, to model the behaviour of truss structures subjected to fire. This extension also enables the modelling of trusses under “fire following earthquake” scenarios within the same framework. Two truss elements have been developed using Co-rotational and Total Lagrangian formulation taking into account an exact geometric transformation between local and global frames of reference. Furthermore the element can use a material with nonlinear stress and strain relationship with temperature dependent material properties so inelastic effects are accounted for by utilizing appropriate constitutive relationships. Several numerical examples are presented to demonstrate the accuracy of the proposed numerical procedure.

1 INTRODUCTION

This study describes the procedures for conducting large displacement inelastic analysis of trusses in fire. The adopted formulation has been embedded into the object oriented and open source nonlinear finite element software framework OpenSees by creating new thermal load, element and material classes.

OpenSees is an object-oriented nonlinear finite element framework primarily designed for earthquake engineering simulations. The fact that OpenSees is open-source, modular and object-oriented makes it suitable for adding new capabilities which then will be accessible to users or researchers for modification of existing methods and procedures.

The total Lagrangian and co-rotational formulations are adopted in this study. It is important for these formulations allow for the large displacements that are experienced in a real fire as well to take into account the inelastic effects from material degradation due to elevated temperatures.

Excluding the strain due to creep effect the total strain is equal to the mechanical strain and the thermal strain: [1]

$$\varepsilon_t = \varepsilon_m + \varepsilon_{th}$$

Where the thermal strain for a truss element, which considers only thermal expansion of the member, will be

$$\varepsilon_{th} = \alpha \Delta T = \alpha (T_{heated} - T_{ambient})$$

Furthermore the total strain varies for different formulations. For the TL formulation the total strain will be equal the Green-Lagrange strain, while for the co-rotational formulation it will be equal to the engineering strain. Thermal strain does not produce any stress, which comes only from the mechanical strain.

$$\sigma = \sigma(\epsilon_m)$$

A set of new classes were added in the OpenSees framework to make possible the analysis of trusses in fire. These include an elemental load class that provides a uniform temperature load for the elements (BarUniformThermalLoad), and elements based on the Total Lagrangian (ThermalTLTruss) and Co-rotational (ThermalCorrotTruss) theory. These elements are also capable of including the inelastic effect of material degradation in fire, combined with temperature dependent uniaxial materials that were also developed inside the OpenSees framework [2].

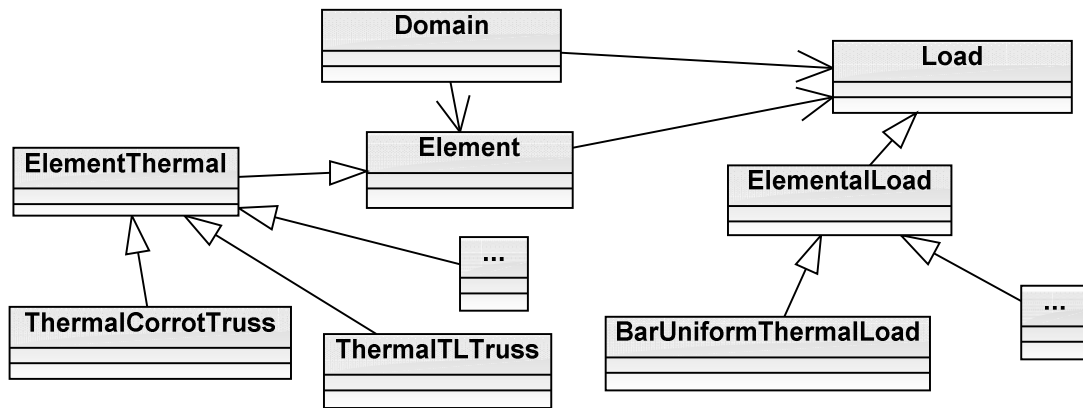


Figure 1: A class diagram of the hierarchy of the class added in OpenSees

2 PROCEDURE

In this study the incremental – iterative Newton Raphson algorithm is used for solving the finite element equations using a load control integrator. The mechanical load is first applied as the first load step and remains constant for the second thermal load step. The temperature of the element is provided as an input. The temperature is multiplied by the load factor, as in mechanical analysis, to give the first temperature increment. During that increment, the material tangent and the thermal strain are queried from the material class in order to obtain a guess for the thermal force in the element for the first iteration which will be equal to $EA\epsilon_{th}$ (*addLoad* method). Then, further iterations (*update* method) follow until the equilibrium conditions are satisfied inside a convergence limit and the next increment is then applied. During each iteration the tangent stiffness matrix of the element gets updated (*getTangentStiff* method) as well as the material stress gets calculated. At the end of the iterations and before the next increment, the resisting force gets updated by removing the thermal force found in that increment from the load resulting from the material stress in order to find the actual force in the element (*getResistingForce* method).

Figure 2 below also shows the main typical methods of an element in OpenSees.

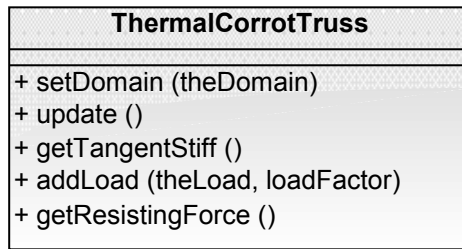


Figure 2: A class diagram showing the main methods of an element in OpenSees

The drawback of this load controlled procedure is that it cannot follow the equilibrium path beyond the limit points and cannot capture snap-through and snap-back buckling. This is the point where failure of the element takes place or a temporary loss of stability is experienced and then a post buckling path is followed. This drawback is not so important for most simple or determinate structures, but for redundant structures local (element) failure does not imply global failure of the whole structure which may be able to carry the loads, without the failed member contributing to its load carrying capacity. This is explained because redundant structures can find different load paths by which to support additional load when its local strength is reached at a single location [3]. Hence, alternative step by step procedures have also to be employed to check if the structure will continue to be stable or collapse. For this reason a dynamic procedure is also under development to make that possible in the OpenSees framework [4].

3 NUMERICAL EXAMPLE

A numerical example is presented to verify the proposed procedure. The example selected is the benchmark provided by Lin et al [5] which was solved analytically using a Total Lagrangian approach. For comparison purposes both Total Lagrangian and Co-rotational procedures developed are examined.

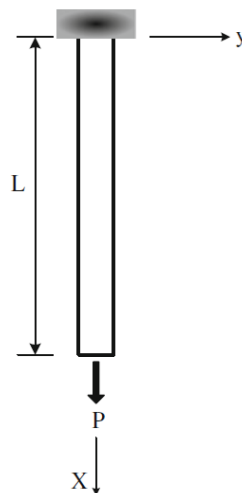
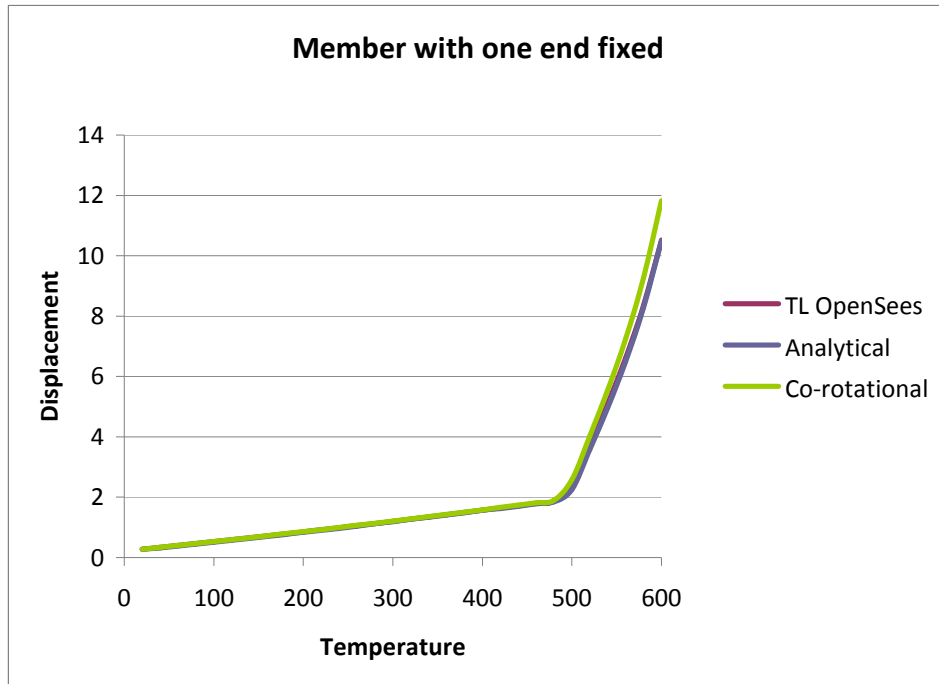


Figure 3: Member with one fixed end example

A uniaxial bilinear steel material with kinematic hardening (*Steel01Thermal*) is employed in this study. The information required for this material are yield strength (f_y), Young's modulus (E_0) and strain hardening parameter (b). This material is approximate but computationally efficient. Furthermore, this is the same material that was used also by Lin et al. The strain hardening parameter is temperature dependent, as reported by Shen and Zhao [6].

The temperature increments for the OpenSees modelling were applied in 10°C steps.



The comparison between the analytical and OpenSees results shows very good agreement. Furthermore, as expected the OpenSees TL solution is almost identical to the analytical one as it is also based in a TL formulation. The CR solution finds slightly higher result by 1mm.

References

- [1] Usmani A. S. , Rotter J. M., Lamont S., Sanad A. M., Gillie M., Fundamental principles of structural behaviour under thermal effects, *Fire Safety Journal*, 36(8), 721-744 (2001).
- [2] Usmani A., Zhang J., Jiang J., Jiang Y., Kotsovinos P., May I., Zhang J., Using OpenSees for Structures in Fire, Proceedings of International Conference on Structures in Fire, Michigan, 2010, 1089-94
- [3] J.M.Rotter, A.M.Sanad, A.S.Usmani, and M.A.O'Connor. Structural performance of redundant structures under local fires. In *Proceedings of Interflam'99*, Edinburgh, Scotland, June-July 1999.
- [4] Franssen J.M., Gens F., Dynamic analysis used to cope with partial and temporary failures, Proceedings of International Workshop on Structures in Fire, Ottawa, 2004, 1089-94.
- [5] Lin T.J., Yang Y.B., Huang C.W., Inelastic nonlinear behaviour of steel trusses cooled down from a heating stage, *International Journal of Mechanical Sciences* 52 (2010) 982-992.
- [6] Shen J.Y., Zhao J.C., Modelling fire resistance behaviour of multi-storey steel frames, Proceedings of International Conference on Computing in Civil and Building Engineering, Berlin, 1995, 1089-94.

Finite Element Analysis of a Novel Aircraft Seat against Static Certification Requirements (CS 25.561)

*Omkar Gulavani¹, Kevin Hughes²

^{1,2}Crashworthiness, Impact and Structural Mechanics Group.
Cranfield University, Bedfordshire, MK43 0AL, United Kingdom.
Web page : <http://www.cranfield.ac.uk/soe/structures/>

¹Presenter: O.gulavani@cranfield.ac.uk, ² Correspondance: k.hughes@cranfield.ac.uk

Key Words: *Aircraft seat, CS 25.561, Non-linear FEA, Bolt Preload, Seat interface loads*

ABSTRACT

Due to the competitive nature of the airline industry and the desire to minimise aircraft weight, there is a continual drive to develop lightweight, reliable and more comfortable seating solutions, in particular, the development of a new generation slim economy seat. The key design challenge is to maximise the “living space” for the passenger, with strict adherence / compliance to Safety Regulations.

This paper presents the analysis led design using finite element analysis of an innovative seat concept developed by BlueSKy Designers Limited, which has been acclaimed as “The most exciting development in aviation in over 30 years” and has won the company numerous awards. A generous angle of recline (40 degrees), movement of the “Seat Pan” along different gradients, and unique single “Forward Beam” design, distinguishes “Sleep Seat” from current generation seats.

Compliance against Static Strength requirements (CS25.561) through a sequential model development approach was performed, in order to predict the stress induced in the primary seat structure, against static certification requirements. A critical design parameter is ensuring seat interface loads are below airline limits, which resulted in the inclusion of seat stud and track details in the finite element model.

This stepwise and validated analysis framework, which includes mesh sensitivity studies, modelling of bolt-preload, representing bolted joints in FEA and obtaining a converged solution for non-linear FEA was essential in order to allow different concepts to be assessed virtually, thereby reducing development cycle time. The findings from this paper demonstrate that the seat is safe against CS 25.561.

1 INTRODUCTION

This research provides an assessment of an innovative design called “Sleep Seat” [1], which consists of a forward beam, seat leg, Boomerang, and Seat pan as shown in Figure 1. This innovative design includes movement of the seat pan along the gradient maximising the space for leg spread, 40 degree generous recline of the backrest within a fixed outer shell, single Forward (FWD) beam design eradicating the undercarriage below the seat pan, significant reduction in the part count, and an ultra lightweight design saving more than 3kg of mass over existing products [1], [2].

The objective of the research is to develop a practical modelling methodology that can be used to assist designers in assessing the suitability of a chosen seat configuration, through a sound understanding / application of the FE Method, together with demonstrating a critical assessment of the quality of the numerical results through appropriate verification methods.

2 CERTIFICATION SPECIFICATIONS (CS) USED AS SAFETY GUIDELINES

CS has been followed as a guideline for safety in this research as it encompasses works of all relevant governing bodies in international commercial aviation and agrees to some extent with its US equivalent FAR (Federal Aviation Regulations) [3]. CS sections 25.561 and 25.562 give static and dynamic loads during emergency landing conditions respectively [4]. As a first step, this paper focuses on static 9g compliance in the forward direction, as defined in CS 25.561.

As this project was in the conceptual phase, Finite Element Analysis (FEA) was used to compare different designs. Going further, this can be considered as a baby step towards “Certification By Analysis (CBA)” a programme undertaken by “Federal Aviation Administration (FAA) [5]. To reduce the number of variables at initial stage, focus was on successful design of Forward (FWD) beam and leg which are critical components of “Primary Load Path (PLP)” subjected to “Forward 9g”.

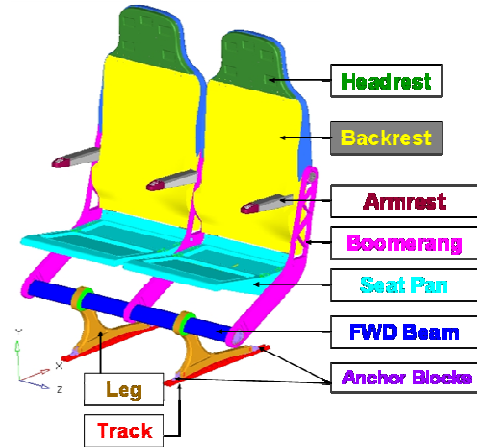


Figure 1 Nomenclature of “Sleep Seat” (Courtesy BlueSky) [1]

3. SPREADSHEET FOR INITIAL SIZING OF FORWARD BEAM

Analytical model for the “FWD beam” was developed (Spreadsheet), which could estimate the bending stress induced in it for “Forward 9g” loads, with design variables such as its cross-section and thickness. C3D8I (linear brick element with incompatible modes) used in Abaqus/Standard) gave satisfactory results, when two brick elements through thickness with aspect ratio of 1:1 in critical areas and 3:1 in non-critical areas gave reliable results with optimum solution time and storage requirements. Good agreement between spreadsheet and FEA verified the FE model and demonstrated the usefulness of the spreadsheet as a quick and simple conceptual design tool for initial sizing of the FWD beam.

4 SEQUENTIAL FE MODEL DEVELOPMENT FOR THE PRIMARY LOAD PATH

A stepwise procedure for the development of the leg required an evolution in detailed FE model, where each model contains the refinements suggested by results supplied by previous models, resulting in the final model containing all necessary details, optimum mesh and boundary conditions (Figure 2) [6].

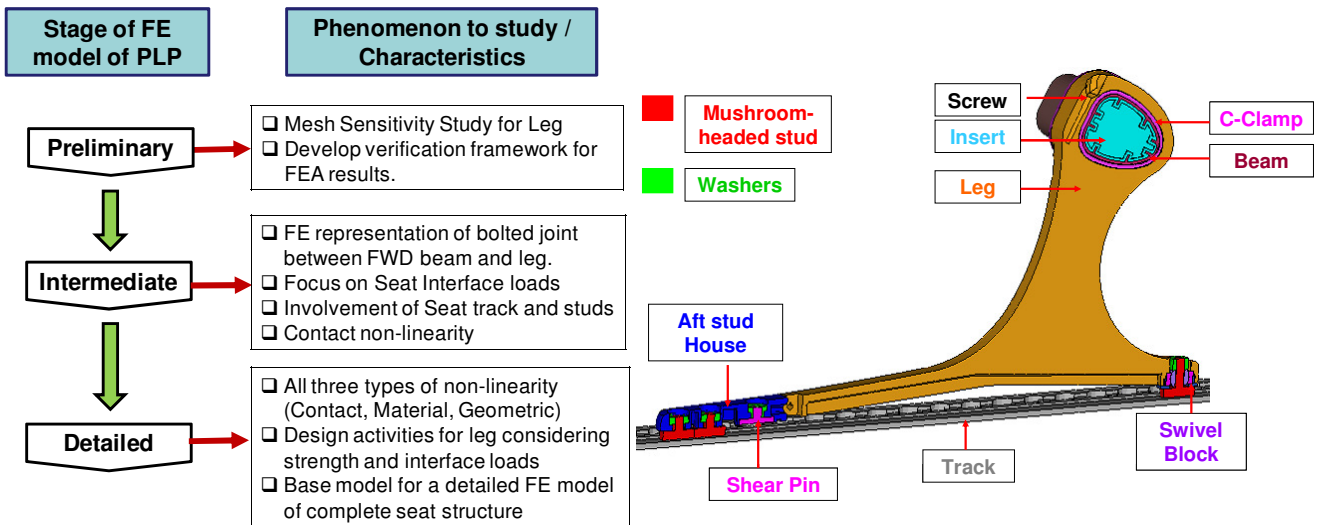


Figure 2 Sequential Development Approach for FE model of the “Primary Load Path (PLP)” (left) and cross sectional view of the detailed FE model generated for FWD beam / leg (right)

The mesh studies for the leg showed that geometrically versatile tetrahedral elements were a very attractive option compared to brick elements, as they provided an 85% reduction in the FE model building time and 40% in the solution time, whilst still providing reasonably accurate results. Care should be taken to ensure two elements through thickness are used.

During this stepwise development, a procedure to verify computational accuracy of FEA results was drafted. It included checks as reaction force equilibrium, stress difference between “with nodal averaging” and “without nodal averaging” and displacement continuity. It was found that, results satisfy all the checks. For non-linear FEA, checks such as residual force and moment, ratio of artificial damping energy to strain energy, distribution of contact pressure and forces transmitted across interfaces were added to above checks.

4.1 FE REPRESENTATION OF BOLTED JOINT IN SEAT

FWD beam is attached to the leg with the help of two M5 bolts. Three different ways to represent this bolted joint in FEA were studied: coincident nodes at FWD beam and leg interface (Case I- preliminary model), tied contact (Case II) and actual modelling of studs and corresponding contacts (Case III). Flexibility (to absorb initial penetrations), less pre-processing time required (80% lesser than that in Case III) and acceptable results; favoured the used of “Tied contact” definition at “FWD beam and leg” interface.

During study of bolted joint between “FWD beam and leg”, a stepwise procedure for FE modelling of “Bolt-preload” and its integration with inertia loads (CS 25.561); was developed and implemented.

4.2 METHODOLOGY TO EXTRACT “SEAT INTERFACE LOADS (SIL)”

Leg designing depends on its strength as well as on SIL i.e. static loads applied by the seat to the floor [7]. The challenge was to develop an FE model, which could give enable designers to perform sensitivity studies to assess the changes in the resulting stress due to different stud configurations for the applied “Forward 9g” loads. Going further, classification of contact pairs in suitable groups for evaluating SIL was accomplished through pilot studies, and a systematic approach for extracting SIL using FEA was developed. With this study, an “Intermediate” FE model of PLP was completed.

4.3 TECHNIQUES TO HANDLE “RIGID BODY MOTION”

For static non-linear contact FEA of “Sleep Seat”, two prominent reasons for non-convergence were initial penetrations and clearances. Model with initial penetrations, suffers from very high stress levels during as penetration is considered as interference fit by the solver, even though unintentional [8]. In case of initial clearances, FEA algorithms undergo unrestrained motion and frictional sticking is not effective [8]. Use of same element faces in mating area, clever use of “Mesh algorithm” e.g. use “Union Jack R-tri” instead of “Standard R-tri” element and a nominal “Bolt Pre-load” of 1KN – 2KN to close initial gaps were some of the techniques, which were successfully used to deal with “Rigid Body Motion”.

5 DESIGN PHASE AND NON-LINEAR FEA OF COMPLETE SEAT

An elliptical cross-section with two millimetres thickness was chosen for FWD beam using spreadsheet. Inserts were added at high stress locations for local reinforcements. “I” section was chosen for leg considering the second moment of area, while length of the leg was decided by carefully studying SIL induced.

A non-linear FE model of complete seat structure with total 62 contact pairs with penalty algorithm, 11 tied contacts, 32 MPC connections (rigid) and 2 MPC connectors with “End Release”, involving material and geometric non-linearity was developed, which could give outputs such as stress and interface loads when subjected to loads as specified in CS 25.561. Total number of nodes and elements are 354862 and 285679 respectively. Total mass of this seat structure is around 7 kg.

The total weight considered for the load application was 87.48kg, which included an occupant mass of 77

kg and additional mass to represent in-plane entertainment items. Bottom surfaces of track were constrained for all dofs during the simulation and loads were applied at the point, as specified in National Aerospace Standard (NAS 809) [9]. It was found that the components of PLP (FWD beam and leg) are “Safe” against the critical loads as specified in CS 25.561.

6. SUMMARY

The development of a practical methodology was successfully used during the conceptual design phase, which led to significant structural design modifications, which now allows the company to build and test a prototype with more confidence. Methodology includes:

- FE modelling strategy for individual components through Mesh Sensitivity Study,
- Framework to critically assess the FEA results,
- Solutions to deal with “Rigid Body Motion” and “Initial Penetration”.
- Modelling of “Bolt Pre-load” using Abaqus / Standard,
- Simplified yet reasonable FE representation of bolted joint in seat structure,
- Extraction of “Seat Interface loads”,
- To obtain the converged solution for the complete seat subject to static loads (CS 25.561) including all types of non-linearities i.e. contact, material and geometry; using Abaqus / Standard.

7 FUTURE SCOPE

The next phase of this work is to perform experimental tests to support model validation. Once static compliance has been demonstrated, this project will then consider the dynamic certification requirements through the incorporation of an anthropometric hybrid III numerical dummy. Based upon the findings, the numerical tools will be used to optimise the seat structure for minimum weight.

8. REFERENCES

- [1] D. Robinson, “BlueSky Designers Ltd.” 57, Surrey Technology Centre, “Surrey Research Park”, Guildford GU27YG. <http://www.blueskydesigners.com/>
- [2] <http://www.aviationweek.com/events/current/sic/>
- [3] C. Olschinka, A. Schumacher. *Dynamic Simulation of Flight Passenger Seats*, LS-Dyna Anwenderforum, Hamburg University of Applied Sciences, 2006
- [4] European Aviation Safety Agency, Certification Specifications (CS) for Large Aeroplanes CS25; Amendment 8, 18 December 2009.
- [5] P Bhonge. *A methodology for aircraft seat certification by dynamic finite element analysis*, PhD thesis, Wichita State University, December 2008.
- [6] Cook, Malkus, Plesha, Witt, *Concepts and applications of Finite Element Analysis*, 4th Edition, John Wiley and Sons Publication. ISBN 9814-12-683-7
- [7] Boeing Specifications (1993) ‘D6 36238 Passenger Seat Structural Design and Interface Criteria Rev C’
- [8] Abaqus 6.9 Documentation
- [9] Department of Transportation, Federal Aviation Administration Aircraft Certification Service. *TSO-C39a AIRCRAFT SEATS AND BERTHS*, Washington, DC 24 February 1972

APPLICATION FRAMEWORK AND DATA STRUCTURE TO INTRODUCE REAL-TIME STRESS ANALYSIS INTO EARLY DESIGN STAGES

*M.S. Mohamed, T.M. Foster, J. Trevelyan and G. Coates

School of Engineering & Computing Sciences, University of Durham, Durham, DH1 3LE

m.s.mohamed@durham.ac.uk

Key Words: *Real-time stress analysis, Early design stages, Interactivity, Application framework, Data structure.*

ABSTRACT

The use of computational stress analysis as a tool in early design stages faces some challenges. An application framework and a data structure are proposed to overcome some of the difficulties arising with such use. The proposed application framework and data structure are implemented using an open-source CAD kernel and an in-house developed stress analysis software.

1 INTRODUCTION

Designing mechanical products relies strongly on computational stress analysis. This trend is encouraged by the rapid developments in computer technologies and in numerical methods. The computational stress analysis became more accessible to engineers by integrating the stress analysis and CAD into the same environment where the geometry, the boundary conditions and the analysis results are defined and displayed graphically.

Despite being integrated into the same working environment the stress analysis and CAD function under two different modes such that whenever the CAD model is modified the stress results are lost and a new analysis is required. This limitation should not be a problem if only few modifications are needed. However, for preliminary models where many modifications are necessary this limitation becomes severe. Therefore to a large extent the use of numerical stress analysis is avoided at early design stages where approximation methods are used instead. When considering that more than 70% of the total life-cycle costs of a product are determined at the early stages [1] introducing numerical stress analysis to these stages may significantly reduce the costs. To achieve this it is important to update the stress results in real-time as the model is being modified.

Different approaches were investigated to achieve real-time stress analysis. One approach is to use the knowledge available about the model in order to reduce the reanalysis time. Trevelyan *et al.* used the first analysis results in order to save time in the reanalysis given that the system matrices and the solution vectors have certain similarities before and after the modifications [2]. Another approach is to

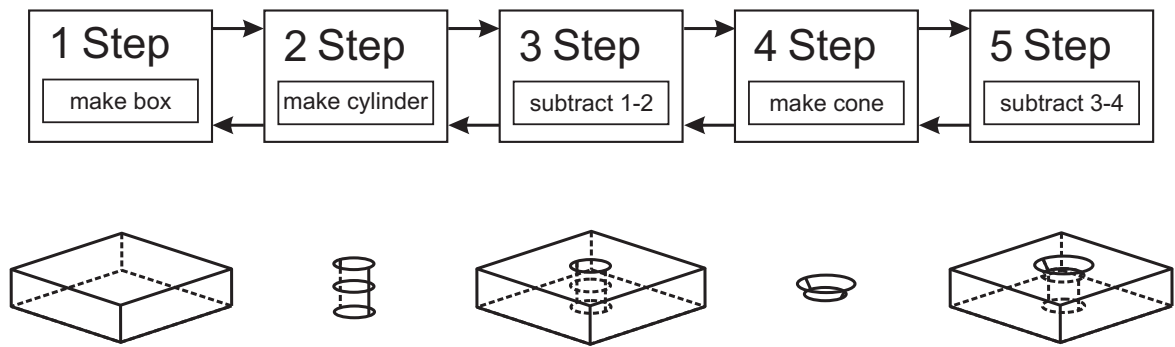


Figure 1: List of steps used to create an object.

reduce the analysis time by using high performance computing [3]. The ultimate aim of this work is to make computational stress analysis accessible by a wide range of engineers therefore we consider the first approach here. In particular we expand the approach developed by Trevelyan *et al.* into three-dimensional problems.

A key issue in this approach is to establish a relation between the CAD model and the numerical analysis input so that after modifying the model only the necessary parts of the linear system are recomputed while the unchanged parts are reused as they are. In this work, we propose an application framework and a data structure that can serve this purpose. An implementation example is shown using an open source CAD kernel [4] and a real-time stress analysis tool [5].

2 APPLICATION FRAMEWORK AND DATA STRUCTURE

When the first stress analysis software packages were introduced they mainly relied on pre-prepared data to be input at run time. With the advancement of CAD applications, CAD and analysis were integrated so that the CAD model is automatically transformed into input data at the analysis run time. This remains the mainstream level of integration for most of the stress analysis tools available today. However, for real-time stress analysis this may not be the most suitable level of integration.

A CAD model is usually developed gradually with the geometry evolving through a series of operations. This series is considered from the analysis point of view as a sequence of models that are not necessarily related. To overcome this we propose to generate the analysis input when the first model is introduced and prepare a first set of results. Then it is sufficient to only modify the linear system according to the operations added to the series and subsequently update the results.

The proposed framework here describes the solid model as a list of operations/steps, as illustrated in Figure 1. The last step of the list builds/updates the data structure. Using Object Oriented Programming (OOP) the operations can be constructed as objects while the list can be expressed as a double linked list where operations can easily be added or removed. Table 1 displays a list of the classes that are used to build the application framework and the data structure. The letter C at the beginning of a name indicates a class while S indicates a structure. Double precision is used for numerical quantities.

The structures SLocation and SSize define the location and the dimensions of a geometrical shape while STRactions and SDisplacements define a set of boundary conditions. The CStep class may only store a single operation that is needed to create a shape, modify it or apply boundary conditions to it. The CList class is the list of steps that defines the solid model and any modifications to this model. The structures SVertex, SEdge and SFace represent the geometry of the solid model in the data structure while SBC represents the boundary conditions. The CBoundaryGeom class stores

| Class name | Member function | Data member |
|---------------|-----------------------|---------------------|
| CStep | CreateBox() | SLocation[] |
| | CreateCone() | SSize[] |
| | CreateCyl() | SDisplacements[] |
| | CreateBoolean() | STractions[] |
| | AddBoundryCond() | |
| CList | GetFirst() | CurrentStep : CStep |
| | GetLast() | FirstStep : CStep |
| | GetCurrent() | LastStep : CStep |
| | Remove(CStep) | |
| | Add(CStep) | |
| | Replace(CStep, CStep) | |
| CDoc | Update() | ListOfSteps : CList |
| CBoundaryGeom | UpdateGeom() | SVertex[] |
| | UpdateBC() | SEdge[] |
| | | SFace[] |
| | | SBC[] |
| CMesh | CreateMesh() | SNode[] |
| | UpdateMesh() | SElement[] |
| CAnalysis | BuildElmtMtrx() | ElmMtrx[] |
| | BuildLnrSys() | SLinearSys[] |
| | UpdateLnrSys() | |

Table 1: Classes used to create and manipulate the objects of the application framework and data structure.

the geometric data structure and updates it. The CMesh class creates, stores and updates the mesh. The CAnalysis class creates the elementary matrices and assembles them into the system matrix to build the linear system and updates it. The CDoc class stores the model list of steps and communicates with the CBoundaryGeom, the CMesh and the CAnalysis classes whenever a step is added to or removed from the list. This is done through the procedure Update() in CDoc which activates the procedures UpdateGeom() and UpdateBC() in CBoundaryGeom, CreateMesh() or UpdateMesh() in CMesh and BuildLnrSys() or UpdateLnrSys() in CAnalysis to update the data structure and to build or to update the mesh and the linear system of equations.

3 IMPLEMENTATION IN A REAL-TIME STRESS ANALYSIS TOOL

The application framework and data structure have been developed in MS Visual C++ 2005 and using OpenCASCADE, an open-source CAD kernel [4], which provides a ready means of implementation of general solid modelling functionality. The application framework is applied using an in-house developed stress analysis software [5] that uses the boundary element method. However, the application framework might equally be useful when implemented with other methods such as the finite

element method. The solid model is built by creating instances of the class `CStep` and adding them to `ListOfSteps`. When the stress results are to be displayed for the first time the model is meshed, the system matrix is assembled and the linear system is solved. If the model is to be modified a new instance of `CStep` is added to `ListOfSteps`. This activates the `Update()` procedure in the `CDoc` class instance, thus, the data structure, the mesh and the linear system are updated. Subsequently, the linear system is re-solved.

The real-time aspect provides the user with the results while the modification is still being applied. For example, when the user moves a face of the solid model from position A to position B the data structure, the mesh and the linear system are updated simultaneously as the mouse cursor is still being moved between the two positions. Updating the linear system frequently ensures smaller changes between two consecutive updates and, hence, the solution of the system before being updated can be a good approximation of the updated system solution. This can be useful in different ways. For example, this approximation can be used as an initial guess for solving the updated system iteratively, which may efficiently reduce the required number of iterations. However, updating the linear system too often may become prohibitively expensive in term of computations. Optimisation of this aspect is a topic that remains under consideration by the authors.

To reduce the time needed to update the system matrix and re-solve the linear system, the `UpdateMesh()` procedure minimizes the number of elements to be modified which minimizes the number of entries in the system matrix that must be updated. Before adding or removing any elements the procedure distorts the existing elements as long as they are of an acceptable quality, which retains the size of the system matrix. Keeping the size of the system matrix and minimizing the number of to-be-updated entries reduce the time needed to assemble the system matrix. Other strategies to reduce the reanalysis time of a two-dimensional problem by up to 80% are proposed in [2]. However, the solution of three-dimensional problems is more time demanding and an 80% reduction may not be sufficient to achieve real-time. This will be discussed further in future work.

4 CONCLUSION

An application framework and a data structure that are useful to achieve real-time performance in stress analysis software are proposed. The application framework and data structure can effectively reduce the reanalysis time by improving the integration level of CAD and stress analysis. Their implementation using an open-source solid modeling kernel is explained.

References

- [1] Y. Asiedu, P. Gu, Product life cycle cost analysis: State of the art review *INT J PROD RES*, 4, 883-908, 36, 1998.
- [2] J. Trevelyan and D.J. Scales, Techniques to accelerate BEM computation to provide virtual reality update of stress solutions, *ENG ANAL BOUND ELEM*, 31, 875-889, 2007.
- [3] G.R. Joldes, A. Wittek and K. Miller, Real-time nonlinear finite element computations on GPU Application to neurosurgical simulation, *COMPUT METHOD APPL M*, 199, 3305-3314, 2010.
- [4] Open CASCADE S.A.S. Open CASCADE, [Online] www.opencascade.org, 1999.
- [5] J. Trevelyan Concept Analyst, [Online] www.conceptanalyst.com, 2006.

Development and Application of OpenSees for a RC Frame in Fire

Jian Zhang², *Asif Usmani¹, Jian Jiang¹, Yaqiang Jiang¹, Panagiotis Kotsovinos¹ and Ian May²

1. School of Engineering, The University of Edinburgh, Edinburgh EH9 3JF, United Kingdom

2. School of Built Environment, Heriot-Watt University, Edinburgh EH14 4AS, United Kingdom

* asif.usmani@ed.ac.uk

Key Words: *structures; OpenSees; Fire; Finite element; computational methods*

ABSTRACT

An experiment is being undertaken to understand the response of earthquake damaged reinforced concrete frames subjected to a post earthquake fire. To model the experiment, a number of new modules are being developed for the open source and object-oriented finite element software framework, OpenSees, so that the software could be used to perform thermo-mechanical analyses. The development began with modification of the elastic beam-column element and the elemental load classes. In addition to the existing 2D linear element 3D linear element and thermal load classes have been developed. A series of benchmark problems (an elastic beam with various boundary constraints subjected to uniformly distributed and thermal loads) have been solved using OpenSees and ABAQUS. The results obtained match well with each other and with analytical solutions (where available). New two dimensional nonlinear beam-column elements have been added to OpenSees by introducing thermally induced load, temperature dependent materials and section force-deformation relationships. These elements have been developed from the existing *dispbeamcolumn2d* and *forcebeamcolumn2d* OpenSees classes. The results from undertaking a number of benchmark tests and modelling a real fire test using the newly developed classes show that the additions so far have been reasonably successful.

1 INTRODUCTION

With increasing urbanisation and industrialisation earthquakes represent an ever greater risk to life, livelihoods and to the sustainability of society's rapid development. In built-up areas, especially major cities with tall buildings and extensive gas mains, this risk is compounded by post earthquake fires. In fact, losses resulting from fires developing soon after the earthquake may be comparable to those resulting from the shaking [1]. The risk is certainly increased by the hampering of fire response due to the extreme traffic congestion, collapsed houses and buildings, rubble in the streets, the concomitance of multiple fires and the possible difficulties in water supply soon after the earthquake [2].

To develop a comprehensive earthquake and fire research programme based on exploiting the complementary strengths of the collaborating institutions, a project funded by UKIERI is currently underway. Objectives of this project may be stated as: a) Developing a detailed understanding of the mechanics of the response of earthquake damaged structures (primarily reinforced concrete frames) subjected to fire (through small and large scale testing and developing computational models); b) Developing mathematical models for determining the reliability of structural components and structures subjected to compound seismic and fire loading, which account for the uncertainties associated with the loading and damage estimation, to enable realistic quantification of performance.

To model the experiment, a software named OpenSees has been developed so that it could be used to perform thermo-mechanical analyses. OpenSees is an open source object oriented software framework developed at UC Berkeley and currently supported by PEER and Nees. OpenSees has so far been focussed on providing an advanced computational tool for analysing the non-linear response of structural frames subjected to seismic excitations [3]. A key feature of OpenSees is the interchangeability of components and the ability to integrate existing libraries and new components into the framework (not

just new element classes) without the need to change the existing code [4]. However one of the limitations of OpenSees is that thermal analysis can not be carried out by it up to date. In order to overcome this flaw so that it can be used to model the experiment of UKIERI, some new classes have been added into OpenSees and the some thermal analysis has been performed. The compared results show an acceptable agreement between theory, OpenSees, Abaqus.

2 NEWLY ADDED OPENSEES CLASSES

As mentioned above, there is not much work to do to let the OpenSees “recognize” a new class, and this advantage can be shown by the progress of introducing thermal action to the elastic beam-column element. A new derived class of *ElementalLoad*, called *Beam2dThermalAction* or *Beam3dThermalAction*, and a new member function of elastic beam-column element were all required to add into OpenSees to perform the linear analysis of elastic element in thermal loading.

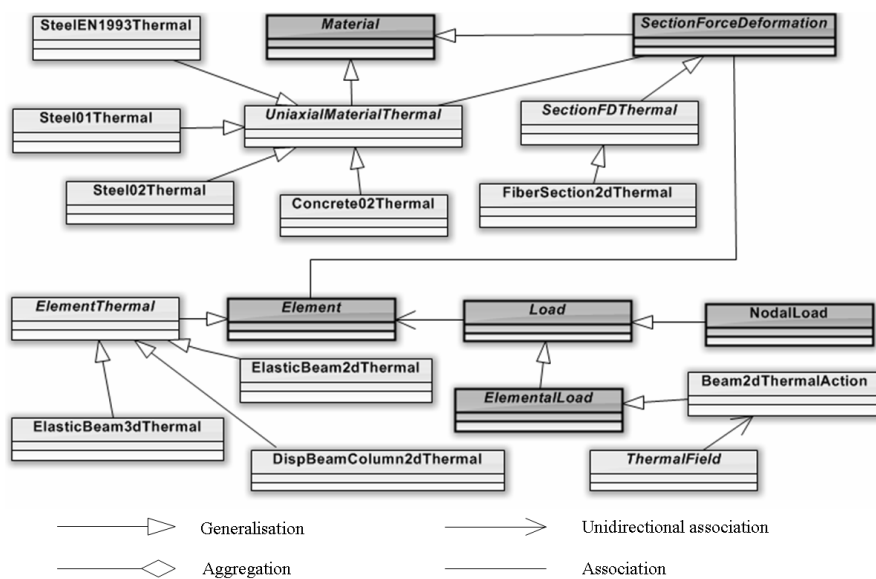


Fig. 1 New classes introduced to the current OpenSees framework for performing thermo-mechanical analyses

It is more complicated to perform a thermal analysis to the nonlinear beam-column element. *Material* and *SectionForceDeformation* classes’ information has to be passed to the element class while carrying out the nonlinear analysis and all of these classes must be temperature related. Fig. 1 above shows the new classes that have been implemented within the existing framework (the original OpenSees classes are identified by the greyed boxes).

3 A BENCHMARK TEST FOR ELASTIC BEAM-COLUMN ELEMENT

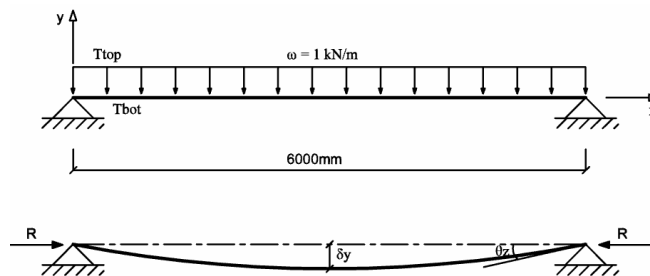


Fig. 2 An end-restrained elastic beam under udl and thermal loading

A series of benchmark problems have been used to test the new thermo-mechanical code in OpenSees. For instance one was to predict the mid-span deflection, end rotation and axial force in an elastic beam

(Young's Modulus $E = 10\text{GPa}$, area of cross section $A = 9 \times 10^4\text{mm}^2$) under udl and thermal loading ($T_{\text{top}} = 20\text{C}$, $T_{\text{bottom}} = 800\text{C}$, thermal expansion coefficient $\alpha = 12 \times 10^6 /\text{C}$) both ends of which are restrained in translation (Fig. 2), however the rotations are free. Analytical, OpenSees and ABAQUS solutions are shown in Table 1, all of which are in agreement.

| | udl | | | thermal | | | udl and thermal | | |
|------------------------|------------|----------|--------|------------|----------|--------|-----------------|----------|--------|
| | analytical | OpenSees | ABAQUS | analytical | OpenSees | ABAQUS | analytical | OpenSees | ABAQUS |
| $\delta y(\text{mm})$ | 2.5 | 2.5 | 2.51 | 140.678 | 140.4 | 140.4 | 143.178 | 142.9 | 142.91 |
| $\theta z(\text{rad})$ | 0.133 | 0.133 | 0.133 | 0.936 | 0.936 | 0.936 | 0.0949 | 0.0949 | 0.0949 |
| $R(\text{kN})$ | 0 | 0 | 0 | 4212 | 4212 | 4120 | 4212 | 4212 | 4120 |

Table 1 compared results among analytical, OpenSees and ABAQUS

4 MODELLING OF AN TEST FRAME

An RC frame is being tested in India under simulated earthquake damage and a subsequent fire. To predict the behaviour of the frame, a two dimension frame model has been analysed. The model was at first subjected to a gradually increased cycle of lateral displacements after loading the columns and the slab/beams with gravity loads. The complete analysis was carried out over a number of steps. In the first step the frame was subjected to increasing quasi-static cyclic displacements as shown in Figure 3. Displacement control was used for the analysis with node 1 (see Figure 4) regarded as the control point with a maximum displacement of approximately 200mm.

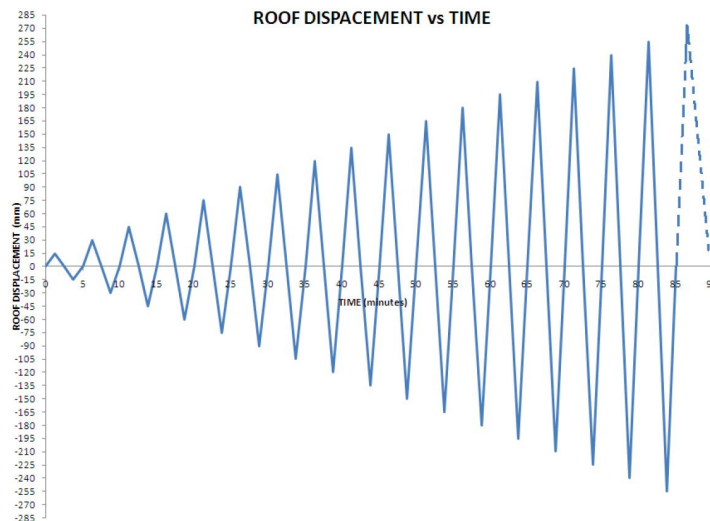


Fig.3. Frame model and the displacement – force curve of control node 1

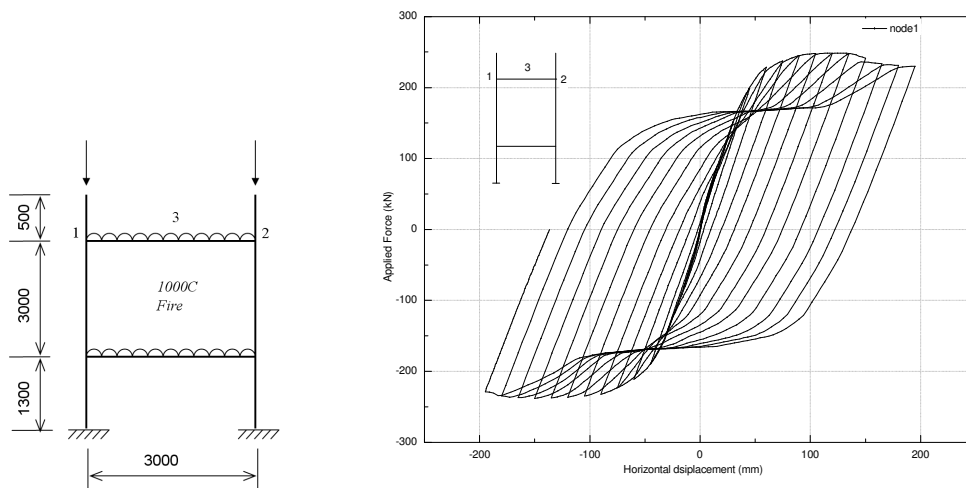


Fig.4. Frame model and the displacement – force curve of control node 1

The Figure 4 shows the complete force-displacement plot node 1. The plot shows that the analysis was carried until maximum displacements of just under 200mm were reached on both sides. The displacement was then reduced until the force at the control point become zero, leaving a permanent residual displacement of approximately 130mm. The displacement corresponding to zero force was obtained from an earlier analysis.

After the damage inducing cyclic displacement step, the frame was subjected to a 1000°C constant fire lasting 3600 seconds. An interesting feature of the behaviour was that the frame seemed to “stiffen” because of the fire. The absolute displacement of node 1 decreased from around -140mm to -80mm under fire until the maximum (exposed face) temperature of the beam reached 450°C, and then it dropped to around -130mm at the end of the heating (Fig. 5). The deflection at the midspan of the upper beam is also shown in Fig. 5 which shows relatively low values as the current model lumps the slab and beam sections together to form the beam. The test results are still awaited, however it is expected that the slab will produce greater deflections after the fire than possible with this 2D model

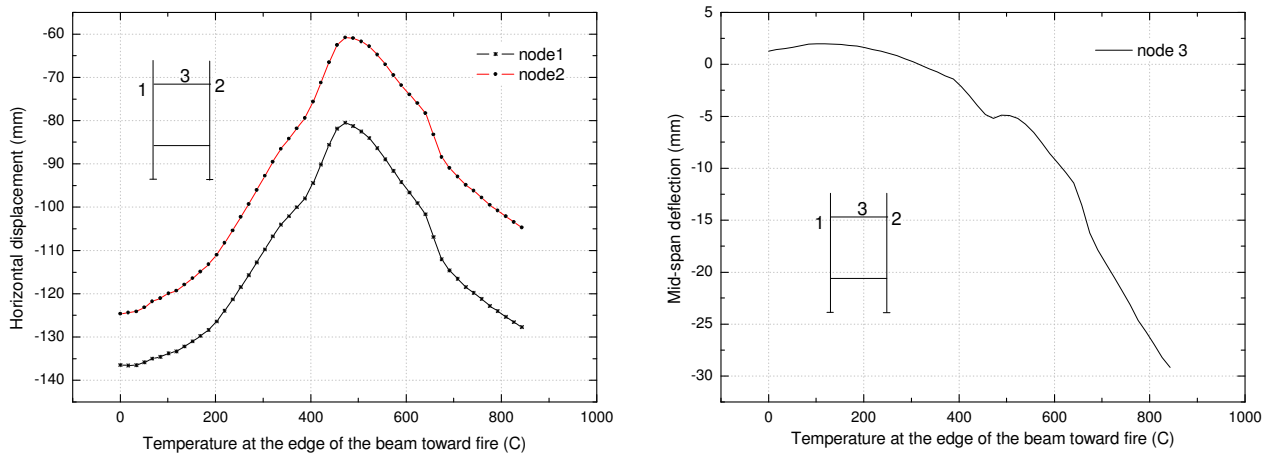


Fig.4. Displacements of node 1, 2 and 3

4 CONCLUSION

A fully nonlinear 2D thermo-mechanical frame analysis capability has been added to OpenSees and had been tested against a number of benchmark problems to ensure that it is working correctly. It has also been combined with the native nonlinear static analysis capability in OpenSees to model damaged frames subjected to fire. Open source codes offer an excellent opportunity for researchers to collaborate across geographical boundaries and build a truly international community to solve engineering problems that are of common concern. This work is a small contribution to the OpenSees movement and considerable further development is in train. Future developments will include full 3D thermo-mechanical analyses for frames by further developing OpenSees beam and shell elements.

References

- [1] EQE International. *The January 17, 1995 Kobe earthquake—an EQE summary report*. April, 1995..
- [2] Buchanan AH. *Structural design for fire safety*. Chichester, England: Wiley; 2001.
- [3] A. Usmani, J. Zhang, J. Jiang, Y. Jiang, P. Kotsovinos, J. Zhang And I. May. Using OpenSees for structures in fire. 6th International Conference on Structures In Fire, 2010.
- [4] S. Mazzoni, F. Mckenna, et al, *OpenSees Command Language Manual*, 2007.

DAMAGE-BASED FRACTURE ANALYSIS FOR THE EVALUATION OF SEISMIC PERFORMANCE OF RC BRIDGE COULMNS

*M. O. Benamer¹, Y. T. Feng²

Civil and Computational Engineering Centre
Swansea University
SA2 8PP, Wales, UK

¹474825@swansea.ac.uk ²y.feng@swansea.ac.uk

Key Words: *seismic performance, fracture state, energy dissipation, bridge piers*

ABSTRACT

It is an important practice to implement the methodology of Performance-based seismic evaluation (PBSE) for reinforced concrete (RC) substructures in bridges. With PBSE, more considerations have been focused on preserving the structure's serviceability and integrity during and after the earthquake incident.

To investigate the rate of damage at a structure due to a seismic motion, a dynamic FE analysis, with Rankine fracture model for quasi-brittle materials, is conducted for a shaking table multidimensional seismic excitation experiment. The aim is to seismically evaluate the bridge substructure based on the fracture state that develops at the column base. Crack initiation and propagation, spalling of the concrete cover, and buckling of the rebar are all detected along the time history of the analysis. Such information can be used to evaluate the seismic behaviour of bridge piers. The evaluation can also be extended for piers with seismically isolated bearings (SIB), to achieve an optimum energy dissipation with suitable structural serviceability.

Introduction

From 1990-to date, the Eurocode 8 has laid a new base for the so called capacity design strategy which has adopted deformation-based and energy-based approaches to reach a seismic design. The philosophy of the capacity design is to dissipate energy throughout the building itself, throughout 'plastic hinges', i.e. controlling the failure mode & position.

A strong-column weak-beam design strategy would be adopted to control the initiation of plastic hinges, which act as 'hysteretic damping devices' that would bring the structure to some balanced energy state and force equilibrium. Plastic hinges would control the failure of a structure to the minimum extent in order to increase life safety measures, but the resulting damage is still not repairable.

Both 1994's North Bridge earthquake and 1995's Kobe earthquake resulted a huge economic loss, and people started to think about preserving a structure's serviceability as much as life safety. This brought up what is known as Performance-based strategy which focuses on limiting the expected damage in the design to maintain the structure's serviceability after the earthquake incident.

This should bring us to the field of seismic evaluation of damage in RC structures, which requires knowledge of fracture mechanism and simulation of crack growth as the structure is subjected to the seismic excitement. Performance-based seismic design is used to ensure that specific damage-based criteria are met [1]. A performance objective represents a specific risk, stated in terms of the desired structural behaviour (or damage state) associated with a specific level of earthquake demand (or seismic hazard) [2]. In concern with bridges, Sung et al [3] stated that conventional seismic evaluation of existing bridges show inaccurate and unreliable information since that they use a strength-based concept to indirectly estimate the non-linear behaviour of structures.

Recent studies have advised the use of energy concepts as an alternative way to the traditional design strategies for the identification of both seismic demands imposed by the earthquakes and the structure

capacities to meet with such demands [4]. Decanini and Mollaioli [4] stated that the energy balance formulation is much more effective in concept than the force equilibrium equation since it provides an explicit control of balance over the input and dissipated energy. The considered energy is the inelastic energy, which is the sum of the hysteretic energy (E_H) and damping energy (E_ϵ). The hysteretic energy (E_H) is an important demand descriptor for damage potential of the ground motion, and it is a function of the Displacement-Ductility ratio of the structure ($u_y = u_{\max}/\mu$).

A seismic performance-based design of a structure implies that the seismic capacity of a structural response should meet the seismic demand of that structure under the target ground motion excitations. However, when a shortage of seismic capacity exists, certain damage would occur as corresponding to that shortage. It is the damage index (d) that expresses that shortage of efficiency in the structure, or it is the fragility index (P_f) that describes the probability of exceeding the damage state [5]. Most studies on fragility analysis of bridges use column ductility as the primary damage measure [5]. However, other effective damage indicators are based on energy dissipation. One of the best known local damage indices is the one proposed by Park and Ang [6], which defines a linear relationship between the displacement and a damage index, yet involves the ductility and rate of dissipative energy.

As a qualitative descriptive approach, the HAZUS 97 technical manual to estimate structure loss in bridges due to lateral earthquake movements determines the damage states as they vary between (No damage –to- Complete damage state) [7]. HAZUS was used in an analytical study on typical bridges [5], in which damage states were classified in terms of ductility measures and displacement-based domains. There seems to be an agreement between researchers on the fact that the earthquake damage occurs not only due to maximum deformation (or max ductility) attained, but it is associated with the hysteretic energy dissipated by the structure as well [2].

Simulation of fracture and Modelling of Specimen

It is quite significant to understand the way fracture occurs theoretically and computationally. In the previously discussed literature, damage was determined through measuring energy and deformation parameters but not through inelastic stresses and softening strains, which control the fracturing mechanism. Once Gauss stresses reach the failure point, the material is said to have entered the softening stage, in which inelastic strains are determined according to the softening curve stiffness E_t , which is a function of the fracture energy G_f of the material.

Release of the fracture energy rate ∂G_f is dependent on the degree of damage. Integrating over a localization band width l_c for a constant slope softening model gives:

$$-\frac{f_t^2 l_c}{2G_f} = E_t = \frac{\partial \sigma}{\partial \epsilon}$$

Where, f_t is the concrete tensile strength, and E_t is the stress-strain modulus at the softening stage. The fracture energy G_f for concrete is ranging between 100 and 150 (N/m) (J/m), which is assumed to be released during the softening stage. Once all of the fracture energy in the infinitesimal element is released, i.e. work of softening strains is completed and stresses at that Gauss point drop to zero, a crack initiates.

In this research, conducted a computational dynamic analysis of 3D Finite/Discrete tetrahedral elements using the (ELFEN 3.7.1) software. The ELFEN Explicit code is provided with rate independent models such as the Rankine fracture model and the Mohr-Coulomb Model with tension cut-off envelope, which are designated to model fracture in quasi-Brittle materials such as concrete. The analysed model simulates a shaking table experiment that was conducted for a RC bridge column, subjected to a bidirectional seismic excitation of Kobe earthquake. This loading implements many structural hazards and raise challenges for seismic design tasks. However, it is a low strain-rate motion, and thus, a plastic strain-rate function is not required in the non-linear algorithm to update the plastic strains.

The model is vertically symmetric and subjected to x-direction loading only to reduce the substantial computation time and memory required. In addition, only 10-seconds time history is analysed.

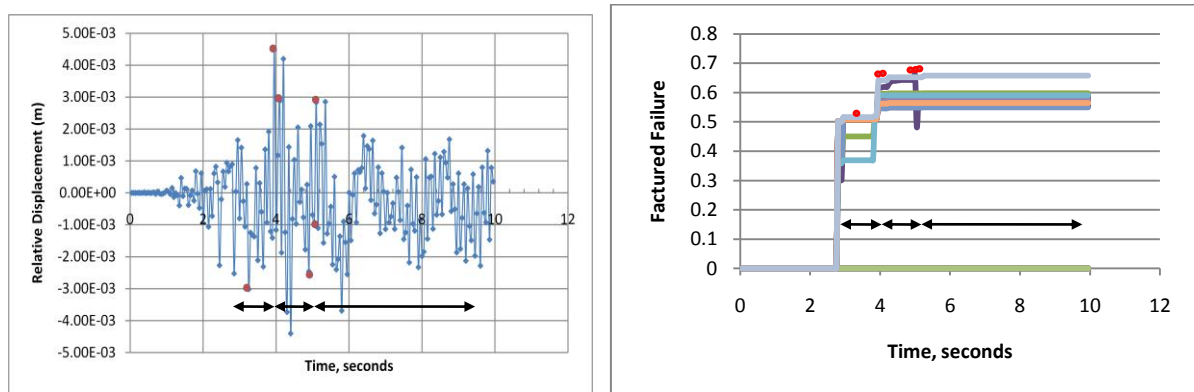
The discrete properties such as the normal penalties, tangential penalties, buffer zone, smallest element size and others belong to the Post-fracture process. However, in this particular seismic motion both Normal and Tangential Penalties of the Post-fracture parameters are quite effective in conducting the overall fracture process, and need to be tolerated until the simulated damage match the damaged column of the experiment. No specific interpretation was found for this cause and effect, but it was concluded that oscillatory low-rate strains motions may require special values for the post-fracture parameters.

Analysis and discussion of Results

The bridge column is modelled by the ELFEN code to analyse its response when it is subjected to Kobe Ground motion. It can be clearly noticed, in this particular example, that neither time-history nor hysteresis loops representations of the structure's mass are able to predict the rate of damage in its early or late stages. However, failure fracture state of elements (or FAILFC) expresses the percentage of fracture propagation that those elements experience. However, not all failed elements could become fully damaged, but rather have initiative fractures and micro fractures, as according to the fracture theory. Elements probability to reach severe fracture propagation depends on the seismic demand of the oscillation of the non-periodic ground motion imposed on the structure.

Such failure-fracture history can be useful to researchers to understand the probability of fracture propagation in conjunction with other measures of a structure's response such as the time history and hysteresis loops. Figures (1) and (2) show a 3-category display on the time history based on the change of fractured failure detected at the column base. They are; as follows: 1st category starts at 2.7 seconds, 2^{ed} category starts at 4.0 seconds and 3^{ed} category starts at 5.05 seconds until end of analysis. The time history of the top mass displacement relative to base displacement can also be classified based on this categorization. Points of crack propagations, in figure (1), are mostly seen when relative displacements reach maximum values, but this is not necessarily true for every crack propagation. In fact, few other large displacements are not associated with any crack propagation. This classification of the fractured failure can be very useful to define a range of qualitative damage severity for the specific problem, starting from trivial damage rates till non-repairable damage.

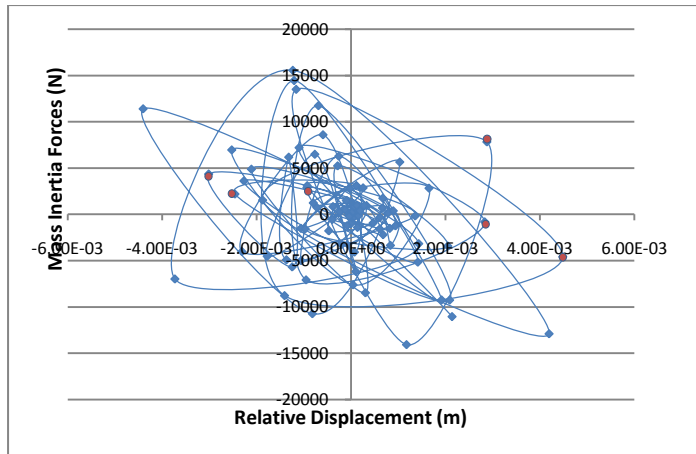
Images of simulated fractures show that the first crack occurs at 3.3 seconds with elements' fractured failure between 0.37 and 0.51. Then a second crack occurs at 3.95 seconds with failure between 0.53 and 0.62. The 3rd, 4th, 5th and 6th cracks occur at 4.0, 4.95, 5.05 and 5.10 seconds respectively. At further excitements, the structure remains the same with no more propagation until the end of analysis.



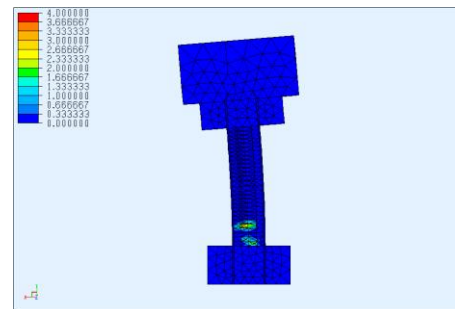
Figure(1):Crack points &failure stages in Time History Figure(2):Crack points & failure stages in fracture index

In contrast to other oscillation responses, the hysteresis loops by Kobe motion shown in figure (3) shows some degree of inconsistency of path in the force-deformation relation. This is due to the shear mode response of this particular RC column under the Kobe excitement. In this analysis, the consequent damage has been relatively low, and the structure did not suffer spalling of the column concrete cover or buckling of the rebar. This investigation has been made to cover light failure

responses. Severe cases are to be conducted respectively under stronger ground motions to investigate progressive failure responses. Moreover, this analysis could be extended with base-isolated structures, in which seismic energy is dissipated through both isolation mechanism and the plastic hinge at the column base.



Figure(3): Crack points in Hysteresis Loops.



Figure(4): Fracture failure spots in model

Conclusion

- 1- Evaluation of seismic performance for reinforced concrete bridge columns can rely on damaged-based fracture analyses, with low uncertainty, to interpret dissipative energy, probability of damage propagation and the structure's capacity to resist earthquake demand imposed on the structure.
- 2- In this specific example, neither time-history nor the hysteresis loops displays were able to predict the rate of damage in its early or late stages.
- 3- Based on failure of fracture outcome, time history of this specimen can be divided into 3 categories which specify different failure stages for the excited structure. The fracture classification can be very useful to define a qualitative range of damage severity for the specific problem, starting from trivial damage till non-repairable damage.
- 4- In respect to this analysis, further extended work can be conducted concerning a structure's progressive failure and seismic isolation analysis. Both are needed in earthquake engineering and bridge structures dynamics.

References

- [1] Rafael Riddell, Jaime E. Garcia and Eugenio Garces. Inelastic deformation response of SDOF systems subjected to earthquakes, *Earthquake Engn Struct. Dyn.*;31:515–538 (DOI:10.1002/eqe.142), 2002.
- [2] Rafael Riddell and Jaime E. Garcia. Hysteretic energy spectrum and damage control. *Earthquake Engn Struct. Dyn.*; 30:1791–1816 (DOI: 10.1002/eqe.93), 2001.
- [3] Yu-Chi Sung, Wen-I Liao and W. Phillip Yen. Performance-based concept on seismic evaluation of existing bridges. *Earthq Eng & Eng Vib*; 8:127-135 DOI: 10.1007/s11803-009-8151-3, 2009.
- [4] Luis D. Decanini, Fabrizio Mollaioli. An energy-based methodology for the assessment of seismic demand. *Soil Dynamics and Earthquake Engineering*; 21, 113-137, 2001.
- [5] Eunsoo Choi, Reginald DesRoches, Bryant Nielson. Seismic fragility of typical bridges in moderate seismic zones. *Engineering Structures*; 26, 187–199, 2004.
- [6] Park YJ, Ang AH-S. Mechanistic seismic damage model for reinforced concrete. *Journal of Structural Engineering*; 111(4) or (3) :722–39. ASCE1985.
- [7] HAZUS, Earthquake loss estimation methodology. Technical Manual, *National Institute of Building for the Federal Emergency Management Agency FEMA*, Washington (DC), 1997.

Natural frequencies of cracked isotropic & specially orthotropic plates using the extended finite element method

*S Natarajan¹, P Baiz², D Roy Mahapatra³, T Rabczuk⁴, P Kerfriden¹ and S Bordas¹

¹Institute of Theoretical, Applied and Computational Mechanics, Cardiff University, Cardiff, Wales,
U.K.

²Department of Aeronautics, Imperial College, London, U.K.

³Department of Aerospace Engineering, Indian Institute of Science, Bangalore, India.

⁴Department of Civil Engineering, Bauhaus-Universität Weimar, Germany.

*sundararajan.natarajan@gmail.com

Key Words: *extended finite element method; first order shear deformation; mindlin plate theory; vibration; cracked isotropic plate.*

ABSTRACT

In this paper, the linear free flexural vibration of cracked isotropic and specially orthotropic plates is studied using the extended finite element method. The mixed interpolation technique of the well-established MITC4 [1] quadrilateral finite element with 12 standard degrees of freedom per element is used for this study. The natural frequencies of simply supported square plates are computed as a function of crack length and crack location.

1 INTRODUCTION

In this paper, we apply the extended finite element method (XFEM) to study the free flexural vibrations of cracked isotropic and specially orthotropic plates. It is known that cracks or local defects affect the dynamic response of a structural member. This is because, the presence of the crack introduces local flexibility and anisotropy. Moreover the crack will open and close depending on the vibration amplitude. The vibration of cracked plates was studied as early as 1969 by Lynn and Kumbasar [2] who used a Green's function approach. Later, in 1972, Stahl and Keer [3] studied the vibration of cracked rectangular plates using elasticity methods. The other numerical methods that are used to study the dynamic response and instability of plates with cracks or local defects are: (1) Finite fourier series transform [4]; (2) Rayleigh-Ritz Method [5]; (3) harmonic balance method [6]; and (4) finite element method [7, 8]. And recently, XFEM has been applied to study the vibration of cracked isotropic plates [9]. Their study focussed on center and edge cracks with simply supported and clamped boundary conditions. In this paper, we carry out a parametric study on the influence of crack location and crack length on the natural frequencies of isotropic plates with proper use of enrichment functions described in [10] using the stabilized MITC4 element [1].

2 Numerical results

In this section, we present the natural frequencies of cracked isotropic plates using the extended MITC4 formulation [10] for simply supported square plate. In all cases, we present the non-dimensionalized free flexural frequencies as, $\Omega = \omega a^2 \sqrt{\frac{\rho h}{D}}$, where $D = \frac{Eh^3}{12(1-\nu^2)}$ is the bending rigidity of the plate and ρ is the mass density. The effect of crack length and crack location on the natural frequencies are studied. Based on progressive mesh refinement, a 30×30 structured mesh is found to be adequate to model the full plate for the present analysis. Consider a plate of uniform thickness, h and with length and width as a and b , respectively. Figure (1) shows a plate with all edges simply supported with a center crack of length c . The boundary conditions for this study are:

$$w_o = \theta_y = 0 \quad \text{along} \quad x = 0, a \quad (1a)$$

$$w_o = \theta_x = 0 \quad \text{along} \quad y = 0, b \quad (1b)$$

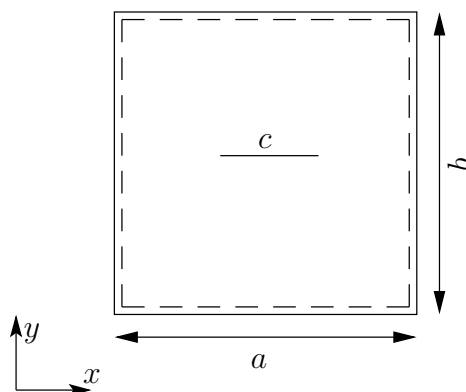


Figure 1: Plate with a center crack and all edges simply supported

Table 1: Non-dimensionalized natural frequency for a simply supported square plate with a center crack for $h/a=0.001$

| c/a | Mode 1 | | Mode 2 | |
|-------|----------|---------|----------|---------|
| | Ref [11] | Present | Ref [11] | Present |
| 0.0 | 19.74 | 19.74 | 49.35 | 49.38 |
| 0.2 | 19.38 | 19.40 | 49.16 | 49.85 |
| 0.4 | 18.44 | 18.50 | 46.44 | 47.27 |
| 0.6 | 17.33 | 17.37 | 37.75 | 38.92 |
| 0.8 | 16.47 | 16.54 | 27.43 | 28.28 |

The influence of the crack length ratio (c/a) on the first two natural frequencies for a square plate ($a/b = 1$) with thickness, $h/a = 0.001$ are shown in Table 1. It is observed that as the crack length ratio increases, the frequency decreases for both modes. This is due to the fact that increasing the crack length increases local flexibility and thus decreases the frequency.

Figure (2) shows the influence of the crack location on the natural frequency of a square plate with thickness $h/a = 0.001$ and crack length ratio, $c/a = 0.2$. It is observed that the natural frequency of

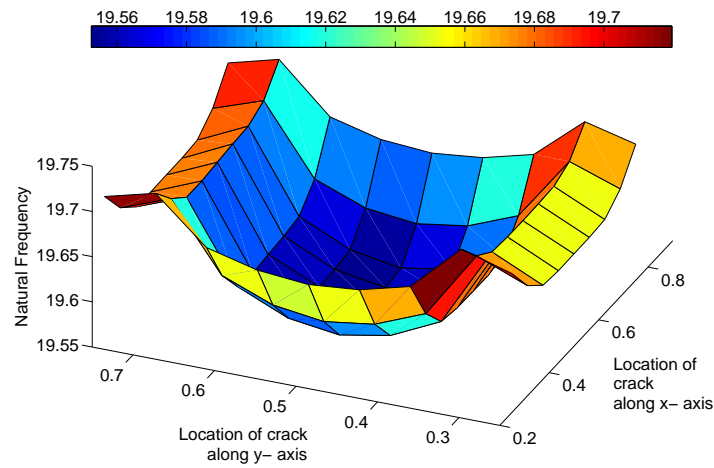


Figure 2: Natural frequency (first mode) vs position of crack along the x - and the y - axis for a square plate with $(a/b = 1)$ with thickness, $h/a = 0.001$ and crack length, $c/a = 0.2$.

the plate monotonically decreases as the crack moves along the edges and towards the center of these edges. The natural frequency of the plate is maximum when the damage is situated at the corner. As the crack moves along the center lines of the plate from the edges and towards the center of the plate, the natural frequency increases up to a certain distance and then decreases. When the crack is situated at the center of the plate, the frequency is minimum.

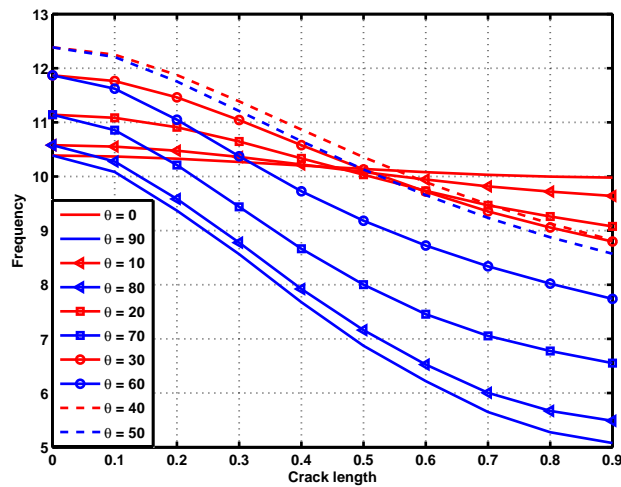


Figure 3: Fundamental frequency (mode 1) as a function of crack length for different fiber orientation ($E_1/E_2 = 25, G_{12} = G_{13} = 0.5E_2, G_{23} = 0.2E_2, \nu_{12} = 0.2E_2$). θ is the orientation of the fiber.

Next, the influence of fiber orientation and the crack length on the fundamental frequency of a square specially orthotropic plate is studied. The non-dimensionalized frequency, $\Omega = \omega(a^2/h)\sqrt{\rho/E_2}$ is plotted as a function of crack length for different fiber orientations. It can be seen that the frequency decreases as the crack length increases due to the loss of material stiffness. For a fixed crack length,

the frequency initially increases until the fiber orientation reaches, $\theta = 45^\circ$. With further increase in the fiber orientation, the frequency decreases. Due to the inherent anisotropic property of the material, the solution lacks symmetry. This is shown in Figure (3).

3 Conclusion

In this paper, we used the extended finite element method to study the dynamic response of cracked isotropic and specially orthotropic plates. A stabilized MITC4 element with appropriate enrichment is used for the study. The influence of the crack length and crack location on the natural frequency are studied. It is seen that with increase in crack length, the natural frequency decreases and is minimum when the crack is situated at the center of the plate. The effect of fiber orientation and the crack length on the fundamental frequency of specially orthotropic material is also studied. The unsymmetric nature of material property is reflected in the response of the plate. It is seen that XFEM is an effective method to study the dynamic response of cracked structures.

References

- [1] K. Bathe and E. Dvorkin. A four node plate bending element based on Mindlin-Reissner plate theory and mixed interpolation. *IJNME*, 21, 367–383, 1985.
- [2] P. Lynn and N. Kumbasar. Free vibrations of thin rectangular plates having narrow cracks with simply supported edges. In: *Developments in Mechanics, Proc. of the 10th Midwestern Mechanics Conf.*, 911–928, 1967.
- [3] B. Stahl and L. Keer. Vibration and stability of cracked rectangular plates. *IJSS*, 8, 69–91, 1972.
- [4] R. Solecki. Bending vibration of rectangular plate with arbitrarily located rectilinear crack. *EFM*, 22, 687–695, 1985.
- [5] S. Khadem and M. Rexaee. Introduction of modified comparison functions for vibration analysis of a rectangular cracked plate. *JSV*, 236, 245–258, 2000.
- [6] G. Wu and Y. Shih. Dynamic instability of rectangular plate with an edge crack. *Comp. Struct.*, 84, 1–10, 2005.
- [7] G. Qian and S. Gu and J. Jiang. A finite element model of cracked plates and application to vibration problems. *Comp. Struct.*, 39, 483–487, 1991.
- [8] H. Lee and S. Lim. Vibration of cracked rectangular plates including transverse shear deformation and rotary inertia. *Comp. Struct.*, 49, 715–718, 1993.
- [9] M. Bachene and R. Tiberkak and S. Rechak. Vibration analysis of cracked plates using the extended finite element method. *Arch. Appl. Mech.*, 79, 249–262, 2009.
- [10] J. Dolbow and N. Moës and T. Belytschko. Modeling fracture in mindlin-reissner plates with extended finite element method. *IJSS*, 37, 7161–7183, 2000.
- [11] K. Liew and K. Hung and K. Lim. A solution method for analysis of cracked plates under vibration. *EFM*, 48, 393–404, 1994.

A PROJECTED QUASI-NEWTON METHOD FOR DYNAMIC MULTIBODY FRICTIONAL CONTACT PROBLEMS

Tomasz Koziara, Nenad Bićanić

Department of Civil Engineering, University of Glasgow, Glasgow G12 8LT, UK

t.koziara@civil.gla.ac.uk

Key Words: *friction; contact; multibody; solver*

ABSTRACT

We present a simple projected quasi-Newton (PQN) approach for dealing with frictional contact constraints in multibody dynamic simulations. A single matrix-vector product is required per iteration, rendering the method attractive in the context of parallel computations. Our approach often performs comparably with the commonly used Gauss-Seidel scheme, while having a much lower communication cost in parallel. The implementation is available at <http://code.google.com/p/solfec>.

1 METHOD

Let \mathbf{U} collect 3-component relative contact point velocities and \mathbf{R} collect 3-component contact reactions. At contact points we consider a minimalistic interface law, reflecting the core difficulties related to the lack of smoothness and the non-associated character of friction. In terms of normal behaviour we employ the velocity Signorini condition, $U_{\alpha N} \geq 0$, $R_{\alpha N} \geq 0$, $U_{\alpha N} R_{\alpha N} = 0$. In terms of shearing behavior we utilize the Coulomb law, $\mathbf{R}_{\alpha} \in \text{interior}(K_{\alpha}) \Rightarrow \mathbf{U}_{\alpha T} = 0$ and $\mathbf{R}_{\alpha} \in \text{boundary}(K_{\alpha}) \Rightarrow \mathbf{U}_{\alpha T} = -\gamma \mathbf{R}_{\alpha T}$, where $\gamma > 0$. The friction cone K_{α} is defined as

$$K_{\alpha} = \{\mathbf{R}_{\alpha} : \|\mathbf{R}_{\alpha T}\| \leq \mu_{\alpha} R_{\alpha N}, R_{\alpha N} \geq 0\} \quad (1)$$

where μ_{α} is the coefficient of friction. It has been shown by De Saxcé and Feng [1], that the Signorini-Coulomb law can be expressed in a compact form

$$-\begin{bmatrix} \mathbf{U}_{\alpha T} \\ U_{\alpha N} + \mu_{\alpha} \|\mathbf{U}_{\alpha T}\| \end{bmatrix} \in N_{K_{\alpha}}(\mathbf{R}_{\alpha}) \quad (2)$$

where $N_{K_{\alpha}}$ stands for the normal cone of the set K_{α} . For a convex set A the normal cone $N_A(\mathbf{R})$ at point $\mathbf{R} \in A$ is defined as the set of all vectors \mathbf{V} such that $\langle \mathbf{V}, \mathbf{S} - \mathbf{R} \rangle \leq 0$ for all $\mathbf{S} \in A$. Let us now define

$$\mathbf{F}(\mathbf{R}) = \begin{bmatrix} \dots \\ \mathbf{U}_{\alpha T}(\mathbf{R}) \\ U_{\alpha N}(\mathbf{R}) + \mu_{\alpha} \|\mathbf{U}_{\alpha T}(\mathbf{R})\| \\ \dots \end{bmatrix} \quad (3)$$

and

$$K = \bigcup_{\alpha} K_{\alpha} \quad (4)$$

where the dependence $\mathbf{U}_{\alpha}(\mathbf{R})$ is linear $\mathbf{U} = \mathbf{W}\mathbf{R} + \mathbf{B}$, and \mathbf{R} is a collection of \mathbf{R}_{α} for $\alpha \in \{1, \dots, \nu\}$. Formula (2) states, that the frictional contact constraints are satisfied if $-\mathbf{F}(\mathbf{R})$ belongs to the normal cone of the friction cone at \mathbf{R} . Hence

$$-\mathbf{F}(\mathbf{R}) = \mathbf{R} - \mathbf{F}(\mathbf{R}) - \text{proj}_K(\mathbf{R} - \mathbf{F}(\mathbf{R})) \quad (5)$$

which can be reduced to the usual projection formula $\mathbf{R} = \text{proj}_K(\mathbf{R} - \mathbf{F}(\mathbf{R}))$. Let us not do it though, but rather define a vector field

$$\mathbf{m}(\mathbf{S}) = \mathbf{S} - \text{proj}_K(\mathbf{S}). \quad (6)$$

We can rewrite (2) as

$$\mathbf{C}(\mathbf{R}) = \mathbf{F}(\mathbf{R}) + \mathbf{m}(\mathbf{R} - \mathbf{F}(\mathbf{R})) = \mathbf{0} \text{ and } \mathbf{R} \in K, \quad (7)$$

a root finding problem defined within the friction cone. Since $\mathbf{C}(\mathbf{R})$ is not smooth, to compute $\nabla \mathbf{C}$ we generalize the approach from [2], where only the self-dual case (friction coefficient equal to 1) was considered. Our idea is to employ the following projected Newton step

$$\mathbf{R}^{k+1} = \text{proj}_K \left[\mathbf{R}^k - \mathbf{A}^{-1} \mathbf{C}(\mathbf{R}) \right] \quad (8)$$

so that, as required, the iterates remain within the friction cone and where $\mathbf{A} \simeq \nabla \mathbf{C}$ is an easy to invert approximation of $\nabla \mathbf{C}$. Since in many practical situations $\nabla \mathbf{C}$ is singular, we cannot hope to employ $\nabla \mathbf{C}$. The relative velocity \mathbf{U} is first updated in step (a) of Algorithm 1. This is the only step requiring parallel communication: each processor stores a subset of constraints and a portion of the \mathbf{W} operator. We then compute the right hand side \mathbf{C} and the diagonal 3×3 blocks $\nabla \mathbf{C}_{\alpha\alpha}$. Since \mathbf{A} is a rather poor approximation of $\nabla \mathbf{C}$, in step (c) we employ a θ -damping involving the previous increment, where $\theta \in (0, 1]$. We note that smoothing is only employed in step (b). Projection $\text{proj}_K[\cdot]$ and the merit function $g(\mathbf{R})$ do not employ smoothing, where

$$g(\mathbf{R}) = \sum_{\alpha=1}^{\nu} \langle \mathbf{W}_{\alpha\alpha}^{-1} \mathbf{C}_{\alpha}(\mathbf{R}), \mathbf{C}_{\alpha}(\mathbf{R}) \rangle / \sum_{\alpha=1}^{\nu} \langle \mathbf{W}_{\alpha\alpha}^{-1} \mathbf{B}_{\alpha}, \mathbf{B}_{\alpha} \rangle, \quad (9)$$

\mathbf{B} collects the relative local velocities of an unconstrained motion, $\mathbf{C}(\mathbf{R})$ has the dimension of velocity, and $\mathbf{W}_{\alpha\alpha}$ are the diagonal 3×3 blocks of \mathbf{W} .

Algorithm 1 The projected quasi-Newton method.

PQN($\mathbf{R}, \theta, \gamma, n, \omega$):

1. $\Delta \mathbf{R}^0 = \mathbf{0}, k = 0$.
2. Do
 - (a) $\mathbf{U}^k = \mathbf{W}\mathbf{R}^k + \mathbf{B}$.
 - (b) Compute \mathbf{C}^k and $\mathbf{A}^k = \text{diag}_{3 \times 3} [\nabla \mathbf{C}_{\alpha\alpha}^k]$ using smoothing ω .
 - (c) $\Delta \mathbf{R}^{k+1} = (1 - \theta) \Delta \mathbf{R}^k - \theta (\mathbf{A}^k)^{-1} \mathbf{C}^k$.
 - (d) $\mathbf{R}^{k+1} = \text{proj}_K [\mathbf{R}^k + \Delta \mathbf{R}^{k+1}]$.
 - (e) $k = k + 1$.

while $g(\mathbf{R}^k) \geq \gamma$ and $k < n$.

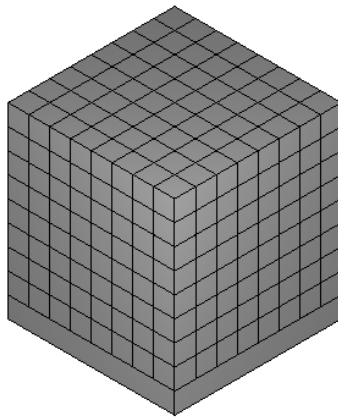


Figure 1: Stack of rigid cubes.

2 EXAMPLE

Figure 1 pictures an 8x8x8 stack of 1x1x1 rigid cubes with material properties 1E3, 0.3 for the mass density and the coefficient of Coulomb friction. The cubes rest on a rigid foundation and are subject to the gravity of value 10. Two cases are compared: a statically overdetermined case with 5000 contact points (includes edge to edge, vertex to vertex and surface to surface contacts) and a well conditioned case with 1400 (surface to surface) contacts. The PQN solver from Algorithm 1 is compared against the classical Gauss-Seidel (GS) solver [3]. The damping parameter $\theta = 0.25$. The iteration histories for time zero and zero initial reaction guess are presented in Figure 2. The PQN solver converges, even though it is a nonlinear solver based on the Jacobi update paradigm (noteworthy in itself). The convergence rate of PQN is slower than of GS for the case with 1400 contact points. On the other hand, for the ill-conditioned case the convergence rate of both solvers is comparable. In the context of distributed memory computations we take advantage of the latter property and use the PQN solver, which allows for a significant saving of communication time which dominates the solver runtimes for large numbers of processors.

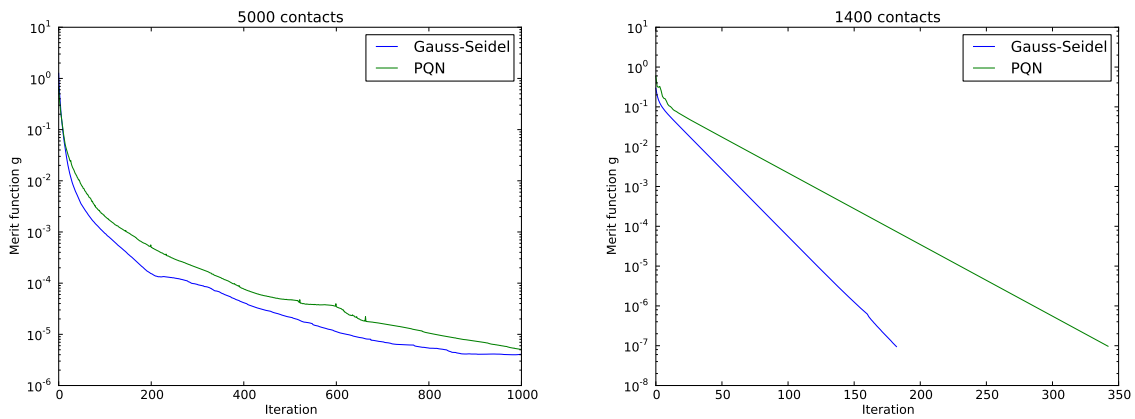


Figure 2: Iteration histories for time zero and zero initial reaction guess. The ill-conditioned case on the left and the well-conditioned case on the right.

References

- [1] G. De Saxcé and Z. Q. Feng. The bipotential method: a constructive approach to design the complete contact law with friction and improved numerical algorithms. *Mathematical and Computer Modelling*, 28:225–245, 1998.
- [2] Masao Fukushima, Zhi-Quan Luo, and Paul Tseng. Smoothing functions for second-order-cone complementarity problems. *SIAM Journal on Optimization*, 12(2):436–460, 2002.
- [3] F. Jourdan, P. Alart, and M. Jean. A Gauss-Seidel like algorithm to solve frictional contact problems. *Computer Methods in Applied Mechanics and Engineering*, 155:31–47, 1998.

MODELLING OF A POST-TENSIONED MODULAR STRUCTURE SYSTEM

Tianxin Zheng, Yong Lu *, Asif Usmani

Institute for Infrastructure and Environment, School of Engineering, University of Edinburgh, The King's Buildings, Edinburgh EH9 3JL, UK

* Correspondence: yong.lu@ed.ac.uk

Key Words: *Modular system; modular frame; tie rods, post-tension; computational model*

ABSTRACT

This paper deals with the structural analysis of a novel post-tensioned modular system (PTMS) made of tubular steel frames and tie rods. It firstly introduces the structural characteristics of the post-tensioned modular system. A simplified computational model is then presented, which incorporates the interaction between the modular frames and the tensioning rods. Example analysis is given to illustrate the effectiveness of the simplified modelling methodology in predicting the global as well as the essential local responses under gravitational and applied lateral loads.

1 INTRODUCTION

Lightweight steel structure is increasingly used in the modern building construction. Apart from pre-fabricated structural components such as curtain wall, ceiling and floor, self-contained modular units are also being developed. Building systems constructed by assembling modular units are sometimes called open house system [1], volumetric structure [2], or modular steel building [3]. The general advantages of module systems include higher accuracy and efficiency of production, shorter construction period, reduced use of skilled labour for on-site work, lower life-cycle cost, less construction waste, and thus generally improved sustainability.

In this study, a novel modular system, referred to herein as post-tensioned modular system (PTMS), is considered. Full details of the system can be found in [2]. Structurally the system is formed by assembling modular frame units through connectors at the floor levels and tie (tension) rods. The pre-stress installed through the tensioning rods effectively keeps the whole system tight, and in conjunction with the connectors it also provides a mechanism for lateral load resistance. Such a system has unique structural features due to the pre-stressing system, and hence requires special modelling considerations.



Fig. 1. Building structure made from modular units and tie rods (courtesy Powerwall [2])

2 STRUCTURAL CHARACTERISTICS OF PTMS

As indicated in Fig. 1, the PTMS is an assembly of a number of modular frames integrated by tie rods. Each modular unit is a basic rectangular frame made by steel tubular members. The modular frame units are stacked on top of (and next to) each other, usually via a connector at each joint. Tie rods are passed vertically through the tubular columns, and attached to the connector via a lock nut as each storey is erected. Final tightening (post-tensioning) is applied at the top when the whole structure is erected. The relative movement between the modular units in the transverse direction is resisted by friction or gripping, in conjunction with the shear resistance provided via the connectors. Fig. 2 schematically illustrates the force paths in a post-tensioned modular system.

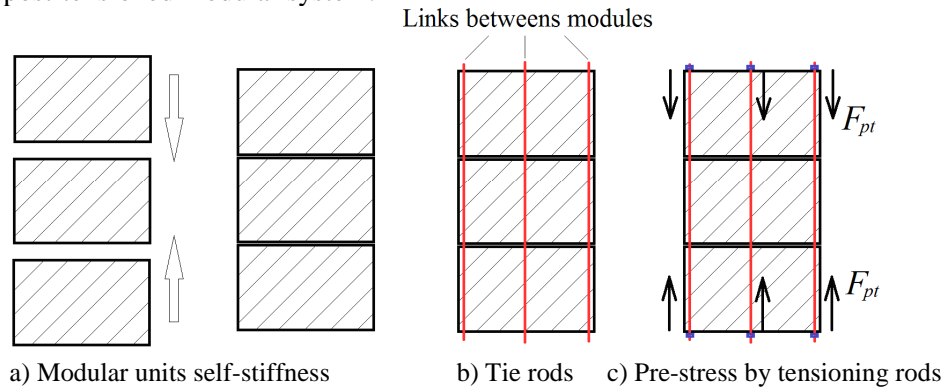


Fig. 2. A typical PTMS

When subjected to lateral (wind or seismic) loads, the load resistance mechanisms in a PTMS will exhibit the following features:

- 1) Re-distribution of stress and associated nonlinearity: As lateral load are applied, re-distribution of stresses occur between the tensioning rods and the modular frame members. Vertical separation (uplifting) in the vertical direction could occur when the pre-stress in the frame columns is overtaken by the effect due to the lateral load-induced overturning moment. This marks a critical situation concerning the overall integrity and rigidity of the entire system. A separation between modular units will lead to a step reduction in the global stiffness because the contribution of the affected modular columns to the axial stiffness reduces to zero. Consecutive separations will manifest in the load vs. (vertical) deformation response with a piece-wise linear behaviour (without involving material nonlinearity).
- 2) Interaction between modular frames and tension rods: tension rods may be attached to the modular frames directly or via the connectors by lock-nuts at the floor levels. The presence of lock nuts provides redundancy allowing for staged re-distribution of the axial force when separation (uplifting) occurs, as will be illustrated in section 4.
- 3) Failure modes: Three failure modes can be identified in a PTMS when it is subjected to (lateral) external loading: a) failure of tubular components within a modular frame, with buckling of a tubular column or bending failure in columns/beams; b) rupture of tension rods; c) connection failure at the modular joints, normally with local failure in the tubular columns around the connectors.

3 SIMPLIFIED FE MODELLING METHODOLOGY

3.1 Basic modelling considerations

Due to the complexity in the contact behaviour between the modular frames and the tensioning rods, a detailed analysis involving detailed contact simulation can be difficult and problematic. Herein a simplified method is adopted.

- 1) Tie rods and post-tensioning force: The tie rods in a PTMS are modelled using bar elements (tension only). The post-tensioning force is established by setting an initial tensile strain in the bar elements. Consider a PTMS with tensioning rods being fixed at the top and bottom ends. Let the pre-tension force to be installed in the rod be F_{pt} , the axial rigidity of the tie rods and the tubular column be $E_t A_t$ and $E_m A_m$, respectively, and the total length (height) of the PTMS be L , the required initial strain can be calculated as follows:

$$d_t = \frac{F_{pt}L}{E_t A_t}, \quad d_m = \frac{F_{pt}L}{E_m A_m} \quad (1)$$

$$\varepsilon = \frac{d_t + d_m}{L} = F_{pt} \left(\frac{1}{E_t A_t} + \frac{1}{E_m A_m} \right) \quad (2)$$

2) Modular frame-connector contact: The contact between the modular frames in the vertical direction is modelled by mass-less, rigid, and compression-only bar elements, as shown in Fig. 3(a). Where the modular frames are actually connected through a connector, two compression-only bars are used at each connection, Fig. 3(b). The interaction between the modular frames and the connectors in the transverse direction can also be simulated, using transverse links, Fig. 3(c). The properties of the transverse links may be assigned to simulate different coupling behaviour between the tubular columns and the connectors, which may also vary before and after separation.

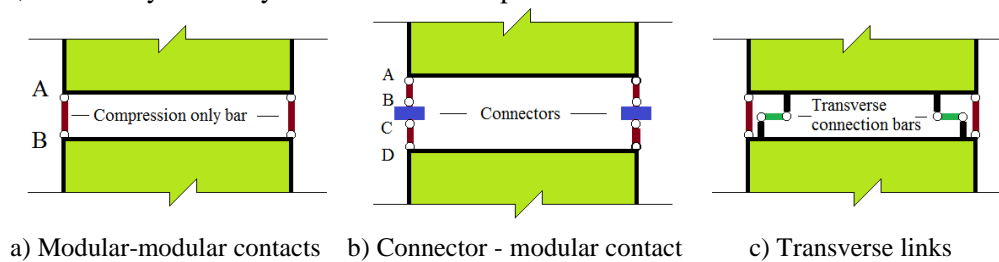


Fig. 3. Connection between modules and connector

3) Tie rod-connector contact: The connection between tie rods and connectors can be modelled in a similar way as described above. Fig. 4(a) is the simple case where the tie rod directly connects to the connector. If the tie rod is attached to the connector through a lock-nut, a link element (compression-only bar) may be inserted between a node (the lock-nut) in the tie rod and the connector, Fig. 4(b).

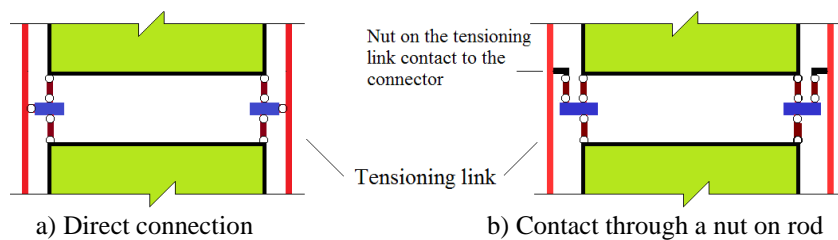


Fig. 4. Connection between tie rods and connectors

3.2 Example analysis of a PTMS

A single span, five-storey PTMS is modelled with the above described modelling scheme using ANSYS. Fig. 5 shows the configuration and relevant properties of the structure. Ties rods are made of steel with a diameter of 25mm, and they are fixed to the foundation and the top of the structure. The pre-tensioning force in the rods is 60.0 kN. Uniform lateral loads are applied at storey levels. To highlight the force paths and re-distribution due to the interaction between the modular frames and the pre-tensioning system, the material nonlinearity is not considered in this example, while geometric nonlinearity is included.

The structural response is analysed by gradually increasing the lateral loads. Fig. 6(a) shows the vertical displacement at the foundation and floor levels. It can be seen that, when the lateral load at each floor, F , reaches 48kN, vertical displacement at the left bottom (Node 1LB) begins to emerge, indicating separation (uplifting) from the left support. Separation between the first and second storey frames occurs when F further increases to 71 kN, as line 1LT (top of first storey) and 2LB (bottom of second storey) begins to depart. A step reduction of the stiffness occurs when separation takes place.

The stress re-distribution in the tension rods is shown in Fig. 6(b). After the first separation (uplifting) occurs at the left support, for example when $F = 58\text{kN}$, the lock nut at the top of the first storey is engaged to limit the separation effect within the first storey. After the horizontal force exceeds the second separation threshold, for instance $F = 87\text{kN} > 71\text{kN}$, similar phenomenon extends to the second storey. Because the right hand side of the structure is being compressed by the lateral-load induced overturning moment, the connections at the floor levels remain in contact during the entire course of loading; however, the tension force in the tie rod decreases as the lateral loads increase.

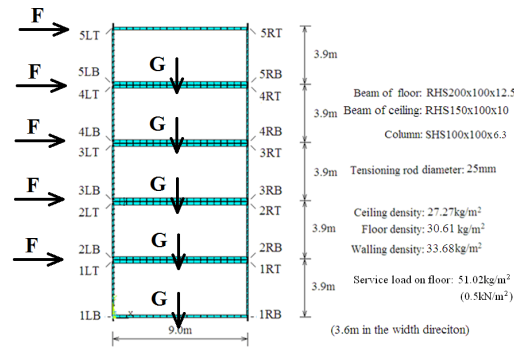


Fig. 5. Simplified FE model of a PTMS with five modular units

Different modular configurations have been analysed using such a simplified methodology, including material nonlinearities. Refined finite element model with shell elements for the critical regions of the frames and with contact have also been carried out to provide verification of the simplified analysis results, and generate more realistic constitutive descriptions for the link elements used in the simplified model. Results indicate that the simplified scheme works well within its capacity of providing results regarding the global behaviour and the stress re-distributions.

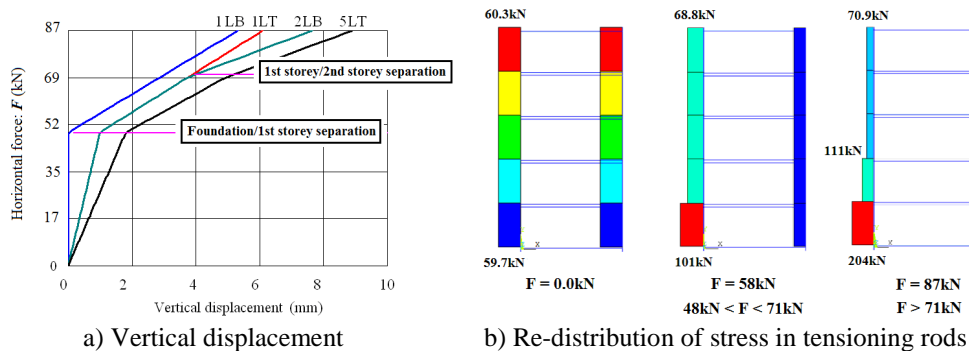


Fig. 6. Analysis of an example five-storey PTMS

4 CONCLUSIONS

A simplified modelling scheme is presented to model the global behaviour and the stress re-distribution for a novel post-tensioned modular system (PTMS). Characteristic phenomena pertinent to the analysis and structural behaviour of such system, including establishment of tensioning force in the tie rods (and hence pre-stress in the modular frame), separation (uplifting) at modular foundation and floor joints, the axial force redistribution between tension rods and the tubular columns, as well the primary failure modes, can be well incorporated and described using such a simplified approach.

References

- [1] M. Veljkovic, and B. Johansson, Light steel framing for residential buildings. *Thin-Walled Structures*, 44(12), 1272-1279, 2006.
- [2] Powerwall, *Powerwall building systems*. Powerwall Spaceframe System Ltd., 2008
- [3] C.D. Annan, M.A. Youssef, and M.H. El Naggari, Experimental evaluation of the seismic performance of modular steel-braced frames. *Engineering Structures*, 31(7), 1435-1446, 2009.
- [4] F.L.M. Pedrazzi and S. Lozano, The development of lightweight steel structures for housing in Argentina. *Journal of Constructional Steel Research*, 46(1-3), 178-178, 1998.
- [5] O. Popovic, Sustainable aspects of long-span lightweight steel structures. *Journal of Constructional Steel Research*, 46(1-3), 288-289, 1998.
- [6] J.M. Davies, Recent research advances in cold-formed steel structures. *Journal of Constructional Steel Research*, 55(1-3), 267-288, 2000.

ENHANCED RECOVERY TECHNIQUES FOR ACCURATE EVALUATION OF ERROR ESTIMATES IN FE APPROXIMATIONS

*Octavio A. González-Estrada^{1,4}, Juan José Ródenas⁵, Stéphane P.A. Bordas^{1,2},
Pierre Kerfriden^{1,3}

²Professor of Engineering, ³Lecturer in Engineering, ⁴Research Associate,

¹Institute of Modelling and Simulation in Mechanics and Materials, Cardiff School of Engineering,
Cardiff University, Queen's Buildings, The Parade, Cardiff CF24 3AA Wales, UK.

⁵Centro de Investigación de Tecnología de Vehículos(CITV),
Universidad Politécnica de Valencia, E-46022-Valencia, Spain.

*agestrada@gmail.com

Key Words: *error estimation; FEM; XFEM; recovery; fracture mechanics*

ABSTRACT

When modelling critical structures, it is crucial to rationally assess the outcome of numerical simulations. Specifically, error estimation strategies are key tools in critical decision-based processes. The development of design tools that enhance performance of the final product and give reliability on the calculations is essential in today's industrial environment, which increasingly seeks to reduce development times for new products while improving the quality.

During the last years there has been an increasing interest on the use of error estimates which help to measure and control the error committed in standard or enriched finite element approximations. The error can be defined in terms of energy norm or in quantities relevant for design purposes (such as the mean stress value in a particular area, displacements, the stress intensity factor for fracture problems).

In this work, we discuss the use of different a posteriori recovery techniques to evaluate error estimates for different finite element (FE) approximations. These techniques are based on equilibrated superconvergent patch recovery or equilibrated moving least squares procedures and can be used in smooth or singular problems. Numerical results show the capabilities of the proposed techniques to provide good error estimates.

1 INTRODUCTION

The use of powerful computers together with effective numerical methods have change our view on how to move from theories derived from mechanics and physics to the effective simulation of real phenomena both in industry and in research, and increased our capacity to tackle complex problems in countless engineering applications. However, on major drawback of any simulation process is that in

general the computational results obtained from it are affected by a numerical error. In particular, we are interested in the error introduced when discretizing a continuum model in order to be able to obtain a solution through a numerical approximation. This error can be large, pervasive and in some cases it can even invalidate the numerical results. To assess the quality of these approximations and guarantee the validity of the simulation it is necessary to measure, control and finally minimize the error obtained.

The error control techniques used in finite element (FE) analysis are well known and can be usually classified into different families [1]: residual based error estimators, recovery based error estimators, dual techniques, *etc.* Residual based error estimators were substantially improved with the introduction of the *residual equilibration* by Ainsworth and Oden [1]. These error estimators have a strong mathematical basis and have been frequently used to obtain lower and upper bounds of the error [1, 2]. Recovery based error estimates were first introduced by Zienkiewicz and Zhu [3] and are often preferred by practitioners because they are robust, simple to use and, additionally, provide a more accurate solution. Further improvements were made with the introduction of new recovery processes such as the SPR technique proposed by the same authors [4, 5]. Dual techniques based on the evaluation of two different fields, one compatible in displacements and another equilibrated in stresses, have also been used in [6] to obtain bounds of the error. Herein we are going to focus on recovery based techniques which follow the ideas of the Zienkiewicz-Zhu (ZZ) error estimator proposed in [3].

During the last decade new numerical techniques, such as the extended finite element method (XFEM) and the smooth finite element method (SFEM), have emerged as powerful alternatives to the standard FEM, extending even more the capabilities of the method. The XFEM increases the number of degrees of freedom of the FE approximation space to properly describe the singularity and discontinuity typical of fracture mechanics problems. The SFEM extends strain smoothing techniques previously used in meshless methods to FE approximations, redefining the way in which the problem is formulated. It avoids the use of isoparametric mapping and the integration is performed along the boundaries of subcells defined within the domain of the element. This method allows the use of arbitrary polygonal elements, diminishes the sensitivity to mesh distortion and locking, as well as other useful properties. Like in FEM, the XFEM and SFEM results are affected by the discretization error and, therefore, there is a need to develop tools capable of providing accurate error estimates for these methods.

In this paper we present an overview of recently developed recovery based error estimators in the context of standard and non standard FE approximations. The literature on error estimation techniques for enriched FE approximations is still scarce. Strouboulis *et al.* [7] proposed a recovery-based error estimator which provides good results for h -adapted meshes in the context of the Generalized Finite Element Method (GFEM). Pannachet *et al.* [8] worked on error estimation for mesh adaptivity in XFEM for cohesive crack problems. Two error estimates were used, one based on the error in the energy norm and another that considers the error in a local quantity of interest. The error estimation was based on solving a series of local problems with prescribed homogeneous boundary conditions. Panetier *et al.* [9] presented an extension to enriched approximations of the constitutive relation error (CRE) technique already available to evaluate error bounds in FEM. Bordas and Duflo [10] and Bordas *et al.* [11] proposed a recovery based error estimator for XFEM called the extended moving least squares (XMLS), which intrinsically enriched an MLS formulation to include information about the singular fields near the crack tip. Later, Duflo and Bordas [12] proposed a global derivative recovery formulation extended to XFEM problems. Ródenas *et al.* [13] presented a modification of the superconvergent patch recovery (SPR) technique tailored to the XFEM framework named SPR_{XFEM} , which enforces the fulfilment of equilibrium constraints and decomposes the stress field in singular and smooth parts. Here, we discuss the use of two recovery based techniques for FEM, XFEM and SFEM. The first one is the SPRCX technique which is based on a superconvergent patch recovery procedure. The second one is the MSLCX based on a moving least squares formulation.

2 SPRCX

For a 2D problem the recovered stress field σ^* in a patch of elements connected to a node is expressed as the polynomial expansion

$$\sigma^*(\mathbf{x}) = \begin{Bmatrix} \sigma_{xx}^*(\mathbf{x}) \\ \sigma_{yy}^*(\mathbf{x}) \\ \sigma_{xy}^*(\mathbf{x}) \end{Bmatrix} = \mathbf{P}(\mathbf{x})\mathbf{A}(\mathbf{x}) = \begin{bmatrix} \mathbf{p}(\mathbf{x}) & 0 & 0 \\ 0 & \mathbf{p}(\mathbf{x}) & 0 \\ 0 & 0 & \mathbf{p}(\mathbf{x}) \end{bmatrix} \begin{Bmatrix} \mathbf{a}_{xx}(\mathbf{x}) \\ \mathbf{a}_{yy}(\mathbf{x}) \\ \mathbf{a}_{xy}(\mathbf{x}) \end{Bmatrix} \quad (1)$$

where \mathbf{P} represents a polynomial basis and \mathbf{A} are the coefficients to evaluate. The SPRCX technique introduces the enforcement of the boundary and internal equilibrium equations in the functional minimized locally at each patch, using Lagrange multipliers.

For singular problems the SPRCX performs a decomposition of the stress field into two parts: singular and smooth, then each part is recovered separately:

$$\sigma^* = \sigma_{smo}^* + \sigma_{sing}^* \quad (2)$$

To obtain an approximation to the singular part of the problem, an estimation of the generalised stress intensity factor (GSIF) is calculated. The GSIF is used to evaluate the expressions that describe the stress field near the singularity. Continuity of the global recovered field is enforced using a conjoint polynomials procedure.

3 MLSCX

We use a moving least squares formulation to directly obtain a continuous and equilibrated recovered stress field. To obtain values for the coefficients \mathbf{A} that define the polynomial expansion, the following functional is minimized:

$$\begin{aligned} \chi &= \sum_{l=1}^n W(\mathbf{x} - \mathbf{x}_l) \left[\sigma^*(\mathbf{x}, \mathbf{x}_l) - \sigma^h(\mathbf{x}_l) \right]^2 \\ &= \sum_{l=1}^n W(\mathbf{x} - \mathbf{x}_l) \left[\mathbf{P}(\mathbf{x}_l) \mathbf{A}(\mathbf{x}) - \sigma^h(\mathbf{x}_l) \right]^2 \end{aligned} \quad (3)$$

The MLS functional is modified to enforce the internal equilibrium equation. Normally in the literature only the first part of the equilibrium constraint is enforced. Here we fully enforce the internal equilibrium constraint. A second order expansion of the boundary tractions is also enforced using e.g. Lagrange multipliers. For singular problems a decomposition technique similar to the one used in SPRCX is implemented.

4 CONCLUSIONS

The numerical results indicate that both techniques provide error estimates that converge to the exact value and can be considered as asymptotically exact. These techniques could be effectively used to estimate the error in different types of FE approximations of smooth and singular problems, while other conventional recovery procedures which do not include the enrichment functions in the recovery process have proved not to converge to the exact error. This shows the need for the use of extended recovery techniques especially when considering problems with singular solution.

References

- [1] Ainsworth M, Oden JT. *A posteriori Error Estimation in Finite Element Analysis*. John Wiley & Sons: Chichester, 2000.
- [2] Díez P, Parés N, Huerta A. Accurate upper and lower error bounds by solving flux-free local problems in stars. *Revue européenne des éléments finis* 2004; **13**(5-6-7):497.
- [3] Zienkiewicz OC, Zhu JZ. A simple error estimation and adaptive procedure for practical engineering analysis. *International Journal for Numerical Methods in Engineering* 1987; **24**:337–357.
- [4] Zienkiewicz OC, Zhu JZ. The superconvergent patch recovery and *a posteriori* error estimates. Part I: The recovery technique. *International Journal for Numerical Methods in Engineering* 1992; **33**(7):1331–1364.
- [5] Zienkiewicz OC, Zhu JZ. The superconvergent patch recovery and *a posteriori* error estimates. Part II: Error estimates and adaptivity. *International Journal for Numerical Methods in Engineering* 1992; **33**(7):1365–1382.
- [6] Pereira OJBA, de Almeida JPM, Maunder EAW. Adaptive methods for hybrid equilibrium finite element models. *Computer Methods in Applied Mechanics and Engineering* 7/6 1999; **176**(1-4):19–39.
- [7] Strouboulis T, Cops K, Babuška I. The generalized finite element method. *Computer Methods in Applied Mechanics and Engineering* 2001; **190**(32-33):4081–4193, doi:10.1016/S0045-7825(01)00188-8.
- [8] Pannachet T, Sluys LJ, Askes H. Error estimation and adaptivity for discontinuous failure. *International Journal for Numerical Methods in Engineering* 11-20 2009; **78**(5):528–563.
- [9] Panetier J, Ladevèze P, Chamoin L. Strict and effective bounds in goal-oriented error estimation applied to fracture mechanics problems solved with XFEM. *International Journal for Numerical Methods in Engineering* 2010; **81**(6):671–700, doi:10.1002/nme.2705.
- [10] Bordas S, Duflot M. Derivative recovery and *a posteriori* error estimate for extended finite elements. *Computer Methods in Applied Mechanics and Engineering* 07/15 2007; **196**(35-36):3381–3399, doi:10.1016/j.cma.2007.03.011.
- [11] Bordas S, Duflot M, Le P. A simple error estimator for extended finite elements. *Communications in Numerical Methods in Engineering* 2008; **24**(11):961–971, doi:10.1002/cnm.1001.
- [12] Duflot M, Bordas S. *A posteriori* error estimation for extended finite element by an extended global recovery. *International Journal for Numerical Methods in Engineering* 2008; **76**(8):1123–1138.
- [13] Ródenas JJ, González-Estrada OA, Tarancón JE, Fuenmayor FJ. A recovery-type error estimator for the extended finite element method based on singular+smooth stress field splitting. *International Journal for Numerical Methods in Engineering* 2008; **76**(4):545–571, doi:10.1002/nme.2313.

MESH IMPROVEMENT METHODOLOGY FOR EVOLVING GEOMETRIES

*Alan Kelly¹, Prof. Chris Pearce¹ and Dr Lukasz Kaczmarczyk¹

¹School of Engineering, University of Glasgow, Glasgow, G12 8LT

*a.kelly.2@research.gla.ac.uk

Key Words: *mesh quality measure, evolving geometry*

ABSTRACT

The accuracy of the Finite Element Method is partly dependent on the quality of the underlying mesh. Automatic mesh generation packages are available to generate good quality meshes. However, for problems with changing domains, moving boundaries, crack propagations, large deformations, etc. these packages are not always appropriate as they cannot deal with the complex geometries. Poor quality elements can result in a badly conditioned stiffness matrix, resulting in long solution times and a greater discretisation error. In this paper we will discuss how to measure mesh quality and how to automatically adapt the mesh to improve its quality, based on these mesh quality measures.

1 INTRODUCTION

In recent years, High Performance Computing (HPC) systems have become increasingly more powerful and affordable allowing the widespread use of HPC for numerical simulations. The major developments in this area has made it possible to model physical phenomena on a much greater scale than ever before. However, in order to fully exploit the power of massively parallel machines, high quality, robust and reliable software packages must be produced. The availability of such packages allows engineers and scientists to focus their attention on the physical problem and not on the extremely complex computational aspects of it.

The finite element method (FEM) and its many variations are some of many methods used to model physical problems. These methods require that the domain under consideration be discretised using a mesh. There are many freely available and powerful mesh generation packages available. These packages are very effective in meshing standard shapes and non-complex domains. The meshing of complex domains is much more challenging and thus, requires specialised software to achieve a high quality mesh. A high quality mesh is essential to producing accurate results within an acceptable time frame. Furthermore, for problems in which the mesh must evolves (e.g. finite deformations, fluids, fractures,

| Error | Cause |
|------------------------------|--------------------------------------------------------------------|
| Interpolation Error | Element size major factor. Element Shape has very little influence |
| Gradient Interpolation Error | Element size. Large angles bad, small angles OK. |
| Matrix Conditioning | Element Shape. Small angles bad, large OK. |

Table 2.1: Mesh errors and causes [1]

moving boundaries, etc.), maintaining a high quality mesh throughout the simulation increases this challenge. Therefore, the objective of this project is to produce a mesh improvement library which takes an existing mesh as input and performs local improvement on poor quality elements, with the goal of producing a higher quality mesh and thus, more accurate analysis whilst using less computational resources. The resulting package must be easily integratable with existing software to ensure its accessibility to computational scientists and hopefully, to encourage its use in complex scientific codes.

2 WHAT IS A HIGH QUALITY ELEMENT

The purpose of performing mesh improvement is to reduce or eliminate the errors associated with the discretisation of a domain, i.e. mesh errors. These errors may be classified as: interpolation error, gradient interpolation error and stiffness matrix conditioning [1].

The errors presented in Table 2.1 often occur when a complex domain is meshed using an automatic mesh generation package. This project aims to produce a high quality mesh according to the criteria in Table 2.1 using a poor quality mesh as input. Many problems require re-meshing at every time step such as problems with continuously changing domains, crack propagation for example. As one of the reasons for producing a high quality mesh is to improve matrix conditioning, and hence reduce the time required to solve the systems of equations, mesh improvement must be achieved as efficiently as possible.

3 QUANTITATIVE QUALITY MEASURES

The ability to quantitatively measure the quality of a mesh is essential if the quality of a mesh is to be improved. There are many such measures discussed in literature [1-3]. We will focus on the ones presented in [3] which are the minimum sine measure and volume-length ratio as these have been shown to be highly effective and possible to implement efficiently.

3.1 Minimum Sine

The minimum sine measure of a triangle is the minimum of the sines of its three angles. This measure penalises both small and large angles as the sine of 0° and 180° are both zero. This therefore improves discretisation accuracy and matrix conditioning (Table 2.1). This measure reaches its maximum of $\arcsin(\sqrt{3}/2)$ for an equilateral triangle. It is possible to calculate this measure without using computationally expensive trigonometric functions. While the minimum sine measure is relatively inexpensive to calculate, its gradient is not. This measure has been shown to be highly effective at improving poor quality triangular mesh. From Table 2.1, it may be seen that large angles affect the accuracy of the solution, not just the speed of the analysis. Therefore, large angles are more harmful than small ones.

| | Measure | Gradient |
|--------------|--------------------------------------------------|--------------------------------------------------------------------------------------|
| minimum sine | $2 \min_{1 \leq k < l \leq 3} \frac{A}{l_a l_b}$ | $2 \frac{l_a l_b \nabla A + A [\frac{l_b}{l_a} a - \frac{l_a}{l_b} b]}{l_a^2 l_b^2}$ |
| area-length | $\frac{A}{l_{rms}}$ | $\frac{l_{rms} \nabla A - A \nabla l_{rms}}{l_{rms}^2}$ |

Table 3.1: Quality measures and their Gradients (adapted from [3])

To account for this, the biased minimum sine measures is used, whereby the sine of obtuse angles are multiplied by 0.7 before choosing the minimum.

3.2 AREA-LENGTH RATIO

This measure is an adaptation of the volume-length ratio [3] used for tetrahedral mesh. The measure punishes triangles with extreme angles, be they small or large as these triangles tend to have a small area compared with their edge lengths. The gradient for this measure is much cheaper to compute than that of the minimum sine measure, thus making this measure more attractive from an efficiency point of view.

4 IMPLEMENTATION

4.1 Minimum Sine

The sine of every angle in the mesh is calculated and the element with the lowest sine is found. The vertex at which the lowest sine occurs is identified. Generally, vertices which lie on the boundary of the domain cannot be moved or have restrictions on which directions they may be moved, i.e. fixed in the x or y directions, for example.. If the vertex with the lowest sine cannot be moved the vertex in that element which will have the greatest impact on the minimum sine is chosen. As each internal vertex will lie on more than one element, a search direction must be chosen which will give the greatest overall improvement to the local mesh. This is achieved by calculating the gradient of the sine of every affected angle. These gradients are superimposed over the relevant vertex and a convex hull is formed from which the search direction is calculated. A line search algorithm is then used to determine the optimum distance to move the vertex in the search direction. If the vertex lies within the convex hull, [3] states that no further improvement is possible. However, it has been found that moving the vertex to the centroid of the hull results in significant improvement to the local mesh. This requires further investigation.

4.2 Area-Length Ratio

The area of every triangle in the mesh and the root mean square length of every triangles' edges are calculated. The element with the lowest ratio is found and the gradient of this measure is found for each vertex. The vertex with the largest magnitude gradient is identified. Moving this vertex will have the greatest impact on the quality of the local mesh. Once the gradients have been calculated, a convex hull is formed and a search direction determined in a simliar manner to the minium sine measure.

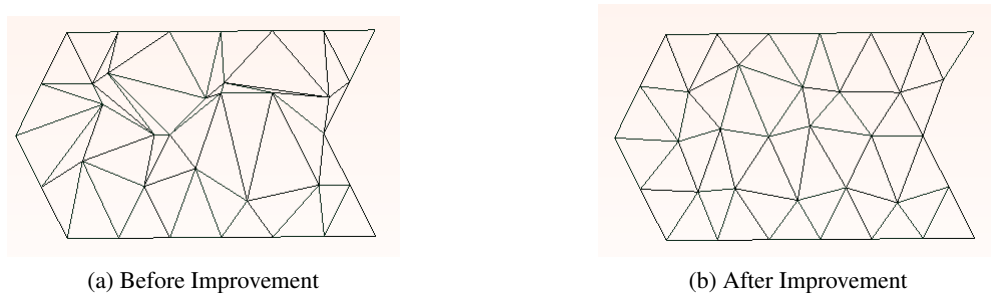


Figure 5.1: Before and After Improvement

4.3 Future Work

The next step in this is to fully implement the area-length measure and compare the results from this with those obtained from the minimum sine measure. The quality of the resulting mesh and a profile of the code will be used to determine which method is best in terms of effectiveness and efficiency. This will then be tested using mesh from physical simulations with the aim of improving the accuracy of the calculations whilst reducing the time required to find the solution.

5 RESULTS

The mesh improvement strategy using the Minimum Sine measure was tested on a small triangular mesh with poorly shaped elements. After running the improvement code on this mesh, significant improvement was achieved, with all extreme angles eliminated (Figure 5.1).

6 Conclusions

From the results presented above, it is clear that it is possible to significantly improve the quality of a mesh. With further work, it should be possible to apply this to large scale simulations, thus improving the accuracy and decreasing the runtime of these simulations. In large simulations where iterative solvers are used, there is significant scope for reducing runtime as a better conditioned matrix is produced from a higher quality mesh.

References

- [1] J. R. Shewchuk. What is a Good Linear Finite Element. *Earthquake Engineering and Structural Dynamics*, 11, 689–710, 1983., 1989.
- [2] V. N. Parthasarathy, C.M. Graichen and A.F. Hathaway. A comparison of tetrahedron quality measures *Finite Elements in Analysis and Design*, 15, 255–261, 1993.
- [3] B. Klingner 2008. Tetrahedral Mesh Improvement. Thesis (PhD). Department of Electrical Engineering and Computer Sciences University of California at Berkeley.

RAPID RE-MESHING FOR REAL-TIME THREE-DIMENSIONAL BOUNDARY ELEMENT ANALYSIS

***T.M. Foster, M.S. Mohamed, J. Trevelyan and G. Coates**

School of Engineering and Computer Sciences, Durham University, South Road, Durham, DH1 3LE

*timothy.foster@durham.ac.uk

Key Words: *real-time; boundary element method; stress analysis; re-meshing.*

ABSTRACT

Structural design of mechanical components is an iterative process that involves multiple stress analysis runs; this can be time consuming and expensive. It is becoming increasingly possible to make significant improvements in the efficiency of this process by increasing the level of interactivity. One approach is through real-time re-analysis of models with continuously updating geometry. A key part of such a strategy is the ability to accommodate such changes in geometry with minimal perturbation to an existing mesh. A new re-meshing algorithm that can generate and update a boundary element (BE) mesh in real time as a series of small changes are sequentially applied to the associated model is introduced. The algorithm is designed to make minimal updates to the mesh between each step whilst preserving a suitable mesh quality. This significantly reduces the number of terms that need to be updated in the system matrix, thereby reducing the time required to carry out a re-analysis of the model.

1 INTRODUCTION

This research aims to produce an integrated modelling and analysis tool that can be used intuitively by engineers at the conceptual design stage to analyse 3D components rapidly without lengthy training. Parts of an initial design model, such as a fillet radius, may be updated and, as the geometry is altered, stress contours displayed on the object will update in real-time. This will aid the designer to optimise rapidly components for any mechanical application. Various finite element (FE) schemes that aim to provide such a level of interactivity, eg. [1], have been conceived. Concept Analyst [2], a 2D BE stress analysis package that features real-time functionality, has been developed at Durham University. The current work aims to take the simplicity of the user interface and the speed of this package and extend it into 3D. This will involve the development of innovative techniques to generate, update and analyse the mesh. A key part of this work is the subject of this paper, creating an efficient re-meshing algorithm.

Many algorithms have been proposed for re-meshing FE and BE models, often using adaptive refinement schemes [3] to inform re-meshing through the errors in an initial analysis. These schemes do not usually allow geometrical changes and usually require regeneration of the entire mesh with a full re-analysis. If the geometry is changed, it is possible to refresh only affected areas of the mesh. This has

been applied to FE fluid flow problems [4], however, the methods can be adapted for BEs. It is important to minimise the number of elements updated during re-meshing. Trevelyan *et al.* [5] have shown this to be the major factor in reducing re-analysis time, Figure 1, this reduces the time required to update and solve the BE equations. A fast linear solver, eg. [6], may be employed to accelerate the solution time.

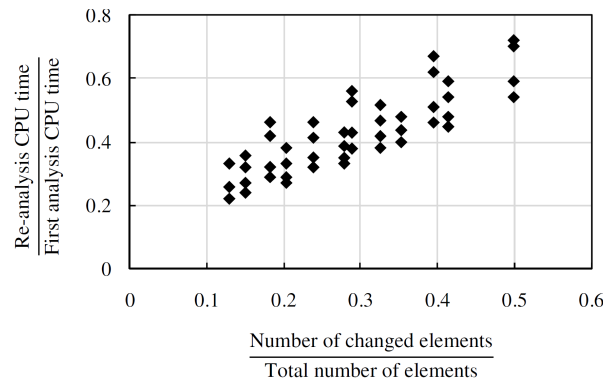


Figure 1: Re-analysis performance for 3D applications (Reproduced from [5])

2 THE BOUNDARY ELEMENT METHOD

The boundary integral equation (BIE) can be formulated for displacements at a source point, p , on the boundary, Γ , of an object due to tractions and displacements at field point, q , also on Γ . For $p \in \Gamma$:

$$c(p)u_j(p) + \int_{\Gamma} T_{ij}(p, q)u_i(q)d\Gamma = \int_{\Gamma} U_{ij}(p, q)t_i(q)d\Gamma \quad (1)$$

where u and t refer to the tractions and displacements experienced at q . T_{ij} and U_{ij} refer to the traction and displacement kernels for every p - q pairing, taking into account the material properties and the distance from p to q . The equations are given in most BE literature. The subscripts refer to a traction or displacement in the Cartesian direction, i , at q caused by a unit load in direction j at p . $c(p)$ is introduced due to the limits applied to allow evaluation of the strongly singular traction kernel. Shape functions, N , are defined as a discretization of Γ leading to a discretized BIE:

$$c(p)u_j(p) + \sum_{elemk} \int_{-1}^1 \int_{-1}^1 T_{ij}(p, q)N_k J d\xi d\eta \{u\} = \sum_{elemk} \int_{-1}^1 \int_{-1}^1 U_{ij}(p, q)N_k J d\xi d\eta \{t\} \quad (2)$$

where J is the Jacobian. Evaluating (2) considering p at all nodes in turn, and applying sufficient boundary conditions, yields a set of linear equations in matrix form:

$$[A]\{x\} = \{b\} \quad (3)$$

The system can now be solved to find the unknown tractions and displacements in $\{x\}$. Internal stresses may be found by declaring p at the point of interest and substituting the now fully defined values of displacement and traction at the nodes into equation (2) and solving at p .

3 RE-MESHING STRATEGY

The mesh updating procedure minimises the number of elements affected when the model geometry is updated. This minimises the number of integrals, contained in matrix $[A]$ of (3), that need to be

recalculated before re-analysis and improves the convergence rate of a preconditioned iterative solver. During re-meshing, each updated face of the model is considered individually. A face may be translated, distorted in plane or distorted out of plane. If translated, all the nodes and elements on the face are translated through the same vector, the integrals between these elements do not need to be recalculated. If distorted out of plane the mesh across the face must be regenerated and all integrals recalculated. If the face is distorted but remains in plane, efficiency gains can be made by only updating elements local to the change. We propose a new algorithm to propagate these changes across the face.

The algorithm assumes that all elements on these faces are triangular. The quality, Q , of each element can be assessed using an adaption of the radius ratio discussed by Topping *et al.* [7]. This is defined as the ratio of the radius of the incircle to the circumcircle of the element and can be formulated such that:

$$Q = \frac{16A^2}{abc(a+b+c)} \quad (4)$$

where A is the area of the element and a , b and c are the side lengths. Q takes a value between 0 and 1, where 1 indicates the highest quality element (an equilateral triangle) and 0 a fully collapsed element. The global mesh quality can be assessed using the mean, \bar{Q} , and standard deviation, S , of the collected element quality measures. We define measures \bar{Q}_{min} and S_{max} to be the minimum acceptable mean quality and the maximum acceptable standard deviation of element quality.

Nodes, $N_i (i = 1, 2, 3, \dots, n_N)$, distributed along updated edges are repositioned by translating or scaling the original distribution. The vector through which they have moved, V_i , is stored. Each element that includes N_i , $E_{ki} (k = 1, 2, 3, \dots, n_{Ei})$, is assessed for quality, Q_{ki} , using 4. If $Q_{ki} < Q_{min}$ and the update will further reduce the element quality, the un-updated corner node(s) of E_{ki} are also moved through vector V_i . The changes propagate through the mesh until all the elements return $Q_k < Q_{min}$. Experimentation has suggested 0.6 as an appropriate value of Q_{min} , a higher value will result in a more accurate analysis but requires a larger number of elements to be updated. The re-meshing process is summarised in Figure 2. A node may be moved only once in each update pass. All updates are initially applied to the corner nodes of each element. Once all the required updates have been applied, the mid-side node positions for updated elements are recalculated. Flags inform the re-analysis algorithm of how each element has been transformed. This algorithm can only distort an existing mesh. It is efficient for small to medium perturbations but for larger changes additional strategies must be employed to prevent excessive propagation of updates. A crude method involves periodically regenerating the mesh across any poorly meshed faces. Once the updates across face j have finished propagating, \bar{Q}_j and S_j are calculated. If $\bar{Q}_j < \bar{Q}_{min}$ or $S_j > S_{max}$ the mesh across j is regenerated. As this only has to be done occasionally the additional computational expense is relatively small. An apparently more efficient technique is to add or remove elements from poorly/over refined areas, however, this necessitates regeneration of the preconditioning matrices used during the analysis.

Additional strategies may be employed to maintain the accuracy of the analysis in key areas such as around a hole or notch. If high quality elements are generated immediately adjacent to these features and are not allowed to distort but instead move with the geometry the accuracy of the results in these key areas is much improved. However, this leads to updates affecting a larger number of elements.

4 CONCLUSIONS

A robust algorithm has been introduced for updating a BE mesh to accommodate geometric perturbation whilst preserving the majority of the mesh. The scheme is efficient for small perturbations; methods to improve it for larger changes have also been discussed. Using these techniques, a BE mesh can be updated in a computationally inexpensive manner and the time required for re-analysis can be reduced.

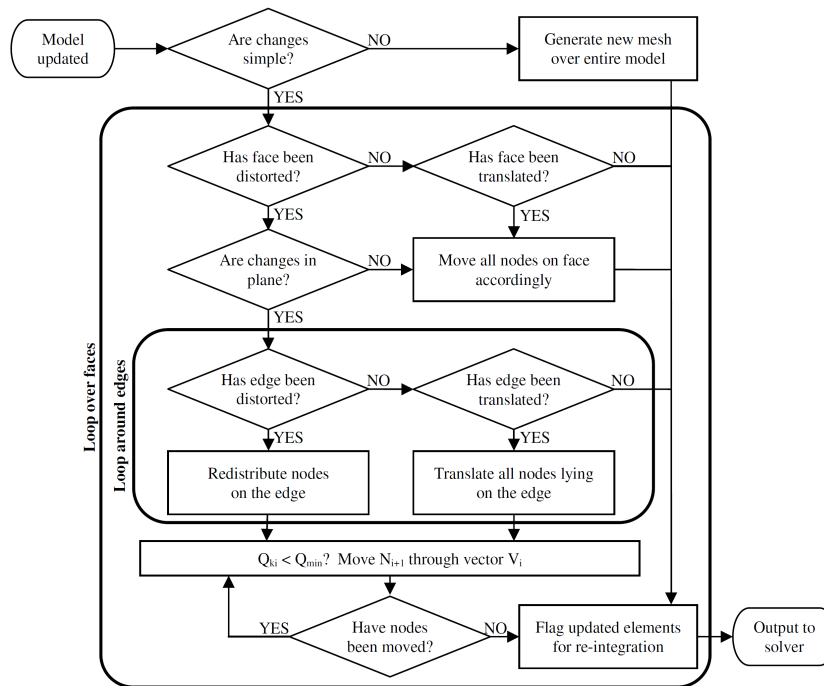


Figure 2: Flowchart showing a single re-meshing iteration

Acknowledgements

The authors acknowledge funding received from EPSRC grant EP/H000046/1. They also thank Dr. Stuart Spence of BAE Systems and Mr. Simon Walker of Jesmond Engineering for their input.

References

- [1] R. Mackie. An object-orientated to fully interactive finite element software. *Advances in Engineering Software*, 29, 139–149, 1998.
- [2] J. Trevelyan. Concept Analyst. [Online] www.conceptanalyst.com, 2006.
- [3] E. Kita and N. Kamiya. Error estimation and adaptive mesh refinement in boundary element method, an overview. *Engineering Analysis with Boundary Elements*, 25, 479–495, 2001.
- [4] K.F.C. Yiu, D.M. Greaves, S. Cruz, A. Saalehi, and A.G.L. Borthwick. Quadtree grid generation: Information handling, boundary fitting and CFD applications. *Computers and Fluids*, 25, 159–169, 1996.
- [5] J. Trevelyan, P. Wang, and S.K. Walker. A scheme for engineer-driven mechanical design improvement. *Engineering Analysis with Boundary Elements*, 26, 425–433, 2002.
- [6] L.J. Leu. A reduction method for boundary element reanalysis. *Computer Methods in Applied Mechanics and Engineering*, 178, 125–139, 1999.
- [7] B.H.V. Topping, J. Muylle, P. Ivanyi, R. Putanowicz, and B. Cheng. *Finite Element Mesh Generation*, Saxe-Coburg, 2004.

Determination of polynomial C^1 shape functions on triangular finite elements

*Stefanos-Aldo Papanicolopoulos¹ and Antonis Zervos²

¹Department of Mechanics, National Technical University of Athens, Zografou, 15773, Greece

²Faculty of Engineering and the Environment, University of Southampton, Southampton, SO17 1BJ

*stefanos@mechan.ntua.gr

Key Words: *finite element methods, C^1 elements, triangular elements*

ABSTRACT

We present an algorithm to generate all C^1 continuous polynomial shape functions for triangular elements without first prescribing the type of the degrees of freedom. We describe the derivation of the algorithm and consider the ways in which the resulting shape functions can be grouped to generate specific elements. A first comparison is made with existing elements.

1 INTRODUCTION

A displacement-only discretisation of continuum mechanics problems involving a fourth-order partial differential equation introduces the need for finite elements with C^1 continuous interpolation of the displacements. Such elements have been developed and used for modelling bending of thin plates and more recently for modelling strain-gradient dependent materials. A C^1 triangular element with polynomial interpolation and 21 degrees of freedom has been presented by Argyris *et al.* [1], as well as by other authors, from which a simpler element with 18 degrees of freedom has also been produced.

We have recently presented an algorithm to directly derive elements like the latter, without first having to formulate more complex ones like the former [2]. In that algorithm, the interpolation is obtained by determining a priori the location and type of the degrees of freedom. This restriction is lifted here, by presenting an algorithm to generate all possible C^1 continuous polynomial shape functions for triangular elements without first prescribing the type of the degrees of freedom.

2 SHAPE FUNCTIONS

Consider a shape function ϕ that multiplies a degree of freedom which lies on a given node. The node can lie on a vertex, on a side (excluding its endpoints) or on the interior of the element—we do not consider the case of nodes lying outside the element. We therefore distinguish between vertex shape functions, side shape functions and internal shape functions.

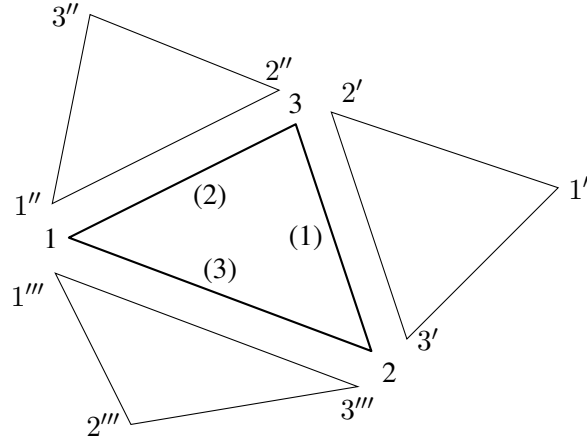


Figure 1: A triangle element with its neighbouring elements

Since we use a polynomial interpolation of order n_p , the shape functions are also polynomials of order n_p . The generic form of the shape function ϕ can therefore be written as

$$\phi = \sum_{i=0}^{n_p} \sum_{k=0}^{n_p-i} t_{i,k} L_1^{n_p-i-k} L_2^i L_3^k \quad (1)$$

where the coefficients $t_{i,k}$ depend on the geometry of the element (expressed through the quantities $x_{ij} = x_i - x_j$ and $y_{ij} = y_i - y_j$). To determine the coefficients $t_{i,k}$ for a given shape function ϕ associated with a given node, we distinguish between the sides which include the node (“near” sides) and those that do not include it (“far” sides). The value of ϕ and its normal derivative must be zero on the far sides and it must match the respective values of the shape function on neighbouring elements on near sides (Figure 1).

2.1 Internal shape functions

For internal nodes, all three sides are “far” sides, therefore the shape function and its normal derivative must be zero on all sides, so that the shape function is a “ C^1 bubble function”. This yields

$$t_{i,n_p-i} = t_{0,i} = t_{i,0} = 0, \quad t_{j,n_p-1-j} = t_{1,j} = t_{j,1} = 0 \quad (2)$$

where $i = 0, \dots, n_p$ and $j = 0, \dots, n_p - 1$. The remaining coefficients can be selected arbitrarily, as they do not affect C^1 continuity. For $n_p \leq 5$ there exist no internal shape functions.

2.2 Side shape functions

We consider a node on side 1 (shape functions for nodes on other sides will then be obtained by cycling the appropriate indices). Considering the far sides (sides 2 and 3) we easily obtain

$$t_{0,i} = t_{i,0} = 0, \quad t_{1,j} = t_{j,1} = 0 \quad (3)$$

where again $i = 0, \dots, n_p$ and $j = 0, \dots, n_p - 1$. The value of ϕ on side 1 must only depend on the geometry of side 1, so

$$t_{i,n_p-i} = \hat{t}_{i,n_p-i}(x_{32}, y_{32}) \quad (4)$$

Requiring rotational symmetry for the triangle, we consider the matching triangle that has its side 1 in common with side 1 of the initial triangle. Matching the value of ϕ on side 1 for the two triangles yields

$$\hat{t}_{i,n_p-i}(x_{32}, y_{32}) = \hat{t}_{n_p-i,i}(-x_{32}, -y_{32}) \quad (5)$$

The value of the normal derivative of ϕ on side 1 must also depend only on the geometry of the side, so we can write

$$\sqrt{x_{32}^2 + y_{32}^2} \frac{\partial \phi}{\partial \hat{n}(1)} = \sum_{j=0}^{n_p-1} L_2^j (1 - L_2)^{n_p-1-j} G_j(x_{32}, y_{32}) \quad (6)$$

where $G_j(x_{32}, y_{32})$ are arbitrary functions. Matching the normal derivatives of the two elements sharing the side, we obtain $G_j(x_{32}, y_{32}) = -G_{n_p-1-j}(-x_{32}, -y_{32})$ and, after some calculations,

$$t_{j,n_p-1-j} = -\frac{1}{\kappa_2 + \kappa_3} G_j(x_{32}, y_{32}) + \frac{\kappa_2}{\kappa_2 + \kappa_3} (n_p - j) \hat{t}_{j,n_p-j}(x_{32}, y_{32}) + \frac{\kappa_3}{\kappa_2 + \kappa_3} (j + 1) \hat{t}_{j+1,n_p-1-j}(x_{32}, y_{32}) \quad (7)$$

where κ_α is the cotangent of the angle on vertex α of the triangle. Using the above equations we also obtain $G_0 = G_1 = G_{n_p-2} = G_{n_p-1} = 0$ and $t_{2,n_p-2} = t_{n_p-2,2} = 0$. Therefore for $n_p \leq 4$ there exist no side shape functions.

2.3 Vertex shape functions

Considering a shape function for vertex 1 and using a procedure similar to the one for side shape functions, but now with two near sides and one far side, we obtain

$$t_{i,n_p-i} = 0, \quad t_{j,n_p-1-j} = 0 \quad (8)$$

$$t_{i,0} = \hat{t}_{i,0}(x_{21}, y_{21}), \quad t_{0,i} = \hat{t}_{0,i}(x_{31}, y_{31}), \quad \hat{t}_{i,0}(u, v) \equiv \hat{t}_{0,i}(u, v) \quad (9)$$

$$t_{1,j} = -\frac{1}{\kappa_1 + \kappa_3} F_j(x_{31}, y_{31}) + \frac{\kappa_3}{\kappa_1 + \kappa_3} (n_p - j) \hat{t}_{0,j}(x_{31}, y_{31}) + \frac{\kappa_1}{\kappa_1 + \kappa_3} (j + 1) \hat{t}_{0,j+1}(x_{31}, y_{31}) \quad (10)$$

$$t_{j,1} = \frac{1}{\kappa_1 + \kappa_2} F_j(x_{21}, y_{21}) + \frac{\kappa_2}{\kappa_1 + \kappa_2} (n_p - j) \hat{t}_{j,0}(x_{21}, y_{21}) + \frac{\kappa_1}{\kappa_1 + \kappa_2} (j + 1) \hat{t}_{j+1,0}(x_{21}, y_{21}) \quad (11)$$

where F_j are arbitrary functions, $i = 0, \dots, n_p$ and $j = 0, \dots, n_p - 1$. For $j = 2, \dots, n_p - 3$, equations (10) and (11) yield the respective values of $t_{1,j}$ and $t_{j,1}$. For $j = n_p - 2$ we obtain

$$t_{n_p-2,0} = t_{0,n_p-2} = 0 \quad (12)$$

while for $j = 0$ and $j = 1$ the equations are coupled and yield, after a few calculations,

$$t_{0,0} = C_0 \quad (13)$$

$$t_{0,1} = n_p C_0 + C_1 x_{31} + C_2 y_{31} \quad (14)$$

$$t_{1,0} = n_p C_0 + C_1 x_{21} + C_2 y_{21} \quad (15)$$

$$t_{0,2} = \frac{1}{2} n_p (n_p - 1) C_0 + (n_p - 1) C_1 x_{31} + (n_p - 1) C_2 y_{31} + \frac{1}{2} C_3 x_{31}^2 + \frac{1}{2} C_4 y_{31}^2 + C_5 x_{31} y_{31} \quad (16)$$

$$t_{2,0} = \frac{1}{2} n_p (n_p - 1) C_0 + (n_p - 1) C_1 x_{21} + (n_p - 1) C_2 y_{21} + \frac{1}{2} C_3 x_{21}^2 + \frac{1}{2} C_4 y_{21}^2 + C_5 x_{21} y_{21} \quad (17)$$

$$t_{1,1} = n_p (n_p - 1) C_0 + (n_p - 1) C_1 (x_{31} + x_{21}) + (n_p - 1) C_2 (y_{31} + y_{21}) + C_3 x_{31} x_{21} + C_4 y_{21} y_{31} + C_5 (x_{21} y_{31} + x_{31} y_{21}) \quad (18)$$

where C_0, \dots, C_5 are arbitrary constants.

3 COMBINING SHAPE FUNCTIONS

The expressions derived in the previous section give all the possible forms of a polynomial C^1 shape function of order n_p , even in the case that the element considered uses also non-polynomial shape functions. It can be easily seen that for $n_p < 5$ there exist no polynomial C^1 shape functions, as demonstrated by Ženíšek [3].

It is more interesting, however, to consider the case of a C^1 element where only polynomial shape functions are employed. Calculating the value of a vertex shape function ϕ and its first and second derivatives *on the vertex 1* we obtain

$$\phi = C_0, \quad \frac{\partial \phi}{\partial x} = C_1, \quad \frac{\partial \phi}{\partial y} = C_2, \quad \frac{\partial^2 \phi}{\partial x^2} = C_3, \quad \frac{\partial^2 \phi}{\partial y^2} = C_4, \quad \frac{\partial^2 \phi}{\partial x \partial y} = C_5 \quad (19)$$

The respective values for vertex shape functions of vertices 2 and 3, as well as for all side and internal shape functions, are all zero. Thus by setting only one of C_0, \dots, C_5 equal to one and the others equal to zero we obtain six shape functions whose corresponding degrees of freedom are the value at the vertex of the function being interpolated and its first and second derivatives. These shape functions will depend on at least one function, whose value is determined by requiring that the resulting element can exactly interpolate a polynomial of a given order.

Considering fifth-order shape functions, the above six (for each vertex) shape functions can be used to derive the C^1 triangle with 18 degrees of freedom. One side shape function can be added for each side (for side 1 this is $\phi = t_{2,2}L_1L_2^2L_3^2$) to obtain the complete fifth-order element with 21 degrees of freedom. Considering however the vertex shape functions, even for $C_{0\dots5} = 0$ there exists a shape function (for vertex 1 this is $\phi = t_{1,2}L_1^2L_2L_3^2 + t_{2,1}L_1^2L_2^2L_3$). It is therefore possible that a complete fifth-order element can be obtained using only vertex nodes.

For elements with higher-order polynomial interpolation, a larger number of arbitrary functions is introduced in the expressions for the shape functions. These allows greater freedom in the choice of the additional degrees of freedom (e.g. for seventh-order elements it is possible to use up to second-order or up to third-order derivatives). An extension to the present algorithm is however needed to easily determine which combinations of shape functions provide adequate interpolations.

References

- [1] J.H. Argyris, I. Fried and D.W. Scharpf. The TUBA family of plate elements for the matrix displacement method. *The Aeronautical Journal of the Royal Aeronautical Society*, 72, 701–709, 1968.
- [2] S.-A. Papanicolopoulos and A. Zervos. A method for creating a class of triangular C^1 finite elements. *Submitted to International Journal for Numerical Methods in Engineering*.
- [3] A. Ženíšek. Interpolation polynomials on the triangle. *Numerische Mathematik*, 15, 283–296, 1970.

A stabilised finite element method using residual-free bubble enrichment for semiconductor device simulation

***R. Simpson¹, S. Bordas¹, P. Kerfriden¹ and A. Asenov²**

¹School of Engineering, Cardiff University, The Parade, Cardiff, Wales, UK, CF24 3AA,

²Department of Electronics and Electrical Engineering, University of Glasgow, Glasgow, UK, G12
8QQ

*simpsonr4@cardiff.ac.uk

Key Words: *semiconductor device simulation, enrichment, residual-free bubbles*

ABSTRACT

The need to predict the operating characteristics of semiconductor devices that exhibit various geometries and are subject to differing boundary conditions is great, and with the current exponential increase in semiconductor device usage, this need is becoming greater through time. The majority of current numerical simulations are carried out using the finite difference method, where the well-known Scharfetter-Gummel approximation [1] is used to provide stabilisation to the current continuity equations. However, the restrictions of using a finite-difference grid are clear, particularly when modelling curved boundaries, and the finite element method seems to present a more attractive solution. After implementation though, it is found that severe restrictions are placed on the geometry of elements and meshing becomes a cumbersome task.

The present work implements a stabilisation method through the use of residual-free bubble functions [2]. The method can be interpreted as a two-scale approach where in the fine scale a bubble function is used to solve the differential equation analytically. The bubble enrichment approximation is applied to a simple 1D p-n junction problem where it is found that the method is equivalent to the Scharfetter-Gummel approximation and the Streamline Upwind Petrov Galerkin method [3]. However, the advantages of the method become clear in two dimensions. It is shown that the bubble approximation successfully stabilises the current continuity equations in the presence of curved boundaries and, even when the method is subject to very distorted meshes, stable results are obtained.

1 INTRODUCTION

For semiconductor device simulation, the most widely used model is the drift-diffusion (DD) model [4] which comprises of a set of three coupled partial differential equations. These consist of Poisson's equation (conservation of charge) and two current continuity (CC) equations (conservation of hole and

electron current). For the case of the stationary semiconductor equations and ignoring recombination terms, these are given by

$$\nabla^2 \psi(\mathbf{x}) = \frac{q}{\varepsilon} (n(\psi(\mathbf{x})) - p(\psi(\mathbf{x})) + N_a^-(\mathbf{x}) - N_d^+(\mathbf{x})) \quad (1a)$$

$$\nabla \cdot \mathbf{J}_n = 0 \quad (1b)$$

$$\nabla \cdot \mathbf{J}_p = 0 \quad (1c)$$

where the electron and hole current density write, respectively

$$\mathbf{J}_n = -q(\mu_n \cdot \nabla \psi \cdot n - D_n \nabla n) \quad (2a)$$

$$\mathbf{J}_p = -q(\mu_p \cdot \nabla \psi \cdot p + D_p \nabla p), \quad (2b)$$

In Poisson's equation (1a) ψ refers to the electrostatic potential, q is the electron charge, ε is the absolute permittivity of the material, n is the electron concentration, p is the hole concentration and N_a^- , N_d^+ are the acceptor and donor concentrations respectively. \mathbf{J}_n and \mathbf{J}_p represent the electron and hole current respectively. In Eq. (2a), μ_n is defined as the electron permeability and D_n the electron diffusivity. The terms for the hole current equation are directly analogous. However, before we proceed to the numerical solution of these equations, some comments need to be made on their behaviour.

First of all, due the dependence of n and p on ψ , we find that Eq. (1a) is in fact a non-linear Poisson equation and therefore must be solved using an appropriate solver. Second, close inspection of Eqns (2a) and (2b) shows that they are in fact advection-diffusion equations where, in the case of the electron CC equation, we find that the term $\mu_n \cdot \nabla \psi$ is an advection velocity and the term D_n represents a diffusion coefficient. As explained by Brooks et al. [3], equations of this type can exhibit boundary layers for strong advection velocities leading to oscillations in the numerical solution. In the case of the semiconductor equations, these oscillations can lead to much slower convergence rates and in some cases, may even cause the solution to fail to converge. For this reason, care must be taken in their numerical solution.

2 RESIDUAL-FREE BUBBLE ENRICHMENT

One technique which can be used to overcome the problems created by large advection-dominated problems is residual-free bubble (RFB) enrichment [5]. The idea is as follows: taking the domain of a single element, and assuming that the advection term varies linearly within this element, it is possible to solve the differential equation with homogenous boundary conditions. The solution to this problem results in a function that is non-zero in the element interior, but zero on the nodes of the element. In this way, *no additional degrees of freedom* are introduced, but the resulting integrands in the stiffness matrix may become exponential.

In the case of the electron current continuity equations, applying the RFB enrichment results in the following 1D shape function approximation:

$$N_1(\xi, \text{Pe}_n) = \frac{\exp(\text{Pe}_n(\xi + 1)) - \exp(2\text{Pe}_n)}{1 - \exp(2\text{Pe}_n)}, \quad N_2(\xi, \text{Pe}_n) = \frac{1 - \exp(\text{Pe}_n(\xi + 1))}{1 - \exp(2\text{Pe}_n)} \quad (3)$$

where the element Peclet number is defined as

$$\text{Pe}_n = \frac{\mu_n \nabla \psi \Delta x}{2D_n} \quad (4)$$

and Δx refers to the distance between nodes in an element. Similar expressions are obtained for the hole current continuity equation.

3 RESULTS

In order to highlight the improvements seen when using RBF enrichment, two problems were analysed: the first consisted of a p-n junction with a straight interface and the second consisted of a p-n junction with a curved interface (Fig. 3). In the first problem, a very distorted mesh was used to test the robustness of the method (Fig. 1) while a comparison was made with the Bubnov-Galerkin method throughout. The results for the electron concentration for both methods are shown in Fig. 2 where oscillations are clearly seen in the Bubnov-Galerkin method while none are apparent in the RBF enrichment results. The same results are also seen for the curved junction (Fig 4).

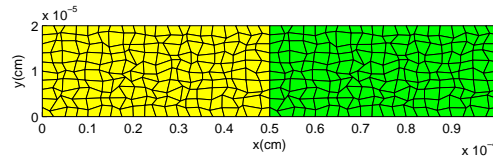


Figure 1: 2D p-n junction with straight interface with distorted quadrilateral elements

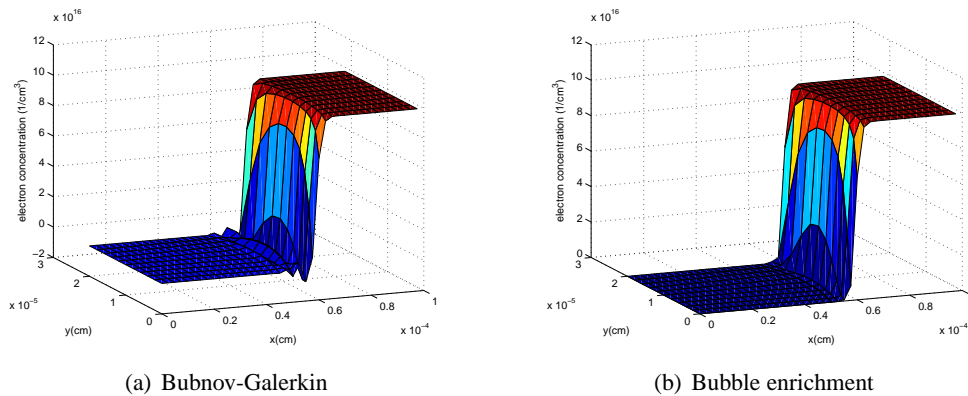


Figure 2: Electron concentration profiles for p-n junction with straight interface

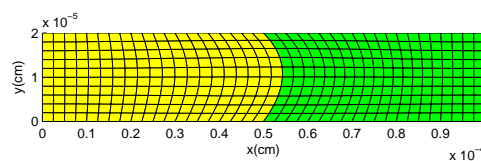


Figure 3: 2D p-n junction with curved interface

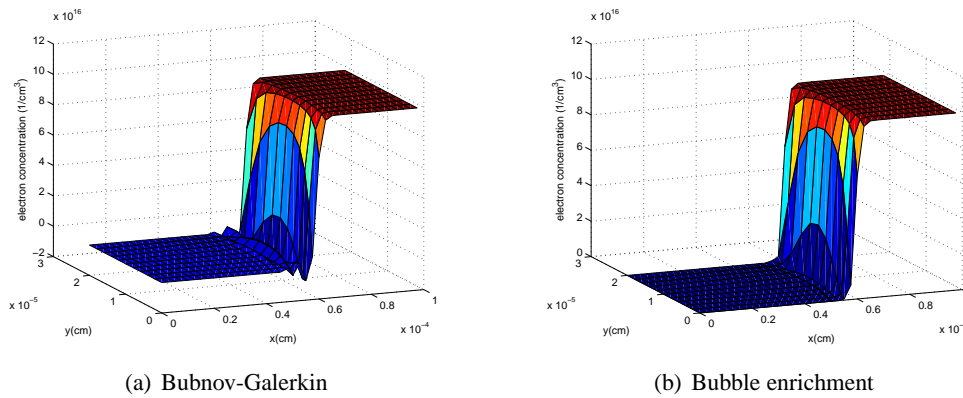


Figure 4: Electron concentration profiles for p-n junction with curved interface

4 CONCLUSION

In this paper the problems created by advection-diffusion equations in semiconductor device simulation has been briefly discussed. In addition, the use of the residual-free bubble enrichment to provide stabilisation to the current continuity equations has been outlined while results show that the method is capable of removing oscillations in the numerical solution for 2D problems, even when subjected to highly distorted meshes.

References

- [1] D. Scharfetter and H. Gummel, "Large-signal analysis of a silicon read diode oscillator," *IEEE Transactions Electron Devices*, vol. 16, no. 1, pp. 64–77, 1969.
- [2] M. Brezzi, "A relationship between stabilized finite element methods and the galerkin method with bubble functions," *Computer Methods in Applied Mechanics and Engineering*, vol. 96, no. 1, pp. 117–129, 1992.
- [3] A. Brooks and T. Hughes, "Streamline upwind/petrov-galerkin formulations for convection dominated flows with particular emphasis on the incompressible navier-stokes equations," *Computer Methods in Applied Mechanics and Engineering*, vol. 32, no. 1-3, pp. 199–259, 1982.
- [4] S. Selberherr, "Analysis and simulation of semiconductor devices?," Jan 1984.
- [5] F. Brezzi, L. Franca, and A. Russo, "Further considerations on residual-free bubbles for advective-diffusive equations," *Computer Methods in Applied Mechanics and Engineering*, vol. 166, no. 1-2, pp. 25–33, 1998.

THE ANNIHILATION OF PHYSICAL DISCONTINUITIES IN FINITE ELEMENTS

R. Darvizeh and K. Davey*

School of Mechanical, Aerospace and Civil Engineering,
The University of Manchester, Manchester, M13 9PL, UK

*keith.davey@manchester.ac.uk

Key Words: *non-physical, discontinuities, transport equations, finite element method.*

ABSTRACT

Numerical modelling of material or weak discontinuities is presently an area of research interest although mesh-based methods are thought not to be ideally suited to their treatment. Adaptive meshing and adaptive mesh-free methods are recognised to be computationally expensive when applied to large deformation and weak/strong discontinuities in solids. Some advances have been made with enriched finite element methods, which involve extending element shape functions using enrichment typically facilitated by the standard partition-of-unity property of standard Lagrange interpolation. Enrichment functions for elements are required to be selected and tested for the type of problem under consideration and only moderate success has been reported with space-time problems.

The theory proposed in the present work is a new approach for the modelling of weak discontinuities. The approach is founded on the transport form of the governing conservation laws and the non-physical variable concept. The advantage of the non-physical methodology is that it permits the precise annihilation of discontinuous behaviour from the governing finite element equations by means of a distribution like source term at the discontinuity location. Equivalent transport equations written in terms of non-physical variables describe the behaviour and are exact replacements for the original governing equations. Hence, continuous finite element approximations can be used to solve the equivalent governing equations numerically. The methodology is demonstrated in the paper through application to a 1-D cellular impact bar, which displays a shock-like behaviour at a discontinuous crush front.

1 INTRODUCTION

This work is concerned with the development of a moving control-volume finite element method for the solution of transport problems involving non-physical variables. The governing equations are presented in the form of transport equations. A control volume can be selected to be moving, stationary, mass tracking, part of, or enclosing the whole system domain. To model the discontinuity, a moving control volume (CV) which is in another moving CV has been selected. The first CV includes the discontinuity and the second CV encloses part of, or whole system domain. Transport equation (TEs) can be written for the first CV in the frame of second CV. The novel concept of non-physical variables are introduced to remove the discontinuity of the field variable through the domain and distribute it as a source term (at the discontinuity location) and discontinuity at the domain boundaries (Figure 1(b)). Non-physical field variables have limiting continuity and source-like behaviour at a physical discontinuity [1]. Equivalent transport equations written in terms of non-physical variables describe the behaviour of non-physical variables and are exact replacements for the original governing equations. A weighted-transport method is applied to solve the TEs. By choosing Galerkin weighting functions the FEM has been used to solve TEs numerically. The level set method is applied to solve FE formulations numerically.

The main aim of the work is to increase the capability of FE formulation to model discontinuities. The problems selected here are restricted to “cellular material crushing” for demonstration purposes to showcase the methodology although the theory is presented in a generic form.

2 CONSERVATION LAW FOR A MOVING CV

The formulation proposed here can be considered as an arbitrary Lagrangian-Eulerian (ALE) formulation [2]. The ALE formulation permits independent control volume (CV) movement in a computational reference system (CRS). The Material reference system (MRS), spatial and CRS co-ordinates are denoted by \mathbf{X} , \mathbf{x} , and χ^* , respectively. The material derivative $D/Dt = \partial/\partial t|_{\mathbf{x}}$ and CV derivative $D^*/D^*t = \partial/\partial t|_{\chi^*}$ are related to the spatial derivative by the following expressions:

$$\frac{D}{Dt} = \frac{\partial}{\partial t}\bigg|_{\mathbf{x}} + \underline{\mathbf{v}} \cdot \nabla \quad (1)$$

$$\frac{D^*}{D^*t} = \frac{\partial}{\partial t}\bigg|_{\mathbf{x}} + \underline{\mathbf{v}}^* \cdot \nabla \quad (2)$$

where $\underline{\mathbf{v}} = D\mathbf{x}/Dt$ and $\underline{\mathbf{v}}^* = D^*\mathbf{x}/D^*t$.

A conservation law for a moving domain Ω defined by the diffeomorphism $\mathbf{x}(\chi^*, t)$, is,

$$\frac{D^*}{D^*t} \int_{\Omega} \rho \psi dV + \int_{\Gamma} \rho \psi (\underline{\mathbf{v}} - \underline{\mathbf{v}}^*) \cdot \underline{\mathbf{n}} d\Gamma = - \int_{\Gamma} \underline{\mathbf{J}} \cdot \underline{\mathbf{n}} d\Gamma + \int_{\Omega} \rho b dV \quad (3)$$

where, Ω is CRS moving control volume, Γ is its boundary, ψ is physical field variable per unit of density, ρ is density, $\underline{\mathbf{v}}$ is material velocity, $\underline{\mathbf{n}}$ is a unit normal, $\underline{\mathbf{J}} \cdot \underline{\mathbf{n}}$ is a flux and b is a body force.

3 EQUIVALENT GOVERNING EQUATIONS

The concept of an equivalent governing equation is introduced in reference [1] but limits to solidification modelling. The idea is to form alternative transport equations that can be more readily solved using numerical techniques. The transport equation is to be constructed so that its solution is precisely that which satisfies equations (2.3). Consider then the identity

$$\frac{D^*}{D^*t} \int_{\Omega} \hat{\psi} dV = \frac{D^*}{D^*t} \int_{\Omega} \rho \psi dV + \int_{\Gamma} \rho \psi (\underline{\mathbf{v}} - \underline{\mathbf{v}}^*) \cdot \underline{\mathbf{n}} d\Gamma = - \int_{\Gamma} \underline{\mathbf{J}} \cdot \underline{\mathbf{n}} d\Gamma + \int_{\Omega} \rho b dV \quad (4)$$

where $\hat{\psi}$ is called non-physical variable and it is shown in Ref.[1] that the function $\hat{\psi}$ exists.

To ascertain the behaviour of the non-physical variable $\hat{\psi}$ at the discontinuity requires careful treatment. Because of non-uniqueness of $\hat{\psi}$, different strategies can be made for its behaviour [1]. The selected strategy in this paper is to assume a continuous distribution for the non-physical variable through the element which experiences the discontinuity and account the non-physical source term ($\hat{\psi}'$) at discontinuity (Figure 1(b)).

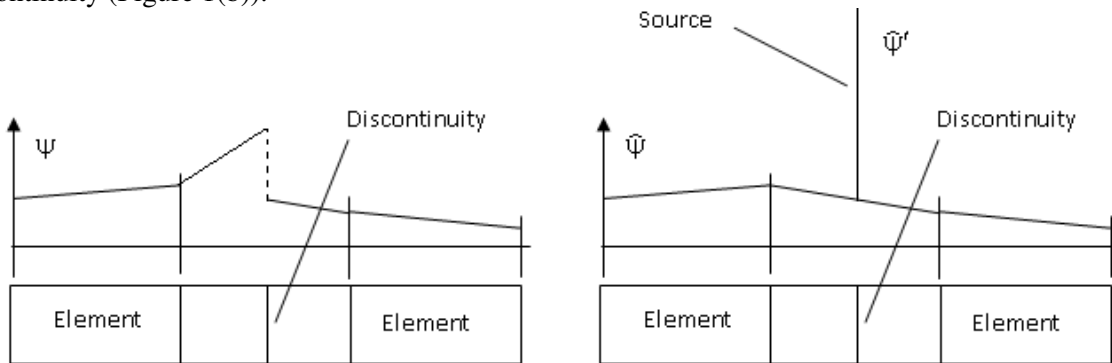


Figure 1. (a) Real model of discontinuity (b) Equivalent model.

To model the discontinuity using the non-physical variable concept another moving control volume enclosing discontinuity (Γ_i) is considered. The transport of this arbitrary small control volume (Ω^x) is

assumed to be governed by the regular velocity field \underline{v}^\times where $\underline{v}^\times \cdot \underline{n} = \underline{v}_i \cdot \underline{n}$ at Γ_i and \underline{v}_i is the velocity of the moving discontinuity. The equivalent transport equation for this control volume is

$$\frac{D^\times}{D^\times t} \int_{\Gamma_i} \hat{\psi}' d\Gamma + \int_{\Sigma_i} \hat{\psi}' (\underline{v}^* - \underline{v}_i) \cdot \underline{t} n d\Sigma + \int_{\Gamma_i} [\hat{\psi}' (\underline{v}^* - \underline{v}_i) \cdot \underline{n}_s] d\Gamma = \int_{\Gamma_i} [\rho \psi (\underline{v}^* - \underline{v}_i) \cdot \underline{n}_s] d\Gamma = - \int_{\Gamma_i} [\underline{J} \cdot \underline{n}_s] d\Gamma \quad (5)$$

where the square bracket signifies a jump and $\underline{t}n$ is a outward pointing unit normal on $\Sigma_i = \Gamma \cap \Gamma_i$ (Σ_i is the boundary for Γ_i) that is in a tangent plane of Γ_i .

Modifying Equation (4) by using the MCV in a MCV¹ concept to account for modelling of discontinuity gives

$$\frac{D^*}{D^* t} \int_{\Omega_e/\Gamma_i} N_i \hat{\psi} dV = \frac{D^*}{D^* t} \int_{\Omega_e} \rho \psi dV + \int_{\Gamma_e} \rho \psi (\underline{v} - \underline{v}^*) \cdot \underline{n} d\Gamma - \frac{D^\times}{D^\times t} \int_{\Gamma_i^e} \hat{\psi}' dV - \int_{\Sigma_i^e} \hat{\psi}' (\underline{v}^* - \underline{v}^\times) \cdot \underline{t} n d\Gamma \quad (6)$$

$$\frac{D^*}{D^* t} \int_{\Omega_e/\Gamma_i} \hat{\psi} dV = - \int_{\Gamma_e} \underline{J} \cdot \underline{n} d\Gamma + \int_{\Omega_e} \rho b dV - \frac{D^\times}{D^\times t} \int_{\Gamma_i^e} \hat{\psi}' dV - \int_{\Sigma_i^e} \hat{\psi}' (\underline{v}^* - \underline{v}^\times) \cdot \underline{t} n d\Gamma \quad (7)$$

Hence there are three relations instead of two presented in Equation (4) which should be solved using the FEM. These three relations are denoted: source equation (Eq. 5), equivalent governing equation (Eq. 6) and linkage equation (Eq. 7).

4 FINITE ELEMENT FORMULATION

By applying the standard Galerkin weighting functions (N_i) to an element domain Ω_e and establishing relationships between different transport derivatives, the weighted form of the equivalent, the linkage and the source equations can be written as below respectively.

$$\begin{aligned} \frac{D^*}{D^* t} \int_{\Omega_e/\Gamma_i} N_i \hat{\psi} dV &= \int_{\Omega_e} \nabla N_i \cdot \underline{J} dV - \int_{\Gamma_e} N_i \underline{J} \cdot \underline{n} d\Gamma + \int_{\Omega_e} \rho N_i \cdot b dV \\ &+ \int_{\Gamma_i^e} N_i [\underline{J} \cdot \underline{n}_s] d\Gamma + \int_{\Gamma_i^e} \hat{\psi}' (\underline{v}_N^* - \underline{v}_N^\times) \cdot \nabla N_i d\Gamma \end{aligned} \quad (8)$$

$$\begin{aligned} \frac{D^*}{D^* t} \int_{\Omega_e/\Gamma_i} N_i \hat{\psi} dV &= \frac{D^*}{D^* t} \int_{\Omega_e} N_i \rho \psi dV - \int_{\Omega_e} \rho \psi (\underline{v} - \underline{v}^*) \cdot \nabla N_i dV + \int_{\Gamma_e} N_i \rho \psi (\underline{v} - \underline{v}^*) \cdot \underline{n} d\Gamma \\ &- \int_{\Gamma_i^e} N_i \rho_s (\underline{v}_s - \underline{v}_i) \cdot \underline{n}_s [\psi] d\Gamma + \int_{\Gamma_i^e} \hat{\psi}' (\underline{v}_N^* - \underline{v}_N^\times) \cdot \nabla N_i d\Gamma \end{aligned} \quad (9)$$

$$\begin{aligned} \frac{D^\times}{D^\times t} \int_{\Gamma_i^e} N_i \hat{\psi}' d\Gamma &+ \int_{\Sigma_i^e} N_i \hat{\psi}' (\underline{v}^* - \underline{v}^\times) \cdot \underline{t} n d\Sigma + \int_{\Gamma_i^e} \hat{\psi}' (\underline{v}_N^* - \underline{v}_N^\times) \cdot \nabla N_i d\Gamma \\ &= \int_{\Gamma_i^e} N_i \rho_s (\underline{v}_s - \underline{v}_i) \cdot \underline{n}_s [\psi] d\Gamma = - \int_{\Gamma_i^e} N_i [\underline{J} \cdot \underline{n}_s] d\Gamma \end{aligned} \quad (10)$$

where \underline{v}_N^* and \underline{v}_N^\times are normal components of Ω and Ω^\times control volumes velocities respectively.

For the conservation of mass equations, $\hat{\psi} = \hat{\rho}$, $\hat{\psi}' = 0$, $\underline{J} = 0$ and they are called respectively non-physical density, non-physical density source and mass flux. And for the conservation of linear momentum equations, $\hat{\psi} = \hat{v}$, $\hat{\psi}' = \hat{v}'$, $\underline{J} = \underline{\sigma}$ and they are called respectively non-physical velocity, non-physical velocity source and stress field vector.

¹ MCV in a MCV: Moving Control Volume in a Moving Control Volume.

5 NUMERICAL RESULTS

A 1-D cellular impact bar is considered to study as a model to illustrate the concepts. A crush front propagates through the bar as a moving weak discontinuity and results a jump in density, velocity and internal energy. A schematic model of 1D cellular impact bar has been shown in Figure 2(a), where its cross section area is assumed to remain constant during the deformation process. The FE solution algorithm is based on the level set method (LSM) and the non-physical variable is defined as a linear function of the level set variable ϕ ; i.e. $\hat{\psi}_e(\phi) = \hat{C}_e \phi_e = \hat{C}_e (N_1 \phi_e + N_2 \phi_{(e+1)})^2$. The variable \hat{C}_e is called the non-physical capacitance (e.g. non-physical density capacitance for the non-physical density and non-physical velocity capacitance for the non-physical velocity). The elemental weighted equivalent equation (Eq.8) is required to be assembled with other element equations to form the FE system. But the linkage and the source equations (Eq. 9 and Eq. 10) should be calculated only for the elements which experience the moving discontinuity and are automatically satisfied for the other elements. Hence there is no need to weight and assemble them (i.e. $N_i = 1$). The variation of non-physical density and velocity capacitances and the non-physical velocity source of the 3 elements model with respect to time is presented in the below figures. The behaviour of the numerical results exactly matches with the theory predictions.

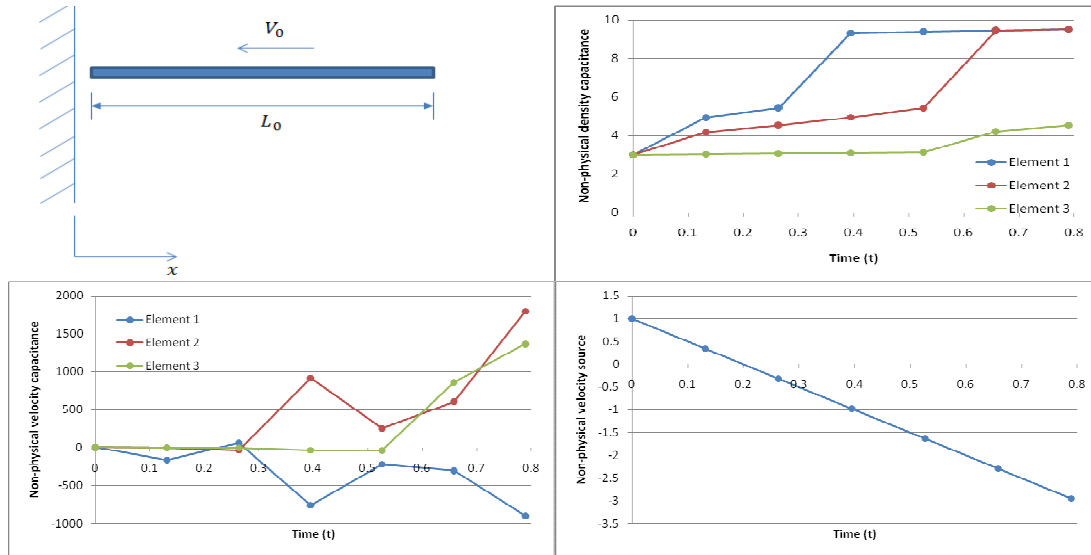


Figure 2. (a) 1D cellular impact bar (b) The variation of non-physical density capacitance (c) The variation of non-physical velocity capacitance (d) Non-physical velocity source.

CONCLUSION

The temporal derivatives of $\hat{\psi}$ and ψ are avoided, making the governing equations applicable when a discontinuity is in Ω . The continuous and source like behaviour of $\hat{\psi}$ facilitates the precise removal of discontinuous from the governing system of transport FE equations. The results presented in the previous section show that there exists a numerical solution for the system of FE equations based on LSM.

References

- [1] Davey, K and Mondragon, R, *A Non-Physical Enthalpy Method for the Numerical Solution of Isothermal Solidification*, Int. Journal for Numerical Methods in Engineering, 2010. **84**, pp. 214-252.
- [2] Donea, J., P. Fasoli, and S.S. Guiliani, *Lagrangian and Eulerian Finite Element Techniques for Transient Fluid-Structure Interaction problems*, in Trans. 4th Int. Conf. on SMIRT, 1977.

² $\phi_{(e)}$ is the value of ϕ variable at node (e) .

FE-EFGM COUPLING USING MAXIMUM ENTROPY SHAPE FUNCTIONS AND ITS APPLICATION TO SMALL AND FINITE DEFORMATION

*Zahur Ullah¹, Charles E. Augarde¹, Roger S. Crouch¹ and William M. Coombs¹

¹Durham University, School of Engineering and Computing Sciences, South Road, Durham, DH1 3LE. UK.

*zahur.ullah@durham.ac.uk

Key Words: *FE-EFGM coupling; local maximum entropy shape functions; finite deformation*

ABSTRACT

The element-free Galerkin method (EFGM) is superior to its counterpart the finite element method (FEM) in terms of accuracy and convergence but is computationally expensive. Therefore it is more practical to use the EFGM only in a region, which is difficult to model using the FEM, while the FEM can be used in the remaining part of the problem domain. In the conventional EFGM, moving least squares (MLS) shape functions are used for the approximation of the field variables. These shape functions do not possess the Kronecker delta property and it is therefore not straightforward to couple the EFGM with the FEM. Local maximum entropy (max-ent) shape functions are an alternative way to couple the EFGM and FEM. These shape functions possess a weak Kronecker delta property at boundaries, which provides a natural way to couple the EFGM with the FEM as compared to the MLS basis functions, which need extra care to properly couple the two regions. This formulation removes the need for interface elements between the FEM and the EFGM, unlike the approach adopted by most researchers. This approach is verified using benchmark problems from small and finite deformation.

1 INTRODUCTION

The EFGM [1] is an excellent tool for the solution of boundary value problems in computational mechanics. In the conventional EFGM, MLS shape functions are used for the approximation of the field variables, background cells are used for numerical integration and essential boundary conditions are implemented with Lagrange multipliers. Compared to the FEM, the EFGM is more accurate with a high rate of convergence, post processing is simple and there is no need for element connectivity information, so nodes can be added and deleted without computationally expensive remeshing. These advantages makes the EFGM very suitable for certain classes of problems, e.g. those with large deformation and moving boundaries.

On the other hand due to the use of the MLS basis functions, the EFGM is computationally more expensive, especially for three-dimensional and nonlinear problems. At each integration point, a system of linear equations are solved to calculate the MLS shape functions, a high integration order needs to be used for accurate results due to the non-polynomial nature of the shape functions and essential boundary conditions cannot be implemented directly as in the case of FEM due to the lack of Kronecker delta property. Therefore it is more practical to use the EFGM only in a region where high accuracy is required, while FEM can be used in the remaining part of the problem domain. Coupling between EFGM and FEM is therefore a key issue.

The coupling between EFGM and FEM was first proposed in [2] based on interface elements. Hybrid shape functions for these elements, consisting of both the FEM and the EFGM shape functions, are formed using ramp functions. A detailed overview and analysis of the coupling between meshless and

FEM can be found in [3]. In this paper a new way of coupling the EFGM and the FEM using local max-ent shape functions is proposed. These shape functions possess a weak Kronecker delta property at the boundaries. This property provides a natural way to couple the EFGM with the FEM as compared to the MLS basis functions, which need extra care properly to couple the same regions.

2 LOCAL MAXIMUM ENTROPY SHAPE FUNCTIONS

For completeness a very brief overview of local max-ent shape functions are given, the detail can be found in [4] and the references therein. The two-dimensional formulation is given here, which is straightforward to modify for one- or three-dimensions. The expression for the local max-ent shape function ϕ_i for node i at point of interest $\mathbf{x} = [x \ y]^T$ is written as

$$\phi_i = \frac{Z_i}{Z}, \quad Z_i = w_i e^{-\lambda_1 \tilde{x}_i - \lambda_2 \tilde{y}_i}, \quad Z = \sum_{j=1}^n Z_j. \quad (1)$$

Here w_i is the weight function associated with node i , evaluated at point \mathbf{x} , $\tilde{x}_i = x_i - x$ and $\tilde{y}_i = y_i - y$ are shifted coordinates, n is the number of nodes in support of point \mathbf{x} and λ_1 and λ_2 are Lagrange multipliers and can be written as

$$\boldsymbol{\lambda} = \operatorname{argmin} F(\boldsymbol{\lambda}), \quad \text{where } F(\boldsymbol{\lambda}) = \log(Z), \quad (2)$$

i.e. the set of values for which F attains its minimum. The expressions for the shape function derivatives are

$$\nabla \phi_i = \phi_i \left(\nabla f_i - \sum_{i=1}^n \phi_i \nabla f_i \right), \quad (3)$$

where

$$\nabla f_i = \frac{\nabla w_i}{w_i} + \boldsymbol{\lambda} + \tilde{\mathbf{x}}_i [H^{-1} - H^{-1}A], \quad A = \sum_{k=1}^n \phi_k \tilde{\mathbf{x}}_k \otimes \frac{\nabla w_k}{w_k}. \quad (4)$$

3 NUMERICAL EXAMPLES

One- and two-dimensional numerical examples from small and finite deformation are now given to demonstrate the implementation and performance of the current approach in linear and nonlinear problems.

3.1 Small deformation

In this section the behaviour of a one-dimensional bar of unit length subjected to body force and fixed at a point $x = 0$ and a two-dimensional cantilever beam subjected to parabolic traction at the free end are examined. In the 1D example the modulus of elasticity $E = 1$. Figure 1(a) shows the FEM and the EFGM regions with the shape functions for all the nodes in the problem domain and Figure 1(b) shows solution for the nodal displacement. The two-dimensional example is the famous Timoshenko beam problem, for which the analytical solution is given in [5]. The problem is solved for the plane stress case with $P = 1000$, $\nu = 0.3$, $E = 30 \times 10^6$, all in compatible units. Figure 2(a) shows the FEM and EFGM regions, Figure 2(b) shows the deflection at $y = 0$ and Figures 2(c) and 2(d) shows the normal and shear stresses σ_{xx} and σ_{xy} at $x = L/2$.

3.2 Finite deformation

An updated Lagrangian formulation is used to model problems subjected to finite deformation. Here the deformation gradient F provides the link between the current and the reference configurations. The logarithmic strain $\varepsilon = \ln(v)$ and Kirchhoff stress $\tau = J\sigma$ are used in this case, where $v = \sqrt{FF^T}$ is the left stretch matrix, J is the determinant of the deformation gradient and σ is the Cauchy or true stress. Two problems are solved in this case: a uniform loaded rectangular plate with simply supported edges, the analytical solution for which is available in [6] and a cantilever beam with uniform loading, the reference solution for which is given in [7]. The geometry for the plate problem is shown in Figure 3(a), due to symmetry only half of the plate is modelled. The problem is solved with $q = 40$, $h = 0.2$,

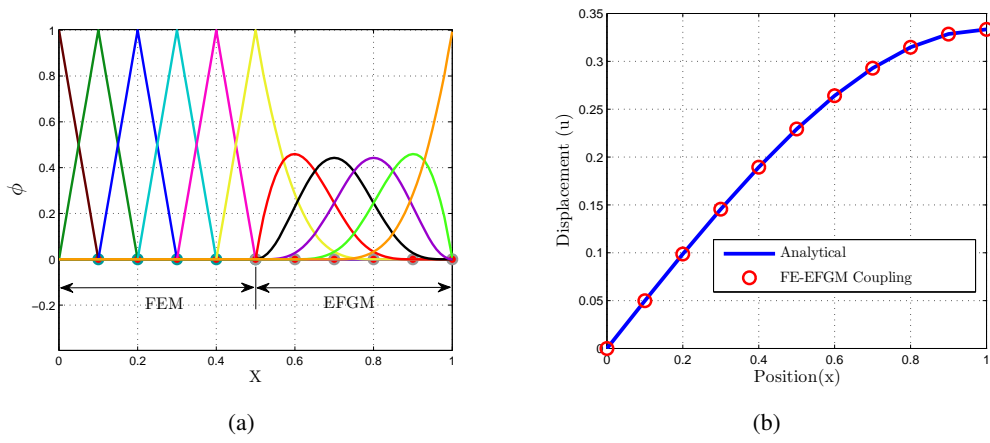


Figure 1: FE-EFGM regions, shape functions and nodal displacements for the 1D bar problem

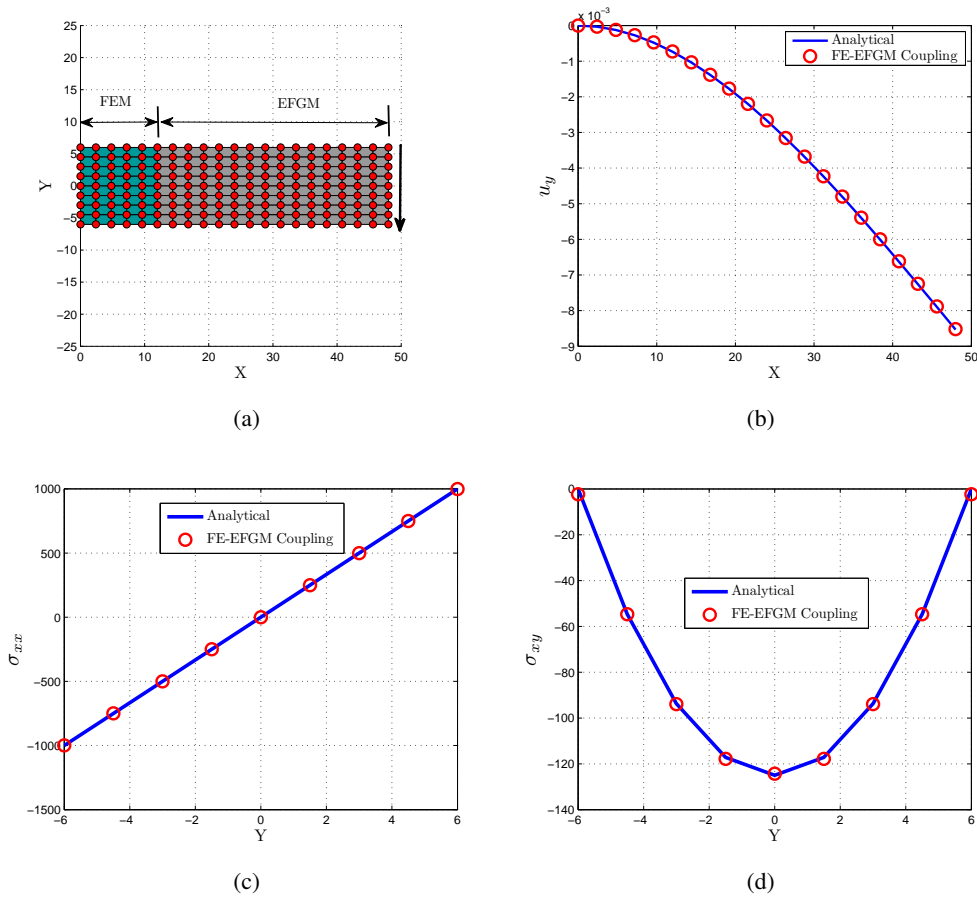


Figure 2: FE-EFGM regions, deflection and stresses for the 2D beam problem

$L = 10$, $E = 10^7$, $\nu = 0.25$ all in compatible units with 20 load steps. Half of the plate is modelled with the EFGM and other half is modelled with the FEM. Figure 3(b) shows the pressure vs w/h for the plate problem. The beam problem is solved with $q = 10$, $h = 1$, $L = 10$, $E = 1.2 \times 10^4$, $\nu = 0.2$ with 20 load steps all in compatible units. Half of the beam is modelled with the EFGM and other half is modelled with the FEM. Figure 4(a) shows the deformed and un-deformed configuration at the end of solution with the EFGM and the FEM regions for the problem. Figure 4(b) shows the pressure vs u_y/L for the beam problem.

4 Conclusion

In this paper a new method of coupling the FEM with the EFGM based on local max-ent shape functions is proposed. Numerical examples are solved from small and finite deformation. In the small deformation case, numerical results for displacement and stresses are compared with the available analytical

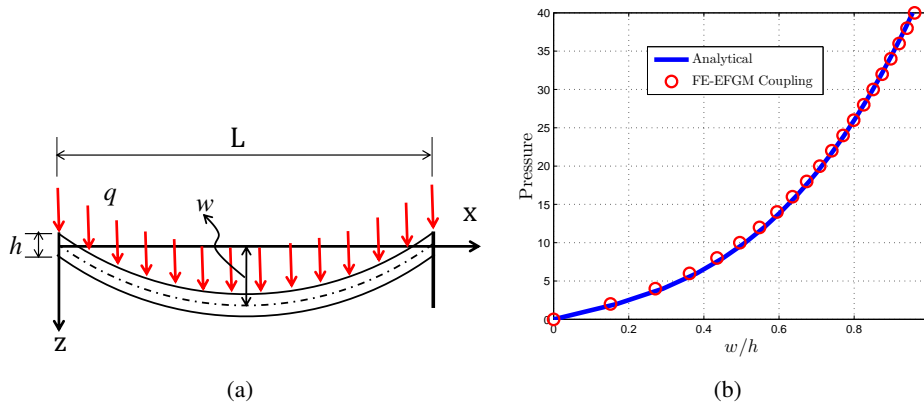


Figure 3: Geometry and pressure vs w/h for the plate problem

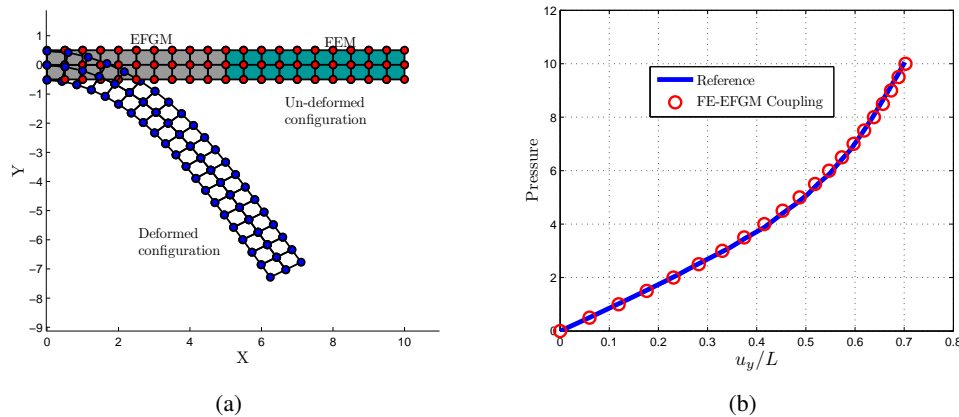


Figure 4: Deformed and un-deformed Configuration with pressure vs u_y/L for the beam problem

solution, which shows excellent agreement. In finite deformation case, the analytical solution for the pressure vs deflection curve is available for the plate problem, while for the beam problem a reference solution is used for comparison. In both cases the numerical results are in a very good agreement with the analytical/reference solutions.

References

- [1] T. Belytschko, Y. Y. Lu, and L. Gu. Element-free Galerkin methods. *International Journal for Numerical Methods in Engineering*, 37:227–256, 1994.
- [2] T. Belytschko, D. Organ, and Y. Krongauz. A coupled finite element-element-free Galerkin method. *Computational Mechanics*, 17:186–195, 1995.
- [3] T. Rabczuk, S. P. Xiao, and M. Sauer. Coupling of mesh-free methods with finite elements: basic concepts and test results. *Communications in Numerical Methods in Engineering*, 22(10):1031–1065, 2006.
- [4] M. Arroyo and M. Ortiz. Local maximum-entropy approximation schemes: a seamless bridge between finite elements and meshfree methods. *International Journal for Numerical Methods in Engineering*, 65:2167–2202, 2006.
- [5] S. P. Timoshenko and J. N. Goodier. *Theory of Elasticity*. McGraw-Hill, New York, 3rd edition, 1970.
- [6] S. P. Timoshenko and S. Woinowsky-Krieger. *Theory of plates and shells*. McGraw-Hill Book Company, NY, 1959.
- [7] J. T. Holden. On the finite deflections of thin beams. *International Journal of Solids and Structures*, 8:1051 – 1055, 1972.

Drilling Rotations and Partition of Unity Boundary Element Method (PUBEM)

Hing Leung and Pedro M. Baiz*

Department of Aeronautics, Imperial College London, London SW7 2AZ, UK.

*p.m.baiz@imperial.ac.uk

Key Words: *drilling rotation; partition of unity; boundary element method*

ABSTRACT

This work presents novel applications of partition of unity (PU) enrichment within the boundary element method (BEM). In the present work, an approach to include drilling rotations in the classical two-dimensional boundary element method will be considered. The approach is based on a simple partition of unity strategy that gives rise to a fictitious rotational degree of freedom (using the well known Allman's triangle strategy). The approach maintains the boundary only character of BEM and the partition of unity enrichment makes it general (totally kernel independent) and efficient (just certain areas of the boundary could be enriched).

1 INTRODUCTION

Drilling rotations (also referred as out of plane rotations) refer to an additional degree of freedom that is associated with the classical d.o.f. in 2D elasticity (u_1 and u_2). This d.o.f. is particularly important when dealing with general plate/shell assemblies in which 6 d.o.f. per node are necessary (3 displacements and 3 rotation, one in each coordinate axis). Drilling rotations in FEM have been introduced primarily as a way to improve the element performance (e.g. avoiding higher order elements) or in order to simplify/improve the treatment of plate/shell intersections [1, 2]. The most common approaches in FEM employ various special devices to develop successful elements. The first successful technique was proposed by Allman [3] in 1984, who introduced a quadratic displacement approximation in the normal direction to supplement drilling d.o.f. to nodes of a triangular element (commonly referred as Allman's triangle). This technique has been continuously extended to other triangular and quadrilateral elements. Other works in FEM include more rigorous mathematical development based on variational principles employing independent rotation fields by Hughes and Brezzi [4]. In the BEM community, drilling rotations have been neglected. The common approach for plate/shell assemblies relies on the assumption that the plate flexural rigidity in its own plane is so large that it is possible to ignore its associated deformation [5] (good approximation for wide plates, but not for narrow ones that behave like beams). Very recently, Tian and Yagawa [8] found that Allman's formulation takes a typical form of partition of unity [9] approximation that offers merits and convenience in formulation and practical

applications. The partition of unity notion also enables a straightforward and general formulation that makes possible to extend Allman's rotational d.o.f. to meshfree approximations. Finally, applications of partition of unity in BEM (also known as PUBEM) started within Trevelyan's group in 2002 with the work of Perrey-Debain *et al.* [10] on short wave problems. In all reported cases, PUBEM has shown to be a powerful new method for a variety of engineering problems.

2 FORMULATION

Enriched Shape Functions

The shape functions for a boundary could that includes drilling rotations could be written as a partition of unity approximation, as recently proposed in [8, 6]:

$$\begin{bmatrix} u_1^e \\ u_2^e \end{bmatrix} = \sum_{\beta=1}^2 N_{\beta} \begin{bmatrix} 1 & 0 \\ 0 & 1 \end{bmatrix} \begin{bmatrix} \widehat{\xi}_{\beta}(-n_1) \\ \widehat{\xi}_{\beta}(n_2) \end{bmatrix} \begin{bmatrix} u_1^{\beta} \\ u_2^{\beta} \\ w^{\beta} \end{bmatrix} \quad (1)$$

where shape functions N_{β} are the classical linear (2 nodes) shape functions used in BEM (continuous or not). n_{β} are the components of the normal. $\widehat{\xi}_i = \xi - \xi_i$ for $i = 1, 2$, and ξ_i is defined as the collocation point, where $[\xi_1 \ \xi_2]$ is $[-1 \ 1]$ (continuous element); $[-2/3 \ 2/3]$ (discontinuous element); $[-2/3 \ 1]$ (semi-discontinuous element node 1) and $[-1 \ 2/3]$ (semi-discontinuous element node 2). As pointed in [8], this theoretically explains why these rotation formulae can be easily extended to meshfree method and, as shown in this work, to boundary element methods.

Enriched 2D BEM formulation and relation between true and assumed rotations

The discretised enriched BEM formulation is obtained after equation (1) is introduced in the classical BEM 2D equation as follows:

$$\begin{bmatrix} C_{11}^c & C_{12}^c \\ C_{21}^c & C_{22}^c \end{bmatrix} \begin{bmatrix} u_1^c \\ u_2^c \end{bmatrix} + \sum_{\beta=1}^{N_e^{enr}} \sum_{\beta=1}^2 \begin{bmatrix} P_{11}^{*m\beta} & P_{12}^{*m\beta} & P_{13}^{*m\beta} \\ P_{21}^{*m\beta} & P_{22}^{*m\beta} & P_{23}^{*m\beta} \end{bmatrix} \begin{bmatrix} u_1^{m\beta} \\ u_2^{m\beta} \\ w^{m\beta} \end{bmatrix} + \sum_{\beta=1}^{N_e^{std}} \sum_{\beta=1}^2 \begin{bmatrix} P_{11}^{m\beta} & P_{12}^{m\beta} \\ P_{21}^{m\beta} & P_{22}^{m\beta} \end{bmatrix} \begin{bmatrix} u_1^{m\beta} \\ u_2^{m\beta} \end{bmatrix} = \sum_{m=1}^{N_e} \sum_{\beta=1}^2 \begin{bmatrix} Q_{11}^{m\beta} & Q_{12}^{m\beta} \\ Q_{21}^{m\beta} & Q_{22}^{m\beta} \end{bmatrix} \begin{bmatrix} t_1^{m\beta} \\ t_2^{m\beta} \end{bmatrix} \quad (2)$$

where

$$\begin{bmatrix} P_{11}^{*m\beta} & P_{12}^{*m\beta} & P_{13}^{*m\beta} \\ P_{21}^{*m\beta} & P_{22}^{*m\beta} & P_{23}^{*m\beta} \end{bmatrix} = \int_{-1}^1 \begin{bmatrix} T_{11}(\mathbf{x}^c, \mathbf{x}(\xi)) & T_{12}(\mathbf{x}^c, \mathbf{x}(\xi)) \\ T_{21}(\mathbf{x}^c, \mathbf{x}(\xi)) & T_{22}(\mathbf{x}^c, \mathbf{x}(\xi)) \end{bmatrix} \left\{ N_{\beta} \begin{bmatrix} 1 & 0 \\ 0 & 1 \end{bmatrix} \begin{bmatrix} \widehat{\xi}_{\beta}(-n_{m1}) \\ \widehat{\xi}_{\beta}(n_{m2}) \end{bmatrix} \right\} J^m(\xi) d\xi$$

where N_e^{enr} is the number of the elements enriched and N_e^{std} is the number of elements using the traditional linear displacement interpolation. In equation (2), left hand side contains displacements, while right hand side contains forces applied on the system. Similar equations to (2) have been introduced by Trevelyan's group for wave propagation and fracture analysis [10, 11].

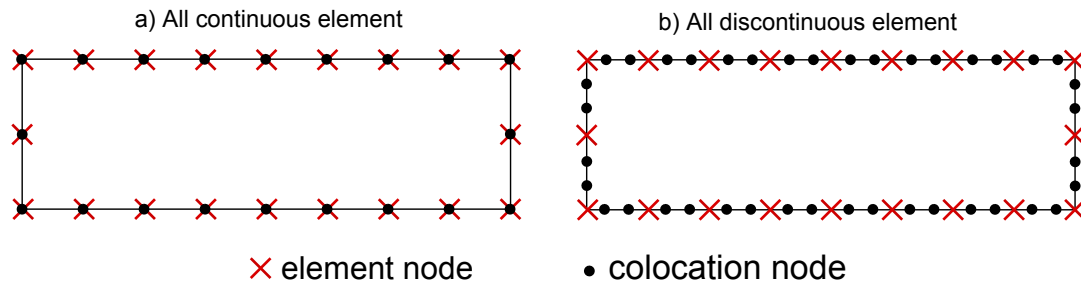


Figure 1: Short cantilever mesh configuration

As shown in [10, 11], implementing an enriched BEM formulation introduces additional d.o.f. to the classical BEM for which additional equations are necessary. In their work, a technique based on additional collocations points have been implemented. In the present work a more physically based approach will be used to obtain the additional equations necessary to have a well posed problem. Following a similar approach continuously used in FEM, the following functional could be considered [2]:

$$\Pi(u, \bar{w}) = \frac{\gamma}{2} \int_{\Gamma} (\Psi - \bar{w})^2 d\Gamma \quad (3)$$

This penalty term ties the average drilling rotation field \bar{w} to the true rotation Ψ induced from u_{α} ($\Psi = 1/2(u_{2,1} - u_{1,2})$ [3, 2]). The penalty parameter (γ) is only necessary if the above expression is introduced in the functional of the total potential energy in order to balance its contribution to the classical two-dimensional problem.

3 NUMERICAL RESULTS

The enriched BEM formulation proposed above was verified using a common benchmark example in FEM (cantilever beam with shear end load). This is a simple structure for which analytical solution is available. The short cantilever tested is shown in Figure 1, the cantilever with length(L)= 48m, height(D)= 12m and depth(h)= 1m is clamped at one end and a upward shear load of 40 is applied on the other end. Other information of the cantilever is as follow: Young's Modulus is 30000, Poisson's ratio is 0.25. A convergence study with different types of enrichment (all boundary or just the right end) and elements (all continuous elements, all discontinuous, and mixed cases). Figure 2 shows the very good rate of convergence of deflection and rotation for different cases (except for totally continuous elements).

4 CONCLUSIONS

This works presents applications of PUBEM to drilling rotations. The approach is based on a recently proposed formulation of the well known Allman's triangle following a partition of unity enrichment (PUFEM) strategy. A functional based on a weighted rotation residual is used as the additional equation in order to obtain a mathematically well posed problem. Results show good convergence characteristics, particularly for totally discontinuous elements while for totally continuous elements (sharing nodes at corners) results are very unstable for rotation results.

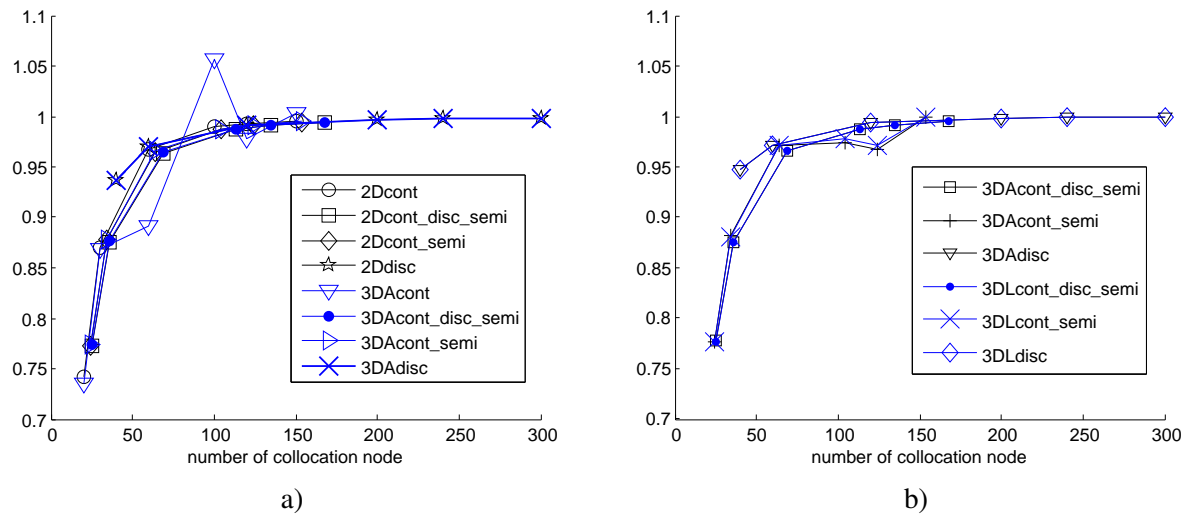


Figure 2: Normalised convergence of short cantilever under shear load. a) results in vertical displacement, b) result in rotation.

References

- [1] C.A. Felippa, A study of optimal membrane triangles with drilling freedoms, *CMAME*, 192:2125-168 (2003).
- [2] O.C. Zienkiewicz, L.R. Taylor, *The Finite Element Method (vol. 2, Solid Mechanics)*, Butterworth-Heinemann, 5 edition (2000).
- [3] D.J. Allman, A compatible triangular element including vertex rotations for plane elasticity analysis, *Comp. Struct.*, 57:1-8 (1984).
- [4] T.R.J. Hughes, F.Brezzi, On drilling degrees of freedom, *CMAME*, 72:105-121 (1989).
- [5] P.M. Baiz, M.H. Aliabadi, Local buckling of thin-walled structures by the boundary element method, *Eng. Anal. Bound. Elem.*, 33:302-313 (2009).
- [6] P.M. Baiz, Drilling Rotations in BEM, in *Advances in Boundary Element Techniques XI*, Berlin, Germany, 12-14 July (2010).
- [7] M.H. Aliabadi, *The Boundary Element Method, vol II: Application to Solids and Structures*, Chichester, Wiley (2002).
- [8] R. Tian, G. Yagawa, Allmans triangle, rotational DOF and PU, *IJNME*, 69:837-858 (2007).
- [9] I. Babuska, G. Caloz, J. Osborn, Special finite element methods for a class of second order elliptic problems with rough coefficients, *SIAM Journal of Numerical Analysis*, v31, pp. 945-98 (1994).
- [10] E. Perrey-Debain, J. Trevelyan, P. Bettess, New special wave boundary elements for short wave problems, *Commun. Numer. Meth. Engng*, v18, pp. 259268 (2002).
- [11] R. Simpson, J. Trevelyan, A partition of unity enriched Dual Boundary Element Method for accurate computations in fracture mechanics, *CMAME*, 200:1-10 (2010).

An isogeometric boundary element method for elastostatic problems

*R.N. Simpson¹, S.P.A. Bordas¹, J. Trevelyan² and P. Kerfriden¹

¹School of Engineering, Cardiff University, The Parade, Cardiff, CF24 3AA, Wales, UK,

²School of Engineering and Computing Sciences, Durham University, South Road,
Durham, DH1 3LE, UK

*simpsonr4@cardiff.ac.uk

Key Words: *isogeometric analysis, boundary element method, NURBS*

ABSTRACT

Over the last few years the topic of isogeometric analysis has received much attention, and represents a fundamental shift in the engineering solution procedure using numerical methods. The aim of the method is to take a model generated in CAD and use the functions that describe the geometry to perform a numerical analysis directly - the often tedious meshing procedure has been bypassed. Hughes et al. [1] were the first to present the method, and since this seminal paper, much research has been carried out in the context of the finite element method. But the natural extension of isogeometric analysis to the boundary element method (BEM) has been lacking, and it is the goal of this paper to propose a new isogeometric BEM which we term isoBEM. We find it is a natural fit with the isogeometric concept since both the NURBS approximation and BEM deal with quantities entirely on the boundary. An outline of isoBEM is given followed by application to an elastostatic problem. A comparison is made with the standard BEM with quadratic elements, and it seen that superior accuracies are achieved.

1 INTRODUCTION

In the majority of CAD packages, non-uniform rational B-splines (NURBS) are used to describe the geometry of a surface due to their ability to represent complex geometries that would otherwise be difficult using polynomial functions. To see why this is the case we can take the example of a quarter-circle and approximate it using both a NURBS and quadratic polynomial interpolation. Fig. 1 shows that we are able to represent the geometry *exactly* while the polynomial interpolation is only approximate in nature. From this we can start to understand the power of NURBS and why its use is widespread throughout CAD software. But to gain insight into the concept of isogeometric analysis [1] - where the same NURBS are used to approximate the unknown fields - the basis functions that comprise NURBS need some explanation.

2 NURBS BASIS FUNCTIONS

NURBS are a variant of B-splines, where it is possible to interpolate a line given the following: a knot vector, control points and degree of the basis. The geometry approximation is given by

$$\mathbf{C}(\xi) = \sum_{i=1}^n N_{i,p}(\xi) \mathbf{B}_i \quad (1)$$

where \mathbf{B}_i is a set of nodal coordinates known as 'control points' and $N_{i,p}(\xi)$ are the B-spline basis functions given by

$$N_{i,0}(\xi) = \begin{cases} 1 & \xi_i \leq \xi < \xi_{i+1} \\ 0 & \text{otherwise} \end{cases} \quad (2)$$

for $p = 0$ and

$$N_{i,p}(\xi) = \frac{\xi - \xi_i}{\xi_{i+p} - \xi_i} N_{i,p-1}(\xi) + \frac{\xi_{i+p+1} - \xi}{\xi_{i+p+1} - \xi_{i+1}} N_{i+1,p-1}(\xi) \quad (3)$$

for $p = 1, 2, \dots$

As an example, we can consider a B-spline approximation with the knot vector $\Xi = \{0 \ 0 \ 0 \ 1 \ 2 \ 3 \ 4 \ 4 \ 4\}$, degree $p = 2$ (quadratic) and $n = 6$ control points where the resulting B-spline approximation is plotted in Fig. 2(a) and the associated basis functions shown in Fig. 2(b). NURBS are a variant of B-splines in that they project the B-spline approximation using a set of weightings. This approximation is written as

$$\mathbf{C}(\xi) = \sum_{i=1}^n R_i^p(\xi) \mathbf{B}_i \quad (4)$$

where the NURBS basis functions are given by

$$R_i^p(\xi) = \frac{N_{i,p}(\xi) w_i}{\sum_{i=1}^n N_{i,p}(\xi) w_i} \quad (5)$$

and w_i are an appropriate set of n weightings. These weightings allow features such as cones and circles to be modelled *exactly*.

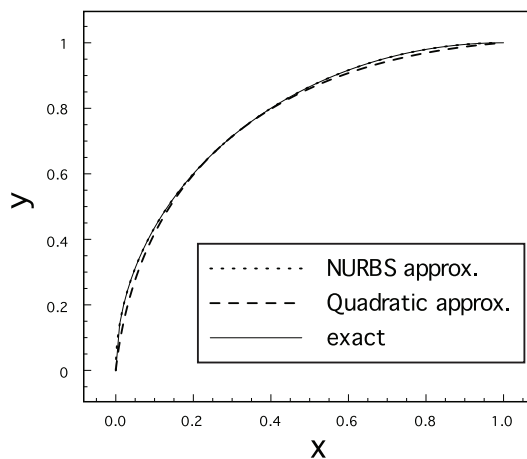
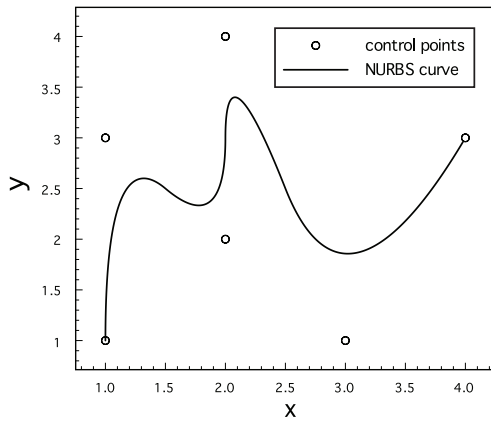
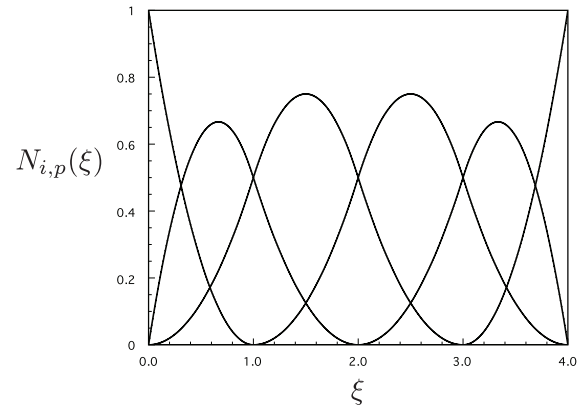


Figure 1: Comparison of NURBS and quadratic approximation of quarter-circle



(a) B-spline curve with associate control points



(b) B-spline basis functions for knot vector $\Xi = \{0 0 1 2 3 4 4 4\}$

Figure 2: B-spline approximation

3 ISOBEM

The isogeometric concept is based on the idea that not only can we approximate the geometry using Eq. (6), but we can also approximate the unknown fields using the same expression. In the Boundary Element Method, this allows the displacement and traction fields to be written as

$$\mathbf{u}(\xi) = \sum_{i=1}^n R_i^p(\xi) \mathbf{a}_i \quad \mathbf{t}(\xi) = \sum_{i=1}^n R_i^p(\xi) \mathbf{b}_i \quad (6)$$

where \mathbf{a}_i and \mathbf{b}_i represent nodal coefficients for displacements and tractions respectively. When these approximations are used, there are some important repercussions on a Boundary Element implementation:

- Control points do not necessarily lie on the boundary
- An algorithm for determining collocation points must be given
- Singular integration routines are required which can evaluate weakly and strongly singular integrals at any general boundary point
- Elements are defined as intervals between unique knot vector values. Numerical integration is performed over these portions of the boundary.

In the present study, we have used the Greville abscissae definition [2] to determine the position of collocation points. Each of the collocation points $\hat{\xi}_i$ is given as

$$\hat{\xi}_i = \frac{\xi_{i+1} + \xi_{i+2} + \cdots + \xi_{i+p}}{p} \quad (7)$$

We have also used the subtraction of singularity routine given by Guiggiani et al. [3] to determine the strongly singular integrals and the Telles' transformation [4] for weakly singular integrals.

4 RESULTS

To illustrate the isoBEM concept, the problem of a hole within an infinite plate subject to a traction at infinity was studied. Since an analytical solution is available for this problem exact errors can be determined. The problem can be modelled using symmetry as shown in Fig. 3(a) where an example mesh of three elements per line has also been shown. Note that the control points on the hole surface do not lie on the boundary. Exact tractions were applied along the top, left and hole surfaces with symmetric conditions on the right and bottom surfaces. Fig. 3(b) shows a comparison between the exaggerated displacement obtained with isoBEM and the exact solution. Excellent agreement is obtained.

In addition, a refinement study was performed in which knots were inserted to the knot vector resulting in a process equivalent to conventional h-refinement. The L_2 norm for displacements around the boundary was calculated for both a quadratic BEM refinement and isoBEM refinement. As can be seen in Fig. 4, the isoBEM shows superior accuracy over the standard quadratic BEM.

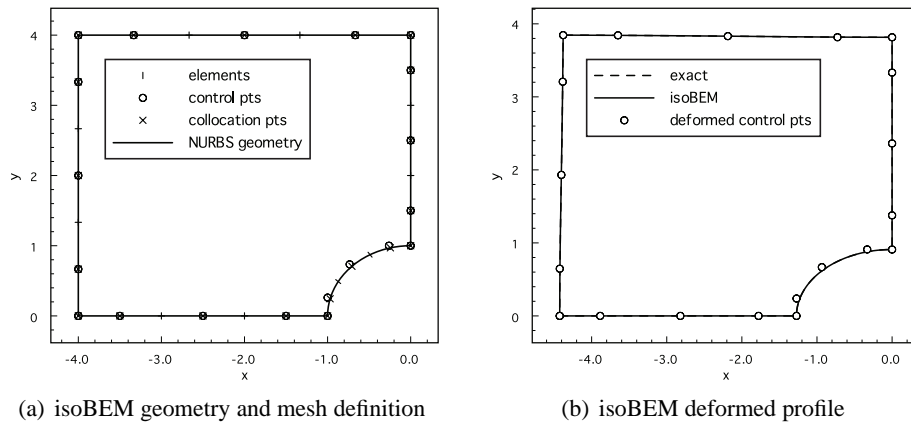


Figure 3: isoBEM analysis - problem of hole in an infinite plate

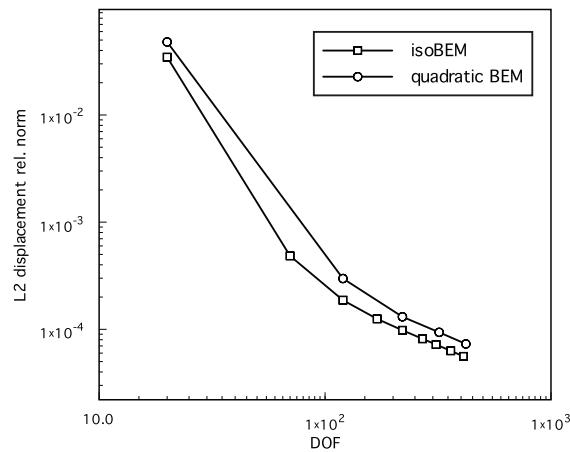


Figure 4: L_2 relative error comparison between quadratic BEM and isoBEM

5 CONCLUSION

This paper has outlined an isogeometric boundary element method for elastostatic problems that approximates both the displacement and traction fields using NURBS basis functions. It is found that the implementation of the method differs from that of a conventional BEM code, where 'elements' and the location of collocation points no longer correspond to conventional definitions. As a result, the numerical integration algorithm must account for these differences. It is seen that when the current method is applied to the problem of an infinite plate with a hole at the centre, higher accuracies are seen for an equivalent number of degrees of freedom compared to the conventional BEM with quadratic elements.

References

- [1] T.J.R. Hughes, J. Cottrell, and Y. Bazilevs, "Isogeometric analysis: CAD, finite elements, NURBS, exact geometry and mesh refinement," *Computer Methods in Applied Mechanics and Engineering*, vol. 194, pp. 4135–4195, Jan 2005.
- [2] R. Johnson, "Higher order B-spline collocation at the greville abscissae," *Applied Numerical Mathematics*, vol. 52, pp. 63–75, Jan 2005.
- [3] M. Guiggiani, G. Krishnasamy, T. Rudolphi and F.J. Rizzo, "A general algorithm for the numerical-solution of hypersingular boundary integral equations," *J Appl Mech – Trans ASME*, vol. 59, pp. 604–614, 1992.
- [4] J.C.F. Telles, "A self-adaptive coordinate transformation for efficient numerical evaluation of general boundary element integrals," *International Journal for Numerical Methods in Engineering*, vol. 24, pp. 953–973, 1987.

An Element-free Galerkin scaled boundary method

*Yiqian He^{1,2}, Haitian Yang¹ and Andrew J. Deeks²

¹Department of Engineering Mechanics, Dalian University of Technology, 116024, Dalian, P.R. China

²School of Engineering and Computing Sciences, Durham University, South Road, Durham, DH1 3LE, UK

*heyiqian@hotmail.com

Key Words: *scaled boundary method; Element-free Galerkin method; high accuracy; smooth stress solution.*

ABSTRACT

This paper presents an Element-free Galerkin (EFG) scaled boundary method. The EFG approach is employed to build approximation in scaled boundary weakened differential equations in circumferential direction. The moving least square (MLS) approximation is used to generate shape function. Numerical tests are shown illustrating the new method has higher accurate and better convergence compared with scaled boundary FEM and MLPG scaled boundary method, and smooth stress field can be obtained in proposed model.

1 INTRODUCTION

The scaled boundary finite element method is a semi-analytical method developed relatively recently by Wolf and Song [1]. The method was shown to be more efficient than the finite element method for problems involving unbounded domains and for problems involving stress singularities or discontinuities [2]. This method works by weakening the governing differential equations in circumferential direction s through the introduction of shape functions, then solving the weakened equations analytically in the radial direction ξ .

This paper investigated the possibility of using the Element-free Galerkin (EFG) approach presented by Belytschko et al [3] to solve the weakened differential equations in circumferential direction in scaled boundary method. EFG method has been proved to have the advantages that high accuracy, rapid rates of convergence and smooth stress field can be obtained [3]. This new EFG scaled boundary method is examined in four benchmark problems. The performance of the new method is compared with the scaled boundary FEM and MLPG scaled boundary method developed by Deeks and Augarde [4].

2 THE SCALED BOUNDARY METHOD

The scaled boundary method introduces such a coordinate system by scaling the domain boundary relative to a scaling centre (x_0, y_0) selected within the domain. The scaled boundary and Cartesian coordinate systems are related by the scaling equations

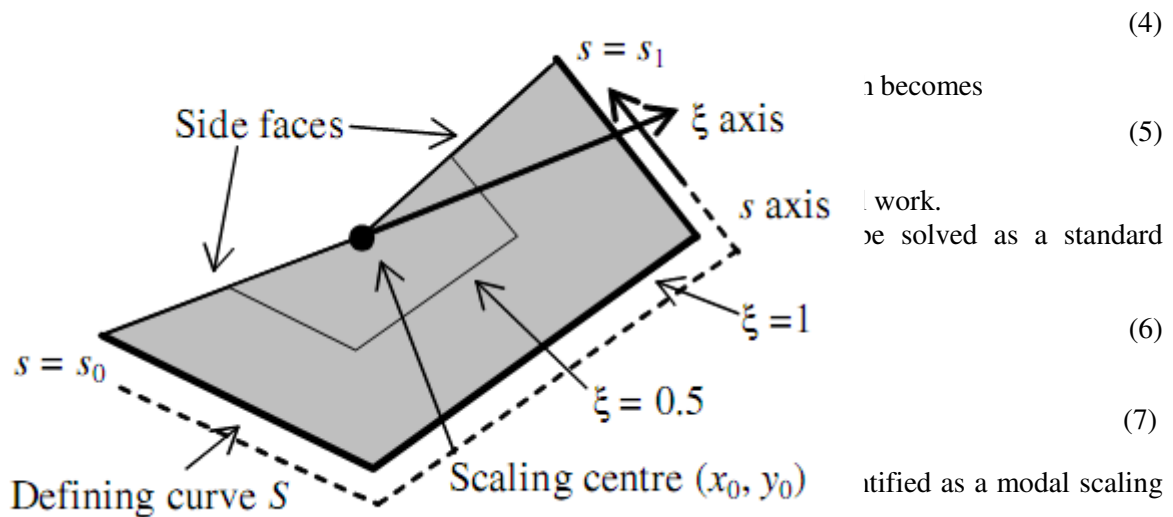
$$x = x_0 + \xi x_s(s) \quad (1)$$

$$y = y_0 + \xi y_s(s) \quad (2)$$

An approximate solution is sought in the form

$$\{u_h(\xi, s)\} = \sum_{i=1}^n [N_i(s)] u_{hi}(\xi) = [N(s)] \{u_h(\xi)\} \quad (3)$$

Mapping the linear operator to the scaled boundary coordinate system, the stresses are obtained in the form



3 AN ELEMENT-FREE GALERKIN APPROACH

This paper employs an Element-free Galerkin (EFG) approach developed by T. Belytschko et al [3] in the circumferential direction. In this method the Galerkin approach is used, and both trial and test functions are built by moving least square (MLS) approximation.

Following Belytschko [3], the MLS approximation yields

$$u_x(s) = \{\phi(s)\}^T \{\hat{u}_x\} \quad (8)$$

where $\phi(s)$ is the MLS shape function, $\{\hat{u}_x\}$ is the nodal ‘fictitious’ value vector.

The actual nodal values can be related to the fictitious nodal values by

$$\{u_x\} = \begin{bmatrix} \phi_1(S_1) & \dots & \phi_n(S_1) \\ \dots & \dots & \dots \\ \phi_1(S_n) & \dots & \phi_n(S_n) \end{bmatrix} \{\hat{u}_x\} = [T] \{\hat{u}_x\} \quad (9)$$

Substituting Eq. (9) to Eq. (8),

$$u_x(s) = \{\phi(s)\}^T [T]^{-1} \{\hat{u}_x\} = \{\varphi(s)\}^T \{\hat{u}_x\} \quad (10)$$

where $\varphi(s)$ can be identified as a shape function associated with a unit value at node i and zero at all other nodes in the conventional manner. That makes the essential boundary condition can be directly imposed [4].

Thus the shape function matrix for the scaled boundary method then becomes

$$[N(s)] = \begin{bmatrix} \varphi_1(s) & 0 & \dots & \varphi_n(s) & 0 \\ 0 & \varphi_1(s) & \dots & 0 & \varphi_n(s) \end{bmatrix} \quad (11)$$

4 PERFORMANCE OF THE METHOD

4.1 Example 1 – An infinite plate with a hole

The geometry of the first example is shown in Fig.1. The centre of the hole is used as the scaling centre. The Fig.2 (a-b) show the error η of energy norm defined in [4] comparing EFG-SB with FEM-SB and MLPG-SB developed by Deeks and Augarde in [4]. It is shown that EFG-SB is more accurate than FEM-SB and it is more accurate than MLPG-SB as the same basis is employed.

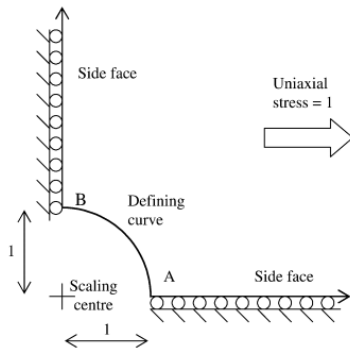


Fig.1 Quarter infinite plate with hole

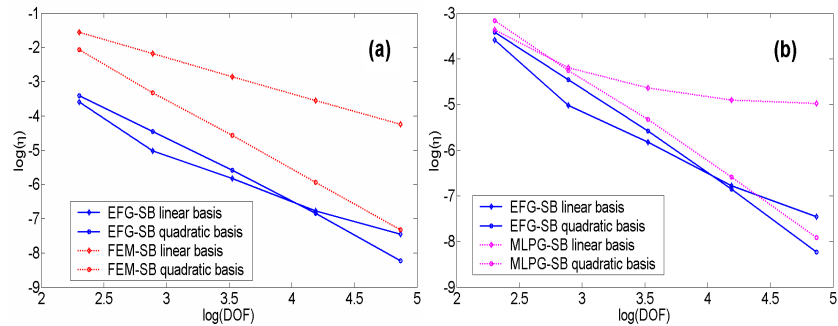


Fig.2 Convergence of EFG approach and conventional approach

4.2 Example 2 - A flexible strip footing of infinite extent

The second example is shown in Fig.3 and only one-half of the plane strain problem is modelled due to symmetry. The comparison of raw stress fields σ_y is made in Fig.4, in which the ability of obtaining smoother stress field in EFG scaled boundary model is shown even only linear basis is used.

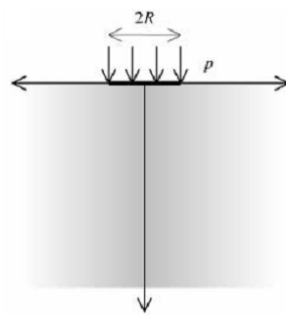


Fig.3 Strip footing model

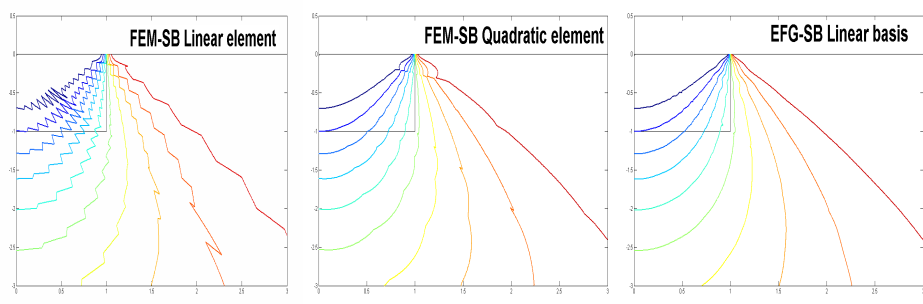


Fig.4 Contour of raw stress

4.3 Example 3 - An infinite plate with a through crack

The third example is shown in Fig.5. As the scaling centre located at the crack tip, the scaled boundary method generates an approximation to the Williams expansion [5]. That makes the determination of stress intensity factors straightforward. Tab.1 shows results of mode I stress intensity factor K_I comparing with exact solution [5]. The EFG-SB model results the value of 1.7724 and 1.7722 with linear and quadratic basis, the MLPG-SB model results 1.7722 using quadratic basis, these three results are very close to the exact value of 1.7725.

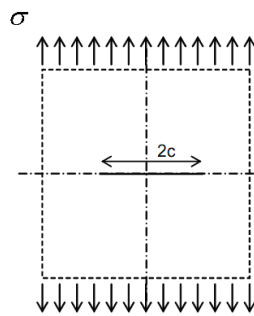


Fig.5 Through crack problem

Tab.1 The values of intensity factor

| Nodes number | EFG linear | EFG quadra. | MLPG linear | MLPG quadra. | FEM linear | FEM quadra. | Exact |
|--------------|------------|-------------|-------------|--------------|------------|-------------|--------|
| 17 | 1.7663 | 1.7599 | 1.7573 | 1.7662 | 1.7843 | 1.7364 | 1.7725 |
| 33 | 1.7723 | 1.7709 | 1.763 | 1.7709 | 1.7755 | 1.7607 | |
| 65 | 1.7724 | 1.7722 | 1.7652 | 1.7722 | 1.7774 | 1.7693 | |

4.4 Example 4 - A single edge cracked plate

The fourth example is illustrated in Fig.6. Fig.7 shows the computed coefficients a_1 and a_3 in Williams expansion in comparison with the EFG-SB with FEM-SB and MLPG-SB, also with reference solutions in [6] and [7]. Better convergence of EFG scaled boundary can be observed.

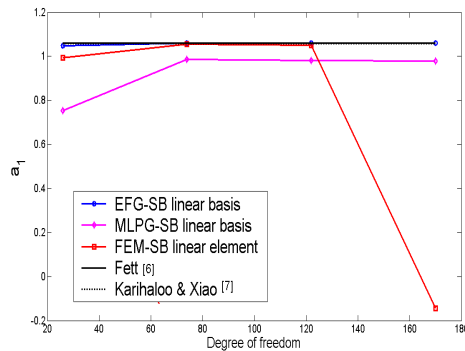
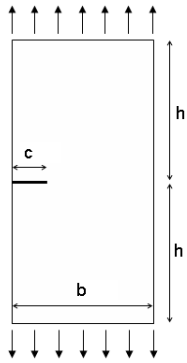


Fig.6 Edge crack model

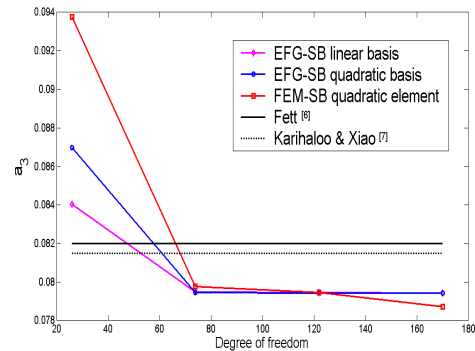


Fig.7 Convergence of EFG approach and conventional approach

5 CONCLUSIONS

An Element-free Galerkin (EFG) scaled boundary method is developed in this paper. EFG approach is used in the weakened differential equations in circumferential direction in the scaled boundary method. Moving least square (MLS) approximation is employed to build shape function. In numerical verifications, this new model is shown with high accuracy, rapid convergence compared with scaled boundary FEM and MLPG scaled boundary, and smooth stress field can be achieved with no post-processing.

References

- [1] J.P. Wolf and C. Song. The scaled boundary finite-element method – a fundamental solution-less boundary-element method. *Computer Methods in Applied Mechanics and Engineering*, 190, 5551–5568, 2001.
- [2] A. J. Deeks and J. P. Wolf. A virtual work derivation of the scaled boundary finite-element method for elastostatics. *Computational Mechanics*, 28, 489–504, 2002.
- [3] T. Belytschko, Y.Y. Lu and L. Gu. Element-free Galerkin methods. *International Journal for Numerical Methods in Engineering*, 37, 229–256, 1994.
- [4] A.J. Deeks and C.E. Augarde. A meshless local Petrov-Galerkin scaled boundary method. *Computational Mechanics*, 36, 159–170, 2005.
- [5] S.R. Chidzey and A.J. Deeks. Determination of coefficients of crack tip asymptotic fields using the scaled boundary finite element method. *Engineering Fracture Mechanics*, 72, 2019–2036, 2005.
- [6] T. Fett. A Green's function for T-stresses in edge-cracked rectangular plate. *Engineering Fracture Mechanics*, 57, 365–373, 1997.
- [7] B.L. Karihaloo and Q.Z. Xiao. Accurate determination of the coefficients of elastic crack tip asymptotic field by a hybrid crack element with p-adaptivity. *Engineering Fracture Mechanics*, 68, 1609–1630, 2001.